Biomechanical study of intervertebral disc degeneration

Ramiro Arturo González Gutiérrez

Doctoral Thesis

Mechanical Engineering Doctoral Program

Supervised by Dr. Damien Lacroix

Departament d' Enginyeria Mecànica

Universitat Politècnica de Catalunya

2012

Biomechanical study of intervertebral disc degeneration

Abstract

It is widely accepted that aging and degeneration are factors that affect the biomechanics of the intervertebral disc. Most important for a disc is to maintain a broad range of flexibility and shock absorption against daily movement and spinal load, as these define normal disc functionality.

Biomechanical characterization of discs is achieved by conducting mechanical testing to spinal motion segments, with or without the posterior elements. The testing is usually done on a servo-hydraulic universal tester using axial, shearing, bending and torsion loads, statically or dynamically, with load magnitudes corresponding to the physiological range. However, traditional testing to motion segments gives mean values of the mechanical properties of the disc treating it as a unit, without giving a view of the loading and deformation states of the disc components: nucleus pulposus, annulus fibrosus and endplate. Thus, the internal state of the stress and strains of the intervertebral disc can not be obtained in this way, and can only be predicted by numerical methods, one of which is the finite element method. The objective of this thesis was, to study the biomechanical response of degenerated intervertebral discs to load conditions in compression, bending and torsion, by using mechanical testing and a finite element model of disc degeneration, based on magnetic resonance imaging (MRI).

Therefore, ten lumbar discs from cadavers corresponding to spinal levels L2-L3 and L4-L5 with mild to severe degeneration based on inspection with magnetic resonance imaging were used. Intervertebral osteochondrosis and spondylosis deformans were found in almost all the discs but especially in those from the L4-L5 level, reaffirming the clinical experience that lower lumbar discs are more susceptible to severe degeneration.

Next, all the discs were tested to static and dynamic conditions and the results gained corresponded to the disc stiffness (to compression, bending, and torsion load), the stress relaxation response, and the disc dynamic response. Of these, the stiffness response was used to validate the finite element model of disc degeneration.

The biomechanical testing included loads of 1000 N compression, a 5 N-m moments in bending and in torsion, and a dynamic load in compression of 500 N at the frequencies between 0.2 Hz and 5 Hz. The results from the testing suggest that discs with advanced degeneration over discs with mild degeneration, are less rigid in compression, are less stiff under bending and torsion and show less bulge in all load modes, and reduce their viscoelastic and damping properties. This study shows that degeneration has an impact on the disc biomechanical properties which can jeopardize disc functionality.

Development of one finite element model of disc degeneration started by choosing a MRI of a degenerated disc that corresponds to spinal level L2-L3. Segmentation of bone and disc materials based on pixel brightness and radiology fundamentals were done, and a finite element mesh was created to account for the disc irregular shape. The disc materials were modeled as hyperelastic using the Mooney-Rivlin solid model, while the bone materials were modeled as elastic orthotropic. Initial values of the material properties were assigned according to literature values, and the final adjustment of the Mooney coefficients for the annulus fibrosus gave values of $C_1 = 0.10$, and $C_2 = 0.025$ (E = 750 KPa) which match the stiffness for a mild degeneration tissue.

The validation of the disc degeneration model was performed, and included a study of the distributions of stress and strain under loads of compression, bending and torsion. Of these, the compression load was simulated first using a step displacement of 1.43 mm axially, and a study of the disc bulge was also performed. Similar strain distributions for the annulus fibrosus and nucleus pulposus were found, with compressive and tensile strain maximum values of 40% and 10% respectively. The stress distributions showed that the annulus develops compressive and tensile stresses of 2 MPa and 0.25 MPa respectively, whereas the nucleus developed only compressive stresses with a maximum of 1 MPa. The disc bulge was found to be symmetrical, but four times larger than the testing values. Next, the flexion, extension and lateral bending loads were simulated using an eccentric vertical step displacement of 5.76 mm applied anteriorly, 5.80 mm posteriorly and 4.54 mm applied laterally, respectively. A study was performed of the compressive and tensile strains, and the stresses developed for each bending load. Similar strain distributions were also found for the annulus and nucleus, with compressive and tensile strain maximum values of 20% and 5% respectively. The stress distributions showed that the maximum principal stresses were of equal value being ± 0.50 MPa for the annulus, and ± 0.20 MPa for the nucleus. Finally, the axial rotation or torsion was simulated using pairs of tangential displacement of 9.84 mm of eccentricity, and a study of the strains and stresses developed was performed. Similar strain distributions were found for the annulus and nucleus, with maximum shear strain values of 40% and 30% respectively. The stress distributions showed that the maximum shear developed in the annulus was 0.40 MPa while the maximum shear in the nucleus only reached 0.20 MPa. The study showed the relevance of soft tissue deformation mostly noticed in advanced degeneration. In contrast, the higher stresses in the bone over those of the intervertebral disc showed the relevance of bone predisposition to fracture.

Such kind of studies, should contribute to the understanding of the biomechanical response of degenerated discs.

Resumen

Es ampliamente aceptado que la edad y la degeneración son factores que afectan la respuesta biomecánica del disco intervertebral. Lo más importante para un disco es mantener una amplia gama de flexibilidad y de absorción al choque contra el movimiento y carga diaria de la columna vertebral, ya que esto define el funcionamiento normal del disco.

La caracterización biomecánica de discos se logra mediante la realización de ensayos mecánicos a segmentos vertebrales funcionales, con o sin los elementos posteriores. Las pruebas mecánicas se realizan en una máquina universal servo-hidráulica aplicando carga axial, transversal, flexión y torsión, de forma estática ó dinámica, con magnitudes de carga correspondientes al intervalo fisiológico. Sin embargo, los ensayos tradicionales a segmentos lumbares proporcionan solo valores medios de las propiedades mecánicas del disco tratándolo como una unidad, sin dar una visión de los estados de carga y deformación de los componentes del disco: núcleo pulposo, anillo fibroso, y la placa terminal de cartílago hialino. Por lo tanto, el estado interno de tensiones y deformaciones del disco intervertebral no puede ser obtenido de esta manera, y sólo se puede predecir por métodos numéricos, uno de los cuales es el método de elementos finitos. El objetivo de esta tesis fue, estudiar la respuesta biomecánica de discos intervertebrales degenerados bajo condiciones de carga en compresión, flexión y torsión, mediante el uso de ensayos mecánicos y de un modelo de elementos finitos de la degeneración de disco, basado en imágenes de resonancia magnética (MRI).

Por lo tanto, se usaron diez discos intervertebrales de cadáveres y correspondientes a los niveles lumbares L2-L3 y L4-L5, con grados leve a severo de degeneración basada en inspección a imágenes de resonancia magnética. Se encontró que la mayoría de los discos presentaron osteocondrosis intervertebral y espondilosis deformante, pero en especial los discos del nivel L4-L5, reafirmando la experiencia clínica sobre la degeneración severa en discos de la zona lumbar baja.

A continuación todos los discos fueron ensayados a condiciones de carga estática y dinámica y los resultados obtenidos correspondieron a la rigidez (a compresión, flexión y torsión), a la relajación de tensiones, y al comportamiento dinámico del disco. De estos, la respuesta a la rigidez se utilizó para validar el modelo de elementos finitos de la degeneración del disco.

Las pruebas biomecánicas incluyeron cargas de compresión de 1000 N, momentos de 5 Nm a flexión y a torsión, y una compresión dinámica de 500 N a frecuencias entre 0.2 Hz y 5 Hz. Los resultados de las pruebas sugieren que los discos con degeneración avanzada sobre aquellos con degeneración leve, son menos rígidos en compresión, son menos flexibles en flexión y torsión, presentan menor protuberancia en todos los modos de carga, y ven reducida sus propiedades viscoelásticas y de amortiguamiento. Este estudio muestra que la degeneración tiene un impacto en las propiedades biomecánicas del disco, poniendo en riesgo su funcionalidad.

El desarrollo de un modelo de elementos finitos de la degeneración de disco comenzó eligiendo una resonancia magnética de un disco degenerado, el cual correspondió al nivel lumbar L2-L3. La segmentación de los tejidos óseos (vértebras) y del disco intervertebral se llevó a cabo basados en la intensidad de brillo del píxel y en fundamentos de radiología, y se creó una malla de elementos finitos correspondiente a la forma irregular del disco. Los materiales del disco se modelaron como hiperelásticos utilizando el modelo de sólido de Mooney-Rivlin, mientras que los tejidos óseos se modelaron como materiales elásticos ortotrópicos. Los valores iniciales de las propiedades de los materiales fueron asignados de acuerdo a los valores de la literatura, y el ajuste final de los coeficientes de Mooney para el anillo fibroso dio magnitudes de $C_1 = 0.10$ y $C_2 = 0.025$ (E = 750 KPa), que coincide con una rigidez para un tejido con degeneración leve.

La validación del modelo de degeneración de disco se llevó a cabo, e incluyó un estudio de las distribuciones de esfuerzo y deformación bajo cargas de compresión, flexión y torsión. De estos, la carga de compresión se simuló primero usando un desplazamiento axial de 1.43 mm, e incluyó un estudio de la protuberancia de disco. Se encontraron similitudes en las distribuciones de deformación del anillo fibroso y el núcleo pulposo, con magnitudes máximas de 40% en compresión y de 10% en tracción. Las distribuciones de esfuerzos mostraron que en el anillo se desarrollan tensiones de compresión y de tracción de 2 MPa y 0.25 MPa respectivamente, mientras que en el núcleo sólo se desarrollan tensiones de compresión, con un máximo de 1 MPa. La protuberancia de disco resultó ser simétrica, pero cuatro veces mayor que las magnitudes experimentales. A continuación, las cargas de flexión, extensión y doblez lateral se simularon aplicando un desplazamiento excéntrico vertical de 5.76 mm anteriormente, 5.80 mm posteriormente y 4.54 mm lateralmente, respectivamente. Se realizó un estudio de las deformaciones de compresión y tracción, y de los esfuerzos desarrollados por cada una de las cargas. Se encontraron similitudes en las distribuciones de deformación del anillo y del núcleo, con magnitudes máximas de 20% en compresión y de 5% en tracción. Las distribuciones de tensión mostraron que los máximos esfuerzos principales eran de igual valor siendo ± 0.50 MPa para el anillo, y ± 0.20 MPa para el núcleo.

Finalmente, la rotación axial o torsión se simuló utilizando pares de desplazamiento tangencial de 9,84 mm de excentricidad, y se llevo a cabo un estudio de las deformaciones y tensiones desarrolladas. Se encontraron similitudes en las distribuciones de deformación del anillo y del núcleo, con magnitudes máximas de deformación de corte de 40% y 30% respectivamente. Las distribuciones de esfuerzo mostraron que el cortante máximo desarrollado en el anillo fue de 0.40 MPa, mientras que el cortante máximo en el núcleo sólo alcanzó 0.20 MPa. El estudio mostró la importancia de las deformaciones de los tejidos blandos, principalmente notados en la degeneración avanzada. Por el contrario, las tensiones mayores observadas en los cuerpos vertebrales sobre las que ocurrieron en los discos intervertebrales mostraron la importancia de la predisposición a las fracturas óseas.

Este tipo de estudio debe contribuir a la comprensión de la respuesta biomecánica de los discos degenerados.

Publications and Presentations Resulting from this Study

Journal Publications

Ramiro González, Manel Llusá, Jaume Pomés, Josep Planell, and Damien Lacroix (2008). “Biomechanical and MRI study of degenerated lumbar intervertebral disc”. Journal of Biomechanics; Vol. 41; Supplement 1: S256.

Congress Oral Presentations

Ramiro González, Francesc García, Francesc Roure, Manel Llusá, Jaume Pomés, Josep Planell and Damien Lacroix (2007). “Degeneration of Human Lumbar Intervertebral Disc: Mechanical Testing and MRI Study”. European School of Materials Science and Engineering Fourth Research Conference. Barcelona, Spain, 7-8 June 2007, p.213-222.

Ramiro González, Francesc García, Francesc Roure, Manel Llusá, Jaume Pomés, Josep Planell and Damien Lacroix (2007). “Biomechanical and MRI study of degenerational lumbar intervertebral disc”. 21st European Conference on Biomaterials. Brighton, England, 9-13 September 2007.

Ramiro González, Manel Llusá, Jaume Pomés, Josep Planell, and Damien Lacroix (2008). “Biomechanical and MRI study of degenerated lumbar intervertebral disc”. 16th Congress of the European Society of Biomechanics. Lucerne, Switzerland, 6-9 July 2008.

Acknowledgements

Dear professors, colleagues, and friends, I will like to express my gratitude for helping me in so many ways to complete another phase in my life. When I started this project I knew little about the whereabouts of most things, much less the people behind them. Barcelona was my home for more than four years, and some of you were the closest thing to a family for me. Which reminds me of a phrase that someone said in the past, “You’re not alone, and thus you’re only as good as you are in group” and in that sense, all of you were part of this.

First, I am grateful for having the opportunity to work with Dr. Damian Lacroix, who has made his support available in a number of ways during all this time. His guidance and leadership has not only made this project possible, but has also encouraged me to pursue my own goals. I wish him the very best in his new role in life as a parent, congratulations!

I would like to thank Professors Dr. Josep Anton Planell, director of the IBEC, Dr. Maria Pau Ginebra, director of the biomaterials, biomechanics and tissue engineering group (BIBITE) at the UPC and Dr. Xavier Gil Mur for their academic support, leadership and giving some new insights of what an academic environment should be. I would also like to thank Dr. Ana Barjau, professor of the mechanical engineering department for being my tutor, Dr. Ludovic Humbert and Dr. Roberto De Santis for their reviews and comments of my research.

This thesis would not have been possible without the help of Dr. Manel Llusá Perez M.D., Faculty of Medicine, University of Barcelona, and Dr. Jaume Pomés Talló M.D., Radiodiagnostic Department, Hospital Clinic of Barcelona, for their expertise in disc degeneration, and MRI, and providing the ex-vivo material for this study.

A special thanks to Professor Francesc Roure and Francesc García Ravella, Department of Strength of Materials and Structural Engineering and Pablo Sevilla for their support in calibrating sensors and introducing external signals to the Bionix system. Also, I will like to thank Rafael Bermúdez, José Manuel Guerrero, Lolo Bermúdez and Don Antonio Llach of the laboratori Comú d'Enginyeria Mecànica for their patience and help with brainstorm during the instrumentation and mechanical testing phase.

An academic department is not without an administrative staff, and in this regard, I would like to thank the CMEM and mechanical department administration staff with special thanks to Imma and Mirabel for keeping me up to date, and also for those moments that we shared “while we were in Japan” in the office.

I will like to express my thanks to the former and current group members of the IBEC and BIBITE: Conrado, Melba, Alex, Carolina, Sergio, Tania, Oscar, *Teresa*, Montse CH, Montse E, Johan, Pablo, Aleix, Lluis, Txell, Pedro, Emiliano, Miguel M, Román, Mijail, Gemma, Marta G, Marta M, Marta P, Dencho, and my fellow countrymen: Ana, Edgar and Lucia for their friendship.

Colleagues and friends of the biomechanics and mechanobiology group. It’s been a while since the last time we met. As you know, I am continuing my profession as an undergraduate teacher in my homeland, a task that never ends, and always gives new teaching. Here I am concluding this project, and proud to say that overall it was worthwhile. Thank you Jérôme, Sebas, Clara, Andrea, Andy, Martin, Oriol, and Jean-Louis for your time, patience, support and friendship, I miss the good times we spent together. To all of you I wish the best!

For helping me get into shape, and focus I would like to express my gratitude to Rafa, from Ramadasa and Karla, who taught me to walk again. Thank you to my roommates Maisa and María for making me feel like home not only in Barcelona, but also in Algeciras, where I am indebted to Pepe and Isabel for their hospitality.

It is a pleasure once more to thank my family for their long distance support at and making me fell very close on the other end of the telephone. To my father and mother for who taught me everything; Omar, Erubey and María Guadalupe for making me feel young again and welcomed me back home, I love you all!

Thank you to my colleagues and co-workers in Tijuana for supporting me all this time. I would like to give my gratitude to the recent directors of my Alma Mater, Instituto Tecnológico de Tijuana (ITT), Rafael Quevedo, Enriqueta González and José Guerrero for their support. I also would like to give a special thanks to Raymundo Aguas, Hernán Castro, Federico Salas, Rafael Ramirez and Vicente Reyes for being there when it needed. Finally, I would also like to acknowledge the Council of Science and Technology of México (CONACYT) for the scholarship and support offered.

Contents

List of Figures

List of Tables

Chapter 1

The intervertebral disc and disc degeneration

Chapter 1

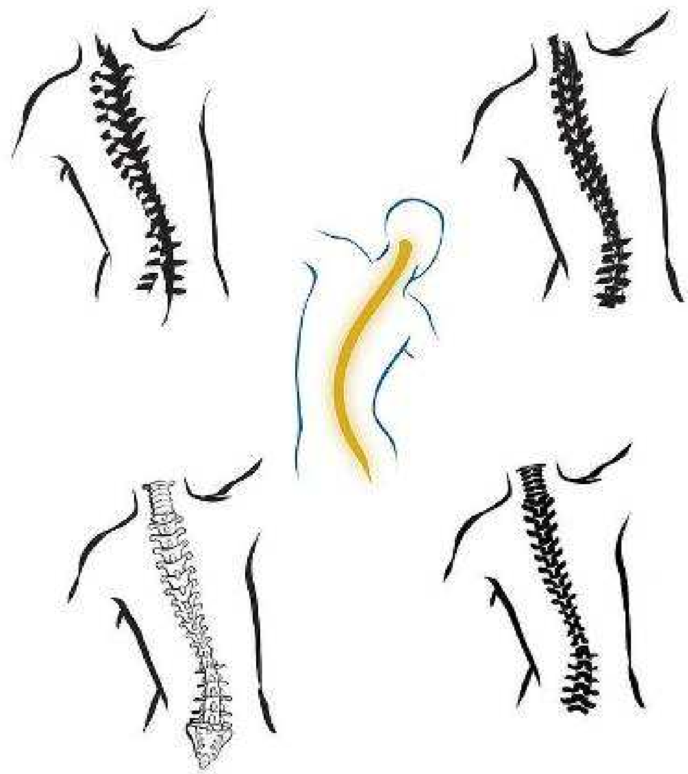

The Intervertebral disc and disc degeneration

The objective of this chapter is to describe the structure, function and pathology of the human lumbar intervertebral disc. The material is organized starting with a description of the spine anatomy, with emphasis in the lumbar region. The study of the intervertebral disc starts with its development and growth, followed by an introduction to the initial signs of disc degeneration, such as vacuum formation and continues to severe cases such as the collapse of disc space. Impact of disc degeneration on material properties and normal disc functions are cover in the section of structure and pathology of the nucleus pulposus and annulus fibrosus. The diagnosis of intervertebral osteochondrosis and spondylosis deformans using MRI are presented and a grading scale for evaluation and scoring the gross anatomy of discs is included. Finally, we present the state of the art in biomechanical studies of discs, using experimental protocols and numerical methods.

A,	Disc cross section	*LVW*,	Lower vertebra width
AF,	Annulus fibrosus	*MRI*,	Magnetic resonance imaging
C1-C7,	Cervical spine	*NP*,	Nucles pulposus
CEP,	Cartilage endplate	*PDH*,	Pedicle height
CS,	Chondroitin	*PDW*,	Pedicle width
CT,	Computer tomography	*SCD*,	Spinal canal depth
DDD,	Disc degeneration disease	*SCW*,	Spinal canal width
GAG,	Sulphated glycosaminoglycan	*SD*,	Spondylosis deformans
HA,	Hyaluronic acid	*T1-T12*,	Thoracic spine
HDa,	Disc height at anterior site (mm)	*TRL*,	Longitude of transversal process
HDp,	Disc height at posterior site (mm)	*UVD*,	Upper vertebra depth
IO,	Intervertebral osteochondrosis	*UVW*,	Upper vertebra width
KS,	Keratan sulphate	*VB*,	Vertebral body
L1-L5,	Lumbar spine	*VBHa*,	Vertebra height at anterior site
LBP,	Low back pain	*VBHp*,	Vertebra height at posterior site
LVD,	Lower vertebra depth		

I. The human spine

a. Spine Anatomy

The human vertebral column is composed of intervertebral discs and vertebrae bone arranged in a sandwich form throughout 4 anatomical regions: cervical, thoracic, lumbar and pelvic, see Figure 1.1.

Located below the skull along the neck is the cervical region which consists of 7 vertebras, labeled C1 to C7. The purpose of the cervical spine is to contain and protect the spinal cord, support the skull, and enable diverse head movement (e.g. rotate side to side, bend forward and backward). Additionally a complex system of ligaments, tendons and muscles (flexors, extensors and rotators) helps to support and stabilize the cervical spine. Ligaments work to prevent excessive movement that could result in a serious injury to the spinal cord, while muscles also help to provide spinal balance and stability, and enable movement.

The thoracic spine is the longest portion of the spine and is located in the chest area containing 12 vertebras, numbered T1 to T12. The ribs connect to the thoracic spine forming the thoracic cage that protects vital organs (heart and lungs). Thus, the flexibility of the thoracic spine is limited by the firmly joined between the sternum or breastbone and the ribs.

In the lower back is the lumbar spine which consists of 5 vertebrae, labeled L1 to L5 and four large intervertebral discs. This area of the spine is the source of much body motion and supports most of the body weight. Finally, the sacrum is a large triangle bone at the base of the spine and at the upper and back part of the pelvic cavity, where is inserted like a wedge between the two hip bones. Its upper part connects with the last lumbar vertebrae, and the bottom part with the coccyx (tailbone), see Figure 1.1b.

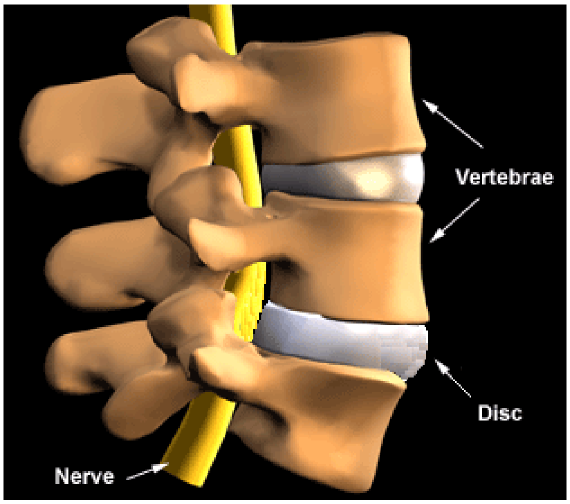

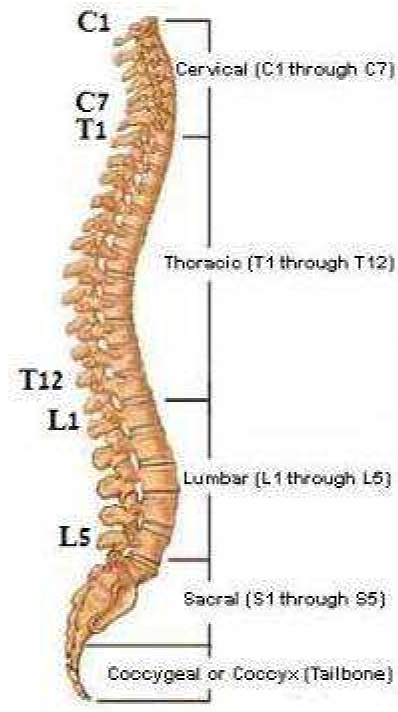

(a) (b)

Figure 1.1. (a) Arrangement of vertebrae-disc-vertebrae. (b) Anatomical regions of the vertebral column. Modification from SpineUniverse^{R}.

Viewed laterally the vertebral column exhibits several curves, each corresponding to one of the four spine regions previously mentioned.

Beginning at the apex of the odontoid process of the second vertebra (the axis) and ending in the middle of the second thoracic vertebra is the cervical curve, which convex forward and attaches to the thoracic curve, concaves forward, and ends at the middle of the twelfth thoracic vertebra. The thoracic most prominent point behind corresponds to the spinous process of the seventh thoracic vertebra. The lumbar curve, convex anteriorly, begins at the middle of the last thoracic vertebra and ends at the start of the sacrum. The convexity of the lower three vertebrae is much greater than that of the upper two. The pelvic curve begins at the sacrovertebral articulation, and ends at the point of the coccyx; its concavity is directed downward and forward, see Figure 1.1.

The development of the spine curvature starts during the fetal life and is characterized by a C-shaped form (up to six weeks). The thoracic and pelvic curves are alone present during this period and are called primarily curves. After birth, when the child achieved to hold up his head (at three or four months) and to sit upright (at nine months), the cervical curve is developed. Finally, the lumbar curve starts to develop when the child begins to walk (after twelve or eighteen months), see Figure 1.2.

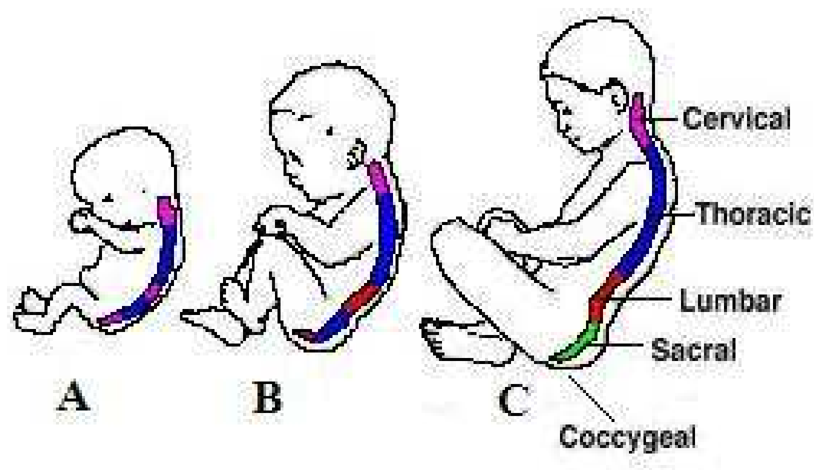

Figure 1.2. Lateral view of the developed spine curvature from: (A) a fetus, (B) a one year old infant and (C) a six year old boy. Modification from"Fundamentals of Anatomy & Physiology". Frederic H. Martini. Prentice Hall International, Inc. 1998.

Each vertebra consist of three elements: (1) a vertebral body, (2) the posterior elements including a spinous, a transversal, an articular process, lamina, pedicles and (3) the vertebral foramen (hole), see Figure 1.3.

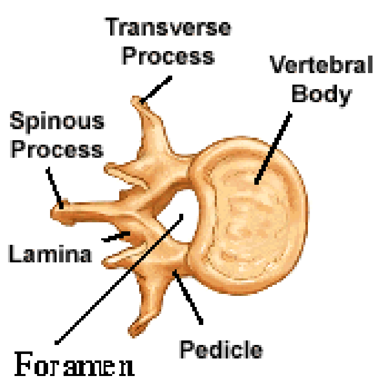

(a)

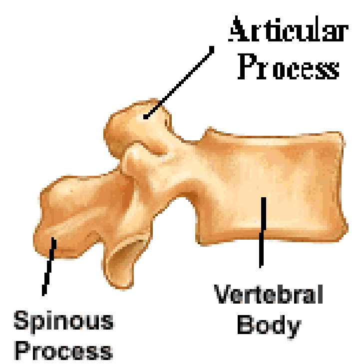

(b)

Figure 1.3. The anatomy of a vertebra, (a) axial view and (b) lateral view. Modification from SpineUniverse^{R}.

Because of its location in the lower back the lumbar spine bears most weight. The five intervertebral discs and vertebrae with the lumbar spinous process are more massive than the cervical and thoracic counterparts. These differences are illustrated in Figure 1.4.

It can be seen that lumbar vertebrae have massive bodies and cervical vertebrae have bigger foramen. In the next section, a description of each vertebra part for the lumbar spine will be given. Our presentation of the spine will now shift to the lumbar section in which are located the intervertebral discs L1 to L5.

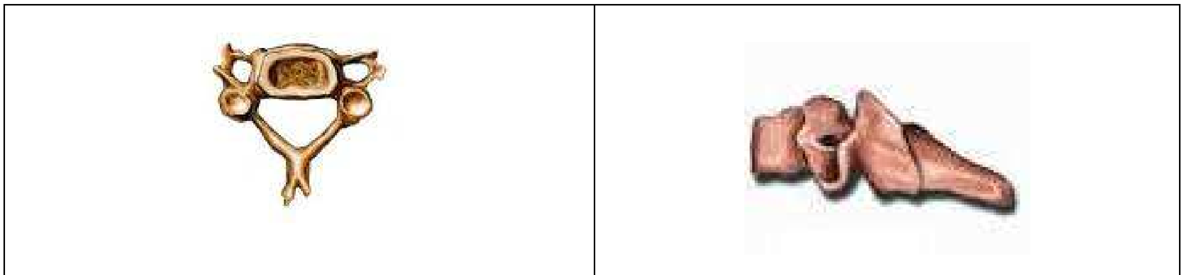

(a) Cervical

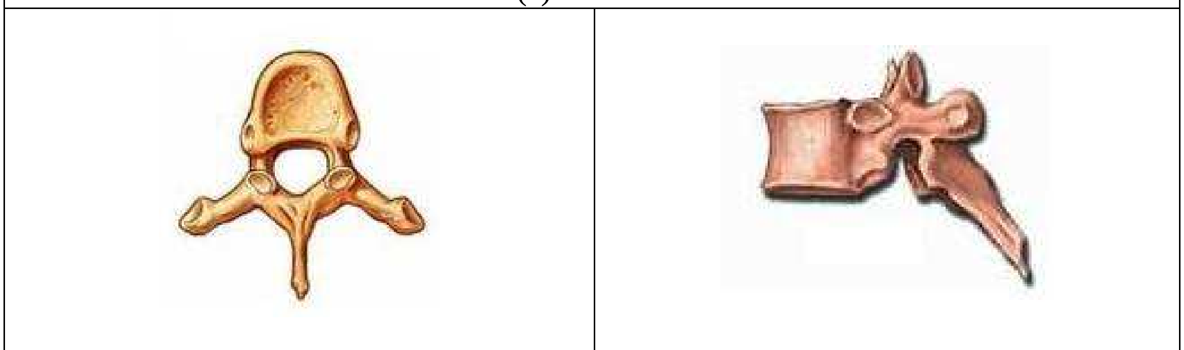

(b) Thoracic

(c) Lumbar

Figure 1.4. Anatomy of the vertebrae from (a) the cervical region, (b) the thoracic region and (c) the lumbar region. Modification from SpineUniverse^{R}.

b. The lumbar spine

Normally, the lumbar spine has five vertebrae which are labeled L1 to L5 corresponding to the first and fifth level respectively, see Figure 1.5. However, some differences arise in individuals showing only four vertebras, while other individuals show six. Lumbar disorders that normally affect L5 level will affect L4 or L6 in these individuals.

The vertebral body is the part of a vertebra that transfers weight along the axis of the vertebral column. The bodies of adjacent vertebras are interconnected by ligaments but are separated by patches of fibrocartilage, called the intervertebral discs. Ligaments connect bone to bone, whereas tendons connect muscle to bone. In the spine, tendons connect muscles to the vertebrae, see Figure 1.6. The ligaments and tendons help to stabilize the spine and guard against excessive movement in any direction.

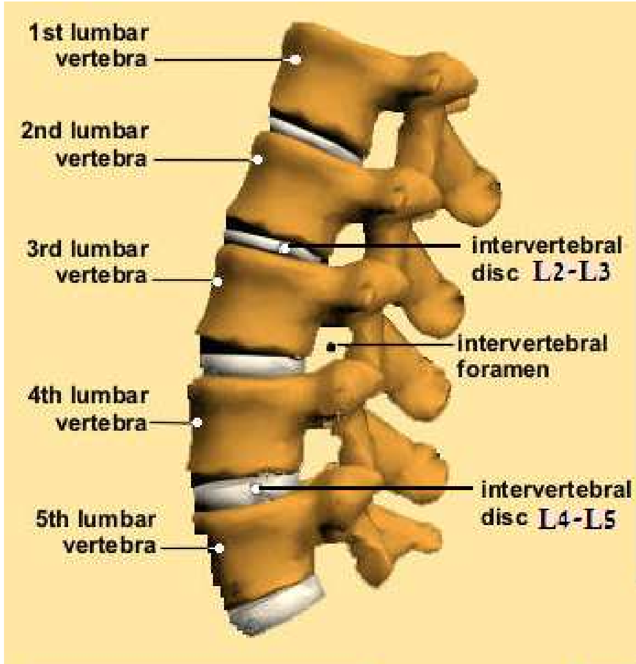

Figure 1.5. The lumbar spine, from the first lumbar vertebra (L1) to the fifth vertebra (L5). Modification from SpineUniverse^R.

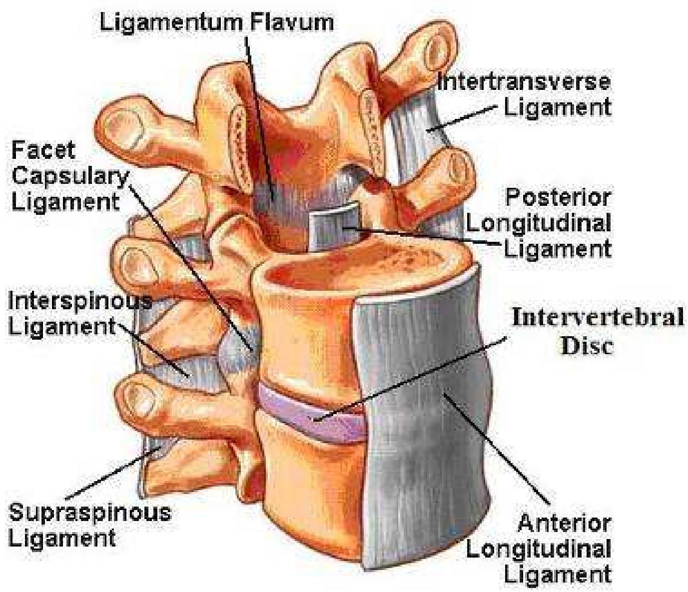

Figure 1.6. Lumbar ligaments. Extraction from "Fundamentals of Anatomy & Physiology". Frederic H. Martini. Prentice Hall International, Inc. 1998.

Each vertebral body is made of two kinds of bone, in the periphery; a thin layer of compact bone called cortical shell encloses the remaining mass that is made of porous tissue, called trabecular or cancellous bone, see Figure 1.7.

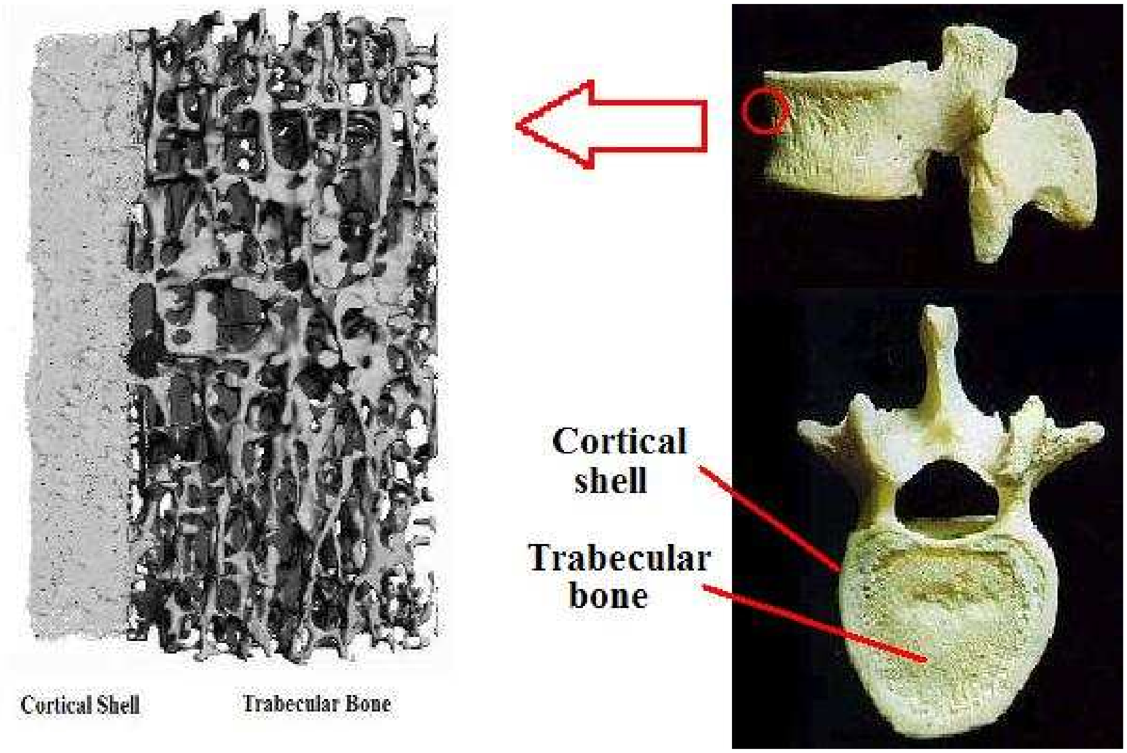

Figure 1.7 Cortical and trabecular bone from the lumbar vertebrae. Modification from SpineUniverse^{R}.

Human bone is an anisotropic, heterogeneous and time dependent material, therefore its mechanical properties change with location, direction and age. Hence, an orthotropic formulation for the behavior of the lumbar vertebrae as been suggested by (Lu et al., 1996) to take into account the higher stiffness of bone over that of the softer intervertebral disc. Such formulation gives three Young's moduli; see Table 1.1, which also show the shear moduli and the Poisson's ratio for the cortical and the cancellous or trabecular bones.

Table 1.1. Mechanical properties for lumbar vertebrae bone. Taken from Lu et al., (1996).

Material	*Young's Modulus (MPa)*	*Poisson's Ratio*
Cortical bone	E_{xx} = 11300	ν_{xy} = 0.484
	E_{yy} = 11300	ν_{yz} = 0.203
	E_{zz} = 22000	ν_{zx}= 0.203
	G_{xy} = 3800	
	G_{yz} = 5400	
	G_{zx} = 5400	
Cancellous or trabecular bone	E_{xx} = 140	ν_{xy} = 0.45
	E_{yy} = 140	ν_{yz} = 0.315
	E_{zz} = 200	ν_{zx}= 0.315
	G_{xy} = 48.3	
	G_{yz} = 48.3	
	G_{zx} = 48.3	

The form of the vertebrae body is complex, an oval type, wider from side to side than from front to back, and a little thicker in front than in back. It is flattened or slightly concave above and below, concave behind, and deeply constricted in front and at the sides. In general, lower lumbar levels, such as L4 and L5 have larger bodies than upper levels. The dimensions of the vertebral body width, depth and height are indicated in Figure 1.8a were (UVW) denotes upper vertebra width, (LVW) denotes lower vertebra width, (UVD) denotes upper vertebra depth, (LVD) denotes lower vertebra depth, (VBHa) denotes vertebra body height in the anterior part and (VBHp) vertebra body height in the posterior part.

The pedicles are two short, thick processes, which project backward, one of each side, from the upper part of the body, at the junction of the posterior and lateral surfaces; consequently, the inferior vertebral notches are of considerable depth. They change in morphology from the upper lumbar to the lower lumbar. An increase in sagittal width from 9 mm to up to 18 mm and an increase in angulations in the axial plane from 10° to 20° at level L5 have been reported (Zhou et al., 2000). Clinically pedicles are used as a portal of entrance into the vertebral body for fixation with pedicle screws or for placement of bone cement as kyphoplasty or vertebroplasty. Pedicle width (PDW) and pedicle height (PDH) locations are shown in Figure 1.8b.

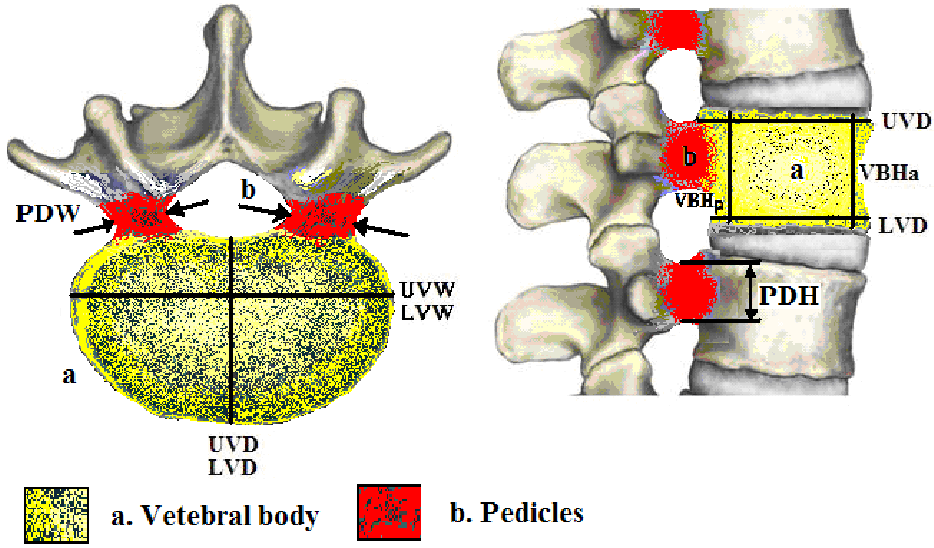

Vertebrae body and pedicles parameters.	Level, L3 (mm)	Level, L4 (mm)	Level, L5 (mm)
UVW	32.3 – 53.3	37.6 – 59.3	42.3 – 67.1
LVW	39.8 – 63.2	42.8 – 68.2	38.1 – 73.1
UVD	24.4 – 41.8	26.4 – 46.2	28.8 – 47.8
LVD	27.8 – 44.8	29.7 – 47.9	27.1 – 50.1
VBHa	23.2 – 35.1	22.9 – 36.1	24.1 – 37.5
VBHp	23.1 – 37.1	21.8 – 34.1	20.6 – 31.6
PDW	5.4 – 14.4	7.1 – 17.1	9 – 22.6
PDH	10.1 – 19	11.1 – 18.3	9.5 – 19.9

Figure 1.8. Dimensions for the lumbar body and the pedicles. Modification from Zhou et al., (2000).

In the posterior side of the vertebrae there are several elements which include protuberance processes for muscle attachment, laminas for structural connection and hollow spaces for the passage of the spinal cord. The laminas are two broad plates, short directed backward and medially from the pedicles. They fuse in the middle line posterior, and so complete the posterior boundary of the vertebral foramen and therefore allow connection between the spinous process and the pedicles, see Figure 1.9. In the upper lumbar region the laminas are taller than wider but in the lower lumbar spine there much wider.

The spinous process is a thick, broad, and somewhat quadrilateral protuberance; it projects backward from the junction of the lamina and ends in a rough, uneven border, thickest below to provide surface area for the attachment of lower back muscles and ligaments that reinforce or adjust the lumbar curvature, see Figure 1.9.

The transverse process projects laterally on both sites from the point were the lamina joints the pedicles. The longitude of the transverse process changes between levels (Zhou et al, 2000). Unlike the spinous process the transversal are long and slender protuberances, see Figure 1.9. They are horizontal in the upper three lumbar vertebrae and inclined a little upward in the lower two. In the upper three vertebrae they arise from the junctions of the pedicles and lamina, but in the lower two they are set farther forward and spring from the pedicles and posterior parts of the vertebral bodies. They are situated in front of the articular processes instead of behind them as in the thoracic vertebrae, and are homologous with the ribs.

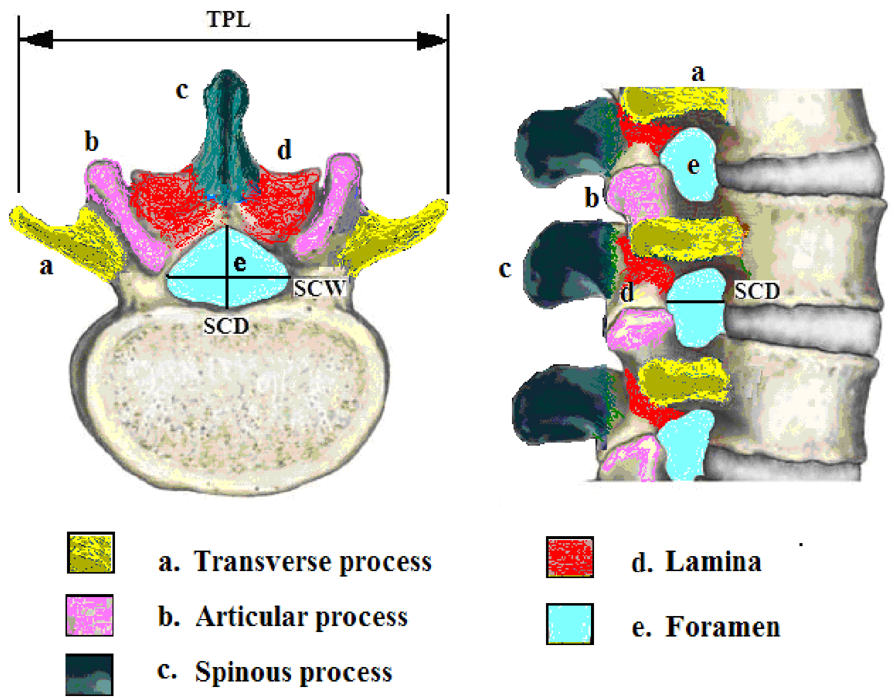

Posterior elements parameters.	Level, L3 (mm)	Level, L4 (mm)	Level, L5 (mm)
TRL	69.8 - 114	65.4 to 108.9	73.3 to 117.8
SCW	16.2 – 34.9	18.9 – 34.4	19.8 – 38
SCD	11.8 – 20.3	11 – 27.5	10.1 – 32.7

Figure 1.9. The posterior elements of the lumbar vertebrae. TRL is the longitude of the transversal process, SCW is the spinal canal width and SCD is the spinal canal depth. Adaptation from Zhou et al., (2000).

The superior and inferior articular processes are well-defined, projecting respectively upward and downward from the junctions of pedicles and laminas. The two articular processes lie on each side of the vertebra. Their function is to connect adjacent vertebras throughout the joints facets, see Figure 1.10. Facets on the superior processes concaves and look backward and medialward; while those on the inferior side convexes and are directed forward and lateralward. The former are wider apart than the latter, since in the articulated column the inferior articular processes are embraced by the superior processes of the subjacent vertebra. In addition, the facet joints help to make the spine flexible.

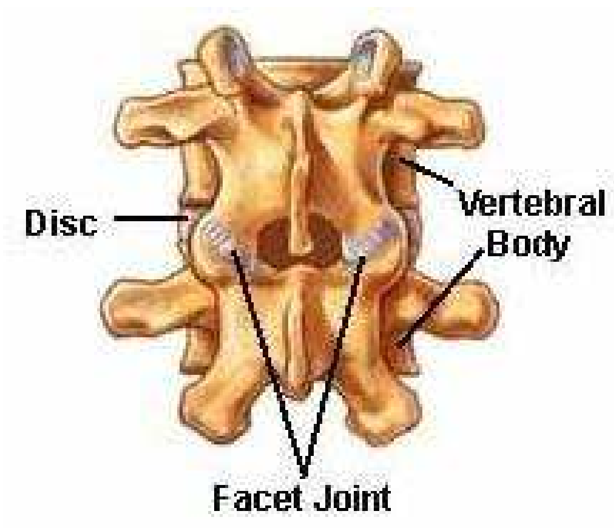

Figure 1.10. Lumbar articular process with facet joints. Extraction from "Fundamentals of Anatomy & Physiology". Frederic H.Martini. Prentice Hall International, Inc. 1998.

The foramen is a hollow space that encloses the spinal canal containing the spinal cord and located between the vertebral body and the posterior elements. The foramen of adjacent vertebrae make the spinal canal, which has a width (SCW) and a depth (SCD), see Figure 1.9. At the lumbar level the size and form of the foramen is a small triangular. At this region the spinal cord contains only the nerves that control the lumbar region and the extremities. As it proceeds cranially along each foramen, the diameter of the spinal cord increases, and so does the diameter of the foramen, given by SCW and SCD, until it reaches the top of the cervical region were the spinal cord contains all the nerves that connect the brain with the rest of the body.

II. Development and function of the intervertebral disc

The human intervertebral disc has an oval structure composed of a nucleus pulposus (NP), an annulus fibrosus (AF) and a cartilage endplate (CEP). Located at the center of the disc is the NP, which is a mixture of proteoglicans cells with water in a gel-like substance. Surrounding the NP at the periphery lies the AF which is a bright white matrix of fibrocartilage strengthen by annular collagen fibers. Covering the NP on the top and bottom lies the CEP which is a permeable layer of hyaline cartilage, see Figure 1.11.

Together, the nucleus, annulus and endplate give to the intervertebral disc its material properties which decay with time and used. Because the lumbar discs bear the most weight and deformation in the spine they are exposed to more damage than upper spine discs. Here, normal lumbar discs will be described, whereas degenerated discs will be cover in the section of disc pathology.

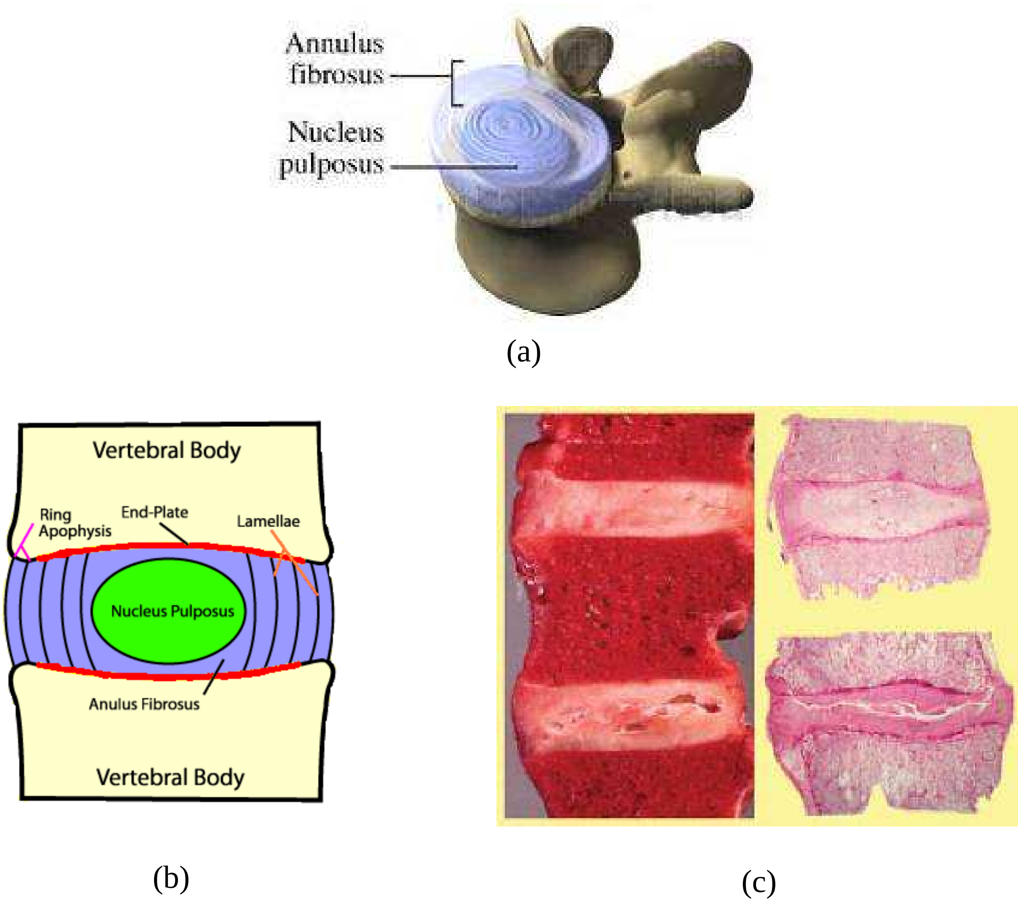

Figure 1.11. (a) The arrangement of the nucleus pulposus and annulus fibrosus. (b) Schematic illustration of the disc in the saggital view. (c) Actual appearance in saggital view for a normal and degenerated disc. Modification from Saunders et al., (2008)."Swellable gels fix bad backs". Chemical Science Vol. 2008(6) p.919.

a. Intervertebral disc development

The origin of the intervertebral disc starts at week four of the embryo development, as mesoderm on either site of the spinal cord and notochord forms a series of mesenchymal blocks called somites. Mesenchyme in the medial portions of each somite, a region known as the sclerotome, will produce the vertebral column. The migrating cells differentiate into chondrocytes and produce a series of cartilaginous blocks that surround the notochord. These cartilaginous blocks, which will develop in to the vertebral bodies, are separated by patches of mesenchyme. Expansion of the vertebral bodies eventually eliminates the notochord, but it remains intact between adjacent vertebrae, forming the nucleus pulposus of the intervertebral discs. Later, surrounding mesenchymal cells differentiate into chondrocytes and produce fibrocartilage within the annulus fibrosus, which surrounds the nucleus pulposus, see Figure 1.12.

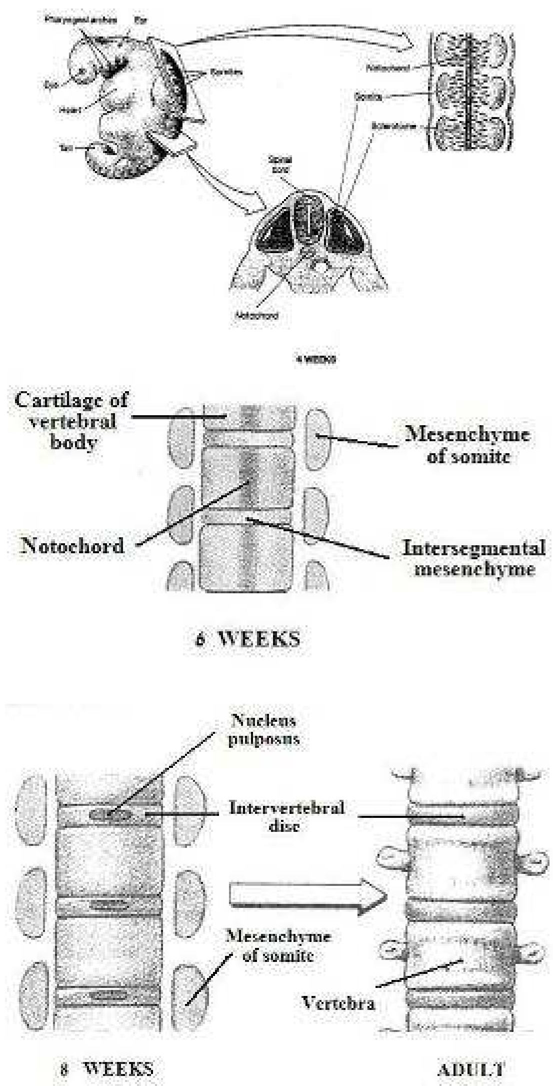

Figure 1.12. Development of the intervertebral disc. From Anatomy and Physiolology. Frederic H. Martini. Prentice Hall International, Inc. 1998.

Disc height and size magnitudes vary from individual's size, age, gender and race. In the adulthood cross section area, A, ranges from 1000 mm^2 in the upper lumbar, e.g. L1 and L2 discs to 3000 mm^2 in the lower lumbar, e.g. L4 and L5 discs. Disc height ranges from 10 to 16 mm in the anterior site, HDa, and from 6 to 10 mm in the posterior site, HDp, see Figure 1.13.

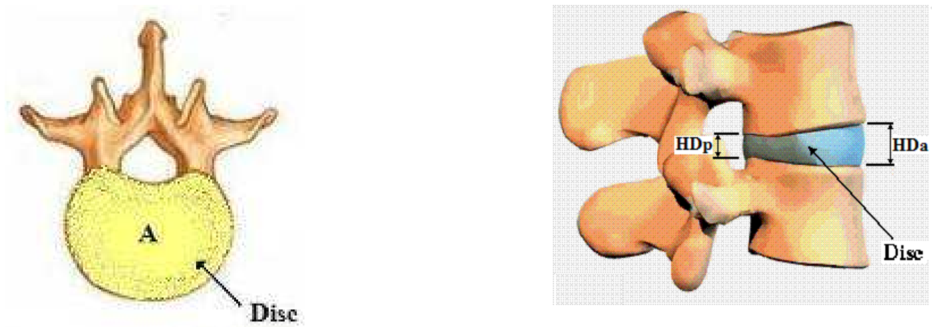

Figure 1.13. Disc cross section area A and height in the anterior site, HDa and posterior site, HDp. Modification from SpineUniverse^R.

b. Disc functions

The basic functions of a healthy intervertebral disc are (1) allowance of spine flexibility during body movement, (2) shock absorption and prevention of excessive wear to the facet joints during spine loading.

Spine movement during daily activities is complex, because it involves a combination of plane movements with couple motions done in the axial, coronal and saggital plane. In the coronal plane, the spine movement takes place when an individual bends forward or backwards, typically when doing exercise and heavy tasks. Forward bending of the spine is defined as **flexion**, while backward bending is called **extension**. Movement in the saggital plane is achieved when bending laterally to the right or to the left. Bending the spine to the right is called **right bending** and to the left is called **left bending**. Spine movement in the axial plane follows after applying an axial rotation clockwise or counterclockwise. Axial rotation of the spine is defined as **torsion**, see Figure 1.14.

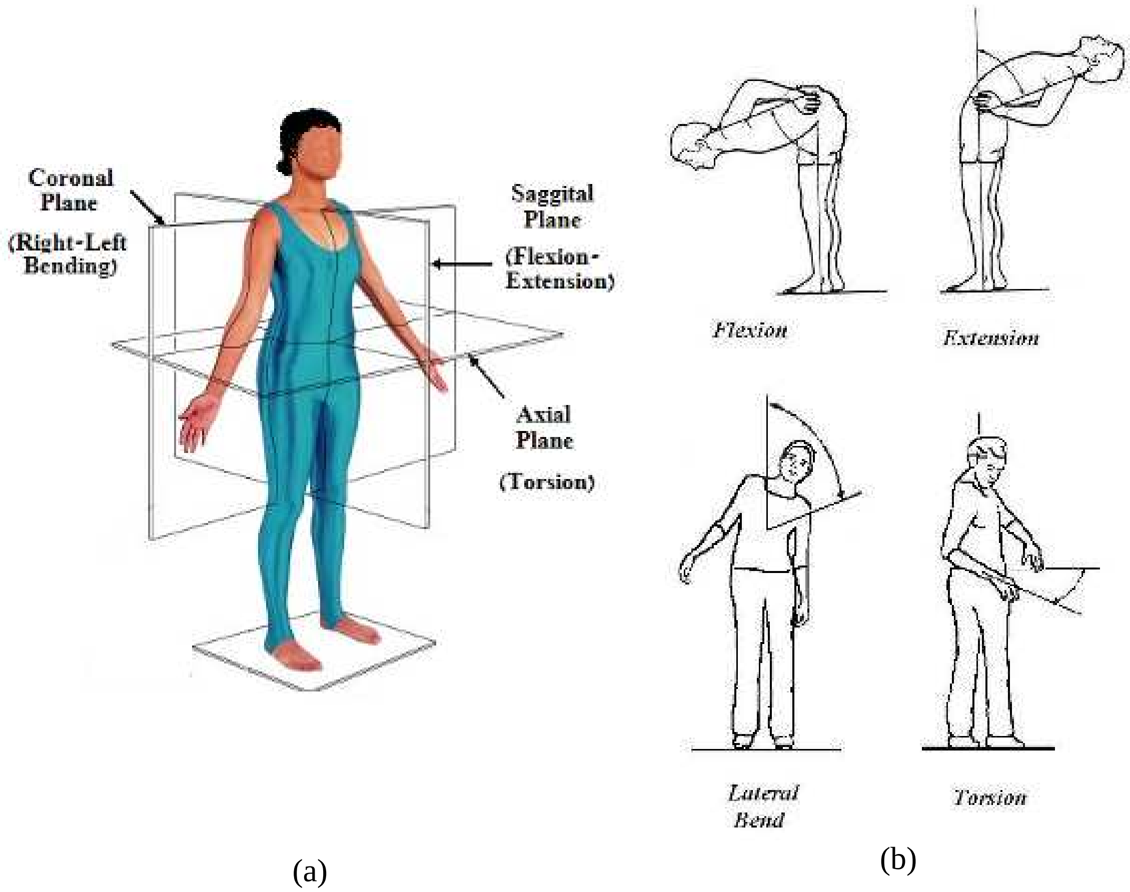

Figure 1.14. (a) Axial, coronal and saggital anatomical planes. (b) Body and spine movement in flexion, extension, lateral bending and torsion. Adaptation from Pearson Educational, Inc. Publishing Benjamin Cummings 2004.

Because the lumbosacral spine carries the heaviest loading and also experienced the largest deformation in the vertical column, its discs, ligaments and vertebra bodies are exposed to severe damage, thus affecting its integrity. The motion response of a normal and degenerated lumbosacral spine in ex-vivo and in-vivo has been a subject of intense study in clinical biomechanics in recent years. Only a few experimental studies involving the whole lumbosacral spine have been done. In a recent kinematics study (Guan et al., 2006) to ten ex-vivo lumbosacral spines columns it was concluded that L5-S1 motions were significantly greater than L1-L5 motions under flexion and extension loadings and were lower than L1-L5 motions under lateral bending, see Figure 1.15.

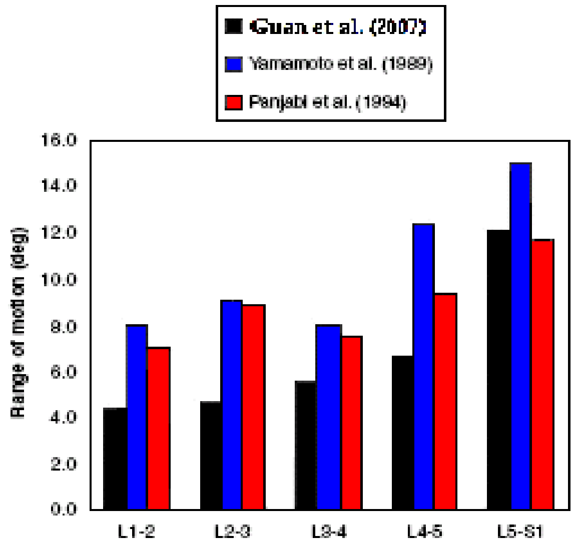

Flexion – Extension.

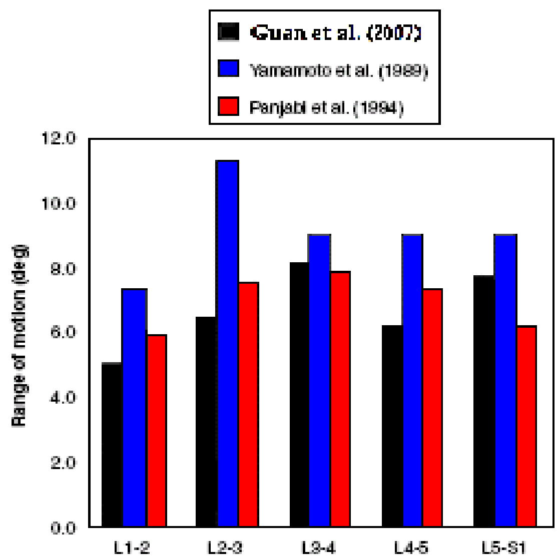

Right – Left Lateral Bending.

Figure 1.15. Ex-vivo lumbosacral spine means motion response to 4 Nm in flexion-extension and right-left lateral bending. Extraction from Guan et al., (2006).

In another kinematics study a 3D analyzing system was developed for tracking the relative motion of individual vertebrae using magnetic resonance imaging (MRI) and analyzed in vivo 3D intervertebral motions of the lumbar spine during trunk rotation (Fujii et al., 2007). Their results shown that trunk rotation promotes axial rotation (torsion) on each lumbar segment accompanied by coupled motions in flexion-extension, and right-left bending. Magnitudes were compared with ex-vivo results and differences found were attributive to the environment and loading conditions, see Figure 1.16.

In vivo studies have the advantage of working with real physiological conditions, whereas in ex-vivo it is not possible. When analyzing in-vivo spine movements, the main disadvantages are couple motions and the influence of muscles. In overall, the significance of the results, both in-vivo and ex-vivo is that they can help in the optimal orthopedic management of lumbar spinal disorders and validation of finite element studies.

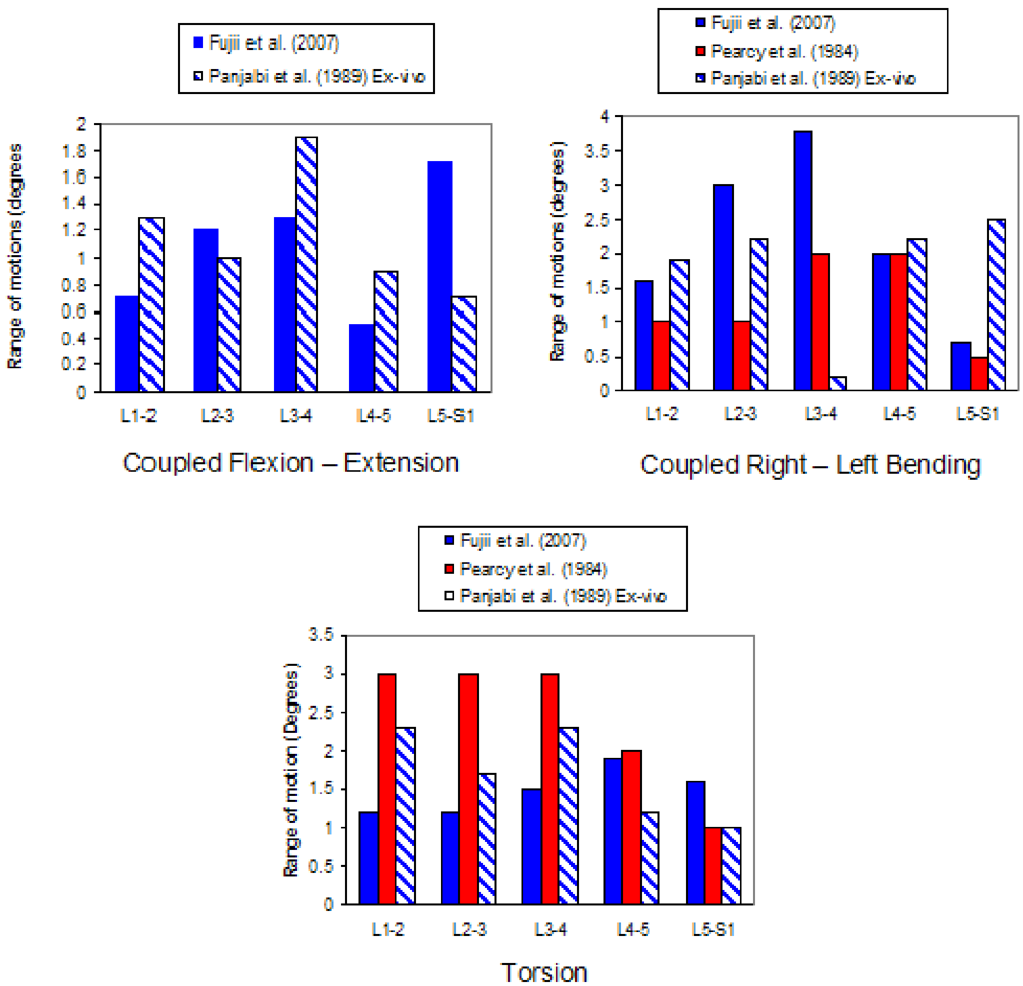

Figure 1.16. In-vivo lumbosacral motion response to 45° trunk rotation. Taken from Fujii et al., (2007).

Spine movement in any one of the three anatomical planes involves disc loading, relative and coupled motion between levels. Disc loading can be achieved by four ways: compression, shearing, bending and torsion, see Figure 1.17. When bending by flexion the anterior part of the disc is in compression and the posterior part is in tension. When bending in extension, the opposite is accomplished.

Bending laterally causes compression on the lateral side and tension on the opposite side. Torsion will cause axial rotation, which is maximum at the disc periphery. Shear loading will cause relative displacement between the upper and lower part of the disc. When applying axial compression, the discs undergo deformation in the longitudinal and transversal directions, thus reducing disc height in the former direction and increasing radial bulging in the latter. Load removal will cause disc height recovery, which will depend on the state of disc tissue.

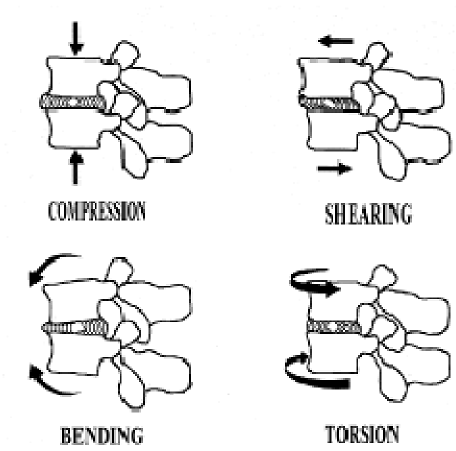

Figure 1.17. Types of loading that are applied to the intervertebral disc upon spine movement. Adaptation from "Biomecanica del raquis y sistemas de reparación". Instituto de Biomecánica de Valencia 2ª edición 1999.

Here, the proteoglycans gives the nucleus the capacity to bind water and confer a high negative fixed charge on the matrix; the concentration of fixed negative charges determines the concentration of extracellular ions in the tissue, which in early life is the highest. When loading the disc, the abundant chains will reject each other, thus creating a swelling pressure that act hydrostatically, distributing pressure evenly to the adjacent annulus and the endplate, and thus acting as a shock absorber, see Figure 1.18.

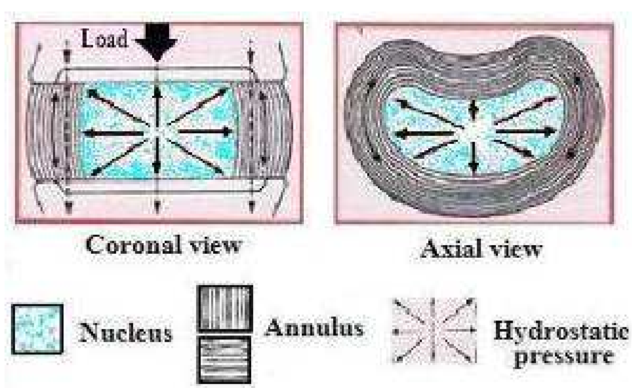

Figure 1.18. Development of the intradiscal pressure in the nucleus pulposus by compressive loading. Modification from SpineUniverse[R].

Early in vivo and ex-vivo measurements of swelling pressure in the nucleus pulposus were reported in the range of 0.2 MPa to 2.5 MPa when applying up to 2000 N of compression to the disc (Nachemson, 1960). This has also been seen on compressive testing on portions of nucleus and annulus tissues were the osmotic pressure measurements were reported in the range of 0.05 MPa to 0.25 MPa for loads up to 300 N (Iatridis et al., 1996). Compressive loading to the disc shows that the nucleus pulposus behaved in a hydrostatic fashion in normal and slightly degenerated discs (Nachemson, 1960), and also spinal movements influence intradiscal pressure and annulus fibrosus loading, see Figure 1.19 (Nachemson, 1960; Wilke et al., 1999).

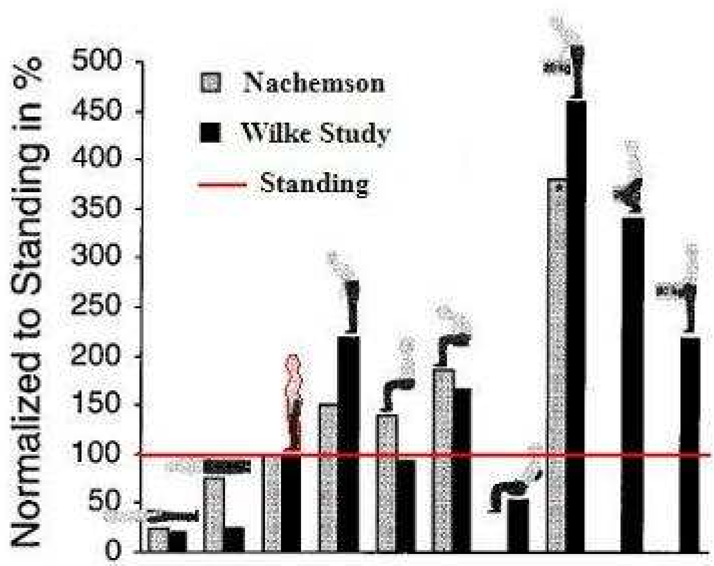

Figure 1.19. Intradiscal pressure in common postures and activities normalized to standing. Taken from Wilke et al., (1999).

In particular, a repetitive motion limited to the craneo-caudal direction, such as jumping or running, will imply a disc loading in compression with a significant coupled motion in torsion. Cyclic compression of the disc gives input data of nucleus pulposus stiffness and damping which decay with age and degeneration. A disc becomes stiffer and less hysteretic as compression frequency is increased from 0.01 to 20 Hz, which is a wide physiological range (Izambert et al., 2003). Stiffness and damping values ranged from 1.9 to 3.66 MN/m and 32 to 2500 Ns/m respectively, see Figure 1.20. Stiffness and damping values increase with loading increase under dynamic flexion and extension, (Crisco et al., 2007). Values of bending stiffness and damping coefficients were reported in the range of 97 to 200 Nm/rad in the former and 1.4 to 4 Ns/m in the latter.

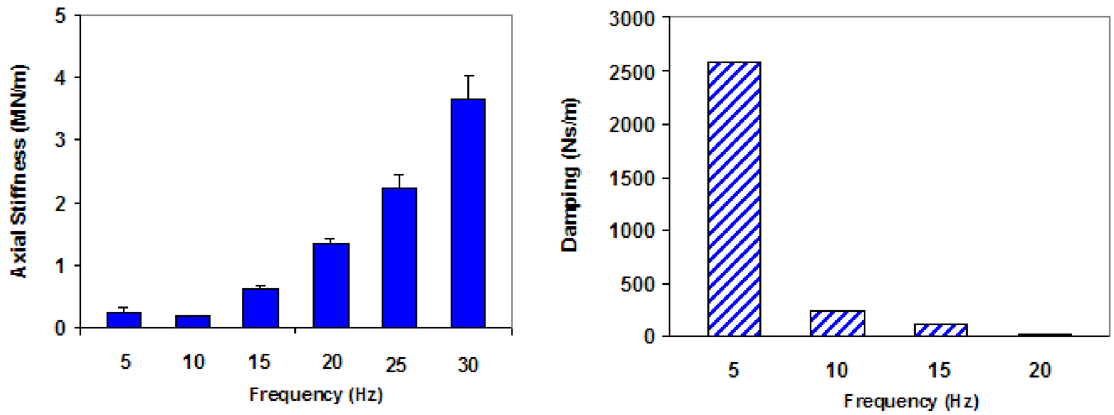

Figure 1.20. Disc stiffness and damping response to dynamic compression. Taken from Izambert et al., (2003).

III. Structure and pathology of the intervertebral disc

As a soft tissue, the intervertebral disc undergoes changes both in its anatomy and its biochemistry with time and degeneration. The three major constituents of the disc are water, fibrillar collagens and aggrecan, the large aggregating proteoglycan. The composition and organization of the collagens and proteoglycans make up the disc tissue, and since they change during development, growth, aging and degeneration they affect how the disc responds to changes in mechanical loading and ultimately affect normal disc functions. A comprehensive study of the structure and function of the disc elements is essential in order to address disc pathology and distinguish normal aging from degenerative disease. *Intervertebral Osteochondrosis (IO)* and *Spondylosis Deformans (SD)* refer to the degenerative disease of the nucleus pulposus and cartilaginous endplate in the case of the former and to the annulus fibrosus for the latter. We begin with a physical description of the disc followed by the physiological changes in degeneration for each disc component. The diagnosis and evaluation of these disorders throughout the used of Magnetic Resonance Imaging (MRI) will be cover in section IV.

a. The nucleus pulposus and intervertebral osteochondrosis

Localized in the central portion of the disc is the nucleus pulposus, being nearer to the posterior than to the anterior border of the annulus fibrosus. In a healthy state, the nucleus can be distinguished from the annulus fibrosus; it occupies about 50 to 60% of the cross sectional area of the disc and the nucleus height is that of the disc. In a newborn, the nucleus appears as a transparent gel-like mass well hydrated, see Figure 1.21; this is due to a high population of notochord cells.

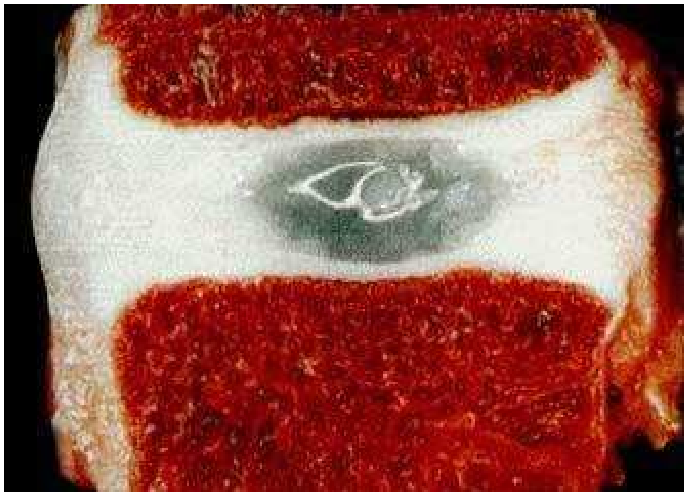

Figure 1.21. The nucleus pulposus of newborns with a transparent gel-like appearance. Adaptation from SpineUniverse^R.

The development of the nucleus pulposus begins at the embrionary stage. The active notochord cells presence in the fetus spine during the gestation period and throughout the child first years of life produce proteoglycans and matrix components, such as hyaluronic acid (HA). The aggrecan proteoglycan cells consist of a protein core to which up to 100 highly sulphated glycosaminoglycan (GAG) chains, principally chondroitin (CS) and keratan sulphate (KS) are covalently attached. The polysaccharine chondroitin sulphate, because of its polar hydroxyl group, gives the nucleus the capacity to bind water, which at this stage is about 90% of weight (Muir, 1995). As mentioned, the population of highly sulphated GAG chains determines the capacity of the nucleus to develop swelling pressure which decreases by age and degeneration. Nucleus permeability decreases with dehydration and rate of deformation, values have been reported in the range of 0.3×10^{-15} to 1×10^{-13} $m^4/N\text{-}s$. These changes in the tissue properties affect the nucleus behavior from fluid in a nondegeneration to a viscoelastic solid or a more elastic solid in a severe degeneration according to Iatridis et al., (1996) and Johannessen et al., (2005).

At four years old, the notochord cells are replaced by those of chondrocytic appearance but of unknown origin. These cells continue to produce proteoglycans but also synthesized collagen type II and significant amounts of collagen, type III, V, VI, IX, XI, XII and XIV (Urban et al., 2000; Roughley, 2004). Nucleus composition has shown also the presence of small proteoglycans such as versican, decorin, biglycan, lumican, perlecan and fibromodulin and proteins such as elastin and fibronectin (Markolf et al., 1974; Sztrolovics et al., 1997). At this stage, the intervertebral disc starts to contain proteases enzymes, which can degrade the macromolecular components collagen and aggrecan at the nucleus, see Figure 1.22.

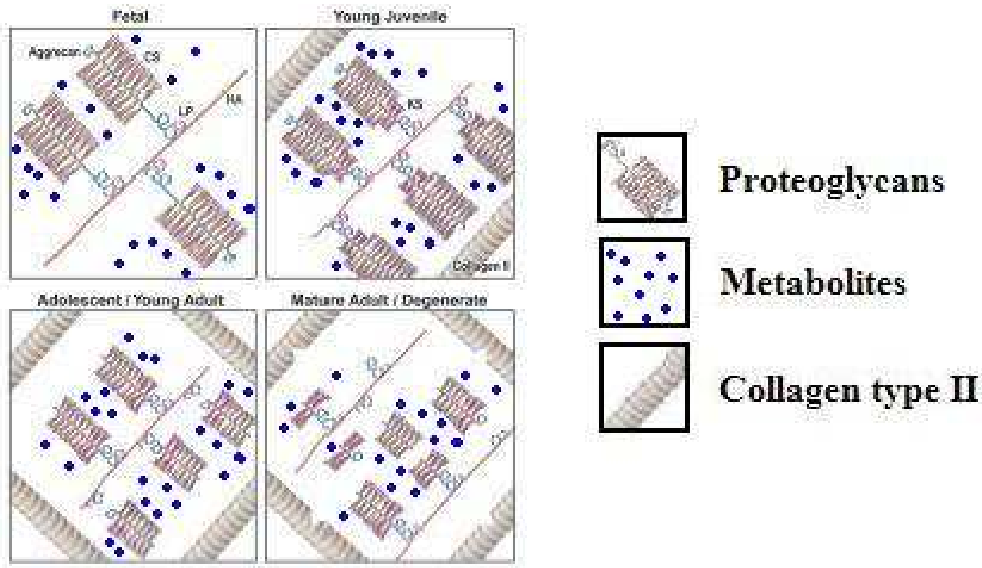

Figure 1.22. Schematic representation of the biology changes in the nucleus pulposus. Taken from Urban et al., (2004).

The composition of the extracellular matrix of the nucleus becomes cartilage-like and in the child and juvenile the appearance turns from a translucent gel-like to a white and opaque, see Figure 1.23, which consists mainly of a high concentration of aggrecan embedded in a fine network of collagen type II fibrils (Urban et al., 2000).

Figure 1.23. The white nucleus appearance of a disc from a juvenile. Adaptation from SpineUniverse[R].

With age, the cell density in the nucleus pulposus changes from about 14 million/cm^3 in an infant to 4 million/cm^3 in the mature adult (Roughley, 2004). The proportions of aggrecan and water in the nucleus fall steeply to approximately 80% at 20 years old, and even further to 70% at more than 60 years old, while the proportion of type II collagen rises (Buckwalter, 1995), see Figure 1.24; a similar change is seen in degenerated discs. But, with age and disc degeneration the levels of active proteases present in the nucleus increases, supporting their suggested role in disc matrix turnover and degradation (Cream et al., 1997). These changes appear to arise from loss of aggrecan rather than an increase in the amount of collagen produced and laid down (Antoniou et al., 1996).

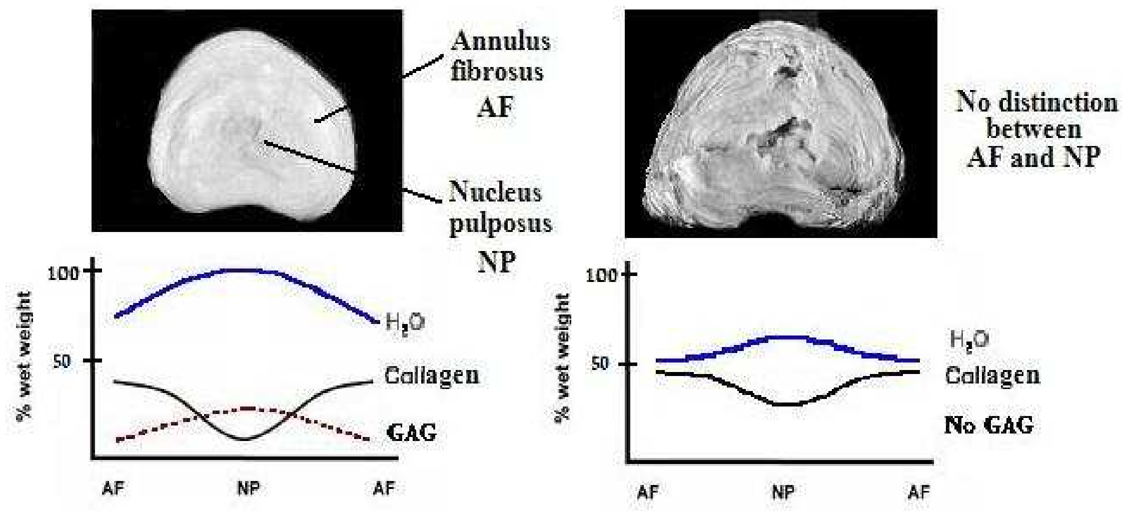

Figure 1.24. Percentage of water, collagen and proteogyicans (GAG) contents in a healthy and a severe degenerated disc. Adaptation from Buckwalter et al., (1995).

The process which causes dehydration of the nucleus pulposus has been termed *Intervertebral Chondrosis* and, when it also involves the neighboring bone is called ***Intervertebral Osteochondrosis***. Typical features of this physiology are loss of disc height and homogeneity between nucleus and annulus fibrosus tissues, see Figure 1.25. In the adult, the nucleus becomes less hydrated and more collagenous. It discolors, changing from white to yellow-brown in color through the accumulation of products of non-enzymatic glycosylation; these can also form crosslink's between polypeptide chains and may reduce tissue's flexibility and resiliency (Hormel et al., 1991; Nerlich et al., 1997).

The disc remains healthy while the rate of macromolecular synthesis and breakdown are in balance. However, if the rate of breakdown increases over synthesis, the nucleus matrix will ultimately disintegrate and the disc will degenerate (Urban et al., 2000). The activity of disc cells can be regulated by growth factors and cytokines and by physical factors such as mechanical stress (Shinmei et al., 1988; Thompson et al., 1991). Nutrient supply to the avascular disc also affects cellular metabolism significantly and loss of nutrient supply is thought to be a major cause of disc degeneration (Nachemson et al., 1970; Urban et al., 1995).

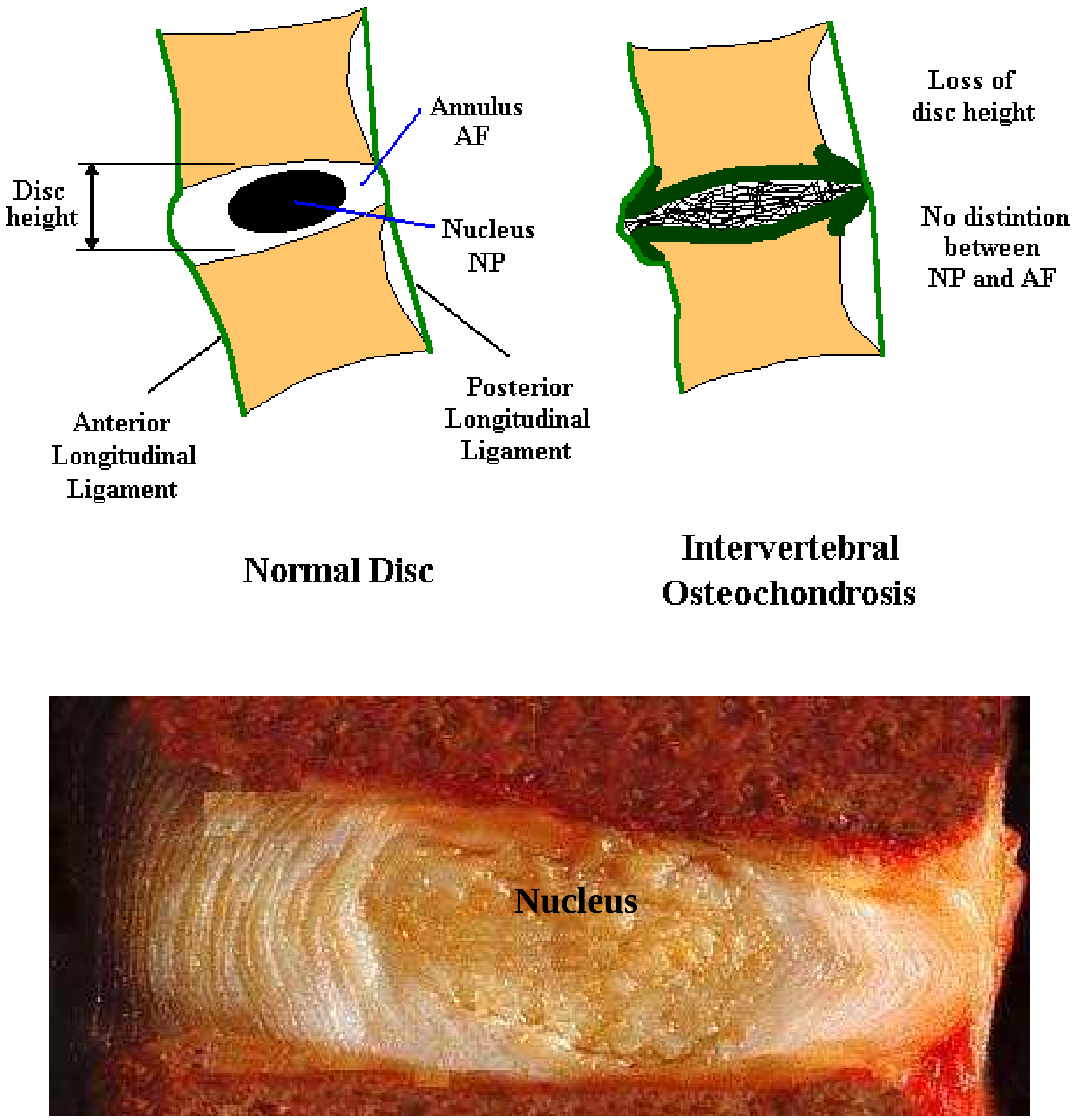

Figure 1.25. Schematic representation of Intervertebral Osteochondrosis and nucleus pulposus dehydration. Modification from Urban et al., 2004.

It is accepted that nucleus nourishment and removal of wasted products is done in two pathways, axially across the endplate and radially throughout the annulus fibrosus (Urban et al., 2004), see Figure 1.26.

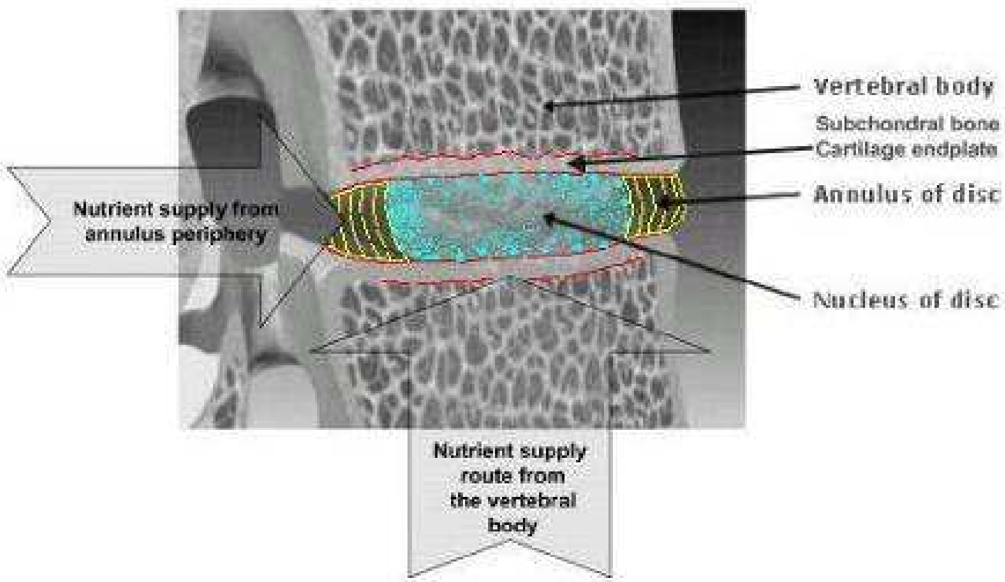

Figure 1.26. Routes of nutrient supply to the avascular intervertebral disc. Adaptation from Urban et al.,(2004).

Since solute transport uses the blood stream, the former trajectory is by far the most used by cells because of the advantage of traveling across the trabecular bone instead of rigid pack collagen fibers. However, it is in this route were most of the changes in nutrient supply takes place, such as: changes in blood supply, sclerosis of the subchondral bone, endplate calcification and most of the cellular activity (Rajasekaran et al., 2004; Urban et al., 2004), which are typical aspects of disc degeneration, see Figure 1.27.

Disc cells require nutrients that include glucose, oxygen and aminoacids to stay alive and function. Their main supply of energy comes from glycolysis; thus, they consume glucose and produce lactic acid at a relatively high rate, as much as 100 times higher than the rate of incorporation of sulphates, an essential component of proteoglycans (Maroudas et al., 1975). Cells will survive under hypoxia and low pH, but not with very low glucose. If glucose concentration drops below 0.5 mmol/L for more than a few days, the cells begin to die (Horner et al., 2001). However, a higher glucose concentration gradient leads to a reduction of pH due to accumulation of lactic acid, a wasted product that has to be removed. If the nucleus pH falls below 6.4 cells viability will be in jeopardy. Cells can survive up to 14 days with no oxygen present but there inactive and matrix synthesis is severely reduced (Bibby et al., 2004).

The cell density through the nucleus is not uniform but is highest at the edge of the endplate and the annulus, which are closer to the glucose and oxygen supply and then falls steeply as we approach the nucleus center (Maroudas et al., 1975). Here, the levels of lactic acid are at maximum and the tissue turns acidic, see Figure 1.28. Therefore, diffusion gradients, which are regulated by cell density, have the higher rates near the endplate.

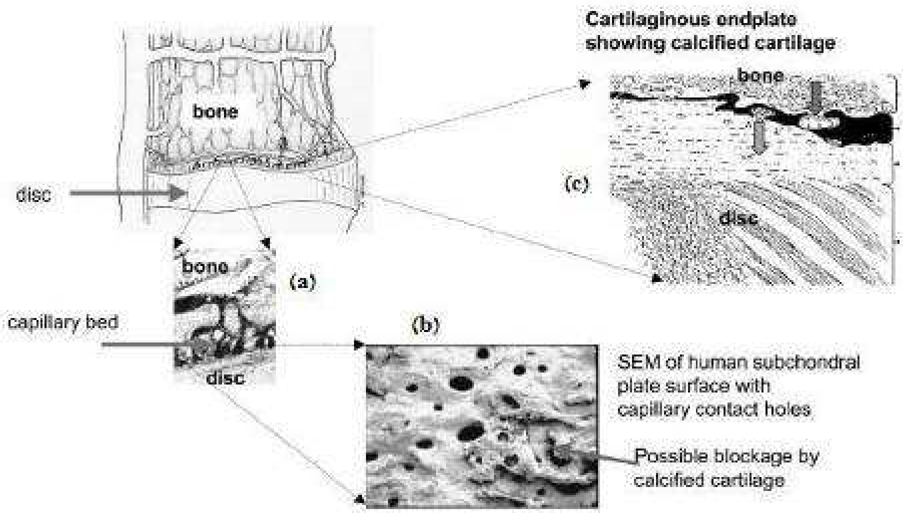

Figure 1.27. Schematic view of the blood supply from the vertebral body to the disc shows (a) details of the capillary bed at the subchondral bone/nucleus junction; (b) "holes" through the subchondral plate allowing capillary penetration with possible evidence of partial blockage by calcified cartilage; and (c) schematic section through the endplate-disc bone junction showing the cartilaginous endplate and calcified cartilage. Taken from Urban et al,(2004).

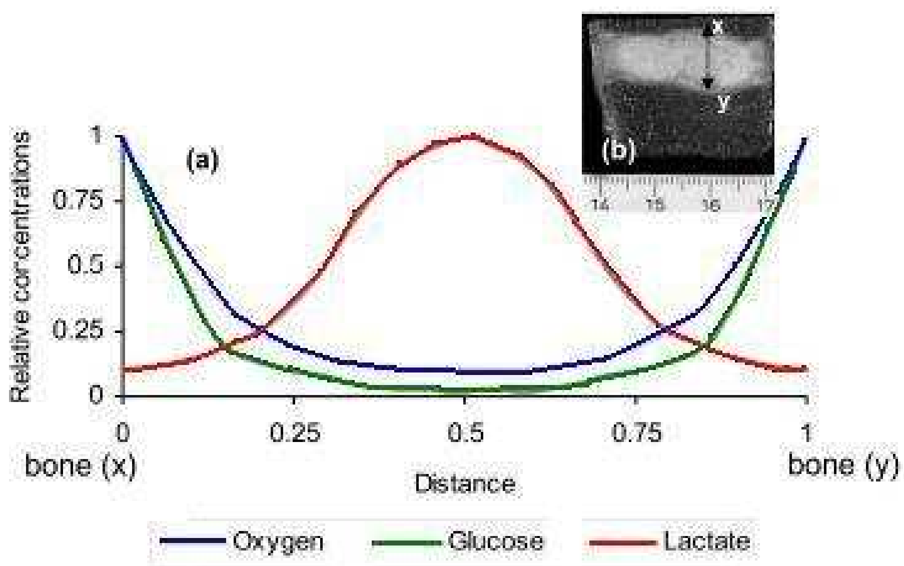

Figure 1.28. (a) Schematic view of nutrient gradients across the disc from top vertebrae x to bottom vertebra y ; (b) saggital section through a human lumbar disc showing the dimensions of the disc and the direction of the gradient shown in a. Extraction from Urban et al.,(2004).

Transport of nutrients from the vertebra into the nucleus is done under gradients through a distance of 7 to 8 mm long and is done mainly by diffusion, but also some convection takes place, both of which are ruled by properties of the nucleus matrix and the solute (Rajasekaran et al., 2004; Urban et al., 2004). The matrix components as well as the cartilage endplate act as a selective permeability barrier to entry of molecules into the disc. Only small particles diffuse, and in the case of large molecules only low concentrations are allowed (Urban et al., 1979).

For macromolecules with lower diffusivity such as growth factors, proteases and their inhibitors, convection movement due to load-induced fluid movement in and out of the disc, may contribute significantly to their movement through the matrix (Boubriak et al., 2003). The role of convection may also be important in ruling movement of newly synthesized matrix molecules through the matrix and in determining the rate of loss of matrix breakdown products and lactic acid (Urban et al., 2004).

Additional literature on nucleus cell behavior and nutrition supply can be found in the studies done by Jackson et al., (2008); Benneker et al., (2005); Kluba et al., (2005); Chiu et al., (2001) and Roberts et al., (1996). In all, the author’s emphasis the continuing changes of bone and cartilage properties and cellular demand, and their impact on normal disc function.

b. The cartilage endplate

Between the vertebral bodies and the intervertebral disc is the cartilage endplate (CEP). It consists of a dense collagen fiber framework which is aligned parallel and horizontally embedded in a thin layer of hyaline cartilage. The CEP expands from the outer 2/3 of the annulus to above the nucleus center a radial distance of 15 to 20 mm with a thickness of up to 1.6 mm (McLauchlan et al., 2002). The CEP contains no fibrillar connections with the collagen of the subchondral bone of the vertebrae above the nucleus pulposus, here the thickness of the CEP ranged from 0.1 to 1 mm. This lack of interconnection between the CEP and the vertebrae may render disc weakness against horizontal shear forces (Inoue H, 1981). In the outer 2/3 of annulus fibrosus the CEP thickness grows to a maximum due to a firmly fibrillar anchored into vertebral bodies, see Figure 1.29.

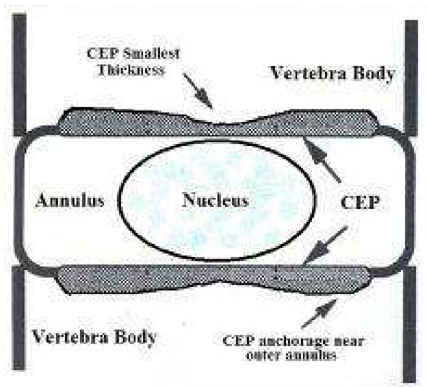

(a)

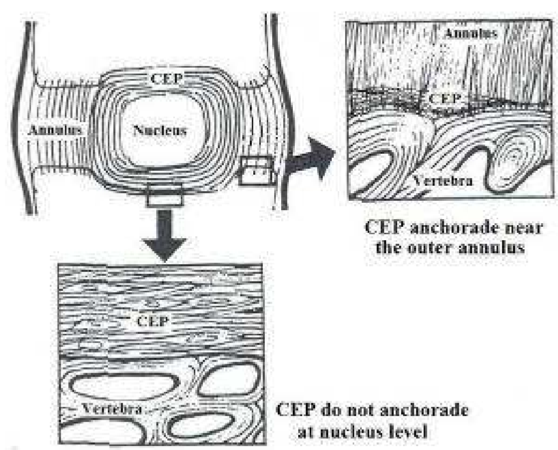

(b)

Figure 1.29. A schematic representation of (a) the cartilage endplate thickness and (b) the collagen framework of the intervertebral disc and the interconnections of the nucleus, annulus and the endplate. Extraction from Inoue, (1981).

Structurally the collagen fibers from the disc continue into the endplate, turning to approximately 120° from the lamellae of the outer annulus and 90° from the nucleus at the disc – endplate interface (Roberts et al., 1989). Here, numerous microscopic irregularities throughout the endplate of degenerated discs have been identified, most notorious are the cartilaginous nodes called Schomorol's nodes which are protrusions from the disc into the bone or viceversa. Where theses anomalies are present there is dehydration accompanied by a significant loss of proteoglycan in both the disc and endplate. With age the hyaline cartilage of the CEP at the interconnection with the bone calcifies blocking the pathway of nutrient diffusion coming from the blood vessels, see Figure 1.30.

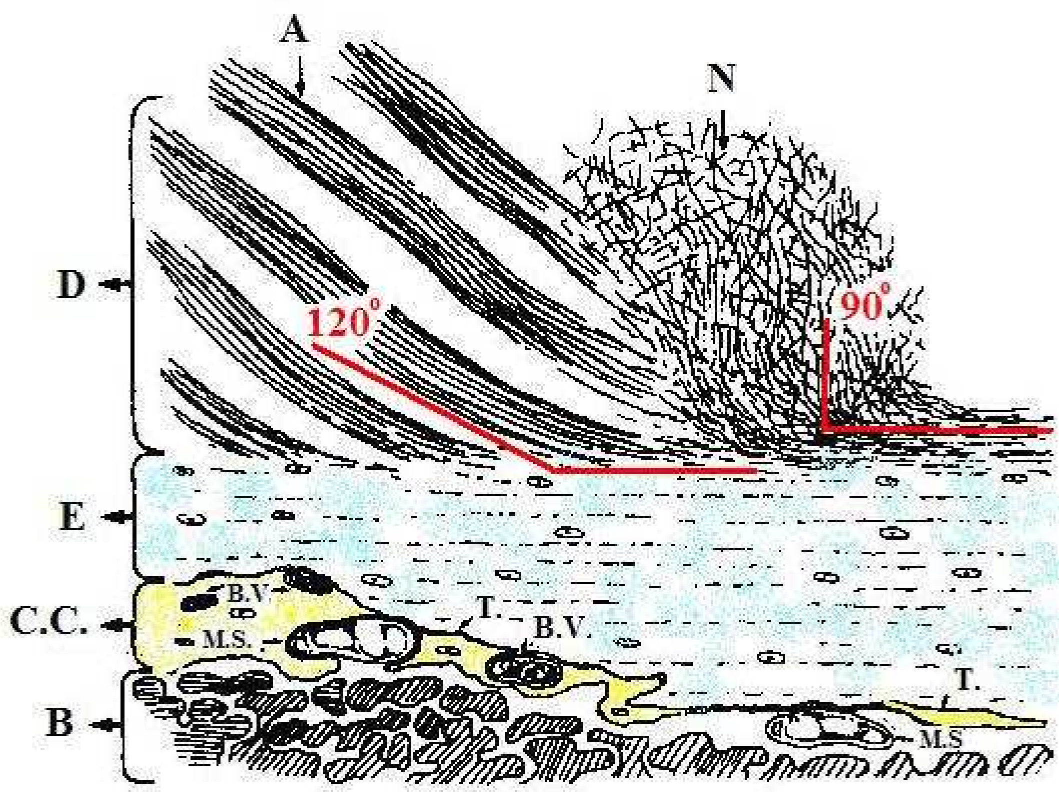

Figure 1.30. A schematic representation of the interconnections between the endplate, the disc, and the vertebrae bone. A= annulus fibrosus; B= vertebra bone; C.C.= calcified cartilage; D= disc; E= endplate (Noncalcified part); M.S.= marrow space; N= nucleus pulposus; T= tidemark. Extraction from Roberts et al., (1989).

With advance degeneration the thickness of the calcified cartilage of the endplate increases up to 60 μm and within cells exhibits fibrosis. This in turn affects the diffusion of nutrients to the nucleus, thus promoting matrix degradation (Baogan et al., 2001). A biochemical study of the cartilage endplate from healthy discs (Roberts et al., 1989, 1996) reveal that the hyaline cartilage of the endplate had a similar composition to that of the articular cartilage which shows less degradation.

The endplate composition is not uniform, but varies with location within any one spinal level. It resembles the disc by having a higher proteoglycan and water content, 20% and 60% respectively, but lower collagen content, 8% in the center adjacent to the nucleus than at the periphery adjacent to the annulus, where the corresponding contents are 15%, 54% and 9% respectively. Cell density was measured to be 325 per mm^2 in the former location and 250 per mm^2 in the latter (Roberts et al., 1996). They show also a chemical gradient with depth through the endplate with the tissue nearest to the bone having a higher collagen content, but lower proteoglycan and water content than that nearest the disc. There were no differences in composition between cranial and caudal endplates or with changes in spinal level. Because of the thinness of the endplate and its similarity in composition to the disc, they suggest that it provided little resistance to the diffusion of nutrients such as glucose and oxygen.

As the nucleus and endplate properties change so does the annulus fibrosus, these changes are focused on collagenous tissue, which are going to be addressed next.

c. The annulus fibrosus and spondylosis deformans

The annulus fibrosus is a ring-like structure that surrounds the nucleus pulposus and is located in between adjacent vertebrae. It is composed of a complex network of collagen fibers embedded in a ground substance and arranged in a series of circumferential laminas that serves to resist the nucleus pressure in the radial and tangential directions.

Characterization of the annulus structure has been done by Cassidy et al., (1989) and Marchand et al., (1990) using human lumbar spine discs. They reported a hierarchical model at the lamellar and fibrillar level base on gradients of lamellar thickness, interlamellar and crimp angle. They found that the circumferential laminas are discontinued and therefore their geometric characteristics change regionally and radially. In the radial direction, the thickness of laminas is smaller in the outer than in the inner annulus, see Figure 1.31. In the anterior region the annulus exhibits two distinct zones of laminas distribution: an outer *peripheral zone* where up to 18 collagenous layers of single thickness between 130 μm to 330 μm are stack one another, and an inner *transitional zone* that borders the nucleus where up to 20 layers of single thickness that ranges from 200μm to 520 μm are organized. In the annulus lateral and posterior regions there is a broad distribution of layer thickness from 80 to 400 μm in the former and from 50 to 250 μm in the latter. Cassidy et al., (1989) found that the layers cross section are not totally rectangular but have crimping profiles with the following geometrical features: an interlamellar angle θ, a crimp length l, a crimp angle $ø$, a crimp period ρ, see Figure 1.31.

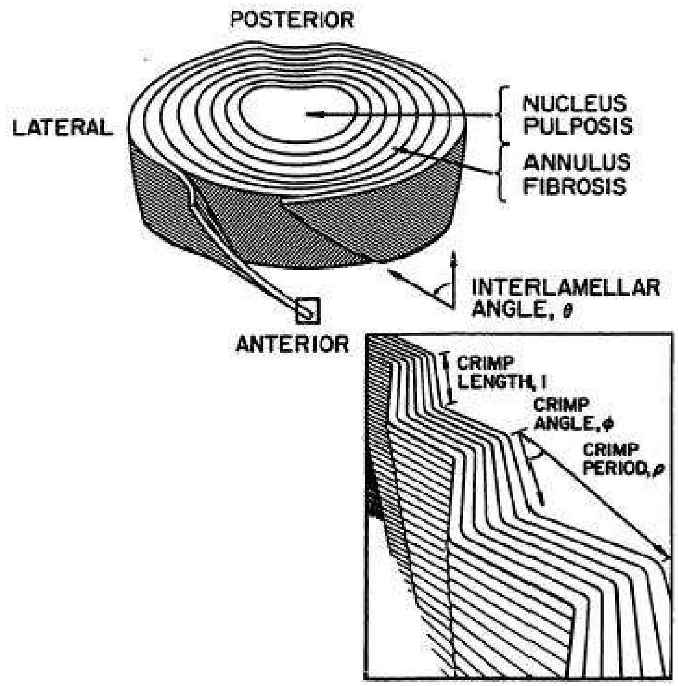

Figure 1.31. Hierarchical model of the annulus fibrosus showing lamellar structure, fiber orientation and crimp morphology. Taken from Cassidy et al., (1988).

The interlamellar fiber angle θ varies from 62° in the outer layers to 47° in the inner layers throughout all the annulus regions. The laminas cross section have a rectangular form where the collagen type I fibers are stacked in bundles and surrounded by the ground substance which is composed mainly by collagen type II and water. The crimp angle ø increases from about 20° at periphery to 45° in the lamellae closest to the nucleus while the crimp period appears to decrease linearly through the depth from 26 to 20 µm (Cassidy et al., 1989). Peripheral lamellae, with a larger interlamellar angle and a smaller crimp angle, are less deformable than those closer to the nucleus according to Galante, (1967) who study the mechanical properties of the lamellae as a function of radial depth through the annulus. He reported that specimens cut from the peripheral lamellae were stiffer and had lower energy dissipation and residual deformation than those of more central lamellae. Values of lamellae tensile modulus were reported for various directions and degeneration grades being greater in less degenerated tissues and in orientations parallel to the fiber direction where values of around 60 MPa were obtained. In posterior studies done by Ebara et al., (1996); Skaggs et al., (1994) and Marchand et al., (1989) they reported tensile modulus values for the annulus lamellae and collagen fibers in the range of 60 to 140 MPa for the former and 210 to 645 MPa for the latter, in all the high tensile values are due to the fiber stiffness. The annulus compressive mechanical properties of non degenerated levels L3-L4 and L4-L5 were investigated by Best et al., (1994). They report values of compressive modulus in the range of 2 to 10 MPa, also the overall hydraulic permeability and swelling pressure were reported to be around 0.25 x 10^{-15} $m^4/(N\text{-}s)$ in the former and 0.12 MPa for the latter.

Studies on mechanisms of layer discontinuity and age related changes in layer thickness and percentage of ground substance per layer were also done by Marchand et al., (1989) and Tsuji et al., (1993). They reported that at least 40% of the annulus layers were circumferentially discontinued or had been altered by merge of adjacent layers. The site where most layer discontinuity takes place is the posterolateral. Also, on older specimens the layer thickness and percentage of volume of ground substance increase from 0.17 mm in the young to 0.44 mm in the elderly for the former and from 13% in the young to 24% in the elderly for the latter. They concluded that in elderly and degenerated discs the annulus tissue losses its viscoelastic behavior. The previous results on the annulus morphology are summarized in Figure 1.32.

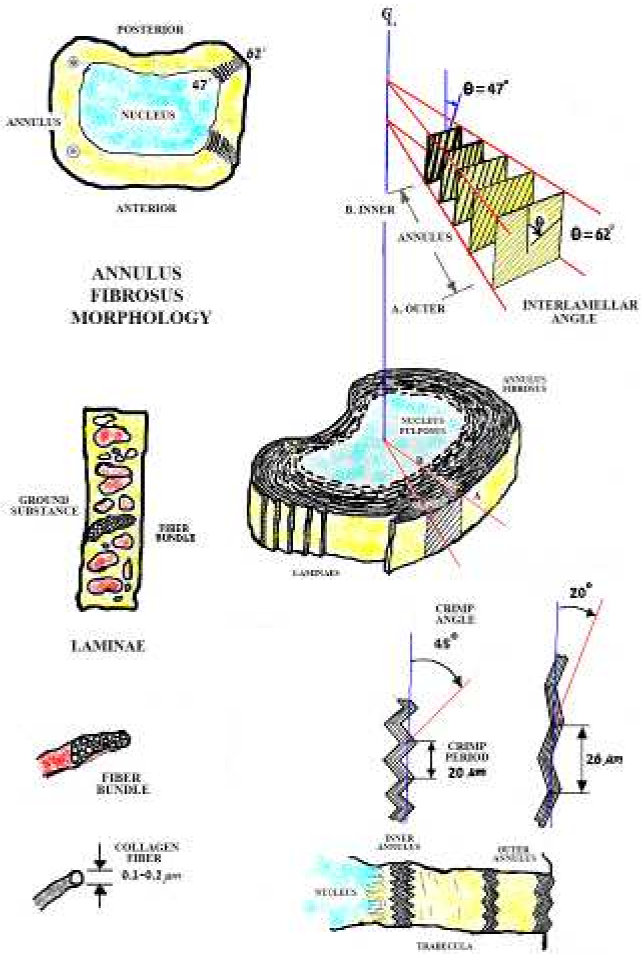

Figure 1.32. Annulus fibrosus morphology.

In addition to the physical characteristics, the annulus biochemical composition and cell morphology have also been studied. In general, the annulus is formed by collagen type I in the periphery and slowly decreases through the inner annulus where type II collagen is more abundant.

The changes in collagen type I and II content in the anterior and posterior sites due to age were studied by Brickley-Parsons et al., (1983) using cadaver lumbar spine discs. They reported a decrease of collagen type I at the anterior outer layers from 78% in young discs to 66% in elderly discs. An opposite trend was observed for the inner layers in which the collagen content increased from 33% in young discs to 45% in the elderly. Analysis of the posterior site shows an increased of collagen at the outer layers from 78% in young discs to 85% in the elderly, while in the inner layers there was a reduction from 34% in young discs to 30% in elderly. The increased of collagen in the posterior site of elderly discs can be explained by the synthesis of new collagen or osteophytes, as a response to mechanical stimulus, as described by Wolff's law of bone remodeling. The formation of new bone or osteophytes at the disc margins is termed *Spondylosis Deformans.* This concept was developed by Christian Schmorl (1932) and emphasizes abnormalities in the peripheral fibers of the annulus fibrosus as the initiating factor. The breakdown and subsequent loss of anchorage of the intervertebral disc to the vertebral body led to movement and thus load stimulus see Figure 1.33. A detail explanation of this process will be given in section IV of this chapter.

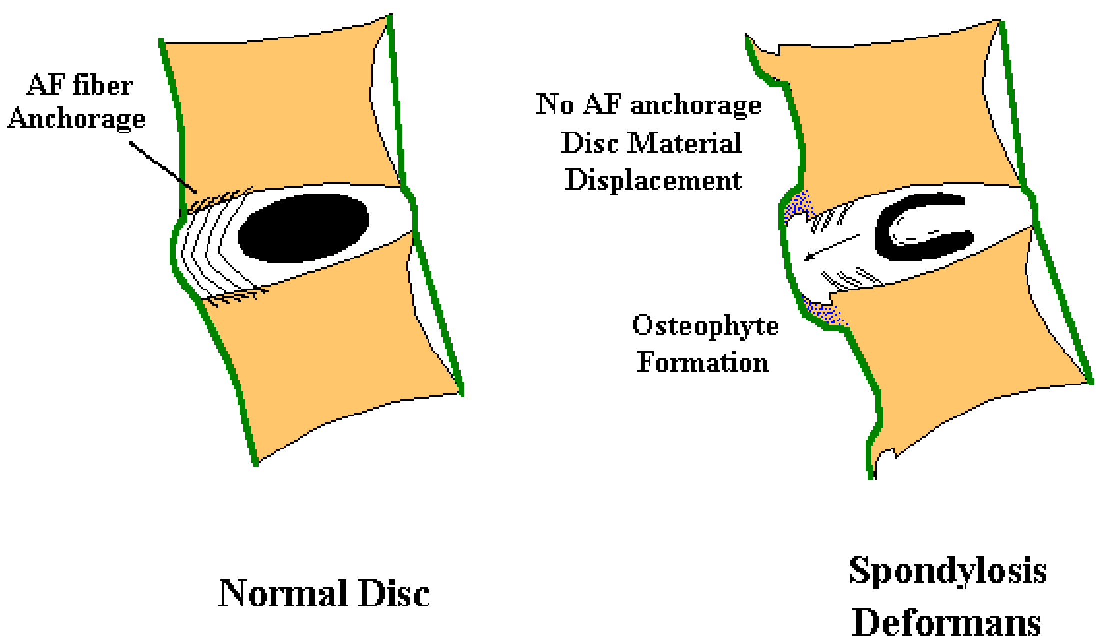

Figure 1.33. Schematic representation of Spondylosis Deformans. Modification from Urban et al.,(2004).

Posterior lumbar spine curve concaves and therefore this shape favor compressive loading which leads to osteophyte formation. In young discs the ratio of collagen type I to type II in the anterior and posterior outer layers are the same and equal to 3.5 (Brickley et al., 1983) with age they changes to 2 and 6 respectively. It is in the annulus posterior site were most biochemical changes occur and in combination with the structural variations affect the tissue mechanical properties and eventually the disc functions.

Cell morphology in the annulus as been characterized, most recently by Bruehlmann et al., (2002) in which they reported differences in the cellular matrix, cell shape, arrangement of cellular process and cytoskeleton architecture between the outer and inner annulus, see Figure 1.34.

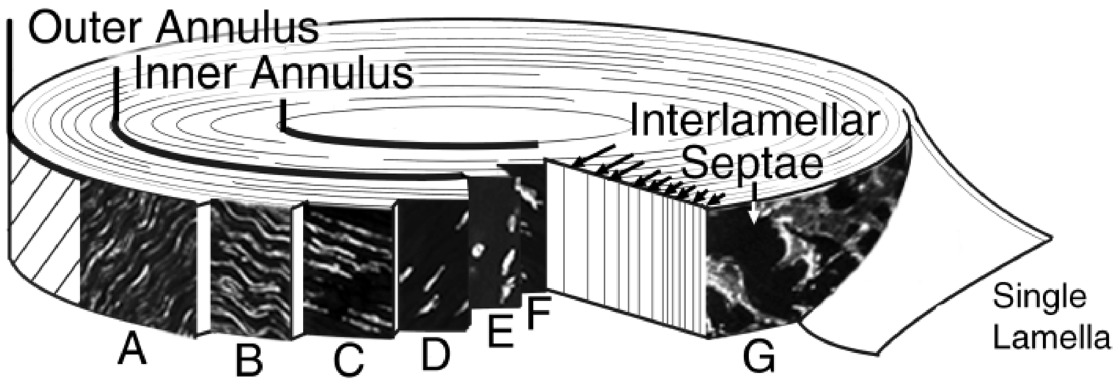

Figure 1.34. Division of the outer and inner annulus zones by identification of cell morphology. Observe also the increase thickness of lamella in the inner annulus. Taken from Bruehlmann et al., (2002).

They distinguish three forms of cells attachment in the radial direction. In the outer annulus cells exhibit an extended cordlike appearance due to a dominant longitudinal process parallel to the collagen fiber, the length of these cells is around 60 μm and favors an interconnected network, see Figure 1.35A-D. In the inner annulus and nucleus pulposus the cells are of spherical shape, their morphology exhibits extensive sinuous process, see Figure 1.35 E-F. In addition, a distinct cell morphology, which also displayed some regional variation, they identified in the space between lamellar layers. These cells exhibit broad branching process. This branching process is perpendicular to the longitudinal process and increases in quantity at the inner annulus, see Figure 1.35 F.

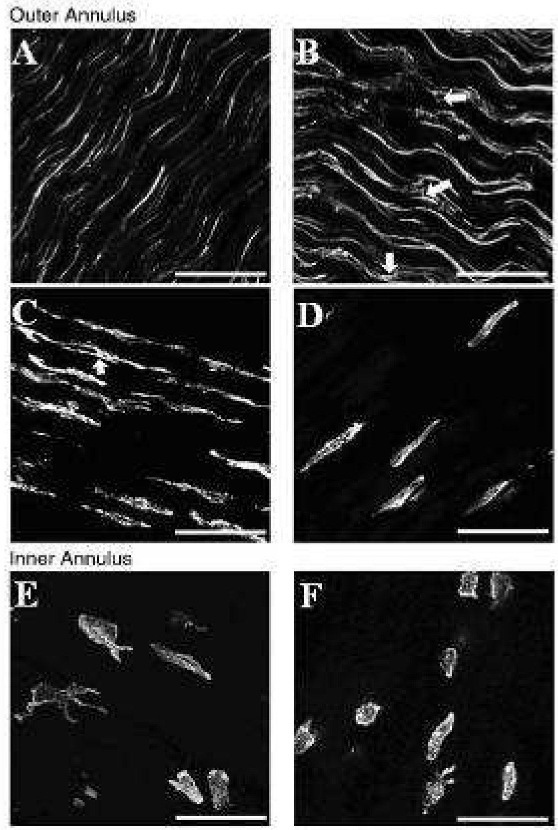

Figure 1.35. Gradual transition of cell morphology through the thickness of the annulus. Scale bar represent 50 μm. A-D. Outer annulus: (A) Cord-like cells at the periphery. (B) Reduction in the length and increase in the thickness of the longitudinal processes and appearance of some lateral process (arrows. (C) The longitudinal process is further reduced in length and isolation of cells is apparent. In addition, lateral process turn and follow the collagen fiber direction, sometimes bifurcating (arrows). (D) Fusiform-shaped cells with no process at the border with the inner annulus. E-F. Inner annulus: Spherical cells with either short or extensive processes or some elongated cells. Taken from Bruehlmann et al., (2002).

From Figure 1.35E-F, the inner annulus biological environment resembles that of the neighboring nucleus. Their changes include a progressive migration of spherical collagen type II cells from the inner annulus to the nucleus as suggested by Antoniou et al., (1996). With age the amount of migrating collagenous into the nucleus increases, supporting their suggested role in disc matrix turnover Cream et al., (1997).

The relevance of these studies is the clinical implications such as understanding low back pain (LBP) diseases and management of diagnosis and therapy. Hence, a basic introduction to radiological imaging using Magnetic Resonance Imaging (MRI) gives a familiarity with the key features of disc degeneration and serves for subsequent application in modeling the complex geometry of the intervertebral disc.

IV. Magnetic resonance imaging (MRI) and radiodiagnostic of intervertebral disc degeneration

Like any other biological tissue, the intervertebral disc exhibits physiological and pathological changes that can be evaluated with medical imaging such as X-Ray, CT scan, Ultrasound or Magnetic Resonance Imaging (MRI). Here, the MRI imaging of the lumbar intervertebral discs will be cover.

Magnetic Resonance Imaging (MRI) is primarily a medical imaging technique most commonly used in Radiology to visualize the structure and function of the body. It provides detailed images of the body in any anatomical plane. MRI provides much greater contrast between the different soft tissues of the body than does computer tomography (CT), making it especially useful in neurological (brain), musculoskeletal, cardiovascular, and oncological (cancer) imaging or where there is a high water content. Unlike CT, it uses no ionizing radiation, but uses a powerful magnetic field to align the nuclear magnetization of usually hydrogen atoms in water in the body. Radiofrequency fields are used to systematically alter the alignment of this magnetization, causing the hydrogen nuclei to produce a rotating magnetic field detectable by the scanner. This signal can be manipulated by additional magnetic fields to build up enough information to reconstruct and image the body.

The radiodiagnostic covered in this section is emphasizes in the physiological features of *Intervertebral Osteochondrosis* e.g. loss of disc height, nucleus vacuum phenomena, radial or longitudinal fissures and of *Spondylosis Deformans* e.g. osteophyte formation, and cartilaginous nodes. Finally a degenerative grading scale based on the amount of these changes will be given in order to classify the anatomy of the intervertebral discs used in this study.

a. Vacuum phenomena and disc space narrowing

As aging progresses, dehydration and loss of tissue resiliency in the nucleus pulposus and annulus fibrosus are more evident. Intervertebral osteochondrosis first appears in the form of vacuum that overlie the intervertebral disc as early as in the juvenile. These manifestations appear as linear or circular dull collections increasingly in the nucleus pulposus (Chevrot et al., 1978). On MRI scans these dull collections appear as opaque areas which are produced by the accumulation of gas in the clefts or cavities, analysis indicated that the gas is around 90% nitrogen (Ford et al., 1977). Upon extension of the spine the disc height in the anterior site increases and attracts gas from the surrounding extracellular fluid. In flexion the disc space is obliterated and the gas is reabsorbed (Knutsson, 1942), see Figure 1.36. Thus, vacuum phenomena are a reliable indicator of disc degeneration, and they are very rare in the presence of disc infection (Kroker, 1949).

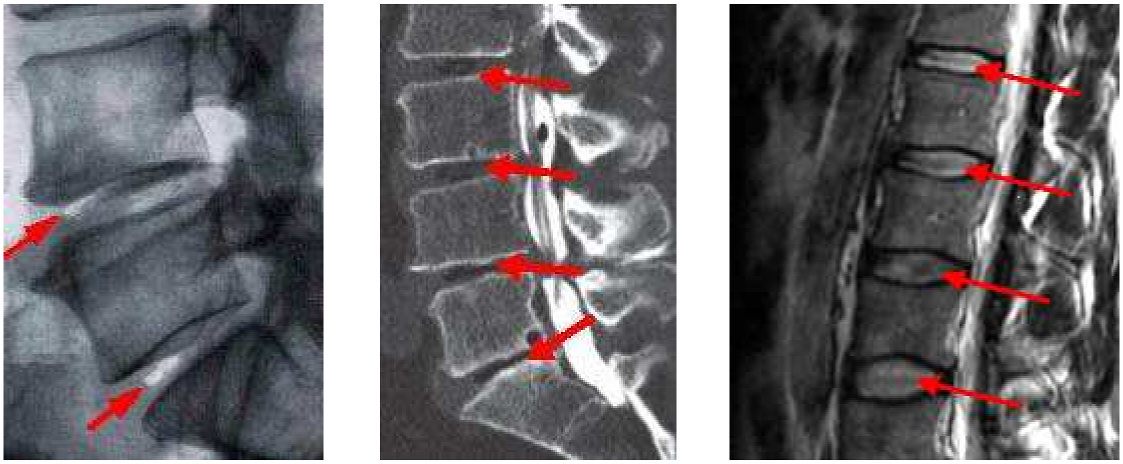

X-ray (white spot) | CT (opaque spot) | MRI (opaque spot)

Figure 1.36. Vacuum phenomena in the nucleus pulposus shown by X-ray, CT and MRI.

In the majority of patients with intervertebral osteochondrosis the dull collections or lesions are most prominent over the nucleus pulposus, although they can extend to the annulus fibrosus. However, a different significance is if an isolated opaque area is shown at the outer limit of the annulus fibrosus adjacent to the vertebral body, here is most likely the case of body fat.

As the process of intervertebral osteochondrosis progresses, the original small clefts enlarge and eventually unite one another until they involve the nucleus and annulus. As the upper body weight compresses the disc, collapse of the cavities and narrowing of disc space or height take place (Pritzer, 1977 and Bernick et al., 1982). This combination of effects produces bulging of the outer fibers of the annulus fibrosus, see Figure 1.37.

(A) (B)

Figure 1.37. Disc space narrowing. (A) Loss of disc height. (B) Disc protrusion with radial bulging.

It is apparent that vacuum phenomena is a frequent finding in the vertebral column and can be localized to the intervertebral disc or, less commonly to the vertebral bodies. In both locations, expertise of the physician or radiologist comes into play when determining the number of differential diagnostic possibilities.

b. Reactive bone sclerosis and schmorl's nodes

The presence of reactive sclerosis seen in the lumbar vertebras is preceded by disc space narrowing. At this stage also bony eburnation is characteristic (Glimer et al., 1975). Although somewhat variable in its appearance, the sclerosis is generally well defined, is linear or triangular, and extends to the intervertebral disc. Subchondral condensation of bone in both vertebral bodies bordering the intervertebral disc is typical (Battikha et al., 1981). Although they may be homogeneous, the sclerotic areas can contain radiolucent lesions of variable size that reflect intraosseous disc displacement; these lesions are termed cartilaginous or Schmorl's nodes see Figure 1.38. The pathogenesis of the sclerosis is not entirely known, but it appears to be produced by trabecular remodeling and thickening as part of the degenerative process and trabecular condensation about intraosseous sites of disc displacement (Resnick et al., 1994). The intervertebral disc displacements of varying size (term cartilaginous nodes) that are associated with intervertebral osteochondrosis are first encountered in the second decade of life and increase in frequency and extent with progressive age (Boos et al., 2002).

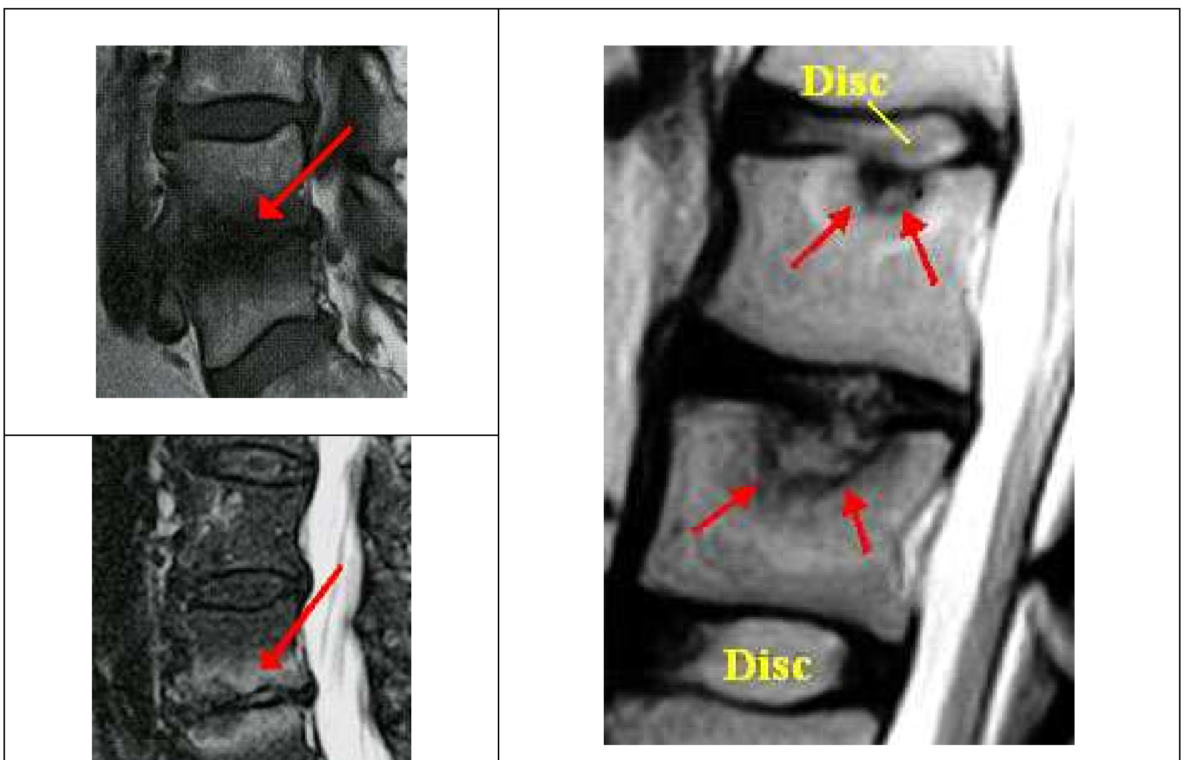

(A) (B)

Figure 1.38. Lumbar reaction bone sclerosis and intraosseous disc displacement. (A) Saggital view of vertebra and adjacent disc reaction sclerosis. (B) Schmorl's nodes.

c. Osteophyte formation

The most obvious pathologic and radiographic degenerative disease of the spine is associated with bone production, particularly in the anterior and lateral margins of the vertebral column. The outgrowths are termed osteophytes and the condition is name *spondylosis deformans*. Spinal osteophytosis is extremely common with advancing age as described by Schmorl's and Junghanns (1932) in a systematic evaluation of over 4000 spines removed at autopsy. As high as 80% of people over 50 years exhibits this excrescences and especially in patients engaged in occupations that require heavy physical labor.

The pathogenesis of spinal osteophytosis is explained by Schmorl's (1932) concept of spondylosis deformans, which is still accepted today. This emphasizes the abnormalities in the peripheral fibers of the annulus fibrosus as the initial factor of spondylosis deformans, see Figure 1.39a.

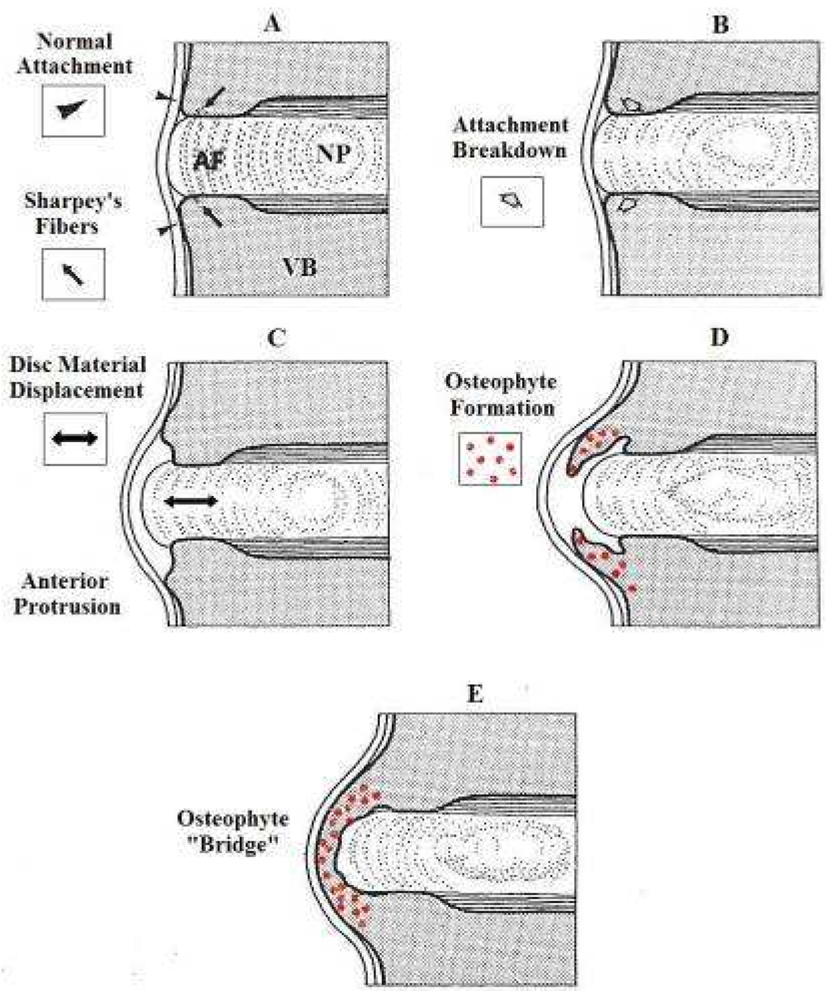

Figure 1.39. Concept and progressive stages of spondylosis deformans according to Schmorl's. AF stands for annulus fibrosus, NP nucleus pulposus and VB vertebral body. Adaptation from Resnick et al., (1994).

At this location, breakdown occurs at the site of attachment of the outer annulus fibers, including the strongly attached Sharpey's fibers, to the vertebral margin, see Figure 1.39b. This discontinuity leads to significant loss of anchorage of the intervertebral disc to the vertebral body, thereby allowing anterior and anterolateral displacement of disc material. The displacement is accentuated when the adjacent nucleus pulposus is relatively normal and saturated with fluid and thus retains most of its turgor. The separated disc tissue produces stretching and displacement of the overlying anterior longitudinal ligament and stress at the site of the vertebral attachment of this ligament, see Figure 1.39c. Osteophytes develop at these stress areas, several millimeters from the actual edge of the vertebra, where the vertebral body and cartilaginous rim unite, see Figure 1.39d. Continued body outgrowth leads to irregular osseous collections that extend first in a horizontal direction and then in a vertical direction and may eventually bridge the intervertebral space, see Figure 1.39e.

Typical appearances of osteophytes in the anterior and lateral margins of the intervertebral disc are shown in Figure 1.40. The junction between the disc and vertebra body seen in adults specimens is mostly of endocondral ossification origin in which the attachment develops during the process of transformation of calcified cartilage to osseous tissue (Francois, 1975, 1983). Endocondral ossification does not produce a strong attachment as in the case of intramembranous tissue formation where the collagen fibers anchorages deeply into the bone, these fibers are term Sharpey's.

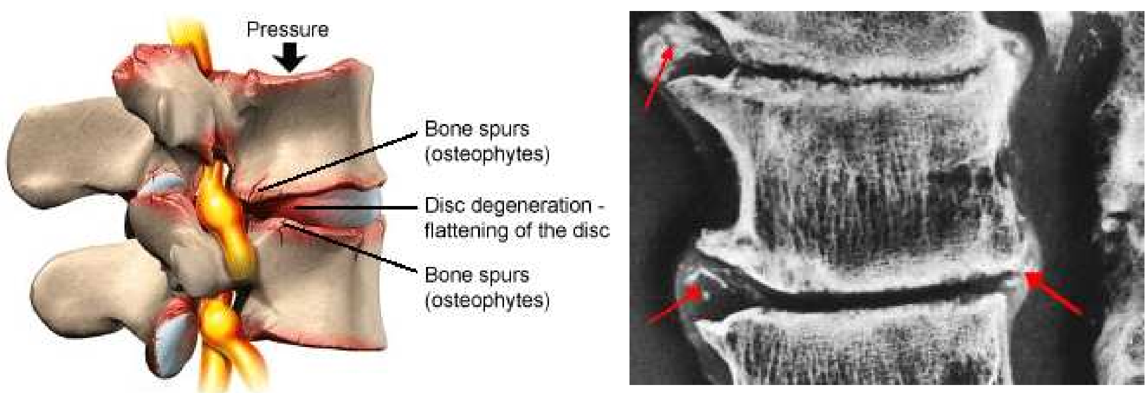

Figure 1.40. Osteophyte formation on the anterior and posterior sides of a lumbar intervertebral disc. Adaptation from Spine Universe^{R} and Adams et al., (2006).

d. Degenerative grading scale

Due to the progressive development of disc degeneration a grading scale is needed to identify and quantify the amount of damage to a specific intervertebral disc. In literature, there are over 20 different grading systems for disc degeneration covering from macroscopic anatomy and histology to plain radiography, discography and magnetic resonance imaging. In a recent review of these grading scales (Kettler et al., 2006) point out the need of usage for multiple grading scales in scoring lumbar disc degeneration for better reliability and agreement from interobservation and intraobservation. Such task will involve grading scales based on anatomy, histology and biochemistry.

A degeneration grading scale based on the photography of the disc macroscopic anatomy of 68 lumbar specimens done by Thompson et al., (1990) to distinguish the pathological features is still widely used. This scale includes involvement of the nucleus pulposus, annulus fibrosus, the cartilaginous and bony endplates, and the periphery of the vertebral body in the process of aging and degeneration. The scale suggested that a minimum of five categories would be required to accommodate the range of gross appearances encountered. A low scoring grade indicates a less degenerated disc and a high scoring grade indicates a severe degenerated disc. The five categories of Thompson degeneration scale are described in Table 1.2.

Table 1.2. Anatomical record for disc degeneration. Taken from Thompson et al., (1990).

Grade	Nucleus	Annulus	Endplate	Vertebral body
I	Bulging Gel	Discrete fibrous lamellas	Hyaline, uniformly thick	Margins rounded
II	White fibrous tissue peripherally	Mucinous material between lamellas	Thickness irregular	Margins pointed
III	Consolidated fibrous tissue	Extensive mucinous infiltration; loss of annular-nuclear demarcation	Focal defects in cartilage	Early osteophytes at margins
IV	Horizontal clefts parallel to endplate	Focal disruptions	Fibrocartilage extending from subchondral bone; irregularity and focal sclerosis in subchondral bone	Osteophytes less than 2 mm
V	Clefts extended through nucleus and annulus		Diffuse sclerosis	Osteophytes greater than 2 mm

A more detailed grading system is the one proposed by Boos et al., (2002). They develop a systematic classification of disc degeneration based on the histology report to the disc and the cartilaginous endplate. The importance of this study is that they used 180 discs from the lumbar spine and classified 9 age groups ranging from fetal age to 88 years. Evaluation included chondrocyte proliferation, mucous degeneration, cell death, tears and cleft formation, granular changes, cartilage disorganization, cartilage cracks, microfractures, new bone formation and bony sclerosis. As with other grading systems a low scoring in each category indicates low degeneration, see Figure 1.41.

Element	Evaluation	Normal = 1	Severe Degenerated = 5
Disc	Cell population	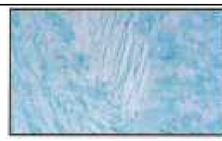	
	Clefts/tears	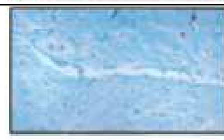	
	Mucoid substance		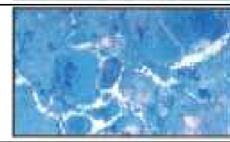
	Cell death	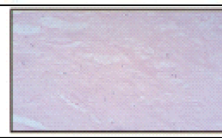	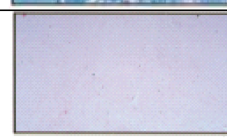
CEP	Cell population		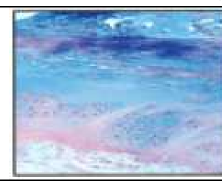
	Cartilage cracks		
	Cartilage organization		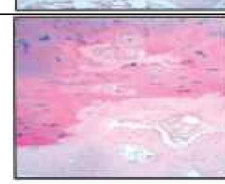

Figure 1.41. Histological classification for disc degeneration. Only shown are the normal and the most degenerated grades. Taken from Boos et al., (2002).

Their study reported an avascularization of the disc for those groups in the first decade of life, so that the nutrient supply is severely impaired with ongoing growth and enlargement of the disc. Such findings were relevant for further identification of nucleus clefts and annulus tears as early as the second decade of life, which prove contrary to the previous findings by Coventry et al., (1945, 1969) in that they appear until the fourth decade.

A very novel and practical disc degeneration grade system is the one based on medical images, one of which is assessed by magnetic resonance imaging (MRI). In MRI a series of pulses of radio waves through a powerful magnetic field are used to generate disc images. Spin echo sequence (T1) and gradient sequence (T2 relaxation) are the two techniques available. In the former anatomical inspection in-vivo is achieved and with the latter the biochemical and changes in the water content of the disc can be establish.

In the case of disc degeneration MRI can detect disc space narrowing, osteophyte formation, Schmorl’s nodes, vacuum phenomena and water content. The relevance of this technique is the clinical feasibility since these changes within the disc are only depicted with MRI and ultrasound, whereas with CT or X-ray only dense materials such as bony structures are assessable. The reliability of MRI is reported in the study done in-vivo by Pfirmann et al. (2001), in which they developed a classification system for lumbar disc degeneration, see Figure 1.42. Their results showed that intra and inter observer agreement were above 80% of over 300 discs from voluntary patients

From the previews degeneration grade scales the reader may ask: which is the suitable scale to be used? It will depend on what is to be identified. In our case we were interested in the gross and volume anatomy changes due to age and degeneration and this can be accomplished by the use of the anatomy grading scale which can be assessed with the MRI grading scale for volume inspection, see Figures 1.42 and 1.43.

While the grading system of Pfirmann et al., (2001) has a high clinical relevance the grading systems of Thompson et al., (1990) and Boos et al., (2002), in contrast , have more academic than clinical value since both systems can not be applied on patients. However, both of them are based on detailed morphological studies, allow an in depth evaluation of the disc and are therefore valuable tools to grade disc degeneration in vitro.

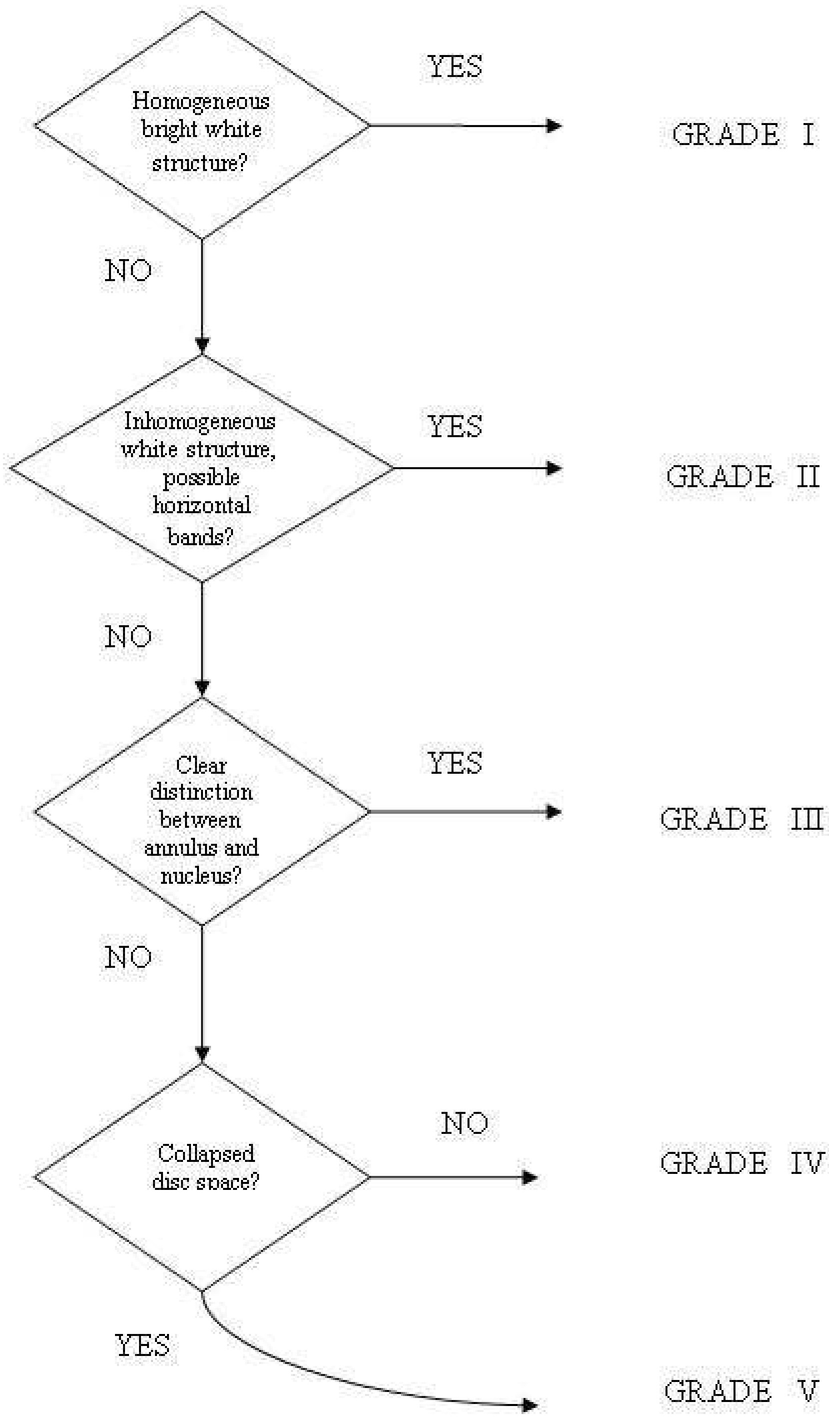

Figure 1.42. Algorithm for the grading system and for the assessment of the lumbar disc degeneration grade. Reconstruction from Pfirmann et al., (2002).

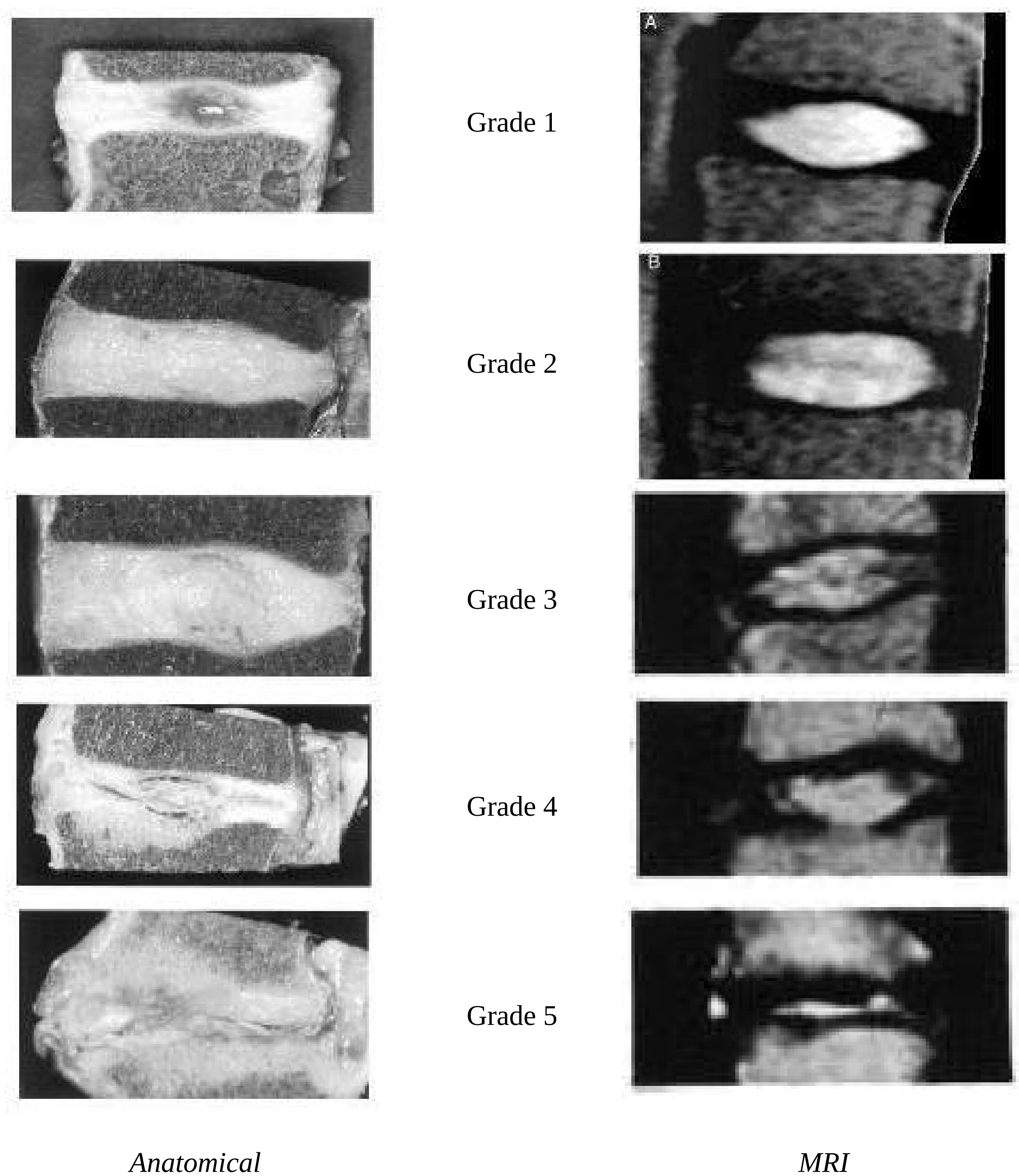

Figure 1.43. Anatomical and MRI grading scale for disc degeneration. A low scoring indicates low degeneration such as a healthy disc. Reconstruction from Thompson et al., (1990).

V. Biomechanichal studies involving spinal lumbar units

As the basis of disc degeneration has been presented it is clear that degeneration changes the biomechanical behavior of the intervertebral disc and also that of its major components: nucleus, annulus and endplate. Therefore, the biomechanical study of the disc and its components in wide range of anatomical stages is a relevant approach to quantify any change in their properties. The results have found application in the medical sciences in both the clinical and the research fields for their respective interpretations, e.g. in the treatments of back pain and related diseases, surgical procedures or in the design of medical devices or implants. Such assessments require studies done firstly to spinal lumbar units consisting of vertebra-disc-vertebra, then to individual disc components with localized dissection. It is important to distinguish the behavior of the disc as a structure from the behavior of its components alone. When conducting testing the former approach gives an overall behavior of the disc as a sole structure, while a more detailed explanation of the internal behavior of the disc components can be obtained with the latter approach. Thus, in the following the biomechanical studies involving spinal lumbar units are presented.

a. Load-deflection testing: stiffness characterization

Compression testing has been the most used loading protocol for studying the intervertebral disc mechanics. Typically, the disc is put into a loading frame where forces or stresses are applied, and the elongation or strain responses are recorded. The curve into which the load (vertical axis) against the displacement (horizontal axis) is plotted is useful for characterizing the mechanical behavior of the specimen, see Figure 1.44.

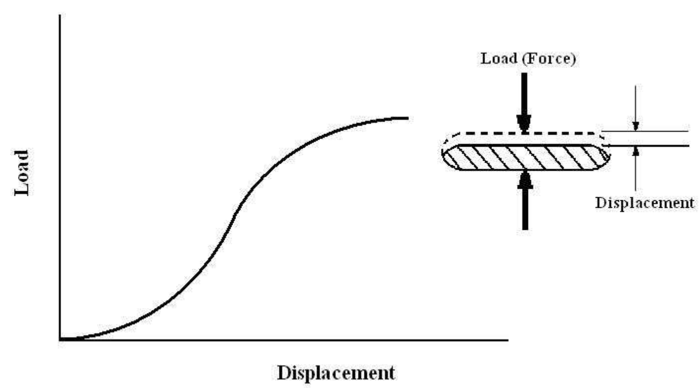

Figure 1.44. Typical load-displacement curve of a lumbar spinal unit subjected to compression loading.

Early biomechanical studies of spinal lumbar units reported the load-deflection response of the disc, and the hysteresis loop using a compression and cyclic loading protocols (Virgin, 1951; Hirsch 1955; Brown et al., 1957; Roaf 1960). These studies proposed a viscoelastic model of the disc based on the nonlinear stiffness relationship, being flexible at low loads and more stable at higher loads and also on the hysteresis shown.

The decrease of hysteresis in subsequent loading was related primarily to the imbibition of tissue fluid by the disc (Virgin, 1951), which lead to further investigation first on intradiscal pressure measurements and then on swelling properties of the disc (Nachemson, 1960).

The deformation and fracture of the spinal lumbar unit without the posterior elements under axial compression loading were studied by Brown et al., (1957); Roaf (1960) and Rolander et al., (1975) they reported that the first elements that failed were the vertebrae due to endplate fracture without failure of the disc. The failure mode was characterized by isolated fractures of one or both endplates adjacent to the disc but without separation from the bone and depended highly on the degree of bone osteoporosis and not on the degree of disc degeneration. Thus, these studies also showed the first insights of the clinical relevance of mechanical testing of the disc and vertebra by relating the type of disc failure to the loading condition.

In the axial loading condition, the disc tends to bulge in the horizontal plane but without any preferred direction, which implies that the tendency of the slipped disc at the posterolateral site, as shown by the large number of clinical cases, is not inherent to the disc structure, but to certain load conditions, other than pure compression (Brown et al., 1957; Rolander et al., 1975; Panjabi et al., 1976). Adams at al., (1996) used bending moment in flexion to show how time-related factors might affect the risk of back injury. Adams study reported the disc stiffness at different loading rates, and after sustaining loading in bending and in compression. Rapid flexion movements increase the stiffness compared with slow movements. In contrast, repeated flexion, or sustained flexion movement reduced the stiffness. Compressive creep loading also reduced the disc stiffness. The changes of such movements suggest that, in life, the risk of bending injury to the lumbar discs and ligaments will depend not only on the loads applied to the spine, but also on loading rate and loading history.

For much of the daily physiological activities the intervertebral disc is subject to compression due to muscle activity. The nucleus pulposus bears most of the compression and develops the intradiscal pressure required to stabilize (Nachemson, 1960; Tencer et al., 1982; Kasra et al., 1992). However, the annulus fibrosus is under tension and compression depending on the physiological conditions. In flexion, the instantaneous axis of rotation is perpendicular to the sagittal plane and passes approximately through the center of the disc. Therefore, the back of the disc is subjected to tensile stresses and the front of the disc is subjected to compressive stresses (Comín and Prat, 1998). From the studies of Brown et al., (1957) it was showed that the disc protrusion took place at the concave side of the column bent where compressive stresses develop. The opposite occurs in extension where the front is subjected to tensile stresses and the back is subjected to compressive stresses. In lateral flexion the instantaneous axis of rotation is perpendicular to the coronal plane and also passes near the center of the disc. In axial rotation (torsion) the tensile stresses appear at 45º to the plane of the disc. Thus, the study of the disc under flexion and torsion is of particular interest, since as noted above, pure compression loads are not sufficient to cause damage to the disc, requiring a complex combination of loads to produce prolapse.

The resistance of the disc to shearing was also investigated by Markolf et al., (1974) and Liu et al., (1975) using tangential loads to the endplate. The force and displacement of the disc in the anterior-posterior and lateral directions were insignificant to cause damage, suggesting that failure of the disc due to pure shearing is unlikely.

The load-deflection and resistance of spinal lumbar units to torsion loading were investigated by Farfan (1970). It was reported that the posterior assembly of the vertebrae bears 2/3 of the load, and the remaining load was sustained by the disc. Also, when removing the facet joints, the remaining disc showed large amounts of tears in the outer periphery of the annulus as a result of the applied torques, suggesting that the intervertebral disc alone is susceptible to shear. Adams et al., (1981) also reported that torsion of spinal lumbar units is resisted primarily by the apophyseal joint which is in compression and that torsion seems unimportant in the etiology of disc degeneration and prolapse when considering complete unit vertebral functions. Under torsion loads, larger discs and healthy ones resist more than smaller and degenerated ones respectively.

The disc flexibility, load-deflection and resistance response to flexion, extension, lateral bending and axial rotation have been characterized widely (Brown et al., 1957; Panjabi et al., 1976, 1984; Nachemson et al., 1979; Schultz et al., 1979; Adams et al., 1980, 1991, 1994, 1996; Goel et al., 1985; Miller et al., 1986; Haugthon et al., 1999; Brown et al., 2002; Patwardhan et al., 2003; Busscher et al., 2009) using off center loads applied anteriorly, posteriorly and laterally throughout custom load frames. These conditions reproduce individual spine movement when bending forwardly, backwardly and laterally. The angular deflection due to the applied load (moment) is recorded and gives the stiffness of the spinal segment and disc, see Figure 1.45. The majority of the studies aggress with the nonlinear response of the disc in the healthy state which becomes stiffer with increasing degeneration and with age. Also, most of these studies tested the hypothesis if age, sex, disc level and degeneration influence the mechanical properties of the disc. They reported that the mean behavior of the different motion segment classes sometimes differs, but these differences are seldom pronounced. Scatter in the behavior of individual motion segments were pronounced, and very often overshadow any class differences.

The axial stiffness of spinal lumbar motion segments and its relation to the applied loads, age, degree of degeneration, bone mineral content, geometry of the motion segment and degree of creep were investigated by Rostedt et al., (1998) and Koeller et al., (1986) using impacts superimposed to a static load. They reported a non linear stiffness which increases with load, bone mineral content and with creep, but there was no significant influence by degeneration and age. In other studies of the structural behavior of spinal motion segments under physiological loading, Stokes et al., (2002) and Gardner-Morse et al., (2004) obtain a linear stiffness matrix expression as an equivalent structure consisting of a truss and a beam with a rigid posterior offset (see Figure 1.46), and assess the linearity and hysteresis of the motion segments under axial load and fluid environment.

In the study by Gardner-Morse et al., (2004) the testing was to intact motion segments and also with removal of the posterior elements and reported an increase in stiffness with increase load, linearity of the load-displacement behavior and reduced hysteresis with advance degeneration. The observed fluid shifts that occurred when specimens equilibrated to changes in load were reported to be insufficient to cause changes in the loss modulus of the disc. With regard to the stiffness components, the largest stiffness occurred along the axial direction and underwent small changes between intact and altered motion segments, and was attributed to the intervertebral disc as the truss element. For the rest of the stiffness components (due to tangential displacements and rotational displacements), they reported a decreased in the stiffness with removal of the posterior elements, and were attributed to the facets and ligaments which act as beams in the equivalent structure, see Figure 1.46.

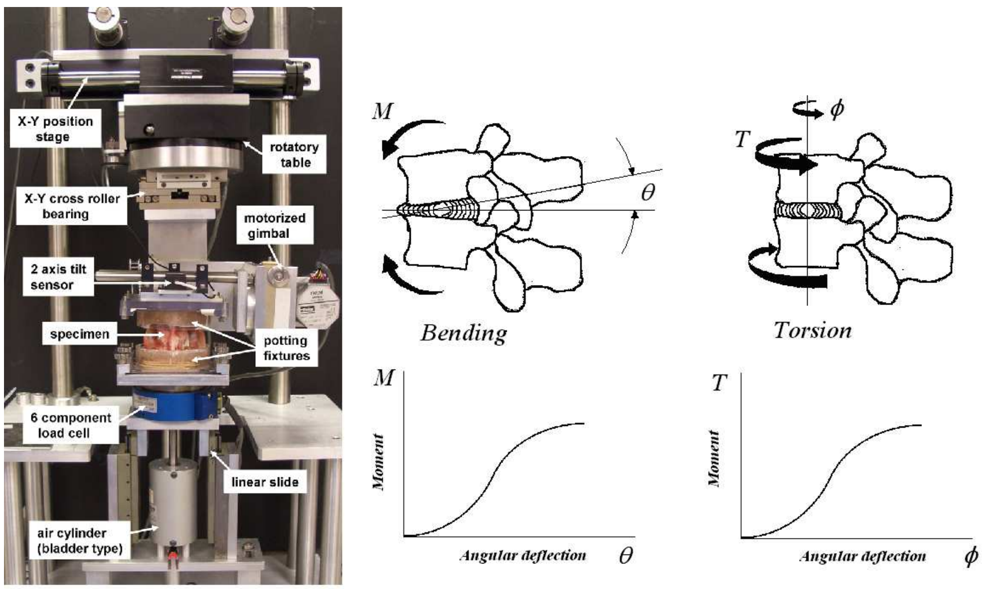

Figure 1.45. Typical loading frame for bending and axial rotation (torsion) of lumbar motion segments and the nonlinear deflection of the intervertebral disc. Adaptation from Gay et al., (2008).

Time dependence is a common feature of biological tissues (Fung, 1967). Also, soft tissues are highly anisotropic, and therefore their mechanical properties have to be measure in the three directions. A versatile testing procedure which can measure mechanical properties in various positions and directions is the indentation test. Such technique has found applications where demand of regional characterization is needed. For example, the effects of degeneration on the elastic modulus of lumbar intervertebral discs were investigated by Umehara et al., (1996) using indentation tests on both discs and polyurethane specimens to establish the relationship between the local elastic modulus and indentation properties for the latter and used it for the disc. The study reported that the elastic moduli in discs with slight degeneration were symmetric about the midsagittal plane while discs with severe degeneration showed irregular distributions of elastic moduli. Also, the values of the elastic modulus in degenerated discs were relatively higher and more various than those in slightly degenerated discs.

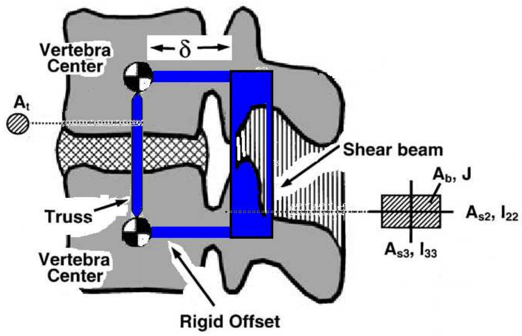

Figure 1.46. Representation of lumbar motion segment stiffness using a structure consisting of a shear beam with rigid offsets and a truss. Adaptation from Gardner-Morse et al., (2004).

For a complete review of the load-deflection studies of spinal lumbar units, see the summary in Tables 1.3 and 1.4.

Table 1.3. Literature summary of the load-deflection response of spinal unit functions to loading conditions in compression and tangential (shear) loading.

Study	***Disc stiffness (N/mm)***	***Applied load (N)***
Compression loading		
Virgin, 1951	2500	4500
Hirsh and Nachemson, 1954	700	1000
Brown et al., 1957	2300	5300
Schultz et al., 1973	1500	1000
Rolander, 1975	3000	5000
Schultz et al., 1979	800	400
Keller et al., 1987	247	253
Rostedt et al., 1998	810	500
Brown et al., 2002	400	200
Stokes et al., 2002	510	500
Gardner-Morse et al., 2004	2420	850
Transverse loading		
Markolf, 1970	260	150
Schultz et al., 1973	685	1000
Liu et al., 1975	300	450
Weis, 1975	830	950
Schultz et al., 1979	1000	980
Miller et al., 1986	115	150

Table 1.4. Literature summary of the load-deflection response of spinal unit functions to loading conditions in flexion, bending and axial rotation (torsion).

Study	***Disc stiffness (N-m/degree)***	***Applied load (N-m)***
Flexion-Extension loading		
Schultz et al., 1973	4.50	20
Panjabi and White, 1978	0.8 - 2	10
Schultz et al., 1979	1.92 – 3.55	10.6
Nachemson et al., 1979	2.03 – 3.53	10
Adams et al., 1980	1.34	10.7
Adams et al., 1996	7.3	80
Miller et al., 1986	5.51 – 7.60	70
Brown et al., 2002	2	20
Patwardhan et al., 2003	1.33	8
Gardner-Morse et al., 2004	2.04	10
Busscher et al., 2009	0.8	4
Van der Veen et al., 2010	0.8	5
Lateral bending loading		
Schultz et al., 1973	2.80	20
Panjabi and White, 1978	0.90	10
Schultz et al., 1979	2	10.6
Miller et al., 1986	4.35	60
Gardner-Morse et al., 2004	1.29	10
Busscher et al., 2009	0.5	4
Van der Veen et al., 2010	0.6	5
Axial rotation (Torsion) loading		
Farfan, 1970	2	31
Schultz et al., 1973	4.50	30
Panjabi and White, 1978	2.22	10
Schultz et al., 1979	7.07	10.6
Nachemson et al., 1979	8.48	10
Adams et al., 1981	1.44	7.4
Miller et al., 1986	10. 9	70
Haughton et al., 1999	7	6.6
Gardner-Morse et al., 2004	2.10	10
Busscher et al., 2009	2.5	4
Van der Veen et al., 2010	1.6	5

b. Creep and stress relaxation testing

A material exhibits viscoelastic behavior when their mechanical properties are time dependent, such as soft tissues (Fung, 1967). For example, if the trials of the previous sections were carried out at different speeds, we find that the stiffness values change. In particular, show an increase in the stiffness with increase loading rate. Another example of viscoelastic behavior of the spine is the fact of decreasing height of people (around 1%) throughout the day (Tyrell et al., 1985; Krag et al., 1990).

The viscoelastic behavior of the intervertebral disc is attributable to the viscoelastic nature of the collagen fibers of the annulus fibrosus, and the flow of internal fluid of the nucleus pulposus through the annulus (Virgin et al., 1951; Hirsh and Nachemson 1954; Yorra 1956; Markolf and Morris 1974; Kazarian 1975). The intervertebral disc has three typical viscoelastic properties, *creep*, *stress relaxation* and *hysteresis*. The *creep* is the tendency of a solid material to slowly move or deform "ε" permanently under the influence of stresses "σ". It occurs as a result of long exposure to levels of stress that are below the yield strength. The rate of deformation in creep is a function of the material properties, exposure time, applied load and exposure temperature. In contrast, the relieve of stress σ under constant strain ε is called *stress relaxation*. Such phenomena occur in soft biological tissues, such the intervertebral disc (Dehoff, 1978; Lin 1978) where the decay of stress tends to be nonlinear, see Figure 1.47.

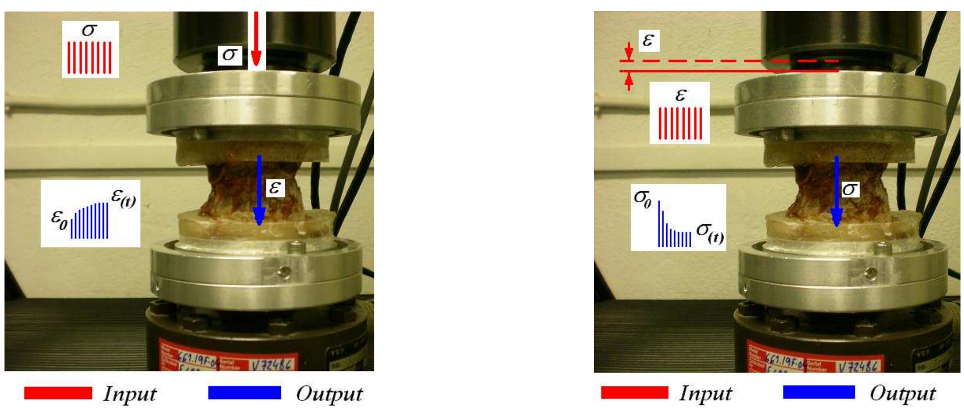

Creep

Stress relaxation

Figure 1.47. Typical set-up for a creep test (left) and a stress relaxation test (right) to a lumbar motion segment without the posterior elements.

The creep and stress relaxation characteristics of spinal lumbar units and their relation with disc degeneration using analytical and computational models were first studied by Kazarian et al., (1975); Burns, Kaleps and Kazarian, (1980, 1984) and reported a decrease in the viscoelastic effects in discs with advanced degeneration. For healthy discs, the total strain was minor and occurred at a longer period of time, implying a loss of ability to mitigate shocks and to distribute the load evenly across the endplates.

Most studies dealing with the creep and stress relaxation responses of complete lumbar unit functions parameterized the testing data using analytical models. Initially, these models were viscoelastic, where the elastic part corresponded to the stiffness of the posterior elements of the unit function and the viscous part was related to the softer disc. The mechanical model that described both behaviors contained springs for the elastic part and a dashpot for the viscous part, see Figure 1.48.

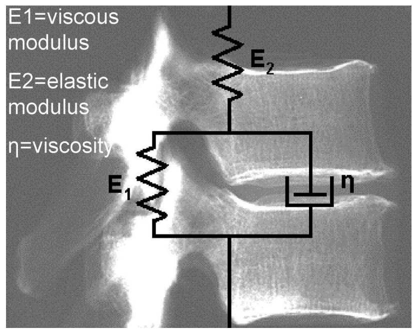

Figure 1.48. An example of a viscoelastic parametric model applied to a complete lumbar spinal function. The spring E_2 resists elastic deformation, a dashpot (η) which resists fluid flow, and a second spring E_1 which resists deformation of the “drained” structure. Adaptation from Pollintine et al., (2010).

Another approach for parameterize the testing data is to take into account the flow of internal fluid in the disc from the loading stage to the unloading. This involves intradiscal pressure studies, soil, porosity and permeability formulations that makes the treatment of the disc as a bi-phasic structure. Currently, such models involve also poroviscoelasticity and could include non constant permeability and osmotic pressure, see Figure 1.49.

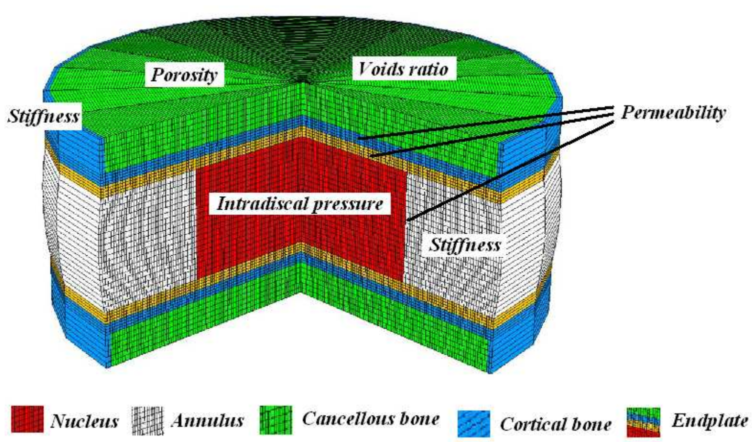

Figure 1.49. An example of a poroelastic finite element structural model of the intervertebral disc. Taken from Ferguson et al., (2004).

For a review of the viscoelasticity studies of spinal motion segments using a parameterize Kelvin solid model, see the summary in Table 1.5.

Table 1.5. Literature summary for the viscoelastic parameters (Young's moduli and viscosity coefficient) using the Kelvin solid model.

Study	*Viscoelastic parameters*	*Loading conditions*
Kazarian, 1975	Normal discs	Creep. Load applied 200 N, initial strain 5 % 5 hours.
	E1 = 3 Mpa	
	E2 = 5.5 Mpa	
	µ = 150 Gpa-s	
	Degenerated discs	
	E1 = 7.5 Mpa	
	E2 = 12.2 Mpa	
	µ = 90 Gpa-s	
Burns et al., 1984	Normal discs	Creep. Load applied 180 N, initial strain 5 % for 8 hours.
	E1 = 2.95 Mpa	
	E2 = 4.93 Mpa	
	µ = 201 Gpa-s	
	Degenerated discs	
	E1 = 8.97 Mpa	
	E2 = 11.21 Mpa	
	µ = 127 Gpa-s	
Keller et al., 1987	Normal discs	Creep. Load applied 253 N, initial strain 15% for 32 minutes.
	E1 = 7.04 Mpa	
	E2 = 1.55 Mpa	
	µ = 8.29 Gpa-s	
	Degenerated discs	
	E1 = 6.30 Mpa	
	E2 = 2 Mpa	
	µ = 6 Gpa-s	
Li et al., 1995	Normal discs	Creep. Load applied 450 N, initial strain 10% for 1 hour.
	E1 = 9.25 Mpa	
	E2 = 6.35 Mpa	
	µ = 27.4 Gpa-s	
	Degenerated discs	
	E1 = 6.63 Mpa	
	E2 = 4.29 Mpa	
	µ = 15 Gpa-s	
Pollintine et al., 2010	Normal discs	Creep. Load applied 1150 N, initial strain 2.5% for 2 hours.
	E1 = 4.57 Mpa	
	E2 = 10.43 Mpa	
	µ = 45.1 Gpa-s	
	Degenerated discs	
	E1 = 4.98 Mpa	
	E2 = 7.08 Mpa	
	µ = 30.2 Gpa-s	

c. Dynamic testing: fatigue, hysteresis and dynamic analysis

The intervertebral disc capacity to regenerated and heal is limited, therefore the study of the fatigue behavior is relevant. The typical testing of fatigue consists of applying dynamic compression and establishing the number of cycles that the disc can sustain before any cracks or tears appear, see Figure 1.50.

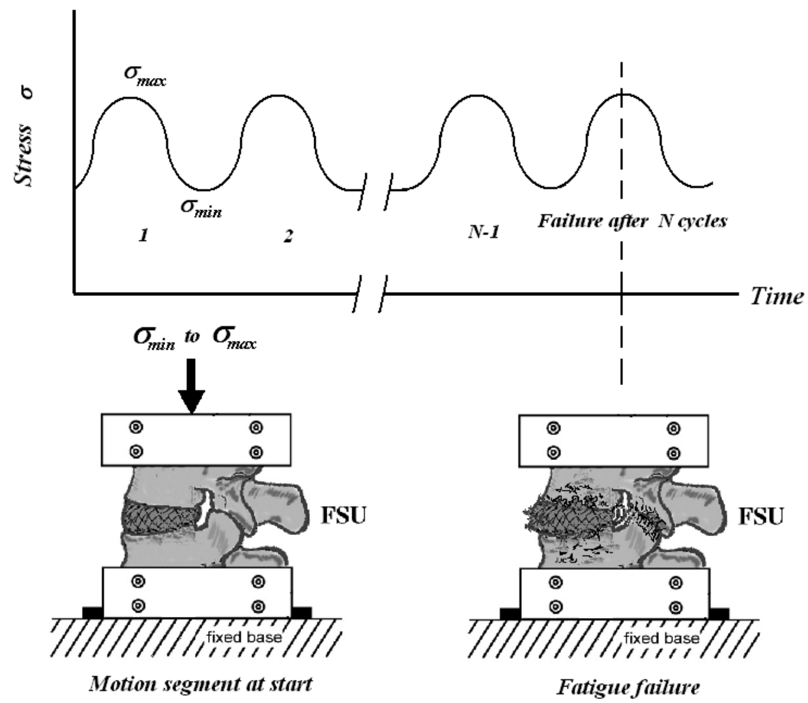

Figure 1.50. Cyclic compression load signal typically used to test a spine motion segment. Adaptation from Crisco et al., (2007).

Brown et al., (1957) conducted fatigue testing on discs, using pure cyclic compression and a combine load of axial compression with an overlap cyclic flexion. They reported a low resistance of the disc (200 cycles) against a combine dynamic loading. The initial signs of disc failure were formations of small cracks, at the posterior annulus, which eventually grew to larger ones. Additionally, the use of a combine cyclic loading, such as compression with bending or torsion is relevant for addressing epidemiologic studies on work habits, especially when heavy physical demand is involve such as construction, mining and farming. Studies have shown that jobs involving significant lifting (National Institute for Occupational Safety and Health, 1997) or frequent bending (Marras et al., 1993) are associated with increased low back disorders risk. Thus, most fatigue testing on spinal motion segments is done with dynamic combine loading.

Adams and Hutton (1985) used a dynamic loading in compression with flexion in 52 spinal motion segments from a wide range of ages. Failure of 80% of the discs occur fast with formation of annular tears (in the juvenile discs) followed by fracture of the endplate or the vertebra. Subsequent studies by Hannson et al., (1987) and Kasra et al., (1992) in lumbar spinal units also showed that the nodes of Schmorl's fracture were predominantly associated with motion segments with normal discs, and the central endplate fracture occurred in segments with moderately degenerated discs. More recently Gallagher et al., (2005, 2007) tested lumbar motion segments from elderly and juvenile spines to cyclic torsion and flexion and compare their fatigue life, and also evaluate the influence of bone mineral content on cycles to failure. It was reported that the most common failure in elderly lumbar motion segments were a combination of endplate failure, disc disruption and vertebral body fracture. In juvenile lumbar motion segments the main failure was endplate fracture and occurred in 2/3 of the discs. Thus, compared with the older motion segments, the middle-aged motion segments exhibited increased fatigue life, which they associated with the increased bone mineral content in younger motion segments. Increasing bone mineral content had a protective influence with each additional gram increasing survival times.

Hyteresis is a dissipation of energy from deformation, it happens when the spinal motion segment is submitted to continuous cycles of loading and unloading. The resulting nonlinear load-displacement curve, which has a large hysteresis loop, gives the tendency of the disc to dissipate energy. This phenomenon occurs when a person jumps; the energy of the impact is absorbed in its transmission from toe to head by the discs and the vertebrae due to hysteresis. Thus, this phenomenon suggests a protective nature of this mechanism (Comin et al., 1998).

Early studies on the phenomenon of hysteresis in lumbar motion segments and intervertebral discs corresponded to Virgin (1951). He used compression load and carried out cyclic and creep testing to spinal motion segments. The study reported that hysteresis varied with load application, with age of the discs and with lumbar level. For larger loads or faster rates of application the hysteresis was more evident, being also greater in younger discs. In lower lumbar discs the hysteresis was also more relevant than the rest of the spine levels. He suggested that the recovery of the disc after deformation depended upon the imbibition of tissue fluid by the disc and by the removal of the deforming force, and that complete recovery of the disc depended on the duration of the force.

Kazarian (1975) reported that the creep recovery rate decreased as time increased. In general, the relative amount of recovery and hysteresis was found to be greater after a short creep test than after a long one. He also showed that the hysteresis response of the disc between successive tests differs from that when the disc is allowed to recover before the next load is applied. In successive tests the disc continuously dissipates energy, indicating that the mechanical efficiency of the disc increases with used. While for testing with a recovery period, the energy loss was less during the unloading phase, suggesting also an influence of fluid redistribution within the disc. In another biomechanical study of the intervertebral disc subjected to dynamic compression Koeller et al., (1986) emphasized that a multiple regional assessment of water content, biochemical composition, structural changes of the collagen fibers, the proteoglycans, and the fibrilar framework was necessary to better address the influence of age and degeneration on the viscoelastic state and hysteresis response of intervertebral discs subjected to dynamic compression. On a posterior study of fatigue strength of intervertebral discs by Hansson et al., (1987) they showed that the hysteresis loops at equilibrium and failure were more marked in motion segments with degenerated discs than with normal discs corroborating with the previous studies. The relevance of the posterior elements of spinal motion segments with regard to the biomechanics of jumping and twisting was addressed by Asano et al., (1992). They used cyclic compression and torsion loading to measured the hysteresis and stiffness response of lumbar spinal units with and without the posterior elements and reported that the posterior elements contributed around 30% in compression and around 55% in torsion of the total hysteresis of the intact motion segment. In general, it has been reported that the proportion of energy dissipated in hysteresis is lower at increased loading rates and that it increase with decreasing loading rates (Race et al., 2000). More recently Costi et al., (2008) study the frequency-dependent behavior of the intervertebral disc in response to dynamic loading done in the three translations and three rotations (six degrees of freedom) using frequencies below 1 Hz. They suggest that the degrees of freedom (compression, lateral bending, flexion and extension) should have large poroelastic (fluid flow) effects, and that the degrees of freedom (anterior/posterior/lateral shear and axial rotation) should exhibit primarily intrinsic (solid phase) viscoelastic behavior. Their report showed that the time-dependent energy storage and energy absorption by the intervertebral discs results from both flow-dependent solid-fluid interactions (poroelasticity) and intrinsic (solid phase) viscoelasticity. As with previous studies, the stiffness increase and phase angle decrease with frequency, and these differences were greater for deformation modes in which fluid flow effects were thought to be greater.

Other parameters that can be obtained with dynamic loading to the disc are the dynamic stiffness and the dynamic modulus given by the storage and loss moduli. In dynamic loading, the viscoelastic behavior of the disc can be described in terms of its elastic component given by the storage modulus, and by its viscous component given by the loss modulus. The phase lag between stress and strain, which gives an indication of the tendency of a material to dissipate energy, is used to determine the dynamic modulus. Several studies investigating the disc response to cyclic loading, mostly in compression reported varying results. Hannson et al., (1987) correlated the segment stiffness with disc degeneration, age and segment bone mineral content. Kazarian at al., (1975); Koeller et al., (1984); Race et al., (2000); and Costi et al., (2008) concluded that intervertebral disc compressive mechanical properties under dynamic loading are significantly dependent on loading rate and hydration. For a review of the studies involving dynamic compression testing to spinal motion segments see Table 1.6.

Table 1.6. Literature summary for the dynamic parameters (Dynamic modulus, dynamic stiffness and Hysteresis) using a sinusoidal wave front.

Study	*Dynamic stiffness (N/mm)*	*Loading conditions (N)*
Koeller et al., (1984)	*1800*	*450*
Kasra et al., (1992)	*1500*	*300*
Li et al., (1995)	*2400*	*450*
Brown et al., (2002)	*300*	*200*
Izambert et al., (2003)	*250*	*400*
Costi et al., (2008)	*5141*	*1285*
Study	*Dynamic modulus (MPa)*	*Stress conditions (MPa)*
Koeller et al., (1984)	*22*	*0.8*
Hansson et al., (1987)	*25*	*1.5*
Ohshima et al., (1989)	*25*	*1.5*
Li et al., (1995)	*15*	*0.4*
Holmes et al.,(1996)	*20*	*1.3*
Race et al., (2000)	*16*	*0.8*
Costi et al., (2008)	*34*	*0.9*
Study	*Hysteresis (Joules)*	*Loading conditions (N)*
Virgin (1951)	*0.50*	*1100*
Kazarian (1975)	*0.25*	*900*
Koeller et al., (1986)	*0.25*	*950*
Hansson et al., (1987)	*0.63*	*2000*
Asano et al., (1992)	*0.15*	*1000*
Li et al., (1995)	*0.11*	*450*
Race et al., (2000)	*0.16*	*450*
Brown et al., (2002)	*0.10*	*100*
Costi et al., (2008)	*0.55*	*2000*
Gay et al., (2008)	*0.50*	*1500*

VI. Constitutive models of the intervertebral disc

a. Viscoelasticity models

The prominence of viscoelastic behavior in the intervertebral joint, as suggested by the biomechanical studies of Virgin (1951), Hirsch and Nachemson (1954), Markolf and Morris (1974), Kazarian (1975) and others, prompted analytical modeling efforts by Kazarian and Kaleps (1979), Burns and Kaleps (1980, 1984) and Sanjeevi (1982). In the latter study by Burns and Kaleps, they recognized viscoelastic characteristics in compressive deformation-time data reported and employed a Kelvin body model with two, three and four parameters (springs and dampers) in a series-parallel arrangement to simulate the creep behavior of the disc under compression. In this theoretical model consisting of ideal elements, the linear springs with *stiffness K* represent the elastic part and the shock absorbers with a *viscosity μ* represent the viscous behavior, see Figure 1.51.

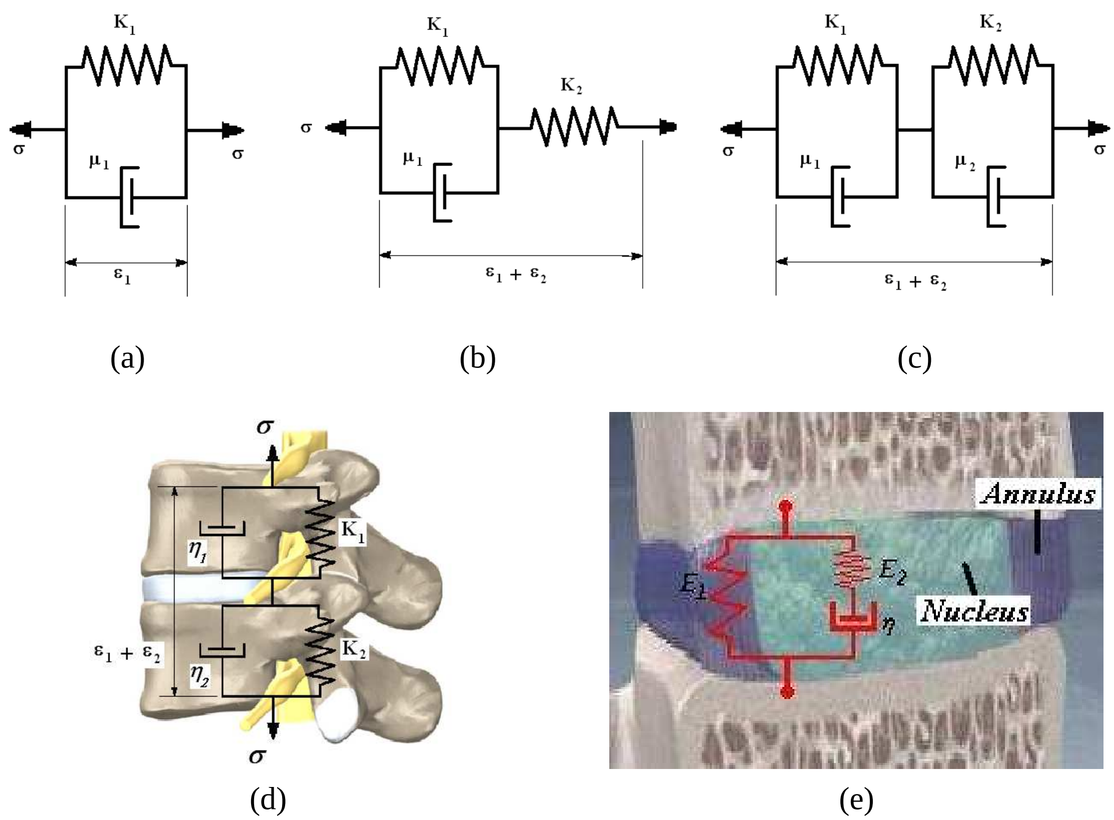

Figure 1.51. Kelvin solid model with (a) two parameter, (b) three parameter, and (c) four parameter used to study the viscoelastic effects of (d) the lumbar spinal unit and (e) the intervertebral disc (Burn and Kaleps, 1984).

The mechanical properties (Young's moduli and viscosity coefficients) associated with the Kelvin solid model (see Figure 1.48) were also characterized using a classification of experimental creep curves in which features of disc degeneration (Schmorl's nodes, cleavage fractures, Scheuermann's disease) were taken into account, see Table 1.4.

The in vitro creep behavior of lumbar motion segments subjected to static axial compressive and dynamic loading can be found in the studies by Keller et al. (1987) and Li et al. (1995). In the former study they used the Kelvin linear viscoelastic model and reported the compressive material constants (moduli and viscosity coefficients) for each disc using a linearization method based on a Taylor series expansion of experimental data, see Table 1.4. The motion segments from older and more degenerated lumbar discs were less stable and had lower material constants than segments from younger and less degenerated discs. No correlation between the creep characteristics and disc height, disc area, segment level, or sex was reported. In the latter study they investigate the disc properties related to stress relaxation, dynamic modulus, and hysteresis and reported that the parameters of the Kelvin solid model were influenced by the disc level and degree of degeneration in lumbar discs. The time of relaxation, dynamic stiffness and dynamic modulus decreased with increasing disc degeneration in lumbar discs, indicating that the equilibrium state will be reached faster in lumbar discs with moderate-severe degeneration as compared to mildly degenerated discs. The Increased disc degeneration reduced the value of the dynamic modulus in lumbar discs by up to 40% (Li et al., 1995). With regard to hysteresis, they reported a correlation with disc degeneration but not with frequencies (range tested between 0.01 and 1 Hz).

Burns, Kaleps and Kazarian (1984) reported that the two-parameter-solid model gave poor prediction of the observed compressive creep behavior of normal spinal segments; although, it may be a reasonable model for simulating creep characteristics of diseased spinal segments, such as degenerated discs. Also, the Young's moduli and viscosity coefficient resulting from the three-parameter-solid model analysis were optimum, while prediction of the observed strain-time behavior immediately following initial loading were best achieved using the four-parameter-solid model. Similar results were obtained by Li et al., (1995); Holmes et al., (1996); and Rostedt et al., (1998) indicating that the standard linear solid model was able to qualitatively simulate the effects of disc level and degeneration on the ability of an intervertebral disc to resist both prolonged loading and low-frequency vibration. However, the model underestimated the stress relaxation, dynamic modulus and hysteresis of lumbar discs subjected to low-frequency vibration. Moreover, the strength of the model predictions decreases with increasing frequency.

Recently, van der Veen et al., (2008) quantified the separate contributions of vertebral bodies and intervertebral discs to creep of a lumbar spinal segment in compression. They showed that the endplate contributes significantly to the creep of a single vertebra and that the vertebral body contributes to the creep of a segment. Creep deformation of a complete motion segment is thus determined by the behavior of the bone, the endplates, the annulus and the nucleus. Each part has a separate time scale. Creep of bone is present during the early creep phase; however, it is small compared to creep of the endplate. Creep of the endplate was substantial during the early creep phase and finally creep of the soft tissue of nucleus and annulus dominates the late creep phase.

Stress relaxation is common feature in viscoelasticity; the decay of stress with time is a measure of the disc ability to mitigate loads. Panagiotacopulos et al., (1987) conducted experimental tests to establish the viscoelastic response of the disc and in particular the relaxation response of the nucleus and annulus. Using the testing data they suggest a phenomenological model of the disc that considers the water content of both the annulus and the lamellae. A master relaxation curve was proposed, and they found that the short term master curve for the lamellae of the annulus and the nucleus were similar, whereas the long term rubbery plateau is different between the lamellae and the nucleus. Also they reported sensitivity between changes in water content in the disc tissues and the corresponding time domain in the relaxation curve. The relaxation modulus of the disc was reported by averaging the properties between the annulus and the nucleus. The model was then used for studies of Schmorl's nodes of degenerated discs and for circumstances in which hydration is important.

Holmes et al., (1996) used compression loading to investigate the load-relaxation response of lumbar motion segments and the ability of the disc to dissipate energy. Using a Kelvin model with four parameters, and Fourier transformations of the load-relaxation curves they showed a gradual increased in the storage modulus and a gradual decrease in the loss modulus for frequencies in the range of 0.1 Hz to about 5 Hz suggesting that at these frequencies the lumbar spine cannot function as a shock-absorber in pure compression, and its most likely that a bending load (mainly in flexion) is associated with disc dissipation at these frequencies. However, no study of load relaxation using flexion was reported.

The effects of frozen storage on the creep and stress relaxation behavior of human intervertebral discs has been investigated in the past (Galante, 1967) and more recently by Dhillon et al., (2001) in both studies they reported no significant effect of freezing on the elastic or creep response of the discs. Dhillon at al., (2001) suggest that freezing for a reasonable time with good packaging may produce subtle effects, but these potential artifacts do not appear to alter the discs time-dependent behavior in any consequential way. However, the degree of pre-existing degeneration had a significant effect on the compressive creep response, with the more degenerated discs appearing more permeable, according to the fluid transport model used to parameterize the creep data.

Thus, from the previous studies it is generally accepted that the Kelvin solid viscoelastic model is particularly suited to describing static creep behavior. However, in the general case of axial and dynamic loading, these models which are based on loading rates variations cannot explain or account for the interactions of the other experimentally demonstrated intervertebral disc phenomena: the poroelastic flow of water that has been observed in association with creep in the disc (Simon et al., 1985; Iatridis, 1996; Race at al., 2000) and the considerable swelling pressure that the nucleus has been shown to generate (Nachemson, 1960). Thus, the use of a fluid transport model with a validation phase is suggested by the above studies.

b. Fiber-reinforced, incompressible fluid and strain energy models

One of the first studies of disc modeling characterized the disc in relation to the basic behavioral equations of its elements. Broberg et al., (1980) modeled the disc with cylindrical symmetry, a nucleus pulposus consists of an incompressible fluid, and 11 layers in the annulus with inclined fibers alternately, see Figure 1.52. With this model, the behavior under axial compression load was studied; reported values of intradiscal pressure, fibre strains and disc protrusion were adjusted to the experimental values and a good approximation was obtained. However, the absence of layer interconnectivity in the model limited its use to compression loading, and further geometrical modifications to the disc shape, annulus structure and endplate curvature were added to analyze the general case of loading such as bending in combination with torsion (Broberg, 1983).

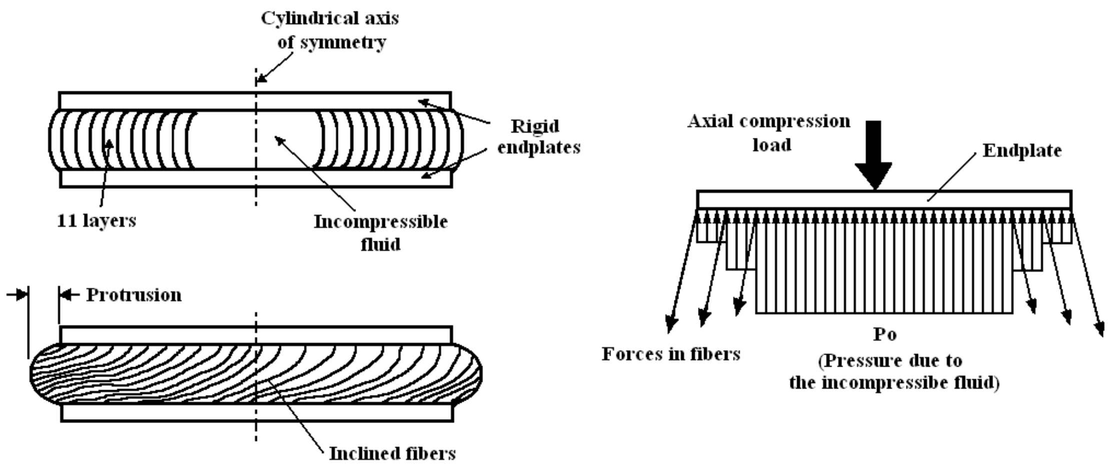

Figure 1.52. Theoretical and physical model of the intervertebral disc developed by Broberg and Von Essen, (1980).

To take into account the annulus fibrosus behavior, a mathematical description is required, yet is particularly difficult to achieve due to tissue nonlinearity and anisotropy. To facilitate disc model development, the tissue is generally either represented as a composite with discreet collagen fibers embedded in an isotropic matrix or as an orthotropic continuum.

Examples of the first representation include thick wall pressure vessel theory applied to develop a model for the structure of the annulus fibrosus and the function and failure of the intervertebral disc (Hickey and Hukins, 1980). The model explains the observed function and failure of the disc in compression, torsion, and bending; the model was based upon the observed arrangement of collagenous fibers in the annulus which were considered to have the same mechanical properties as tendon; thus the stress required to produced a given deformation and which irreversibly damage the fibers was predicted. The annulus was treated as isotropic material and the nucleus consisted of an incompressible fluid, see Figure 1.53.

Fiber composite strain energy theory has been used to model the disc mechanics (Wu and Yao, 1976; Klisch and Lotz, 1999) and the membrane theory (McNally et al., 1995). The former theory gives a model which is suitable for fiber stress analysis in axial compression, such as for strips of annulus under tension. In the latter theory, the disc model is treated as an axially symmetric structure comprising a fluid filled centre, retained by a thin, doubly curved, fiber reinforced membrane under tensile stress.

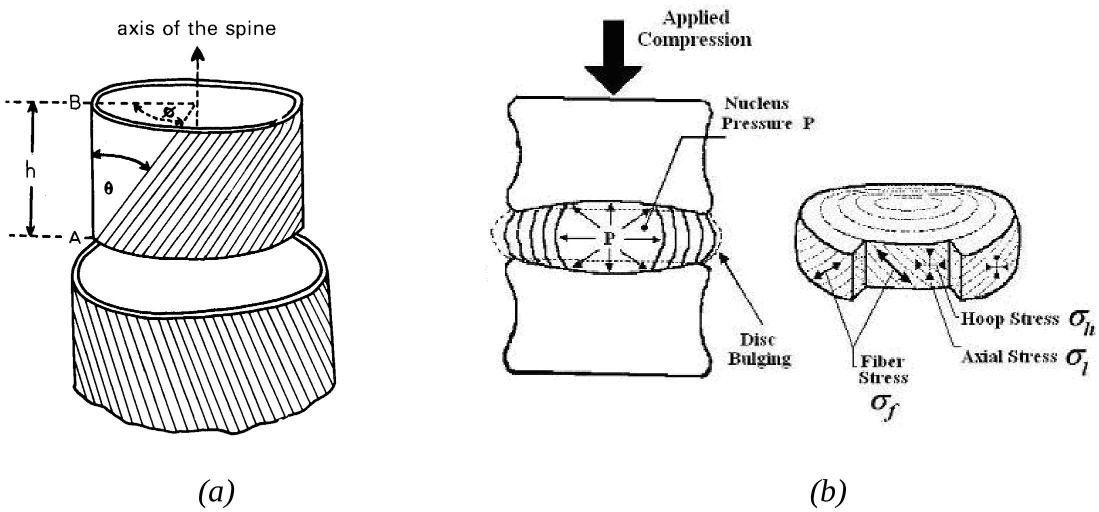

Figure 1.53. (a) Arrangement of consecutive lamellae of the annulus fibrosus. (b) Stress directions according to the theory of pressure vessels. Extraction from Hickey and Hukins, (1980).

In the strain energy theory, a strain energy function is develop to represent the different interactions of the disc tissues (Wagner et al., 2004; Gundiah et al., 2007). Fiber-reinforce strain energy models incorporate annulus fibrosus microstructure as a homogenous continuum, where fibers are represented as directional unit tensors (Wu and Yao, 1976; Klisch and Lotz, 1999). Thus, fiber-reinforce energy models have provided insights into the structure-function relationships of the tissue (e.g., evaluating the role of fiber-matrix interactions, fiber-fiber interactions and crosslinks). One advantage of these models is they do not required input of the currently unknown isolated fiber and matrix properties and volume fraction. Some limitations of these models include many invariant terms which can be combined into a large number of permissible energy functions. Therefore, knowledge and a good selection of the more important invariants and the appropriate energy formulations are needed to judge the wide range of model descriptions. Additional limitations include difficulties in uniquely determining the material properties and interpreting the physical significance of the mathematical expression. These limitations in energy models suggest the need for additional evaluation of annulus fibrosus tissue mechanics.

The example of the fiber-reinforce model of the disc by Wagner et al., (2004) used a strain energy function with separate terms to represent the matrix, the fibers, and the interactions between the disc constituents, and applied to tensile and compressive stress-strain data of the annulus in the circumferential, radial and longitudinal direction. Thus, giving a comprehensive formulation for the multiaxial annular elastic behavior and for elucidating structure-function relationships of the annulus fibrosus, as its physical properties are critical to the intervertebral disc's biomechanical function.

An example of a model of the disc using the membrane and strain energy theory is given in Figure 1.54. The annulus fibrosus consisted of two lamellae reinforced by oppositely oriented collagen fibers that were free to follow paths defined by the cross-ply tyre model, which represents a plane stress state, see Figure 1.54. The behavior of the disc under compression was also studied using this model; calculation of the membrane surface shape, fiber path and angle, fiber loads, volume of disc, and area of annulus were in reasonable agreement with published experimental studies.

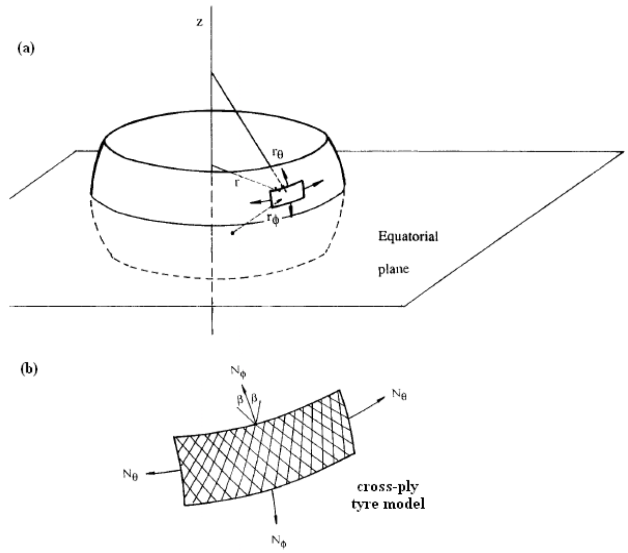

Figure 1.54. (a) Schematic diagram of the coordinate system used in the mathematical model by McNally at al., (1995) using membrane theory. (b) Schematic diagram showing definitions of fiber angle β and the two membrane stress resultants N_ϕ and N_θ.

Another approach to model the intervertebral disc is the homogenization theory (Bensoussan et al., 1978; Sanchez Palencia and Zaoui, 1987; Jones, 1999). This theory describes the effect of microstructure on macroscopic material properties by assuming the material is composed of repeating representative volume elements. An example of this theory can be found in the study by Yin et al., (2004). A homogenization model of the annulus fibrosus for prediction in plane single and multi-lamellae annulus properties: tensile moduli in the longitudinal and circumferential directions and the shear modulus were developed. The predictions of the model were consistent with measure values, and the parametric analysis showed strong relationship between matrix modulus and tensile module, which in turn suggest the contribution of the matrix in annulus load support, which may play a role when proteolysis are decreased in disc degeneration, and also be an important design factor in tissue engineering.

c. Constitutive models of fluid transport: pore pressure, poroelasticity, poroviscoelasticity

In the last two decades, there has been an increasing interest in modeling soft tissues, such as the intervertebral disc, as saturated porous media where pore fluid moves through the voids until equilibrium state is attained under a given applied load. These kinds of models are referred as poroelastic formulation and take into account the flow of internal fluid in the disc. The poroelasticity theory was proposed by Biot (1941), later refined by Rice and Cleary (1976), as a theoretical extension of soil consolidation models developed to calculate the settlement of structures placed on fluid-saturated porous soils. It is a theory that models the influence of solid deformation on fluid flow (and vice versa). A load applied to a block of fluid-saturated porous elastic material will be carried partly by the solid and partly by the fluid. As the fluid is forced from the pores, the solid material will carry an increasing portion of the load. The mechanical behavior is, therefore, governed both by the elastic deformation of the solid and the flow of fluid in the pores. In essence, poroelasticity replaces de biphasic fluid-saturated solid with a single-phase material whose behavior matches that of the two phases acting in concert (Goulet et al., 2008).

A number of linear poroelastic model studies of the intervertebral disc have been performed (Laible et al., 1993; Simon et al., 1985a, b). In these early studies, the disc annulus was simplified as being isotropic. However, composite theory has been used to address appropriately the complex structure of the annulus fibrosus morphology (Argoubi and Shirazi, 1996) and quantify the elastic, osmotic and viscous contributions of the annulus fibrosus to the overall behavior of the intervertebral disc (Huyghe et al., 2003), see Figure 1.55. Also, poroelastic formulation has been used to study the coupling of bone fluid flow and mechanical deformation of the trabeculae (Cowin, 1999; Goulet et al., 2008) and cartilage modeling (Shirazi et al., 2000).

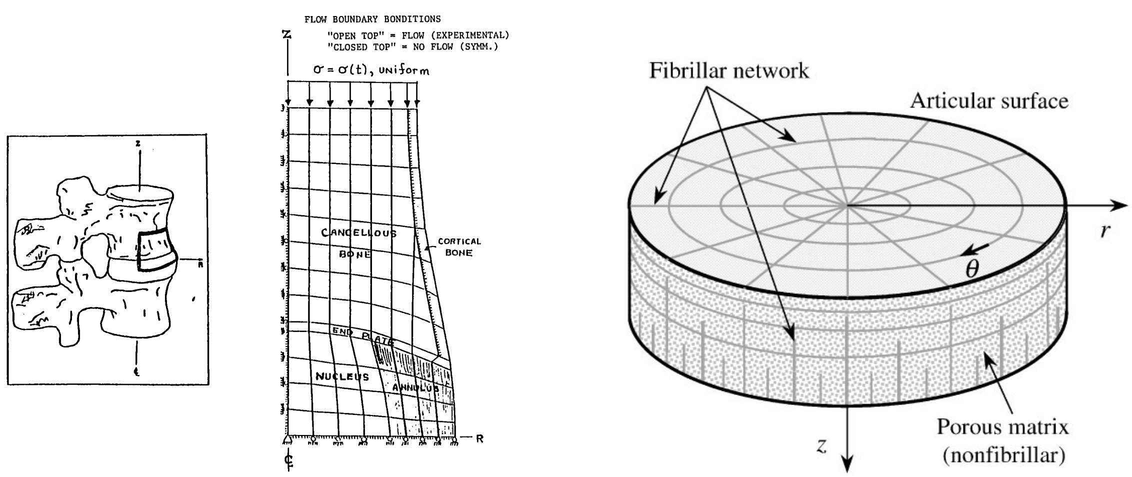

Figure 1.55. Intervertebral disc and cancellous bone mesh modeled as poroelastic material taken from Simon study (left) and Shirazi study (right).

The creep response of the intervertebral disc has also been studied using poroelastic models (Rostedt et al., 1998; Palmer et al., 2004). Using a Burger fluid model they related the creep response with the non linear stiffness of the lumbar motion segments and reported an increase in stiffness with creep. Additionally, they characterized the in-vitro compressive creep properties of normal and degenerated discs using a fluid-transport model, and reported that degenerated discs became less stiff and crept more. The model results suggested that the increased creep response was mainly due to a diminished strain-dependent nuclear swelling pressure. They noted that the calculated tissue properties varied with the applied load magnitude and rate for both normal and degenerated discs.

In the foregoing analytical models an understanding of the principles of disc mechanics was given by simplifying the geometry and modeling the disc as a complete structure with a few boundary conditions and assumptions. However, in instances where the geometry of the disc is important, then numerical models, such as the finite element is a better alternative. Here the disc is modeled as a summation of many simple units and consequently many boundary parameters and assumptions, but can have highly complex and realistic geometry, for this matter some of the relevant finite element studies with lumbar motion segments are presented next.

VII. Finite element simulation of intervertebral disc degeneration

In this section the simulation response of loading spinal motion segments with normal and degenerated discs using the finite element method (FEM) is presented. Finite element models generally have components representing areas of the disc and the vertebrae, but the exact way these are modeled varies widely between models. The nucleus pulposus is normally modeled as an inviscid incompressible liquid (Shirazi-Adl and Drouin, 1987). The annulus fibrosus has been represented by: linear, elastic orthotropic elements (Spilker et al., 1986); non-linear cable elements embedded in a ground matrix (Rao and Dumas, 1991); hyper-elastic bar elements in a ground matrix (Natali, 1991) and anisotropic membranes in an isotropic, homogeneous matrix (Shirazi-Adl, 1989). Similarly, the properties of vertebral cortical and trabecular bone have received a wide variety of treatments. Fluid flow and porosity within the elements have also been used in an attempt to model the visco-elastic behavior of motion segments (Simon et al., 1985). All these models are highly dependent upon their choice of the material properties of the various elements (Rao and Dumas, 1991) most of which have to be estimations. Additionally, when medical imaging techniques are not available, the relative sizes of the different areas of the disc, fiber orientations, etc. are usually derived from morphological investigations of disc structure based on sectioned, unloaded (Cassidy et al., 1989) and dehydrated (Marchand and Ahmed, 1990) motion segments; the artifacts introduced in this way undermine the superficial anatomical accuracy of many models.

Most FE studies dealing with disc degeneration carry out a stress-strain analysis of the intervertebral disc in response to applied external loads. The type and role of the loading used in the simulation is a simplification from the one in reality. In vivo, the loading on a disc is a complex combination of nonlinear distributions that are applied statically or cyclically, and clinically are associated with heavy physical work, lifting stationary work postures and vibrations, which lead to disc degeneration and are difficult to reproduce in vitro. Thus, these loads are often simulated as occurring singularly and with a single cycle and neglects complex loading conditions (Natarajan et al., 2004). Initial models included nonlinear and viscoelastic formulations which were further implemented and developed to include poroelastic and poroviscoelastic formulations to better address disc functionality e.g. intradiscal pressure and nutrient supply.

a. Studies with material and geometric nonlinearity: Single loading simulation

When the stress of a tissue surpasses its strength, failure occurs. Therefore, in order to understand the mechanism of disc failure, we must know the type, direction and magnitude of the stresses generated in response to the applied loads, one at a time. In general, the determination of the stress-strain state inside the intervertebral disc is an arduous task that has been treated by numerous studies involving mathematical models which includes the finite element method.

Early finite element studies of stress analysis in healthy and degenerated discs included models with axisymmetry, linear (Belytschko et al., 1974), and nonlinear with an incompressible hydrostatic fluid (Kulak et al., 1976). Both studies used axial compressive load and hypothesized a plane stress condition in the laminae, and thus proposed an orthotropic formulation for the annulus fibrosus, see Figure 1.56. In the second study the nucleus was formulated as incompressible. In both studies degeneration was simulated in two ways: denucleation due to desiccation, and radial tears in the annulus fibrosus. In the former, the nucleus was modeled as a void while the material properties of the annulus fibrosus were assumed to be unaltered. In the second case, the annulus was modeled with a reduction of the effective elastic modulus in the fiber direction. Belytschko et al., (1974) reported the effects of material properties and geometry on the stress-distribution and intradiscal pressures. They showed that: (1) an adequate representation of the disc behavior requires the inclusion of material anisotropy; (2) material properties of the annulus obtained by direct measurements underestimate the stiffness of the material; (3) reasonable predictions of variations of disc stiffness with vertebral level can be made on the basis of geometry; and (4) degenerative changes associated with loss of elasticity had little effect on the intradiscal pressure, while annular tears result in reduced pressure and are in agreement with clinical observations. Additionally, the model by Kulak et al., (1976) predicted that hoop or tangential stresses were dominant in lumbar discs over thoracic discs and that the change in the load-deflection curve produced by annular tears was not as drastic as that produced by denucleation. Thus, the decrease of computed stiffness when the nucleus is absent, lead to suggest that the nucleus plays a significant role in carrying compressive axial loads.

Parametric studies have been used to examine the effects of gross disc geometry and material property parameters on the predicted response of the disc: intradiscal pressure, disc bulge, vertical deflection, etc. under compressive loading (Spilker, 1980) and complex loading (Spilker et al., 1984). If significant effect of parameters on disc response occurs, then this can help to explain the wide scatter often observed in raw experimental data.

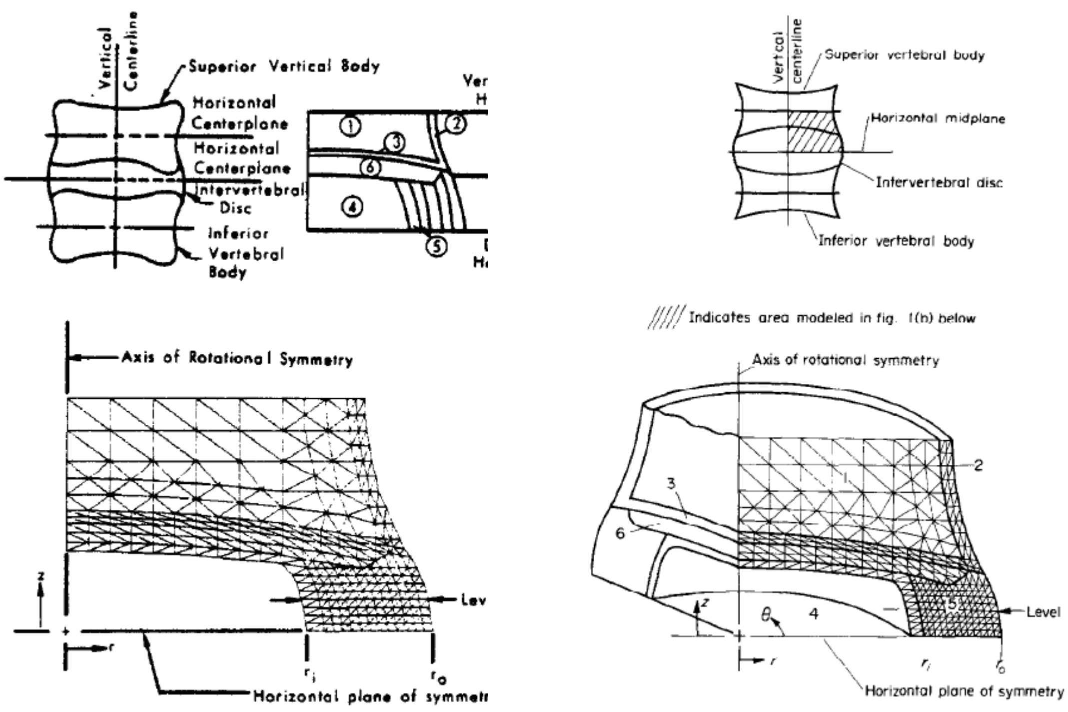

(a) *(b)*

Figure 1.56. Two dimensional finite element models of the intervertebral disc (fine mesh) and the vertebral bodies (coarse mesh) assuming the conditions of plane stress and orthotropy for studying compressive loading, (a) linear model taken from Belytschko et al., 1974, (b) nonlinear model taken from Kulak et al., 1976.

Three-dimensional finite element models of the intervertebral joint for tested specimens were developed to study the behavior of the intervertebral disc under direct shear (Liu et al., 1975) and axial compressive load (Lin et al., 1978). Both studies reported parametric studies of the material properties of the annulus fibrosus, and showed that in the lumbar region, the Young's and Shear moduli decrease linearly as a function of the degree of degeneration of the disc.

Validation of a model require that the overall material constants of the disc, which are gained from experimental studies (Rolander, 1966; Galante, 1967; Markolf, 1972), be recalculate optimally, by minimizing the error between the experimental data and the predicted response (deformations, forces, pressure etc.) from the finite element analysis. A large number of finite element studies include programs for optimization of deformations (Belytschko et al., 1974; Liu et al., 1975; Lin et al., 1978; Spilker, 1980), reactive forces (Kulak et al., 1976) and intradiscal pressure (Yang et al., 1983), see Figure 1.57.

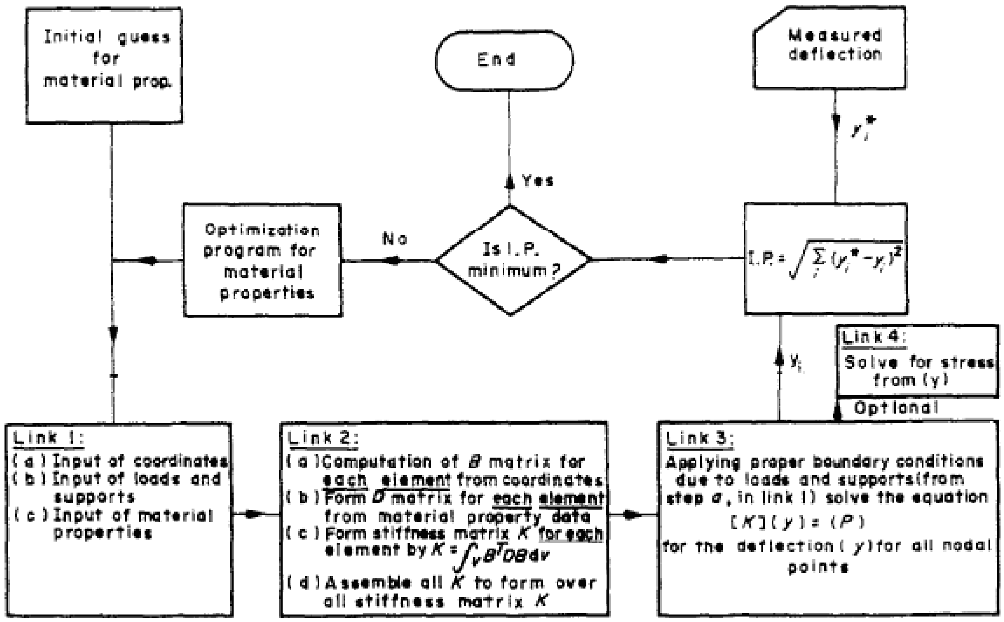

Figure 1.57. Flow diagram of the optimization technique used by Li et al., (1978) to yield material properties of the intervertebral disc.

The detailed structure of the annulus fibrosus (composite of collagenous fibers embedded in a matrix of ground substance) was included in a 3D nonlinear finite element model of a lumbar spinal segment to study the effects of the variations of the intradiscal pressure, the fiber angle and removal of the nucleus pulposus (severe case of disc degeneration) on the behavior of the disc-vertebrae unit under compressive load (Shirazi-Adl et al., 1983, 1984), see Figure 1.58. They showed that removal of the nucleus leads to: (1) reduction of the disc stiffness; (2) an alteration in the pattern of stress distribution in the vertebral body and in the thickness of the annulus fibrosus; (3) an alteration in the pattern of tensile strains in the fibers; (4) an alteration in the pattern of the annulus bulge and the occurrence of maximum bulge site. For a normal disc, continuing increase in the disc stiffness was predicted with decreasing fiber orientation. Their results show good agreement with reported experimental results, and noteworthy that modeling of the annulus fibrosus as a composite material is crucial in predicting axial stresses in the disc which are consistent with measurements. Their results indicate that under a compressive load, the most vulnerable elements in a normal disc are the cancellous bone and the endplates. Their predictions correlate with the frequent occurrence of Schmorl's nodes in non-degenerated discs. For the disc without nucleus, their analysis predicts the bulk material of the annulus also to be susceptible to failure. While the annulus fibers do not appear vulnerable to rupture under the compressive load.

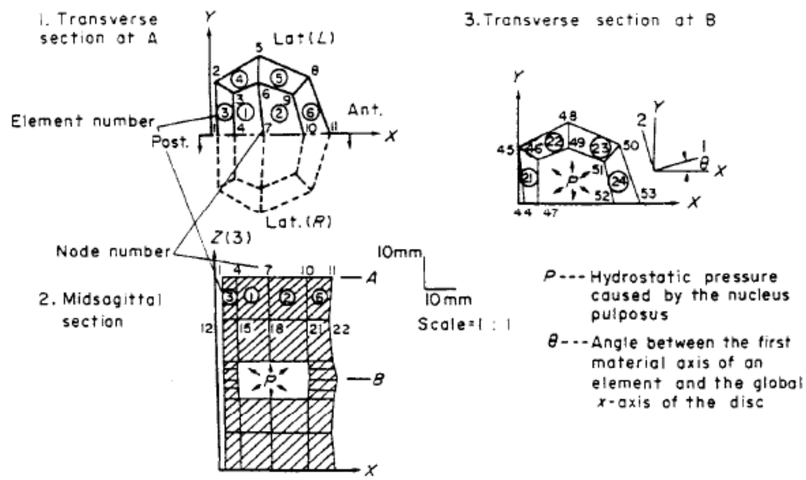

(a)

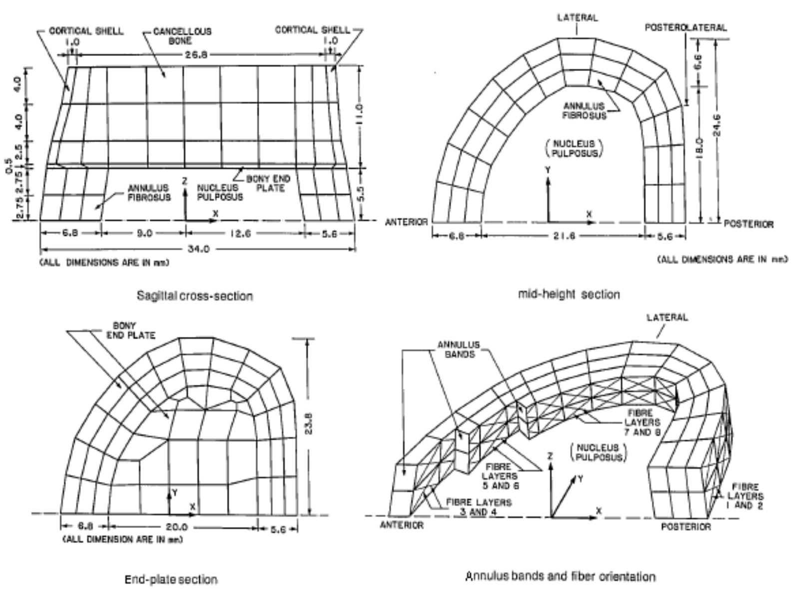

(b)

Figure 1.58. Three-dimensional finite element models of the intervertebral disc for studying compressive loading. (a) Assuming a hydrostatic pressure in the nucleus and an orthotropic behavior in the annulus, taken from Lin et al., (1978). (b) Assuming the annulus as a composite, taken from Shirazi-Adl et al., (1983, 1984).

In a subsequent study with the lumbar segment model developed by Shirazi-Adl et al., (1983), the posterior elements were added to the model and a nonlinear finite element program developed was developed and implemented for the analysis of loading in the saggital plane, (Shirazi-Adl et al., 1986). The effects of the loss of intradiscal pressure in flexion and of facetectomy during extension (typical in disc degeneration) were examined to verify their effects on the predicted response of the model to stiffness, bulge, and stress-strain distributions, see Figure 1.59.

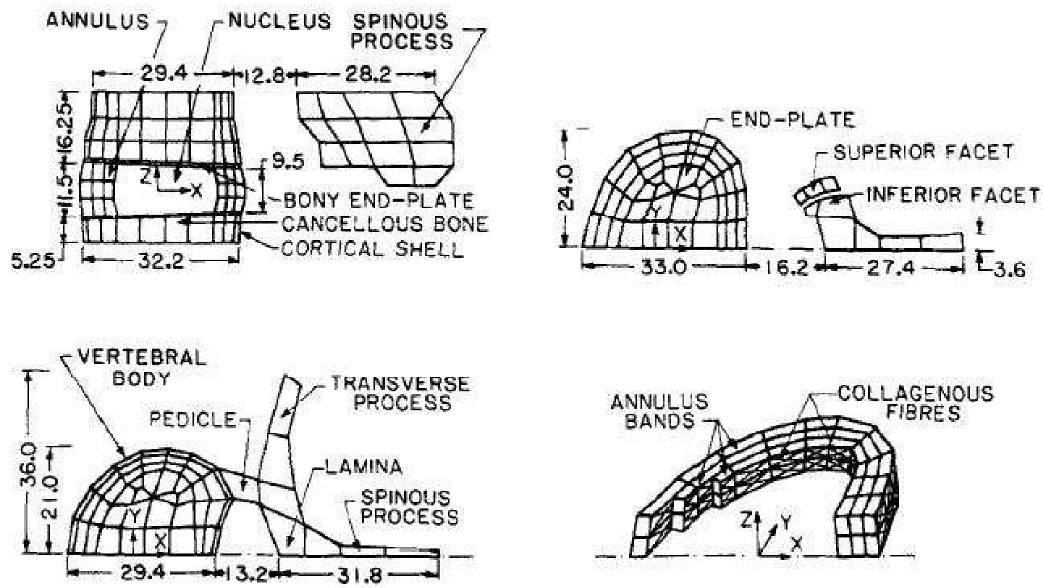

Figure 1.59. Three-dimensional finite element model of the intervertebral disc for studying bending loading, taken from Shirazi-Adl et al., (1986).

They reported that the disc-vertebra segment showed stiffening effects with increasing loading, being stiffer in extension than in flexion. Also, removal of the facets caused a larger impact on stiffness decrease, than in loss of intradiscal pressure. On the other hand, loss of intradiscal pressure caused a larger impact on the predicted bulge response, than that in facetectomy. In flexion, a large intradiscal pressure was generated, while in extension negative pressures (suctions) of low magnitude were predicted. The stress distribution results showed that the pathway of load transfer from the upper vertebra to the lower one through the posterior elements occurs in different paths in flexion, and in extension. In flexion, the ligaments are the means for such transfer; in extension, the load is transferred through the pedicles, laminae and the articular processes. Large tensile strains: radially and axially, occur at the anterior, and posterolateral site of the annulus under flexion and extension, respectively. Loss of intradiscal pressure in flexion and facecetomy in extension increased these strains, suggesting a cause for clefts formation between annulus layers, which frequency of occurrence increases with age. In the annulus the maximum fiber strain occur in flexion and was located posterolaterally in the innermost layer. Their suggestions indicate that large flexion moments in combination with other loads is a likely cause of disc prolapse, which are commonly found at these posterior locations.

In a posterior study of the mechanical response of the whole lumbar spine in torsion, Shirazi-Adl (1994) used a three-dimensional finite element model (L1-S1) and also reported stiffening effects at increasing loads, see Figure 1.60. Axial rotation caused couple movements, mainly in transversal direction and flexion rotation. Structural alteration in the form of facetectomy or loss of nucleus fluid in a lumbar level decreased the torsion stiffness, increased the maximum fibre strain and strains in the capsular ligaments for the remaining levels, which were severely impaired for the former.

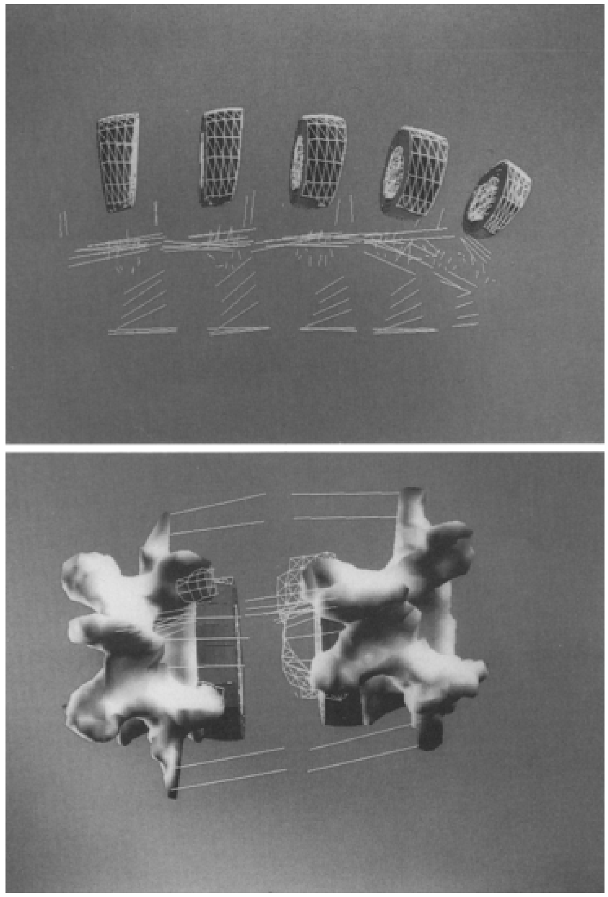

Figure 1.60. A three-dimensional finite element model of the ligamentous lumbar spine based on a CT scan and showing intervertebral disc, ligaments and beam elements connecting rigid bodies, taken from Shirazi-Adl et al., (1994).

The decrease of intradiscal pressure is known to be connected with the aging of the disc (Kanematsu, 1970), eventually leading to the loss of its hydrostatic properties (Nachemson, 1960). Thus, another approach to study disc degeneration was one which consisted on modeling the droop of intradiscal pressure (Kurowski and Kubo, 1986). In this study, an axial compressive load applied to a two dimensional finite element model showed the influence of decreasing the intradiscal pressure on the mechanism of load transmission, stress concentration and failure modes through the lumbar vertebral body, for healthy discs and with degeneration. In the analyses, it was assumed that the degenerated disc model do not represent the advanced stages of degenerated discs but the beginning of the degeneration process when the nucleus still acts like a fluid. Nonetheless, they reported a common site for concentration of stresses, regardless of degeneration, and which occur near the boundary between the cortical shell and the cancellous bone. For healthy discs, the largest stresses were located centrally in the endplates, and with progress in disc degeneration (decreasing intradiscal pressure) they move to the peripheral parts of the endplate and to the cortical wall. Their patterns of stress distribution suggest that load transmission through the vertebral bodies also depended on the state of disc degeneration. For healthy discs, it passes mainly through the center of the vertebral body. When the disc is degenerated, more loads are transmitted through the cortical wall. Based on their stress distributions and load transfer pathways, they suggest that prediction of the mode of damage to a vertebral body also depended on the state of disc degeneration. Thus, compression of motion segment with healthy disc is likely to produce cracks in the central portions of the vertebral endplates. While compression of motion segment with degenerated disc is likely to collapse the cortical wall and/or the lateral portions of the endplate. Regardless of the disc condition, local damage may also occur in the boundary between the cortical and cancellous bone, where the blood vessel foramen is located.

A nonlinear three dimensional finite element model was used by Kim et al., (1991) to study how disc degeneration at one level affects the mechanics of the adjacent levels. The analyses were restricted to compressive loading mode alone. Again, disc degeneration was simulated by removing the hydrostatic capability of the nucleus and substituting the nucleus with a much stiffer material. Using a lumbar L3–L5 model, the authors showed that the intradiscal pressure and the bulging in a normal disc increased with respect to the degenerated disc, and with time may trigger the degenerative process at the adjacent level as well. Their report shows that with a more refined finite element model, the predictions of degeneration as a cascading event were possible, and that disc degeneration at one level can induce changes in adjacent segments, a clinically observed event. A posterior study with loadings in bending and torsion showed the same tendencies (Ruberté et al., 2009).

Another feature of disc degeneration that has been modeled is the delamination of the annulus fibrosus, which is a clinically observed structural change, associated with disc prolapse, rupture and herniations. This mode of degeneration was explained using a nonlinear finite element model developed by Goel et al., (1995) and later by Kim (2000). In both studies, the lamina separation by shear stress as a result of external loading was studied. In the disc model by Goel et al., (1995) only a mild state of degeneration was analyzed, and the delaminations predicted were small and occurred in the anterior and lateral margins of the annulus. A more detailed model of the delamination process was given by Kim (2000) by modeling the annulus as a fiber composite material: fiber-reinforced elements with a tension-only option for the collagenous fibers and embedded in an isotropic matrix. The study also included two disc conditions: healthy disc and degenerated disc. Again, degeneration was modeled by an increase of the disc area, a reduction of the disc height and a decreasing in the stiffness of the nucleus pulposus. The finite element analyses showed that interlaminar shear stresses were highest in the innermost layers of the posterolateral regions, where most of the annular tears are clinically identified. The analyses also showed that these shear stresses grow further with presence of radial and/or circumferential annular tears. Kim (2000) further included failure modes of the fiber and matrix, either by breakage or folding, and showed that matrix breakage mode is more prominent in healthy discs and occurs in the anterior outer part of the annulus. The folding failure mode in the matrix occurs in both disc models with a location in the posterior and posterolateral part of the annulus.

Osteoporosis is a disease of bones, which is characterized by loss of mass, in particular the bone mineral density is decreased and leads to an increased risk of fracture. Lumbar vertebrae are more susceptible to fracture due to their position in the human spine. Thus, it is relevant to differentiate the biomechanical behavior of lumbar spinal segments in a healthy state and with osteoporosis. For this matter, several finite element studies have been done, two of which have developed an anisotropic finite element model of a human L3-L4 lumbar segment to study the load-sharing in compression (Pitzen et al., 2002; Mizrahi et al., 1993), for healthy bone, osteoporotic bone and disc degeneration. Osteoporosis and degeneration were modeled as a reduction of the stiffness. The model predicted a drastic change in the load-sharing between healthy vertebrae and osteoporotic vertebrae. As the stiffness is decreased, the role of the posterior elements as a load-bearing structure is more pronounced with respect to a healthy lumbar spinal segment. They showed that osteoporosis changes the load pathways in the vertebrae, in the same way that disc degeneration does. Thus, when osteoporosis is present, more loads are transmitted through the cortical shell.

Disc injury, has been modeled in many ways, e.g. Shirazi-Adl et al., (1989) used an analysis of progressive failure which was based on an accumulation of strain in the annulus fibers due to lifting, leading to localized failure and the appearance of tears. In a posterior study of mechanical and clinical implications of a nucleus injury, Shirazi-Adl, (1992) modeled the changes in the fluid content of a lumbar intervertebral disc model through a loss or gain of the nucleus volume. Loss of fluid, leads to high forces of contact in the facets and diminished the tensile forces in the annulus fiber layers. Also, inward bulge appeared at the inner annulus layers causing a progressive damage to the adjacent layers which alter the stress distribution in the vertebral bodies.

In another finite element study, the removal of the nucleus was used as a model of disc injury to analyzed the disc vibration response to the dynamic loading (Guo et al., 2005). Little et al., (2007) simulated disc injury and degeneration with rim, radial and circumferential annular lesions and by reducing the nucleus pressure to zero, respectively. In all the previous studies, they showed that loss of nucleus pressure had a much greater effect on the disc mechanics than the presence of annular lesions. Indicating that the development of annular lesions alone (prior to degeneration of the nucleus) has minimal effect on disc mechanics, but that disc stiffness is significantly reduced by the loss of hydrostatic pressure in the nucleus.

The finite element method has also been used to analyze the mechanical interaction of medical devices and prosthesis with the lumbar spine. In a recent study to a new artificial disc model, Noailly et al., (2005) evaluated the L3-L4 prosthesis segment mobility, articular contact and stress analysis in a L3-L5 lumbar spine physiologic model. The finite element predictions showed that models with disc substitute are much stiffer than the physiologic model. In case of good contact with the adjacent vertebrae, the implant behaves like a physiological intervertebral disc and respects the surrounding motion segment biomechanics. The distribution of stress in the vertebrae for the disc substitute model showed the same tendencies as for the physiologic model, suggesting that bone remodeling would be expected in the trabecular bone.

b. Studies with material and geometric nonlinearity: Multiple loading simulation

Finite element studies with multiple loading simulation include axial loading (compression or tension), transverse or shear, bending (flexion-extension and lateral bend loads), and axial rotation (torsion) loading. In the previous section, it was shown that simulation of loading with axial compression gives insights of the disc response to stress distribution, intradiscal pressure, bulging, and load-deflection characteristics. Moreover, transverse or shear force simulation is used to study displacements and tilt of the endplate in the loading direction, at the upper and lower site of the disc, where the joint between the vertebrae and the disc occurs. Torsion simulation is used to predict axial rotations of the annulus fibrosus while bending simulation is used to predict couple motions, such as flexibility and displacements of the disc. However none of the previous studies consider multiple loadings, which occur on a daily basis, and represent a more realistic approach of analyzing the biomechanics of the intervertebral disc.

One of the first studies with finite element involving complex loading was done by Spilker et al., (1984). They examined the response of an axisymmetric finite element model of a human spine segment, containing two adjacent vertebrae and the intervertebral disc to compression, shear, torsion, and bending loads, and using strength of materials theory determined the effects of disc geometry and material properties on response. They reported that intradiscal pressure increases and disc displacements vary linearly with the axial compressive pressure. The vertical displacement and radial bulge was found to decrease for increasing disc radius and increased for increasing disc height. Their predictions for shear loading in the endplate region include radial and tangential displacements, bulge, and tilting which showed similar trends that in axial load. Also, predictions for torsion and bending loading gave similar tendencies: rotation increased with increasing disc height, and decreased with increasing disc radius. Some of their conclusions were, model displacements and strains varied inversely with the elastic modulus of the annulus; except for compression response, model intradiscal pressure did not change considerably, which is consistent with experimental observations. In general, disc radius and disc height were major determinants of disc displacements. Typically, displacements at a given load increased with increasing disc height and decreased with increasing disc radius.

A study of combined loading in torsion and compression in a 3D nonlinear finite element model of a lumbar spinal segment was done by Shirazi-Adl et al., (1986) to examined the effects of the loss of intradiscal pressure (typical in disc degeneration), and removal of the facets on the predicted response of the model to couple displacements, stiffness, bulge, and stress-strain distributions, see Figure 1.61. For the intact segment their results showed, the stiffening behavior of the motion segment with increasing applied torque and compression. Loss of disc pressure and removal of the posterior elements decreased torsion stiffness, being more markedly in the latter case.

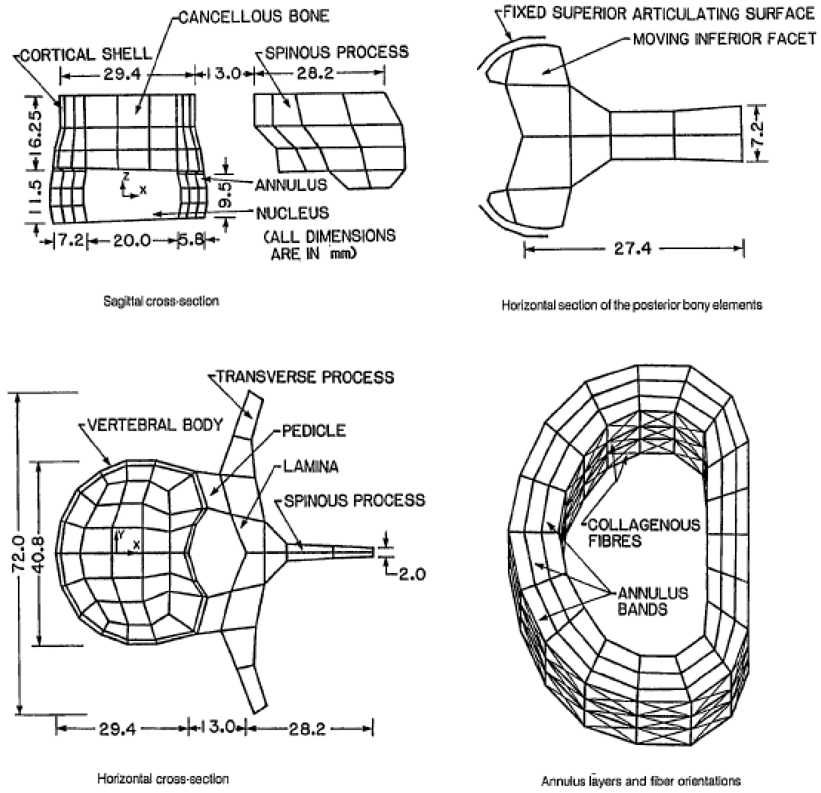

Figure 1.61. Three-dimensional finite element grid of the motion segment used by Shirazi-Adl et al., (1986) for studying torsion in combined with compression loading.

Also, the relative contributions of an axial compressive load and the posterior elements to the segmental rotational stiffness were associated with the annulus fibers (which offers a more effective resistance to rotation at low torques) and the facet interaction (which plays the dominant role in the segmental resistance to rotation at large torques), respectively. The predicted deformation of the disc showed, that loss of intradiscal pressure caused a larger impact on the predicted bulge response, than removal of the posterior elements. Their results from the stress-strain distribution predict the highest strains occurred in the annulus outermost fibers, growing with additional loading or with removal of the posterior elements. In the posterior bony elements, the maximum stresses occurred in the articular facets that are always in contact, suggesting that in torsion, the articular facets and the disc annulus are the main load carriers.

Disc prolapse is a medical condition related to injury due to complex loading. It occurs because a group of tears in the outer annulus fibrosus allows extrusion of the soft nucleus pulposus. The tear is the result of fiber failure by breakage. Thus, the influence of loading on the prediction of fiber strain has been study using finite element models of the disc, such as the one developed by Shirazi-Adl (1989). Lift tasks done symmetrically and none symmetrically were simulated as pure bending and a combination of bending with torsion, respectively. The model predicted that the maximum fiber strain occurs in the innermost annulus layer at the posterolateral location. Failure analysis showed that the rupture started also at these sites and progresses radially to the adjacent layer with only a slight increment of load. Further progress in the rupture of fibers toward the annulus outer periphery, resulted in a complete radial fissure, and disc prolapse occurred. The predicted failure mechanism was in agreement with the findings from clinical, epidemiologic and experimental studies. In a posterior simulation of combined loading in flexion-extension, lateral bending and axial rotation to a nonlinear finite element model of a lumbar spinal segment L4-L5 (Schmidt et al., 2007) also reported that the posterior and posterolateral annulus layers were susceptible to develop large strains.

The finite element method was also used to investigate the role of axial rotation in the etiology of disc prolapse (Duncan et al., 1991). They used a L2-L3 lumbar disc model to study the relevance of axial rotation as a cause of disc degeneration and the role of facet asymmetry in the injury mechanism. The finite element predictions showed minimum effect of facet asymmetry on the couple motions and on the annular strains. Also the predictions showed minimum effect of the variation of facet geometric parameters on the segment response. They concluded that, without facet damage, it is unusual that the annulus fibers experience unusual levels of stress and strain, either as a result of increased axial rotation or any of the associated couple motions.

Muscles are connected to the ligamentous lumbar spine and are able to carry load. Hence, the effects of muscles activity on the biomechanics of the normal and degenerated lumbar spine are a relevant issue that has been study in vitro widely (Andersson et al., 1980; Panjabi et al., 1989; Crisco and Panjabi, 1991). However, only a few studies with finite element have been done, one of which is Goel et al., (1993) in which degeneration was simulated as a reduction of the muscle forces. They used a combined, nonlinear, finite element model of a ligamentous L3-L4 motion segment in which the predicted muscle forces were used to calculate and compared displacements and rotations, bulge, intradiscal pressure, foramen gap, facet loading, ligament tension, compressive load in the disc, and stress distribution in the vertebral body. Their results indicated that the segment becomes more stable in the presence of muscles forces. Also, the forces transmitted by the facets, grew, and the remaining parameters (intradiscal pressure, stress, and forces in other structures) decreased with increase muscle activity, suggesting that muscle strength is essential for maintaining the spinal function, which supports the concept of degeneration as a cascade event, that describes various stages of the degenerative process that takes place with age.

A three dimensional finite element model of a motion segment without the posterior elements was developed by Natarajan et al., (1994) to study how degeneration might start and progress in a disc under various loading conditions. In particular, the model was used to study the development of annular tears, nuclear clefts, endplate fracture and the subsequent propagation of these degenerative processes due to compression and bending loads. Based on the pressure vessel theory, an iterative approach was used to determine the location and magnitude of the highest stresses in the endplates and in the annulus fibrosus, at which failure can initiate, see Figure 1.62. The initiation of disc failure was identified by one of the following: breakage of a fiber in the annulus (tensile or shear), failure of the annular matrix (tension/compression, or shear), or fracture of the endplate. The analyses showed that the disc failure always started in the endplate, and not in the annulus, indicating that the endplates are the weakest link in the body-disc-body unit. The model predicted that the fracture of the endplates occurs at the junction of the annulus and the endplate and in the posterolateral direction, which agrees with clinical observations. The analyses also showed that the compressive load required to initiate failure in the annulus was about twice as high as that required to initiate a fracture in the endplate, indicating that annular injuries are unlikely to be produced by pure compressive loads. Prediction of large moments in extension as compared to flexion was required to initiate and propagate failure in a motion segment, which supports the conclusion that the motion segment is much stiffer in extension. The model also suggested that the presence of peripheral tears in the annulus fibrosus may have a role in the formation of concentric annular tears and in accelerating the degenerating process of the disc.

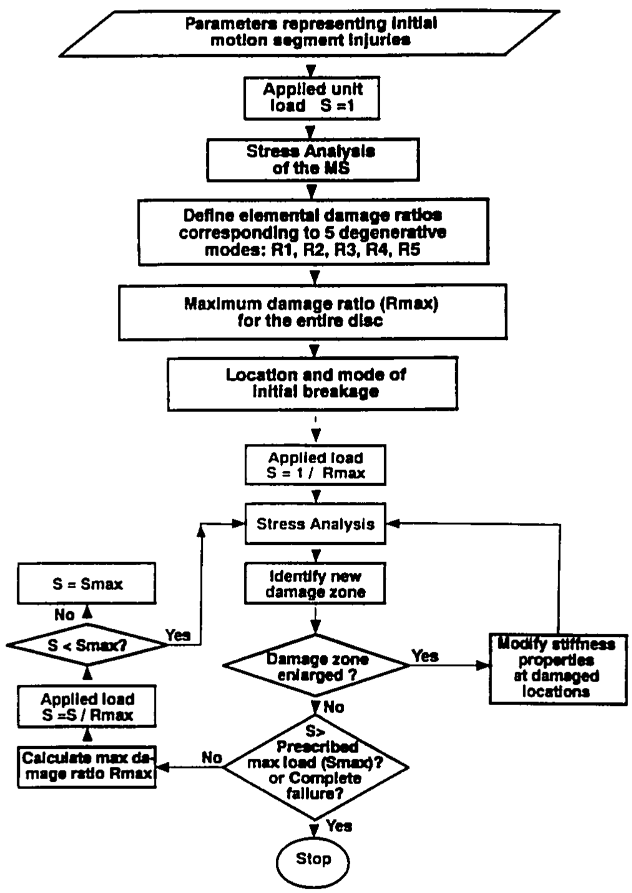

Figure 1.62. Flow chart for the model used by Natarajan et al. (1994) to study the initiation and progression of the disc degeneration process.

Another finite element study under loading conditions of compression and bending (Lu et al., 1996), reported similar results using a viscoelastic formulation for the annular fibers and a decremental function to account for the diurnal fluid change in the nucleus. Also, the analysis showed that a saturated disc was the weakest in combined loading of bending and compression. These conclusions are in agreement with clinical observations and illustrate how finite element techniques can be used to study the disc degeneration process in a way that cannot be accomplished using in vivo or in vitro models.

The disc height reduction, which is a clinical evidence of intervertebral disc aging, has also been modeled (Natarajan and Andersson, 1999). For this matter, a nonlinear finite element model generated from a computer tomography (CT) scan of an L3-L4 lumbar segment was further developed by including variation of the disc height and disc area, and was used to identify disc geometric characteristics which are related to the biomechanical response of the disc: flexibility, fiber stress, disc bulge, and nucleus pressure in response to loads in compression, shear, bending and torsion, see Figure 1.63.
This model did not include any change in the mechanical properties of the disc, but only the decrease in height, and assumed material properties for a case of mild degeneration, in all disc heights considered. The analyses showed that, flexibility, fiber stress, facet contact forces, and disc bulge were increased and the nucleus pressure was decreased, as a result of an increased in the disc height alone, suggesting that discs with low ratio of area to height are exposed to much higher risk of failure than other combinations of disc height and geometry, confirming clinical experience and the in vitro evidence.

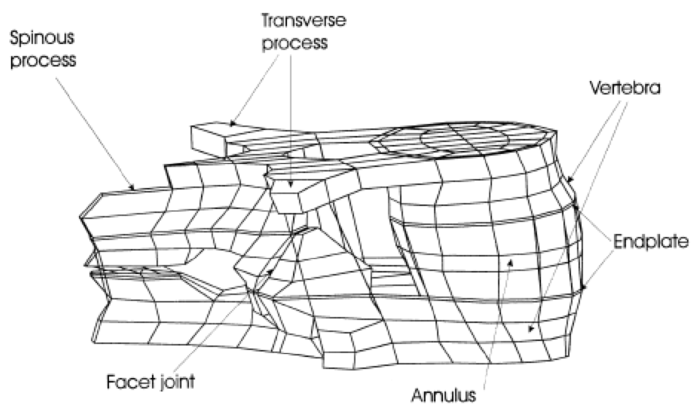

Figure 1.63. Finite element model of a L3-L4 lumbar segment with varying disc height and cross sectional area, taken from Natarajan et al., 1999.

More recently, Ruberté et al., (2009) also modeled disc degeneration in the lower lumbar spine throughout decreasing the disc height and area of the nucleus pulposus and by modifying the Young's modulus and the Poisson ratio of the annulus ground substance and the nucleus. In particular, they varied the degree of degeneration in the L4-L5 lumbar level and predict the motion response, intradiscal pressure and stress in the adjacent lumbar levels, L3-L4 and L5-S1 due to flexion-extension, bending laterally and torsion. They showed that degeneration causes a decrease in motion response in the L4-L5 level and below, and also caused a small increase in motion response in the above level, L3-L4. Except for lumbar level, L4-L5, the intradiscal pressure decrease was negligible for the rest of levels. In general, they reported that disc degeneration caused an increased in the maximum normal stress and maximum shear stress in the annulus, which was more evident below the affected level. Their conclusions also point out that degeneration altered the loading and motion patterns of both, the degenerated disc and the adjacent segments, suggesting that single-level degeneration can lead to an increased risk of injury at the adjacent levels.

Weightbath hydrotraction treatment (WHT) is a simple noninvasive effective method of hydro or balneotherapy to stretch the spine or lower limbs, applied successfully in hospitals and health resort sanitaria in Hungary for over fifthly years. However, it is not understood the biomechanical and clinical effects of the treatment in a single spine segment. For this purpose, a three-dimensional finite element model of a lumbar spine segment was developed by Kurutz and Oroszváry, (2010), in which five grades of degeneration from healthy to fully degenerate were introduced, see Figure 1.64. They modeled the loss of hydrostatic pressure in the nucleus by decreasing the Poisson's ratio, accompanied by nucleus hardening modeled by increasing Young's modulus, respectively. In the annulus matrix a gradual increase, while in the vertebral cancellous bone and endplates a gradual decrease of Young's modulus were considered with aging.

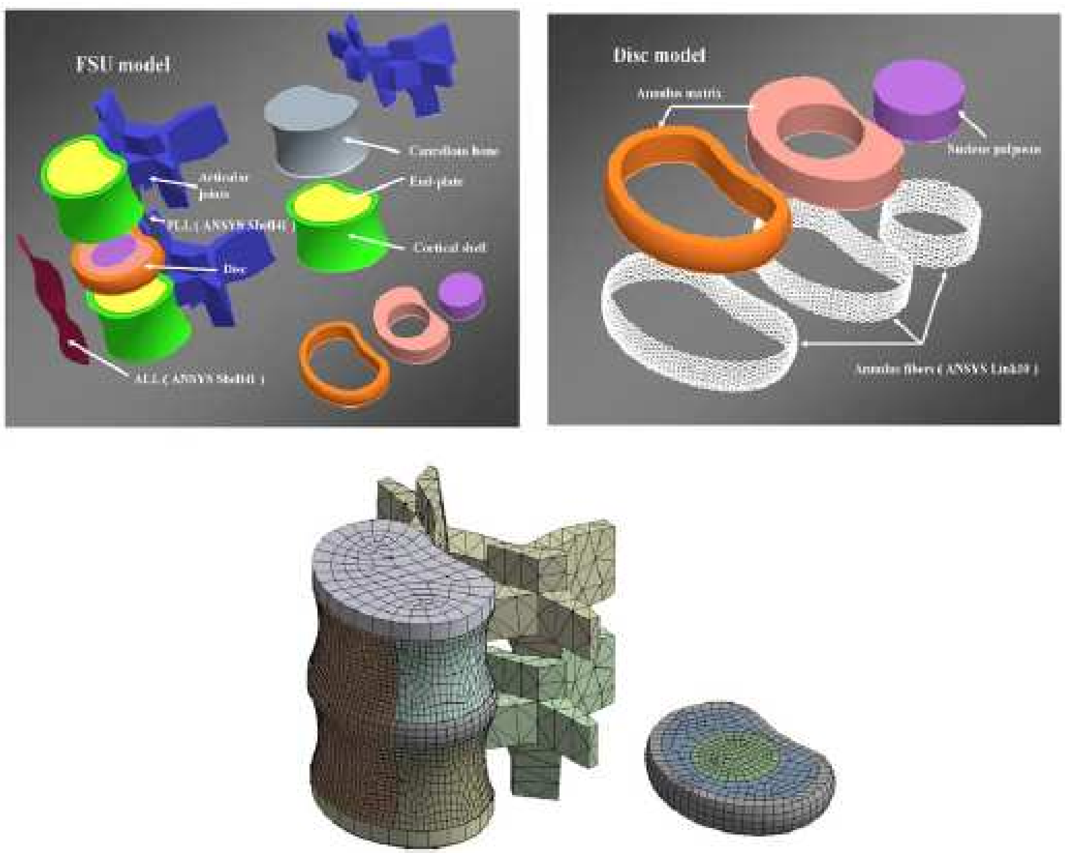

Figure 1.64. Finite element model of a lumbar spinal segment used to analyzed the biomechanical effects of weightbath hydrotraction treatment (WHT), taken from Kurutz et al., 2010.

Their predictions of the effects of degeneration showed a change in the smooth distribution of compressive stresses in the sagittal section seen in healthy discs, to a profile with a sharp stress increase, being maximum in the annulus-nucleus boundary, and minimum in the nucleus, these results were in agreement with previous reports (Adams et al., 1996, 2002). In WHT the compressed and hardened state of the nucleus in degeneration is reduced by the removal of compressive preload of body (indirect traction), and by the active tensile force of buoyancy with applied extra loads as direct traction loads. The traction loads causes an extension, and partial disc height recovery. Their degeneration model showed that WHT unloads the compressed disc: extends disc height; decreases bulging, stresses and fiber forces; increases joint flexibility; relaxes muscles; relaxes muscles and unloads nerve roots.

c. Studies with poroelastic behavior

In all the models described previously, the fluid flow during loading and unloading processes was not considered. The fluid flow in and out of the disc is an important component, because it allows the spine to carry heavy loads. Also, it is the decrease in fluid content in the disc that occurs due to degeneration, in addition to the material of the nucleus which becomes more fibrosus and leads to a stiffer disc. Also, the fluid phase may have a significant effect on the mechanical response of the disc, which may affect the nutritional paths to the avascular interior of the disc (Natarajan et al., 2004). Poroelastic models suggest that the biphasic nature of the disc is an important factor in load transfer and stress distribution. Thus, to understand disc degeneration, and predict better response of degenerated discs, the finite element models should include not only a change in geometry of the disc and an increase in the elastic properties of the nucleus, but also the change in permeability and porosity of various disc components and the reduction of water content of the nucleus. To this effect, some of the relevant finite element studies are presented.

The first implementation of a poroelastic formulation into a finite element modeling of a spinal motion segment was done by Simon et al., (1985) by using radiographic images of a rhesus monkey disc. Only the anterior portion of the disc was modeled as having two distinct phases: a fluid phase and a permeable solid phase, see Figure 1.65. The study of Simon et al., (1985) also includes an analytical and experimental model development, which consisted of creep testing for validation of the FE model. With the poroelastic constants: drained elastic moduli of the annulus and nucleus, compressibility of the solid and fluid phase, the permeability and porosity of the solid phase, the FE model was used to predict the overall internal fields included deformation, fluid motion relative to the deforming solid and the effective stress. Once the model was validated, they modified it to analyze disc degeneration, which was simulated as an increase of the disc permeability, and a decrease in the drained annular and nuclear moduli. They showed that the relative fluid motion is highly sensitive to small changes in disc stiffness, and that the externally applied loads cause a reduction in the disc volume, resulting in expression of the fluid from the disc, being larger in the degenerated disc case, suggesting that this may affect the nutritional path to the avascular interior of the disc. The creep analyses also showed that gross failure of the endplates is possible as well as failure of the cancellous bone adjacent to the endplate. They suggest that these failures could alter the fluid flow patterns and perhaps change nutritional channels.

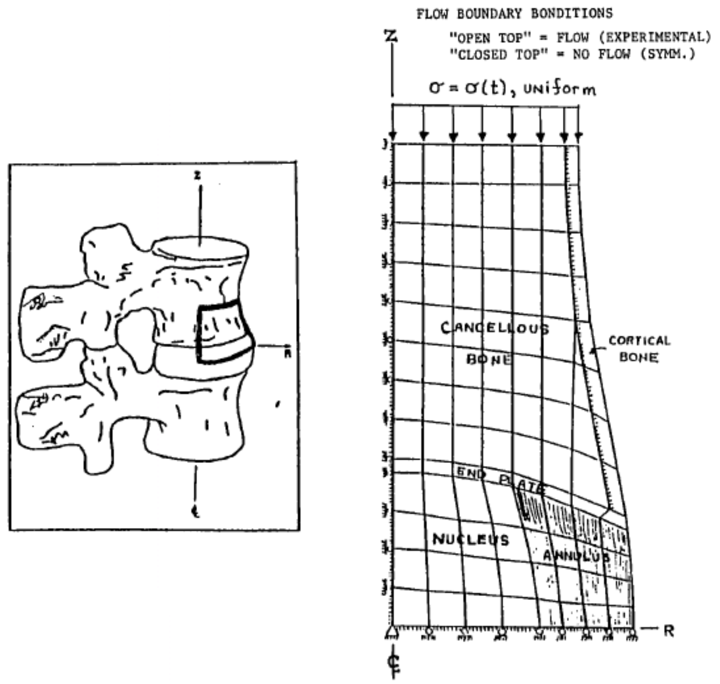

Figure 1.65. Poroelastic finite element model of the anterior portion of a motion segment used by Simon et al., (1985) for studying the creep response of healthy and degenerated discs.

Other finite element models with poroelasticity were developed by Wu and Cheng (1996) and Lee et al., (2000) which include the motion segment with the posterior elements. In the former model, a creep loading was simulated, while in the latter model, the study of the response of a lumbar motion segment to impact load was included. In both studies, the conclusions for creep loading, stress distribution and failure modes in impact were similar than those by Simon et al., (1985). The results suggested that fractures are likely to occur under short duration impact loads and that they are likely initiated in the endplate region or the posterior wall of the cortical shell. However, neither the swelling pressure nor the initial disc pressures were included in the analyses.

The variation of the void ratio and hence the porosity change of the disc material with load increment was included in the finite element model developed by Agouti and Shirazi-Adl (1996). Inclusion of the initial disc pressure was made possible by adopting a two step analyses. Using a finite element model of half of the lumbar L2–L3 motion segment including facet joints, it was shown that under creep load, the variable permeability markedly stiffens the creep response, reduces the fluid loss from the nucleus, and decreases facet contact forces, see Figure 1.66.

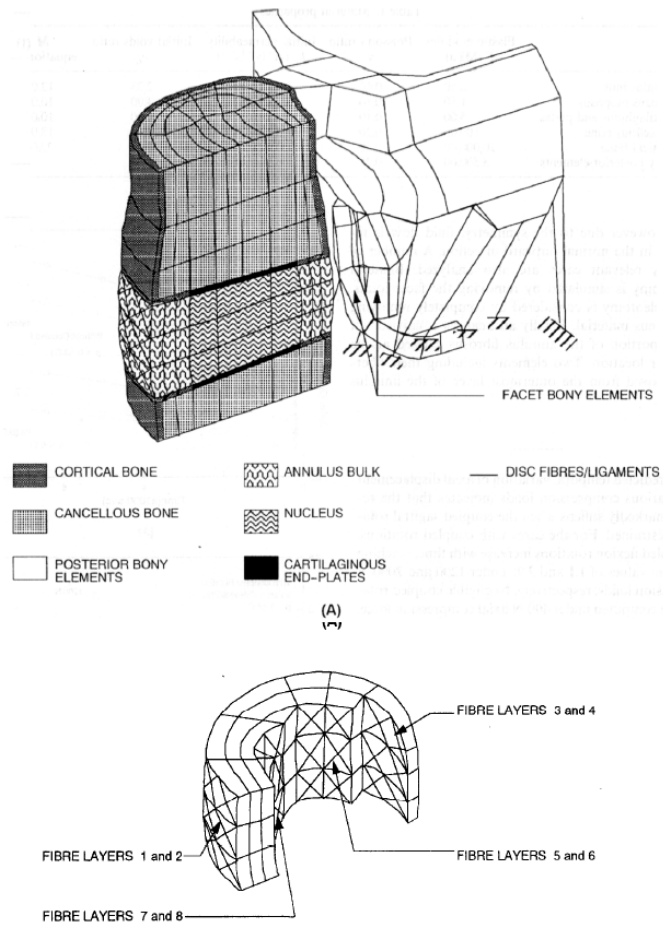

Figure 1.66. Poroelastic finite element model of one half of the lumbar L2-L3 motion segment with inclusion of variable porosity, taken from Argoubi and Shirazi-Adl (1996).

Prediction of fluid flow back into the disc that occurs during removal of the load, i.e., during relaxation of the disc, requires inclusion of the swelling pressure into the models.
The swelling process that occurs in soft tissue was incorporated into the poroelastic finite element model by Laible et al., (1993). Using a finite element model of a disc-vertebra-disc without the posterior elements, they showed that inclusion of swelling pressure reduced the load on the solid phase while increases the load in the fluid phase. Overall, the effect was a stiffening of the segment and reversal of the bulging of the inner portion of the disc. Inclusions of strain-dependent permeability and osmotic potential into a poroelastic model of a lumbar segment was done by Riches et al., (2002) to investigate the disc mechanics associated with multiple cycles of creep compression and expansion. They also reported that inclusion of swelling pressure increases the load in the fluid phase. These results were corroborated by Cheung et al., (2003) using vibration loading to analyze the biomechanical response of the disc; they reported that the fluid flow and the deformation of the intervertebral disc were dependent on the loading frequency.

The combination of an animal model (murine) and a related poroelastic model was proposed to explain how compression can induce disc degeneration (Lotz et al., 1998). The authors showed that a sustained compression load could maintain tension in the outer annulus, while a tensionless state was developed in the middle and inner regions. The model predictions correlated well with the in vivo findings that the inner and middle annulus became progressively more disorganized with an increase in apoptosis and associated loss of cellularity, which may have implications for disc nutrition and modulation in cellular activities. Wognum et al., (2006) showed that these sites were susceptible for crack opening and propagation even under decreasing osmotic pressure.

Hence, the intervertebral disc nutrition is a key issue to understand disc degeneration. In the last decade there has been numerous studies modeling the mechanics for disc nutrition. For instance, Ferguson (2004) predicted the influence of load-induced interstitial fluid flow due to compression or swelling within the disc, on mass transport using a poroelastic model, see Figure 1.49. However, mainly macromolecules, such as cytokines and the proteoglycans were reported as transported solutes by convection. Additionally, he showed that fluid flow did not enhance the transport of low-weight solutes, such as glucose and oxygen, which depended more on diffusivity, suggesting that the permeability and deformation of the endplate and annulus bulk material played a relevant role in the transport of solutes, and that fluid flow and solute transport should be coupled. Their results were in agreement with the reports by Sélard et al., (2003) regarding predictions of concentration gradients of solutes throughout the disc in response to changes in disc and endplate morphology, disc properties, and cellular activities.

In a posterior study of coupling diffusion of oxygen and lactid acid in the disc (Shirazi-Adl et al., 2005) it was shown that the lactic production rate to lactic concentration, and oxygen consumption rate to oxygen concentration, reached their critical values between the disc mid-height and the nucleus-annulus boundary. Their results were also in agreement with the predictions by Sélard et al., (2003) regarding the concentrations of oxygen and glucose, which are consumed by cells, fell towards the disc center. Concentration decreased with decreased diffusivity, or with an increase in disc height and consumption rate. In contrast, the concentration of lactate, produce by the cells, was highest in the center and fell towards the disc-blood vessel interface. A recent sensitivity study of the poroelastic material properties in a L3-L4 disc FE model reveal a strong influence of the strain-dependent permeability of the endplate and annulus fibrosus on the fluid pore pressure and velocity fields, suggesting the importance of endplate permeability at these regions in the normal mechanical behavior of lumbar discs (Malandrino et al., 2009).

To better understand the transport of nutrients and the cellular activity in the disc, Shirazi-Adl (2010) introduce cell viability criteria (based on decreasing the levels of glucose and pH) into nonlinear coupled nutrition transport equations thereby evaluating the dynamic nutritional processes governing viable cell population and concentration of oxygen, glucose and lactic acid in the disc as the endplates exchange area dropped from a fully permeable condition to an almost impermeable one. Consisting with previous predictions, it was reported that the nucleus region was the most affected one, being farthest away from supply sources, and that cell death initiated first as the endplate calcified.

The interactions of the fluid with the proteoglycans contained within the nucleus were considered by Williams et al., (2004). The changes in the fluid volume within the disc on the biomechanics of the motion segment under various loading conditions were analyzed. Swelling pressure was simulated by imposing a boundary pore pressure around the disc tissue. Their predictions were that the presence of proteoglycans within the nucleus is the driving force behind the fluid flow from the surrounding tissues into the disc, as well as the resistance of the flow of fluid out of the disc. They showed that the concentration of proteoglycans creates an increase of swelling pressure, and that this should change the fixed charge density of the nucleus, although no attempt was made to develop an electrical model of the disc. The model initially was used for better prediction of the change in disc height during short term and long term loading, and later was implemented for analyzing changes in disc height during heavy physical work, involving creep and dynamic loading with inclusion of standing recovery (Williams et al., 2007). Recently, this approach was used to investigated the biomechanical response (stiffness, fluid velocity, flexibility and daily disc height variation) to compression and bending of a L4-L5 FE disc model in three grades of disc degeneration: mild, moderate and severe (Galbusera at al., 2010). They modeled disc degeneration in six different ways: (1) reduction of water content was modeled with changing the void ratio; (2) formation of radial tears in the annulus was modeled with imposing discontinuities in the FE mesh; (3) endplate collapse and calcification was modeled with reducing its thickness and increasing its Young’s modulus; (4) disc height loss was modeled with reducing up to 75% the height; (5) osteophyte formation was modeled with increasing the Young’s modulus of the anterior annulus; (6) diffuse sclerosis in the cancellous bone was modeled with increasing its Young’s modulus. They reported a tendency to an increase of disc stiffness, and a decrease of fluid velocity, flexibility and daily variation of disc height with progressive disc degeneration. A similar study was done to investigated the whole lumbar spine response during daily dynamic physiological activities (Schmidt et al., 2010) yielding fairly good results.

In the foregoing studies, the bi-phasic theory was applied to poroelasticity and used to model the disc biomechanics. However, no attempt was made to consider the hydrophilic and electrical nature of the proteoglycans in the disc. Such consideration can give insights of the functionality of the nucleus in terms of the population of proteoglycans and the presence of a respective electrical potential. Since the most significant biochemical change seen in a degenerated disc is the loss of proteoglycan, resulting in the decrease in fixed charge density (Lyons et al., 1981), its analysis can help to better understand the biomechanics, nutrition and mechanobiology of discs, normal and degenerated. To this end, Iatridis et al., (2003) introduced a finite element model of a slice of lumbar disc material, which included electrical potential, and chloride and sodium concentrations, and showed that the mechanical, chemical and electrical behaviors were all strongly influenced by the density of fixed charge distribution throughout the disc.
They concluded that changes in the fixed charge density from a healthy distribution to a degenerate distribution will cause a stress increase in the solid matrix and can cause fluid loss. In another study, a tri-phasic finite element model of an intervertebral disc which included electrical chargeability, inhomogeneity, anisotropy and porosity was proposed (Yao et al., 2007). In such model, the effects of tissue properties: stiffness, porosity and fixed charge density, on the mechanical, chemical and electrical signals, and the transport of fluid and solute within the disc under axial compression load were investigated. Their

predictions showed that the fluid pressurization and the effective stress in the solid phase were more pronounced in the region between the annulus fibrosus and the nucleus pulposus. In the nucleus, the distribution of the fluid pressure, effective stress, and electrical potential were more uniform than those in the annulus. Changes in modulus and water content affected the effective stress, fluid pressure and solute transport in the disc. However, the most drastic affectation was the electrical potential by changes in the fixed charge density, which suggest being a reliable indicator of disc degeneration, at least from a biochemical point of view.

d. Studies with medical imaging: CT, MRI and Ultrasound

Obtaining the precise geometry of soft and hard biological tissues, such as a lumbar spinal unit is a challenge. In the majority of the foregoing studies, the complex profile of the cross sectional area, and height of the disc and vertebrae were not defined precisely, and their true forms were replaced by approximations to a circular area, or an ellipse with uniform section. The identification of the complex geometry of lumbar spinal units requires medical imaging techniques: computer tomography (CT), ultrasonic, or magnetic resonance imaging (MRI). In the last two decades there has been an increasing use of such techniques for implementation of database, concerning disc degeneration: anatomical background, water content, annulus, nucleus and vertebral structure (Roberts et al., 1997; Wehrli et al., 2004). For example, Wong et al., (2003) developed a nonlinear finite element model of a lumbar disc-body unit based on CT-scan. The vertebral body consisted of solid tetrahedral elements (cancellous bone) surrounded by shell elements (cortical bone), the disc consisted of an incompressible nucleus, surrounded by the annulus fibers embedded in a matrix of ground substance. They showed the model validation, with good agreement for loading conditions in compression and flexion.

Computer tomography and MRI were used to generated a finite element model of a L2-L3 lumbar spinal unit to study the biomechanical response of the intervertebral disc to axial loading (Wang et al., 2005), see Figure 1.67. The disc was considered as incompressible and the vertebrae bodies were considered as orthotropic. The model predicted that the stress around the disc was higher than on the central disc during compression.

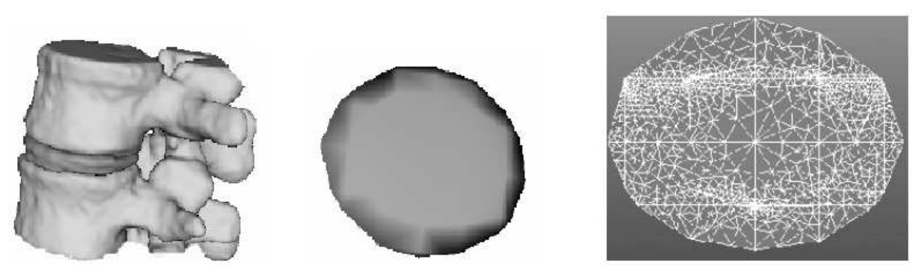

a b c

Figure 1.67. (a) CT geometric model of the L2-L3 lumbar spine unit. (b) CT geometric model of the intervertebral disc. (c) Finite element model of the L2-L3 intervertebral disc, taken from Wang et al., (2005).

Computer tomography was also used to developed finite element models of disc degeneration (Rohlmann et al., 2006; Schmidt et al., 2007). In the former, they used a three-dimensional nonlinear finite element model of an L3-L4 lumbar segment, and in the posterior study, an L4-L5 segment. Rohlmann et al., (2006) studied the influence of disc degeneration on motion segment mechanics. A healthy disc and three grades of disc degeneration (mild, moderately and severe cases) were simulated by decreasing the disc height and the bulk modulus of the nucleus pulposus, see Figure 1.68. They loaded the model in flexion, extension, lateral bending and torsion. The finite element predictions showed that the intersegmental rotation and intradiscal pressure were in good agreement with the reported values from the in vitro studies. For mild degenerated discs, the intersegmental rotation showed an increase for all loading cases. However, this trend changed for the rest of the degeneration grades, increasing disc degeneration caused a decreased in intersegmental rotation. For torsion, the decrease in flexibility took place only in severe degeneration. Intradiscal pressure was lower, while facet joint force and maximum von Mises stress in the annulus were higher in a degenerated compared to a healthy disc.

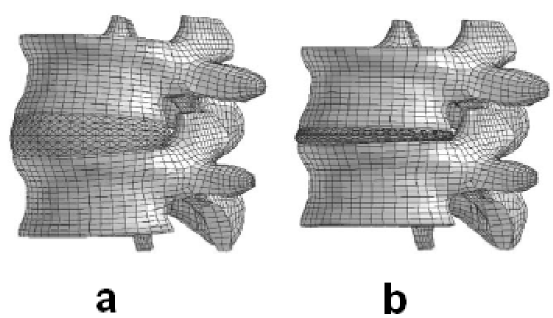

Figure 1.68. Finite element meshes of the L3-L4 lumbar spinal segment. a) Healthy disc. b) Severely degenerated disc, taken from Rohlmann et al., (2006).

In another finite element study with CT scan of the lumbar spine, Noailly et al., (2007) modified an existing model of an L3-L5 bi-segmental finite element model and conducted a sensitivity and validation study in order to evaluate the influence of the approximations inherent to modeling, see Figure 1.69. They investigated the effects of changes in bone geometry, ligaments fibres distribution, nucleus position and disc height in flexion-extension, lateral bending and axial rotation. Results from mobility were in agreement with the experimental results, independently of the geometrical changes. Also, they showed that the geometrical parameters affects the distribution of stress and strain energy in the zygapophysial joints, the ligaments and the intervertebral disc, changing qualitatively and quantitatively their relative role in resisting the imposed loads. Thus, the authors concluded that the validation of the lumbar spine model should be based on the relative role of its structural components and not only on its global mobility.

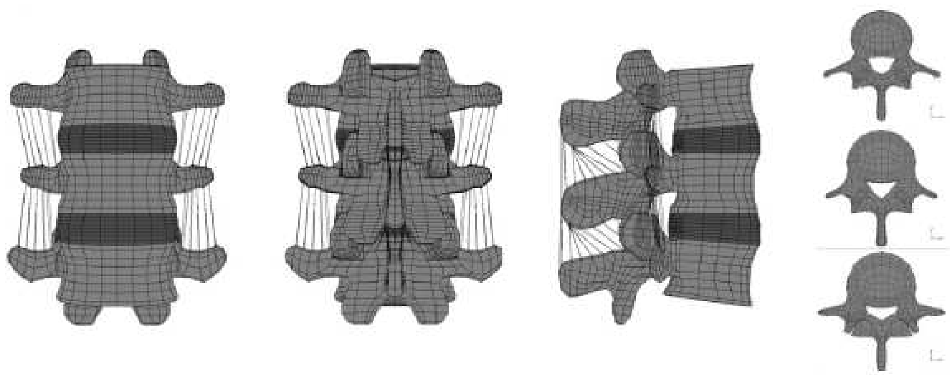

Figure 1.69. The L3-L5 lumbar spine bi-segment model used for the sensitivity study, taken from Noailly et al., (2007).

The creep response of a 3D L5-S1 reconstructed disc model from MRI was computed using substructuring techniques, this was based on dividing the complex structure into a series of smaller structures, called substructures (Swider et al., 2010), see Figure 1.70. In such model, the reduction of the computational task was achieved, and the displacement fields in three different loading conditions: compression, bending and torsion gave fair results.
From the foregoing presentations, one can say that the finite element method has evolved to become a standard technique that gives new insights for modeling and prediction of intervertebral disc degeneration. Whether the modeling involves linearities, nonlinearities, viscoelasticity or poroelasticity, it is evident that the detailed stress distributions that occur within the intervertebral disc is an arduous task that can be predicted only by using numerical solutions, and when geometrical aspects are taken into account, the use of medical imaging is advised.

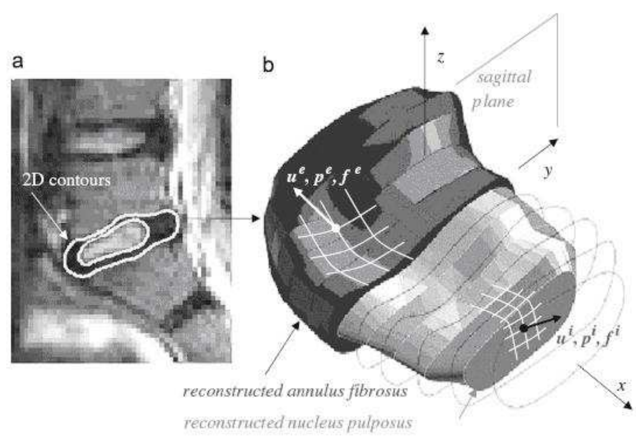

Figure 1.70. Application of the substructuring to a MRI of a L5-S1 intervertebral disc: (a) T2-weighted image in the saggital plane and segmentation of contours, and (b) volume reconstruction of nucleus pulposus and annulus fibrosus, taken from Swider et al., 2010.

VIII. References

Adams MA, Hutton WC and Stott JR (1980). “The resistence to flexion of the lumbar intervertebral joint”. Spine 5(3) pp. 245-253.

Adams MA, Hutton WC (1981). “The relevance of torsion to the mechanical derangement of the lumbar spine”. Spine 6(3): 241-248.

Adams MA, Hutton WC (1985). “Gradual disc prolapse”. Spine 10(6): 524-531

Adams MA, Dolan P. (1991). “ A technique for quatifying bending moment acting on the lumbar spine in vivo”. Journal of Biomechanics 24: 117-126.

Adams MA, Dolan P, Earley M,. (1994). “Bending and compressive stresses acting on the lumbar spine during lifting activities”. Journal of Biomechanics 27:1237-1248.

Adams, M.A., McNally, D.S., Dolan, P., (1996). Stress distributions inside interverteb- ral discs. The effects of age and degeneration. Journal of Bone and Joint Surgery. British Volume 78 (6), 965–972.

Adams, M.A., Bogduk, N., Burton, K., Dolan, P., (2002). The Biomechanics of Back Pain, Churchill Livingstone, Edinburgh, London, New York, Oxford, Philadelphia, St Louis, Sydney, Toronto, p. 238.

Allen L. and A.N. Palazotto (1983) “An analysis of the human intervertebral joint considering orthotropic and viscoelastic properties” J. Biomechanics 16(4): 287

Andersson GBJ, Ortengren R, Schultz A. (1980). “ Analysis and measurement of the loads on the lumbar spine during work at a table”. Journal of Biomechanics 15, pp. 513-529.

Antoniou J, Steffen T, Nelson E, Winterbottom N, Hollander AP, Poole PA, Aebi M and Alini M. (1996). “The human lumbar intervertebral disc: Evidence for changes in the biosynthesis and denaturation of the extracellular matrix with growth, maturation, ageing, and degeneration”. J. Clin. Invest. 98:996-1003.

Argoubi M and Shirazi-Adl A. (1996). “Poroelastic creep response analysis of a lumbar motion segment in compression”. Journal of Biomechanics Vol.29(10): 1331-1339.

Asano S, Kaneda K, Umehara S and Tadano S. (1992). “The Mechanical Properties of the Human L4-5 Functional Spinal Unit During Cyclic Loading: The Structural Effects of the Posterior Elements”. Spine 17(11) pp. 1343-1352.

Baogan P, Shuxun H, Qi S and Lianshun J. (2001). “The relationship between cartilage endplate calcification and disc degeneration: an experimental study”. Chinese Medical Journal 114(3): 308-312.

Belytschko T, Kulak RF, Schultz AB, Galante JO. (1974). “Finite element stress analysis of an intervertebral disc”. Journal of biomechanics 7: 276-285.

Benneker L, Heini PF, Alini M, Anderson SE and Ito K. (2005). “Vertebral Endplate Marrow Contact Chanell Occlusions and Intervertebral Disc Degeneration”. Spine 30(2): 167-173.

Bensoussan A, Lions JL, Papanicolaou G. (1978). “Asymptotic analysis for periodic structures”. North-Holland , Amsterdam.

Bernick S, Walker JM and Paule WJ. (1991). “Age Changes to the Annulus Fibrosus in Human Intervertebral Discs”. Spine 16(5): 520-524.

Best B, Guilak F, Setton LA, Zhu W, Saed-Nejad F, Ratcliffe A, Weidenbaum M and Mow VC. (1994). “Compressive Mechanical Properties of the Human Annulus Fibrosus and Their relationship to Biochemical Composition”. Spine 19(2): 212-221.

Bibby SR, Jones DA, Ripley RM et al. (2004). “Metabolismof the intervertebral disc: effects of low levels of oxygen, glucose and pH on rates of energy metabolism of bovine nucleus pulposus cells. Trans Am Orthop Res Soc..

Bick EM. (1955). “Vertebral osteophytosis: Pathologic basisof its roentgenology”. American Journal of Roentgenology 73: p.979

Biot MA. (1941). “General theory of three-dimensional consolidation”. Journal of applied physics, vol 12, pp. 155-164.

Bloch-Michel H, Benoist M and Peyron J. (1958). Images condensantes localisees des corps vertebraux.Rev Rhum Mal Osteoartic 25: p.732.

Boos N, Weissbach S, Rohrbach H, Weiler C, Spratt K and Nerlich A.(2002). “ Classification of Age-Related Changes in Lumbar Intervertebral Disc“. Spine 27(23): 2631-2644.

Boubriak OA and Urban JPG. (2003). “Nutrient supply to the cells of the intervertebral disc: effect of diurnal hydration changes”. Trans Am Othop Res 28: 1127.

Brickley-Parson D and Glimcher MJ (1983). “Is the chemistry of collagen in the intervertebral disc an expression of Wolff’s law? A study of the human lumbar spine. Spine 9. 148-163.

Broberg KB, Essen H.O. Von. (1980). “Modeling of Intervertebral Discas”. Spine 5(2) pp. 155-167.

Broberg KB (1983). “On the mechanical behavior of Intervertebral Discs”. Spine 8(2) pp. 151-165.

Brown T., Hanson, R. y Yorra, A.J. (Oct 1957). “Some mechanical tests on the lumbo-sacral spine with particular reference to the intervertebral discs”. J. Bone and joint surgery, 39-A: 1135-1164.

Brown MD, Holmes DC and Anneliese D. (2002). “Measurement of cadaver lumbar spine motion segment stiffness”. Spine 27(9): 918-922.

Bruehlmann S.B., Rattner J.B., Matyas J.R. and Duncan N.A. (2002). “Regional variations in the cellular matrix of the annulus fibrosus of the intervertebral disc”. Journal of Anatomy 201: pp. 159-171.

Buckwalter JA. (1995) “Aging and degeneration of the human intervertebral disc”. Spine 20:1307-14.

Burns, M.L. y Kaleps, I. (1980). Analysis of load-deflection behaviour of intervertebral discsunder axial compression using exact parametric solutions of Kelvin-solid models. J. Biomechanics 13, 959.

Burns, M. L., Kaleps, I. y Kazarian, L.E. (1984). Analysis of compressive creep behavior of the vertebral unit subjected to a uniform axial loading using exact parametric solution equations of Kelvin-solid models—Part I. Human intervertebral joints. Journal of Biomechanics, Vol 17(2): 113-130.

Busscher I, van Dieën J, Kingma I, van der Veen A, Verkerke G, Veldhuizen A. (2009). “Biomechanical characteristics of different regions of the human spine: An in vitro study on multilevel spinal segments”. Spine 34(26): pp. 2858-2864.

Cassidy J.J., Hiltner A. and Baer, E., (1989). “Hierarchical Structure of the Intervertebral Disc”. Connective Tissue Research 23: pp.75-88.

Cheung JT-M, Zhang M, Chow DH-K, (2003). “Biomechanical responses of the intervertebral joints to static and vibrational loading : a finite element study”. Clinical Biomechanics 18, pp. 790-799.

Chevrot A, Pillon B and Revel M (1978): “Phenomene radiologique du vide discal lombaire (vacuum-disc”. J. Radiol Electrol Med Nucl 59: p. 267.

Chiu EJ, Newitt DC, Segal MR, Hu SS, Lotz JC and Majumdar S. (2001). “Magnetic Resonance Imaging Measurements of Relaxation and Water Diffusion in the Human Lumbar Intervertebral Disc under Compression in Vitro”. Spine 26(23): E437-444.

Comin M and Prat J. (1998). “Biomecánica del raquis y sistemas de reparación”. Instituto de Biomecánica de Valencia. Ed. Generalitat Valenciana. pp 37-81.

Costi J, Stokes I, Gardner-Morse MS, Iatridis J. (2008). “Frequency-Dependent Behavior of the Intervertebral Disc in Response to Each of the Six Degree of Freedom Dynamic Loading: Solid Phase and Fluid Phase Contributions”. Spine 33 (16): pp1731-1738.

Coventry MB, Ghormley RK and Kernohan JW. (1945) “The intervertebral disc: Its microscopic anatomy and pathology. II. Changes in the intervertebral disc concomitant with age. J. Bone Joint Surgery 27:233.

Coventry MB. (1969). Anatomy of the intervertebral disc. Clinical Orthopeadic 67:9.

Cowin SC. (1999). “Bone poroelasticity”. Journal of Biomechanics vol. 32, pp.217-238

Cream JK, Roberts S, Jaffray DC, Eisenstein SM, and Duance VC. (1997). “Matrix metalloproteinases in the human intervertebral disc: Role in disc degeneration and scoliosis”. Spine 22:2877-2884.

Crisco JJ, Fujita L and Spenciner D. (2007). “ The dynamic flexion/extension properties of the lumbar spine in vitro using a novel pendulum system”. Journal of Biomechanics 40: 2767-2773.

Crisco JJ, Panjabi MM. (1991). “The intersegmental and multisegmental muscles of the lumbar spine – A biomechanical model comparing lateral stabilizing potential”. Spine 16, pp. 793-799.

Dehoff PH. (1978). “On the nonlinear viscoelastic behavior of soft biological tissues”. Journal of Biomechanics 11: pp. 35-40.

Dhillon N, Bass E and Lotz J. (2001). “Effects of frozen storage on the creep behavior of human intervertebral discs”. Spine 26(8): 883-888.

Duncan NA and Ahmed AM. (1991). “The role of axial rotation in the etiology of unilateral disc prolapse: An experimental and finite-element analysis”. Spine 16(9), pp. 1089-1098

Ebara S, Iatridis JC, Setton LA, Foster RJ, Mow VC and Weidenbaum M. (1996)“ Tensile Properties of Nondegenerate Human Lumbar Annulus Fibrosus”. Spine 21(4): 452-461.

Farfan, H.F. (1970). “The effects of torsion on the lumbar intervertebral joints: Role of torsion in the production of disc degeneration.” J. Bone and joint surgery Vol. 52-A, No. 3.

Ferguson S, Ito K and Nolte L. (2004). “Fluid flow and convective transport of solutes within the intervertebral disc”. Journal of Biomechanics 37: 213-221.

Ford LT, Gilula LA, Murphy and WA. (1977). “Analysis of gas in vacuum lumbar disc”. American Journal of Roentgenology 128: p.1056.

Fujii R, Sakaura H, Mukai Y, Hosono N, Ishii T, Iwasaki M, Yoshikawa H and Sugamoto K. (2007). “Kinematics of the lumbar spine in trunk rotation: in vivo three dimensional analysis using magnetic resonance imaging”. European Spine Journal 16(11): 1867-74.

Fung YC. (1967). “Elasticity of soft tissues in simple elongation”. American journal of physiology. Vol 213 (6): 1532-1544.

Galante J. (1967). “Tensile Properties of the human lumbar annulus fibrosus”. Acta Orthopedica Scandinavika (Supp) 100.

Galbusera F, Schmidt H, Neidlinger-Wilke C, Gottschalk A, Wilke H-J, (2011). “The mechanical response of the lumbar spine to different combinations of disc degenerative changes investigated using randomized poroelastic finite element models”. Eurospine Journal 20 (4), pp. 563-571.

Gallagher S, Marras W, Litsky A, Burr D, Landoll J and Matkovic V. (2007). “A comparison of fatigue failure responses of old versus middle-aged lumbar motion segments in simulated flexed lifting”. Spine 32(17) pp. 1832-1839.

Gallagher S, Marras W, Litsky A and Burr D. (2005). “Torso Flexion Loads and the Fatigue Failure of Human Lumbosacral Motion Segments”. Spine 30(20) pp 2265-2273.

Gardner-Morse MG and Stokes I. (2004). “Structural behavior of human lumbar spinal motion segments”. Journal of Biomechanics 37. pp. 205-212.

Glimer T, Sibue M and Ryckewaert A. (1975). “Les condensations vertebrales etendues des discophaties degeneratives. Semin Hop Paris 51:p.1199.

Goel VK, Monroe BT, Gilbertson LG, et al. (1995). “Interlaminar shear stresses and laminae separation in a disc”. Spine 20: 689-698.

Goel VK, Kong W, Han J, Weinstein JN and Gilbertson LG. (1993). “A combined finite element and optimization investigation of lumbar spine mechanics with and without muscles”. Spine 18(11), pp. 1531-1541.

Goel VK, Fromknecht K, Nishiyama K, and Weinstein JN. (1985). “The role of lumbar spinal elements in flexion”. Spine 10 (6): 516-523.

Goulet G, Coombe D, Tran D, Martinuzzi RJ, Zernickr RF. (2008). “Validation and application of iterative coupling to poroelastic problems in bone fluid flow”. Bulletin of applied mechanics 5(17): 6-17

Guan Y, Yoganandan N, Moore J, Pintar FA, Zhang J, Maiman DJ and Laud P. (2007). “Moment – rotation responses of the human lumbosacral spinal column”. Journal of Biomechanics 40:1975-1980.

Gundiah N, Ratcliffe M and Pruitt L. (2007). “Determination of a strain energy function for arterial elastin: experiments using histology and mechanical test”. Journal of Biomechanics 40: 586-594.

Guo LX, Teo EC, Lee KK, and Zhang QH. (2005). “ Vibration characteristics of the human spine under axial cyclic loads: effects of frequency and damping”. Spine 30(6), pp. 631-637.

Hansson TH, Keller TS and Spengler DM. (1987). Mechanical Behavior of the Human Lumbar Spine. II. Fatigue Strength During Dynamic Compressive Loading. Journal of Othopaedic Research Vol.5(4) pp.479-487.

Haughton V, Lim T and An H. (1999). “Intervertebral disc appearance correlated with stiffness of lumbar spinal motion segments”. AJRN American Journal of Neroradiology 20. pp. 1161-1165.

Hickey DS, and Hukins DW. (1980). “Relation between the structure of the annulus fibrosus and the function and failure of the intervertebral disc”. Spine 5(2): 106-116.

Hirsch, C and Nachemson, A (1954). “New observations on the mechanical behavior of lumbar discs” Acta orthopedica scandinavica 23: 254-283.

Hirsch C.(1955). “The reaction of intervertebral discs to compresion forces”. J. Bone Joint and Surg 37(A):1188.

Holmes AD, Hukins DWL. (1996). “Analysis of load-relaxation in compressed segments of lumbar spine. Med. Eng. Physics 18: 99-104.

Horner H and Urban JPG. Urban. (2001). Volvo Award Winner in Basic Science Studies. “Effect of nutrient supply on the viability of cells from the nucleus pulposus of the intervertebral disc”. Spine 26(23): 2543-2549.

Hormel SE. and Eyre DR. (1991). “Collagen in the ageing human intervertebral disc: An increase in covalently bound fluorophores and chromophores”. Biochim. Biophys. Acta: Protein Structure and Molecular Enzymology 1078:243-250.

Huyghe JM, Houben GB, Drost MR and van Donkelaar CC. (2003). “An ionised/non ionised dual porosity model of intervertebral disc tissue: experimental quatification of parameters”. Biomechanics model mechanobiology 2. pp. 3-19.

Iatridis JC, Weidenbaum M, Setton LA and Mow VC.(1996). “Is the Nucleus Pulposus a Solid or a Fluid? Mechanical Behaviors of the Nucleus Pulposus of the Human Intervertebral Disc”. Spine 21(10): 1174-1184.

Iatridis JC, Laible JP, Krag MH. (2003). “Influence of fixed charge density magnitude and distribution on the intervertebral disc: applications of a poroelastic and chemical electric (PEACE) model”. Journal of Biomechanical Engineering 125: 12-24.

Inkinen RI, Lammi MJ, Agren U, Tammi R, Puustjarvi K and Tammi MI. (1999). “Hyaluronan distribution in the human and canine intervertebral disc and cartilage endplate”. The Histochemical Journal 31: 579-587.

Inoue H. (1981). “Three dimensional Architecture of Lumbar Intervertebral Discs”. Spine 6(2): 139-146.

Izambert O, Mitton D, Thourot M, Lavaste F. (2003). “ Dynamic stiffness and damping of human intervertebral disc using oscillatory displacement under a free mass system”. European Spine Journal 12: 562-566.

Jackson A, Yuan T, Huang CY, Travascio F and Yong W. (2008). “Effect of Compression and Anisotrophy on the Diffusion of Glucose in Annulus Fibrosus”. Spine 33(1): 1-7.

Jackson A, Yao H, Brown MD and Gu WY. (2006). “Anisotropic Ion Diffusivity in Intervertebral Disc: An Electrical Conductivity Approach”. Spine 31(24): 2783-2789.

Johannessen W and Elliot DM. (2005). “Effects of Degeneration on the Biphasic Material Properties of Human Nucleus Pulposus in Confined Compression”. Spine 30(24): E724-729.

Jones RM. (1999). “Mechanics of composite materials, second ed. Taylor and Francis, London.

Kanematsu H. (1970). “An experimental study of intradiscal pressure”. Journal of Japanease orthopeadic association 44, pp. 589-599.

Kasra M, Shirazi-Adl and Grouin G. (1992). Dynamic of human lumbar intervertebral joints-experimental and finite element investigations. Spine 17, 93-102.

Kazarian, L.E. (1975). Creep charactaristicsof the human spinal column. Orthop. Clin. North A.. 6(1) 3-18.

Kazarian, L.E. and Kaleps I. (1979). Mechanical and physical properties of the human intervertebral joint. Technical report AMRL-TR-79-3, Aerospace medical research laboratory. Wrigth Patterson air force base, OH.

Keller, T.S., Spengler, D.M. y Hansson, T.H. (1987). Mechanical behaviour of the human lumbar spine. I Creep analysis during static compressive loading. J. Orthop. Research, Vol. 5, No. 4. pp.467-478.

Kettler A and Wilke H-J. (2006). “Review of existing grading systems for cervical or lumbar disc and facet joint degeneration” Europaen Spine Journal 15: 705-718.

Kim YE, Goel VK, Weinstein JN, et al. (1991). “Effects of disc degeneration at one level on the adjacent level in axial mode”. Spine 16:331-335.

Kim Y. (2000). “Prediction of peripheral tears in the annulus of the intervertebral disc”. Spine 25: 1771-1774.

Klisch S and Lotz J. (1999). “Application of a fiber-reinforced continuum theory to multiple deformations of the annulus fibrosus”. Journal of Biomechanics 32: 1027-1036.

Knutsson F. (1942). “The vacuum phenomenon in the intervertebral discs” . Acta Radiologika 23: p. 173

Koeller, W., Muehlhaus, S., Meier, W., Hartmann, F. (1986). “Biomechanical properties of human intervertebral disks subjected to axial dynamic compression - infuence on age and degeneration”. Journal of Biomechanics 19(10): 807-816.

Koeller W, Meier W, Hartmann F. (1984). “Biomechanical properties of human intervertebral discs subjected to axial dynamic compression: A comparison of lumbar and thoracic discs“. Spine 9: 725-733.

Krag MH, Cohen MC, Haugh LD and Pope MH. (1990). “Body height change during upright and recumbent postura“. Spine 15(3): 202-207.

Kroker P. (1949). “Sichtbare Rissbildungen in den Bandscheiben der Wirbelsaule“. ROFO 72:p.1

Kubla T, Niemeger T, Gaissmaier C and Grunder T. (2005). “ Human Annulus Fibrosus and Nucleus Pulposus Cells of the Intervertebral Disc: Effect of Degeneration and Culture Systemon cell phenotype“. Spine 30(24): 2743-2748.

Kulak RF, Belytschko T, Schultz AB, Galante JO. (1976). “Nonlinear behavior of the human intervertebral disc under axial load”. Journal of biomechanics Vol. 9: pp. 377-386.

Kurowsky P and Kubo A. (1986). “The relationship of degeneration of the intervertebral disc to mechanical loading conditions on lumbar vertebrae”. Spine 11(7), pp. 726-731

Kurutz M and Oroszváry (2010). “Finite element analysis of weightbath hydrotraction treatment of degenerated lumbar spine segments in elastic phase”. Journal of Biomechanics 43, pp. 433-441.

Laible, JF, Pfaster DS, Krag MH, Simon BR and Haugh LD. (1993). “A poroelastic-swelling finite element model with application to the intervertebral disc”. Spine 18, 659-670.

Lee CK, Kim YE, Lee CS, et al. (2000). “Impact response of the intervertebral disc in a finite element model”. Spine 25: 2431-2439.

Li S, Patwardhan AG, Amirouche FML, Havey R and Meade K. (1995). “Limitations of the standard linear solid model of intervertebral disc subject to prolonged loading and low-frequency vibration in axial compression”. Journal of Biomechanics Vol. 28(7): pp. 779-790.

Lin HS, Liu YK, Gautman R, Nikravesh P. (1978). "Systems identification for material properties of the intervertebral joint". Journal of Biomechanics 11: pp. 1-14.

Little JP, Adam CJ, Evans JH, Pettet GJ and Pearcy MJ. (2007). "Nonlinear finite element analysis of anular lesions in the L4-L5 intervertebral disc". Journal of Biomechanics 40, pp. 2744-2751.

Liu YK, Gautman R, and Hirsch C. (1975). "The resistance of the lumbar spine to direct shear". Orthopedic clinics of North America Vol. 6(1): pp. 33-49.

Lotz JC, Colliou KC Chin JR et al. (1998). "Compression-induced degeneration of the intervertebral disc: an in vivo mouse model and finite element study". Spine 23: 2493-2506.

Lu, Y.M, Hutton, WC and Gharpuray VM (1996). "Do bending, twisting and diurnal fluid changes in the disc affect the propensity to prolapse? A viscoelastic finite element model". Spine 21(22): 2570-2579.

Lyons G, Eisenstein SM, Sweet MB, (1981). "Biochemical changes in intervertebral disc degeneration" . Biochemica et Biophysica, Acta 673, pp 443-453.

Magnusson W. (1937). "Uber die Bedin gungen des Hervortretens der wirklichen Gelankspalte auf dem Rontgen bilde". Acta Radiologika 18:p. 733.

Malandrino A, Planell J, Lacroix D, (2009). "Statistical factorial analysis of the poroelastic material properties sensitivity on the lumbar intervertebral disc under compression, flexion and axial rotation". Journal of Biomechanics 42, pp. 2780-2788.

Marchand F. and Abdul M.A. (1990). "Investigation of the Laminate Structure of Lumbar Disc Anulus Fibrosus". Spine 15(5): pp 402-410.

Markolf KL. (1972). "Deformation of the thoracolumbar intervertebral joints in response to external loads". Journal of bone and joint surgery 54A, 511-533.

Markolf KL and Morris JM. (1974). " The structural components of the intervertebral disc". The journal of bone and joint surgery 56-A (4):675-687.

Maroudas A, Nachemson A, Stockwell R et al. (1975). "Factors involved in the nutrition of the human lumbar intervertebral disc: cellularity and diffusion of glucose in vitro". Journal of Anatomy 120: 113-130.

Marras WS, Lavander SA, Leugans SE. (1993). "The role of dynamic three-dimensional motion in occupationally-related low back disorders: the effects of work place factors, trunk position, and trunk motion characteristics on risk of injury. Spine 18: 617-628.

Mc Lauchlan GJ and Gardner DL. (2002). "Sacral and iliac articular cartilage thickness and cellularity: relationship to subchondral bone endplate thickness and cancelleous bone density". Rheumatology 41: 375-380.

McNally DS and Arridge RGC. (1995). "An analytical model of the intervertebral disc mechanics" . Journal of Biomechanics 28(1): 53-68.

Miller, J.A., Schultz, A.B., Warwick, D.N. y Spencer, D.L. (1986). Mechanical properties of lumbar spinal motion segments under large loads. J. Biomechanics Vol.19 (1) pp.79-84.

Miller, J.A.A, McGlashen, K.M., Schultz, A.B. y Anderson G.B.J. (1987). Load-displacement behaviour of the human lumbosacral joint. J. Orthop Res. 5, 488-496.

Mizrahi J, Silva MJ, Keaveny TM, Edwards WT, Hayes WC. (1993). "Finite-element stress analysis of the normal and osteoporotic lumbar vertebra body". Spine 18(14), pp. 2088-2096.

Muir, H. 1995."The Chondrocyte, Architect of Cartilage". Bioessays 17:1039-1048.

Nachemson A, Lewin T, Maroudas A, Freeman MA. (1970). "In vitro diffusion of dye through the endplates and annulus fibrosus of human lumbar intervertebral discs". Acta Orthop. Scand. 41: 589-607.

Nachemson A. (1960). "Lumbar intradiscal pressure". Acta Orthopaedica Scandinava 43: 1-105.

Nachemson A, Schultz AB and Berkson MH. (1979) "Mechanical properties of human lumbar spine motion segments. Influence of age, sex, disc level and degeneration. Spine 4(1). pp. 1-8.

Natarajan RN, Ke JH, Anderson GBJ. (1994). “A model to study the disc degeneration process”. Spine 19: 259-265.

Natarajan RN, Anderson GBJ. (1999). “The influence of lumbar disc height and cross-sectional area on the mechanical response of the disc to physiologic loading”. Spine 24: 1873-1881.

Natarajan RN, Williams JR, and Andersson GBJ. (2004). “Recent advances in analytical modeling of lumbar disc degeneration” Spine 29(23) pp. 2733-2741.

Natali, AN (1991). “A hyperelastic and almost incompressible material model as an approach to intervertebral disc analysis”. Journal of biomedical engineering 13, pp. 163-168.

National Institute for occupational safety and health. (1997). Musculoskeletal disorders and the workplace: A critical review of epidemiological evidence for work-related musculoskeletal disorders of the neck, upper extremity, and low back. Cincinnati, OH: U.S. Department of Health and Human Services, National Institute for Occupational Safety and Health, 1997.

Nerlich AG, Schleicher ED, and Boos N. (1997). “Immunohistologic Markers for Age-Related Changes of Human Lumbar Intervertebral discs”. Spine 22:2781-2795.

Noailly J, Wilke HJ, Planell J, Lacroix D. (2007). “How does the geometry affect the internal biomechanics of a lumbar spine bi-segment finite element model ? Consequenceson the validation process”. Journal of Biomechanics 40, pp. 2412-2425.

Noailly J, Planell J, Lacroix D. (2005). “Finite element study of a novel intervertebral disc substitute”. Spine 30(20), pp. 2257-2264.

Ohshima H. and Urban JPG. (1992). “Effect of lactate concentrations and pH on matrix synthesis rates in the intervertebral disc”. Spine 17:1079-1082.

Ohshima H, Tsuji H, Hirano N, Ishihara H, Katoh Y, Yamada H. (1989). “Water difussion pathway, swelling pressure, and biomechanical properties of the intervertebral disc during compression load”. Spine 14: 1234-1244.

Palmer, E. y Lotz, J. (2004). The compressive creep properties of normal and degenerated murine intervertebral discs. J. Orthop. Research. 22, pp. 164-169.

Panagiotacopulos N, Pope M, Krag M and Bloch R. (1987). “A mechanical model for the human intervertebral disc”. Journal of Biomechanics 20(9): 839-850.

Panjabi MM, Brand RA and White AA. (1976). “Mechanical properties of the human thoracic spine. J. Bone Joint Surgery. 58A pp. 642-652.

Panjabi MM, Krag MH and White AA (1984). “Effects of disc injury on mechanical behavior of the human spine”. Spine 9(7) pp. 707-713.

Panjabi MM, Abumi K, Duranceau J, Oxland TR. (1989). “Spinal stability and intersegmental muscles forces – a biomechanical model”. Spine 14, pp. 194-199.

Patwardhan AG, Havey RM, Carandang G, Simonds J, Voronov LI, Ghanayem A, Meade K, Gavin T and Paxinos O. (2003). “Effect of compressive follower preload on the flexion-extension response of the human lumbar spine”. Journal of Orthopaedic research 21: pp 540-546.

Pearcy, M.J. y Tibrewal, S.B. (1984). Axial rotation and lateral bending in the normal lumbar spine measured by three-dimensional radiography. Spine Vol 9 (6) pp.582-587.

Pfirmann, C, Metzdorf, A, Zanetti M, Hodler J and Boos N. (2001). “Magnetic Resonance Classification of Lumbar Intervertebral Disc Degeneration”. Spine 26(17): 1873-1878.

Pitzen T, Geisler F, Matthis D, Möller-Storz H, Barbier D, Steudel WI, Felges A (2002). “A finite element model for predicting the biomechanical behavior of the human lumbar spine”. Control engineering practice 10. pp. 83-90.

Pollintine P, Van Tunen M, Luo J, Brown M, Dolan P and Adams M. (2010). “Time-dependent compressive deformation of the ageing spine: Relevance to spinal stenosis” Spine 35(4): 386-394.

Pritzker KPH. (1977). “Aging and degeneration in the lumbar intervertebral disc”. Orthopedic Clinic North America 8: p.65.

Race, A., Broom, N.D. y Robertson, P. (2000). Effects of loading rate and hydration on the mechanical properties of the disc. Spine Vol. 25, No. 6, pp. 662-669.

Rajasekaran S, Naresh Babu, Arun R, Wilson BR, Shetty AP and Subramaniam M. (2004). “ A study of diffusion in human lumbar discs: A Serial Magnetic Resonance Imaging Study Documenting the influence of the Endplate on diffusion in Normal and Degenerated Discs”. Spine 29(23): 2654-2667.

Rao AA and Dumas GA. (1991). “Influence of material properties of the mechanical behavior of the L5-S1 intervertebral disc in compression: a nonlinear finite element study”. Journal of biomedical engineering 13, pp. 139-151.

Resnick D. (1994). “Diagnosis of Bone and Joint Disorders: Degenerative Disease of the Spine”. W.B. Saunders. Vol.2, Chapter 35: p.1382-1471.

Rice JR, and Cleary MP. (1976). “Some basic stress diffusion solutions for fluid-saturated elastic porous media with compressible constituents”. Reviews in geophysics and space physics, vol. 14, pp. 227-241.

Riches PE, Dhillon N, Lotz JC et al. (2002). “The internal mechanics of the intervertebral disc under cyclic loading”. Journal of Biomechanics 35: 1263-1271.

Roaf, R. (1960). “A study of the mechanics of spinal injury”. J. Boint joint Surg. 42B, 810.

Roberts N, Gratin C, Whitehouse G. (1997). “MRI analysis of lumbar intervertebral disc height in young and elder populations”. Journal of magnetic resonance imaging 7(5). pp. 880-886

Roberts S, Urban JPG, Evans H and Eisenstein S. (1996). “Transport Properties of Human Cartilage Endplate in Relation to its Composition and Calcificaction”. Spine 21(4): 415-420.

Roberts S, Menage J and Urban JPG. (1989). “Biochemical and Structural Properties of the Cartilage Endplate and its Relation to the Intervertebral Disc”. Spine 14(2): 166-174.

Rohlmann A, Zender T, Schmidt H, Wilke HJ, Bergmann G. (2006). “Analysis of the influence of disc degeneration on the mechanical behaviour of a lumbar motion segment using the finite element method”. Journal of Biomechanics 39, pp. 2484-2490.

Rolander SD. (1966). “Motion of the lumbar spine with special reference to the stabilizing effects of posterior fusion”. Acta orthopaedica scandinavica suppl. 90: pp 1-114.

Rostedt M, Ekström L, Broman H and Hansson T. (1998). “Axial stiffness of human lumbar motion segments, force dependence”. Journal of Biomechanics 31: 503-509.

Roughley, PJ. (2004). “Biology of intervertebral disc aging and degeneration: Involvement of the extracellular matrix”. Spine 29: 2691-2699.

Ruberté LM, Natarajan R, Andersson GBJ. (2009). “Influence of single-level lumbar degenerative disc disease on the behavior of the adjacent segments - A finite element study”. Journal of Biomechanics 42, pp. 341-348.

Sanchez-Palencia E, Zaoui A. (1987). “Homogenization techniques for composite media”. Springer, Verlag, Berlin.

Sanjeevi R, Somanathan N, Ramaswamy D. (1982). “A viscoelastic model for collagen fibers”. Journal of Biomechanics 15(3): 181-183

Schmidt H, Shirazi-Adl A, Galbusera F, Wilke HJ, (2010). “Response analysis of the lumbar spine during regular daily activities – A finite element analysis”. Journal of Biomechanics 43, pp. 1849-1856.

Schmidt H. Kettler A, Heuer F, Simon U, Claes L, Wilke HJ. (2007). “Intradiscal pressure, shear strain, and fiber strain in the intervertebral disc under combine loading”. Spine 3297), pp. 748-755.

Schmorl’s G and Junghanns H. (1971). “ The Human Spine in Health and Disease. 2nd Ed. Translated by EF Basemann. New York, Grune & Stratton, p138.

Schultz, A.B., Warwick, D.N., Berkson, M.H. y Nachemson, A.L. (1979). "Mechanical properties of the human lumbar spine motions segments. Part I: Responses in flexion, extension, lateral bending and torsion." J. Biomech. Eng. 101, 46-52.

Sélard E, Shirazi-Adl A, Urban JPG, (2003). "Finite element study of nutrient diffusion in the human intervertebral disc". Spine 28(17), pp. 1945-1953.

Shinmei M., Kikuchi T, Yamagishi M and Shinomura Y. (1988). "The role of interleukin-1 on proteoglycan metabolism of rabbit annulus fibrosus cells cultured in vitro". Spine 13:1284-1290.

Shirazi-Adl A, Taheri M, Urban JPG, (2010). "Analysis of cell viability in intervertebral disc: Effect of endplate permeability on cell population". Journal of Biomechanics 43, pp. 1330-1336.

Shirazi-Adl A , Soukane DM, Urban JPG, (2005). "Analysis of nonlinear coupled diffusion of oxygen and lactic acid in intervertebral discs". Journal of Biomechanical Engineering Vol. 127, pp. 1121-1126.

Shirazi-Adl, Li LP and Buschmann MD. (2000). "A fibril reinforced nonhomogeneous poroelastic model for articular cartilage: inhomogeneous response in unconfined compression". Journal of biomechanics 33. pp. 1533-1541.

Shirazi-Adl. A. (1994). "Nonlinear stress analysis of the whole lumbar spine in torsion - mechanics of facet articulation". Journal of Biomechanics Vol. 27(3), pp. 289-299.

Shirazi-Adl. A. (1992). "Finite-element simulation of changes in the fluid content of human lumbar disc: Mechanical and clinical implications".Spine 17(12): 206-212.

Shirazi-Adl A. (1989). " Strain in fibers of a lumbar disc: analysis of the role of lifting in producing disc prolapse". Spine 14(1) pp. 96-103.

Shirazi-Adl A. (1989). "On the fibre composite material models of disc annulus – comparison of predicted stresses". Journal of biomechanics 22, pp. 357-365.

Shirazi-Adl A and Drouin G (1987). "Load-bearing role of facets in a lumbar segment under saggital plane loadings". Journal of biomechanics 20, pp. 601-613.

ShiraziAdl, Ahmed AM, Shrivastava SC. (1986). "A finite element study of a lumbar motion segment to pure saggital plane moments". Journal of biomechanics 19(4), pp 331-350.

Shirazi-Adl A, Ahmed A, Shrivastava SC. (1986). " Mechanical response of a lumbar motion segment in axial torque alone and combined with compression". Spine 11(9), pp. 914-927.

Shirazi-Adl A, Shrivastava SC, Ahmed A. (1984). "Stress analysis of the lumbar disc-body unit in compression: A three dimensional nonlinear finite element study". Spine 9(2). Pp. 120-134.

Shirazi-Adl A, Shrivastava SC and Ahmed AM. (1983). " A 3-D nonlinear finite element analysis of a lumbar disc with annulus modeled as a composie". Applied mechanics, bioengineering and fluids engineering conference: biomechanical symposium, Houston TX, June 19-22, 1983. pp. 137-140.

Simon BR, Wu JSS, Carlton MW. (1985a). "Structural models for human spinal motion segments based on a poroelastic view of the intervertebral disc". Journal of Biomechanical Engineering 107, 327-335.

Simon BR, Wu JSS, Carlton MW, Kazarian LE, France EP, Evans JH and Zienkiewicz OC. (1985b). "Poroelastic dynamic structural models of rhesus spinal motion segments". Spine 10: 494-507.

Skaggs, DL, Weidenbaum, M, Iatridis, JC, Ratcliffe A and Mow VC. (1994) "Regional Variation in Tensile Properties and Biochemical Composition of the Human Lumbar Annulus Fibrosus". Spine 19(12): 1310-1319.

Spilker RL. (1980). "Mechanical behavior of a simple model of an intervertebral disc under compressive loading". Journal of biomechanics Vol. 13. pp 895-901.

Spilker RL, Daugirda DM, Schultz AB. (1984). "Mechanical response of a simple finite element model of the intervertebral disc under complex loading". Journal of biomechanics 17(2), pp. 103-112.

Spilker RL, Jakobs DM, and Schultz AB. (1986). "Material constants for a finite element model of the intervertebral disc with a fibre composite annulus". Journal of biomechanical engineering 108. pp. 1-11

Stokes I, Gardner-Morse M, Churchill D, and Laible J. (2002). “Measurement of a spinal motion segment stiffness matrix”. Journal of Biomechanics 35. pp. 517-521.

Swider P. Pédrono A, Ambard D, Accadbled F, Sales de Gauzy J, (2010). “Substructuring and poroelastic modeling of the intervertebral disc”. Journal of Biomechanics 43, pp. 1287-1291.

Sztrolovics RM. Alini PJ, Roughley P and Mort JS. (1997). “Aggrecan degradation in human intervertebral disc and articular cartilage”. Biochem J. 326:235-241.

Tencer AF, Ahmed AM and Burke DL. (1982). “Some static mechanical properties of the lumbar intervertebral joint, intact and injured. Journal of Biomechanical Engineering 104: 193-201.

Thompson JP, Oegema TR and Bradford, DS. (1991). “Stimulation of mature canine intervertebral disc by growth factors”. Spine 16:253-260.

Thompson JP, Pearce RH, Schechter MT, Adams ME, Tsang IK and Bishop PB. (1990). Preliminary Evaluation of a Scheme for Grading the Gross Morphology of the Human Intervertebral Disc”. Spine 15(5): 411-415.

Tsuji H., Hirano N., Ohshima H., Ishihara H., Terahata N. and Motoe T (1993). “Structural Variation of the Anterior and Posterior Annulus Fibrosus in the Development of Human Lumbar Intervertebral Disc: A isk Factor for Intervertebral Disc Rupture”. Spine 18(2): 204-210.

Tyrrell AR, Reilly T and Troup JDG (1985). Circadian variation in stature and the effects of spinal loading. Spine 10(2), PP. 161-164.

Umehara S, Tadano S, Abumi K, Katagiri K, Kaneda K, Ukai T. (1996). “Effects of degeneration on the elastic modulus distribution in the lumbar intervertebral disc”. Spine 21(7): pp 811-819.

Urban, JPG, Stanton S and Fairbank, JCT. (2004). “Nutrition of the intervertebal disc”. Spine 29: 2700-2709.

Urban JPG, Roberts S and Ralphs JR. (2000). “The nucleus of the intervertebral disc from development to degeneration”. American Zoologist 40(1): 53-61.

Urban, JPG. and Roberts S. (1995). “Development and degeneration of the intervertebral discs”. Mole. Med. Today 1:329-335.

Urban JPG and Maroudas A. (1979). “Measurements of fixed charge density and partition coefficients in the intervertebral disc”. Biochim Biophys Acta 586: 166-178.

Van der Veen A, Busscher I, van Dieën J, Kingma I, Verkerke G and Veldhuizen A. (2010). “In vitro biomechanical characteristics of the spine: A comparison between human and porcine spinal”. Spine 35(2): E35-E42.

Van der Veen A, Mullender MG, Kingma I, van Jaap H and Smit T. (2008). “Contribution of vertebral bodies, endplates and intervertebral discs to the compression creep of spinal motion segments”. Journal of biomechanics 41. pp. 1260-1268.

Virgin, W.J. (Nov 1951). Experimental Investigations into the physical properties of the intervertebral disc. J. Bone and Joint Surgery., 33-B: 607-611.

Wagner DR and Lotz J. (2004). “Theoretical model and experimental results for the nonlinear behavior of human annulus fibrosus”. Journal of orthopaedic research 22: 901-909.

Wang Z, Li H. (2005). “A novel 3D finite element modeling based on medical image for intervertebral disc biomechanical analysis”. Procedings of the 2005 IEEE Engineering in medicine and biology 27th Annual conference , Shanghai, China, September 1-4, 2005.

Weis EB. (1975). “Stresses at the lumbosacral junction”. Orthopedic clinics of North America Vol. 6(1): pp. 83-91.

Wehrli F, Leonard M, Saha P, Gomberg BR. (2004). “ Quantitative high-resolution magnetic resonance imaging reveals structural implications of renal osteodystrophy on trabecular and cortical bone”. Journal of magnetic resonance imaging 20. pp. 83-89.

Williams JR, Natarajan RN, Anderson GBJ. (2004). “Inclusion of regional variations in the poroelastic material properties of the lumbar disc better predicts the change in disc height during long term as well as short term loadings [poster no. 1147]. Transactions of 50 th Annual Meeting of Orthopedic Research Society, 2004.

Williams JR, Natarajan RN, Anderson GBJ. (2007). “Inclusion of regional poroelastic material properties better predicts biomechanical behavior of lumbar discs subjected to dynamic loading”. Journal of Biomechanics 40, pp. 1981-1987.

Wilke HJ, Neef P, Caimi M, Hoogland T and Claes L. (1999). “New In vivo Measurements of Pressures in the Intervertebral Disc in Daily Life”. Spine 24(8): 755-762.

Wognum S, Huyghe JM, Baaijens PT, (2006). “Influence of osmotic pressure changes on the opening of existing cracks in 2 intervertebral disc models”. Spine 31(16), pp. 1783-1788.

Wong C, Gehrchen PM, Darvann T, Kiaer T. (2003). “Nonlinear finite element analysis and biomechanical evaluation of the lumbar spine”. IEEE Transactions of medical imaging Vol. 20(6) June 2003, pp. 742-746.

Wu JS, Chen JH. (1996). “Clarification of the mechanical behavior of spinal motion segments through a three-dimensional poroelastic mixed finite element model”. Medical Engineering Physics 18: 215-224.

Wu HC and Yao RF. (1976). “ Mechanical behavior of the human annulus fibrosus”. Journal of Biomechanics 9: 1-7.

Yang KH, Khalil T, Tzeng R and King AI. (1983). “Finite element model of a functional spinal unit”. Applied mechanics, bioengineering and fluids engineering conference: biomechanical symposium, Houston TX, June 19-22, 1983. pp. 137-140.

Yin L and Elliot D (2004). “A homogenization model of the annulus fibrosus”. Journal of Biomechanics 37.

Yorra, A.J. (1956). “The investigation of the structural behavior of the intervertebral disc”. Thesis. Massachusetts Institute of Technology.

Zhou SH, McCarthy ID, Mc Gregor AH, Combs RRH and Hagues SPF. (2000). “Geometrical dimensions of the lower lumbar vertebrae – analysis of data from digitised CT images”. Eur Spine J 9: 242-248.

Chapter 2

Materials and Methods:

MRI of disc degeneration, Biomechanical Testing, and Disc modeling

Chapter 2

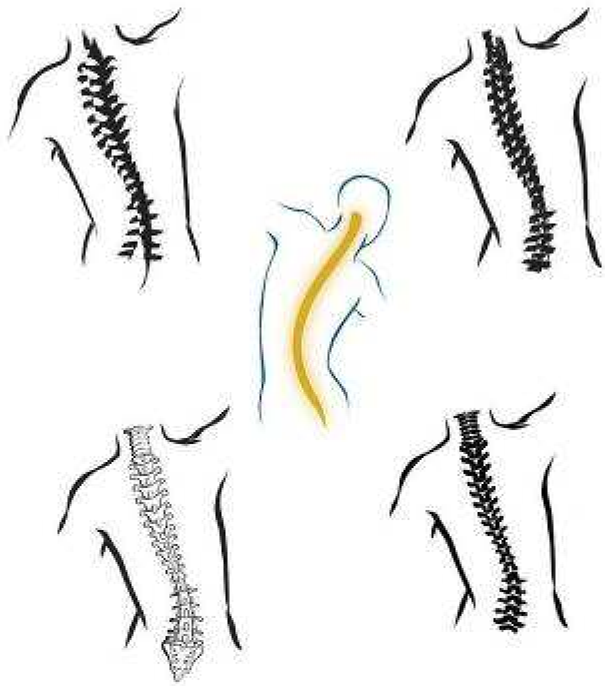

Materials and Methods: MRI of Disc Degeneration, Biomechanical Testing, and Disc modeling

This chapter presents the materials and methods used. Its starts with a description of the methodology used to handle cadaver intervertebral discs, specimen identification, MRI inspection and preparation for testing. Then, the experimental and numerical methodologies are presented. In the former methodology two testing protocols were designed, including a static loading and relaxation period protocol and a cyclic compression protocol applied to all discs. In both experimental tests a period of creep preconditioning was applied to each specimen prior to testing. In the numerical methodology the construction of the finite element mesh starting from the MRI of the discs is presented. Also, the identification of regional disc materials, assignment of the material type, geometric properties and boundary conditions is included.

$1/K_M$,	Disc flexibility.
3D,	Three dimensional.
a,	Major axis of the disc cross section.
b,	Minor axis of the disc cross section.
C_1, C_2,	Mooney-Rivlin deviatoric constants.
D,	Dashpot element.
E,	Young's modulus.
E,*	Complex modulus.
E',	Storage modulus.
E",	Loss modulus.
E_2/η,	Relaxation parameter.
$E_R(t)$,	Relaxation modulus.
Ex,	Extension.
F,	Force.
F(t),	Force over time.
FEA,	Finite element analysis.
FEM,	Finite element method.
Fl,	Flexion.
G,	Shear modulus.
H,	Hysteresis.
HDa,	Disc height at anterior site.
HDp,	Disc height at posterior site.
K,	Disc stiffness to axial load.
K_M,	Disc stiffness to bending.
K_T,	Disc stiffness to torsion.
L2-L3,	Disc from in between lumbar level 2 and 3.
L4-L5,	Disc from in between lumbar level 4 and 5.
LB,	Left lateral bending.
M,	Bending moment.
MRI,	Magnetic resonance imaging.
Ø,	Angular deflection in torsion.
PMMA,	Polymethylmethacrylate.
RB,	Right lateral bending.
S,	Spring element.
SLS,	Standard linear solid model.
STL,	Stereo lithography.
t,	Time.
T,	Torque moment.
t(r),	Relaxation time.
T1,	Weighted spin echo sequence.
T2,	Weighted fast spin echo sequence.
$Tan\ \delta$,	Ratio of loss to storage moduli.
UVF,	Unit vertebral function.
X, Z,	Radial bulging.
Y,	Vertical displacement.
β,	Phase angle difference.
ε,	Normal strain.
θ,	Angular deflection in bending.
ν,	Poisson's ratio.
σ,	Normal stress.
$\sigma(t)$,	Relaxation functions or stress decay.

I. Disc preparation

a. Material identification

Five lumbar spine sections from cadaveric elderly donors with a mean age of 70 years were obtained from Hospital Clinic of Barcelona, Spain. The lumbar sections were further dissected in situ into 10 unit vertebral functions (UVF), five specimens (n=5) corresponding to level L2-L3 and five (n=5) to level L4-L5. Additional removal of the posterior elements and ligaments were done and only the anterior and posterior longitudinal ligaments were preserved. The actual appearance after posterior elements removal of two lumbar level discs used in this study is shown in Figure 2.1.

Hospital and laboratory safety regulations require the use of a protocol for handling post-mortem human tissues and also for biological tissue degradation. For these purposes each specimen was sealed in double plastic bag and always handled using surgical gloves. Specimen identification (ID) such as geometry, anatomical grade and testing history were recorded in a sheet called "traveler", see Figure 2.2. If the specimen with the traveler was not to be tested then it was stored in the freezer at -20°C until the day of testing. Conservation and degradation of biological tissues and their subsequent mechanical properties have been studied by Galante (1967). He concluded that degradation by freezing and subsequent thawing can be neglected if tissue relative humidity is maintained close to 100%.

Figure 2.1. Typical lumbar discs used in the present study. A Level L2-L3 (left) and a level L4-L5 (right).

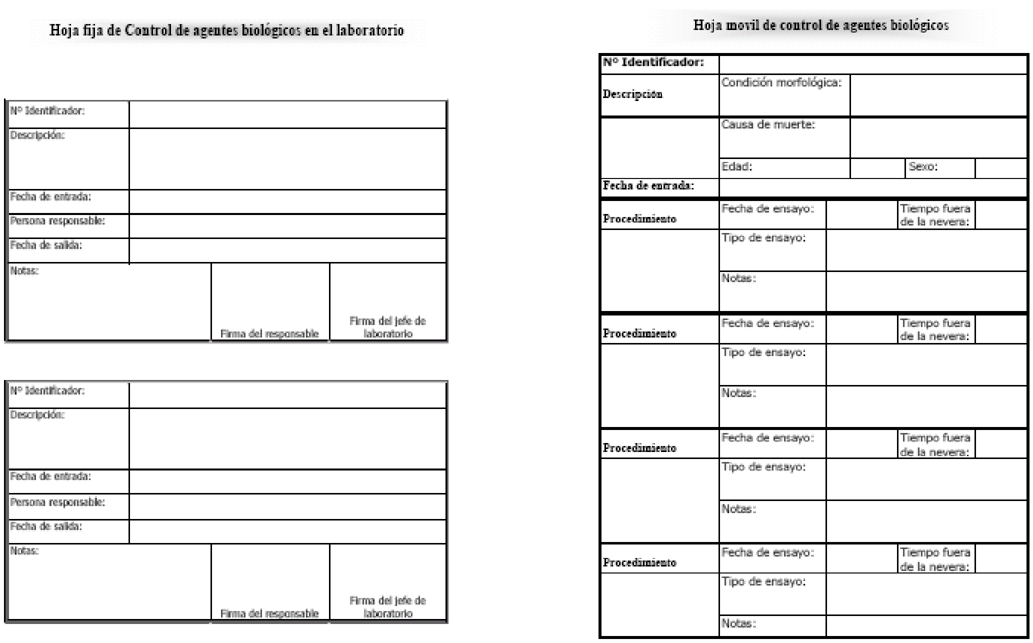

Hoja fija de Control de agentes biológicos en el laboratorio

Nº Identificador:
Descripción:
Fecha de entrada:
Persona responsable:
Fecha de salida:
Notas:
Firma del responsable
Firma del jefe de laboratorio

Nº Identificador:
Descripción:
Fecha de entrada:
Persona responsable:
Fecha de salida:
Notas:
Firma del responsable
Firma del jefe de laboratorio

Hoja movil de control de agentes biológicos

Nº Identificador:
Descripción
Condición morfológica:
Causa de muerte:
Edad:
Sexo:
Fecha de entrada:
Procedimiento
Fecha de ensayo:
Tiempo fuera de la nevera:
Tipo de ensayo:
Notas:
Procedimiento
Fecha de ensayo:
Tiempo fuera de la nevera:
Tipo de ensayo:
Notas:
Procedimiento
Fecha de ensayo:
Tiempo fuera de la nevera:
Tipo de ensayo:
Notas:
Procedimiento
Fecha de ensayo:
Tiempo fuera de la nevera:
Tipo de ensayo:
Notas:

Figure 2.2. Traveler sheets used for specimen documentation in the experimental study.

The sequence of specimen handling during this study is summarized in the flow chart shown in Figure 2.3. Because the discs were to be tested with 6 modes of loading all the travelers had to be updated. Documentation include day of testing, type of loading, magnitude, duration of testing including the thawing time and observations. When it was decided that a disc was no longer needed for testing it was stored in an isolated cage in the freezer along with its traveler. Access to the discs was limited to only the laboratory responsible and me. Additional precautions were taken in the cutting of the vertebral bodies top and bottom surfaces in preparation for the disc setting with polymethylmethacrylate (PMMA) see section 3.I.c.

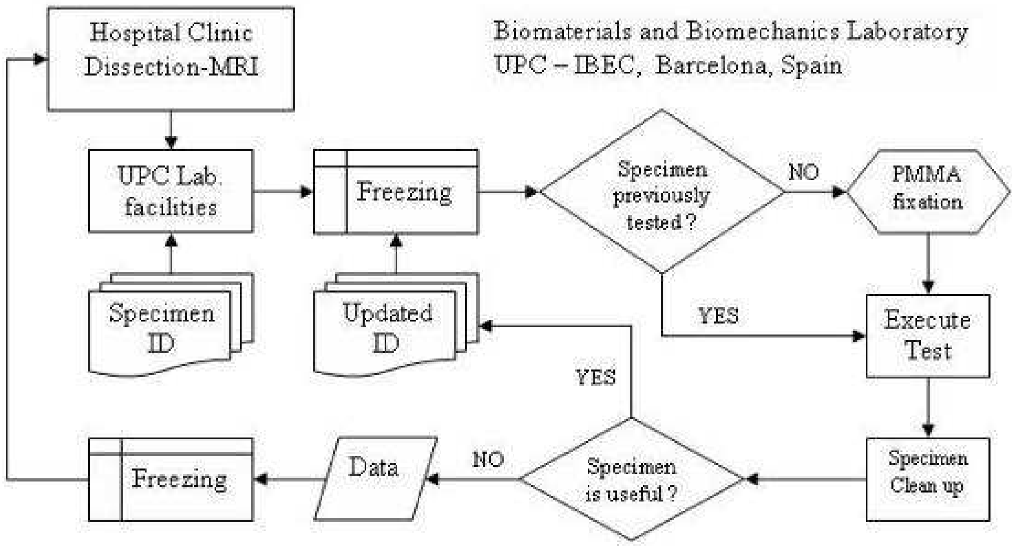

Figure 2.3. (A) Flow chart for the handling of the discs.

Measurements were made to obtain an approximate value of the disc cross section area and its height. For the latter it was assumed that the disc area had an elliptic shape as suggested by Farfan et al., (1970). Definition of the major and minor axis "a" and "b" respectively are shown in Figure 2.4. The disc height was measured with a caliper in the anterior site HD_a; posterior site HD_p, right and left lateral margins and a mean value was assigned.

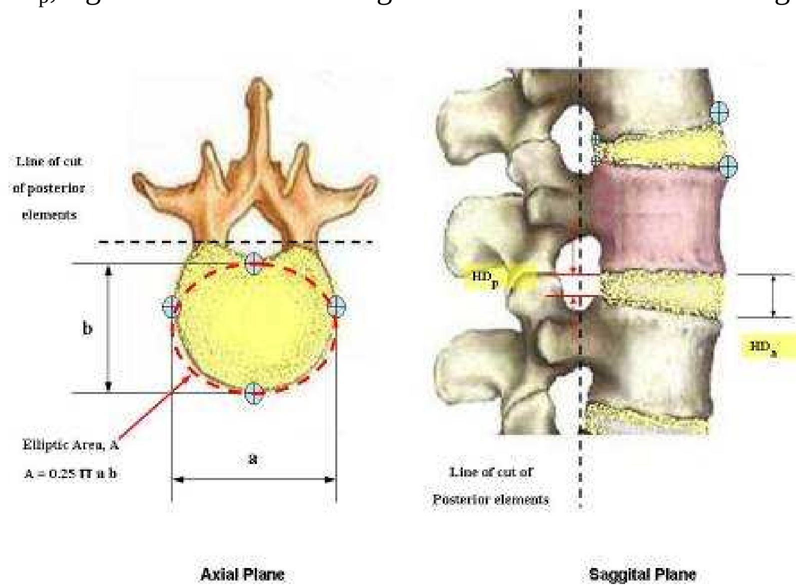

Figure 2.4. Locations for measurements of the cross section and disc height.

Recording of cadaver sex, age, disc levels, disc cross sectional area and disc height are summarized in Table 2.1.

Table 2.1. Anatomical record of the specimen used in this study. Only specimens free of congenital diseases were included.

Specimen	***Level***	***Sex***	***Age (Years)***	***Axis length (mm)***		***Elliptic area, A A=(πab)/4 (mm²)***	***Disc height "h" (mm)***
				major a	***minor b***		
A	***L2-L3***	***M***	***70***	***55***	***44***	***1900***	***10***
B	***L4-L5***	***F***	***70***	***60***	***38***	***1790***	***8***
C	***L4-L5***	***M***	***65***	***60***	***43***	***2026***	***10***
D	***L4-L5***	***M***	***70***	***60***	***49***	***2309***	***9***
F	***L2-L3***	***M***	***75***	***55***	***41***	***1771***	***10***
G	***L2-L3***	***M***	***70***	***57***	***42***	***1880***	***12***
H	***L2-L3***	***M***	***65***	***54***	***40***	***1697***	***10***
I	***L4-L5***	***M***	***75***	***56***	***42***	***1847***	***12***
J	***L4-L5***	***M***	***70***	***54***	***42***	***1782***	***11***
L	***L2-L3***	***F***	***70***	***46***	***40***	***1445***	***7***
Mean			***70***			***1845***	***9.90***
SD			***3.33***			***222.78***	***1.60***

Mean cross sectional area and standard deviation (SD) values for the L2-L3 and L4-L5 disc sets were reported to be 1739 mm^2 with SD=183 mm^2 and 1951 mm^2 with SD=233 mm^2 respectively. The corresponding values for the disc height were 10 mm with a SD=1.60 mm for both lumbar levels. Two specimens (E and K) not shown in Table 2.1 were removed because of severe osteoporosis.
After specimen identification an assessment of volumetric and geometric inspection of the nucleus, annulus and vertebral bodies by magnetic resonance imaging (MRI) was performed to all the discs.

b. Magnetic Resonance Imaging (MRI) of disc degeneration

The objective of performing magnetic resonance imaging (MRI) on all the degenerated discs was to gain the disc geometry and characterized its anatomy. With the geometry of the disc, a model of disc degeneration is proposed. MRI has proven to be an effective procedure for input disc geometry into a finite element model to study the intervertebral disc biomechanics (Wang et al. 2005). Therefore, every disc used was inspected using the MRI Siemens Harmony ™ system, from the Radiodiagnostic facilities of Hospital Clinic in Barcelona, Spain. A needle transducer permitted inspection in the axial, coronal and saggital plane to insure that no tumors, previous fractures, diseases that effect bone or bony abnormalities were present. Only changes due to intervertebral osteochondrosis, and spondylosis deformans were considered, e.g. cavity formation, calcified cartilage and new bone formation were among the morphological features worth identifying.

Inspection with the MRI required that the intervertebral disc be at room temperature. Therefore, discs that were previously stored in the freezer were allowed first to thaw for 12 hours. After which they were inspected, one by one, in the MRI system using the following sequence.

Values for the MRI sequence may change depending on the biological tissue and the ex-vivo condition, but the imaging procedure does not. In a morphological and biochemical assessment of intervertebral disc degeneration to ex-vivo specimens done by Benneker et al., (2005) and Perie et al., (2006) they used the following sequence:

- Axial localizer (spoiler gradient).
- Coronal and Saggital T1-weighted spin-echo.
- Coronal and Saggital T2-weighted Fast Spin Echo (FSE) for anatomical assessment.

The MRI inspection also started with a localized sequence. For this purpose a coronal T1-weighted spin-echo (repetition time [TR] 870 msec/echo time [TE] 19 msec) and a T2-weighted fast spin-echo “FSE” (TR=2300 msec/TE 106 msec) sequence were used.

Once the specimens were localized then the actual imaging protocol was determined, which also included a coronal and saggital T1-weighted spin-echo (repetition time [TR] 24.6 msec/echo time [TE] 7.2 msec) followed by a T2-weighted FSE (TR 3400 msec/TE 94 msec) images with the following parameters for the T1 sequence: matrix 256 x 256; field of view 10.4 x 10.4 mm; slice thickness, 0.4 mm; interslice gap, 0.4 mm; echo train length (ETL), 3 and for the T2 sequence: matrix 128 x 128; field of view 22.8 x 22.8 mm; slice thickness, 3 mm; interslice gap, 0.3 mm; echo train length, 5.

The appearance of a localized sequence image is shown in Figure 2.5. Only the disc and the neighboring sides of the vertebra bodies were inspected as shown by the coronal T2-weighted spin echo images, see Figure 2.6.

Figure 2.5. Localized sequence in the saggital (left) and axial view (right) to a L2-L3 disc.

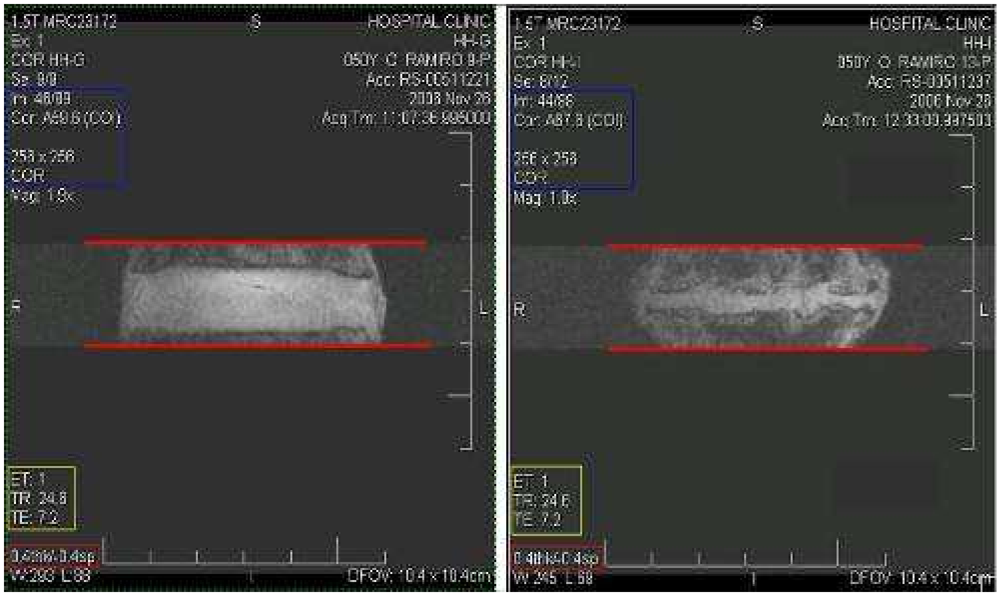

Figure 2.6. Typical MRI showing the T2-weighted spin-echo anatomical record of two degenerated discs, a L2-L3 disc (left) and a L4-L5 disc (right). Resolution is shown on the blue and red boxes while the time sequence is shown in the yellow box. Areas with more bright indicate higher water content typical of soft tissues while opaque areas indicate denser material, e.g. bone structure.

The recorded spin-echo sequences were saved as DICOM files which is widely used format that can be read by many segmentation programs, such as MIMICS, MATERIALISE ™ that was used in this study. After the MRI inspection all the discs were sealed in double plastic bags and were frozen at -20°C until the day of testing.

c. Specimen fixation

Mechanical test of the intervertebral disc requires that each specimen is held fix in a test fixture by mechanical or chemical means without further damaging the disc tissue. Typically the minimum spine segment that can be tested and characterized is a unit vertebral function (UVF) consisting of a vertebra–disc-vertebra. In our case the UVF was further dissected from its posterior elements, this was necessary in order to characterize the full disc response to bending and torsion and eliminate any possible contribution of the posterior processes. Therefore, the fixation procedure was applied to the remaining vertebra-disc-vertebra for all specimens while still frozen and included the use of a plastic acrylic polymethylmethacrylate (PMMA), two testing cylindrical plates and a custom assembly device for achieving parallelism and concentricity of each fixed specimen, see Figure 2.7. Due to the toxic reaction of PMMA polymerization it was advised to work close to an extraction chamber. A general clean up of the workplace was advised before the start of the procedure.

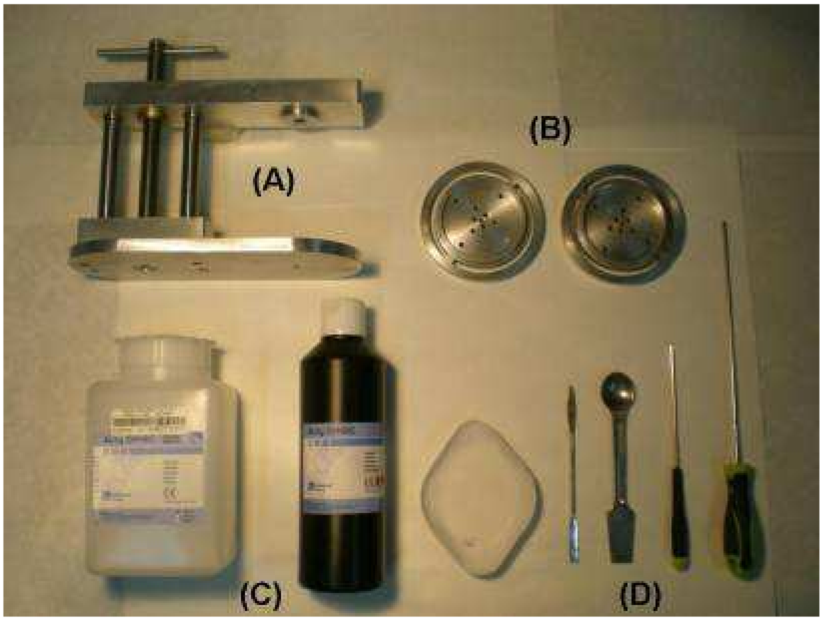

Figure 2.7. Material used for disc setting. (A) Assembly device, (B) testing cylindrical plates, (C) plastic acrylic, Polymethylmethacrylate "PMMA" Acry Ortho^{TM} Ruthinium Group, and (D) tool accessories.

The disc setting procedure is shown in Figure 2.8 and starts with the preparation of one testing cylindrical plate in which the PMMA was polymerized. Using a sheet of acetate, a strip of 10 mm width was cut and sticks it with plasticine into one of the cylindrical plate, as shown in Figures 2.8 (a-d). Anchorage of one end of the specimen into the plate's base was achieved by using screws, which had to be sealed with plasticine (e). The PMMA was formed by mixing the powder with the liquid monomer. First, the powder was deposited into the prepared plates. An amount of 100 g was needed for fixation of a single disc, 50 g for the upper, and 50 g for the lower fixation side (f). After the deposition a wetting of all the powder was done using the liquid monomer (g), until the mixture of powder and liquid achieved a gel consistency (h-i), then in a chamber the specimen was introduced and positioned quickly into the plates containing the gel mixture (j-l). If needed additional powder and liquid were added. The reaction time of polymerization for the used PMMA took about 15 minutes which gave time to prepare the other testing plate by repeating steps (a-f).

A critical aspect of the setting process was the maintenance of parallelism and concentricity between the top and lower plate's surfaces as this determines optimal geometrical conditions for "pure" axial loading in compression. Once the reaction time was set on the first plate containing the specimen, the second plate was positioned into the lower base of the assembly device (m) and the powder wetting was repeated. Then quickly, the first plate containing the specimen was put in the upper base of the assembly device and was hand hold it while turning the handle (n) until the specimen reach the lower plate. Here additional powder and liquid was added while the initial stages of the reaction took place (o-p). After another 15 minutes the reaction ceased and the fixation of the specimen to the testing plates was achieved (q).

Two additional plates were assembled to the fixed specimen (r-t) for connection to the testing frame. After specimen fixation the disc was ready for testing. If the fixed disc was not to be tested then it was returned to the freezer at -20°C.

Figure 2.8. Setting procedure with polymethylmethacrylate (PMMA) for each intervertebral disc.

II. The experimental protocol

The purpose of biomechanical testing to degenerated intervertebral discs was to characterize the mechanical response to static and dynamic loads, which are necessary for gaining input data for finite element studies of disc degeneration. The methodologies consisted of imposing physiological loads and analyze the corresponding response of the discs. For this purpose, a testing protocol was developed and applied to all the discs used in this study. The protocol consisted in two phases: (1) a static loading with a relaxation period to analyze disc stiffness and relaxation response, and (2) a dynamic loading to analyze damping behavior and viscoelasticity. In the static testing protocol, any difference in the deflection and relaxation response between different lumber levels and degeneration scoring were investigated, see Figure 2.9.

Prior to any testing, a period of 12 hours of thawing was allowed to all frozen fixed discs in the laboratory. The testing technique was based on applying static and dynamic loading using a hydraulic actuator. The testing apparatus was a MTS Bionix 858 system with a custom frame build that allowed the application of the different modes of bending and torsion, see Figure 2.10.

Because biological tissues dehydrate with time and this affects its biomechanical behavior, the entire testing protocol was applied in one session for every disc. Disc hydration was observed before and during every testing. As part of the testing protocol the disc was wrapped in a cotton tissue and was subjected to a water spray every 15 minutes.

Also, the ex-vivo condition of the disc causes no pressure in the nucleus to move out fluid, thereby causing water retention in the nucleus while the annulus dehydrates. To better redistribute the water in the disc, it has been suggested to apply a compressive creep of 300 N for a period of 15 minutes before any testing. This creep allows the retained water in the nucleus pulposus to be partially distributed in the annulus fibrosus, thus bringing the disc into a broad physiological range as suggested by Adams et al. (1995). Thus, all the discs were creep preconditioned at the specified values.

In the second experimental protocol, a cyclic compression load in the physiological range was used to investigate the dynamic properties: the storage modulus, the loss modulus, and the amount of hysteresis between different lumbar levels and degeneration scoring, see Figure 2.11.

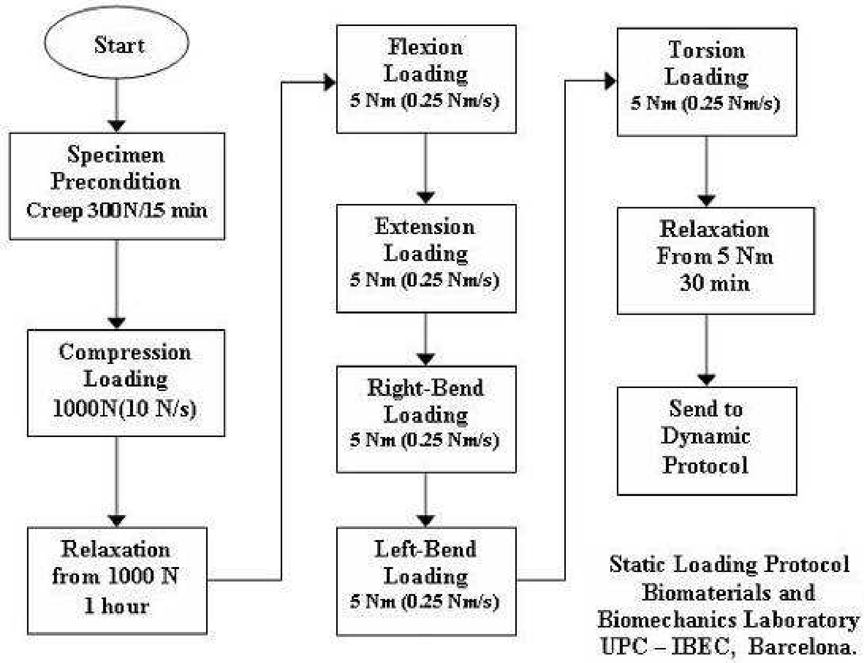

Figure 2.9. Static loading protocol used in this study for characterization of disc stiffness, Young's modulus, deflection response and relaxation time.

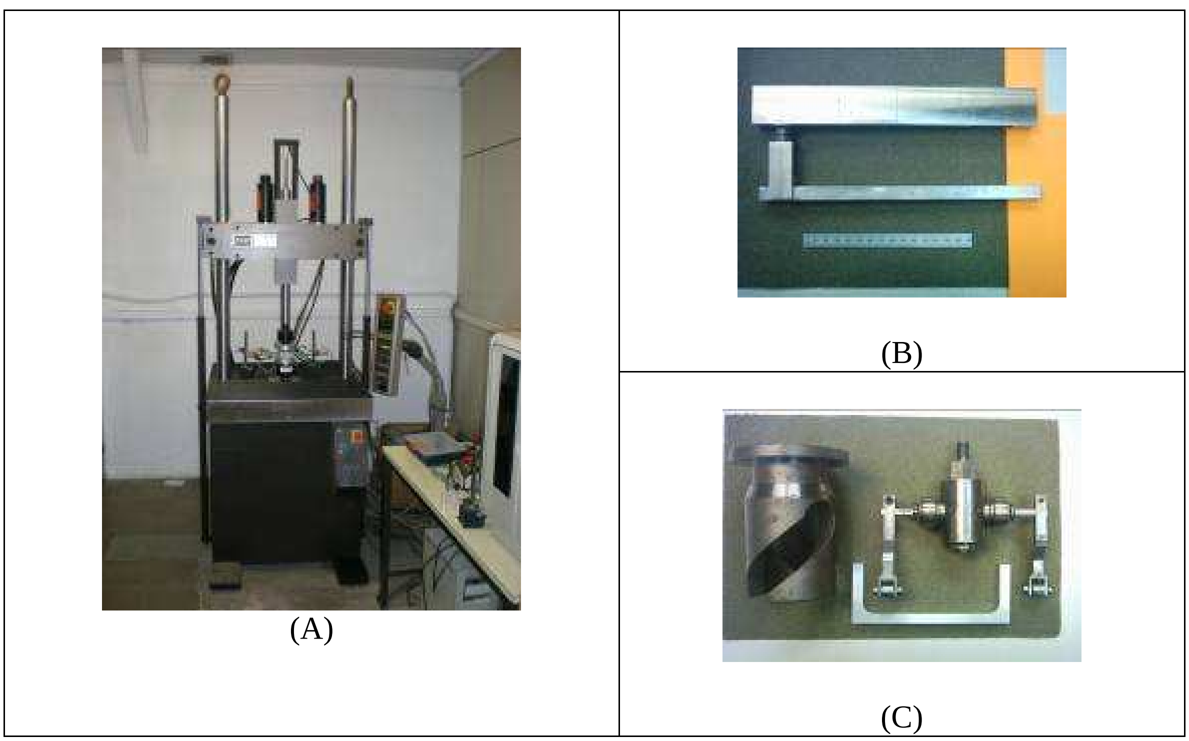

Figure 2.10. (A) MTS Bionix testing 858 system used for the experimental study. (B) Rig frame for applying bending and (C) accessories for applying torsion.

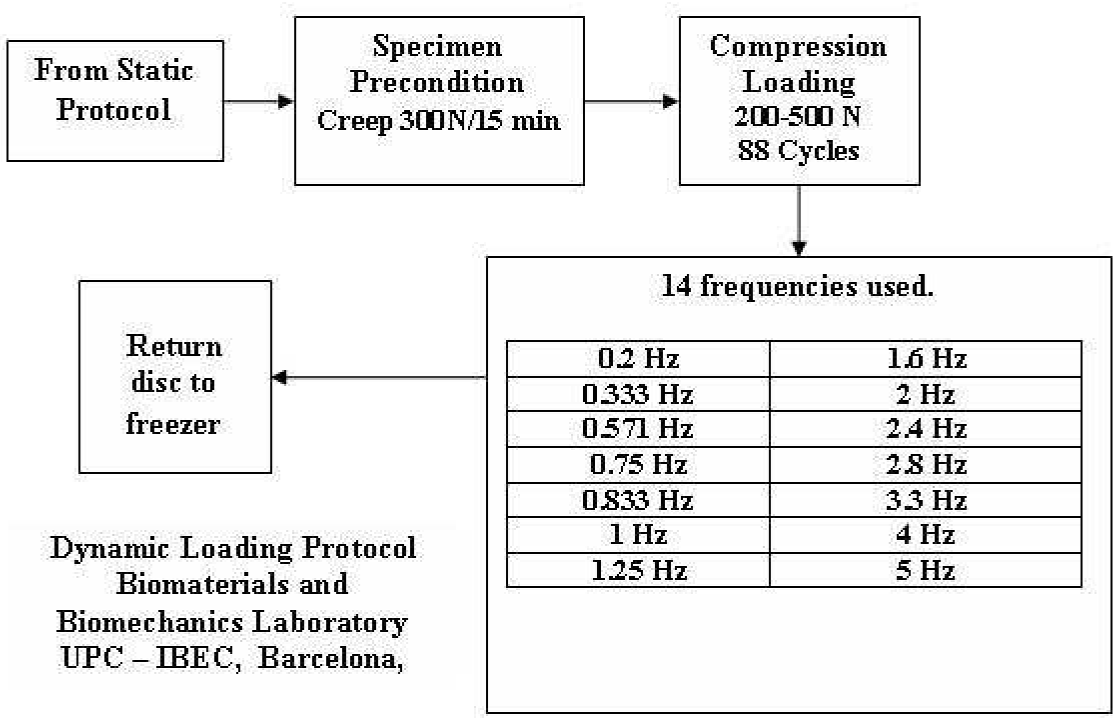

Figure 2.11. Cyclic compression protocol used in this study for characterization of viscoelastic behavior.

a. Compression load protocol

Loading the intervertebral disc to axial compression serves to determine the *disc stiffness K, Young's modulus E, axial deformation* ε, and *radial bulging X, and Z.* The load type and its magnitude were kept in the static physiological range to prevent further damage and failure of the discs. The advanced degeneration stages of the L4-L5 discs used in this study favor the use of force control instead of displacement control. Therefore, a maximum compressive force *F* of 1000 N was applied with a loading rate of 10 N/s, as this simulates a broad range of daily loading activities in accordance with Adams et al. (1995) and also avoids rate effects (Lin et al, 1978). This loading rate gave a corresponding piston displacement rate of about 0.5 mm/min which is adequate for testing biological tissues under static loading. After reaching 1000 N the relaxation test began and lasted 60 minutes were the force decay eventually tends to stabilize.

Measurements of the applied force *F* in Newton (N), the vertical displacement *Y* of the hydraulic actuator in millimeters (mm), and the radial bulging in the anterior side *X* and posterior side *Z* also in millimeters (mm) were recorded during the loading stage. Sensors used included (1) force transducer cell for *F* readings and (2) displacement potentiometers for *X* and *Z* readings, see Figure 2.12 for specifications.

Force Cell

Dealer: MTS
Model 661.18F-02
Service load: 2500 N.
Bridge resistance: 350Ω
Accuracy class: 0.08%
Sensitivity: 1 mV/V

(a)

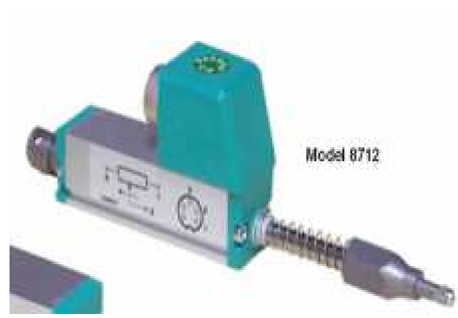

Displacement Sensor

Dealer: Burster
Model: 8712
Range of service: 0-10 mm.
Accuracy: 0.05%.
Resolution: 0.01 mm.

(b)

Figure 2.12. Specification of sensors used in the compression and relaxation test. (a) Force cell and (b) displacement sensor.

A schematic representation and the actual appearance of the set up for the compression and relaxation test are shown in Figure 2.13.

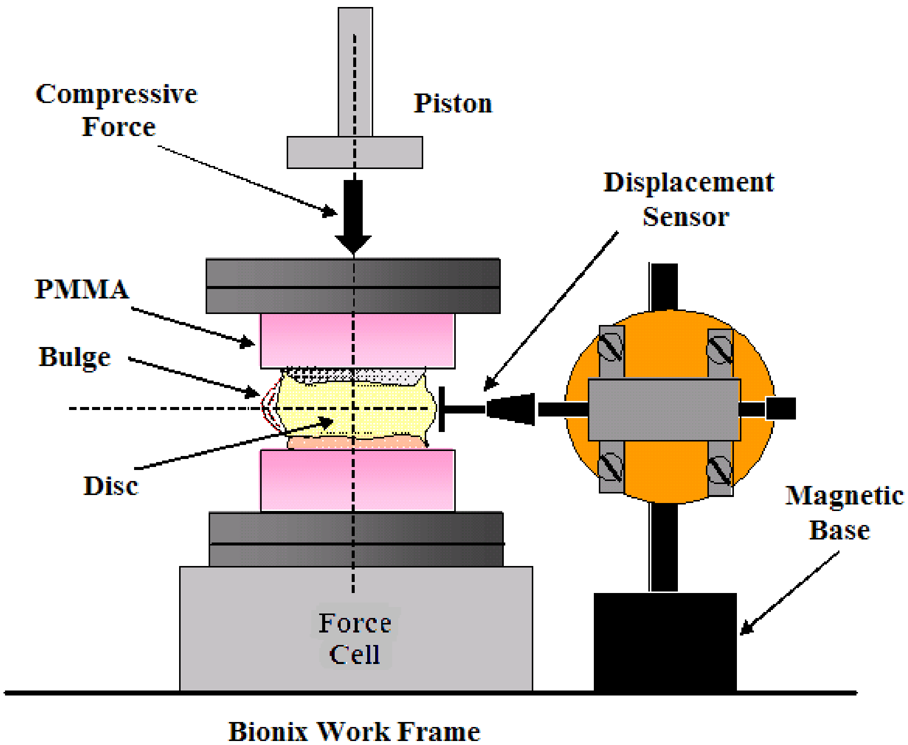

(A)

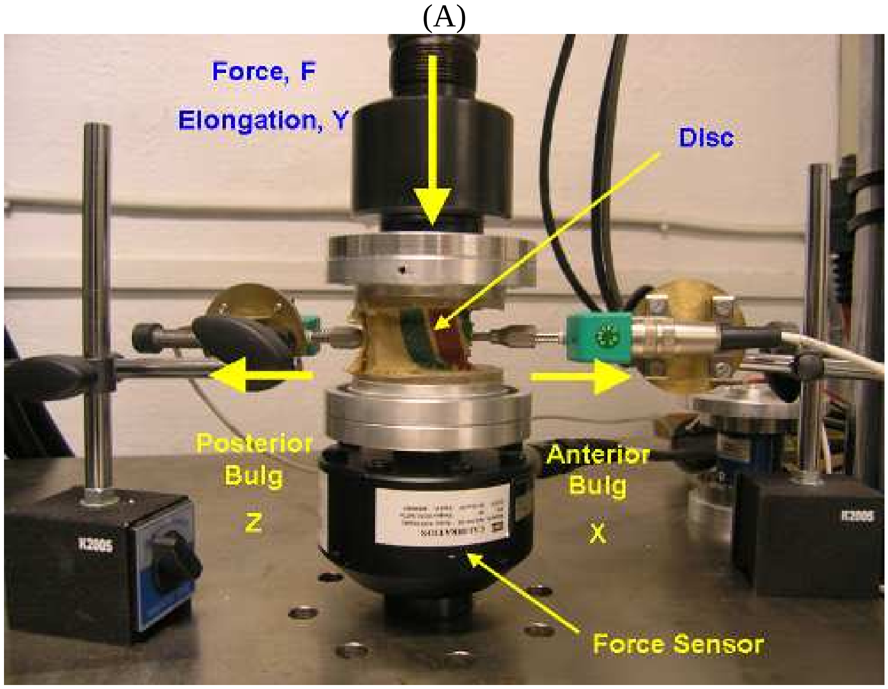

(B)

Figure 2.13. (A) Schematic representation of the compression loading and stress relaxation test set up. (B) Actual appearance.

With the readings of *F* and *Y* from the loading stage a calculation of the plot *stress-strain* σ–ε is usually done. Here, the stress is a *normal stress* σ_C and the strain is also a *normal strain* ε_Y and corresponds to the disc as a whole and not to a particular material.

The relationship between stress and strain for biological tissues, such as the intervertebral disc, tends to be *nonlinear* with *large strains* due to the polymeric nature of the collagen tissues. One explanation is that in the initial stages of the compression loading, the nucleus pulposus develops pressure that acts radially in expansion, and causes also expansion of the outer annulus laminas where the crimped collagen fibers are stretch. This elongation of the fibers will led to a horizontal slope, segment A-B in Figure 2.14, with a low value for the *Young's modulus*, *E*. As the load increases the fiber stretching also increases which leads to a higher slope B-C and a corresponding higher value of the *E* modulus, until the fiber yield is reached, see segment C-D. In practice, the *Young's modulus E* of the disc corresponds to a mean value of 50% to 100% of the peak load.

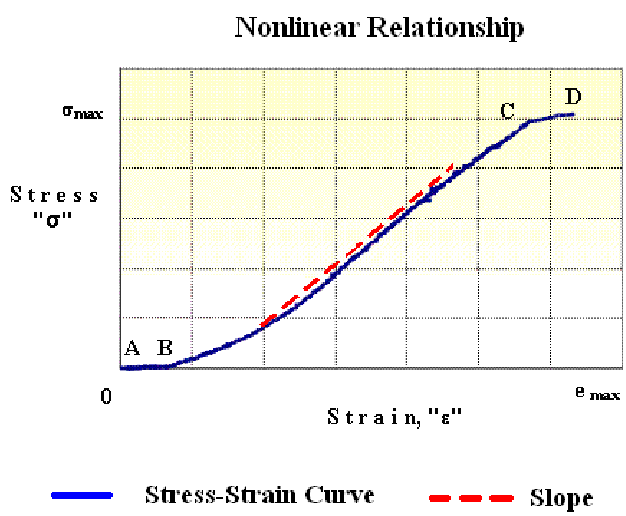

Figure 2.14. Nonlinear relationship between stress σ and strain ε for soft biological tissues.

Under compression loading, the normal stress σ and the normal strain ε were obtained using:

$$\sigma = \frac{F}{A} \qquad \left(\frac{N}{mm^2} \text{ or } MPa\right) \tag{2-1}$$

$$\varepsilon = \frac{Y}{h} \tag{2-2}$$

where *A* and *h* are the cross sectional area (elliptic) and height of the disc and were given in Table 2.1. Units of stress are given in MPa while the strain is adimensional. If assuming that the vertical displacement of the disc is that of the actuator and if the changes to disc cross section *A*, and its height *h* after the loading are too small, then σ will depend only on

F in the same way that ε will depend only of *Y*. Thus, the relationship between σ and ε can be written by Hooke's law of elasticity in the typical form:

$$\sigma = E\varepsilon \qquad (MPa) \tag{2-3}$$

where *E* is the *Young`s modulus in* (MPa) and represents the disc stiffness, which graphically is the slope of segment B-C in Figure 2.14.

The fitting of the test data for a nonlinear relationship can be done using a polynomial function of higher order. Usually a second or third order is sufficient to adjust most of the testing data. A general expression for a polynomial function of σ against ε in the canonical form can be written as follows:

$$\sigma = A\varepsilon^{n} + B\varepsilon^{n-1} + \ldots + C \tag{2-4}$$

If the polynomial function σ is differentiated with respect to ε, the result will give the disc instantaneous *Young's modulus E*. Thus, we can write as follows:

$$E = \left(\frac{d\sigma}{d\varepsilon}\right)_{P=P_{\max}} \tag{2-5}$$

this is taken at peak load and should represent the disc mean response.

To investigate any possible weaker zone of the peripheral annulus, measurements of disc bulging at the middle anterior and posterolateral sides were done using the recorded values of *X*, *Z* against *F*. The bulging increases with loading increase, and usually gives a nonlinear relationship for each disc, see Figure 2.15.

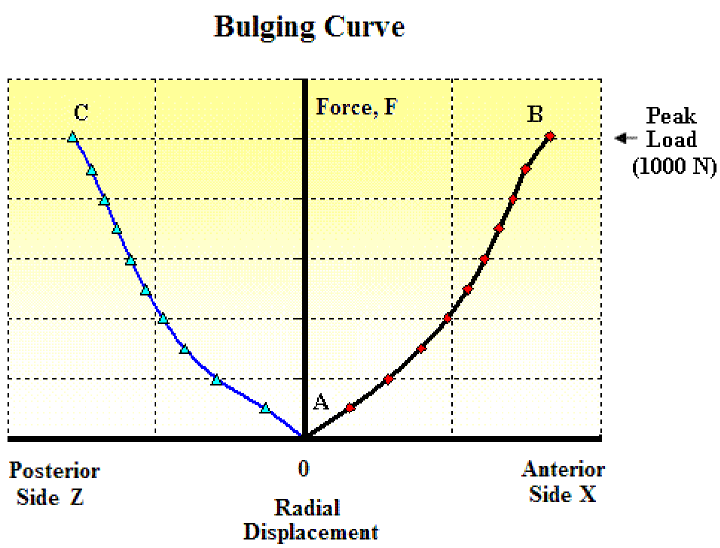

Figure 2.15. Disc bulging upon compression loading.

b. Stress relaxation protocol

Soft biological tissues, such as the intervertebral disc, undergo stress relaxation when they are loaded. Thus, the relaxation response has to be characterized. The stress decay *σ(t)* over time of a soft biological tissue is characterized by an initial rapid decline, which is represented by segment AB in Figure 2.16, followed by a period of transition decay (segment BC) until it achieves the *relaxation stress* (segment CD). The time for which the stable stress is reached is the *relaxation time t(r)* (point C). Thus, the time-dependent response of the disc to the loading is defined by *t(r)*.

Thus, in this protocol the measurement of the force decline over time *F(t)* and the corresponding *stress decay σ(t)* are required to analyze relaxation phenomena. Once the peak load of 1000 N was reached, the displacement *Y* of the hydraulic actuator was put to a hold, and the disc was subjected to a constant *elongation*. Then, immediately after, a sharp decline of force *F(t)* from the peak load took place. The *normal stress σ = F/A* also decreased in an exponential fashion and was investigated until it decreased to ***1/e*** of the initial value σ_0 or achieved stability, known as the *relaxation stress*.

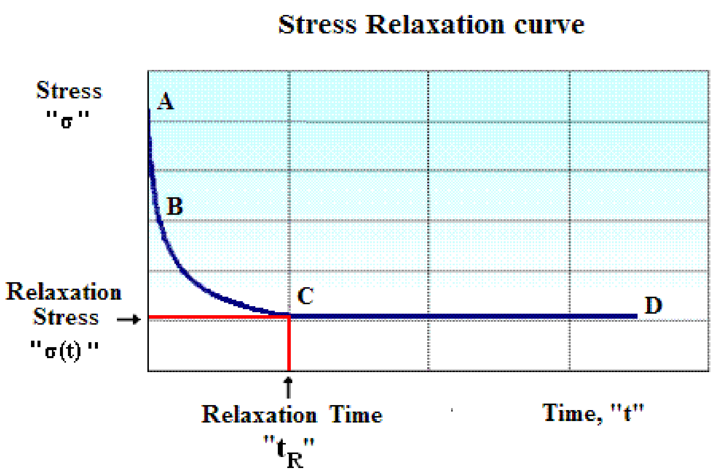

Figure 2.16. Stress behavior in a relaxation test. Point C is were the stable stress is reached and identifies the relaxation time t(r) and the relaxation stress σ(t).

The nonlinear relationship between the *stress decay σ(t)* and the *time t* can be approximated with the basic first order differential equation of exponential growth:

$$\frac{d\sigma}{dt} = -\alpha\sigma \qquad (2.6)$$

where *σ* is the stress at any time, and *α* is a constant of proportionality.

The solution of Eq 2.6 is:

$$\sigma(t) = \sigma_0 e^{-\alpha \cdot t} \ (MPa) \qquad (2.7)$$

where σ_0 is the *peak stress* at the end of the loading stage, t is the time, and α is the *relaxation parameter*, which is a characteristic of each disc.

Because of the high water content, the ex-vivo intervertebral disc can be modeled as a *viscoelastic body*. The viscous part of the disc was assume based on the gel-like structure of the nucleus pulposus, which is a mixture of water with disorganized collagen type II. While the elastic part comes from the annulus fibrosus and its well organized collagen type I laminar structure that favors flexibility. Thus, it was assumed that the annulus fibrosus acts more as a spring element. Thus, the fluid-solid behavior of the disc can be represented by an array of *dashpots* and *springs* in parallel. The dashpot represents the viscous behavior in accordance with a *Newtonian fluid*, while the spring represents the elastic behavior in accordance with a *solid elastic* (Koolstra et al., 2007) and (Allen et al., 2006). This model is known as *the standard linear solid (SLS)* model or *Zener model*, which is used for viscoelastic analysis, see Figure 2.17.

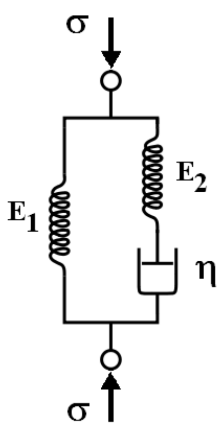

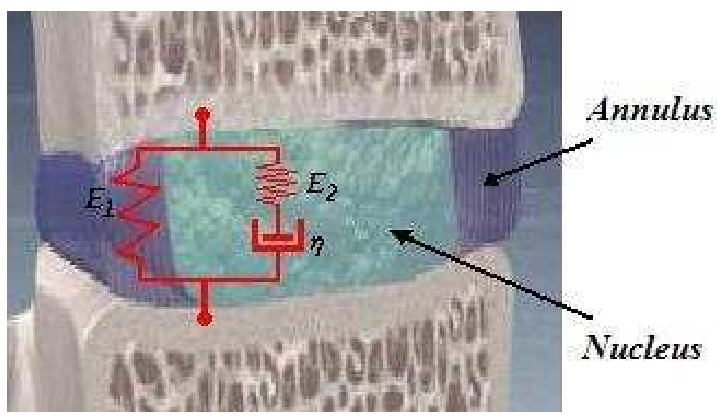

Figure 2.17. (A) Standard linear solid (SLS) model and (B) application to an intervertebral disc. Observe the arrangement of dashpots and springs in the arms located in the nucleus pulposus and the annulus fibrosus.

In a *Newtonian fluid* the constant of proportionality between the *shear stress* τ and the *velocity gradient of deformation* $d\varepsilon/dt$ is known as the *viscosity* η. The equation to describe a *Newtonian fluid* behavior is:

$$\tau = -\eta \frac{d\varepsilon}{dt} \qquad (2\text{-}8)$$

While in a solid elastic, the constant of proportionality between the *normal stress* σ, and the *strain* ε is known as the *Young's modulus, E*. In elasticity, *Hooke's law* describes this relationship as linear, which was introduced previously; see Eq (2-3):

$$\sigma = E\varepsilon \qquad (2\text{-}3)$$

As described previously, the *SLS* model uses two parallel arms to predict a more accurate viscoelastic response in terms of *stress relaxation*, and *creep*. The basic models for the SLS model are the *Maxwell* and the *Voigt* elements, which are linear and are restricted to small deformations (Fung YC, 1993). In the former configuration the elements are connected in series and the strain is additive but not the stress, which is constant. In the latter configuration the elements are connected in parallel and the stress is additive but the strain is maintain constant between the two arms, see Figure 2.18.

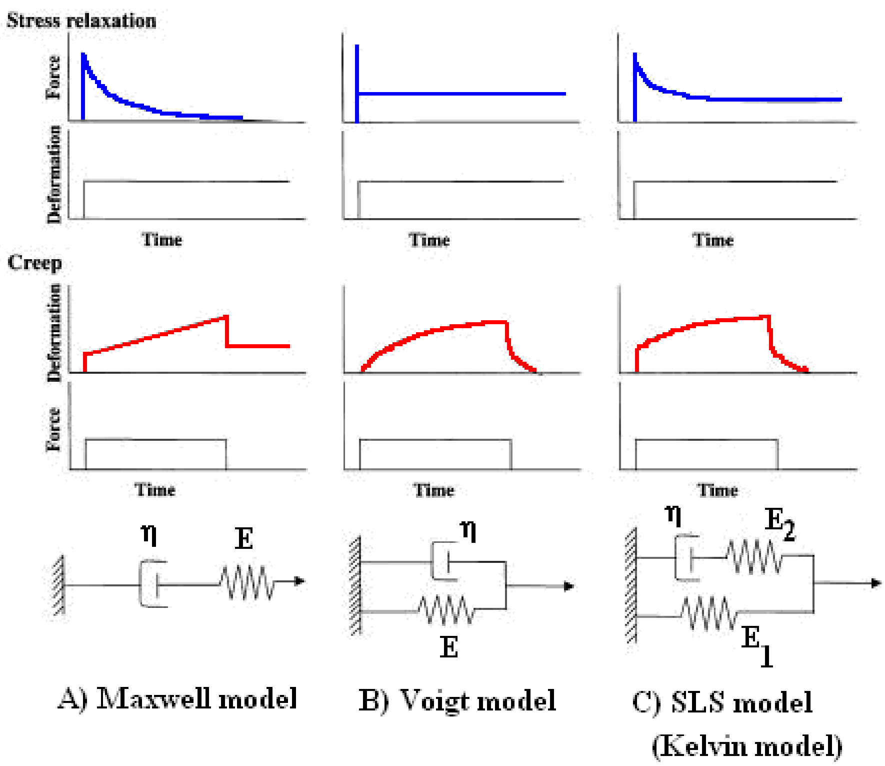

Figure 2.18. Stress relaxation (in blue) and creep (in red) relationships using (A) Maxwell, (B) Voigt, and (C) SLS (Kelvin) models. Adaptation from Tanaka et al. (1993).

From the foregoing, the following relations exist:

For parallel components, such as Voigt model:

$\sigma_{tot} = \sigma_D + \sigma_S$, and $\varepsilon_{tot} = \varepsilon_D = \varepsilon_S$. (2-9)

For series components, such as Maxwell model:

$\sigma_{tot} = \sigma_D = \sigma_S$, and $\varepsilon_{tot} = \varepsilon_D + \varepsilon_S$. (2-10)

where the subscripts *S* and *D* refer to the spring and dashpot respectively.

However, in the Voigt model the rate of deformation *$d\varepsilon/dt$* is zero, and solution for *stress relaxation* is not possible. To take into account relaxation, a second spring is added next to the dashpot of the *Voigt* element forming a *Maxwell* "arm", and an overall *SLS* model is form, see Figure 2.18.

We can relate the various stresses and strains in the overall *SLS model* and the inner Maxwell arm as follows:

For the overall system and using Eq. (2-9)

$$\sigma_{tot} = \sigma_M + \sigma_{S1}. \tag{2-11}$$

$$\varepsilon_{tot} = \varepsilon_M = \varepsilon_{S1}. \tag{2-12}$$

For the Maxwell arm and using Eq. (2-10)

$$\sigma_M = \sigma_D = \sigma_{S2}. \tag{2-13}$$

$$\varepsilon_M = \varepsilon_D + \varepsilon_{S2}. \tag{2-14}$$

where the subscripts M, D, S_1 and S_2 refer to Maxwell, dashpot, spring one, and spring two (in the arm), respectively.

Using these relationships, their time derivatives, and the stress-strain relationships for the spring (Eq. 2-3) and dashpot element (Eq. 2-8), the system can be modeled as follows:

$$\frac{d\varepsilon(t)}{dt} = \frac{\frac{E_2}{\eta}\left(\frac{\eta}{E_2}\frac{d\sigma(t)}{dt} + \sigma(t) - E_1\varepsilon(t)\right)}{E_1 + E_2} \tag{2-15}$$

where E_1, E_2, η and $\sigma(t)$ are the *Young modulus* of each spring, the *viscosity* of the fluid and the *stress relaxation function* respectively.

Prediction of *stress relaxation* requires a strain step or an elongation step. Therefore $\varepsilon(t)$ is a constant, and the rate of deformation is null, $d\varepsilon/dt = 0$, and Eq. 2-15 reduces to:

$$\frac{d\sigma(t)}{dt} + \frac{E_2}{\eta}\sigma(t) - \frac{E_1 E_2}{\eta}\varepsilon = 0 \tag{2-16}$$

This is a first order linear differential equation. Using E_2/η as the integration factor and resolving for $\sigma(t)$ gives:

$$\sigma(t)_{total} = E_1\varepsilon + E_1\varepsilon \cdot e^{-\left(\frac{E_2}{\eta}\right)\cdot t} \tag{2.17}$$

Other form of Eq. (2-17) is:

$$\sigma(t)_{total} = \sigma_0 + \sigma_0 \cdot e^{-\left(\frac{E_2}{\eta}\right)\cdot t} \qquad (2\text{-}18)$$

Where again σ_0 is the *peak stress* at the end of the loading stage. The first term of Eq. (2-18) correspond to the linear response of the single spring element, and the second term contains the relaxation response of the *Maxwell* arm given by the exponential term E_2/η known as the *relaxation parameter* α, and shown also in Eq. 2-7. Thus, we can write:

$$\alpha = \frac{E_2}{\eta} \qquad (s^{-1}) \qquad (2\text{-}19)$$

If the response is $E_2 >> \eta$, then it will imply a dominant solid viscoelastic behavior, and if $E_2 << \eta$ it will imply a fluid like behavior. The inverse of Eq. (2-19) gives the characteristic *relaxation time* (t_R); it is physically the time needed for the stress to fall to ***1/e*** of its initial value σ_0 or achieve stability. Also, it will vary from disc to disc. Thus we can write:

$$t_R = \alpha^{-1} = \frac{\eta}{E_2} \qquad (s) \qquad (2\text{-}20)$$

The *disc modulus* (E_{disc}) may be obtained by dividing Eq. (2-18) by the deformation ε_0:

$$E_{disc} = \frac{\sigma(t)_{total}}{\varepsilon_0} = \frac{\sigma_0}{\varepsilon_0} + \frac{\sigma_0}{\varepsilon_0} e^{-(\frac{E_2}{\eta})\cdot t} \qquad (2\text{-}21)$$

The first term of Eq. (2-21) is the *Young's modulus E*, and the second term is the *relaxation modulus* (E_R); it represents the relative *stiffness* when the stress relaxation ceases which occurs at the *relaxation time* t_R. Replacing α for the *relaxation time* t_R in second term:

$$E_R(t) = \frac{\sigma_0}{\varepsilon_0} e^{-\frac{t}{t_R}} \qquad (2\text{-}22)$$

At $t = 0\ s$, the second term of Eq. (2-18) gives the stress peak value σ_0, and at a particular time t, the corresponding stress decline. However, the decline of stress will follow a straight line since the *SLS model* is also linear. Also, it will end at a none zero value, unlike the Maxwell model, see Figure 2.18.

Finally, the use of an exponential decay expression for stress relaxation is simple and effective, and additional terms in the exponential of Eq. (2-18) may be used to accurately fit any test data. Considerations should be made regarding factors that affect stress relaxation which include: magnitude of the initial load, speed of loading, loading medium, temperature and long term storage, as described by Fung YC (1993).

c. Flexion-extension and right-left bending protocol

The *disc flexibility* is a physical characteristic of healthy discs. *Flexibility* is defined as the amount of motion response θ (in degrees) due to a moment loading M (N-m). The ratio of moment loading to motion response is the *bending stiffness* K_M and the nonlinear relations are analyzed on a graph of motion response θ to moment loading M done in the coronal and saggital planes of the disc. Thus, in this study, moments of 5 N-m in flexion, extension, right and left bending were applied in this order. The magnitudes of the moments were sufficient to produce physiological motions but small enough to not injure the disc. The loading rate of the moments were kept at 0.25 N-m/s, thus it took 20 seconds to reach the peak moment. The corresponding piston displacement rate was about 6 mm/min. After reaching the 5 N-m in flexion every specimen was unloaded and allowed a 10 minute recovery before repeating the next loading in extension.

The testing technique was based on that use by Schultz et al. (1979), the use of an eccentric compression load to produce the desired moment. The hydraulic actuator of the testing machine provided the load F, and the bending accessories previously shown in Figure 2.10 provided the lever arm D. The maximum force F was 50 N and the length D was kept fixed at 100 mm. Thus, the magnitude of the applied moment in any bending M was

$$M = F \times 0.1 \qquad (N\text{-}m) \qquad (2\text{-}23)$$

A schematic representation and the actual appearance of the set up for the flexion-extension and the right-left bending tests are shown in Figure 2.19.

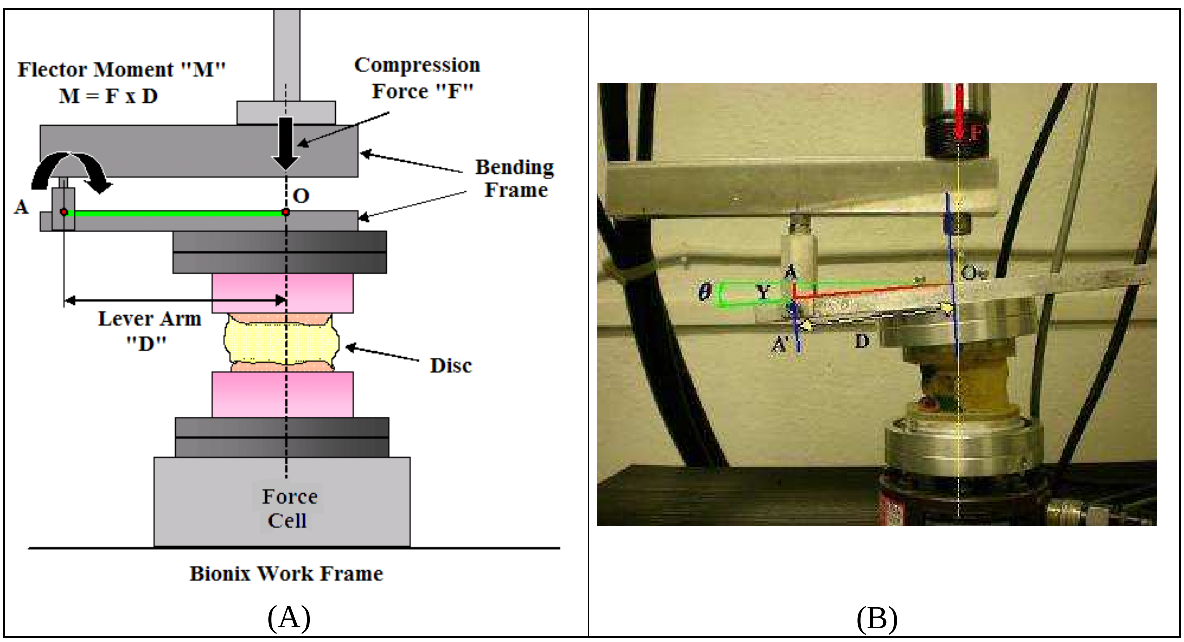

Figure 2.19. Schematic view of the bending test setup. (A) The non deformed configuration of the disc. (B) Actual appearance after applying a 5 N-m moment, first in flexion-extension and then in right-left bending.

Measurements of the applied force *F* and the vertical displacement *Y* were recorded during the loading stage. These values were used determine the motion response of the disc in a graph of *M* against θ. The horizontal line *OA* shown in Figure 2.19A corresponds to the initial configuration of the disc. After the 5 N-m bending, the line *OA* was rotated of an angle θ to the new position, shown as line *OA'* which corresponds to the deformed configuration. Perpendicularly between F and D was maintained initially while any movement of point *O* was assumed to be small. Thus, it can be seen from the triangle *OAA'* that

$$\sin\theta = \frac{Y}{D} \tag{2-24}$$

where, *D* =100 mm. Resolving for θ :

$$\theta = \sin^{-1}\left(\frac{Y}{100}\right) \qquad (rad) \tag{2-25}$$

where θ is given in radians. With the values of *M* and θ obtained from Eq. 2-23 and 2-25 a plot of *M*-θ was drawn to show the nonlinear relationship between moment loading and motion response, as shown in Figure 2.20. This was repeated for the other three moments used: extension (*Ex)*, right bending (*RB)*, and left bending (*LB)*.

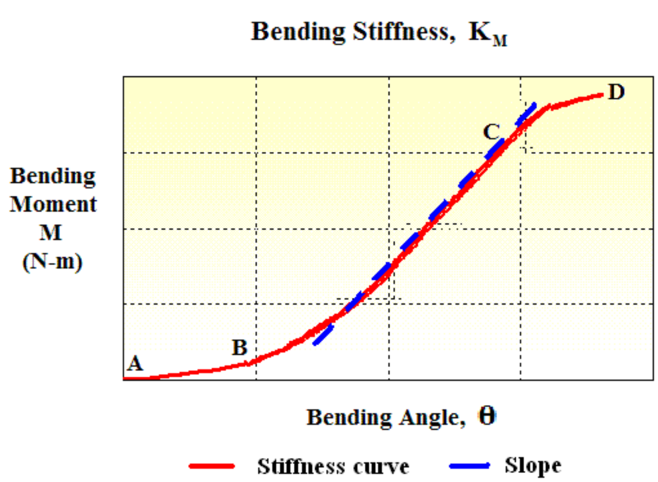

Figure 2.20. Typical motion response of an intervertebral disc when bending it to flexion-extension or to the lateral side.

When dividing equation (2-23) by (2-25) we obtain the bending stiffness K_M of the disc, which will depend only on the applied force *F* and the corresponding elongation *Y*.

$$K_M = \frac{M}{\theta} \qquad \left(\frac{Nm}{rad}\right) \tag{2-26}$$

d. Torsion load protocol

Another type of motion that the intervertebral disc is subjected is rotation or *torsion* done in the transversal plane. The disc flexibility and disc stiffness K_T have the same meaning as it did in the bending case. The literals are now, for motion response *Ø*, and for torsion moment *T*. However, in the intact unit vertebral function UVF the presence of the posterior elements leads to a high torsion strength, which represents a 65% contribution, while the remaining is attributed to the intervertebral disc (Farfan et al. 1970). To investigate the disc strength to torsion, the posterior elements were removed, and was assumed that the main load carrier was the annulus fibrosus. Therefore, the results of this protocol should give inside information of this material.

Thus, in this study a torsion moment of 5 N-m was applied to each disc, and the nonlinear relation between *T* and *Ø* was analyzed. Again, the magnitude of the torque was sufficient to produce physiological motions but small enough not to injure the intervertebral discs. The loading rate of the torsion was kept at 0.25 N-m/s, thus it took 20 seconds to reach the 5 N-m peak torque. The corresponding piston displacement rate was about 2 mm/min. After reaching 5 N-m every disc were unloaded and allowed to recover for 10 minutes before applying the next testing protocol. Measurement of the torque T was done using a torque cell with an amplifier, see Figure 2.21.

(a)

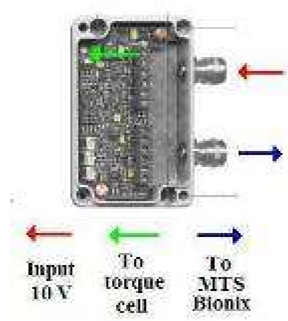

(b)

Torque Cell

Dealer: Lorenz Messtechnik
Model: DF-30
Service torque: 10 Nm +30%
Bridge resistance: 350 Ω
Accuracy class: 0.05%
Sensitivity: 1 mV/V

Amplifier

Dealer: Lorenz Messtechnik
Model: SI-U10
Supply and output: 10 V

Figure 2.21. (a) Torque cell used in this study. (b) Amplifier for torque signal input into the MTS Test Start.

The hydraulic actuator of the MTS Bionix provided the initial vertical displacement *Y* and the torsion device with a cam threaded and rolling follower mechanism allowed the transformation of linear to helical rotation *Ø*, see Figure 2.22. The cam helix thread permits constant torsion *T*. The relationship between Y and *Ø* is called pitch thread and determines the ratio of displacement, which for the torsion device was:

$$Ø = 0.0312\,Y \qquad (rad) \qquad (2\text{-}27)$$

where Y was given in mm. This mechanism allowed the transmission of "pure" torque *T* while the force compression component was eliminated due to rolling and sliding contact, see Figure 2.22.

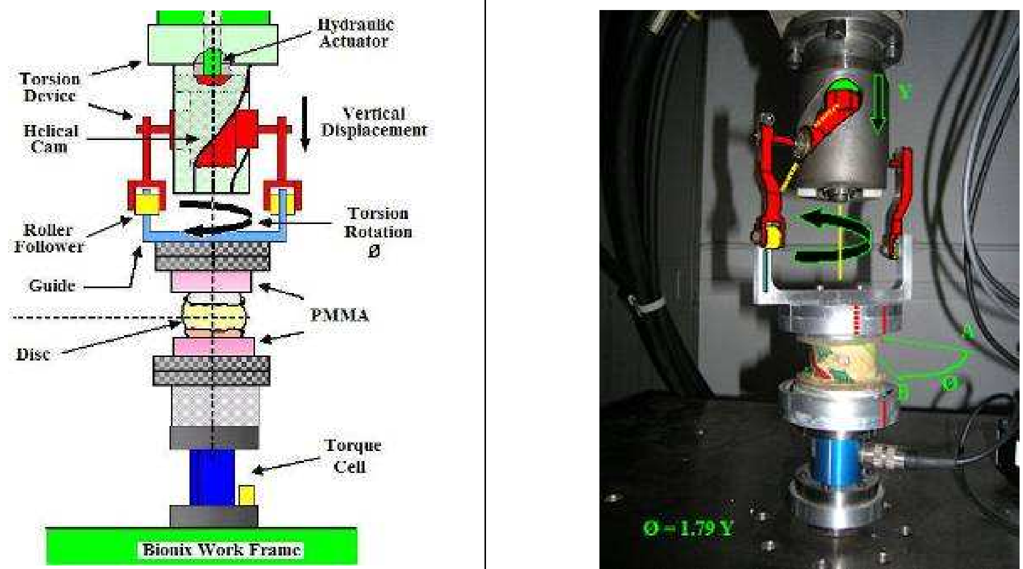

(A) (B)

Figure 2.22. (A) Schematic view of the torsion test set up and (B) actual appearance.

A typical curve of *T- Ø* for the intervertebral disc is shown in Figure 2.23. The initial toe AB of the curve correspond to the uncrimping of the annulus collagen fibers, after then stretching of the fibers takes place and the torsion stiffness of the disc is given by the near straight line BC up to the point of fiber yield CD.

Dividing the torque *T* by the angular deflection *Ø* during the loading stage gives the torsion stiffness K_T :

$$K_T = \frac{T}{\phi}. \qquad (Nm/rad) \qquad (2\text{-}28)$$

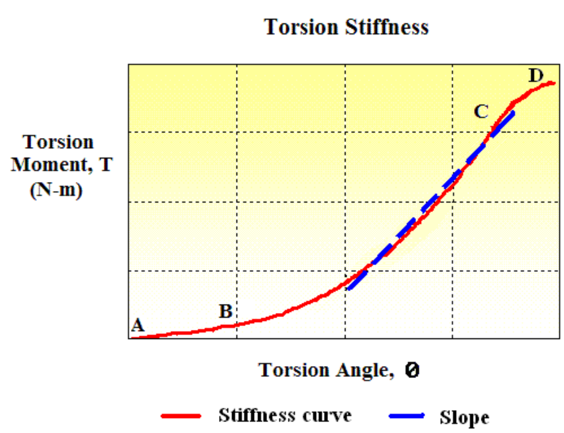

Figure 2.23. Typical motion response of an intervertebral disc to torsion loading.

e. Cyclic compression protocol

The cyclic compression load is used to investigate the damping capacity of the intervertebral disc. The water in the disc makes it somewhat incompressible, a feature that benefit the disc because it act as a cushion against impact loading that results from normal body movement.

Lower lumbar discs are exposed to severe loading and deformation that compromised their ability to shock absorbed. Part of the loading tends to be axial and directed toward the nucleus pulposus which bears initially most of the damping (Kazarian, 1975). Thus, cyclic compression serves to evaluate its damping characteristics. For this purpose, a loading protocol was designed and used to all the specimens tested after the static protocol. The technique consisted of applying 85 cycles using a sinusoidal fluctuating wave, which initially range from a minimum force F_{min} of 200 N to a maximum force F_{max} of 500 N. These loads corresponded to the supine and upright positions according to Nachemson et al., (1964) and Wilke et al., (1999). Thus, the corresponding displacement Y was maintained fixed between a minimum Y_{min} corresponding to the F_{max} and a maximum Y_{max} corresponding to F_{min}, see Figure 2.24. The decay of the mean force F_m between the first and the last cycle, if any, was measured. Due to limitations of PC memory and the architecture of the software controller TestStar of the MTS Bionix system the number of applied cycles was limited to 85.

For a viscoelastic material such as the intervertebral disc, the dominant disc response, e.g. solid or fluid-like behavior will depend on the frequency ω. Low frequencies (low rates) favors elastic behavior while high frequencies favors fluid like behavior according to Iatridis et al., (1996) and Tanaka et al., (2003). The usage of a wide physiological range of frequencies allows the analysis of slow and relative fast loading rates and thus, axial motions without permanent deformation. Testing ex-vivo discs requires using frequencies in the physiological range from 0.1 Hz up to 20 Hz (Kasra et al. 1992 and Adams et al., 1995). Thus, in the present study it was decided to use the range of frequencies from 0.2 Hz to 5 Hz as this range represents most of the frequencies of light tasks done in office and at home. For every frequency, measurements of the *time t* in seconds (s), the *force F* in *Newton (N)*, and the *displacement Y* in millimeters (mm) were recorded 360 times per cycle.

The applied displacement Y shown in Figure 2.24 can be written in the form

$$Y = Y_m + Y_a \sin(\omega t) \quad (mm) \tag{2-29}$$

where t is the time (s), ω is the frequency (rad/s), Y_m and Y_a are the mean displacement and the amplitude respectively, and are constants.

Dividing the expression in Eq.(2-29) by the disc height h, gives the strain ε:

$$\varepsilon = \varepsilon_m + \varepsilon_a \sin(\omega t) \tag{2-30}$$

where ε_m is the mean strain and ε_a is the strain amplitude.

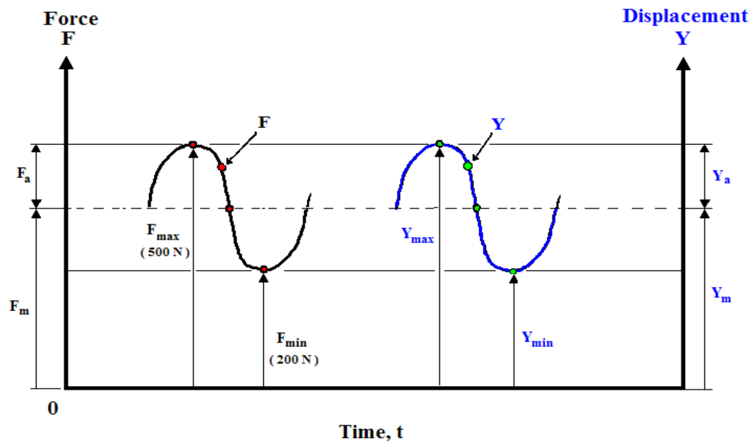

(A)

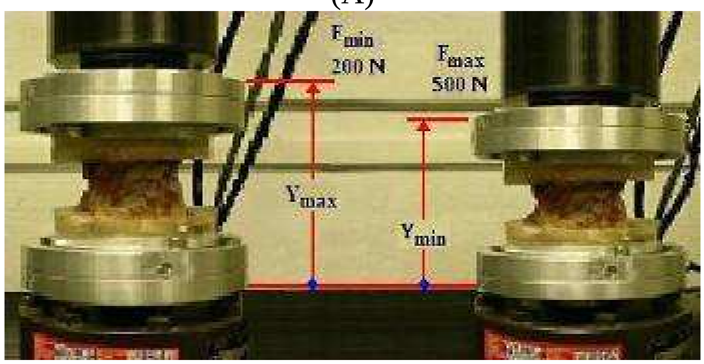

(B)

Figure 2.24. (A) A three axis diagram showing the compression load fluctuation response (right side in black) to an initial sinusoidal displacement (left side in blue). Observe that the force F fluctuate without passing through zero. (B) Actual appearance of the cyclic compression test.

In continuum mechanics, if the applied displacement Y has a sinusoidal wave form, then the response of force F of the medium will also have the same wave form, which may be written in the most general form as

$$F = F_m + F_a \sin(\omega t+\beta) \qquad (N) \qquad (2\text{-}31)$$

where F_m and F_a are the instantaneous mean force and amplitude response respectively and β is the out of phase angle between the applied displacement and the force response. Dividing the force expression in Eq. (2-31) by the disc area A gives the normal stress σ response which can be written

$$\sigma = \sigma_m + \sigma_a \sin(\omega t+\beta) \qquad (MPa) \qquad (2\text{-}32)$$

where σ_m and σ_a are the normal instantaneous mean stress and the stress amplitude, respectively. The out of phase angle β measures the viscous response of the material to dynamic strain.

Then, with the values of ε and σ given by Eq. (2-30) and (2-32) respectively, a graph of stress σ and deformation ε against the time t was plotted in a three axis diagram, see Figure 2.25.

The time space between the peaks of σ and of ε (given by the horizontal distance) determine the value of the angle β, which is given by

$$\beta = \omega t \qquad \text{(rad)} \qquad (2\text{-}33)$$

then, it follows that the angle β is a function of the frequency ω. Also shown in Figure 2.25 is the stress decay represented by the line from σ_m to σ'_m.

Cyclic Stress-Strain, out of phase angle β and Stress Decay

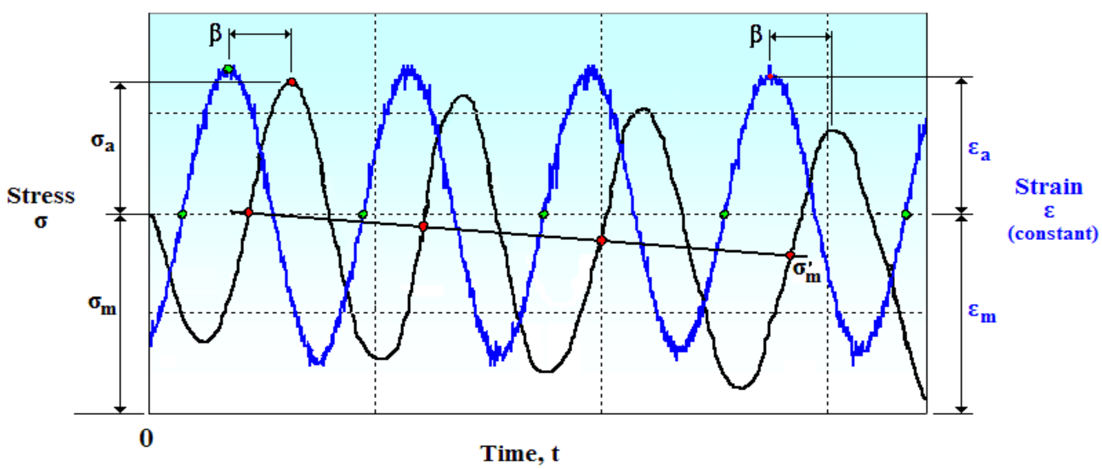

Figure 2.25. Representation of a constant applied sinusoidal strain ε (right side in blue) and the resulting sinusoidal stress σ response (left side in black) of a viscoelastic material. Decay of stress σ'_m will depend on the used frequency while the out of phase angle β do not change between cycles.

In the case of an ideal elastic solid, the stress σ is always in phase with the strain ε (i.e., $\beta=0$ in eq. 2-32). In contrast, the stress of a viscous *Newtonian fluid* is always 90° out of phase (i.e., $\beta = \pi/2$ *rad*) with the strain. This, as a result from Newton's fluids law, given by Eq. (2-8) as

$$\sigma = \eta \left(\frac{d\varepsilon}{dt}\right) \qquad (2\text{-}8)$$

where η is the viscosity. Substitution of the derivative of ε with respect to time, given by (2-30), into eq. (2-8), gives

$$\sigma = \eta\, \omega\, \varepsilon_a \sin\left(\omega t + \frac{\pi}{2}\right) = \sigma_a \sin\left(\omega t + \frac{\pi}{2}\right) \qquad (2\text{-}34)$$

where the amplitude is $\sigma_a = \eta\ \omega\ \varepsilon_a$. Therefore, *the absolute value of β for any material will lie in between 0° and 90°.*
Once the angle β was determined, then the disc *complex modulus E** could be calculated. The usage of complex number notation is the common approach by which a complex strain ε^*, stress σ^* and thereby the modulus E^* (according to Hooke's law) can be represented as:

$$\varepsilon^* = \varepsilon_a\, e^{i\omega t} \tag{2-35}$$

$$\sigma^* = \sigma_a\, e^{i(\omega t+\beta)} \tag{2-36}$$

$$E^* = \left(\frac{\sigma^*}{\varepsilon^*}\right) = \left(\frac{\sigma_a}{\varepsilon_a}\right) e^{i\beta} \tag{2-37}$$

Then, the *complex modulus* can be resolved into two components, one that is in phase (i.e., *E')* and one that is out of phase (i.e., *E")* with the applied strain. Substitution of Euler's identity $e^{i\beta} = \cos\beta + i\sin\beta$ into eq. (2-37) gives

$$E^* = \left(\frac{\sigma_a}{\varepsilon_a}\right)\cos\beta + i\left(\frac{\sigma_a}{\varepsilon_a}\right)\sin\beta \tag{2-38}$$

Equation (3-22) may be written in the following form:

$$E^* = E' + iE'' \tag{2-39}$$

where E' is the ***storage modulus*** given as:

$$E' = \left(\frac{\sigma_a}{\varepsilon_a}\right)\cos\beta \tag{2-40}$$

and E" is the ***loss modulus*** given as:

$$E'' = \left(\frac{\sigma_a}{\varepsilon_a}\right)\sin\beta \tag{2-41}$$

The magnitude of the *complex modulus,* $|E^*|$, was obtained as:

$$|E^*|^2 = (E')^2 + (E'')^2 \tag{2-42}$$

The ratio of loss and stored moduli defines another useful parameter in dynamic mechanical analysis named *tan δ,* where

$$\tan\delta = \frac{\sin\beta}{\cos\beta} = \frac{E''}{E'} \tag{2-43}$$

Another useful concept in dynamic analysis is the energy dissipation or *hysteresis H*. For this purpose, the stress-strain, σ-ε curve was plotted against the loading-unloading cycles and the enclosed area was calculated, as follows:

$$Hysteresis = \left[\int_{\varepsilon_1}^{\varepsilon_2} \sigma \cdot d\varepsilon\right]_{loading} - \left[\int_{\varepsilon_1}^{\varepsilon_2} \sigma \cdot d\varepsilon\right]_{unloading} \tag{2-44}$$

The typical hysteresis for elastic, viscoelastic and fluid behavior, along with the respective linear viscoelastic models with springs and dashpots are shown in Figure 2.26. For a material that exhibits pure elastic behavior the unloading trajectory has the same direction than the loading trajectory, therefore, the enclosed area between trajectories is zero. Most metals exhibit this behavior as long as no permanent deformation is induced. In the stress relaxation protocol, mechanical models that consider only the elastic behavior use a linear spring element to characterize the deflection response. Thus, in the elastic region, metals are characterized by the Young's modulus *E*. However, Figure 2.26A also shows stress relaxation, a feature that is not associated with metals.

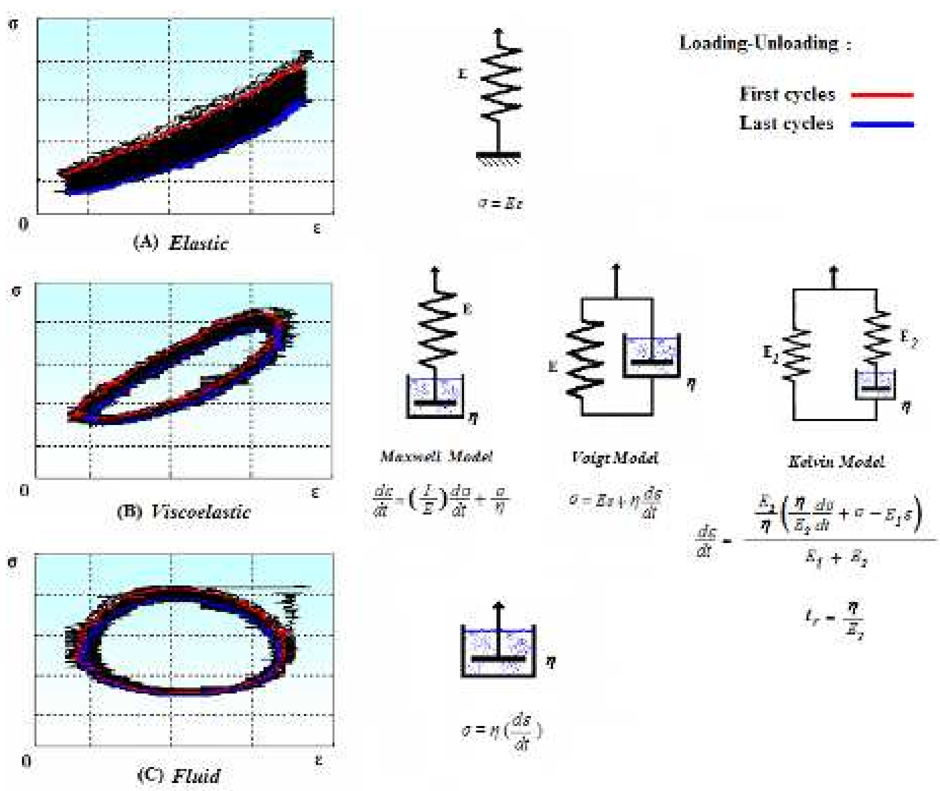

Figure 2.26. Hysteresis curves for a (A) dominant elastic, (B) viscoelastic and (C) fluid behavior with the corresponding mechanical models. In the Kelvin model, an arrangement of springs and dashpots in series and parallel permits predictions of creep and stress relaxation phenomena.

Loading and unloading soft biological tissues gives an *energy dissipation* or *hysteresis*, and also a *stress relaxation*. Thus, the enclosed area between the loading and unloading curves is non zero, see Figure 2.26B. The shape of the hysteresis curve for a pure elastic material resembles a straight line, and that for a viscoelastic material resembles a "banana" shape. While for a *newtonian fluid* the *hysteresis* curve shows a maximum enclosed area, see Figure 2.26C.

III. The Finite Element protocol

The use of the finite element method (FEM) in bioengineering has expanded over the past decades, beginning from the design of sport equipment and medical devices, and continuing with the study of degenerative diseases and most recently in cell mechanobiology and tissue engineering applications. Advances in these branches have been possible due to faster computers, more user friendly implementation of FEM codes into commercial software's and increasing use of high resolution computerized imagining techniques (i.e. computed tomography-CT, magnetic resonance imaging-MRI), which have proven to be reliable and accurate procedures for reconstructing complex geometries of human organs and tissues.

In this study, two MRI, one from a L2-L3 disc, and the other from a L4-L5 disc were used to developed 3D models of each disc. The 2D cross-sectional MRI were imported into an interactive medical imaging control system: MIMICS^{TM} 10.01 (MATERIALISE^{TM}, Leuven, Belgium) for converting anatomical data from images to 3D disc models using segmentation of soft tissue and bone structure. The selected discs were, *specimen G* (L2-L3 level with degeneration scoring = 3) and *specimen I* (L4-L5 level with degeneration scoring = 5), see Table 2.1. Later on, in chapter 3, section I.b, is shown that these two discs best describe significant differences in the amount of *intervertebral osteochondrosis* and *spondylosis deformans*, and therefore can be used as a reference for the development of a finite element model of disc degeneration. After the segmentation procedure, a finite element mesh was created for each disc, with six different sizes, and preprocessed with Marc Mentat^{TM} 2007 (MSC Software^{TM}, Santa Ana CA, USA). However, only the L2-L3 FEM disc was validated with the results from the experimental testing protocol. The validation of the L4-L5 FEM disc is left for future work.

The sequence for removal of air, segmentation of vertebral bone and disc materials for the two discs are shown in the flow charts of Figure 2.27 and 2.28. Once the air was removed (layer by layer), a 3D object containing the disc contour was created. This contour wraps the entire volume of material, corresponding to the intervertebral disc and the side of the vertebrae which were scan. The generation of a contour mesh first, and the mesh of volume later, were done in a copy of the 3D object, while the segmentation of materials were done in the 3D object created initially, along separate layers, forming the *masks*.

The segmentation allowed the identification of the nucleus pulposus, annulus fibrosus, cartilage endplate and cavities from the disc, and also the cortical shell and the trabecular or cancellous bone from the vertebral bodies. Thus, this permitted an eventual anatomical and mechanical characterization of these materials. Additional data needed for the finite element model of disc degeneration included the geometrical properties of the mesh, the type of formulation for the materials, the boundary conditions, and the type of analysis.

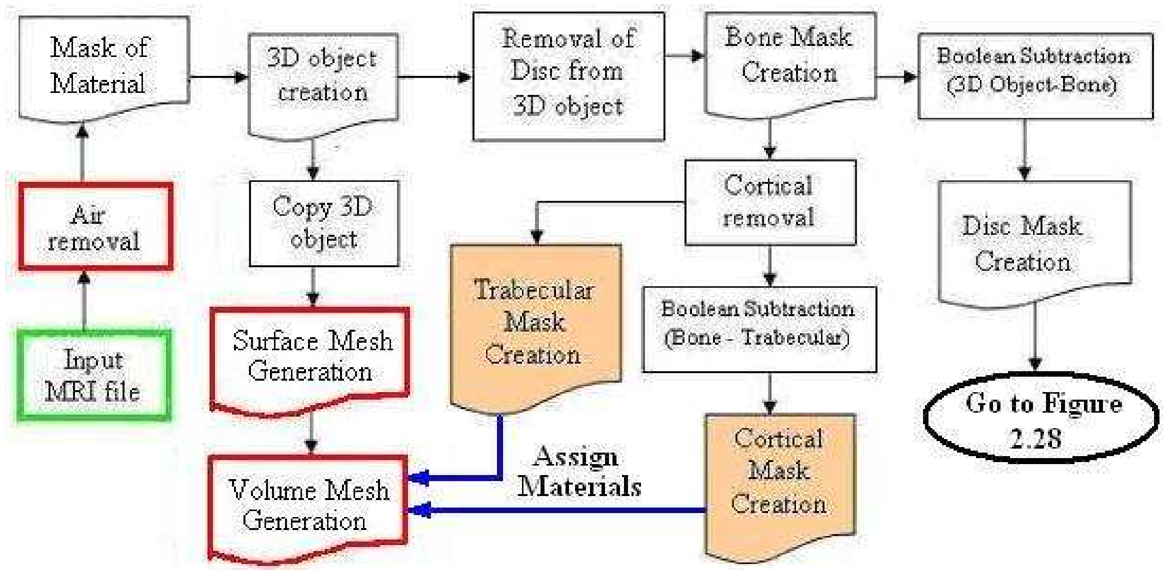

Figure 2.27. Flow chart for the air removal, generation of the contour mesh and segmentation procedure of the vertebra bone.

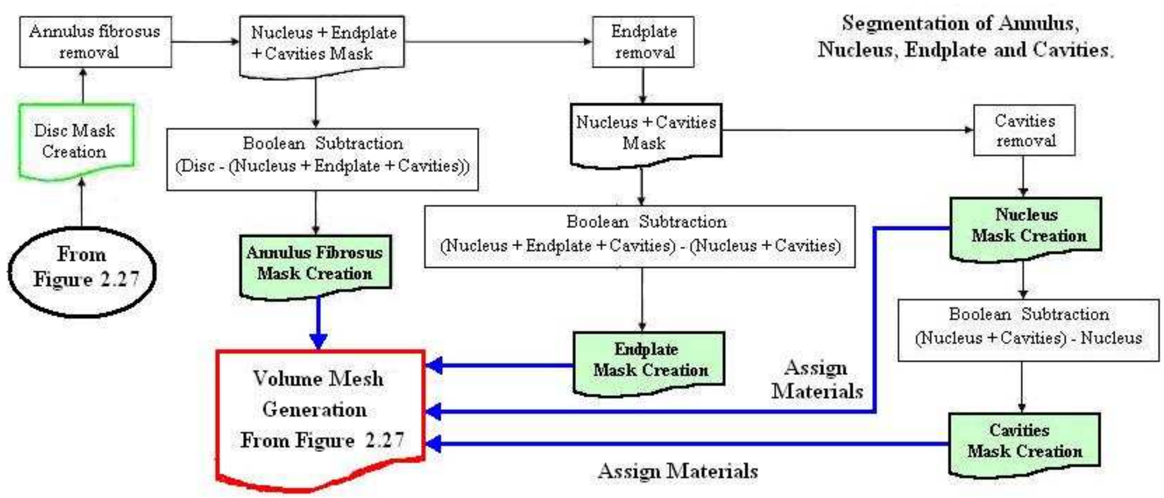

Figure 2.28. Flow chart for the segmentation of the intervertebral disc soft tissues.

a. Removal of air and creation of a 3D finite element surface mesh

At the beginning, MIMICS uses, as an input, a DICOM file containing the MRI of the discs, see Figure 2.29. The green background shown on each of the three references for viewing represent the scanned area in the saggital, coronal and axial planes of the disc and its surrounding air, while the black background represents areas that were not scanned. Thus, the green cubic object in the lower right corner represents the corresponding MRI scan of the selected volume (including air).

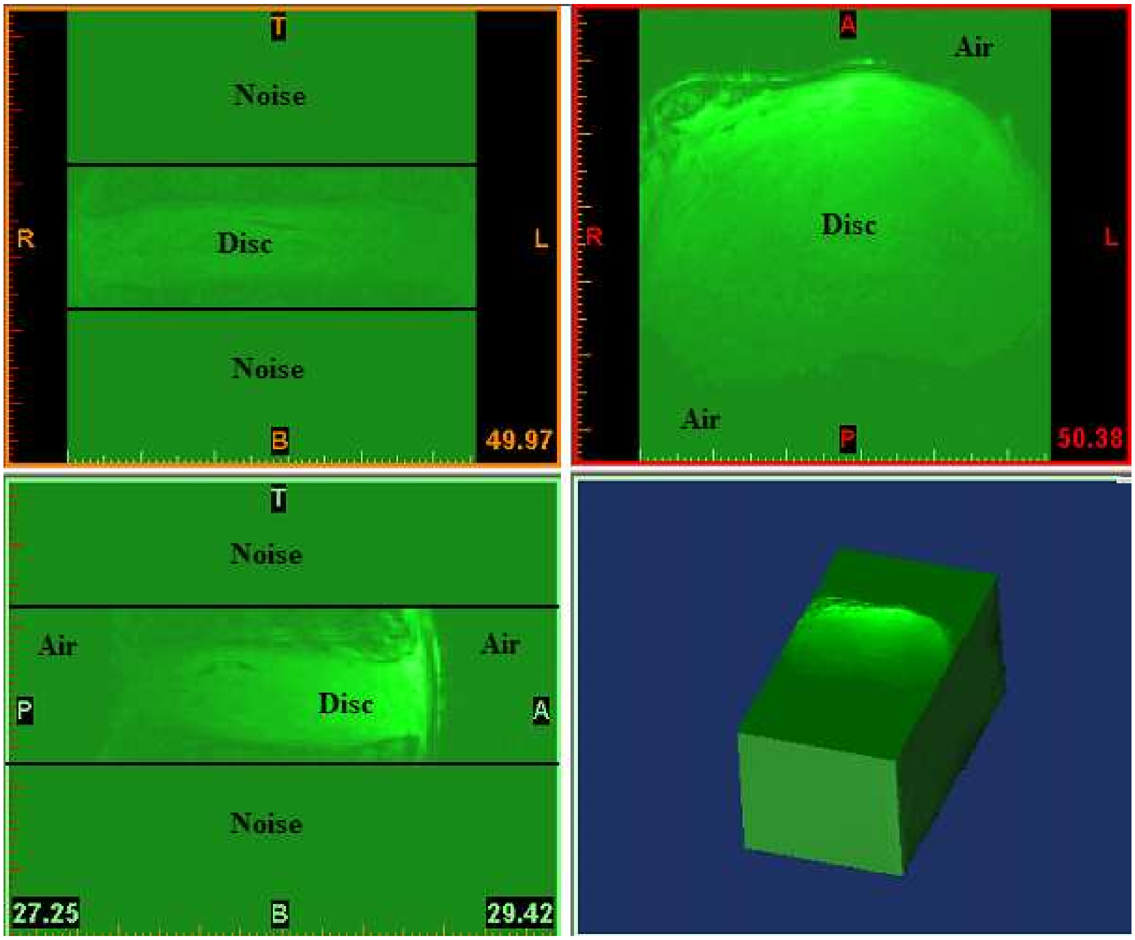

Figure 2.29. Featuring of the DICOM file containing the MRI for the L2-L3 disc in MIMICS™ 10.01, (MATERIALISE™, Leuven, Belgium). Anatomical reference for viewing, starting from the lower left and in clockwise rotation: saggital, coronal, axial and a 3D aspect of the scanned volume.

The MRI from the two selected discs had a display field of view of 104 x 104 mm with a resolution of 256 x 256 pixels, or 256 ppi (pixels per inch) giving a pixel size of 0.406 mm and a 0.4 mm of thickness between the scanned layers. For example, for an anterior-posterior length of 42 mm, a total of 105 scan layers were obtained, which needed to be segmented. Only the disc and the neighboring sides of the vertebra bodies were MRI scanned, and the remaining of the vertebrae was not scan. Thus, only a fraction of the vertebra bone was segmented and modeled, in contrast with the intervertebral disc which was entirely segmented and modeled, see Figure 2.30.

The key to converting anatomical data from the MRI to 3D models is a process called segmentation. During segmentation the user indicates the structure(s) of interest in the sliced image data. This information is then used to recreate a 3D model from the segmented structures. MIMICS™ has several tools to segment, or section, regions of interest, one of which is the *Threshold* level, which is a parameter that acts as a filter to select or discriminate different regions as a function of the intensity of brightness in a color or a grey tone scale. In our case, the MRI was given in 12 bits of grey tone scale per pixel, giving an intensity level (grayvalue) ranging from 0 to 4096. A grayvalue of zero represents a black pixel and that of 4096 represents a white pixel. There is a direct association between material density of the scanned object and the grayvalue assigned to each pixel in the image data. Because of this, segmentation programs have the flexibility to create models from any geometry distinguishable within the scanned data.

Hence, a removal of the volume occupied by air during the MRI scan was done to each disc using the *Threshold* level. With a grayvalue greater than 1040 most of the air was automatically eliminated in both discs. After this initial thresholding, the remaining air was manually eliminated layer by layer, until a 3D mask of only materials was created for each disc, and was called mask of materials, see Figures 2.30 and 2.31. Manual removal of air was mostly carried out at the periphery of the disc. Here, care was taken to maintain the annulus contour from a layer to the next layer. The use of multiple views helped for the coordination of air removal and material segmentation.

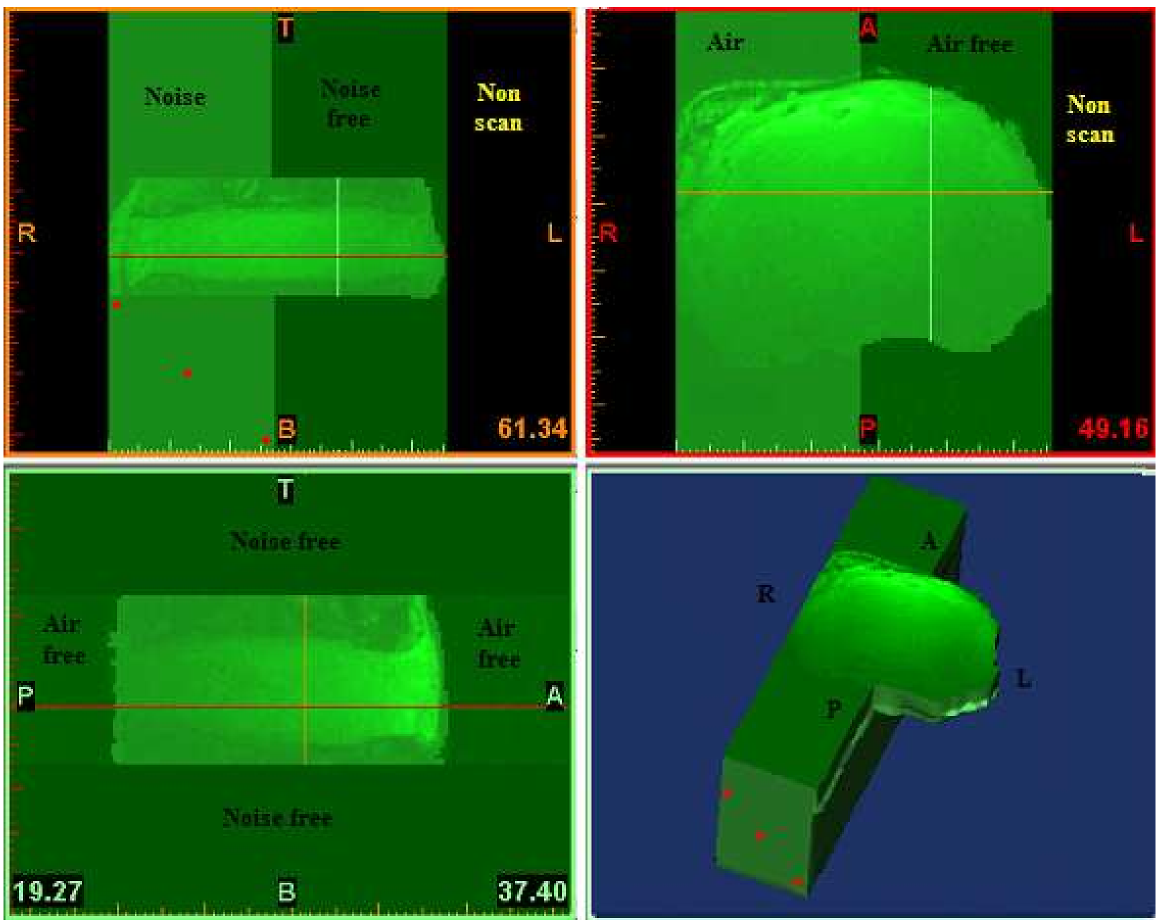

Figure 2.30. Partial removal of air from the L2-L3 disc surroundings using MIMICS™ 10.01, (MATERIALISE™, Leuven, Belgium).

In the MRI from the discs, the air appeared as a blank background pixel located outside the material. The higher concentration of water appeared as the brightest pixels and was located at the central part of the disc. The darker pixels in the region of material were

associated with high density, and appear on top and below the disc, corresponding to the vertebrae, or to the presence of cavities if appear in the disc region. These observations were in agreement with typical interpretations from lumbar spine radiology (Resnick, 1994).
Once the masks of materials were defined for each MRI, a description of the surface or contour of the 3D models was made using a Finite Element (FE) mesh in a stereo lithography (STL) format, which is a triangulated surface mesh file that allowed accurate description of geometrical details, typical of anatomical data which is in general very intricate. The STL surface mesh file contained three nodes for each triangle and defined the normal direction of the triangle. The generation of the mesh follows an iterative algorithm which interpolates with the selected tolerance (0.15 mm) all the layers (105 with 0.40 mm of separation) from the mask of materials (containing the intervertebral disc and vertebrae sides) to conform the contour. Hence, the two meshes were based on a custom quality which was based on a contour interpolation method. This allowed shape preservation with continuity. The parameters used for generating the STL 3D surface meshes are shown in Table 2.2.

Table 2.2. Process parameters used to generate the STL 3D Finite Element surface meshes in MIMICS^{TM} 10.01, (MATERIALISE^{TM}, Leuven, Belgium).

3D object Parameter	**Value**
Quality	Custom
Interpolation method	Contour
Prefer	Accuracy
Slices	Reset
Matrix reduction	XY resolution: 2 x Z resolution: 2 x
Shell reduction	No
Smoothing	Yes
Iterations	5
Smoothing factor	0.70
Compensate shrinkage	Yes
Triangle reduction	Yes
Reduction mode	Edge
Tolerance	0.15 mm
Edge angle	40 degrees
Iteration	10
Working buffer size	Below 31MB

An additional surface smoothing with a factor of 0.70 was applied to simplify complex details, giving the 3D models the contour appearance shown in Figure 2.31.

Initially, the FE surface mesh for each disc was set with a triangulation of 40º edge angle as a minimum, see Figure 2.32. As shown, the generation of the surface mesh creates triangles of different sizes and geometric shapes. The triangle shapes can be seen by its color, the dark green triangles have similar apexes and the dark red triangles have a narrow apex. Since the sum of internal angles in a triangle equals 180º, then it follows that a green triangle would tend to be equilateral. The red triangles with a narrow apex or an obtuse angle tend to have collinear vertices and are not appropriate for structural analysis.

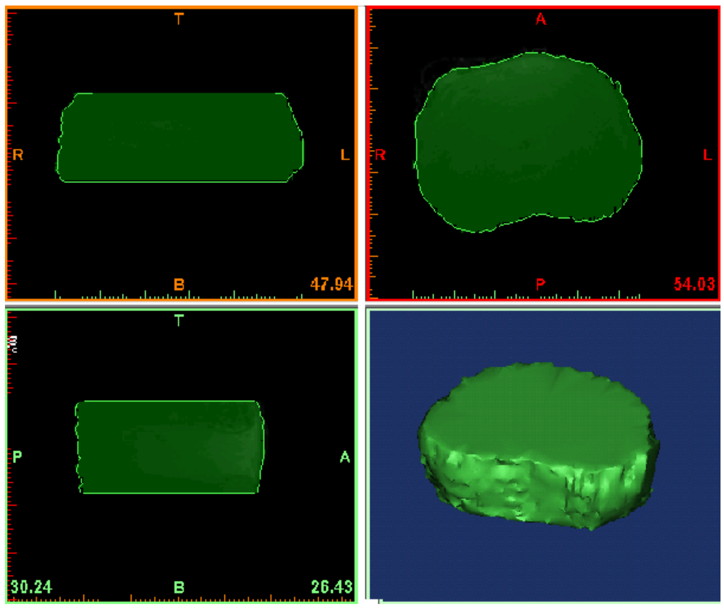

L2-L3 disc

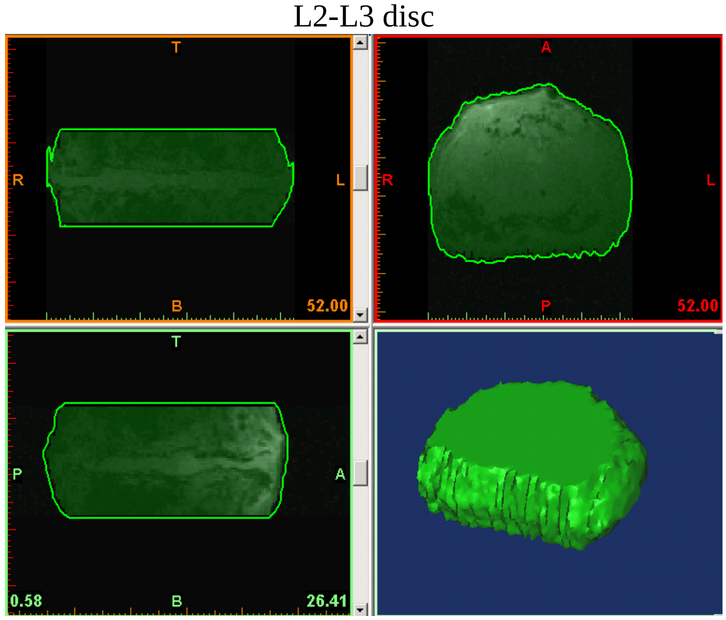

L4-L5 disc

Figure 2.31. Masks of materials showing the surface of the STL 3D models (lower right corner) for the L2-L3 disc (upper), and in the L4-L5 disc (lower) using MIMICS^{TM} 10.01, (MATERIALISE^{TM}, Leuven, Belgium).

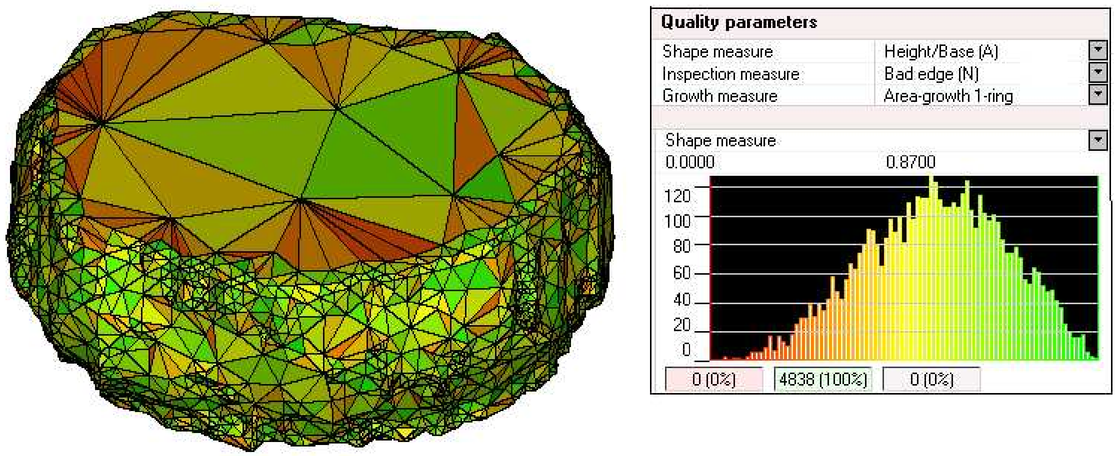

(A)

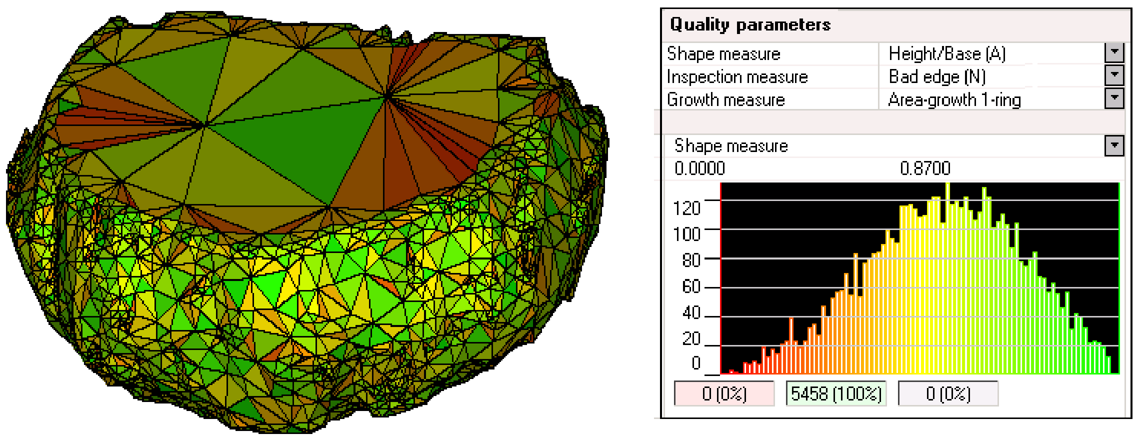

(B)

Figure 2.32. 3D Finite Element surface meshes for (A) the L2-L3 disc and (B) the L4-L5 disc using MIMICS^{TM} 10.01, (MATERIALISE^{TM}, Leuven, Belgium).

The larger triangles in the surface meshes of Figure 2.32 need to be reduced in size to account for a precise stress and strain analysis between points or regions, which is specially needed in the disc section. Also, the geometrical shape of the triangles accounts for maintaining predictable deformation, which in the case of the disc is needed for analyzing large deformations. In this sense, the green triangles tend to maintain the condition of mesh triangulation upon deformation, and are said to have good geometric quality. In contrast, the red triangles tend to show large distortions due to their obtuse angle, and create inconsistencies and instability in the process. Thus, an improvement in the geometric quality of the triangulation imply the reduction of the red triangles, which is mention in the next section.

The geometric characteristics of the 3D surface meshes for discs G (L2-L3), and I (L4-L5) are shown in Table 2.3.

Table 2.3. Geometric characteristics of the STL 3D Finite Element surface meshes for the L2-L3 and the L4-L5 discs.

Specimen	**Volume (mm^3)**	**Surface (mm^2)**	**Number of triangles.**	**Number of Points.**
G, level L2-L3	35654	6578	4838	2421
I, level L4-L5	35148	6518	5458	2731

b. Refinement of the surface meshes

The refinement of the 3D surface meshes in Figure 2.32 were accomplished in three steps using the remeshing tool of MIMICS^{TM}:

1) Reducing the contour details.
2) Reducing the size of the triangles.
3) Improving the ratio of triangles of good quality to low quality.

The remeshing tool is base on improving the quality of the mesh of the STL files from their original rapid prototyping (RP) ready format to a computer aided engineering (CAE) ready format for the preprocess analysis.

Unnecessary details of the surface were reduced by applying a second smoothing to the surface meshes. Elimination of sharp and rough edges, especially in the top and bottom regions of the vertebrae were also done, as these geometric features were the result of the removal of air from the MRI scan, and can be neglected for the modeling, since they are not part of the disc.

The reduction of size of the triangulation was done using criteria which limited the length of the triangles edges to a maximum value and with an established geometrical error. Thus, the meshes contain only triangles of lower size than the maximum edge length permitted, which was set in the range of 1 mm to 5 mm. Thus, this range of sizes for the triangulation was in accordance with the size of the disc, and convenient for the purposes.

For the low geometrical quality triangles (e.g. red triangles), an improvement was done using a criteria based on the quality parameter *Height/Base(A)*, which measures the ratio between the height and the base of the triangle, and normalizes the value to improve their quality. For this criterion, a perfect equilateral triangle has a geometric quality of 1, and a triangle with a sharp apex has a geometric quality near 0. The parameters used for the refinement of the surface meshes are shown in Table 2.4.

Six different sizes for the triangulation were used for the purpose of obtaining the most convenient size model. Recalling the main dimensions of an adult intervertebral disc, height and cross section, it was decided to maintain the maximum edge length of the triangulation in the range between 1 and 5 mm.

Hence, the following edge lengths were used to develop the triangulations: 1 mm, 1.3 mm, 1.5 mm, 2 mm, 3 mm and 5 mm. The meshes appearances for a triangulation of a 1.5 mm are shown in Figure 2.33.

Table 2.4. The remesh parameters for the STL 3D Finite Element surface meshes.

Smooth parameters	
Method	Laplacian 1 order
Smooth factor	0.7
Number of iterations	3
Use compensation	Yes
Reduction of triangles	
Method	Normal
Flip threshold angle	40°
Geometrical error	0.3
Number of iterations	5
Preserve surface contours	Yes
Autoremesh	
Shape quality threshold	0.4
Maximum geometrical error	0.3
Control triangle edge length	Yes
Maximum edge length	1
Number of iterations	10
Skip bad edges	Yes
Preserve surface contours	Yes
Quality preserving reduce parameters	
Shape quality threshold	0.4
Maximum geometrical error	0.25
Control triangle edge length	Yes
Maximum edge length	1, 1.3, 1.5, 2, 3, 5
Number of iterations	10
Skip bad edges	Yes
Preserve surface contours	Yes

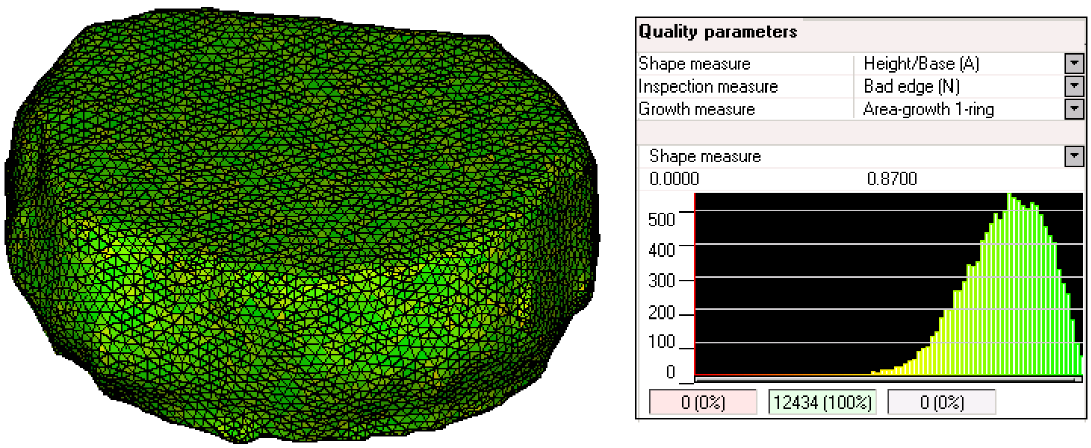

(A)

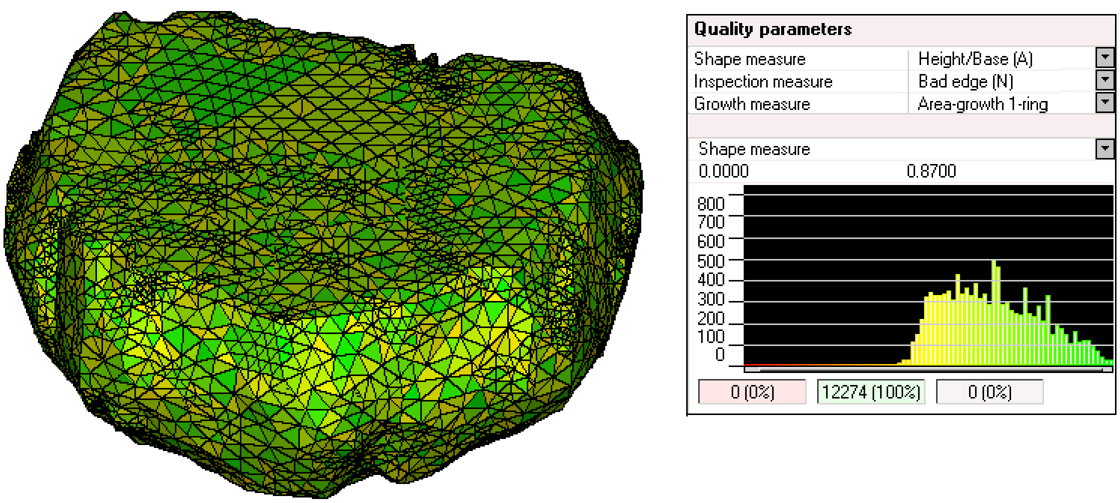

(B)

Figure 2.33. Refinement of the 3D Finite Element surface meshes with a maximum edge length of 1.5 mm for (A) the L2-L3 disc, and (B) the L4-L5 disc using MIMICS™ 10.01, (MATERIALISE™, Leuven, Belgium).

c. Setting of the mesh of volume

Once the refinement of the surface meshes was done for each disc, they were imported to a 3rd party volume mesh generation package (PATRAN™, MSC Software™, Santa Ana CA, USA). STL files are a surface representation. To do an analysis, a complete volume description is needed. Generating a volume mesh from a refined surface mesh is straightforward. This was done by filling the volume described by the triangulation of the contour meshes with a prismatic element. The type of element selected for the filling, was a tetrahedron with 4 nodes. This element is a three-dimensional, isoparametric 4+1-node, low order, tetrahedron with an additional pressure degree of freedom at each of the four corner nodes, see Figure 2.34. It is written for incompressible or nearly incompressible three-dimensional applications, such as rubber, water, or soft biological tissues like the intervertebral disc. The shape function for the center node is a bubble function. Therefore, the displacements and the coordinates for the elements are linearly distributed along the element boundaries. The stiffness of this element is formed using four Gaussian integration points. The degrees of freedom of the center node are condensed out on the element level before the assembly of the global matrix, as described in MSC Marc Mentat™ Tutorial for element type # 157 (MSC Software™, Santa Ana CA, USA).

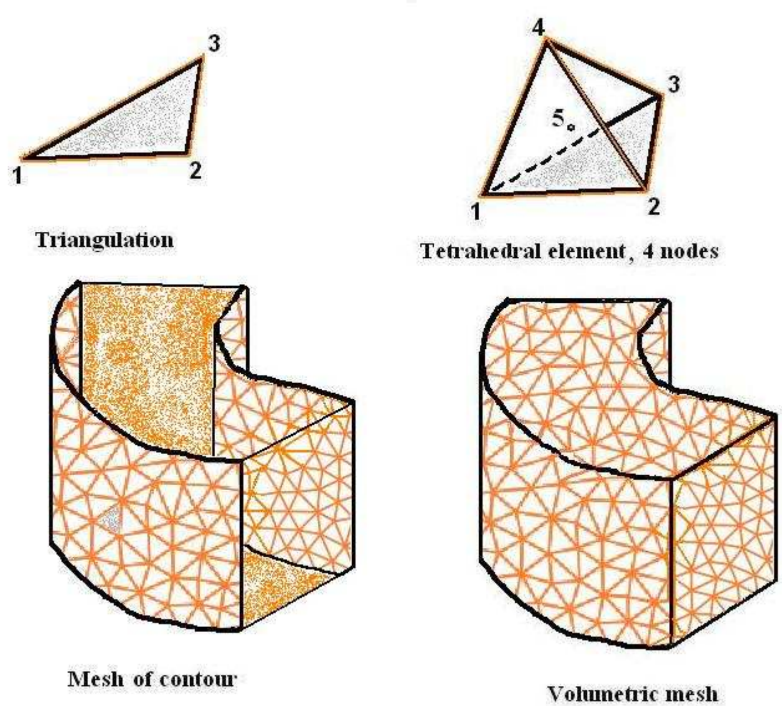

Figure 2.34. Tetrahedral element with 4 nodes used for the construction of the volumetric meshes.

Again, the volumetric meshes for each disc were set with different tetrahedron size, corresponding to the different sizes of the triangulation: 1 mm, 1.3 mm, 1.5 mm, 2 mm, 3 mm and 5 mm. A summary of the geometric characteristics of these volumetric meshes for each disc is given in Table 2.5.

As shown, models G-1 and I-1 corresponded to the meshes with the lowest number of elements and larger size, while models G-6 and I-6 corresponded to the meshes with the highest number of elements and smaller size. The maximum differences in the volume and in the surface of the meshes before and after the remeshing were small with values of 0.68% and 3.24% respectively.

Once the meshes of volume were set they were imported back to MIMICS™ for the assignment of regional materials, as defined by the their respective material masks, a task which involves the segmentation of bone and disc materials, and which is described next.

Table 2.5. The geometrical characteristics for the meshes of volume for the L2-L3 and L4-L5 discs.

L2-L3 disc						
Model Name	**Element size maximum length edge (mm)**	**Volume (mm^3)**	**Surface (mm^2)**	**Number of Elements**	**Number of Nodes**	**Degrees freedom DOF ($x10^6$)**
G-1	5	35411	6365	39788	7950	316
G-2	3	35418	6365	47519	9392	446
G-3	2	35428	6366	105231	19525	2055
G-4	1.5	35438	6369	187746	34172	6405
G-5	1.3	35444	6371	342912	60641	20794
G-6	1	35457	6381	724301	126361	91523
L4-L5 disc						
I-1	5	35335	6728	24596	4907	121
I-2	3	35342	6728	29375	5798	170
I-3	2	35352	6729	65051	12053	784
I-4	1.5	35362	6732	116060	21094	2248
I-5	1.3	35368	6734	211980	37433	7935
I-6	1	35381	6745	447745	78001	34925

d. Bone segmentation and respective masks

The segmentation of bone was done in the mask of materials, corresponding to the 3D object created, see Figure 2.27. This procedure started by differencing the intervertebral disc from the vertebrae. This task was relatively easy to do, as the difference of intensity of brightness of the pixels from the disc region with respect to those from the vertebrae in the MRI was evident. Thus, a clear boundary was established between the bone and the disc, see Figure 2.35.

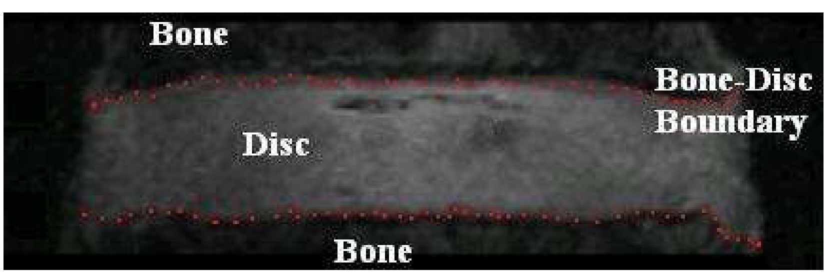

Figure 2.35. Differences in the intensity of brightness of the pixels are used to identify a boundary (red dots) between the disc and the vertebrae.

The procedure used for removal of the intervertebral disc from the mask of materials was also done layer by layer, and gave a mask of only vertebra bone, called Bone mask. Then, by applying a boolean subtraction of the mask of materials minus the Bone mask, gave the mask of the intervertebral disc, called Disc mask, see Figure 2.27. The appearance of the segmentations of bone and disc are shown in Figure 2.36.

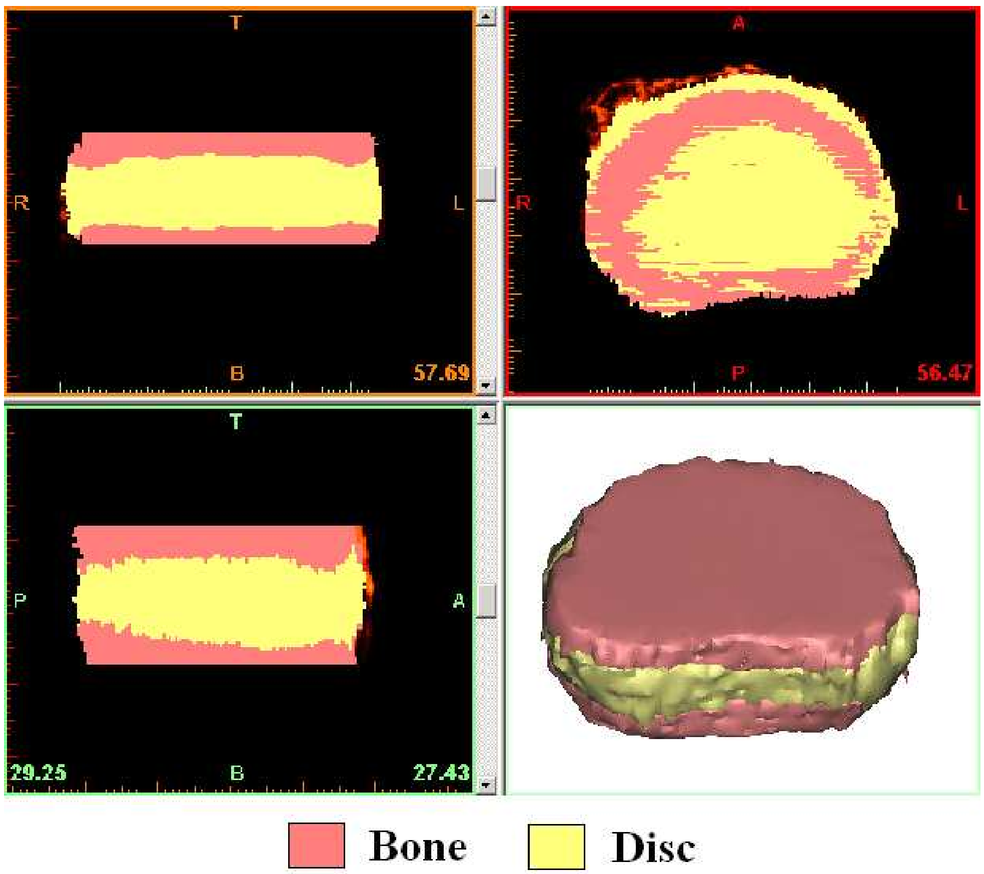

Figure 2.36. Masks showing the segmentation of vertebrae and intervertebral disc for the L2-L3 segment done with MIMICS^{TM} 10.01, (MATERIALISE^{TM}, Leuven, Belgium)..

Once the Bone mask was obtained, then a further segmentation was done to obtain the masks of cancellous bone, compact bone or cortical shell and osteophytes. However, these segmentations were base on assumptions from the anatomical features from the resolution (256 x 256 pixels) of the two MRI. Figures 2.37 and 2.39 shows the regions in the MRI that account for distinguishing differences between the two types of bone, which were: (1) the peripheral contour of the L2-L3 vertebra, as shown by the red dots in the axial view, and (2) the anterior sides of the L4-L5 vertebra, near the boundary with the disc, as shown by the blue dots in the coronal and saggital views.

Thus, for the L2-L3 segment it was proposed to assign a shell of compact bone (cortical) in the entire periphery of the MRI with a thickness of 1 to 2 pixels (0.4 to 1 mm) in accordance with Silva et al. (1994), see Figure 2.37. This shell of compact bone corresponded to a medium grade of disc degeneration, as suggested by Kotha et al (2007).

In juvenile vertebrae there is a clear distinction between cortical and trabecular bone, whereas in elderly bones is not always clear, especially in lower lumbar discs, such as level L4-L5.

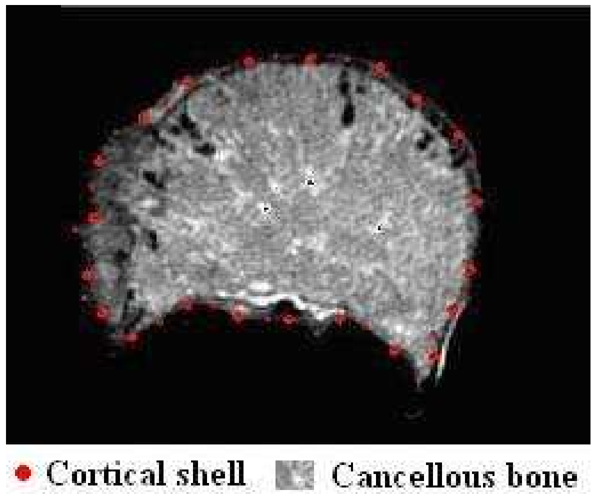

Figure 2.37. A ring of 0.4 to 1 mm of thickness (2 pixels) from the L2-L3 MRI contour of the vertebra account for the segmentation of the cortical shell. The remaining gray color in the view corresponds to the trabecular or cancellous bone.

A ring of a thin wall of compact bone along the craneo-caudal direction was removed from the Bone mask of the L2-L3 segment giving the trabecular bone, which formed the cancellous bone mask. The boolean subtraction of the Bone mask minus the cancellous bone mask, gave the mask of the compact bone or cortical shell, see Figure 2.27. The appearance of the segmentations of cancellous and cortical bone for the L2-L3 segment is shown in Figure 2.38.

For the L4-L5 segment, the visual inspection showed large amounts of osteophytes in the anterior side of the segment, these were seen in the MRI as bright pixels forming a thick layer that extended over and below the anterior side of the disc. With advance age and degeneration, the presence of these bony outgrowths increases, which makes it difficult to distinguish differences between the two bones (Resnick, 1994). Thus, it was suggested that the elongated bright appearances on the MRI of the L4-L5 segment at the anterior level, be treated as osteophyte formation, see Figure 2.39.

The removal of bony outgrowths from the Bone mask of the L4-L5 segment gave the cancellous bone mask. It was assumed that the cortical shell was underexposed by the presence of osteophytes. The boolean subtraction of the Bone mask minus the cancellous bone mask, gave the mask of the osteophytes, see Figure 2.27. The appearance of the segmentations of cancellous bone and osteophytes for the L4-L5 segment are shown in Figure 2.40.

Except for osteophyte formation, any other pathological changes in the bone such as reaction bone sclerosis or protrusions of the disc material into the vertebra bone were not considered for the segmentation.

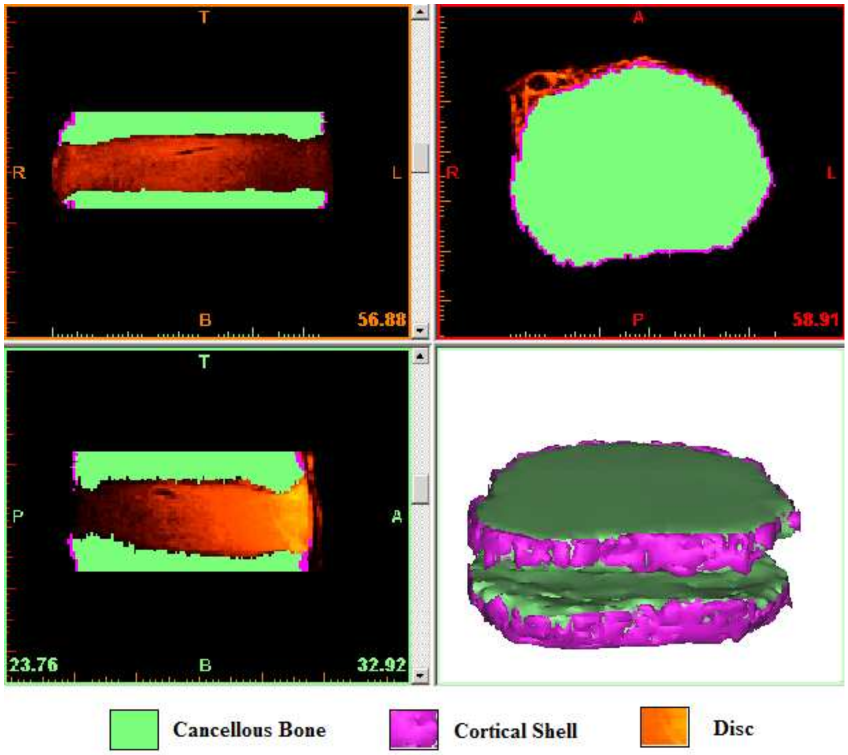

Figure 2.38. Masks showing the segmentation of cancellous and cortical bone for the L2-L3 segment done with MIMICS™ 10.01, (MATERIALISE™, Leuven, Belgium).

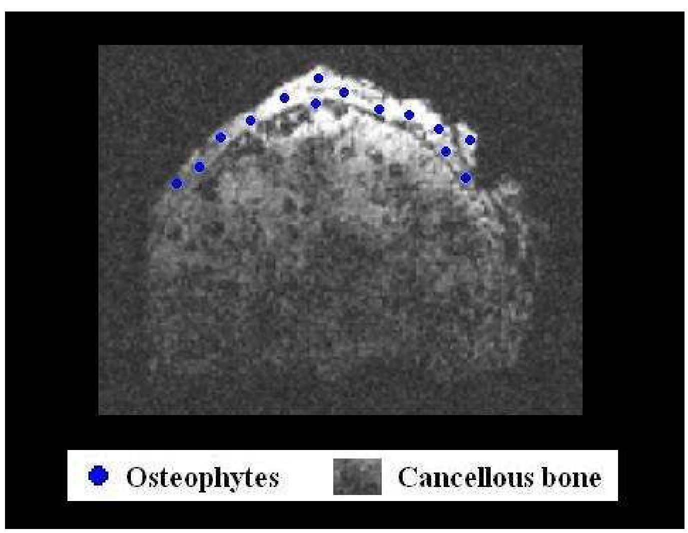

Figure 2.39. A thick wall of osteophytes was identified at the anterior margins of the L4-L5 segment. The remaining gray color corresponds to the trabecular bone.

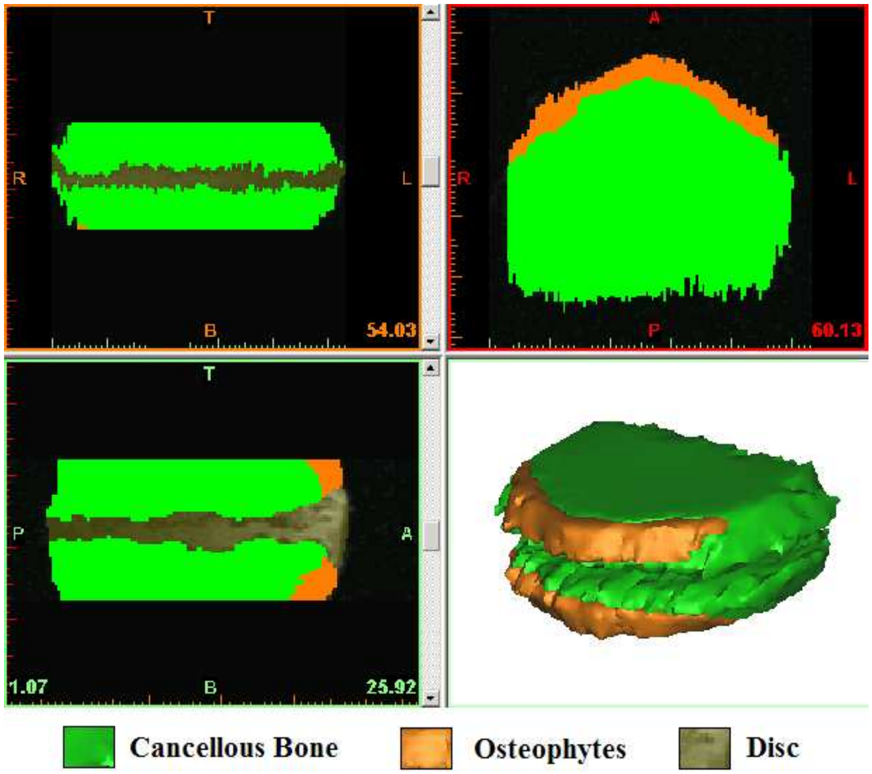

Figure 2.40. Masks showing the segmentation of cancellous bone and osteophyte formation for the L4-L5 disc done with MIMICS^{TM} 10.01, (MATERIALISE^{TM}, Leuven, Belgium)..

e. Intervertebral disc segmentation and respective masks

The segmentation of the disc materials: nucleus pulposus, annulus fibrosus, cartilage endplate and the cavities was done with the help of a radiologist in musculoskeletal, and were based on disc anatomy and geometry, size proportions, fundamentals of disc pathology and degeneration, and pixel brightness. The assignment of soft tissues varied between the two discs, and was done in the mask of the intervertebral disc called Disc mask, which was obtained in the previous sections. The first segmentation of disc material corresponded to the removal of the annulus fibrosus from the Disc mask, which was done for the two models, layer by layer, and gave a mask containing a mixture of the remaining disc materials (nucleus, the endplate and the cavities for the L2-L3 disc) or (nucleus and cavities for the L4-L5 disc). These masks were called Nucleus + Endplate + Cavities mask. A boolean subtraction of the Disc mask minus the Nucleus + Endplate + Cavities mask gave the mask of the annulus fibrosus, called annulus mask. The second segmentation was done in the Nucleus + Endplate + Cavities mask and corresponded to the removal of the endplate (only for the L2-L3 disc), which gave the nucleus pulposus + cavities mask. A boolean subtraction of the Nucleus + Endplate + Cavities mask minus the Nucleus + Cavities mask gave the mask of the endplate. Finally, in a third segmentation done in the two discs, the nucleus pulposus and the cavities masks were created, see Figure 2.28.

The resolution of the MRI (256 x 256 pixels) for the two discs showed a blurry laminar appearance in the outer 1/3 of each of the two elliptical axes at the middle cross section. Thus, it was difficult to distinguish laminas thickness and much less the collagen fibers, but it was decided to treat this region as the annulus fibrosus. The remaining region of inner 2/3 of each of the two elliptical axes at the middle cross section showed the highest intensity of pixel brightness (a level of 4096) and was decided to treated as the nucleus pulposus, see Figure 2.41.

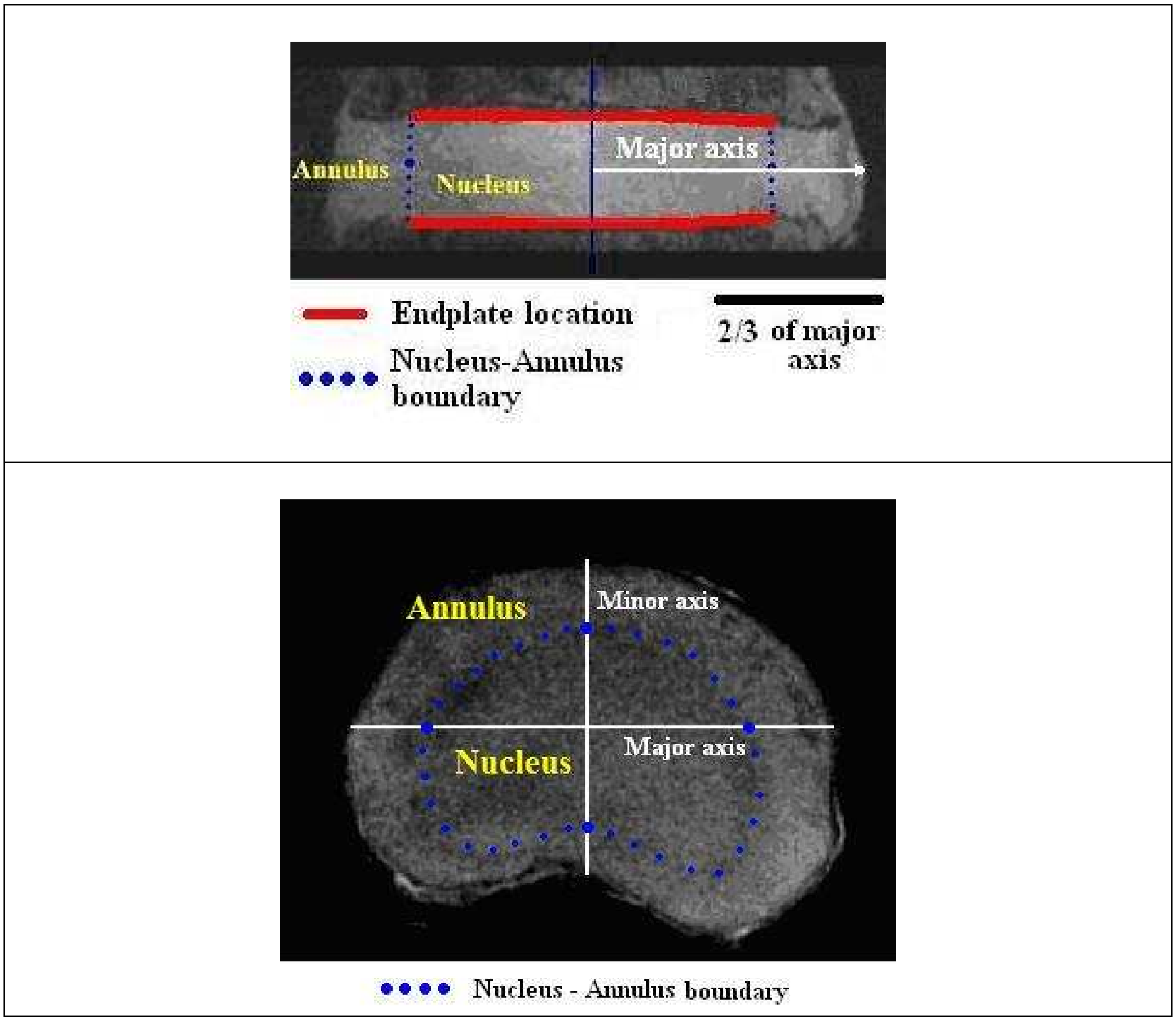

Figure 2.41. Assumptions made for the segmentation of the nucleus pulposus, annulus fibrosus and cartilage endplate.

Also, recognition of the endplate was not possible. However, the clear disc space shown by the MRI of the L2-L3 segment favors the presence of the layer of hyaline cartilage, which was proposed to cover 2/3 of each elliptical axis on the top and bottom cross section, near the boundary with the vertebrae, see Figure 2.41. The thickness of the endplate layer was varied from 1 pixel (0.4 mm in the center) to 2 pixels (1 mm near the annulus). For the case of the L4-L5 segment, no assignment of endplate was given due to the advanced degeneration.

The vacuum phenomenon which is a reliable indicator of disc degeneration was identified as a group of opaque spots corresponding to cavities which were mostly seen in the nucleus pulposus region of the two MRI. The corresponding masks were named cavity mask and were obtained by removing these opaque spots from the nucleus masks, see Figure 2.28.

The appearance of the segmentation of the annulus fibrosus for the L2-L3 segment is shown in Figures 2.42.

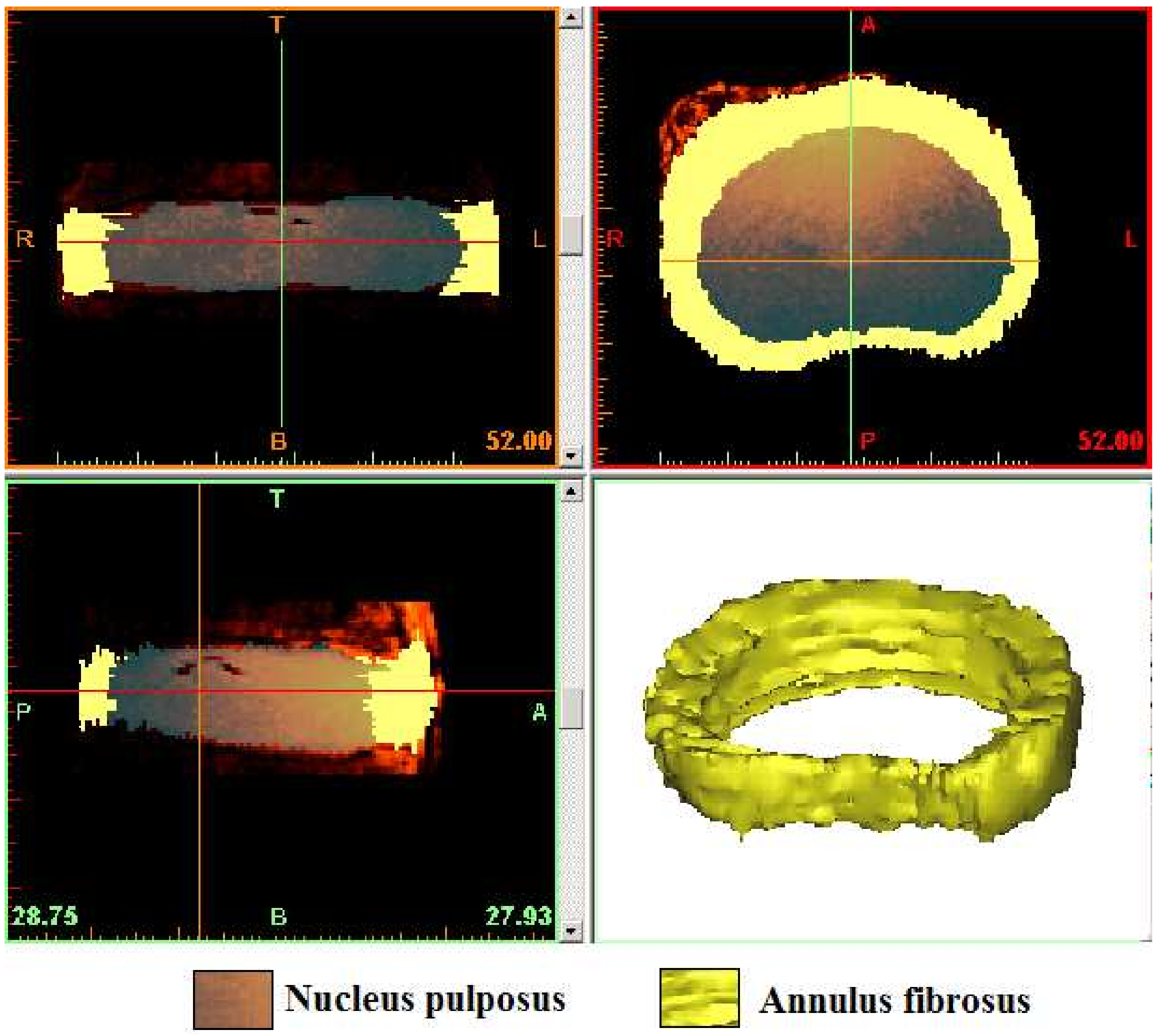

Figure 2.42. Mask showing the segmentation of the annulus fibrosus for the L2-L3 disc using MIMICS™ 10.01, (MATERIALISE™, Leuven, Belgium).

The appearance of the segmentations of the nucleus pulposus and the cartilage endplate for the L2-L3 segment are shown in Figures 2.43.

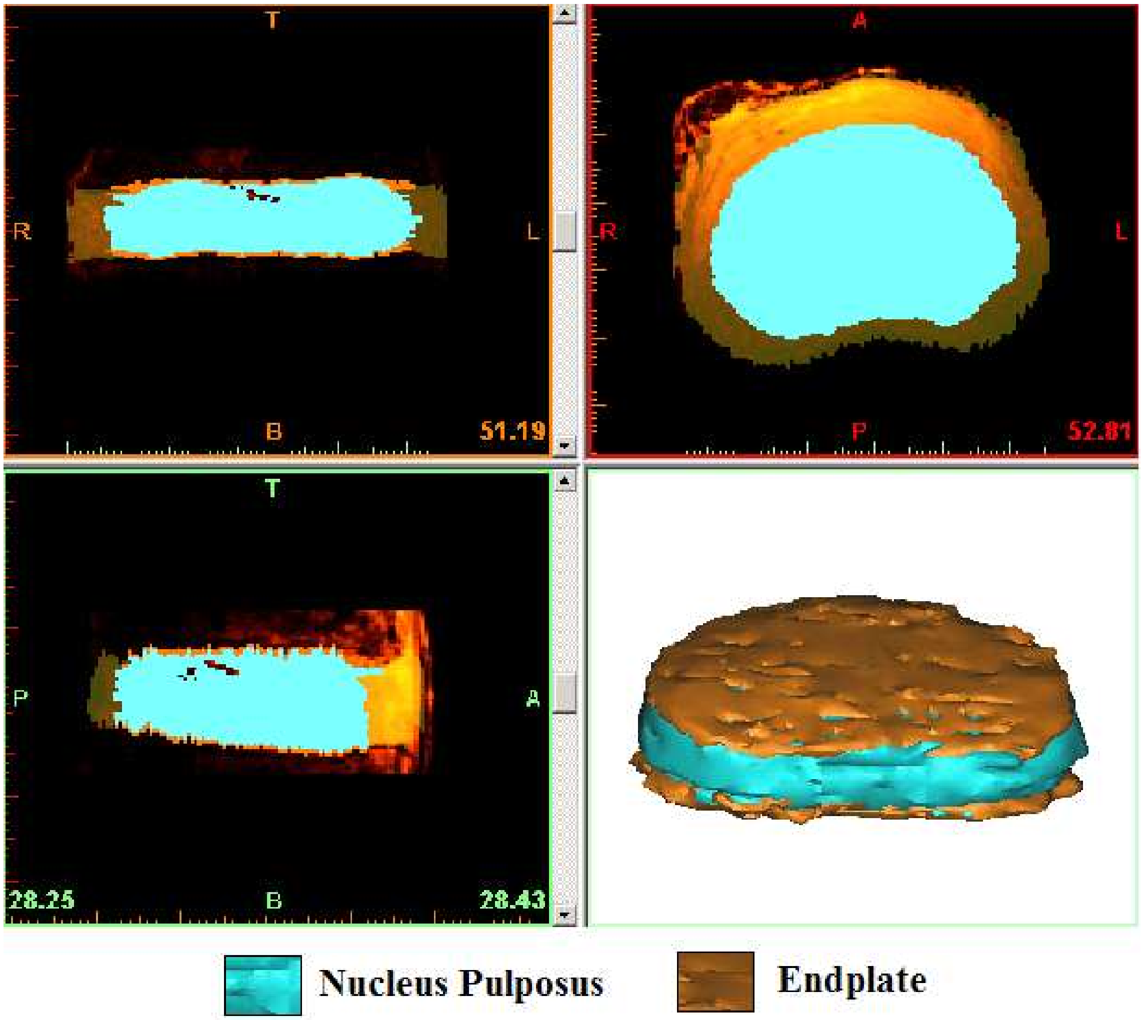

Figure 2.43. Masks showing the segmentation of the nucleus pulposus and the cartilage endplate for the L2-L3 disc using MIMICS™ 10.01, (MATERIALISE™, Leuven, Belgium).

The MRI from the L4-L5 disc showed a clear collapse of the disc space, with the highest intensity of pixel brightness (a level of 4096) showing in the middle cross section. However, the resolution within the cross section was not clear enough to distinguish differences in pixel brightness, and it was decided to maintain the same nucleus–annulus proportion used in the L2-L3 disc, with the exception of the disc height. The appearance of the segmentations of the annulus fibrosus and the nucleus pulposus for the L4-L5 disc are shown in Figure 2.44.

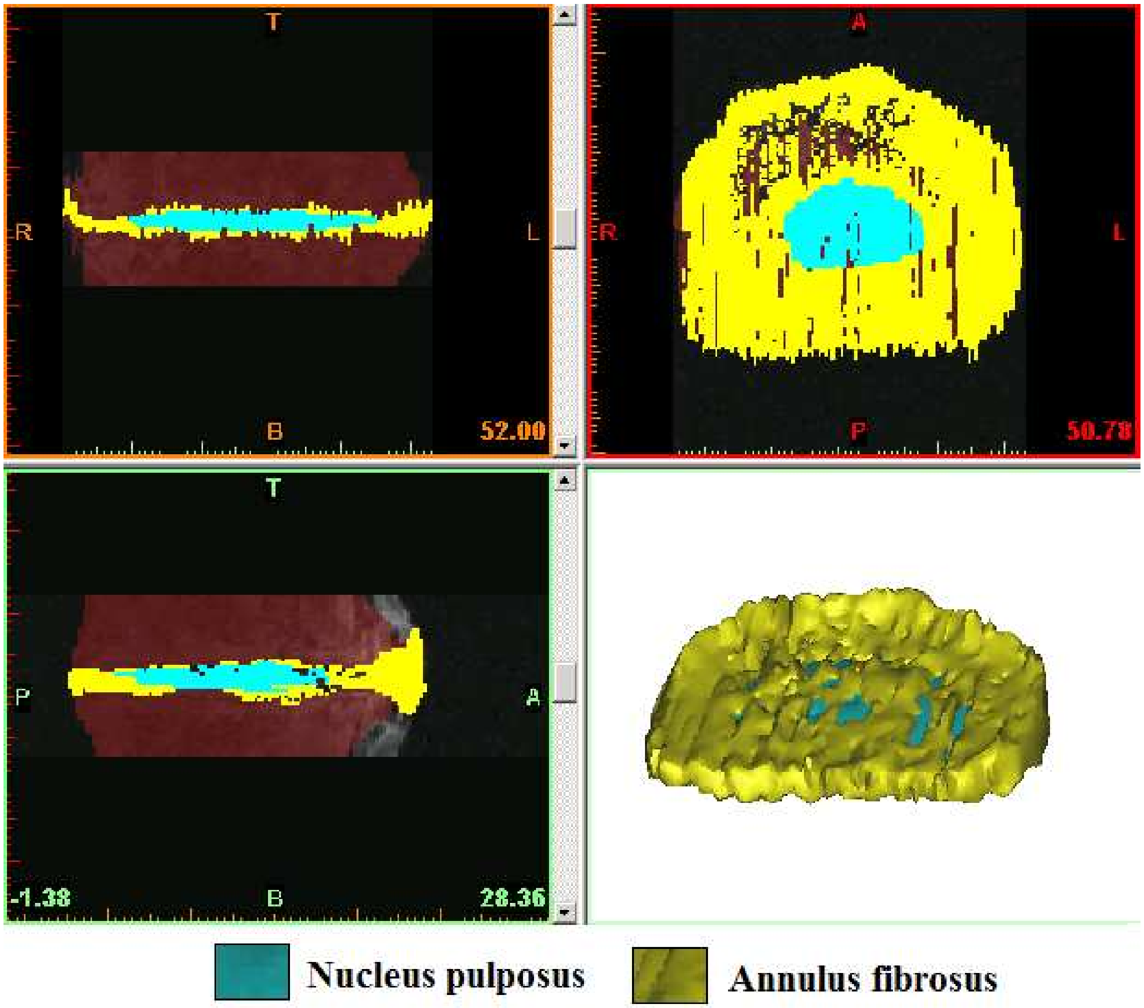

Figure 2.44. Masks showing the segmentation of the annulus fibrosus and the nucleus pulposus for the L4-L5 disc using MIMICS™ 10.01, (MATERIALISE™, Leuven, Belgium).

f. Assigning regional materials to the mesh of volume

The mesh of volume created previously in PATRAN™ was imported back to MIMICS™ for the assignment of regional materials through the material masks of bone and disc. The volume of the finite element mesh was identical to the total volume of all the masks of materials, in accordance with the description of the material segmentation.

Greyvalues of density were not assigned to the different masks of materials in MIMICS™. Instead preliminary values of Young´s modulus and Poisson´s ratio for each material mask were assigned and ratified in Marc Mentat™. Shown in Figure 2.45 are the appearance of the meshes of volume for each disc with their different masks of materials.

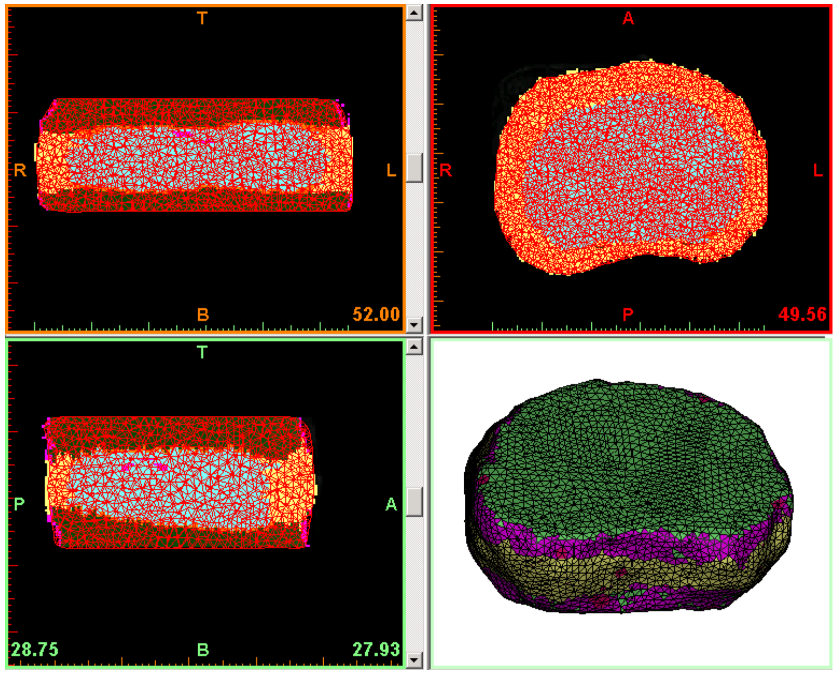

Disc L2-L3

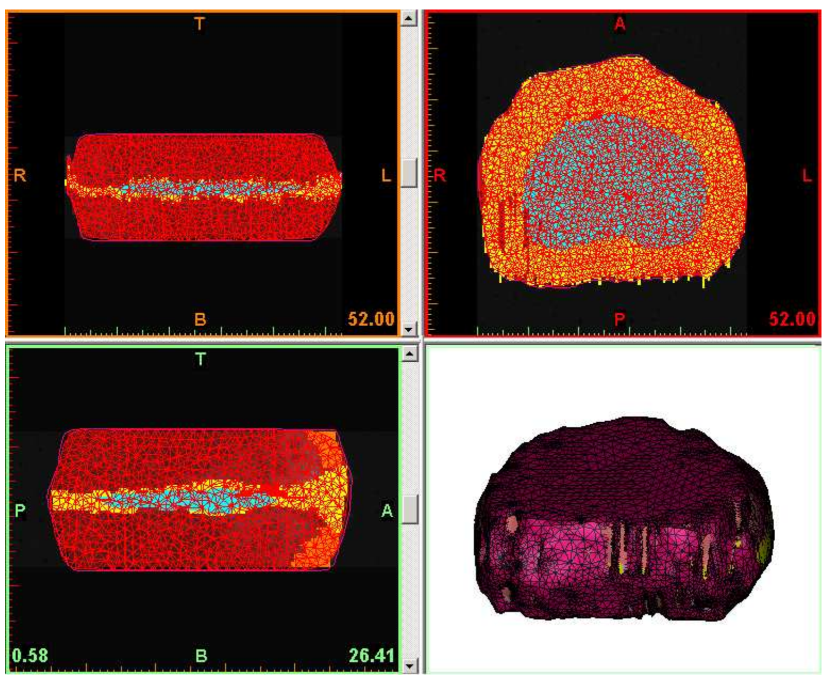

Disc L4-L5

Figure 2.45. Meshes of volume with the assignment of regional materials for the L2-L3 disc and the L4-L5 disc in accordance with the description of Figures 2.27 and 2.28.

The size of the tetrahedron element was the only varying parameter for studying the most convenient FEM disc to preprocess. Hence, six sizes of the tetrahedron element were used for each of the two discs, see Table 2.6 which also shows the total number of tetrahedral elements per mask material for each model.

Table 2.6. Number of tetrahedral elements per mask for each disc.

Number of elements, L2-L3 disc						
Mask Name	**Model G-1 (5 mm)**	**Model G-2 (3 mm)**	**Model G-3 (2 mm)**	**Model G-4 (1.5 mm)**	**Model G-5 (1.3 mm)**	**Model G-6 (1 mm)**
Annulus	13102	14302	26655	48091	82041	168968
Cancellous_bone	13502	18177	42733	82092	141211	302022
Cartilage_CEP	791	1046	3159	5508	11617	25976
Cavities	8	18	67	119	368	786
Cortical_shell	2748	2873	3884	6666	9449	19466
Nucleus	9633	11103	28729	45270	98168	206706
Total	39784	47519	105227	187746	342854	723924
Number of elements, L4-L5 disc						
Mask Name	**Model I-1 (5 mm)**	**Model I-2 (3 mm)**	**Model I-3 (2 mm)**	**Model I-4 (1.5 mm)**	**Model I-5 (1.3 mm)**	**Model I-6 (1 mm)**
Annulus	5274	5757	10729	19358	33024	68014
Cancellous_bone	16399	19291	46061	85398	146898	314185
Cavities	25	55	206	365	1129	2411
Nucleus	1025	1182	3550	4818	10448	21999
Osteophytes	1873	3090	4505	6121	20481	41136
Total	24596	29375	65051	116060	211980	447745

This completed the mesh generation for the two discs, after which the files were ready to be preprocess in Marc Mentat^{TM} 2007 (MSC Software^{TM}, Santa Ana CA, USA). However, only the L2-L3 disc was validated with the experimental results and further developed into a finite element model of disc degeneration.

g. Properties of the materials for the vertebrae and the intervertebral disc

The preprocessing of the L2-L3 FEM disc in Marc Mentat™ started by defining the type of formulation for the different materials, arranged in the segmented masks. Hence, seven masks with different mechanical properties were defined. A summarized of the mechanical properties of these materials is given in Table 2.7.

Table 2.7. Intervertebral disc and vertebrae bone material properties: Young´s modulus E, Poisson´s ratio ν, and Shear Modulus G.

Material	**Type of formulation**	**Young's E, and Shear G Modulus (MPa)**	**Poisson ratio ν**	**Reference**
Cartilage endplate	Isotropic	E = 20	ν = 0.3	Lu et al. (1996) Martinez et. al. (1997)
Nucleus pulposus	Incompressible Mooney-Rivlin	0.5 < E < 1.0	0.4 < ν < 0.5	Smit et al. (1996) Pitzen et al. (2002)
Annulus fibrosus	Incompressible Mooney-Rivlin or Neo-Hookean	0.75 < E < 5	0.35 < ν < 0.5	Goel et al. (1995) Eberlain et al. (2000) Pitzen et al. (2002)
Cancellous_bone	Orthotropic	$E_{11} = 140$ $E_{22} = 200$ $E_{33} = 140$ $G_{12} = 48.3$ $G_{23} = 48.3$ $G_{31} = 48.3$	$\nu_{12} = 0.315$ $\nu_{23} = 0.315$ $\nu_{31} = 0.45$	Goel et al. (1995) Lu et al. (1996) Banse et al. (2002)
Cortical_shell	Orthotropic	$E_{11} = 11000$ $E_{22} = 22000$ $E_{33} = 11000$ $G_{12} = 5400$ $G_{23} = 5400$ $G_{31} = 3800$	$\nu_{12} = 0.20$ $\nu_{23} = 0.20$ $\nu_{31} = 0.48$	Goel et al. (1995) Lu et al. (1996)
Osteophytes	Isotropic	400	0.25	Banse et al. (2002)
Cavities	Isotropic	$1e^{-8}$	0.1	

The bone materials: cortical shell and the cancellous bone, were formulated with orthotropic properties as suggested by Lu et al., (1996) who took into account the anisotropy, heterogeneity and time dependent properties. Also, the collagen from vertebral bone is oriented in the craneo-caudal direction, leading to a dominant stiffness in this direction (Hansson et al., 1980; Brickmann et al. 1989). Thus, an orthotropic formulation with similar stiffness along the radial and circumferential directions, and a higher stiffness along the axial direction is advised (Lu et al., 1996; Rohlmann et al., 2006; Noailly et al., 2007), see Table 2.7. The osteophytes were assigned an isotropic formulation since they do not have a porous structure as the trabecular bone.

The intervertebral disc materials: annulus fibrosus and nucleus pulposus were formulated as hyperelastic with isotropy and incompressibility, while the cartilage endplate was considered isotropic. Hyperelasticity provides a means of modeling the non-linear stress-strain behavior of the disc materials, specially the nucleus pulposus which contains a high water content. In this regard, the use of an elastomeric Mooney-Rivlin solid material formulation is frequently used in modeling lumbar discs mechanics with healthy (Schmidt et al., 2007) and degenerated discs (Rohlmann et al., 2006; Ruberté et al., 2009). Originally, this model was developed and used in the rubber industry by Ronald Rivlin (1915-2005), and Melvin Mooney (1893-1968) in response to the hyperelastic stress-strain behavior. The aplication of this material model in the bioengineering field is evident due to the similarities in the hyperelastic response of soft biological tissues. In the case of the intervertebral disc, the nonlinear large deformations seen upon loading, favors its use. Thus, it was decided that the nucleus pulposus, and the annulus fibrosus be assigned a *Mooney-Rivlin* formulation with the values shown in Table 2.8.

Table 2.8. Mooney-Rivlin incompressible material constants for the nucleus pulposus and annulus fibrosus based on disc degeneration. Adaptation from Schmidt et al.,(2007).

Material	**Degeneration Grade 1**	**Degeneration Grade 2**	**Degeneration Grade 3**	**Degeneration Grade 4**
Nucleus pulposus	C_1=0.066 C_2=0.016 E = 0.5 MPa*	C_1=0.10 C_2=0.025 E = 0.75 MPa	C_1=0.14 C_2=0.035 E = 1.05 MPa	C_1=0.18 C_2=0.045 E = 1.35 MPa
Annulus fibrosus	C_1=0.10 C_2=0.025 E = 0.75 MPa*	C_1=0.14 C_2=0.035 E = 1.05 MPa	C_1=0.18 C_2=0.045 E = 1.35 MPa	C_1=0.20 C_2=0.05 E = 1.50 MPa

* value of E obtained with an approximated equation for incompressible elastomers: $E = 6(C_1+C_2)$ with $C_2=0.25C_1$ obtaing from MSC Marc 2001.

The constants C_1 and C_2 shown in Table 2.8 refers to the material stiffness, and are called the deviatoric constants of the model, which are obtained from experimental and statistical studies of rubber (Marc Mentat, 2005r3). Values for these constants increase as the material stiffens, which in the case of degenerated discs, the stiffening of the disc junction is caused by the mechanisms of intervertebral osteochondrosis and spondylosis deformans (Resnick et al. 1994).

Thus, the incompressibility is reduced due to nucleus dehydration and bony outgrowths in the periphery, and the disc deformation implies some compressibility (Minna et al., 1991; Videman et al., 2008). Thus, in severe disc degeneration an elastic isotropic formulation for the disc tissues is more appropriate, see Table 2.9.

Table 2.9. Elastic material constants for the nucleus pulposus and annulus fibrosus based on disc degeneration scoring. Adaptation from Nataragan et al. (2004).

Material	Non-Degenerated (Grade 1)			Severe Degenerated (Grade 4)		
	Water Content (%)	Young Modulus E (MPa)	Poisson's Ratio ν	Water Content (%)	Young Modulus E (MPa)	Poisson's Ratio ν
Nucleus pulposus	85	1	0.49	75	1.6	0.40
Annulus fibrosus	70	2	0.40	55	12	0.35

h. Criteria for the adjustment of material properties

The higher stiffness of vertebral bone over that of the intervertebral disc materials was assumed. Hence, the *Young's modulus E, Poisson ratio* ν*, and Shear modulus G* values of the vertebral bone and cartilage endplate, and the *bulk modulus* of water for the L2-L3 FEM of disc degeneration were kept constant, with values in accordance with those indicated in Table 2.7.

The nucleus pulposus is a jelly-like substance in a disorganized arrangement of proteoglicans cells mixed with water. With aging and degeneration, the nucleus dehydrates and undergoes biochemical changes (Roughley, 2004; Buckwalter et al., 1995). The height preservation appearance of disc G from the MRI suggested a mild degenerated nucleus with only vacuum phenomena present. Thus, the proposed Mooney-Rivlin coefficients C_1 and C_2 values for the nucleus corresponded to a mild degeneration and were kept fixed.

Mechanically, the annulus fibrosus presents a hierarchical structure, and with disc degeneration undergoes deformation and dehydration, altering its structural arrangement, such as: in delaminations, protrusions, tears and broken fibers much of which affects the annulus mechanical properties *E* and *G* (Cassidy et al., 1989). However, the MRI resolution (256 x 256) of the annulus region was not sufficient to distinguish these anatomical changes, especially in the laminae structure. Still, it was suggested that the osteophytes from the anterior side of the annulus could influence its mechanical properties. Thus, it was decided that the only adjustment of material properties corresponded to the annulus fibrosus.

The criteria used for the adjustment of the Mooney-Rivlin coefficients for the annulus was based on the square of the sum of differences between the reaction force from each simulation and the applied force from the corresponding mechanical testing. The minimum force difference (F.D.) between these two process was defined as the adjustment value. The corresponding magnitude of F.D. was as follows:

$$F.D. = ((F_c(c_1) - 1000)^2 + (F_B(c_1) - 50)^2 + (F_E(c_1) - 50)^2 + (F_{LB}(c_1) - 50)^2 + (F_T(c_1) - 72)^2)^{0.5} \qquad (2\text{-}45)$$

where F_C, F_B, F_E, F_{LB} and F_T correspond to the sum of the reaction forces for all nodal points at the disc base (see nodal set "Fixed base" in Figure 2.48) for loading simulations in compression, flexion, extension, lateral bending and torsion, respectively. The right side of Eq. 2-45 contains the applied forces in the testing: in the first term a 1000 N for the compression load; from the second to the fourth term, a 100 mm off center axial load of 50 N which produced a moment of 5 Nm in flexion, extension and lateral bending; in the last term four tangential loads of 18 N with an off center of 70 mm to produce a moment of 5 Nm in torsion. For a description of these loads see the boundary conditions in the following section.

The technique adopted for finding the minimum force difference was achieved by varying the Mooney-Rivlin deviatoric coefficients C_1 and C_2 of the annulus fibrosus according to the range of values shown in Table 2.8. A schematic flow diagram of the adjustment of material properties for the annulus fibrosus is shown in Figure 2.46.

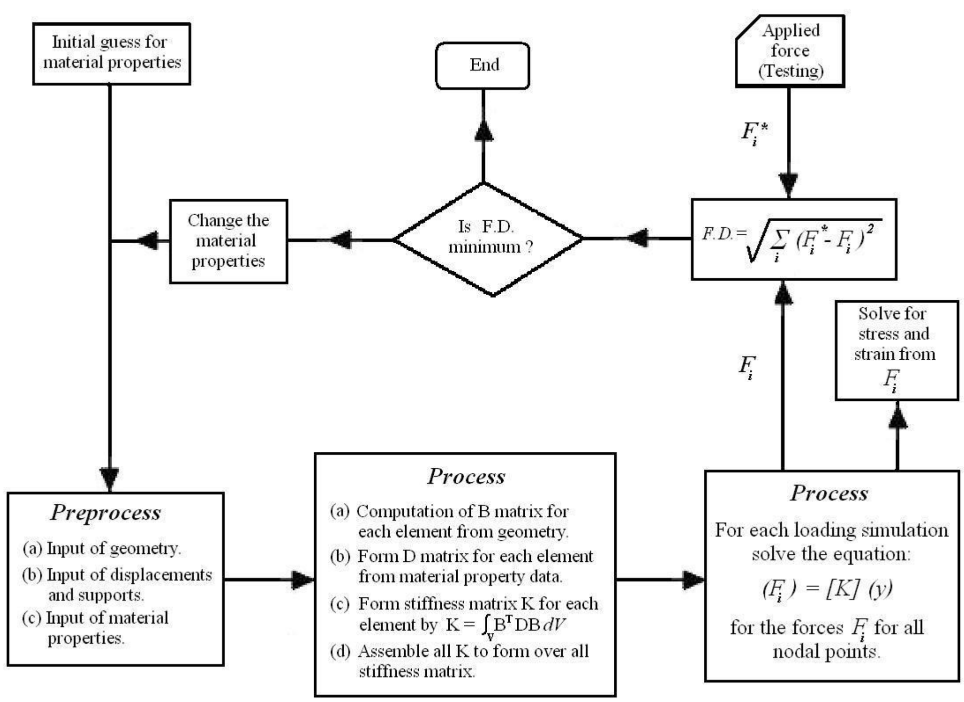

Figure 2.46. Flow diagram for yielding the Mooney-Rivlin deviatoric constants C_1 and C_2 for the annulus fibrosus.

i. Boundary conditions

For an analysis of stress, strain, forces and displacements in the L2-L3 FEM of disc degeneration, a mechanical class of boundary condition was defined in Marc Mentat^{TM}. Within the mechanical boundary class, the restraints, loading type, loading application, creation and selection of nodal sets, definition of loadcases and the implementation of a lever arm for the purpose of simulating bending and torsion loads for the two disc models are presented.

The application of the boundary conditions to the FEM disc require that the displacement versus time response for each loading scenario/case from the testing protocols be collected, saved, and inputted into MSC Marc Mentat^{TM} as a RAW file of data to be processed, which is a common readable format. Similarly, the raw file containing the force-time responses for each loading scenario/case were also inputted. This was done to verify the most predictable simulation results between inputs as a displacement, or as a force. In other words, it must ensure that the simulation results match the testing results, not only with the load or elongation magnitude, but also with the way in which the disc deforms. For example, in the compression testing the vertical displacement response was uniform across the disc upper section. Therefore, this deformation shape had to be reproduced in the simulation. For the case of inputs as displacements, the maximum duration (seconds) and the corresponding maximum displacement (mm) for each loading type for the two models are shown in Table 2.10.

Table. 2.10. The time and deflection response to reach the peak loads for the FEM of disc degeneration L2-L3 and L4-L5.

Loading Type	**Disc Response**			
	Duration (seconds)		**Displacement (mm)**	
	Disc L2-L3	**Disc L4-L5**	**Disc L2-L3**	**Disc L4-L5**
Compression 1000 N	101	101	1.43	1.01
Flexion 5 N-m	44	44	5.76	4.96
Extension 5 N-m	45	43	5.80	4.97
Right-Bend 5 N-m	35	20	4.54	5.00
Left-Bend 5 N-m	29	22	3.73	5.06
Torsion 5 N-m	91	87	9.84	6.32

The most convenient way of applying the boundary conditions to a large number of nodes, and viewing the results, was to create set of nodes. The following sets of nodes were defined for each material of the disc and vertebra, accessories for testing, and the disc sides (lower and upper sides), see Table 2.11.

Table 2.11. List of set of nodes created for the L2-L3 FEM of disc degeneration.

Set name	Description and site of the node set	Model viewing
Fixed Base 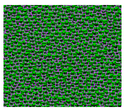	Nodes from the lower flat surface (green) of the lower trabecular body.	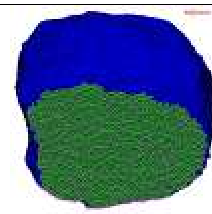
Displacement 	Nodes from the upper flat surface (purple) of the top trabecular body.	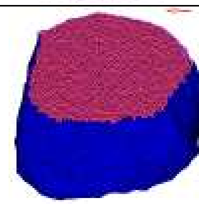
NP 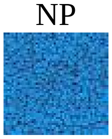	Nodes from all the nucleus pulposus elements.	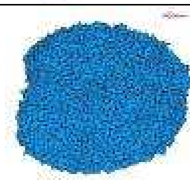
AF 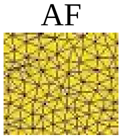	Nodes from all the annulus fibrosus elements.	
CEP 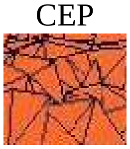	Nodes from all the cartilage endplate elements.	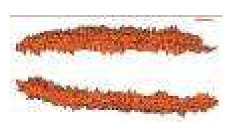
Bone 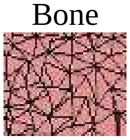	Nodes from all the cancellous, cortical and osteophytes elements.	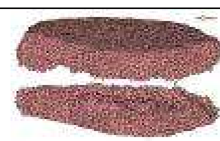
Steel 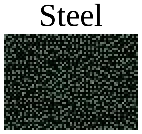	Nodes from the four arm lever arm.	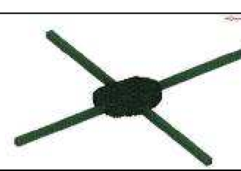

For all loading simulations, the disc model needs to be maintained fixed to the ground. Therefore, a restriction of movement was imposed to all nodes from the lower side of the disc. This set of nodes was called "*Fixed Base*". Hence, the displacements in the three axes: x, y and z were zero, see Figure 2.47.

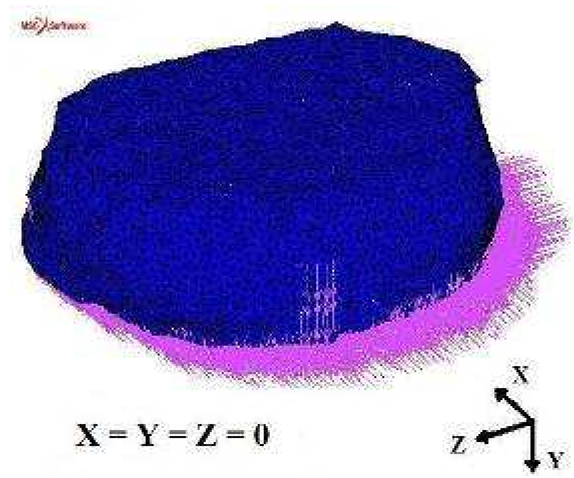

Figure 2.47. Restriction imposed to all nodes at the disc base.

For the simulation of the compression loading, the boundary conditions included an input of the vertical displacement response from the testing to all the nodes from the upper surface of the disc, defined by the nodal set "*Displacement*" in Table 2.11. Hence, only vertical displacement was imposed, and any other possibility for displacement was restrained, see Figure 2.48. For the other approach, the boundary conditions included an input of the fraction of the 1000 N force to each node from the nodal set "*Displacement*" in accordance with the verification of the most predictable result between inputs as a displacement, or as a force.

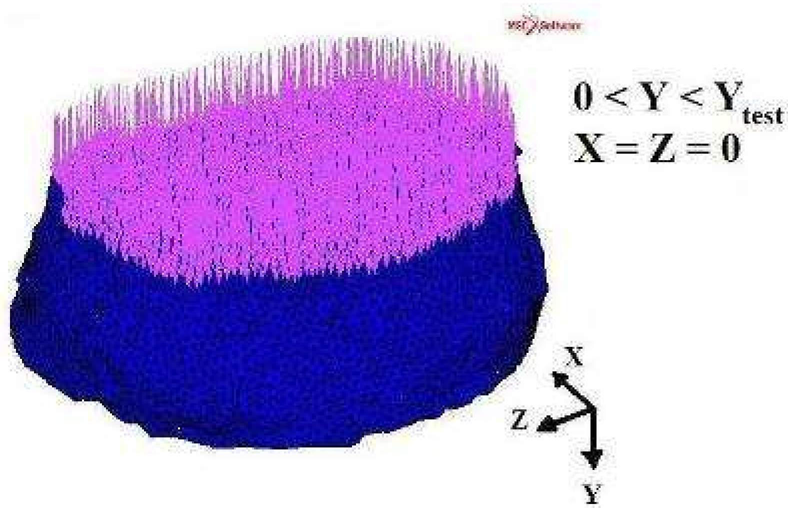

Figure 2.48. Uniform vertical displacement imposed to the upper nodes for the compression simulation.

For the simulations of the flexion, extension, lateral bending, and torsion loadings, it was necessary to implement a four arm lever with a length of 200 mm between opposite sides, and mounted on the upper flat surface of the disc model, as shown in Figure 2.50. A set of all the nodes from this lever was defined and called "Steel". For each simulation, a vertical displacement corresponding to the vertical deflection from the testing was imposed at the free end of each corresponding lever, see Table 2.10. A perspective of the lever arm with the imposed vertical displacement to induce (A) flexion, (B) extension, (C) right bending and (D) left bending are shown in Figure 2.49.

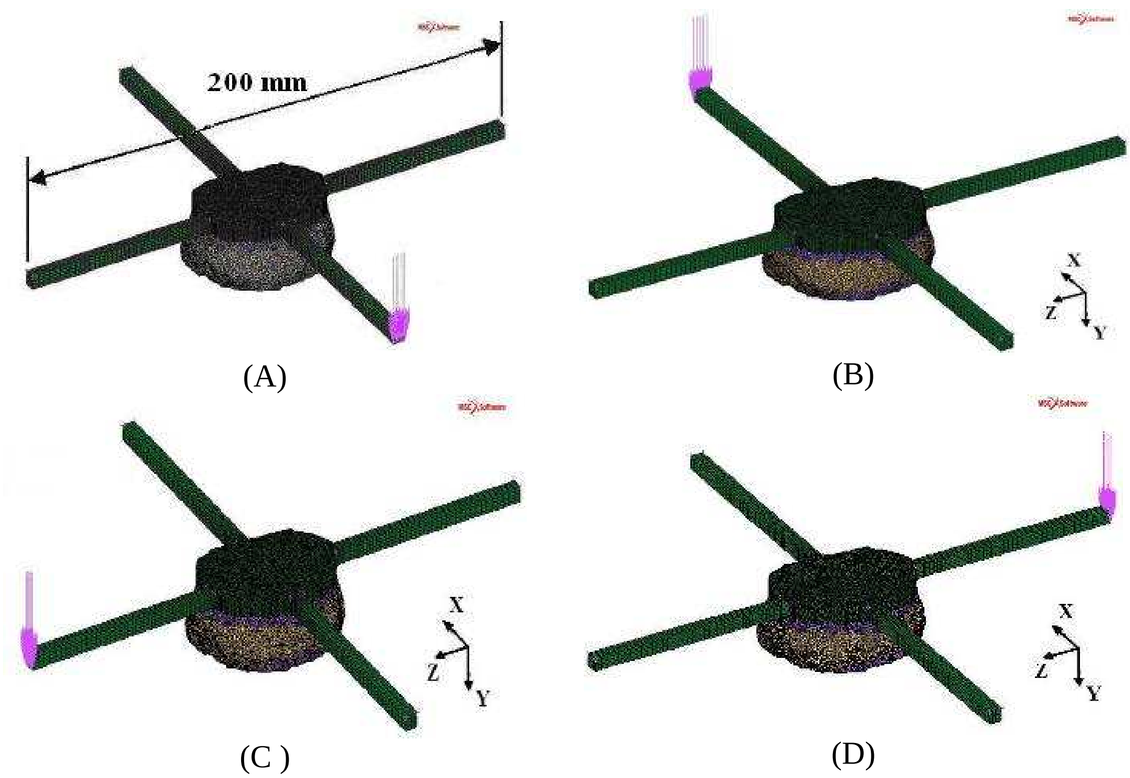

Figure 2.49. Boundary conditions for the bending simulations. Implementation of a 200 mm lever arm, and imposed vertical displacement at the free end of each lever for simulations of (A) flexion, (B) extension, (C) right bending and (D) left bending.

For the torsion simulation, the imposed displacements were parallel to axes X and Z, as shown in Figure 2.50. Thus, with two pairs of displacements of equal value but in opposite directions, and separated by a distance of only 140 mm from one another, the torsion was achieved. The values of the displacements applied in the X and Z directions, were 9.84 mm for disc model L2-L3 and 6.32 mm for disc model L4-L5. These values were obtained considering the length of the arc rotation in the XZ plane of the disc cross section. Thus, it can be written:

$$S = r\theta \qquad (2\text{-}46)$$

where S is the arc length, r is the radius of rotation and is equal to 70 mm, which is one half of the lever arm length, and θ is the angle of torsion. For small deformations it was assumed that $S \sim L$, where L is the straight line between the points A and B of the arc, see Figure 2.51. Thus, the length of this straight line was determined by the cosines law:

$$L^2 = r^2 + r^2 - 2r^2 \cos\theta \qquad (2\text{-}47)$$

when comparing values between S and L their differences were less than 1% indicating that a straight deflection with $\pm L$ value of 9.84 mm and 6.32 mm could be used as input.

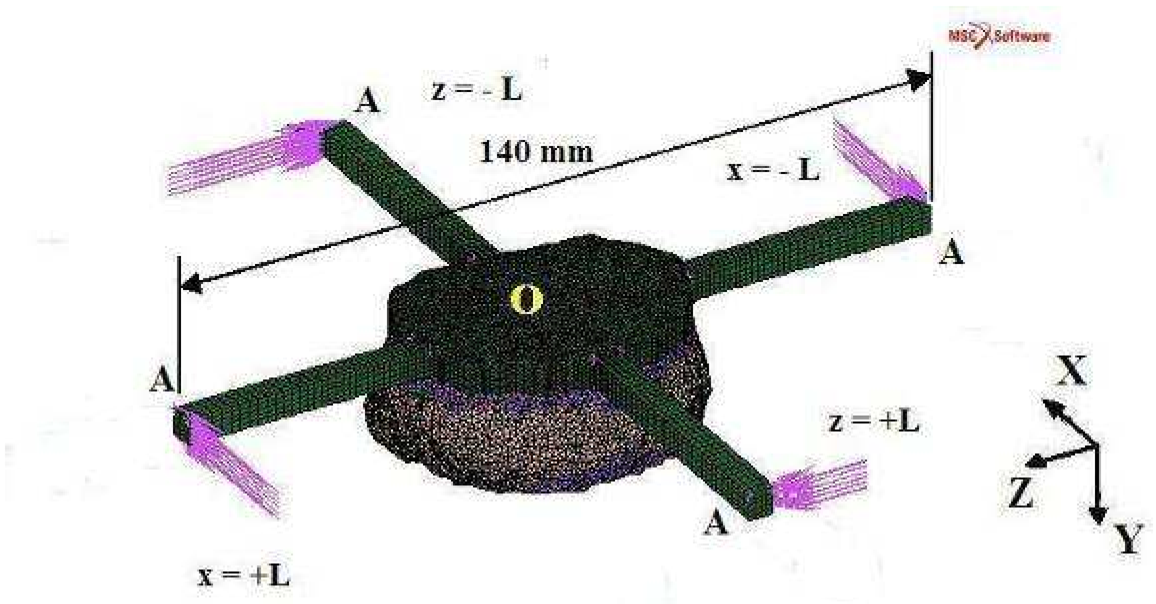

(A)

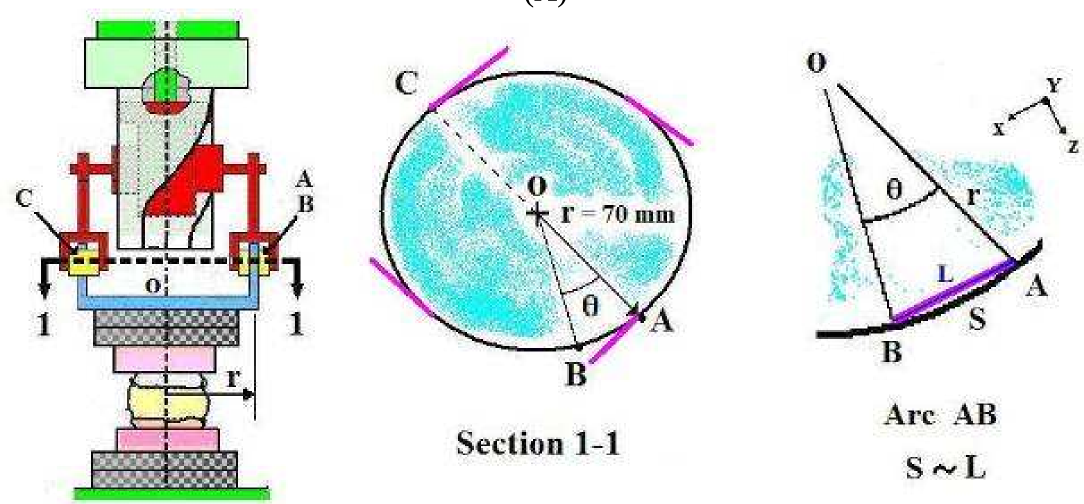

(B)

Figure 2.50. Boundary conditions for the simulation of torsion loading. Displacements applied to the lever are parallel to axes X and Z to cause torsion.

j. Assignment of loadcases and analysis of stress and strain

After establishing the boundary conditions, the next step was to define the type of Finite Element Analysis (FEA) to be submitted, and the load cases for all simulations: compression, flexion, extension, lateral bending and torsion.

Loadcases are used to define how the boundary conditions are going to be applied, and also for viewing the time sequence of a particular result, e.g. displacements, forces, stresses, strains, etc. The parameters used for the loadcases were the same for all simulations and are indicated in Table 2.12.

Table 2.12. Loadcase parameters.

Parameter	**Actions and values**
Load	Compression, Flexion, Extension, Right-Bend, Left-Bend or Torsion
Solution Control	Default
Convergence Testing	Relative with residual or displacement with 0.1 relative force and displacement tolerance
Numerical Preferences	Default
Total Loadcase Time	Test duration in seconds for each loading type
Stepping Procedure	Fixed
Number of Steps	10 steps for Compression, and 5 steps for the each bending loading
Automatic Step Cut Back	On
# of Cut Back Allowed	10

The simulation results are organized into elements (tensors and scalars) and nodal quantities grouped by set of nodes, which included the disc and vertebrae materials. In general, the results for the loading simulations include the following:

1) Displacements.
2) Reaction force.
3) Stress (principal and shear).
4) Strain (principal and shear).

For each simulation, the step displacement in the vertical direction *Y* also included radial displacements in the *X* and *Z* directions, which in the case of the compression simulation were compared with the bulging results from the testing. In the bending and torsion simulations, the radial displacements were not compared with the testing results because the bulging was not measured.

The intervertebral disc undergoes large deformations upon loading, which represents a nonlinear problem with large displacements and small strains. Hence, changes in the stress-strain law can be neglected, but the contributions from the nonlinear terms in the strain displacement relations cannot be neglected, as described in the tutorial “MSC. Marc Volume A: Theory and User Information,” (MSC Software^{TM}, Santa Ana CA, USA).

Nonlinearities considered for the stress and strain distribution profiles included: material behavior, geometry, and boundary conditions and/or loads such as those that were presented in the previous sections. Description of the kinematics of deformation for the case of the intervertebral disc loading favors the use of a Lagrangian formulation approach, which description is given in appendix IV.

IV. References

Adams, M.A. (1995). “Spine Update. Mechanical testing of the spine: An appraisal of methodology, results, and conclusions”. Spine 20(19) pp 2151-2156.

Allen K and Athanasiou K. (2006). “Viscoelastic characterization of the porcine temporomandibular joint disc under unconfined compression”. J. Biomechanics 39. pp. 312-322.

Benneker LM, Heini PF, Anderson SE, Alini M and Ito K. (2005). “ Correlation of radioghapic and MRI parameters to morphological and biochemical assessment of disc degeneration”. Eur Spine Journal 14: 27-35.

Banse X, Sims TJ and Barley AJ (2002). “Mechanical properties of adult vertebral cancellous bone: correlation with collagen intermolecular cross-link”. Journal of Bone and Mineral Research 17(9): pp. 1621-1628.

Brinckmann P, Biggemann M and Hilweg D. (1989). “Prediction of the compressive strength of human lumbar vertebrae“ Spine 14(6), pp. 606-610.

Buckwalter JA. (1995) “Aging and degeneration of the human intervertebral disc”. Spine 20:1307-14.

Cassidy J.J., Hiltner A. and Baer, E., (1989). “Hierarchical Structure of the Intervertebral Disc”. Connective Tissue Research 23: pp.75-88.

Eberlein R, Holzapfel GA and Schulze-Bauer CAJ (2000). “An anisotropic model for annulus tissue and enhanced finite element analysis of intact lumbar disc bodies”. Computer Methods in Biomechanics and Biomedical Engineering 4, 209-229.

Farfan HF, Cossette JW, Robertson GH, Wells RV and Kraus H (1970). “The Effects of Torsion on the Lumbar Intervertebral Joints: The Role of Torsion in the Production of Disc Degeneration”. The Journal of Bone and Joint Surgery. Vol 52-A, No.3 pp.468-497

Fung YC. (1993). Biomechanics, 2nd ed. Springer-Verlag, New York. ISBN 0-387-9747-6

Galante J. (1967). “Tensile Properties of the human lumbar annulus fibrosus”. Acta Orthopedica Scandinavika (Supp) 100.

Goel VK, Monroe BT, Gilberston LG and Brinckmann P. (1995). “Interlaminar shear stresses and laminae separation in a disc. Finite element analysis of the L3-L4 motion segment subjected to axial compression loads”. Spine 20(6), 689-698.

Hansson T, and Roos B. (1980). “The influence of Age, Height, and Weight on the bone mineral content of lumbar vertebrae”. Spine 5(6), pp. 545-551.

Huber G, Linke B, Morlock M and Ito K. (2003). Spinal Implants: Are we evaluating them appropriately? . “The influence of in vitro testing method on measured intervertebral disc characteristics”.. Editor M. Merkelson, J Kirkpatrick and S Griffith. ASTM.

Iatridis JC, Weidenbaum MD, Setton LA and Mow VC. (1996). “Is the nucleus Pulposus a Solid or a Fluid? Mechanical Behaviors of the Nucleus Pulposus of the Human Intervertebral Disc”. Spine 21(10): 1174-1184.

Izambert D, Mitton D, Thourot M and Lavaste F. (2003). “Dynamic stiffness and damping of human intervertebral disc using axial oscillatory displacement under a free mass system”. European Spine Journal 12: 562-566.

Kazarian, L.E. (1975). Creep characteristics of the human spinal column. Orthopedic Clinic of North America. Vol.6(1): 3-18.

Kasra M, Shirazi-Adl A and Drouin G. (1992). “Dynamics of Human Lumbar Intervertebral Joints: Experimental and Finite Element Investigations”. Spine 17(1): pp.93-102.

Koolstra JH, Tanaka E and Van Eijden. (2007). “ Viscoelastic material model for the temporomandibular joint disc derived from dynamic shear tests or stress relaxation test” Journal of Biomechanics 40. pp 2330-2334.

Kotha SP and Guzelsu N (2007). “Tensile behavior of cortical bone: Dependence of organic matrix material properties on bone mineral content” . Journal of Biomechanics 40(1). pp. 36-45.

Lin, H.S., King Liu, Y., Ray, G. y Nikravesh, P. (1978). “Systems identification for material properties of the intervertebral joint”. J. Biomechanics. Vol. 8. pp 1-14.

Lu YM, Hutton WC and Gharpuray VM. (1996). “Do bending, twisting and diurnal fluid changes in the discs affeact the propensity to prolapse?”. A viscoelastic finite element model”. Spine 21(22), 2570-79.

Marc Mentat, (2005). Material Library Vol. A. p.498.

Martinez JB, Oloyede OA and Broom ND (1997). “Biomechanics of load-bearing of the intervertebral disc: an experimental and finite element model”. Med Eng. Phys. Vol. 19 No. 2 pp 145-156.

Minna T, Hannu P, Hatti L, Hekki A, Markku K and Martti K .(1991). “Disc degeneration in magnetic resonance imaging: A comparative biochemical, histologic, and radiologic study in cadaveric spines”. Spine 16(6): pp. 629-634.

Mooney, M., (1940). A theory of large elastic deformation. Journal of applied physics 11, 582-592.

Nachemson , A and Morris, J.M. (1964). In vivo measurements of intradiscal pressure . J.Bone and Joint Surgery. 43 pp. 1077.

Natarajan RN, Williams JR and Anderson GBJ. (2004). “Recent Advances in Analytical Modeling of Lumbar Disc degeneration”. Spine 29(23) pp. 2733-41.

Noailly J, Wilke HJ, Planell J, Lacroix D. (2007). “How does the geometry affect the internal biomechanics of a lumbar spine bi-segment finite element model ? Consequenceson the validation process”. Journal of Biomechanics 40, pp. 2412-2425.

Perie D, Iatridis JC, Demers CN, Goswami T, Beaudoin G, Mwale F and Antoniou J. (2006). “Assessment of compressive modulus, hydraulic permeability and matrix content of trypsin-treated nucleus pulposus using quantitative MRI”. Journal of Biomechanics 39: 1392-1400.

Pitzen T, Geisler F, Matthis D, Muller-Stortz H, Barbier D, Steudel W and Feldges A (2002). “A Finite element model for predicting the biomechanical behavior of the hnuman lumbar spine”. Control Engineering Practice 10. pp. 83-90

Resnick D. (1994). “Diagnosis of Bone and Joint Disorders: Degenerative Disease of the Spine”. W.B. Saunders. Vol.2, Chapter 35: p.1382-1471.

Rohlmann A, Zander T, Schmidt H, Wilke HJ and Bergmann G (2006). “Analysis of the influence of disc degeneration on the mechanical behavior of a lumbar motion segment using the finite element method”. Journal of Biomechanics 39: 2482-2490.

Roughley, PJ. (2004). “Biology of intervertebral disc aging and degeneration: Involvement of the extracellular matrix”. Spine 29: 2691-2699.

Ruberté LM, Natarajan R, Andersson GBJ. (2009). “Influence of single-level lumbar degenerative disc disease on the behavior of the adjacent segments - A finite element study”. Journal of Biomechanics 42, pp. 341-348.

Schmidt H, Kettler A, Rohlmann A, Claes L and Wilke HJ. (2007). “The risk of disc prolapses with complex loading in different degrees of disc degeneration – A finite element analysis”. Clinical Biomechanics, 22(9) pp 988-998.

Schultz, A.B., Warwick, D.N., Berkson, M.H. and Nachemson, A.L. (1979). “Mechanical properties of the human lumbar spine motions segments. Part I: Responses in flexion, extension, lateral bending and torsion”. J. Biomech. Eng. 101, 46-52.

Shigley J. (1979). “ Design in mechanical engineering“. Mc Graw-Hill 1979.

Silva MJ, Wang C, Keaveny TM and Hayes WC (1994). “Direct and computed tomography thickness measurements of the human lumbar vertebral shell and endplate“. Bone 15. 409-414.

Smit, TH, Odgaard A and Schneider E (1997). “Structure and function of vertebral trabecular bone”. Spine 22, pp 2823-2833.

Smit TH. (1996). “The mechanical significance of the trabecular bone architecture in a human vertebra (Ingenieur) ”. Technische Universitat Hamburg-Harburg, Hamburg-Harburg, pp. 49-53.

Tanaka E and Van Eijden T. (2003). “Biomechanical Behavior of the Temperomandibular Joint Disc“. Crit Rev Oral Biology Medicine. 14(2): 138-150.

Treloar, L. (1943). “The elasticity of a network of long-chain molecules”. Transactions of the faraday society 39, 241-246.

Videman T, Gibbons LE, and Battie M (2008). “Age and pathology specific measures of disc degeneration”. Spine 33(25): 2781-2788.

Virgil WJ and Punjab IL. (1951). “Experimental investigation into the physical properties of the intervertebral disc”. The journal of bone and joint surgery 33B(4) Nov. 1951.

Wang Z and Li H. (2005). “ A novel 3D finite element modeling based on medical image for intervertebral disc biomechanical analysis“. Proceedings of the 2005 IEEE engineering in medicine and biology 27 th annual conference. Shanghai, China, Sep 1-4, 2005.

White, A.A and Panjabi, M.M. (1990). “ Clinical Biomechanics of the Spine “. J. B. Lippincott, Philadelphia.

Wilke HJ, Neef P, Caimi M, Hoogland T and Claes L. (1999). “New In vivo Measurements of Pressures in the Intervertebral Disc in Daily Life”. Spine 24(8): 755-762.

Yamamoto I, Panjabi, M.M., Crisco, T. y Oxland T. (1989). Three-dimensional movements of the whole lumbar spine and lumbosacral joint. Spine Vol.14 (11) p.1256-1260.

Chapter 3

Results:

MRI of Disc Degeneration; Biomechanical Testing and Disc modeling

Chapter 3

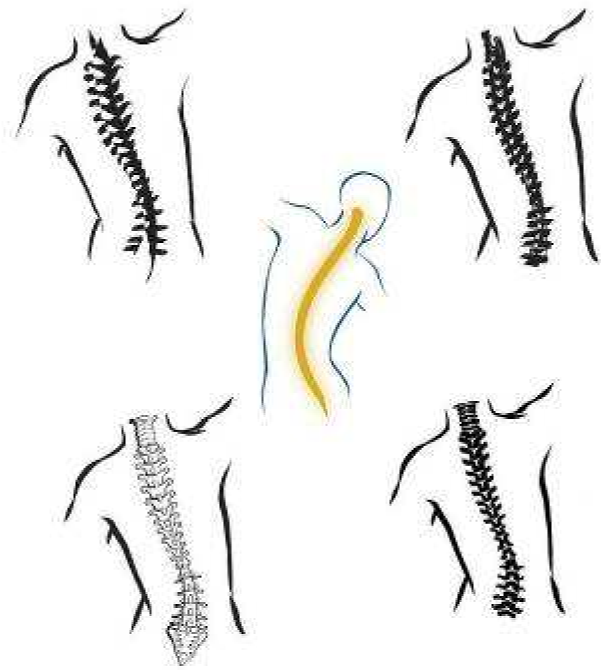

Results:

MRI of Disc Degeneration; Biomechanical Testing and Disc Modeling

This chapter presents the results of the Magnetic Resonance Imaging (MRI) of disc degeneration from a set of elderly lumbar discs, with emphasis in the medical conditions of *intervertebral osteochondrosis (IO)* and *spondylosis deformans (SD)* and their relevance for finite element modeling of disc degeneration. Then, the experimental results from the series of testing protocols which include the use of static, and dynamic loading are presented. The results include the characterization of the motion response, disc stiffness, flexibility, relaxation response and damping behavior, and are organized by lumbar level, and degeneration scoring.

Thereafter, the simulation results of the Finite Element Method (FEM) of disc degeneration model with regard to stress and strain distributions are presented. The outcome of the series of loading testing is used to input the boundary conditions for validation of the disc model. The simulation results of stress and strain distribution are presented with regard to the nucleus pulposus, annulus fibrosus and vertebrae bone. Finally a comparative between simulation and testing response of the disc mechanical behavior is given.

$1/K_M$, Disc flexibility.
3D, Three dimensional.
a, Major axis of the disc cross section.
b, Minor axis of the disc cross section.
C_1, C_2, Mooney-Rivlin deviatoric constants.
D, Dashpot element.
E, Young’s modulus.
*E**, Complex modulus.
E’, Storage modulus.
E”, Loss modulus.
E_2/η, Relaxation parameter.
$E_R(t)$, Relaxation modulus.
Ex, Extension.
F, Force.
F(t), Force over time.
FEA, Finite element analysis.
FEM, Finite element method.
Fl, Flexion.
G, Shear modulus.
H, Hysteresis.
HDa, Disc height at anterior site.
HDp, Disc height at posterior site.
K, Disc stiffness to axial load.
K_M, Disc stiffness to bending.
K_T, Disc stiffness to torsion.
L2-L3, Disc from in between lumbar level 2 and 3.
L4-L5, Disc from in between lumbar level 4 and 5.
LB, Left lateral bending.
M, Bending moment.
MRI, Magnetic resonance imaging.
Ø, Angular deflection in torsion.
PMMA, Polymethylmethacrylate.
RB, Right lateral bending.
S, Spring element.
SLS, Standard linear solid model.
STL, Stereo lithography.
t, Time.
T, Torque moment.
t(r), Relaxation time.
T1, Weighted spin echo sequence.
T2, Weighted fast spin echo sequence.
$\tan\delta$, Ratio of loss to storage moduli.
UVF, Unit vertebral function.
X, Z, Radial bulging.
Y, Vertical displacement.
β, Phase angle difference.
ε, Normal strain.
θ, Angular deflection in bending.
ν, Poisson’s ratio.
σ, Normal stress.
$\sigma(t)$, Relaxation function or stress decay.

I. Intervertebral disc imaging using MRI

a. Disc degeneration scoring and interobserver agreement

Ten lumbar discs were analyzed, five corresponding to the L2-L3 level and the other five to the L4-L5 level. The scoring of disc degeneration by a pathologist and a radiologist were based on the degenerational scales of Pfirmann et al. (2001) and Thompson et al. (1990) and are summarized in Table 3.1. The consensus reading of the degenerated disc resulted in a 35% with grade III, 40% with grade IV, and 25% with grade V scorings. There wasn’t any healthy discs related to grade I or II scorings.

Table 3.1. Assigned and consensus grades scorings done by two observers.

	Degenerational Grade						Total
	III		IV		V		
Observer	Disc Sample	Number	Disc Sample	Number	Disc Sample	Number	
Pathologist	A, G, H	3	B, C, D, F, L	5	I, J	2	10
Radiologist	A, G, H, L	4	B, C, F	3	D, I, J	3	10
Average	3.5 (35%)		4 (40%)		2.5 (25%)		10 (100%)

To assess the accuracy of the observations in the scoring of degeneration a Kappa coefficient calculation was done in accordance with Viera et al. (2005). The observation agreement range from moderate (0.41-0.60) to substantial (0.61-0.80), see Table 3.2.

Since there were no healthy discs in the population and all the specimens came from elderly people, no inquiry was necessary to survey lower degeneration I (normal) and II scorings. Also, because the grading was done only one time no intraobserver analysis was needed.

On average, in nine out of ten discs there was interobserver agreement, being higher for degeneration scorings III and V and lower for grade scoring IV. Upper lumbar discs L2-L3 are subject to lesser body weigh and deflection than lower lumber discs, therefore, the probability of assigning a moderate degeneration scoring (Grade III) was good, K=0.78. Similarly, lower lumbar discs, such as L4-L5, are subject to more weight and motion response that upper lumbar levels, thus, this may explain why this set of discs had also a good probability of assigning the highest degeneration scoring (Grade V), K=0.74. The lower kappa for grade IV can be explained by the fact that two L2-L3 discs, and two L4-L5 discs had the same scoring, anatomically they show significant differences in disc space loss and osteophytes quantity, than the rest of their respective groups.

Table 3.2. Interobserver reliability.

Pathologist- Radiologist interobservation	Agreement					
	Grade III		Grade IV		Grade V	
	n	%	N	%	n	%
Observed agreement	9	80	8	80	9	90
Chance agreement	0.55 (55%)		0.5 (50%)		0.62 (62%)	
Kappa coefficient, K	0.78		0.6		0.74	

b. Anatomical evaluation of the L2-L3 and L4-L5 disc groups

To show the MRI anatomy results of the 10 intervertebral discs, it was decided to separate them by spine level since the clinical experience shows that elderly discs from the lower spine exhibit severe tissue damage and drastic distortions than upper spine discs (Resnick, 1994). Also, the use of axial, coronal and saggital planes is introduced for a complete viewing of the degenerated anatomy. Identification of collapse of disc height, vacuum phenomena, osteophytes formation, cartilaginous protrusions into the vertebra and reactive bone sclerosis for the L2-L3 and L4-L5 discs are summarized in Figures 3.1 and 3.2, respectively.
The MRI procedure was done with a localizer sequence followed by the final scan sequence. The latter sequence was done in the coronal and saggital T1-weighted spin-echo (repetition time [TR] 24.6 msec/echo time [TE] 7.2 msec) followed by a T2-weighted FSE (TR 3400 msec/TE 94 msec) images with the following parameters for the T1 sequence: matrix 256 x 256; field of view 10.4 x 10.4 mm; slice thickness, 0.4 mm; interslice gap, 0.4 mm; echo train length (ETL), 3 and for the T2 sequence: matrix 128 x 128; field of view 22.8 x 22.8 mm; slice thickness, 3 mm; interslice gap, 0.3 mm; echo train length, 5.

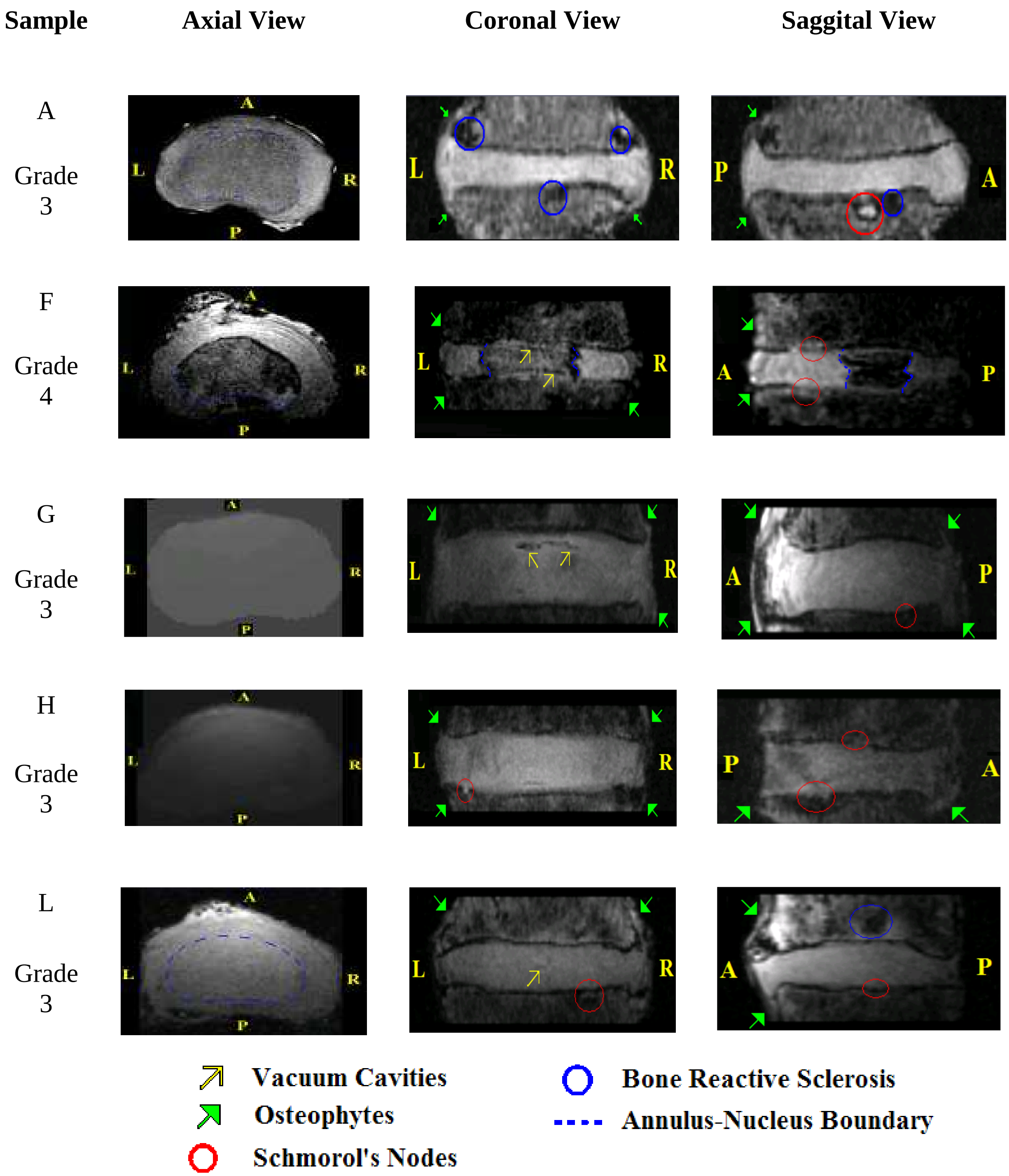

Figure 3.1. Magnetic resonance imaging for the set of L2-L3 discs and their scoring of degeneration.

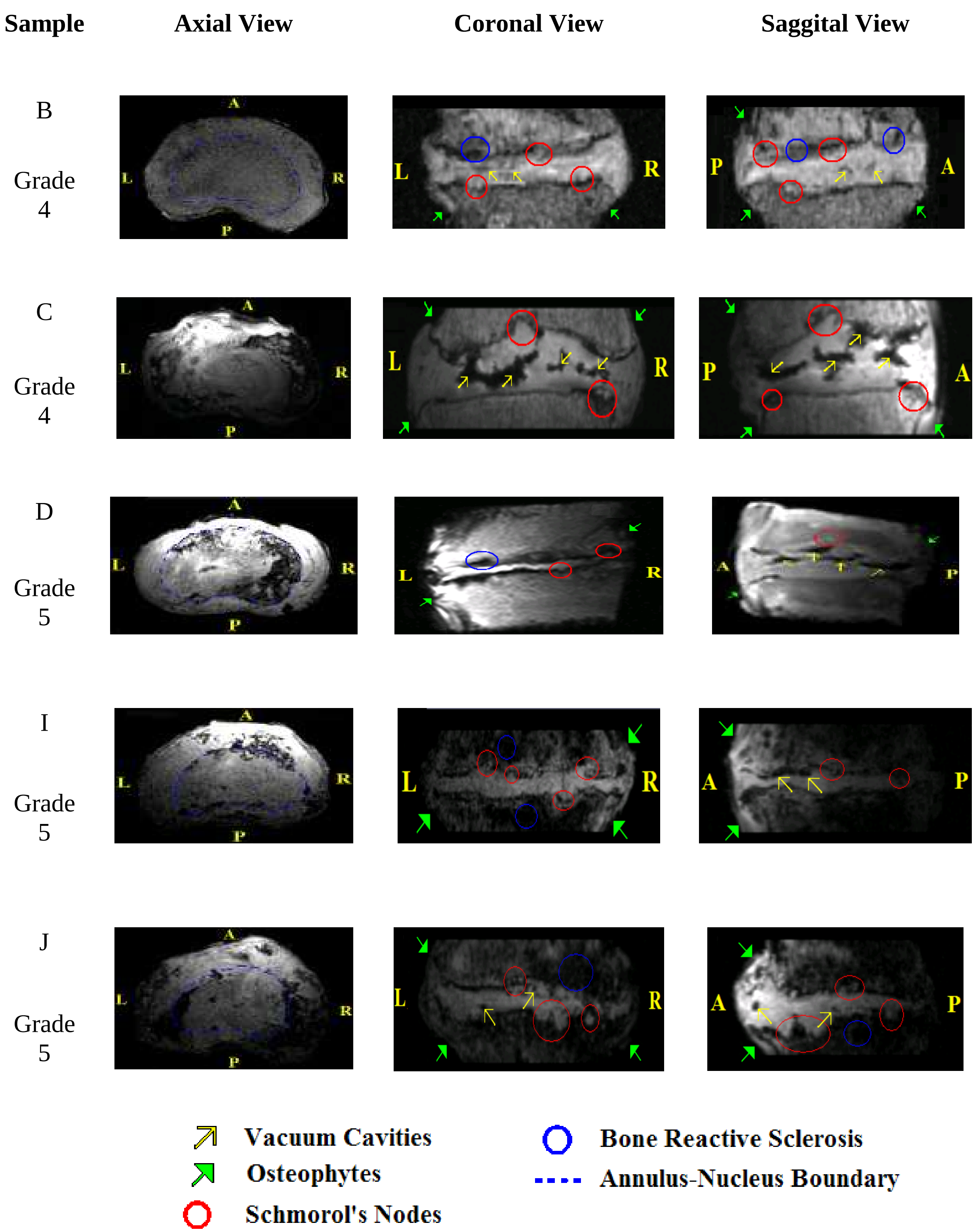

Figure 3.2. Magnetic resonance imaging for the set of L4-L5 discs and their scoring of degeneration.

c. Analysis of the disc composition

The purpose of conducting MRI to all intervertebral discs used in this study was to obtain geometrical data and internal anatomy of elderly discs and use these results to develop a finite element model of disc degeneration based on the severity of damage. Overall this objective was fulfilled using the T1 and T2 weighted spin echo sequences, which allowed to distinguish differences between the anatomy of the intervertebral disc and that of the vertebra bone.
In MRI the signal intensity of the anatomical T1-weighted spin echo for a normal disc is lower than that of the vertebral body, and also the signal intensity of a T2-weighted spin echo and gradient echo images is higher than that of the vertebral body (Resnick et al. 1994). The signal intensity of the intervertebral discs was higher than that of the adjacent vertebra body in the T2-weighted spin echo images suggesting a less water content, which is typical of an aging disc, and as expected, the MRI from the L2-L3 disc set reveals less degeneration than that of the L4-L5 disc set, see Figures 3.1 and 3.2.
A main anatomical feature of the L2-L3 disc set was the maintenance of a disc space, or height of the disc, which was uniform from the anterior to the posterior sides, as shown by the coronal and saggital views of disc samples A, F, G, H, and L of Figure 3.1. The scoring of degeneration for these intervertebral discs was mainly grade scoring 3, and only sample F showed a considerable lost of height mainly seen in the coronal view. This may explain why this sample had a degeneration scoring grade 4. The maintenance of disc height is the most important external sign that is taken into account when scoring disc degeneration (Minna et al. 1991). Such anatomical appearances in post mortem favors the presence of a hydrated nucleus and annulus, which has been reported by Videman et al. (2008). However, in cross examination of the inner nucleus pulposus, in all the discs the MRI revealed to some extent the presence of cavities, showed in the radiographs, as a collection of elongated black shadows. These dull collections correspond to vacuum phenomena, which results from nucleus dehydration throughout age (Boos et al. 1995). A detailed description of the vacuum phenomena and disc space loss is given in section 1.IV.a. Nonetheless, this set of discs are a good representation of a moderate degeneration and were used as guidelines during the segmentation procedure of the finite element model.

Except for disc F, in the rest of the discs the MRI resolution could not clearly distinguish the boundary between annulus and nucleus. During the T1 weighted spin-scho sequence, we maintained constant the relaxation and echo time for all disc samples. Thus, any small differences in nucleus hydration between samples influence the resolution, as this may explain the poor contrast gain between soft tissues in the rest of the discs.

Spinal osteophytosis or *spondylosis deformans* which forms with age were found on all discs and the MRI confirmed as elongated prolongations of the annulus-vertebra junction. The most frequent place where these bony outgrowths or *osteophytes* formed was in the anterior side, although some showed up in the lateral and posterior disc margins, see Figures 3.1 and 3.2. In the anterior side, these bony linkages connected the upper vertebra with the lower one. The length of these "bridges" was in general greater in L4-L5 discs than in L2-L3 discs. However, disc F showed large osteophyte formation, being in the anterior side where the outgrowths reach up to 15 mm in length. For more detail of the description of the mechanism of osteophyte formation see section 1.IV.c.

Cartilaginous or Schmorl's nodes were found in discs A and F but only in small quantities, in contrast with the L4-L5 discs where they appear as multiple collections of protrusions, with different sizes and scatter all across the bone-disc boundary. These protrusions are of calcified origin from the endplate, and can promote a reactive bone sclerosis if in contact with the neighboring sponge's bone of the vertebral bodies (Resnick, 2002). Often in elderly discs, bone sclerosis appears in MRI as an opaque area which indicates a high density zone, see Figure 3.2. Thus, in these areas it is suggested that the trabecular bone stiffens (Wehrli et al. 2004). However, a different meaning can result when these darker signs appear in young adult samples without Schmorl's nodes, which may simply indicate the presence of body fat. Nonetheless, the MRI from all five L4-L5 discs were clear in pointing out that the vertebral bodies were damaged by protrusions.

The evaluation of the MRI from the L4-L5 discs reveals a clear evidence of *intervertebral osteochondrosis*. The decrease in height varies from a partial to a total collapse. While discs B and C show well developed vacuum phenomena in the nucleus and schmorl's nodes formation, they still exhibit a define height, whereas in discs D, I and J they do not, see Figure 3.2. For these reasons, the scoring of degeneration for the former discs were grade scoring 4, while for the latter discs corresponded to the highest, grade scoring 5. Thus, the corresponding anatomical geometry of discs D, I and J were representative of severe degeneration and they were used as a guidelines during the segmentation procedure.

Because the MRI sequence was carried out only to the intervertebral disc and not the entire vertebrae bone, only a small section of the internal anatomical structure of the lumbar bone was considered in the finite element model. Also, due to the resolution obtained, the inspection was limited to collecting and characterizing major anatomical changes, such as disc collapse, osteophytosis, schmorl's nodes and vacuum formation. But, for morphological changes within the annulus in the form of clear delaminations or presence of small tears, or biochemical analysis of the nucleus or annulus, or water content in the disc, there was little information gain.

Finally, of the ten MRI volume inspections previously presented it was decided that two of them should represent the guidelines of the anatomy of disc degeneration for the development of the finite elemet model of disc degeneration. A moderated degeneration stage based on the appearance of a disc with a preserve height, corresponding to a grade scoring 3; and a severe degeneration stage based on the appearance of a disc with a collapse height, corresponding to a grade scoring 5.

II. Experimental results

a. Compression loading

Results presented from the testing protocol correspond to the intervertebral disc as one structure, which is composed mainly of the annulus fibrosus and nucleus pulposus. The annulus being more rigid is considered elastic, and the nucleus being more gelous is considered viscoelastic. Also, the bone is much harder than soft collagenous tissues, then the corresponding bone strain should be much lower than that of the intervertebral disc. Therefore, the results presented in this section should represent the strains within the disc tissues.

Testing of the intervertebral discs in the compression protocol gave results with similarities between samples. The mean motions to 1000 N load were recorded for all discs and the peak value of these responses are shown in Table 3.3. The first aspect to account for mechanical evaluation of the discs was the calculation of the strain ε, and the stiffness K in the vertical direction, in accordance with section 2.II.a. The results show that the strain gave a value ranging from 5.2% in disc A to a maximum of 13.4% in disc B, and a stiffness value ranging from 697 N/mm in disc G to 1923 N/mm in disc A.

The stress-strain (σ-ε) relationship in response to the compression load for the L2-L3 and L4-L5 disc sets are summarized in Figures 3.3 and 3.4 respectively. The nonlinearity of the stress-strain curve was evident with an initial "toe" corresponding to the deformation of the softer nucleus pulposus. The fitting of the σ-ε curve was done with a polynomial function: $\sigma = A\varepsilon^n + B\varepsilon^{n-1} + C\varepsilon^{n-2} + ... + m\varepsilon$ using the program DataFit V.9.0.59 (Oakdale Engineering™) which gave an excellent adjustment (R^2>0.98).

The first derivation of σ with respect to ε gave the instantaneous *Young's modulus E* which was calculated at peak load to ensure a stretching of the annulus fibers. Results shows that the *E modulus* range from 7 MPa in the L4-L5 discs B, C and D to over 20 MPa in discs A and F from the L2-L3 set, see the loading graphs in Figures 3.3 and 3.4. As shown, at low deformations the *E modulus* shows small variations, whereas at large deformations *E* increases in value and in variation. Overall, the fitting showed no significant differences between lumber level nor degeneration scorings.

With the peak load of 1000 N applied, a compression at the nucleus and inner annulus occurred and caused an expansion of the annulus outer walls were bulging was measured. Overall, the cross section area of the disc was subjected to a normal stress which affects both the nucleus and annulus tissues. The corresponding value of the peak normal stress was very similar among discs ranging between 0.43 MPa in disc D, which had the larger cross section, to 0.69 MPa in disc L which had the smallest size. The normal stress mean value for the entire population was 0.55 MPa with a low deviation of 0.067, this mainly due to small differences in the cross section area between discs. The strain had a larger variation than that of the stress due to the large variation in the disc height, which ranges from 7 to 12 mm.

Table 3.3. Single and mean motion response with standard deviation of 10 intervertebral discs tested. All measurements were made while applying 1000 N compression load.

Sample Disc and Level	Motion response to 1000 N compression.					
	Vertical deflection Y (mm)	Radial Bulging		Stiffness, K (N/mm)	Vertical Strain, e* (%)	**Young`s Modulus, E** (MPa)**
		Anterior, X (mm)	Posterior, Z (mm)			
A-L_{23}	0.520	0.675	0.360	1923	5.2	21.52
B-L_{45}	1.072	1.748	0.061	933	13.4	7.54
C-L_{45}	1.200	1.073	0.941	833	12.0	7.83
D-L_{45}	0.918	1.000	0.191	1089	10.2	7.40
F-L_{23}	0.540	0.010	0.020	1852	5.4	29.00
G-L_{23}	1.434	0.855	0.773	697	12.0	11.38
H-L_{23}	1.260	0.898	0.518	794	12.6	8.75
I-L_{45}	1.021	0.293	0.203	980	8.5	12.37
J-L_{45}	1.177	0.243	0.273	850	10.7	12.12
L-L_{23}	0.590	0.341	0.273	1695	8.4	14.65
Complete Set mean values and standard deviation (STD)	**0.971 (0.324)**	**0.714 (0.513)**	**0.361 (0.299)**	**1165 (470)**	**9.84 (2.81)**	**13.26 (7.00)**
Level group L_{23} Values	**0.869 (0.442)**	**0.556 (0.376)**	**0.389 (0.280)**	**1392 (597)**	**8.72 (3.51)**	**17.06 (8.21)**
Level group L_{45} Values	**1.078 (0.116)**	**0.871 (0.624)**	**0.334 (0.348)**	**937 (104)**	**10.96 (1.85)**	**9.45 (2.56)**
Degeneration Grade 3 values	**0.951 (0.464)**	**0.692 (0.253)**	**0.481 (0.219)**	**1277 (622)**	**9.55 (3.44)**	**14.08 (5.52)**
Degeneration Grade 4 values	**0.937 (0.350)**	**0.944 (0.876)**	**0.341 (0.520)**	**1206 (562)**	**10.27 (4.27)**	**14.79 (12.31)**
Degeneration Grade 5 values	**1.039 (0.130)**	**0.512 (0.423)**	**0.222 (0.044)**	**973 (120)**	**9.80 (1.15)**	**10.63 (2.80)**

* approximated values based on dividing the vertical deflection Y with the constant disc height H.

** values were obtained by derivation of σ with respect to the deformation ε at peak load.

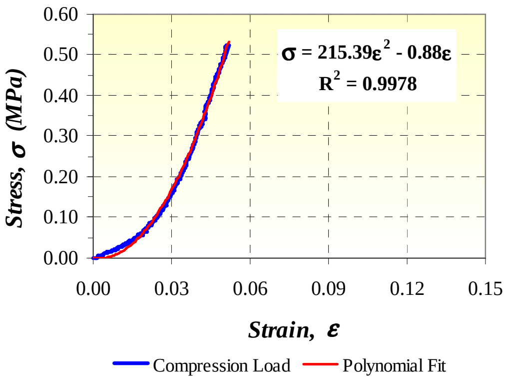

Disc A

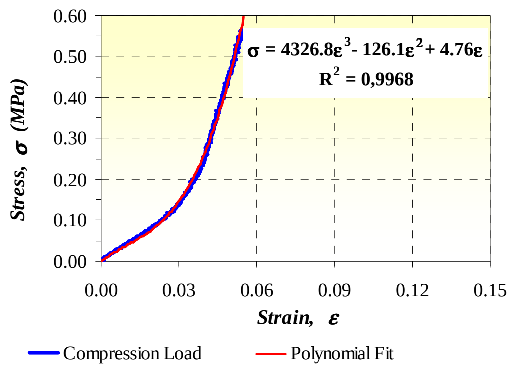

Disc F

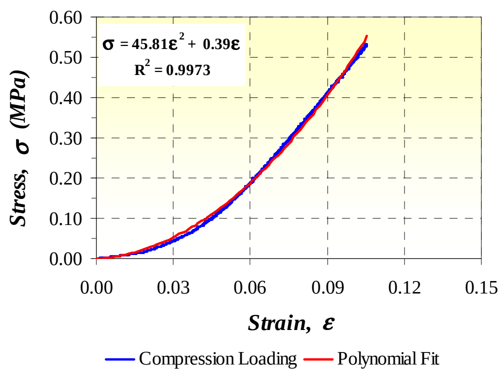

Disc G

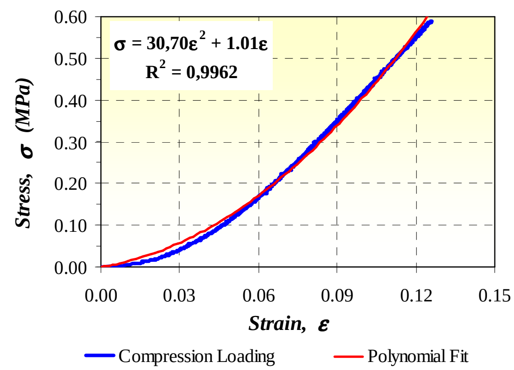

Disc H

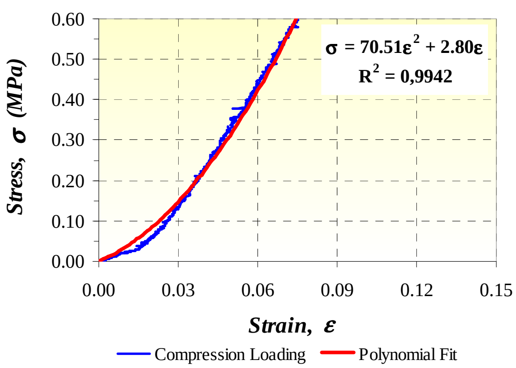

Disc L

Figure 3.3. Stress-strain relationship with polynomial fitting for each of the L2-L3 intervertebral discs tested in this study. All discs were subject to 1000 N of compression load, after which a one hour relaxation period (not shown) was applied.

For disc bulging, in general it was greater in the anterior than in the posterior side. The mean bulge values for the entire population were 0.714 mm in the former position, and 0.361 mm in the latter position. There was a clear distinction in the mean values between the anterior and posterior bulge for the two disc levels, having a larger difference in the lower L4-L5 disc set.

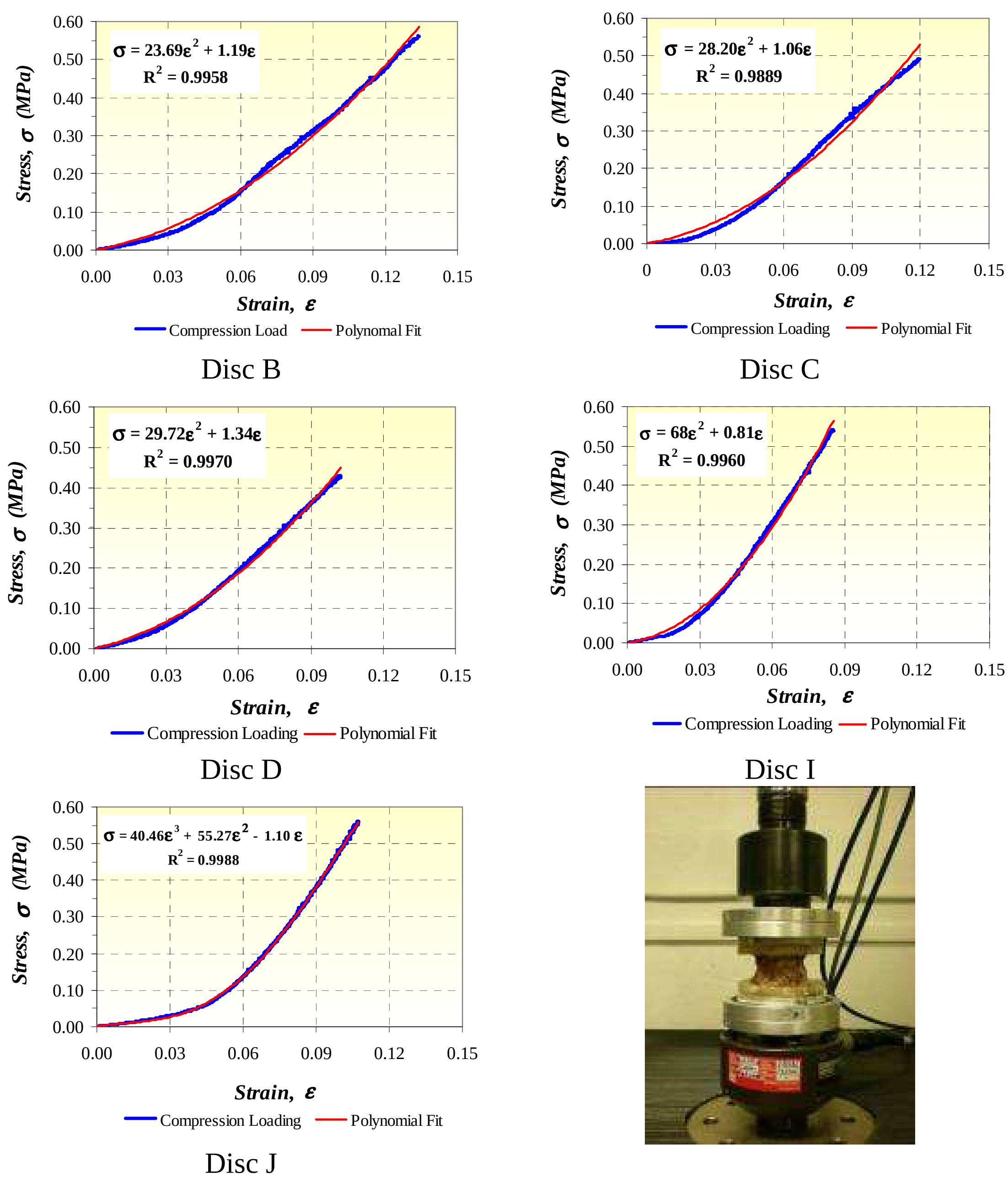

Figure 3.4. Stress-strain relationship with polynomial fitting for each of the L4-L5 intervertebral discs tested in this study. All discs were subject to 1000 N of compression load, after which a one hour relaxation period (not shown) was applied.

However, a student t-test reveals no statistical significance ($P > 0.05$). Nonetheless, the mean bulges between the anterior and posterior sides for both lumbar levels were different, being almost symmetrical in the L2-L3 disc set and asymmetrical in the L4-L5 disc set, see Figure 3.5.

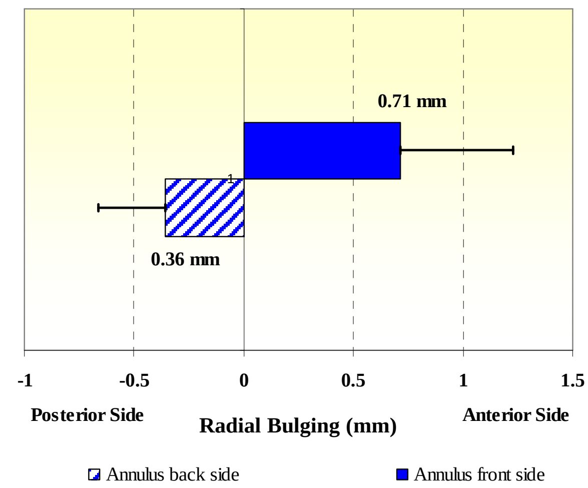

(A)

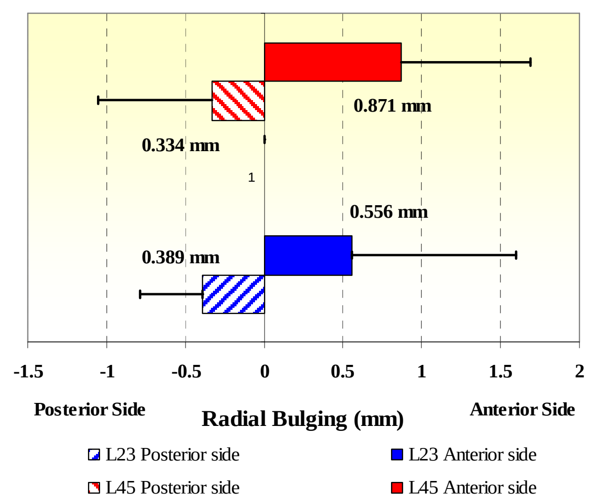

(B)

Figure 3.5. Mean disc bulge and standard deviation for (A) the complete set of discs and (B) among disc levels.

When the discs were classified for disc lumbar level, or degeneration scoring, few marked differences were noticed in their mean mechanical behavior response, due to the large scatter data. The stress-strain relationship was similar between the entire group and the two classifications, see Figure 3.6. Although the L2-L3 disc set had a higher *stiffness K* over that of the L4-L5 disc set, but only after reaching a 50% of the peak load. Thus, the mean values for the *stiffness*, *K* and the *Young's modulus*, *E* for the L2-L3 disc set were equal to 1392 ± 597 N/mm, and 15.36 ± 7 MPa respectively, which were 50% and 70% respectively higher than the corresponding values of the L4-L5 disc set, see Figure 3.6B. These differences were in part because of the high stiffness exhibited by discs A and F over the rest of their group. However, a student t-test revealed no statistical differences between both groups (P>0.05) and much less for any difference between degeneration scoring, see Figure 3.6C.

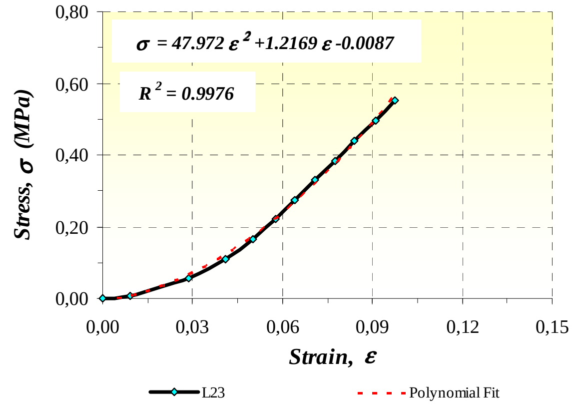

(A)

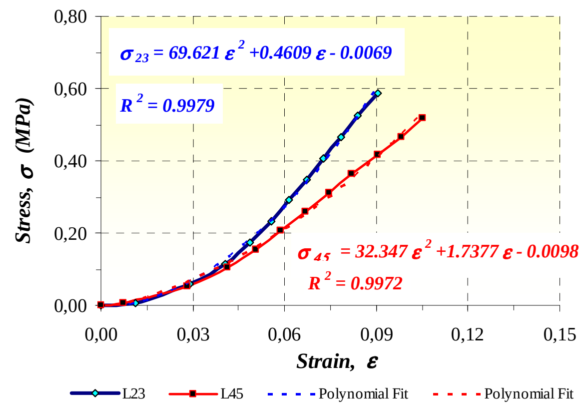

(B)

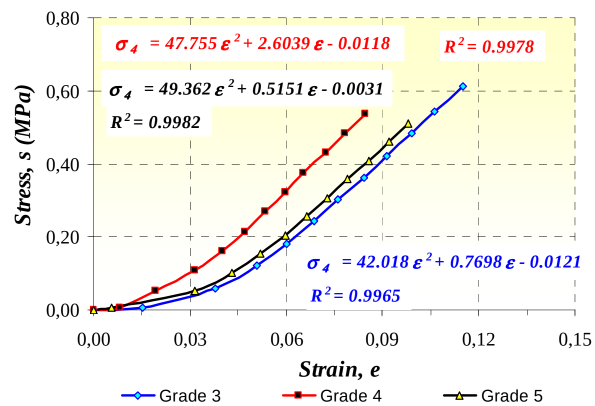

(C)

Figure 3.6. Intervertebral disc stress-strain relationship obtained from the testing and polynomial fitting for (A) the complete set of discs, (B) among disc lumbar levels L2-L3 and L4-L5, and (C) among degeneration scoring 3, 4 and 5.

b. Stress relaxation

Every intervertebral disc showed *stress relaxation* for the entire test, which also decrease with time. At the start of the relaxation test, the peak load of 1000 N underwent a rapid decrease with a variable duration depending on each disc, which ranged from 428 to 615 seconds with an average of 507 s. During this time the *stress* σ also decreases rapidly, and then move on to a slow decline for the rest of the test.

A summary of the values for the *relaxation parameters* for each disc, and those for the classifications by lumbar level and by scoring of degeneration are given in Table 3.4 and includes *the relaxation time t(r)*, the *relaxation stress*, the *relaxation modulus E(t)*, the *relaxation parameter* α, *and the ratio of viscous modulus to viscosity (* η/E_2) of the dashpot-spring assembly of the *Maxwell* arm model, containing the spring-dashpot assembly, see section 2.II.b for the description of the relaxation procedure and the viscoelastic models.

The duration needed for the stress to fall to ***1/e*** of its initial value σ_0 and achieved stability is called the *relaxation time t(r)* and was calculated from the test data. The results showed that the *relaxation time* varied depending on the disc in a range from 272 s in disc A to 1500 s in disc F, with a mean value of 944 s for the entire population. The fastest stress decline occurred in the disc A, where, the initial stress underwent a quick relaxation and decline a 75% value within 10 minutes. In contrast, the smoothest relaxation occurred in disc F, as this sample showed large amounts of osteophytes in the MRI.

After the relaxation time *t(r)*, the stress is called the *relaxation stress* and it's not time dependant. Thus, after *t(r)* the stress was consider constant and represented the stable state of the stress in the disc. Then, for the remaining time of the test, any further decrease of the stress was not accountable for stress relaxation. The results shows that after reaching the time *t(r)* the *relaxation stress* had a narrow range of values from 0.159 MPa in disc D to 0.255 MPa in disc L, with a mean value of 0.200 MPa (200 KPa) for the disc population.

The *relaxation function* $\sigma(t)$ obtained from the exponential fit contained the initial stress σ_0 and the *relaxation parameter* α which is equal to the inverse of the relaxation time *t(r)* and represents the relaxation response of the *Maxwell* arm model. The results show that the values of the parameter α range from $67\text{x}10^{-5}$ (s^{-1}) in disc F to $368\text{x}10^{-5}$ (s^{-1}) in disc A. Again, the disc F gave the smallest value due to its longer relaxation response.

Table 3.4. Stress relaxation parameters for the set of intervertebral discs used in this study. Deviation is shown in parenthesis.

Disc and spine level	*Relaxation Time, t(r) (sec)*	*Relaxation Stress (MPa)*	*Relaxation Modulus, E(t)* (MPa)*	*Relaxation parameter $\alpha = t(r)^{-1}$ (sec^{-1})*	*Ratio E_2/η at time t(r) ($x10^{-4}$ sec)**
$A\text{-}L_{23}$	272	0.193	5.05	0.00368	31
$B\text{-}L_{45}$	887	0.190	1.62	0.00113	10
$C\text{-}L_{45}$	1191	0.181	1.90	0.00084	6
$D\text{-}L_{45}$	443	0.159	1.81	0.00226	19
$F\text{-}L_{23}$	1500	0.208	7.85	0.00067	2
$G\text{-}L_{23}$	862	0.196	1.92	0.00116	10
$H\text{-}L_{23}$	1421	0.217	2.16	0.00070	5
$I\text{-}L_{45}$	826	0.199	3.02	0.00121	10
$J\text{-}L_{45}$	1018	0.200	2.26	0.00098	8
$L\text{-}L_{23}$	1024	0.255	4.03	0.00098	7
Complete Set mean values and standard deviation (STD)	944 (385)	0.200 (0.025)	3.16 (1.99)	0.001361 (0.00093)	11
Lumbar Level L2-L3 set	1016 (494)	0.214 (0.025)	4.20 (2.42)	0.00144 (0.00127)	9
Lumbar Level L4-L5 set	873 (278)	0.186 (0.017)	2.12 (0.55)	0.00128 (0.00056)	12
Degeneration Scoring Grade 3	895 (477)	0.215 (0.029)	3.29 (1.15)	0.00163 (0.00138)	10
Degeneration Scoring Grade 4	1193 (307)	0.193 (0.014)	3.79 (3.52)	0.00088 (0.00023)	8
Degeneration Scoring Grade 5	762 (293)	0.186 (0.023)	2.36 (0.61)	0.00148 (0.00068)	13

*. Values based on fitting the test data with the exponential function: $\sigma = e^{a+bt+ct^2}$

The decrease of stress versus time, or *relaxation function σ(t)*, gave a non linear relationship which was adjust with a second order exponential function: $\sigma = e^{a+bt+ct^2}$ using the program DataFit V.9.0.59 (Oakdale Engineering TM), which gave a good fit (R^2>0.97). However, the initial fit of *σ(t)* differs with respect to the experimental value by as much as 15%. Nonetheless, these differences were limited to the first three minutes where the disc was put to a sudden release of stress. A summary of the *relaxation of stress* curves, indicating the *relaxation of time t(r)*, and the corresponding *relaxation function σ(t)* as an exponential decrease are given for each intervertebral disc for lumbar levels sets L2-L3 and L4-L5 in Figure 3.7 and Figure 3.8, respectively.

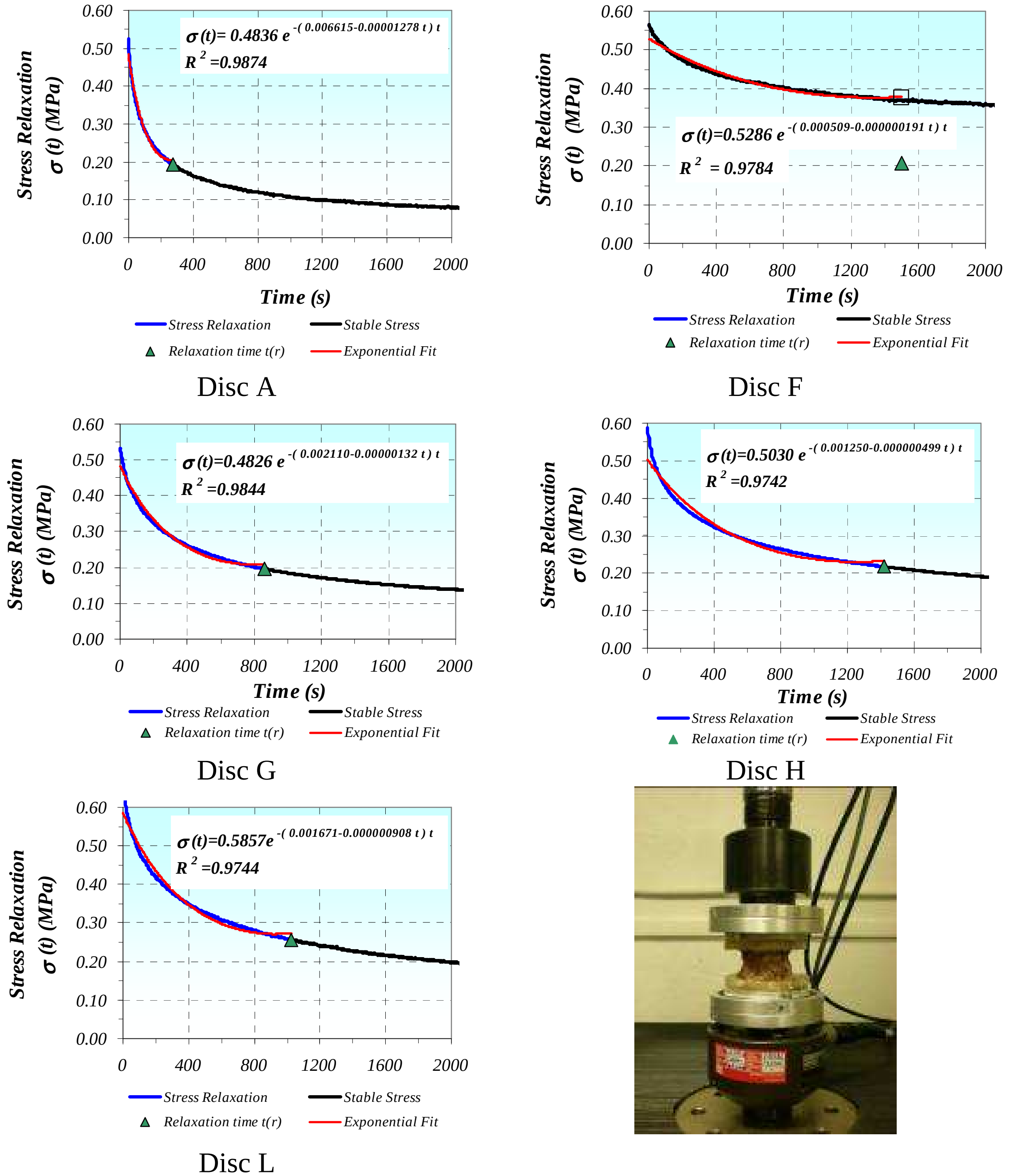

Figure 3.7. Stress relaxation response and exponential fitting for each of the L2-L3 intervertebral discs tested in this study. All discs were submitted to a one hour relaxation after applying a 1000 N compression load.

As shown, the exponential fit of the data curve gave an initial stress σ_0 value which ranged from 0.3931 MPa in disc D to 0.5857 MPa in disc L, in accordance with the peak stress reach in the compression loading. The *relaxation parameter α* localized in the exponential expression showed a linear relation with the time *t* for all the discs.

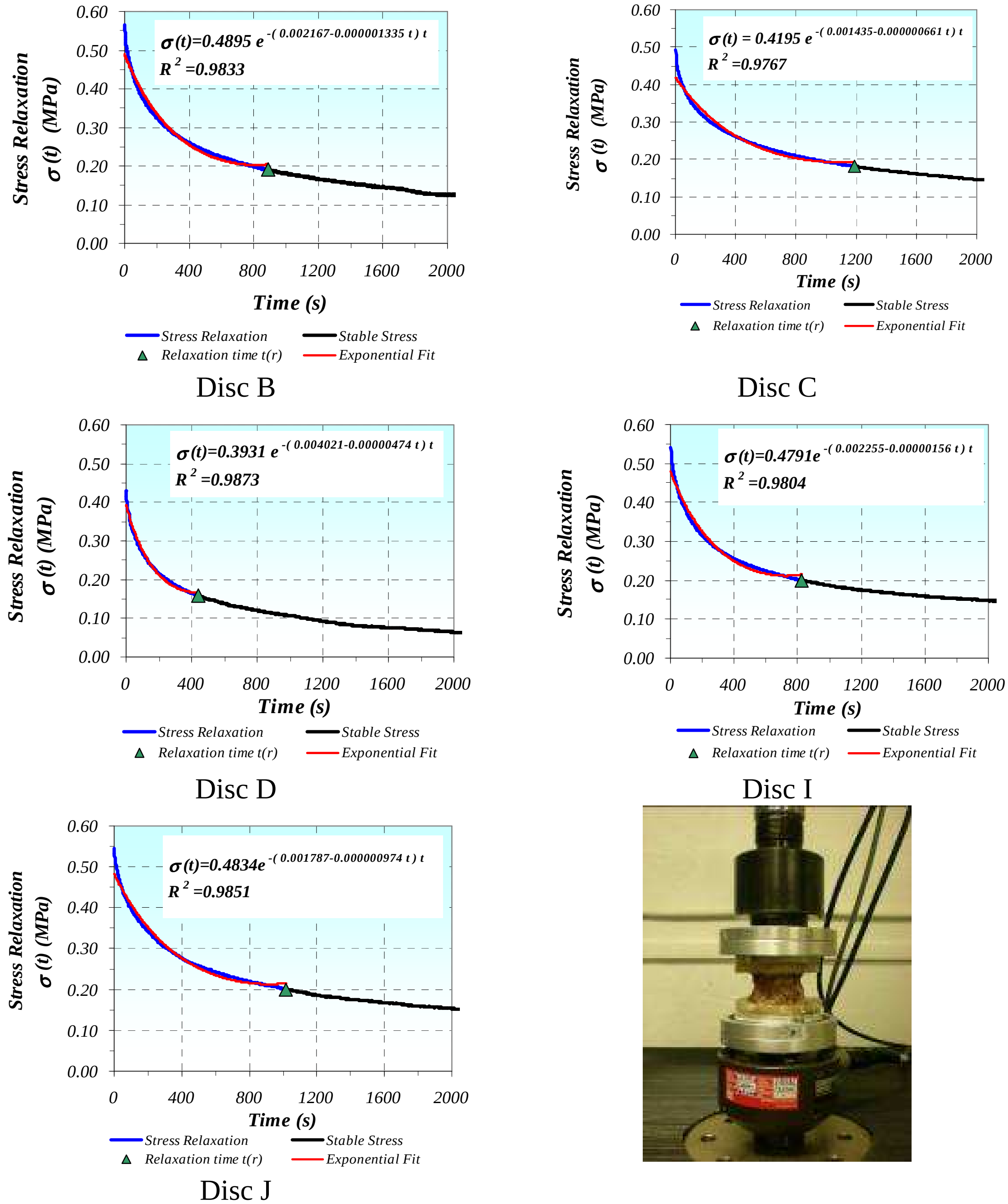

Figure 3.8. Stress relaxation response with exponential fitting for each of the L4-L5 intervertebral discs tested in this study.

In general, the relaxation response *σ(t)* was similar between the entire group and the classifications, and only small differences which were not significant were noticed. Thus, the relaxation stress was 15% higher (0.214 MPa) for the L2-L3 disc set than that for the L4-L5 disc set. This difference grew up to a 60% value in one hour of relaxation, but they were not statistically significant (P>0.05), see Figure 3.9. The relaxation stress response between degeneration scorings showed even closer similarities, being a 16% the maximum difference among the three scoring sets.

The relaxation time *t(r)* varied among lumbar level sets, being longer for the L2-L3 disc set with 1016 s which was 16% higher than that for the L4-L5 disc set. The *t(r)* among degeneration scoring shows that the scoring grade 4 disc set had the longest relaxation time of 1193 s, which was 35% and 60% higher than the other two sets, see Figure 3.9. However, due to the large scatter data they were not statistically different (P>0.05).

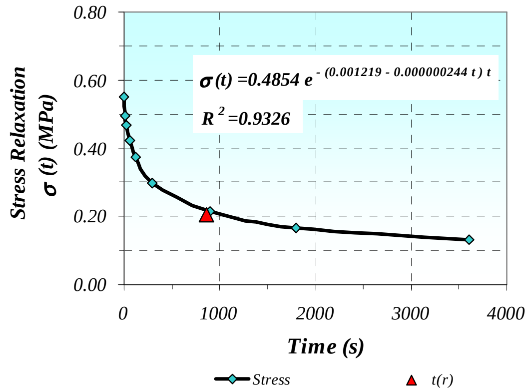

(A)

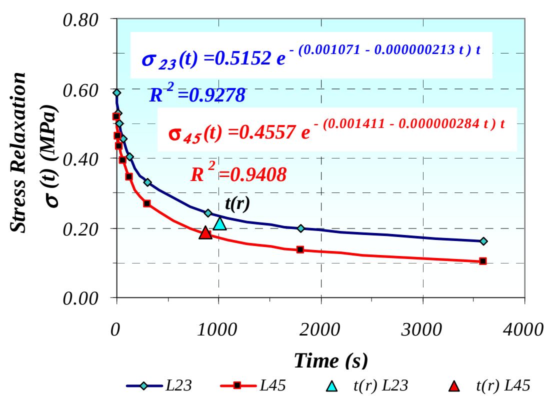

(B)

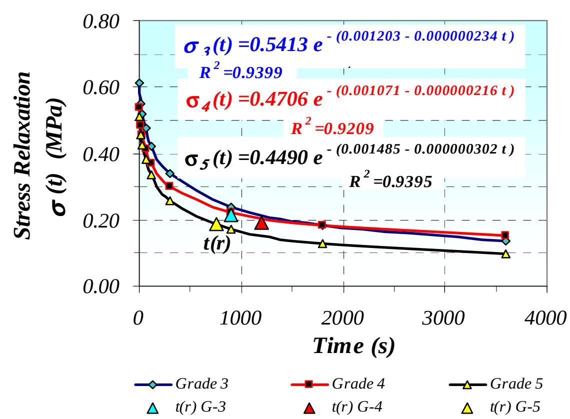

(C)

Figure 3.9. Stress relaxation response and general curve fitting for (A) the complete set of discs, (B) among lumbar levels L2-L3 and L4-L5 and (C) among degeneration scoring grades 3, 4 and 5.

Once the *stress relaxation function* $\sigma(t)$ and the *relaxation parameter* α were obtained from the fit, then they were used to calculate the *relaxation modulus E(t)*, and the *ratio of viscous modulus to viscosity* (E_2/η), corresponding to the dashpot-spring assembly for the *Maxwell arm* of the standard solid model *SLS* in accordance with section 2.II.b. The *relaxation modulus E(t)* represents the relative *stiffness* of the disc when the stress relaxation ceases, which occurs at the *relaxation time t(r)*. The *E(t)* modulus for the entire set of discs was 3.16 ± 2.99 MPa and for the L2-L3 and L4-L5 disc sets were 4.20 ± 2.42 MPa, and 2.12 ± 2.42 MPa, respectively. The degeneration scoring grades 3, 4 and 5 sets had *E(t)* values of 3.29 ± 1.15 MPa, 3.79 ± 3.52 MPa and 2.36 ± 0.61 respectively, see Table 3.4. Again, due to the larger scatter data these differences were not statistically significant (P>0.05).

The ratio E_2/η decrease with time in a linear fashion for all the discs. The values of E_2/η for the entire set of discs range from *0.00002 s* to *0.00031 s* with a mean value of *0.00011 s* at the relaxation time *t(r)*, see Figures 3.10, 3.11 and 3.12. Disc F showed the lowest value for E_2/η in accordance with its longer relaxation response, and disc A showed the highest value due to its faster relaxation response.

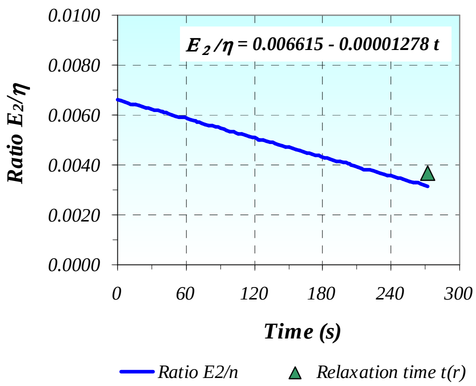

Disc A

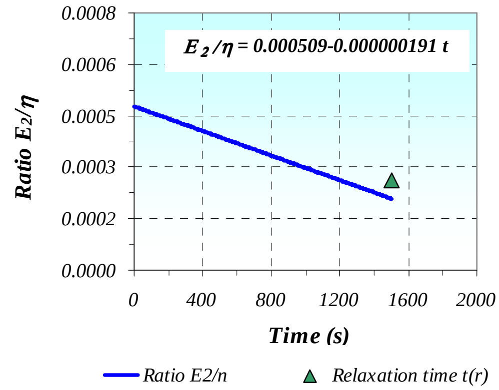

Disc F

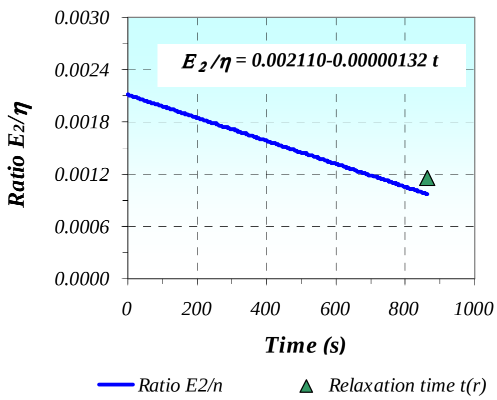

Disc G

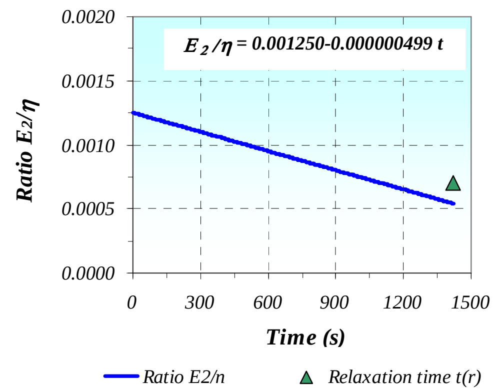

Disc H

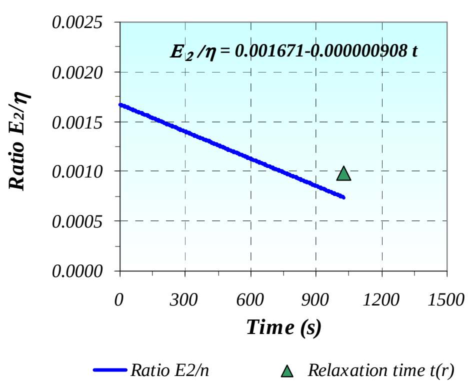

Disc L

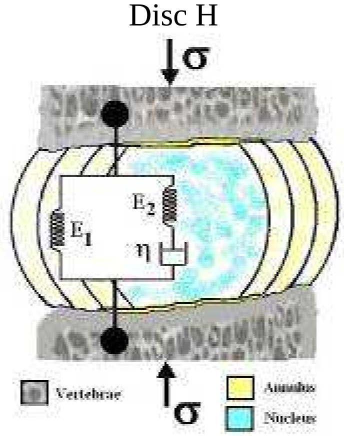

Figure 3.10. Adjusted ratio of viscous modulus to viscosity (E_2/η) for the set of L2-L3 intervertebral discs.

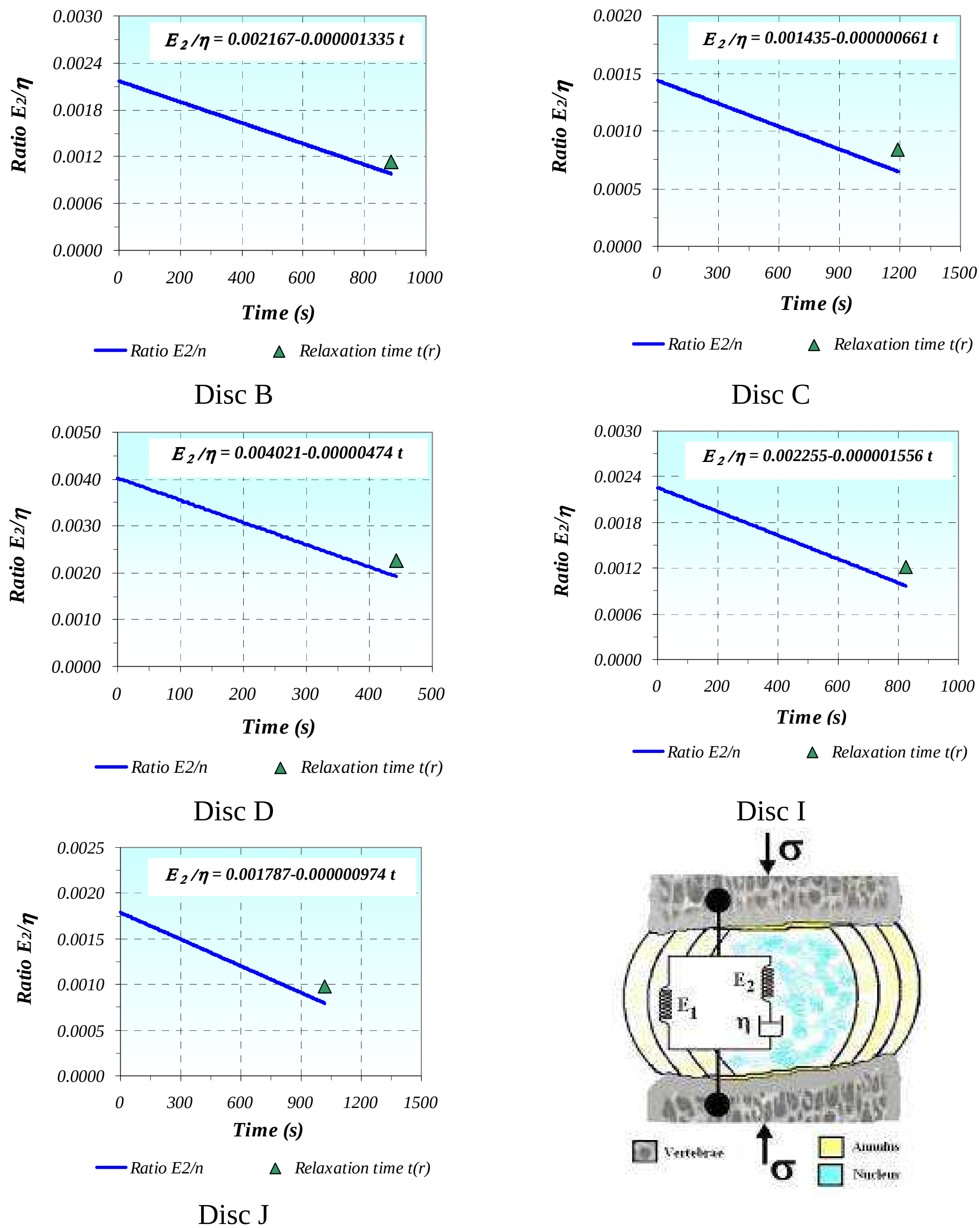

Figure 3.11. Adjusted ratio of viscous modulus to viscosity (E_2/η) for the set of L4-L5 intervertebral discs.

The similarities in the ratio E_2/η among the entire set of discs, lumbar level sets, and degeneration scoring grades are shown in Figure 3.12. Thus, due to the large scatter data any difference that appear was not statistically significant (P>0.05).

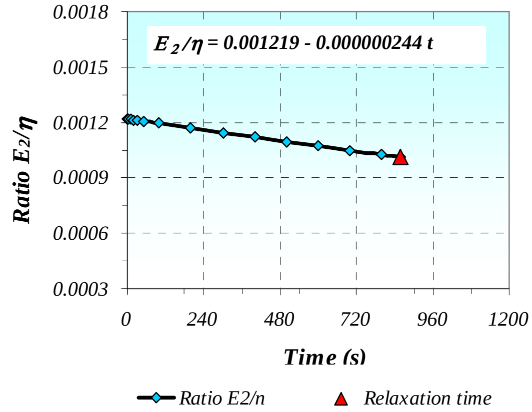

(A)

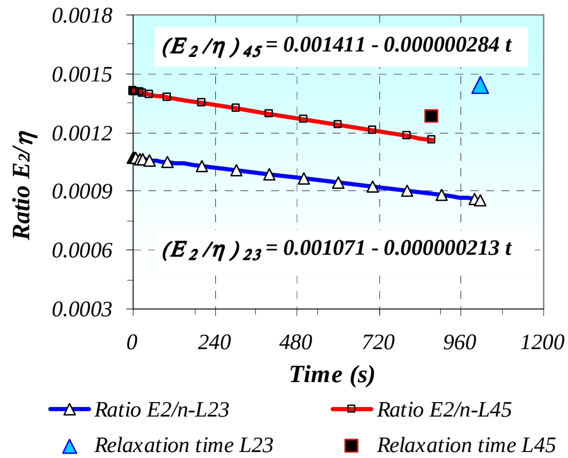

(B)

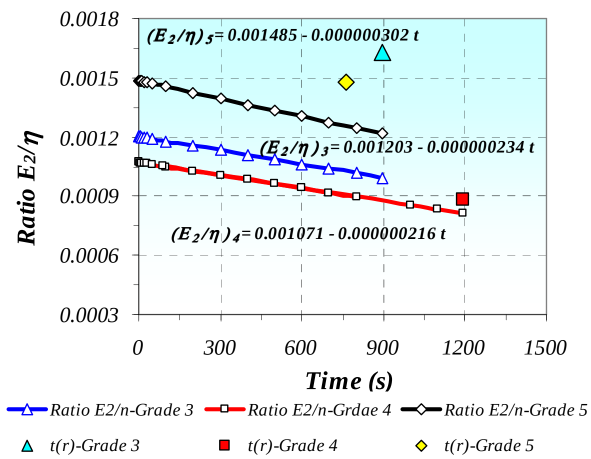

(C)

Figure 3.12. Ratio of viscous modulus to viscosity (E_2/η) for (A) the complete set of discs, (B) among lumbar levels sets L2-L3 and L4-L5, and (C) among degeneration scoring sets 3, 4 and 5.

c. Flexion-extension, right-left bending and torsion deflections

Loading the discs to a 100 mm eccentric load of 50 N gave a bending moment of 5 N-m which caused a rotation response in flexion-extension and right-left bending when were done in the saggital and coronal plane respectively, in accordance with the protocol described in section 2.II.c. While rotation response in the axial plane was achieved with the aid of the torsion device presented in section 2.II.d. The maximum rotation response which corresponded to the peak moment load of 5 N-m for flexion, extension, right lateral bending, left lateral bending and clockwise torsion for the entire set of discs, and classification by lumbar level and degeneration scoring are summarized in Table 3.5.

Table 3.5. Single and mean rotation response to 5 N-m moment for the 10 intervertebral discs tested in this study.

Disc and spine level	*Rotation (°) due to 5 Nm moment.*				
	Flexion	*Extension*	*Right-Bend*	*Left-Bend*	*Torsion*
A-L_{23}	*2.90*	*1.31*	*1.67*	*1.74*	*6.25*
B-L_{45}	*3.12*	*7.04*	*4*	*4.21*	*14.50*
C-L_{45}	*6.39*	*3.46*	*2.20*	*1.86*	*7.55*
D-L_{45}	*4.86*	*4.93*	*3.13*	*3.80*	*10*
F-L_{23}	*0.24*	*0.30*	*0.32*	*0.27*	*2.03*
G-L_{23}	*3.30*	*3.33*	*2.60*	*2.15*	*8.07*
H-L_{23}	*2.36*	*2.85*	*2*	*2.06*	*7.46*
I-L_{45}	*0.80*	*1.63*	*0.72*	*0.77*	*5.18*
J-L_{45}	*2.73*	*2.28*	*2*	*0.81*	*5.29*
L-L_{23}	*1.15*	*0.79*	*1.11*	*1.13*	*4.52*
Complete Set mean values and standard deviation (STD)	***2.79(1.85)***	***2.80(2.04)***	***1.98(1.17)***	***1.88(1.28)***	***7.09(3.41)***
Level group L_{23} values	***1.99(1.27)***	***1.72(1.32)***	***1.54(0.87)***	***1.47(0.78)***	***5.67(2.44)***
Level group L_{45} values	***3.58(2.13)***	***3.87(2.17)***	***2.41(1.24)***	***2.29(1.63)***	***8.50(3.89)***
Degeneration Grade 3 values	***2.43(0.93)***	***2.07(1.21)***	***1.85(0.62)***	***1.77(0.46)***	***6.58(1.56)***
Degeneration Grade 4 values	***3.25(3.08)***	***3.60(3.37)***	***2.17(1.84)***	***2.11(1.98)***	***8.03(6.25)***
Degeneration Grade 5 values	***2.80(2.03)***	***2.95(1.75)***	***1.95(1.21)***	***1.79(1.74)***	***6.82(2.75)***

On average, in the saggital plane the entire set of discs had the same mean range of motion response ranging from +2.79° in flexion, to -2.80° in extension. This tendency was also observed for movement in the coronal plane, were their range from + 1.98° in Right Bending, to -1.88° in Left Bending, see Figure 3.13. However, the mean stiffness values had larger differences, being 241±348 Nm/rad in Flexion, 221±275 Nm/rad in Extension, 241±249 Nm/rad in Right Bending and 277±295 Nm/rad in Left Bending. Disc stiffness in the coronal plane was only 10% higher than that in the saggital plane, where the posterior elements removal may cause an increased motion response. In the axial plane, rotations due to the torque were reported only in the clockwise direction, and ranged from 2° to 14.5° with a mean value of 7.09°, and a mean stiffness of 52±34 Nm/rad, see also Table 3.5.

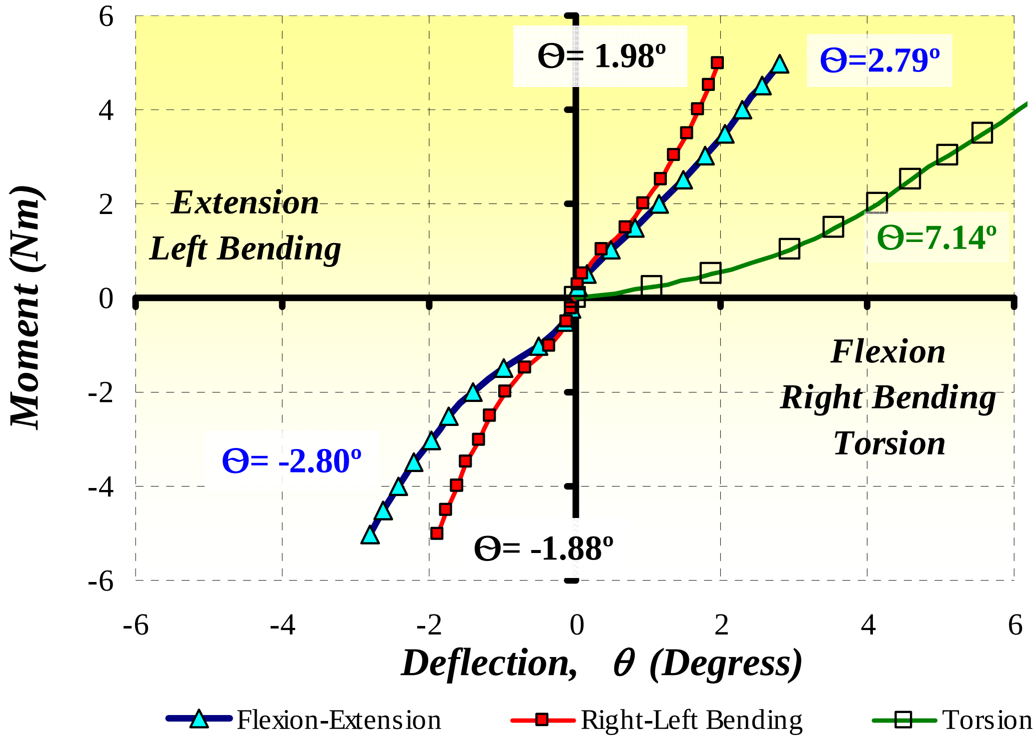

Figure 3.13. Mean load-deflection response to 5 N-m in flexion-extension, right-left lateral bending and axial torsion for the set of intervertebral discs used in this study.

The nonlinear stiffness was evident in the majority of the discs for all the loading modes, as shown by the moment–rotation curves in Figures 3.14 and 3.15. The stiffness curves are organized by loading type, along with lumbar level. Individually, motion response in Flexion-Extension at the peak load of 5 N-m gave discs B, C, and D the highest flexibility, with up to 10° of rotation, while discs F, I, and L were the stiffest with less than 3° of rotation. In six out of ten discs the motion response was about even between flexion and extension, and only in discs A, C, B, and H this did not happen, being flexion the dominant motion in the former pair, and extension in the latter pair, see Table 3.5. In Right-Left lateral bending, discs B, D, and G had up to 7° of rotation while again discs F, I, and L had less than 1° of rotation. In eight discs the motion response was about even between right and left bending, and only in discs G and J this did not happen, being the dominant motion in right bending for the former disc and left bending for the latter disc.

In torsion, discs B, D and G were the most flexible with at least 8° of rotation, while disc F had only 2°, see Figures 3.14 and 3.15. With the exception of disc F, the rest of the discs showed a nonlinear behavior between loading and deflection θ in at least one loading type.

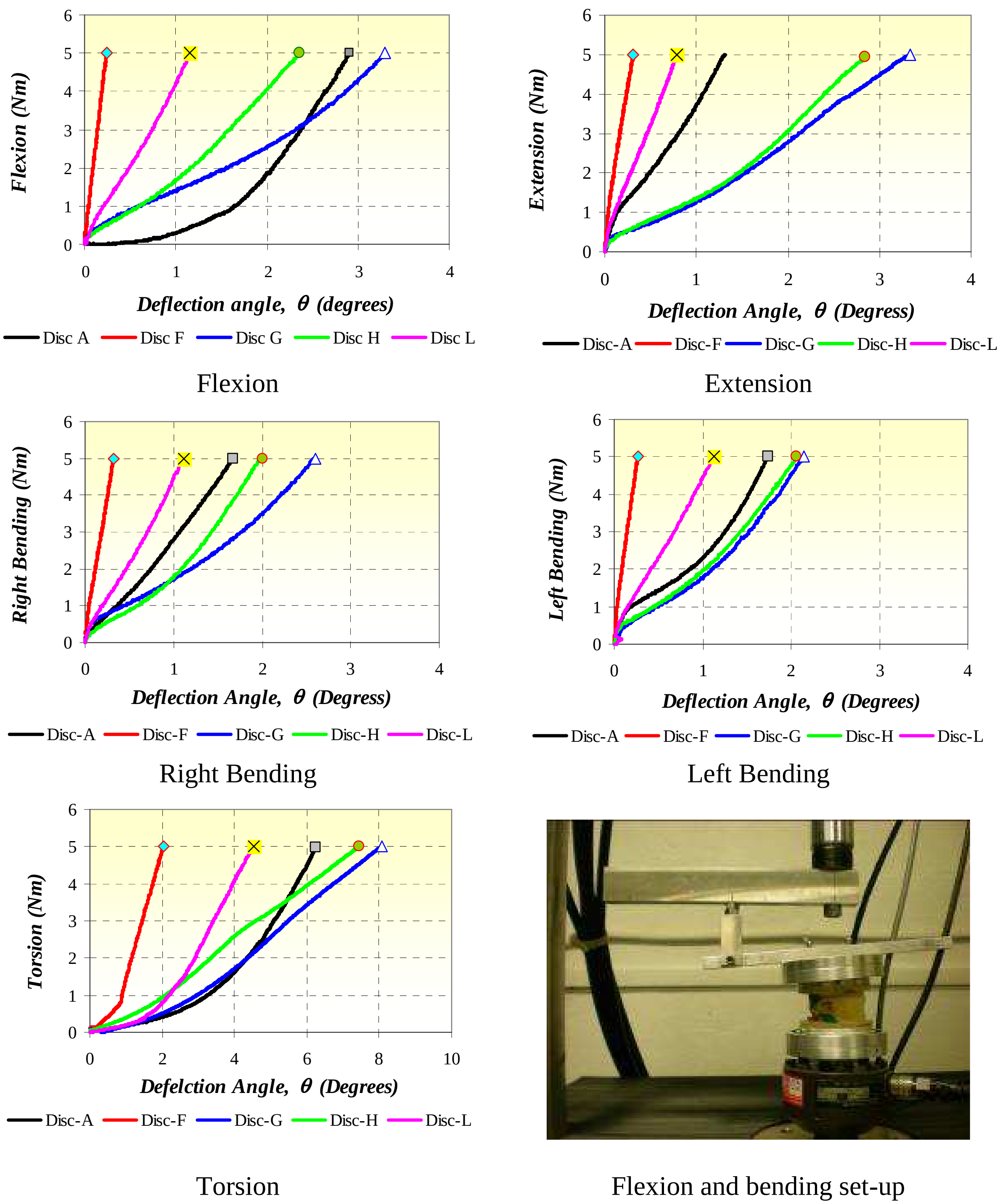

Figure 3.14. Load-deflection response to 5 N-m in flexion-extension, right-left lateral bending and axial torsion for each of the L2-L3 intervertebral discs.

Among lumbar levels, the L4-L5 set of discs showed more flexibility for all modes of rotation than the L2-L3 disc set, see Figure 3.16. Motion response for the L4-L5 disc set gave a mean deflection angle of 3.58° in flexion, and 3.87° in extension, which were 80% and 125% more than the mean values in the L2-L3 disc group.

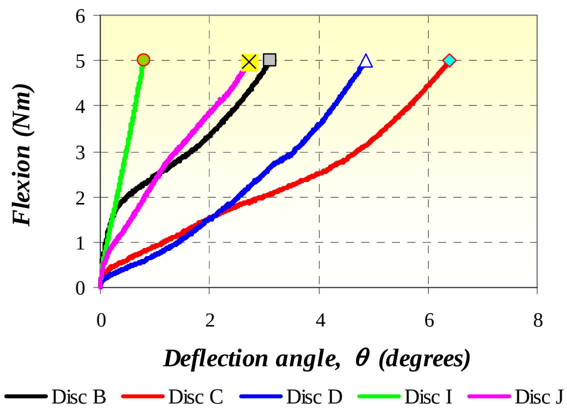

Flexion

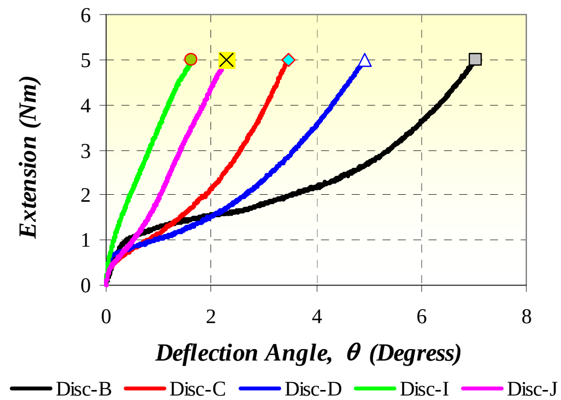

Extension

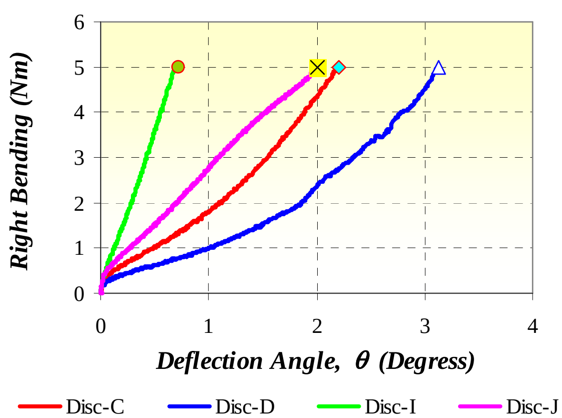

Right Bending

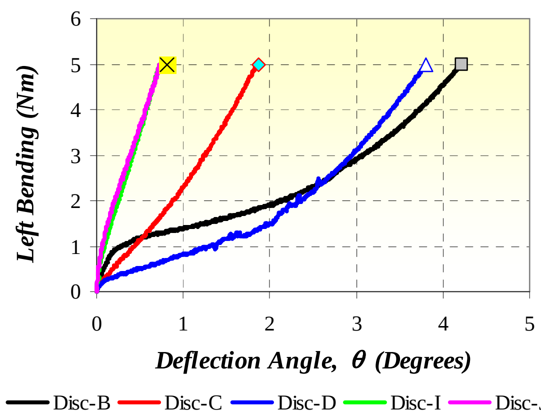

Left Bending

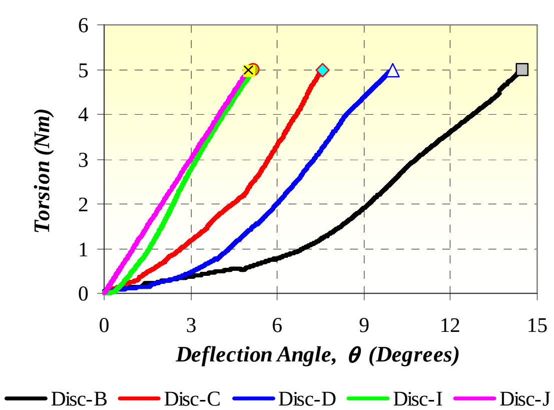

Torsion

Torsion set-up

Figure 3.15. Load-deflection response to 5 N-m in flexion-extension, right-left lateral bending and axial torsion for each of the L4-L5 intervertebral discs.

Mean motion response in the L4-L5 disc set to right-left lateral bending and axial torsion gave deflection angle values of 2.41°, 2.29° and 8.50° respectively, which were about 50% more in all three cases than the corresponding values of the L2-L3 disc group, see also Table 3.5.

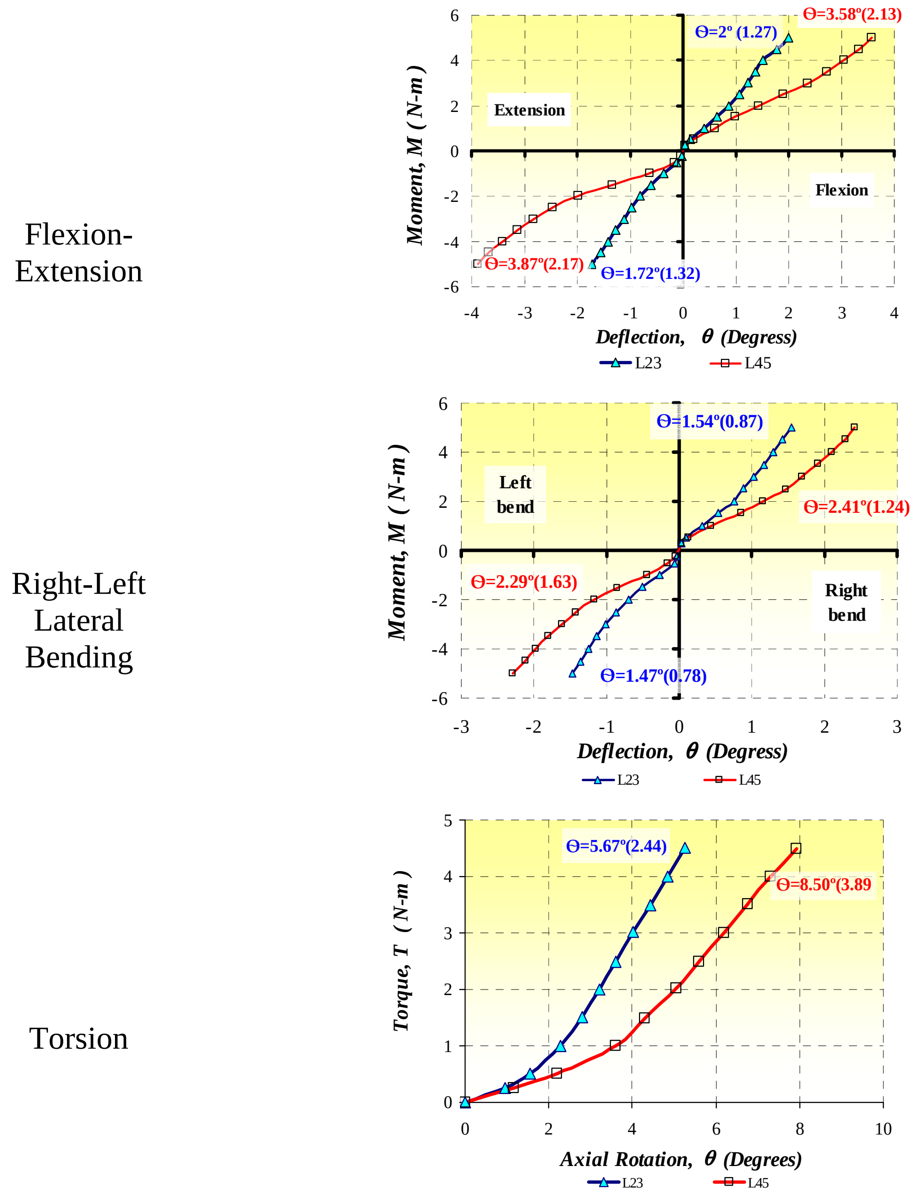

Figure 3.16. Intervertebral disc flexibility in flexion-extension, right-left lateral bending and axial rotation (torsion) between lumbar levels sets L2-L3 and L4-L5.

Mean stiffness values in Flexion and Extension for the L2-L3 disc set were 350±476 Nm/rad, and 345±359 Nm/rad respectively, which were 165% and 255% higher than the corresponding values in the L4-L5 disc group. For Right and Left lateral bending the mean stiffness values for the L2-L3 disc group were 316±329 Nm/rad and 350±400 Nm/rad respectively which were 90% and 70% higher than the corresponding values in the L4-L5 disc set.

Torsion mean stiffness for the L2-L3 disc set was 65±44 Nm/rad which was 66% higher than that in the L4-L5 disc set, see Figure 3.16. Again, because of the large scatter data in the results a student test (P>0.05) reveal no statistical differences in any motion response among disc levels and much less between degeneration scoring, see Figure 3.17.

Flexion-Extension

Right-Left Lateral Bending

Torsion

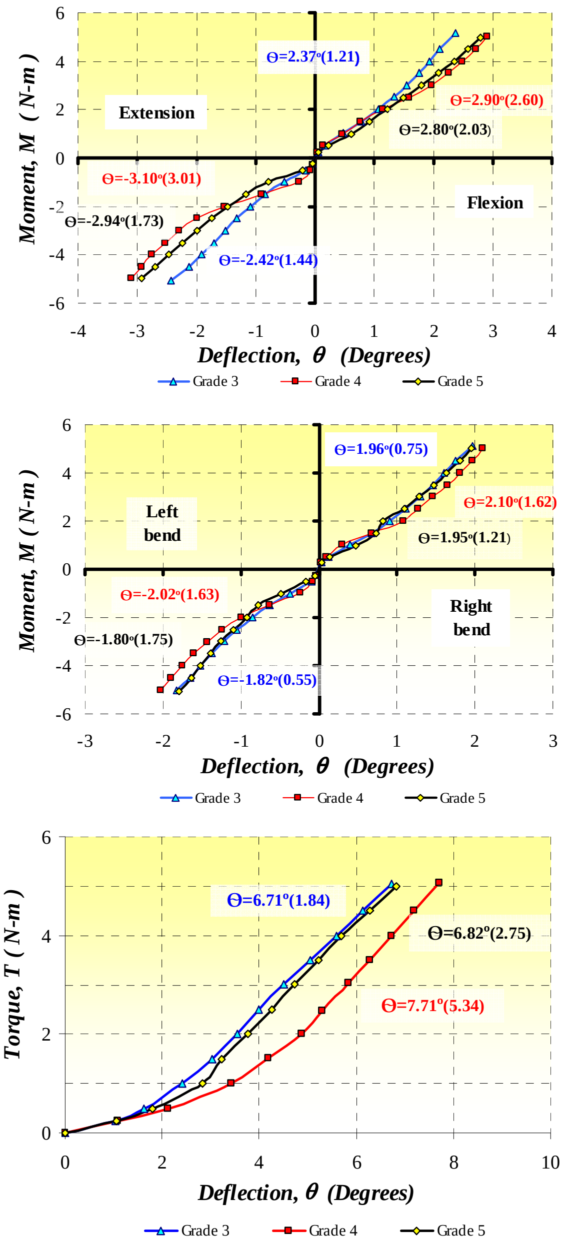

Figure 3.17. Intervertebral disc flexibility in flexion-extension, right-left lateral bending and axial rotation (torsion) between degeneration scoring sets 3, 4 and 5.

d. Cyclic compression

A viscoelastic behavior was shown by all the intervertebral discs tested. This was due to the angle of phase β between the stress and the strain signals, which grew up from 0º to 26º for the range of frequencies from 0.2 to 5 Hz respectively. There was energy dissipation, as the tangent of the *phase angle β* grew with the *frequency ω*. The stiffness value corresponding to an initial 500 N cyclic compression for each disc was around 10% less than those obtained from the static compression protocol. Also, the vertical elongations were less than 10% of the disc height value in all the discs, and were kept constant during the load frequency testing. The results showed that the stress grew and the *phase angle β* also grew with increased *frequency ω*. For the 5 Hz frequency the stress grew up to twice the value of that at 0.2 Hz, and the phase difference or angle β also reached its highest value of 26°. Thus, in all the discs, the values of the *complex modulus |E*|*, *storage modulus |E' |*, and *loss modulus |E''|* also increased as the frequency was increased. The mean and standard deviation of angle β for this range of frequencies are shown in Table 3.6. A zero value of angle β means a pure elastic behavior, and a 90˚ value means a pure viscous behavior. The range of values of β for the low frequency of 0.2 Hz was from 1.33˚ in discs B, G and H to 3.33˚ in disc C with a mean value of about 2˚ for the entire disc set. The 1 Hz frequency gave a range of values of β from 3.67˚ in disc B to 10˚ in disc J with a mean value of 6.5˚. Finally, the frequency of 5 Hz gave a range of values of β from 12.33˚ in disc F to over 20˚ in discs D, I, J and L with a mean value of 19˚.

Table 3.6. Progression of the phase angle β for each intervertebral disc used in this study. All the discs were subjected to an initial 500 N sinusoidal compression load.

Disc	*Phase shift angle β between the load and the elongation.*						
	0.2 Hz	*0.57 Hz*	***1 Hz***	*2 Hz*	*3.3 Hz*	*4 Hz*	***5 Hz***
A	*2*	*3*	***5***	*7.33*	*11*	*14*	***17***
B	*1.33*	*2*	***3.67***	*6*	*9*	*12*	***16***
C	*3.33*	*4*	***8***	*10*	*13.33*	*16.67*	***19***
D	*2*	*3.67*	***7***	*11*	*16.67*	*19*	***23.33***
F	*2.67*	*3*	***5.33***	*6.67*	*8*	*10*	***12.33***
G	*1.33*	*2.33*	***4***	*7*	*10.67*	*12*	***15***
H	*1.33*	*3.33*	***5***	*6.33*	*11.33*	*15*	***18.33***
I	*2.67*	*5*	***9***	*15*	*20.67*	*21*	***24***
J	*2.33*	*6.67*	***10***	*17*	*20*	*23*	***26***
L	*2.33*	*6*	***8***	*12*	*16*	*18*	***20***
Mean	***2.13***	*3.90*	***6.50***	*9.83*	*13.67*	*16.07*	***19.10***
STD	***0.67***	*1.54*	***2.20***	*3.88*	*4.46*	*4.22*	***4.32***

The relationship of angle β with the frequency ω was found to be linear with a slope of 3.449 indicating its rate of change, as shown in Figure 3.18. The fitting of the β curve and all other curves in this section was also done using the program DataFit V.9.0.59 (Oakdale Engineering ™), which for this fit was good (R^2>0.99).

It can be seen that small *phase angles β* (which occur at low frequencies) make the cosine function the dominant part over the sinus expression, as described in equations 2-40 and 2-41 of section 2.II.e. Then, at low frequencies the material response is described mainly by the *storage modulus E'* and to a lesser extent to the *loss modulus E"*.

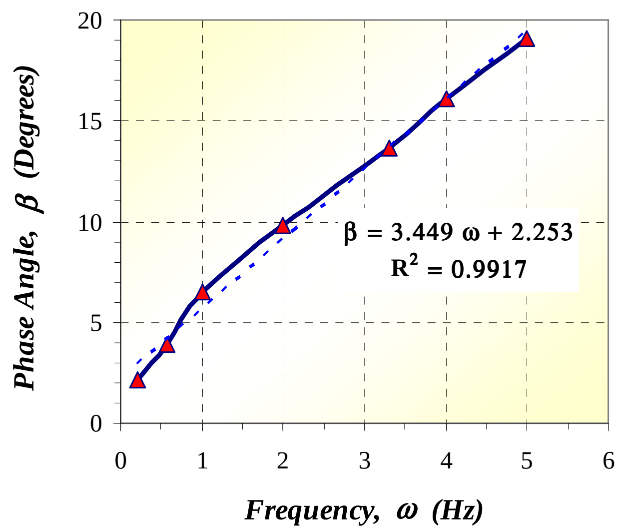

Figure 3.18. The relationship between the phase angle β and the frequency ω for the complete set of discs tested in this study.

The inflexion point of the curve shown in Figure 3.18 is located were the storage, and loss modulus are of equal value, with no dominance. The only possible value of β for which this equity is true is $\beta = 45^\circ$, which for the fit equation gives a frequency ω value of 12.4 Hz, for which $E' = E''$. Thus, because this value falls out of the range used in the protocol (0.2 to 5 Hz), the disc response was given mostly by the storage component *E'*, meaning a more solid viscoelastic disc behavior.

When analyzing the *phase angle β* variation between lumbar levels sets, and degeneration scoring sets it was found that the rate of change was very similar among them. However, the L4-L5 disc set showed a 20% higher β value for frequencies below 1 Hz, and up to 50% higher β value for the rest of the frequencies, than those of the disc group L2-L3. The degeneration scoring grade 5 disc set showed up to a 50% higher value of β than the other two degeneration scoring sets, see Figure 3.19. However, the statistical analysis showed that these differences were not significant (P>0.05).

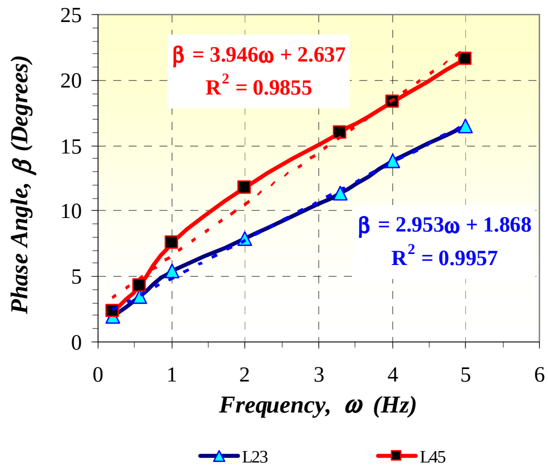

(A)

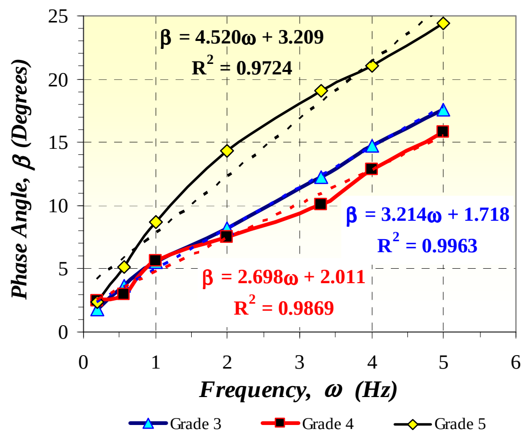

(B)

Figure 3.19. The relationship of the phase angle β with the frequency ω for (A) the lumbar levels disc sets L2-L3 and L4-L5, and (B) the degeneration scoring grades 3, 4 and 5.

The input sinusoidal signals of the load, and elongation gave a response of stress, and strain with similar sinusoidal signals. Then, with the *phase angle β*, the *complex compressive modulus E**, the compressive *storage modulus E'*, the *compressive loss modulus E"*, and the *loss tangent (tan δ)* were determined as dynamic viscoelastic parameters, in accordance with section 2.II.e. Their mean and standard deviation values over the range of frequencies, from 0.2 to 5 Hz, for the complete disc set, lumbar level and degeneration scoring classifications are summarized in Table 3.7. The results indicated that the stresses grew with increased frequency in all the intervertebral discs. At the 0.2 Hz frequency the mean values of E', E" and E* for the entire discs set were 4.64, 0.18 and 4.64 MPa respectively, which grew to 5.62, 0.93 and 5.71 MPa at 2 Hz, and reach there highest values of 7.81, 2.52 and 8.24 MPa at 5 Hz respectively. Also, the *loss tanδ parameter, or ratio of energy lost to energy stored*, increases its magnitude by 10 times, between the load at 0.2 Hz and that at 5 Hz, showing a dissipation tendency, typical of viscoelastic tissues, see Figure 3.20 and also Table 3.7.

Table 3.7. Mean and standard deviation values of the dynamic parameters for the complete set and classifications of intervertebral discs.

Class	Frequency (Hz)	Phase Angle β (Degrees)	Storage Moduli, E' (MPa)	Loss Moduli, E" (MPa)	Complex Moduli, E* (MPa)	Loss Tan δ
Complete set N=10	0.2	2.13(0.67)	4.64(3.13)	0.18(0.15)	4.64(3.13)	0.04(0.01)
	0.57	3.90(1.54)	4.82(3.18)	0.32(0.22)	4.83(3.19)	0.07(0.03)
	1	6.50(2.20)	5.08(3.38)	0.56(0.38)	5.11(3.40)	0.11(0.04)
	2	9.83(3.88)	5.62(3.74)	0.93(0.61)	5.71(3.77)	0.17(0.07)
	3.3	13.67(4.46)	6.58(4.45)	1.48(0.85)	6.77(4.49)	0.25(0.08)
	4	16.07(4.22)	7.31(5.04)	1.96(1.11)	7.59(5.12)	0.29(0.08)
	5	19.10(4.32)	7.82(5.24)	2.52(1.28)	8.24(5.35)	0.35(0.09)
L_{23} Disc Group N=5	0.2	1.93(0.60)	5.68(4.04)	0.21(0.21)	5.68(4.05)	0.03(0.01)
	0.57	3.53(1.43)	5.86(4.12)	0.32(0.20)	5.87(4.13)	0.06(0.03)
	1	5.47(1.50)	6.20(4.37)	0.56(0.40)	6.22(4.39)	0.10(0.03)
	2	7.86(2.34)	6.89(4.93)	0.87(0.56)	6.95(4.96)	0.14(0.04)
	3.3	11.40(2.89)	8.09(5.92)	1.45(0.87)	8.22(5.98)	0.20(0.05)
	4	13.8(3.03)	9.05(6.75)	2.02(1.34)	9.28(6.87)	0.25(0.06)
	5	16.53(2.98)	9.50(7.10)	2.56(1.57)	9.85(7.25)	0.30(0.06)
L_{45} Disc Group N=5	0.2	2.33(0.75)	3.60(1.74)	0.15(0.08)	3.60(1.74)	0.04(0.01)
	0.57	4.27(1.72)	3.78(1.76)	0.31(0.26)	3.80(1.77)	0.08(0.03)
	1	7.53(2.44)	3.95(1.87)	0.56(0.41)	4.00(1.90)	0.13(0.04)
	2	11.80(4.32)	4.36(1.79)	0.98(0.72)	4.48(1.90)	0.21(0.08)
	3.3	15.93(4.86)	5.07(1.95)	1.52(0.92)	5.31(2.11)	0.29(0.09)
	4	18.33(4.25)	5.56(2.01)	1.89(0.99)	5.89(2.18)	0.33(0.08)
	5	21.67(4.07)	6.13(2.10)	2.48(1.10)	6.63(2.31)	0.40(0.08)
Degenerational Grade 3 N=4	0.2	1.75(0.50)	4.19(2.63)	0.13(0.10)	4.19(2.64)	0.03(0.01)
	0.57	3.67(1.61)	4.35(2.75)	0.25(0.12)	4.36(2.75)	0.06(0.03)
	1	5.5(1.73)	4.65(3.07)	0.42(0.25)	4.66(3.08)	0.10(0.03)
	2	8.17(2.59)	5.2(3.65)	0.69(0.44)	5.25(3.67)	0.14(0.05)
	3.3	12.25(2.52)	6.22(4.83)	1.27(0.88)	6.35(4.91)	0.22(0.05)
	4	14.75(2.5)	7.02(5.76)	1.77(1.4)	7.24(5.92)	0.26(0.05)
	5	17.58(2.11)	6.90(4.73)	2.12(1.40)	7.22(4.93)	0.32(0.04)
Degenerational Grade 4 N=3	0.2	2.44(1.02)	5.60(5.28)	0.24(0.26)	5.60(5.28)	0.04(0.02)
	0.57	3(1)	5.8(5.32)	0.29(0.28)	5.81(5.33)	0.05(0.02)
	1	5.66(2.19)	6.04(5.56)	0.56(0.52)	6.07(5.58)	0.10(0.04)
	2	7.55(2.14)	6.87(5.99)	0.83(0.67)	6.92(6.03)	0.13(0.04)
	3.3	10.11(2.83)	8.04(6.69)	1.26(0.82)	8.14(6.73)	0.18(0.05)
	4	12.89(3.42)	8.95(7.35)	1.79(1.10)	9.13(7.41)	0.23(0.06)
	5	15.78(3.34)	10.35(8.49)	2.58(1.59)	10.68(8.62)	0.28(0.06)
Degenerational Grade 5 N=3	0.2	2.33(0.33)	4.28(1.95)	0.18(0.1)	4.28(1.95)	0.04(0.01)
	0.57	5.11(1.5)	4.46(1.98)	0.43(0.29)	4.49(1.99)	0.09(0.03)
	1	8.67(1.53)	4.68(2.10)	0.75(0.43)	4.74(2.14)	0.15(0.03)
	2	14.33(3.06)	4.95(1.96)	1.34(0.75)	5.13(2.08)	0.26(0.06)
	3.3	19.11(2.14)	5.61(2.13)	2(0.9)	5.96(2.30)	0.35(0.04)
	4	21(2)	6.05(2.03)	2.38(1)	6.50(2.25)	0.38(0.04)
	5	24.44(1.39)	6.50(2.06)	2.99(1.10)	7.16(2.33)	0.46(0.03)

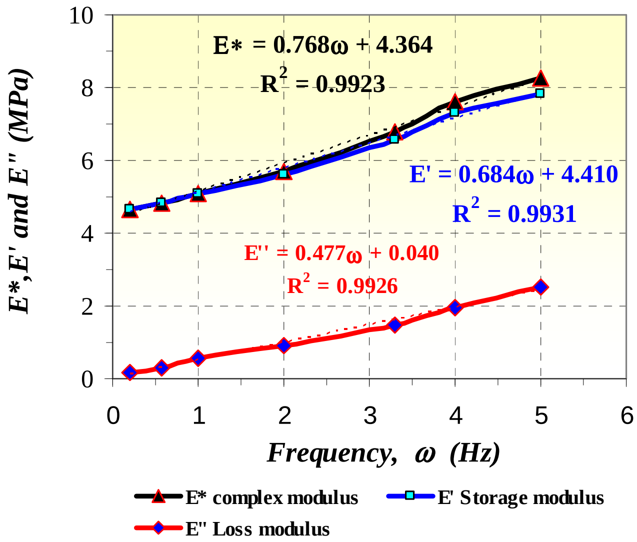

Figure 3.20. Relationship of the Storage E', Loss E"and Complex moduli E with the frequency ω for the complete set of intervertebral discs used in this study.*

As shown, all the dynamic parameters increase in value with increased frequency. Also, the *loss moduli E"* showed about the same increase as the *storage modulus E'* for the entire frequency range. Thus, the disc ratio of dissipation or *tanδ* undergoes small changes, and the *E" moduli* contributed only with a 30% of the dynamic response, meaning an overall elastic response.

The *storage modulus E'* was found to be around 60% larger in discs from the L2-L3 set than discs from the L4-L5 set. These differences arise from the higher stiffness in the former group which showed a define disc height with lesser degeneration. However, the results also indicated that the *loss moduli E"* was similar among lumbar levels sets with less than a 10% value difference. Thus, the larger value of the *E'* moduli from the L2-L3 disc set led to a higher *complex modulus E** which reach a mean value of 9.85 MPa and was 50% higher than that of the L4-L5 disc set, see Figure 3.21 and also Table 3.7. Also, the 50% higher value of *E'*, *E"* and *E** from the L2-L3 disc set over those from the lower L4-L5 disc set, and also, the higher values of these parameters in the degeneration scoring grade 4 set over the other two scoring sets, corroborates their higher stiffness values determined previously with the static compression protocol, see Figure 3.21.

The degenereration scoring classifications gave to the grade 4 set the highest value for the *E' moduli*, with mean values reaching 10 MPa, which were 60% higher than the other two scoring sets. Again, the higher stiffness in disc F can explain the difference. The *E"moduli* was found to be higher in the degeneration scoring 5 disc set, with differences reaching up to 40% with respect to the other two scoring sets, but no statistical differences was found due to the large scatter data (P>0.05). The higher mean value of the *E' moduli* from the degeneration scoring grade 4 disc set led to a higher *complex modulus E** which reach a mean value of 10.7 MPa which was 50% higher than that of the other two scoring sets, see also Table 3.7.

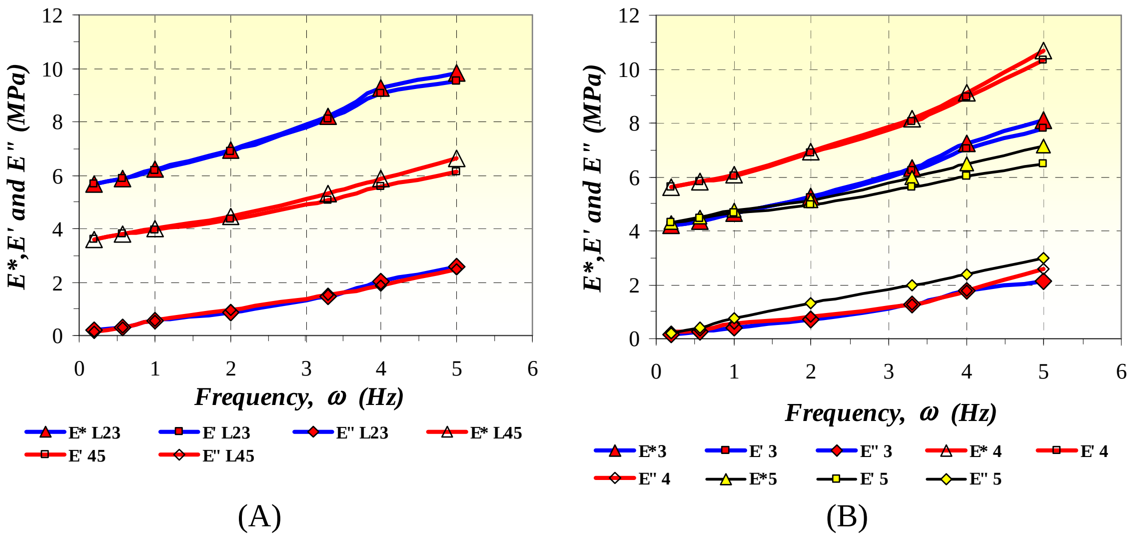

Figure 3.21. Relationship of the Storage E', Loss E"and Complex moduli E with the frequency ω among (A) lumbar level sets and (B) degeneration scoring sets.*

Once the dynamic parameters *E'*, *E"* and *E** were determined, then the ratio of loss to storage moduli or *tanδ* was calculated, and plotted against the frequency *ω*. As shown in Figure 3.22, this turn out to be linear (R^2>0.95). The narrow range of frequencies used in this study may explain this result.

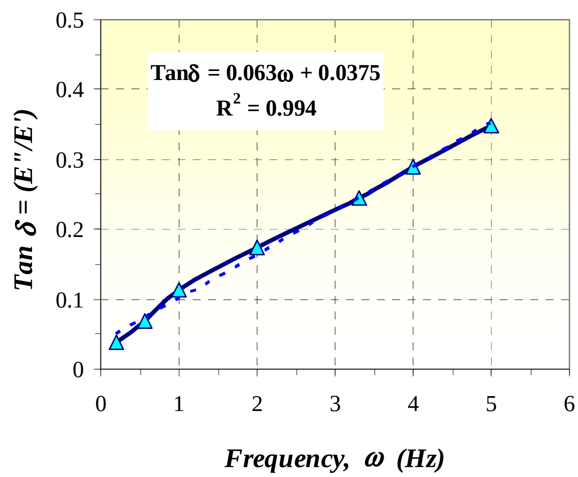

Figure 3.22. The ratio of loss to storage modulus or tanδ for the complete set of discs used in this study.

Additionally, the *ratio tanδ* was plotted for the disc lumbar level, and degeneration scoring sets to see if any differences could exist. As shown in Figure 3.23, there were no differences in response at load frequencies below 1 Hz, and only after 1 Hz these differences started to grew, having the L4-L5 disc set a 30% higher value of dissipation ratio. Also, the degeneration scoring grade 5 disc set had a *tanδ* mean value up to 60% higher than the other two scoring sets.

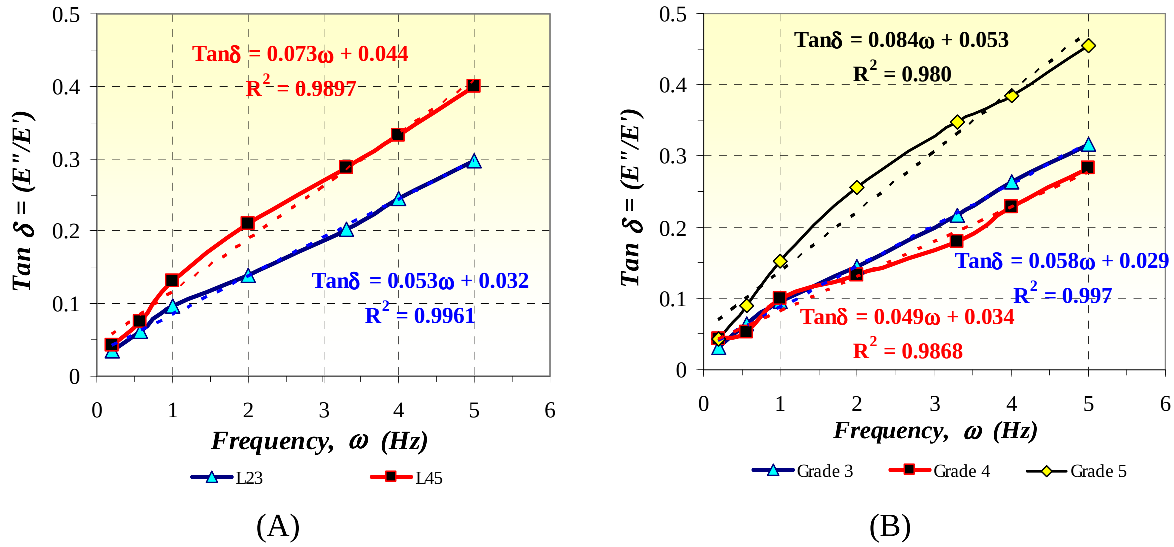

Figure 3.23. The ratio of loss to storage modulus (tanδ) among (A) lumbar level sets and (B) degeneration scoring sets.

As shown in Figures 3.22 and 3.23 the ratio of dissipation values were less than the unit (*tanδ*<1) for almost the entire range of frequencies, indicating a more elastic response of the disc. However, there were significant dissipations at the load frequency of 5 Hz, which were measured as the enclosed area between the loading and unloading curves, in accordance with section 2.II.e. The typical hysteresis curve for the nearby frequency of 5 Hz resembles that which is shown in Figure 3.24.

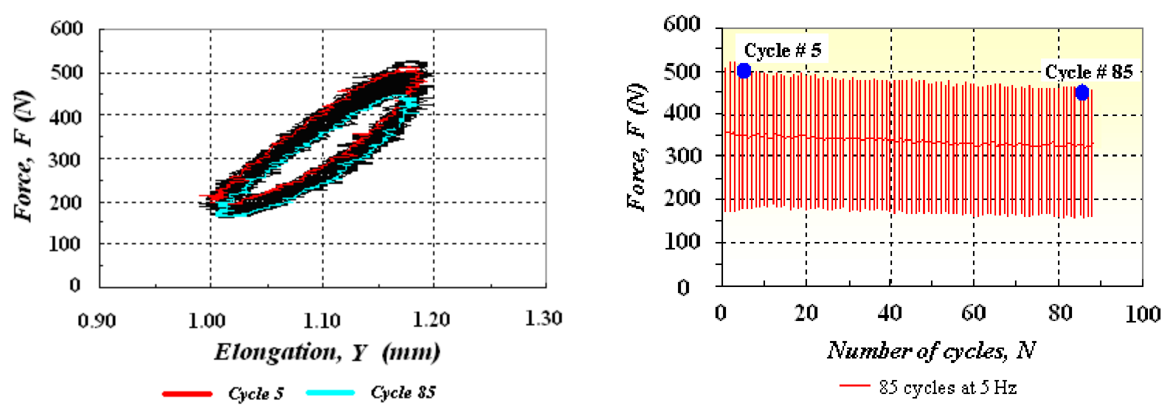

Figure 3.24. Typical hysteresis curve and stress relaxation under cyclic compression for the set of intervertebral discs used in this study. All discs were submitted up to a 5 Hz cyclic compression load. Measurements of hysteresis were done in Nmm (mJ) between the fifth and eighty-fifth cycles.

The mean and standard deviation values of the *hysteresis H* over the range of loading frequencies, from 0.2 Hz to 5 Hz, for the entire set of discs, lumbar level and degeneration scoring classifications showed an increased in energy dissipation as the frequency was increased, see Table 3.8.

Table 3.8. Mean and standard deviation values of the disc hysteresis due to a cyclic compression load. Values are given in milijoules.

.

Disc	*Hysteresis in N m (Joule)*						
	0.2 Hz	*0.57 Hz*	*1 Hz*	*2 Hz*	*3.3 Hz*	*4 Hz*	*5 Hz*
A	*0.02*	*0.04*	*0.26*	*0.76*	*0.88*	*1.06*	*1.19*
B	*0.02*	*0.07*	*0.28*	*1.04*	*1.54*	*1.76*	*2.15*
C	*0.18*	*0.28*	*0.72*	*0.88*	*1.34*	*1.50*	*1.71*
D	*0.01*	*0.35*	*0.68*	*3.12*	*3.52*	*3.92*	*4.12*
F	*0.03*	*0.07*	*0.14*	*0.17*	*0.22*	*0.26*	*0.31*
G	*0.13*	*0.33*	*1.02*	*1.78*	*2.36*	*2.73*	*3.11*
H	*0.21*	*0.66*	*2.24*	*3.36*	*3.87*	*4.22*	*4.81*
I	*0.19*	*0.35*	*0.80*	*1.48*	*2.24*	*2.53*	*3.61*
J	*0.12*	*0.24*	*0.32*	*0.65*	*0.75*	*0.79*	*0.92*
L	*0.06*	*0.18*	*0.57*	*0.83*	*1.41*	*1.63*	*2.57*
Complete set n=10	*0.10 (0.08)*	***0.26 (0.19)***	***0.70 (0.61)***	***1.41 (1.06)***	***1.81 (1.19)***	***2.04 (1.30)***	***2.45 (1.47)***
L_{23} Disc Group n=5	*0.09 (0.08)*	*0.26 (0.25)*	*0.85 (0.85)*	*1.38 (1.25)*	*1.75 (1.42)*	*1.98 (1.54)*	*2.40 (1.75)*
L_{45} Disc Group n=5	*0.10 (0.09)*	*0.26 (0.12)*	*0.56 (0.24)*	*1.44 (0.99*	*1.88 (1.06)*	*2.10 (1.19)_*	*2.50 (1.33)*
Degenerational Grade 3 N=4	*0.11 (0.08)*	*0.30 (0.27)*	*1.02 (0.87)*	*1.68 (1.21)*	*2.13 (1.31)*	*2.41 (1.39)*	*2.92 (1.50)*
Degenerational Grade 4 N=3	*0.08 (0.09)*	*0.14 (0.12)*	*0.38 (0.30)*	*0.70 (0.46)*	*1.03 (0.71)*	*1.17 (0.80)*	*1.39 (0.96)*
Degenerational Grade 5 N=3	*0.11 (0.09)*	*0.31 (0.07)*	*0.60 (0.25)*	*1.75 (1.26)*	*2.17 (1.39)*	*2.41 (1.57)*	*2.89 (1.72)*

A zero value of *H* means that no dissipation is present; however, the results shows that all the discs dissipate energy even at the lowest frequency. Thus, for the low frequency of 0.2 Hz the *hysteresis* ranged from less than 0.05 joule in discs A, B, D and F to 0.20 joule in discs C, H and I, with a mean value of 0.10 joule for the entire set. For the frequency of 1 Hz, the range cover from less than 0.30 joule in discs A, B and F to above 1 joule in discs G and H, with a mean value of 0.70 joule. The 5 Hz load frequency gave *hysteresis* values covering from less than 1 joule in discs F and J to over 4 joules in disc D and H with a mean value of 2.45 joules.

A plot of the hysteresis with frequency for the 85 cycles for the entire set of discs, and also classifications for lumbar level, and degeneration scoring shows a nonlinear relationship and dependence with the *loss moduli E”*. Neither classifications prove that the hysteresis was statistically different among them (P>0.05), being almost identical between lumbar level sets, and different in their mean values between degeneration scoring grade 4 set and the other two scoring sets, see Figure 3.25.

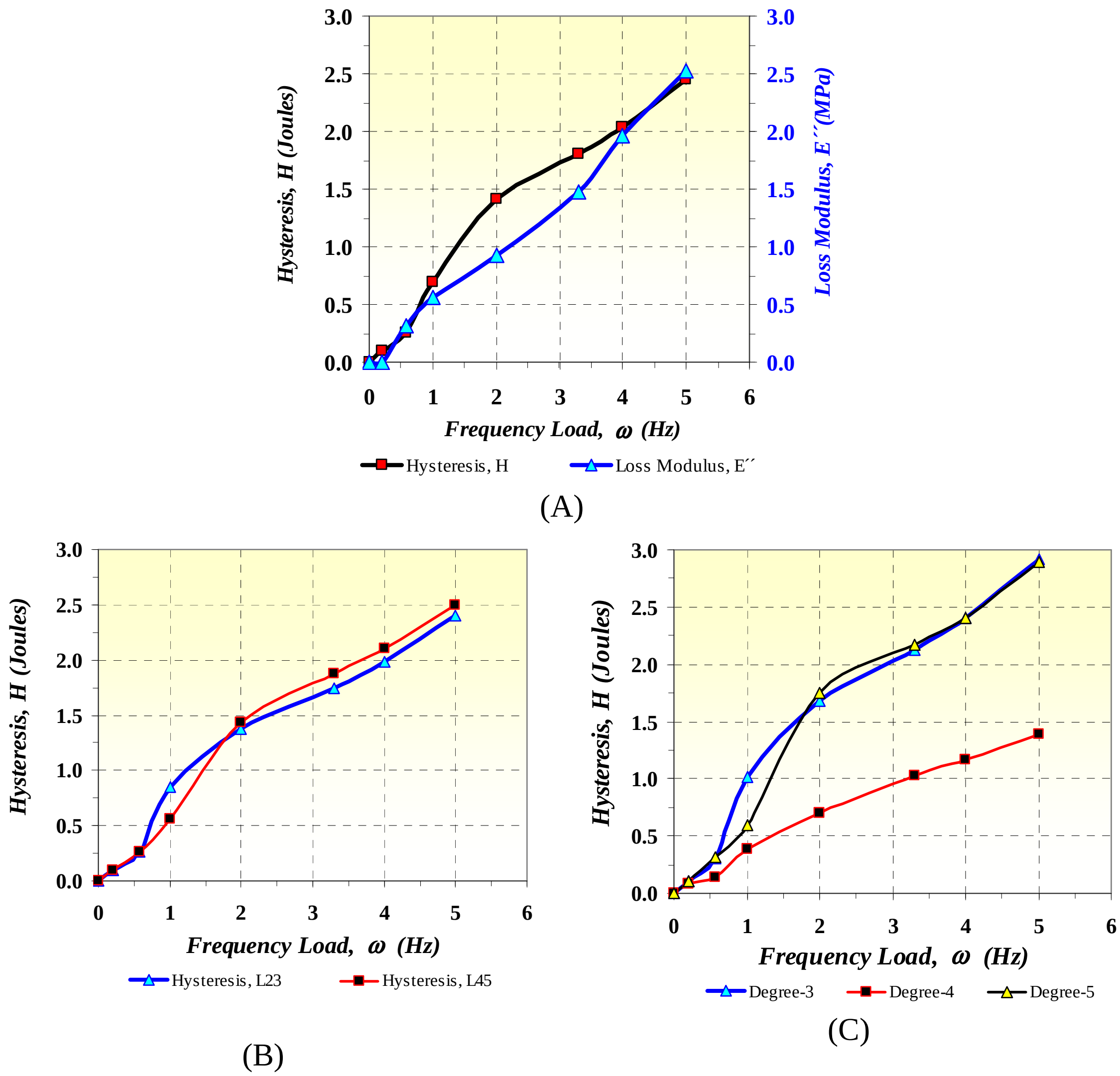

Figure 3.25. Energy dissipation for (A) the complete set of intervertebral discs, (B) among lumbar level sets and (C) among degeneration scoring sets.

Thus, from the results from Figures 3.21, 3.23 and 3.25 the overall dynamic response from the set of degenerated discs indicated a more viscoelastic solid behavior. The dissipation component of the dynamic response was around 30% which may be associated with the remaining fluid in the disc. Whereas the storage part, represented the remaining 70%, and may be associated with stiffer collagenous tissues.

III. Finite Element Model (FEM) results

a. Model convergence

The Finite Element Modeling (FEM) of the sample specific lumbar L2-L3 degenerated disc started by conducting a test of convergence to select the model for analysis. This was done considering the reaction force in compression. The selection of six geometrical models was presented in the mesh generation topic from section 2.III.b. The convergence test was done using MSC Marc Mentat^{TM} software. The reaction force at the nodes from the base of the disc model was compared with the experimental load of 1000 N. Shown in Figure 3.26 is the plot of the reaction force against the number of nodes for each model. It can be seen that the reaction force tends to stabilized at around 1160 N, and the initial points corresponding to models G-1 to G-3, have a downside slope indicating a poor convergence, whereas models G-4 to G-6 there is a more "flat-like" slope indicating more convergence. However, in the interest of reducing file size and time consuming computational calculations; the model G-4 was selected which had a triangle length edge of up to 1.5 mm which was sufficient to detail the disc geometry. The stress-strain run simulation for the selected model was done on a workstation with a CPU of 3 GHz and 64 GB of RAM and took between 2 to 4 hours each run.

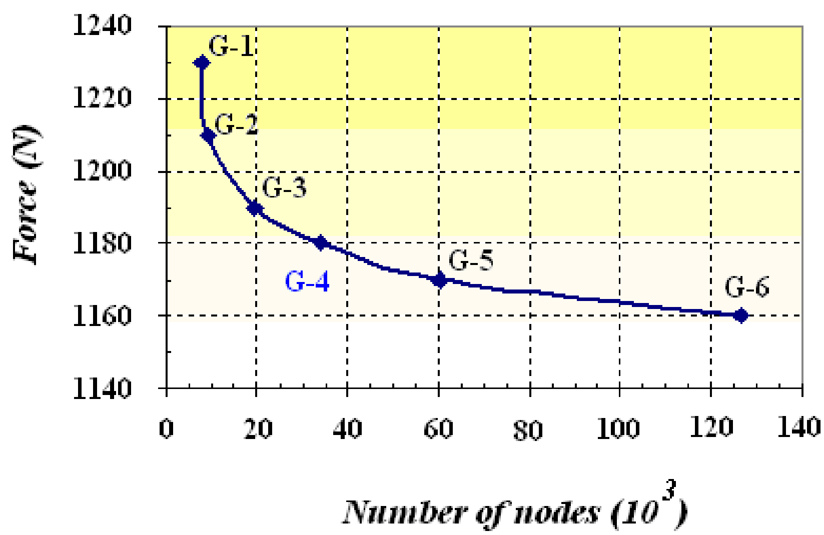

Figure 3.26. Convergence testing for the reaction force of the six L2-L3 FEM disc degeneration models (G-1 to G-6). Model G-4 in blue, was chosen which gave an 18% larger value of the reaction force at the nodes from the disc base. Tetrahedron element size was limited to 1.5 mm length edge.

The geometrical characteristics of the G-4 model are given in Table 3.9. As shown, all elements for the model are solid 3D structures composed of tetrahedrons, pentahedrons, and hexahedrons.

Table 3.9. Geometrical characteristics of the L2-L3 disc degeneration model.

Material	Name of mask	Number of elements	Class and type of elements			
			Compression		**Bending and Torsion**	
Intervertebral disc and vertebrae	Cartilage	5508	Tetrahedron 4 node Marc # 157	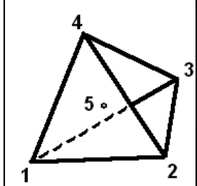	Tetrahedron 4 nodes Marc # 157	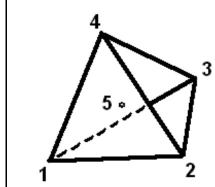
	Nucleus	45270				
	Cavities	119				
	Cancellous Bone	82092				
	Annulus	48082				
	Cortical Shell	6655				
Accessories	Lever Base	31330			Pentahedron 6 nodes Marc # 136	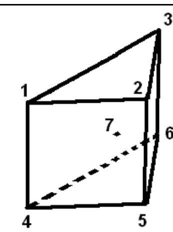
	Lever Arm	5000			Hexahedron 8 nodes Marc # 84	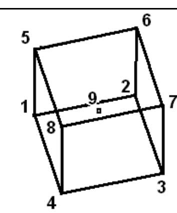

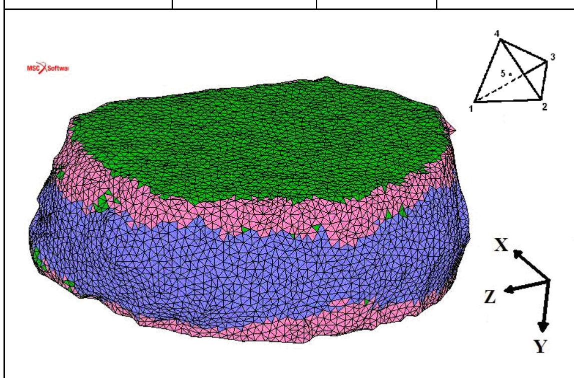

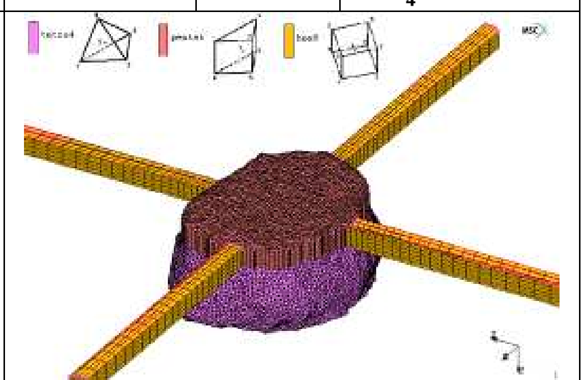

In the finite element simulation of disc compression, the soft tissues of the disc and adjacent vertebral bodies were modelled using element type 157 which in Marc Mentat^{TM} is suitable for rubber, plastics and biological tissues that exhibit non linear behavior. The soft tissues of the disc were treated as *elastomers* with incompressibility, while the hard bone structures as *orthotropic*, as described in section 2.III.g.

The tetrahedral 4 nodes element type 157 is written for incompressible or nearly incompressible three dimensional applications based on Herrmann formulations. The shape function for the center node is a bubble function. Therefore, the displacements and the coordinates for the element are linearly distributed along the element boundaries. The stiffness of this element is formed using four Gaussian integration points. The degrees of freedom of the center node are condensed out on the element level before the assembly of the global matrix, as described in (MSC Marc Mentat 2005r3^{TM}).

The advantage of working with tetrahedrons over brick elements is a better approximation of the disc geometry with fewer elements, although characterization of material behavior is better described with brick elements, where the displacements are distributed along the three orthogonal axes.

The FE simulation and analysis of the loading phase starts with the step displacement compression, after which the bending and torsional loading were simulated and are presented next.

b. Step displacement procedure and adjustment of material properties

A step displacement and a step force procedures were applied (see section 2.III.i) in the loading simulation of compression. In the first case, the nodes on the top surface of the L2-L3 FEM disc were assigned an equal vertical displacement of 1.434 mm to guarantee a uniform elongation in the upper surface, as was seen in the testing, see Figures 3.27 (a). In contrast, when a step force was applied to the nodes located at the upper surface of the disc model, the resulting vertical displacement did not show a uniform distribution; see Figure 3.27 (b).

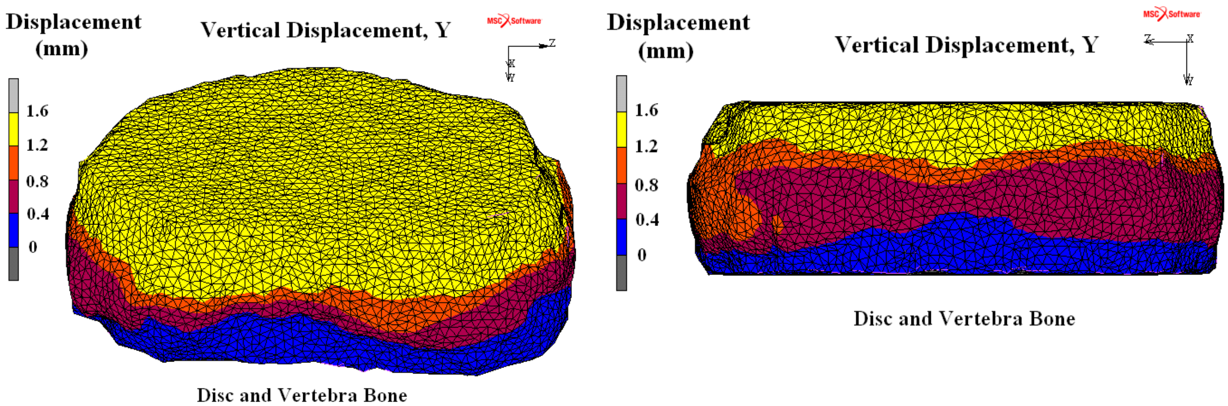

(a)

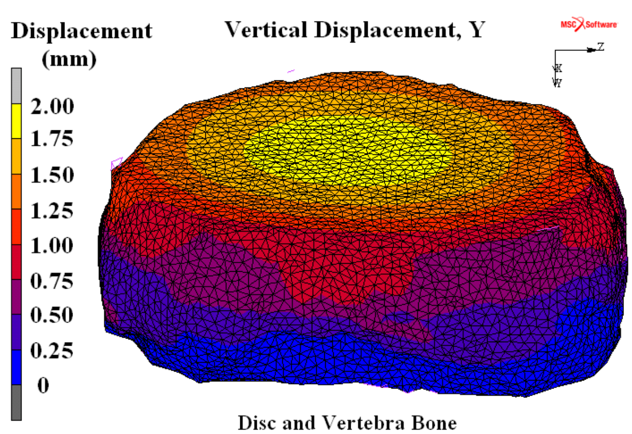

(b)

Figure 3.27. Computational simulation of a displacement step and force step applied to the L2-L3 FEM of disc degeneration. In (a) the disc uniform elongation as a result of an imposed 1.434 mm displacement at the upper nodes. In (b) the varying elongation as a result of applying a force of 0.72 N at each of the 1395 nodes of the upper surface.

The ring-like distribution of elongations due to the force application shown on Figure 3.27 (b) had to take into consideration the stiffness differences between the disc materials and that of the vertebrae, such difference was as high as two to three orders of magnitude, see section 2.III.g. As a result, a 1 mm of depth difference was developed between the periphery of the upper surface (where the stiffer layer of cortical bone is present) and the center of the upper surface (where the nucleus pulposus lies underneath). Thus, the disc configuration exhibited a concave profile, as shown in Figure 3.28 (b), which clearly did not occur in the compression test.

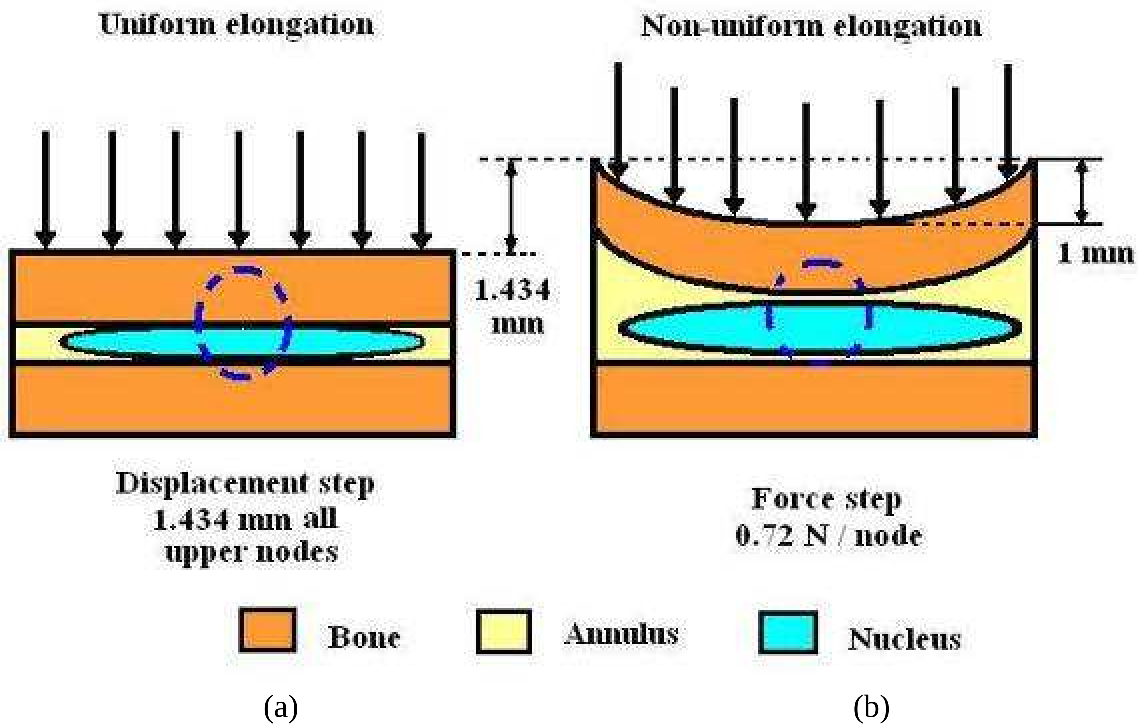

Figure 3.28. Upper surface disc elongation profile in (a) displacement step simulation and (b) force step simulation.

Thus, for the displacement step simulation shown in Figures 3.27 (a) and Figure 3.28 (a) the reaction force at the disc base nodes gave a value of 1180 N, which was 18% higher than that from the experimental test (1000 N). This difference was the smallest possible when considering the additional simulations involving bending, and torsional loading. For such additional loads, the reaction force was measured at the extreme nodes of the lever where the displacement step took place. Measurements of force were done at the 100 mm of the lever for bending, and at 70 mm of the lever for torsion.

The simulation results show that the magnitude of the reaction moment for bending range between 2.1 N-m in left bending, and 8.8 N-m in extension, and for torsion the reaction moment was only 50% of the experimental value of 5 N-m, see Table 3.10.

Table 3.10. Reaction force and moment at the nodes from the disc base for the final fitting of the disc material properties.

Loading Condition and displacement step	Simulation of loading	
	Reaction force (N) and Reaction Moment (N-m)	% of difference with the experimentation
Compression with Y= 1.434 mm	1180 N	+ 18
Flexion with Y= 6.270 mm	7 N-m	+ 40
Extension with Y= 6.300 mm	8.8 N-m	+76
Right Lateral Bending Y= 4.656 mm	5.6 N-m	+ 12
Left Lateral Bending Y= 3.864 mm	2.1 N-m	- 58
Axial Torsion X,Z= 9.824 mm	2.4 N-m	- 52

The *Young's modulus E*, *Poisson's ratio v*, and *Mooney-Rivlin* coefficients C_1 and C_2 for the degenerated annulus fibrosus were obtained in a trial and error method, see section 2.III.h. The initial values for C_1 and C_2 were 0.2 and 0.05 MPa respectively, which corresponded to an *E* value of 1.5 MPa according to Marc Mentat™ approximation method for incompressible materials, see section 2.III.g. Also, to account for the incompressibility of water, a *bulk modulus K* of 2200 MPa was assigned with a high value of *v* equal to 0.4999.

Initial results from the simulations to compression showed that the reaction force was 50% higher than the experimental value. Also, for the flexion and extension run simulations, the reaction moments gave values of 8 N-m and 9.5 N-m respectively. For right and left bending simulations, the reaction moment gave values of 6.6 N-m and 3.1 N-m respectively, while for axial torsion simulation, the reaction torque was 3.9 N-m. A second try was carried out using a lower value of the Mooney constants, such as C_1= 0.15 and C_2= 0.0375 MPa leading to a reduction in all reaction forces and moments, but still higher than the experimental values. Thus, another pair of runs were undertaken until the Mooney constants values of C_1= 0.10 and C_2=0.025 gave the best fitting possible, see Figure 3.29.

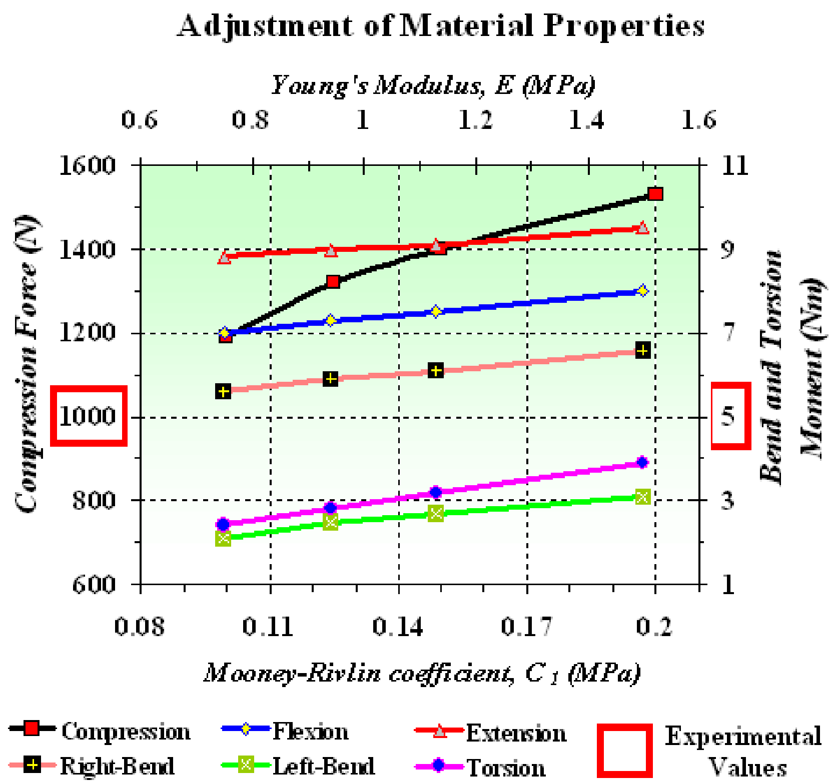

Figure 3.29. Adjustment of annulus fibrosus material properties and comparison with the experimental forces.

Thus, the adjustment of the *Mooney-Rivlin* coefficients of the annulus fibrosus and nucleus pulposus gave the values shown in Table 3.11.

Table 3.11. Annulus fibrosus and nucleus pulposus adjust material properties.

Disc material	*Mooney-Rivlin coefficients (MPa)*		*Young's Modulus E (MPa)*	*Poisson ratio ν*	*Bulk Modulus K (MPa)*
	C_1	*C_2*			
Annulus Fibrosus	0.1	0.025	0.75	0.4999	2200
Nucleus Pulposus	0.0666	0.0166	0.50	0.4999	2200

Further lowering the constants C_1 and C_2 may give better results, but their significance is meaningless since they fail to fall into the range of stiffness values used in the literature: Smit et al. (1996), Pitzen et al. (2002), Goel et al. (1995), Eberlain et al. (2000) y Schmidt (2007).

c. Simulation in compression

Once the disc materials properties were adjusted, then a simulation run with a displacement step in compression was done to check strains and stresses. Of these, the main or principal strains and stresses were calculated along the entire disc volume as these define the state of stress of the disc materials. Also, the bulging in the radial direction was investigated as large strains are expected with a non linear material behavior, typical of biological tissues. The initial run consisted of a disc compression of 1.434 mm in the vertical direction, which caused large negative stresses (compression) and radial bulging along the disc periphery with irregular distributions.

i. Radial bulge

In the experimentation, the axial compression caused a radial bulging at the posterior and anterior side. The magnitude varied from disc to disc, and also with the amount of disc degeneration. Results from the compression simulation shows a bulging magnitude increase by four times that of the experimentation. A maximum bulging of 3.2 mm occurred at the anterior side, while a minimum of 2.2 mm occurred at the left lateral side, see Figure 3.30.

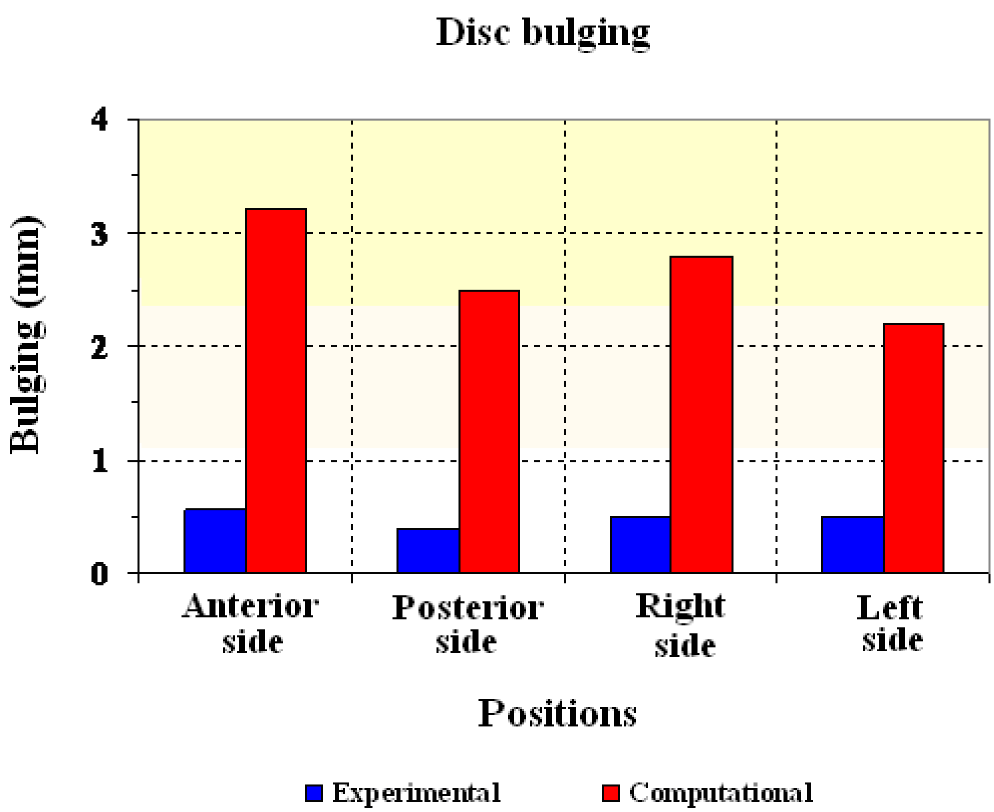

Figure 3.30. Comparison of disc bulge between simulation and experimentation. The large differences suggest that the Young's modulus used for the annulus fibrosus was low due to the absence of fiber modelization.

Bulging distribution in the saggital and coronal planes shows that the majority of the bulging took place at the anterior side where the annulus thickness and its height is greater. While only a small region at the posterior side bulge, due to the thinner annulus. A more symmetrical bulge occurred between the right and left lateral sides, as seen by the cuts in the saggital and coronal plane of Figure 3.31. In the nucleus pulposus the radial bulge had the smallest value, as expected, while in the inner annulus the bulge grew up to 2 mm, and up to 3 mm at the outer layers. These large radial displacements contrasted with the ones from the bone structures, which remained intact, having a near zero value.

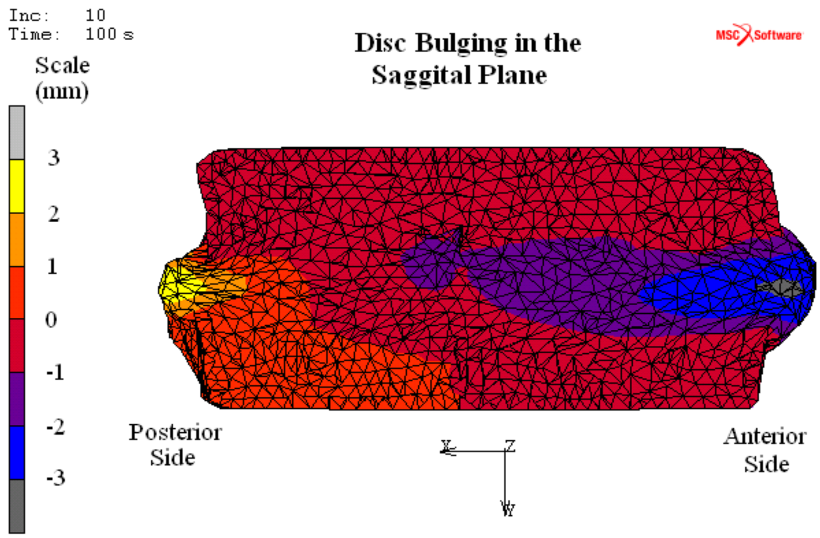

(a)

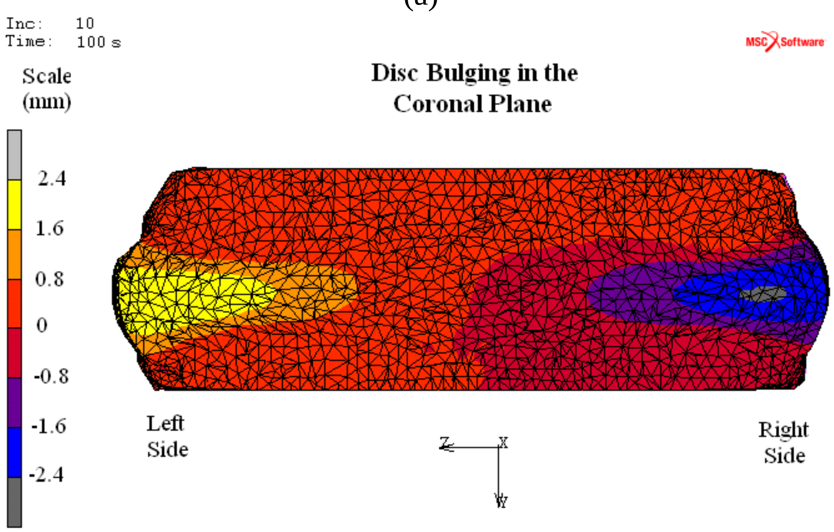

(b)

Figure 3.31. Computational simulation of disc bulging in the (a) anterior-posterior and (b) right-left directions of the L2-L3 disc degeneration model. Observed the symmetrical distribution in the coronal plane view over that in the saggital view, were the thicker section of the anterior side bears most of the bulging.

ii. Intervertebral disc strains

Upon compression, the lower stiffness of the nucleus pulposus and annulus fibrosus led to larger deformations than those of the adjacent trabecular, and cortical bone, see Figure 3.32. The differences in the principal strains between the disc and bone tissues where as high as two orders of magnitude. Strain distribution in the FE mesh shows that the cortical bone deformation was below a 0.25% and the cancellous bone just over 1%, in contrast with the deformation of the disc which reaches values over 40%.

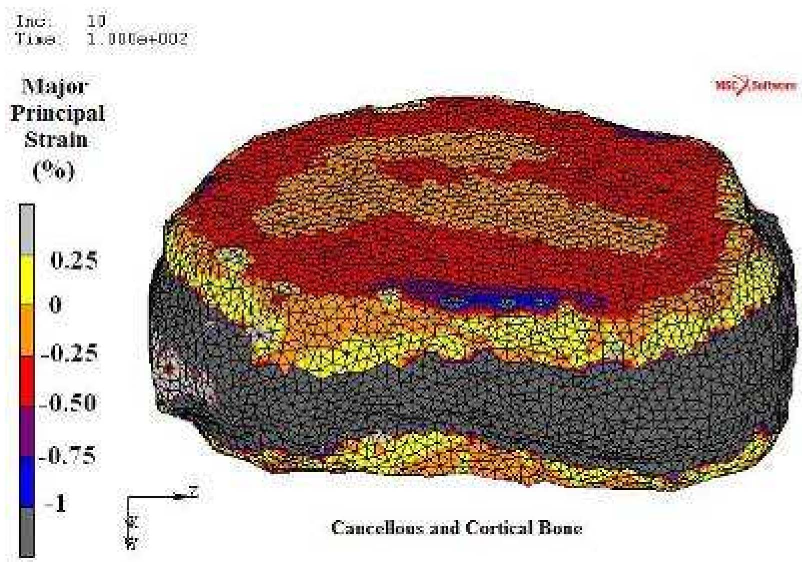

(a)

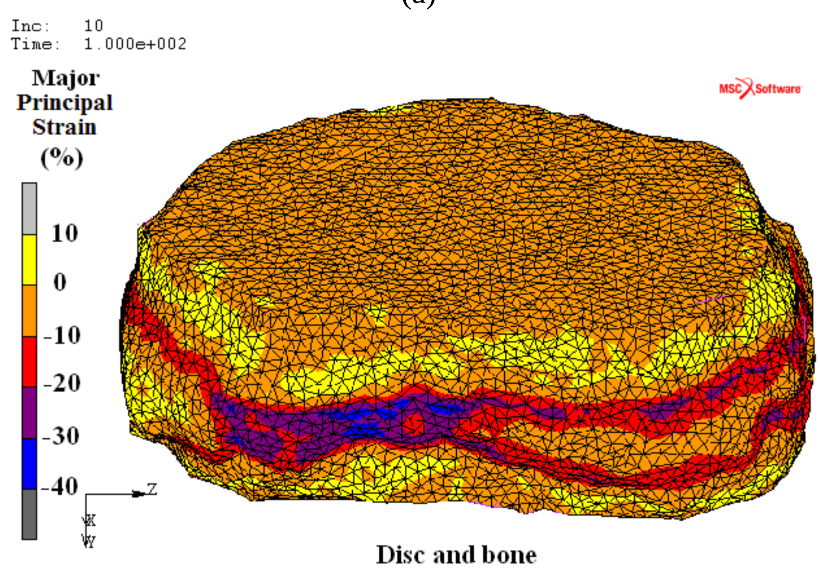

(b)

Figure 3.32. Major principal strain distribution in the L2-L3 model of disc degeneration at the posterior side in (a) vertebral bone and (b) the intervertebral disc with adjacent vertebral bone.

The highest strains in the disc occurred near the boundaries of the nucleus pulposus and annulus fibrosus, where cavities were assigned based in the MRI. The amount of these voids in the FEM disc model was limited to 119 tetrahedral elements, which represented the vacuum phenomena seen in the MRI. Thus, these sites showed a 55% deformation, as shown by the saggital and coronal plane views, see Figure 3.33.

As shown, the mid-section of the nucleus seen in orange, is deformed in compression between 15 and 25%. A larger deformation occurred at the nucleus-annulus boundary which range from 25 to 45% in part due to voids in the disc model. Shown in gray are the cortical and cancellous bone strains which actually deform below 1%.

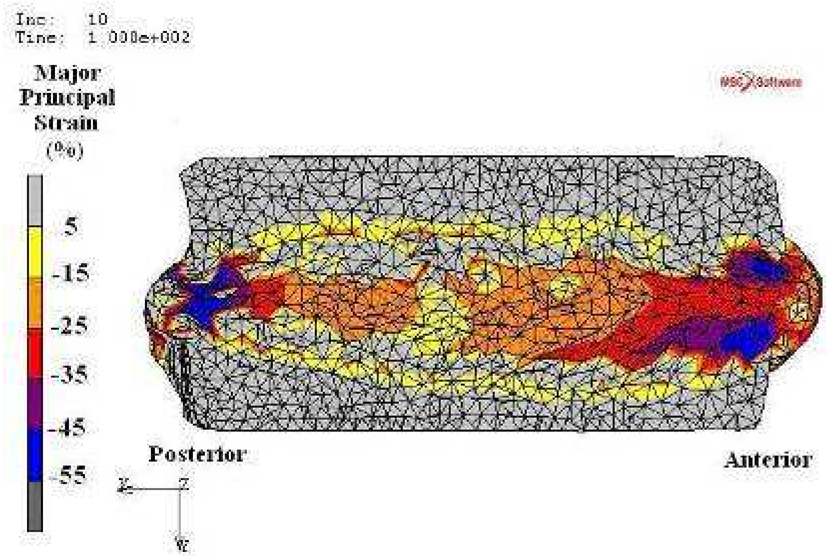

(a)

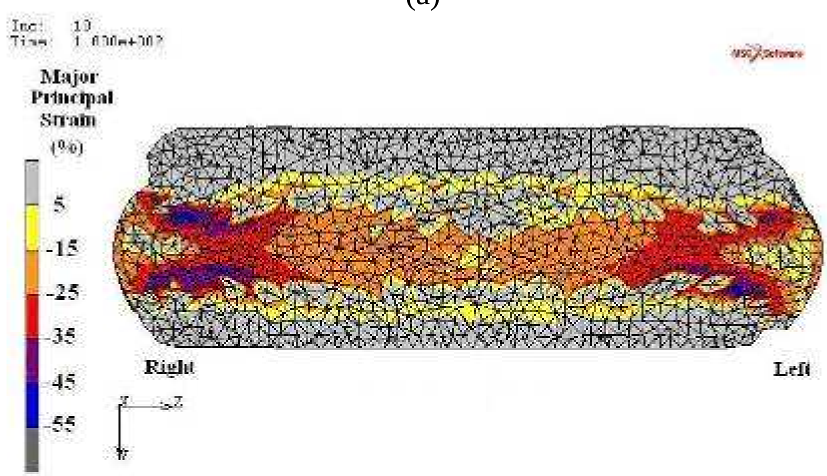

(b)

Figure 3.33. Major principal strain distribution in the L2-L3 disc model along the (a) saggital plane and (b) coronal plane. The highest strains occurred along the boundaries between the nucleus pulposus and annulus fibrosus were also voids appeared in the MRI.

When isolating the nucleus pulposus, the FE strain distribution showed a radial growth with all the mesh elements having negative strain values. The deformation type calculated was an axial strain which was associated with the applied displacement step. The strain values ranged from a minimum at the nucleus center, to a maximum value of -40% located at its posterolateral side, with most of the nucleus periphery having a uniform negative strain, ranging from -16% to -32%. A comparison of the strains between the computational simulation and the experimentation results, shows that the strain of the intervertebral disc as a unit obtained with the testing protocol, falls between the stiffer bone tissues and the softer nucleus and annulus, see Figure 3.34.

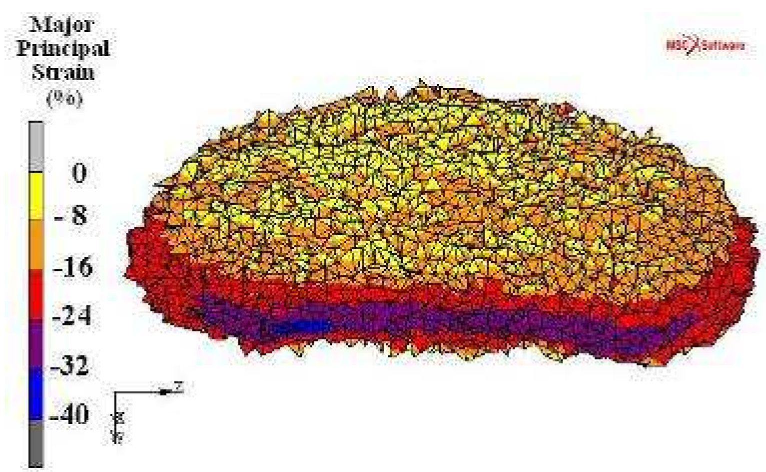

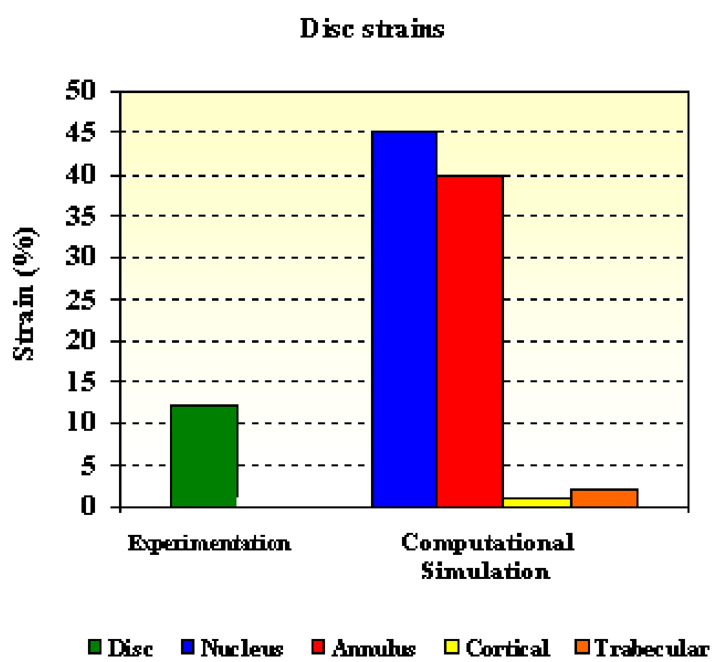

Figure 3.34. Major principal strain distribution in the nucleus pulposus. The highest strains occurred along the disc posterior side. Above is a comparison between the strains from the compression testing protocol and those from the FEA simulation.

In the annulus fibrosus, the FE strain distribution showed a ring-like appearance with a radial growth. The mesh distortion included positive and negative strains with values ranging from +10% to -40%. As with the nucleus pulposus, the larger strains were negative and located at the posterolateral side of the annulus inner wall, where contraction strains between -20% and -40% developed. In contrast, the annulus outer walls at the anterior side showed the highest positive strains, see Figure 3.35.

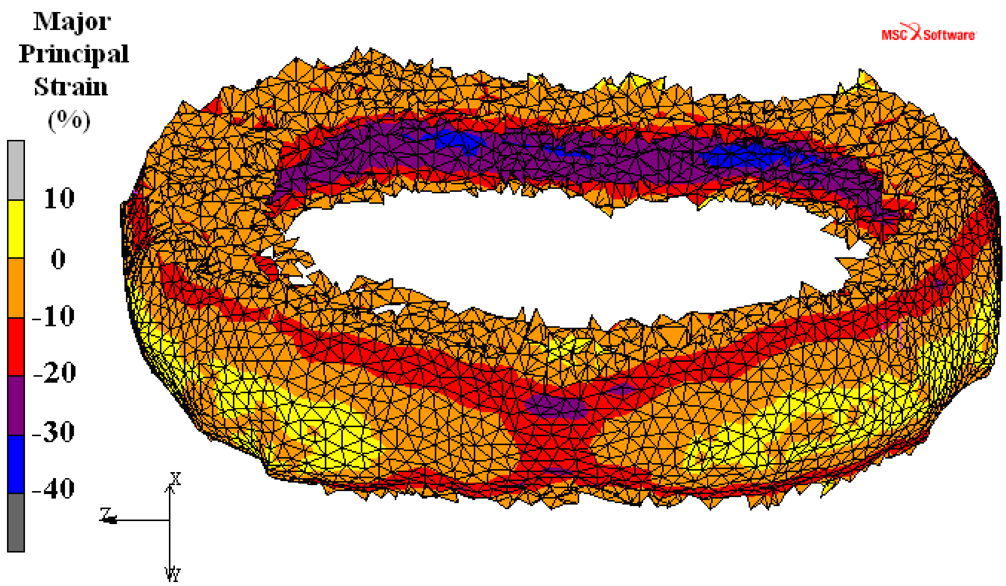

(a)

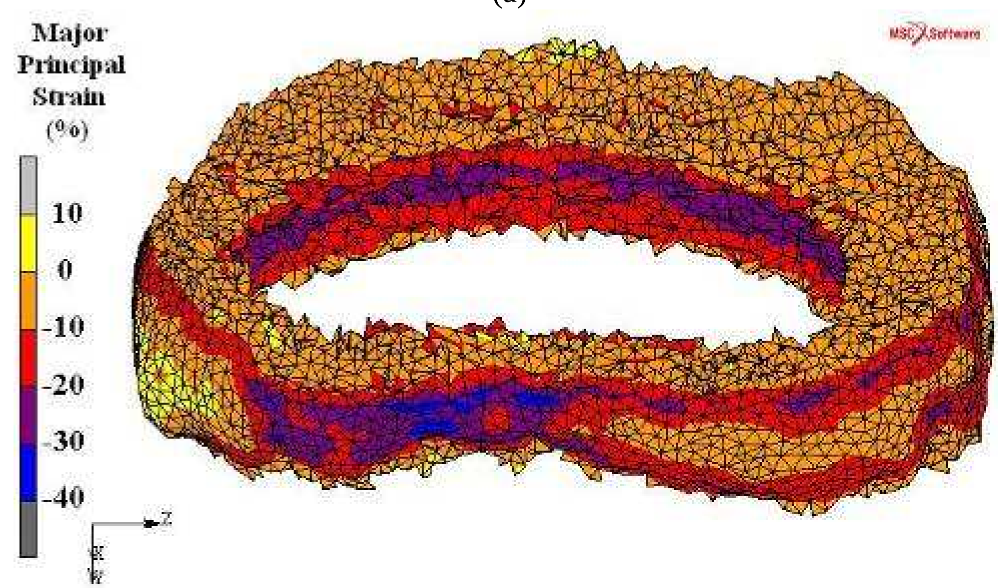

(b)

Figure 3.35. Major principal strain distribution in the annulus fibrosus. The highest strains were located at the posterior side, where the annulus wall is thinner, with deformation values reaching 40%.

iii. Intervertebral disc stresses

The displacement step in the FE disc model caused stresses, of which the most relevant are the *principal stresses* σ_1, σ_2, σ_3 as they represent the largest normal stresses develop, according to section 2.III.j. Shown in Figure 3.36 are the major principal stresses σ_1 and σ_3 in the cortical bone shell with values reaching over 4 MPa in traction (shown on light gray) and also reaching over 8 MPa in compression (shown on dark grey), respectively. As shown, the posterior and posterolateral disc side concentrate these high stresses in a wide zone in comparison with the anterior side. In contrast, the mid section where the disc is located, the major principal stresses σ_1 and σ_3 fell in between ± 2 MPa, which were lower than those in the stiffer bone structures.

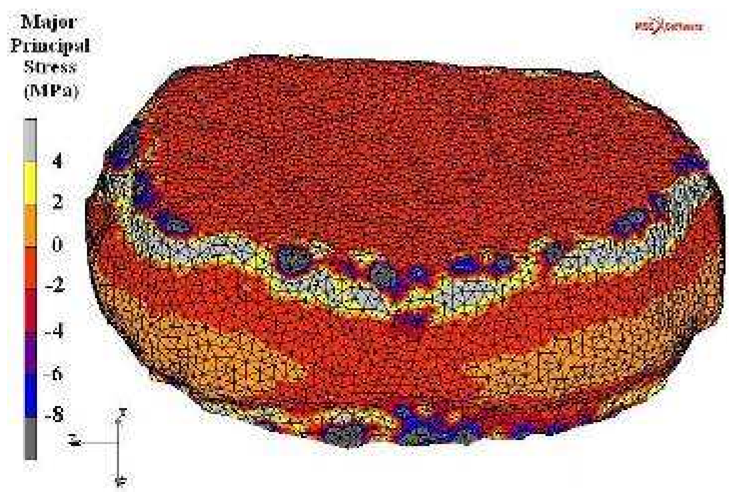

(a)

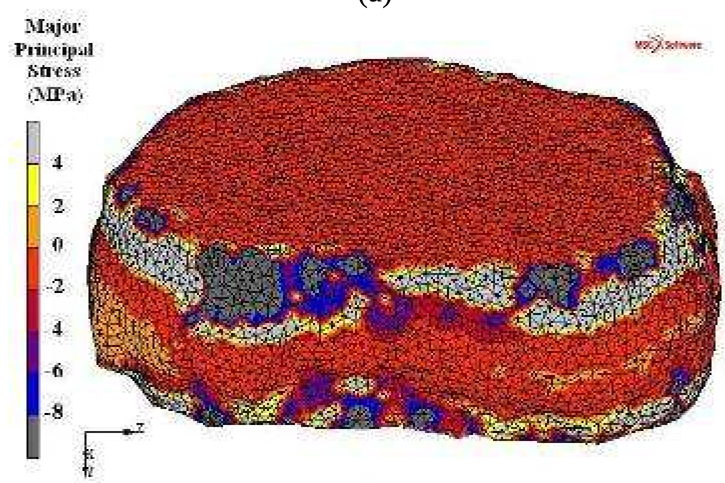

(b)

Figure 3.36. Major principal stress distribution in the L2-L3 model of disc degeneration. A positive sign means a stress in traction, and a negative sign means a stress in compression. The highest stress areas were along the posterolateral side.

When isolating the nucleus pulposus, the principal stress distribution shows a clear negative stress state around the entire nucleus. The principal stresses reached maximum values of 1 MPa in compression, which were located at posterior side. For the rest of the nucleus pulposus the stresses fell in between -0.4 and -0.6 MPa. A comparison between the stresses of the intervertebral disc obtained with the testing protocol, and those from the intervertebral disc materials: nucleus pulposus and annulus fibrosus obtained from the computational simulation, leads to a large difference, being as high as 4 times in the latter procedure, see Figure 3.37.

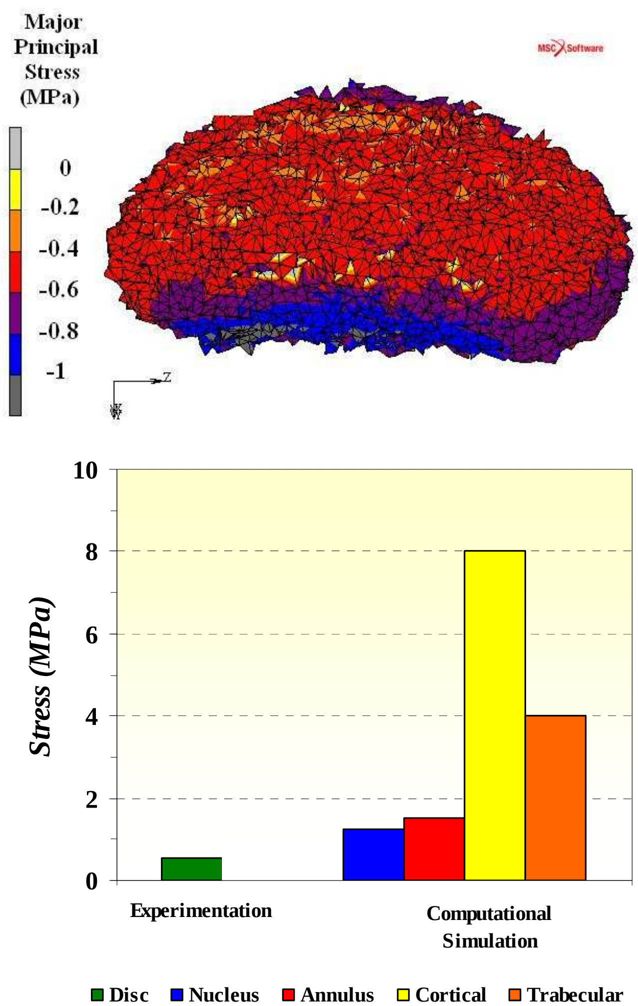

Figure 3.37. Major principal stress distribution in the nucleus pulposus with the overall state of stress in compression, and comparison between the stresses from the mechanical testing and those from the FEM analysis.

The principal stress distribution in the annulus fibrosus shows a ring-like appearance with positive and negative stresses. However, the highest stresses were in compression, and occurred at the outer and inner wall of the posterior side of the annulus, with values reaching -2 MPa and -1.25 MPa, respectively. While the rest of the annulus showed stresses values that fall in the range between + 0.25 and – 1.25 MPa, see Figure 3.38.

The highest traction stresses occurred along the upper and lower rim of the boundary between the annulus and the cortical shell, were stresses up to 0.5 MPa developed. However, the largest zone of traction stresses was the outer wall of the annulus anterior side, where stresses of 0.25 MPa developed, see Figure 3.38.

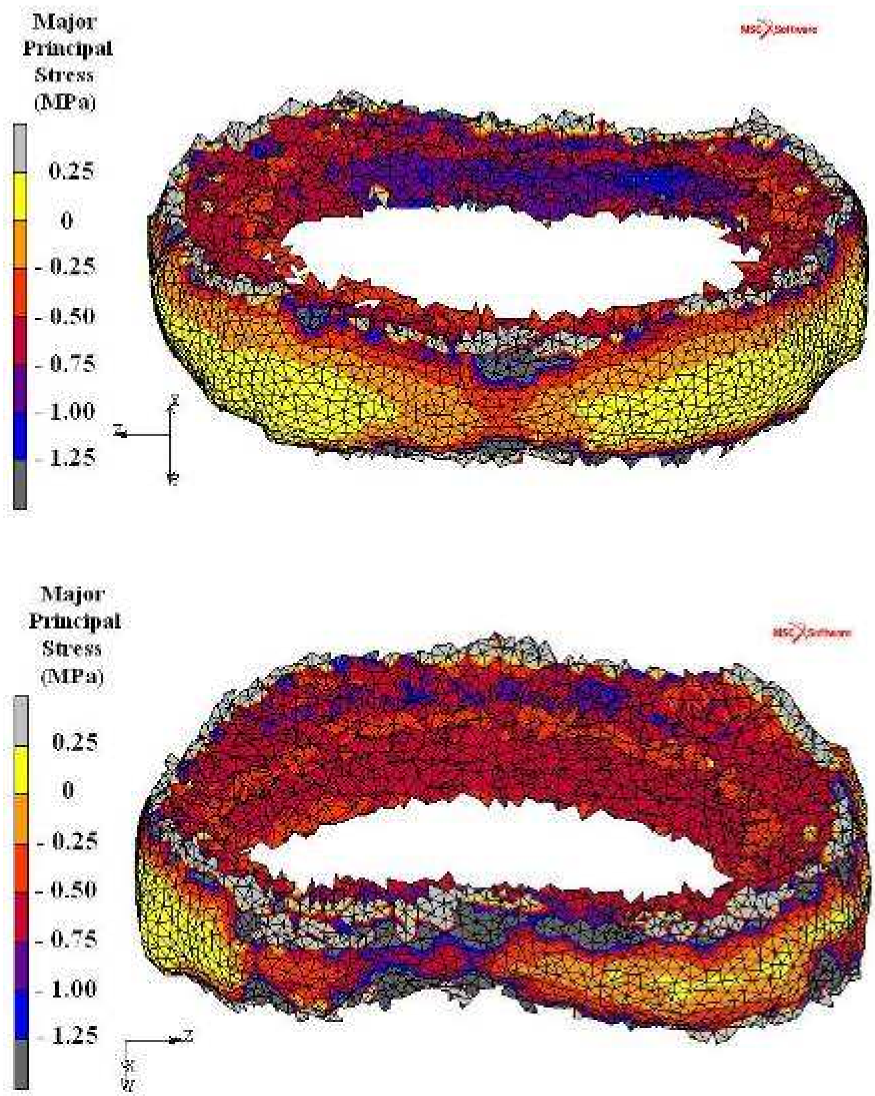

Figure 3.38. Major principal stress distribution in the annulus fibrosus. The highest stresses were located at the posterior side, where the annulus wall is thinner, with compressive tensions reaching up to -2 MPa.

d. Simulation in flexion-extension, right-left bending, and axial rotation (torsion)

The bending simulations in flexion, extension, right and left lateral bending, and axial rotation (torsion) to the L2-L3 disc model were also subjected to a displacement step procedure, according with the results from the experimental protocols, which are summarized in Table 3.10. Of these, the first simulation done was in flexion with an eccentric anterior axial displacement of 5.76 mm downward and applied at the anterior side, see Figure 3.39. Loading in extension, right and left lateral bending used also an eccentric downward axial displacement, with values of 5.80 mm, 4.54 mm, and 3.73 mm respectively, and applied at the arm levers of the disc posterior side, right side, and left side, respectively. While in the simulation of torsion, the 9.84 mm displacement step was applied tangentially to the disc cross section (in the X and Z directions) at the free end of each of the four lever bars, see Figure 3.39.

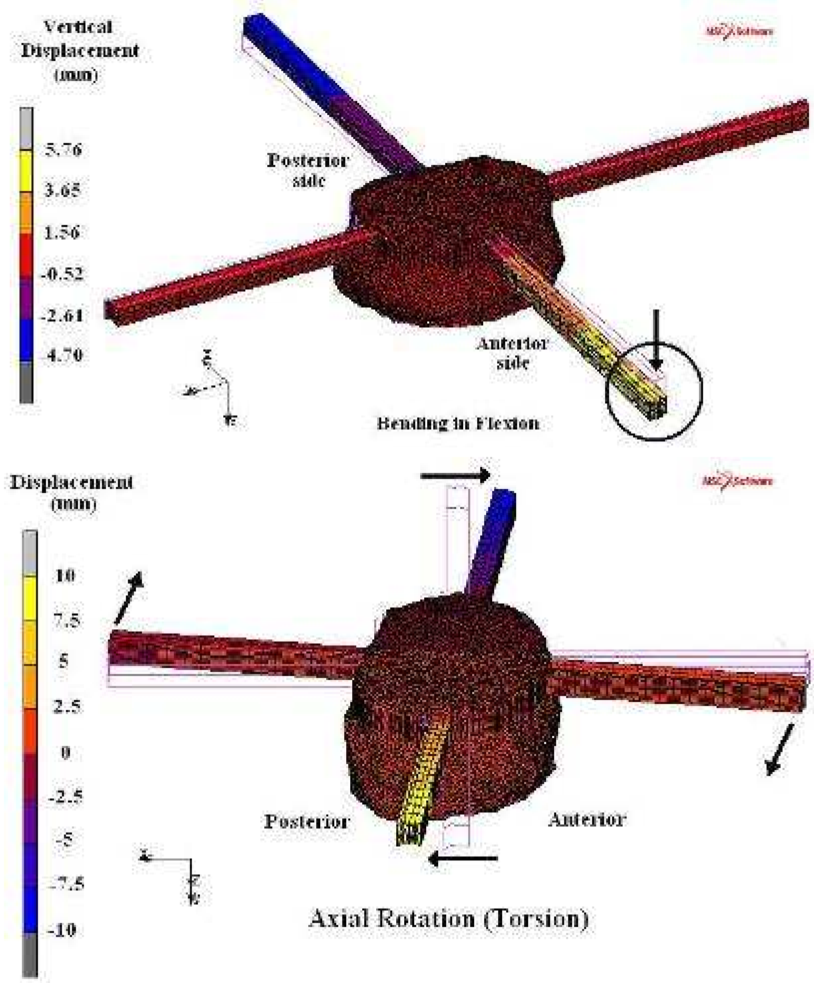

Figure 3.39. Step displacement procedure for simulations of bending (flexion) and torsion in the L2-L3 disc degeneration model.

In bending loading, such as flexion, extension and lateral bend, the stresses generated over the disc cross section are known to be in compression at the disc side of the applied moment, and in traction at the opposite side. A different case result when loading in torsion, where the stresses generated over the disc cross section are known to be in shear, and reach a maximum value at the outer walls of the annulus fibrosus. Since bending cause opposite normal stresses, and torsion cause shear, then the resulting stress distribution across the disc and inside the soft tissues is relevant. Also, high stresses develop near the areas of the applied loading or deformation, and such occurrence was evident from the testing protocols. Thereby, the strains and stresses developed inside the intervertebral disc by bending and torsion loading are presented next, with attention to the nucleus pulposus and annulus fibrosus as these materials have shown large deformations.

i. Intervertebral disc strains in flexion-extension, right-left bending and torsion

The results from the bending and torsion simulation shows that the intervertebral disc is exposed to large deformations, in comparison with those from the vertebrae bone, which deform less than -1%.

In the flexion mode, the model was subjected mostly to negative strains, with values reaching up to -18% at the anterior side where large areas of contraction appeared, as these elements are the closest to the applied step displacement. In the extension mode, the disc central and posterior elements showed large strain values ranging between -10% and -18%, which were more than those elements from the disc anterior side, which deformation only reached -11%, see Figure 3.40. For the lateral right and left bending modes, the disc model strain distribution showed the same tendency, the larger strains occurred at the loading side and were -20%, while at the opposite side the elements deform less than 1% negative, see Figure 3.40. The torsion simulation showed that most of the model was subjected to large strains which reach up to 30%, while the bony structures deform below 1%. The larger strains took place at the outer walls of the annulus fibrosus, see Figure 3.40.

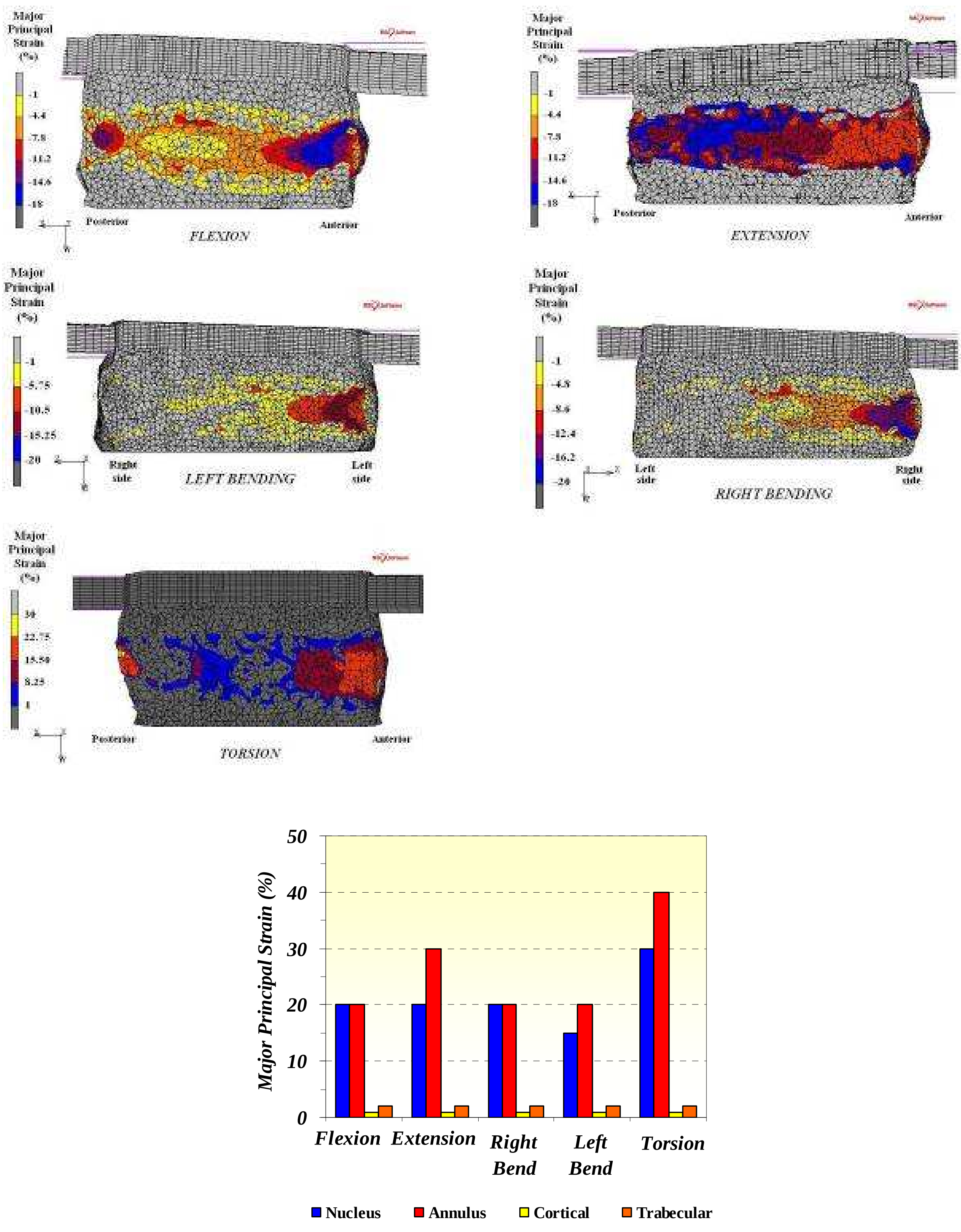

Figure 3.40. Major principal strain distribution in the L2-L3 disc degeneration model for loading simulations in flexion, extension, right and left lateral bending and torsion.

When isolating the nucleus pulposus, the strain distribution for all bending modes showed a transition from a negative strain (at the side of the displacement step) to a positive strain at the opposite side, with the appearance of a neutral axis in between. In the forward flexion and in the backward extension simulations, the largest principal strains reached a 20% value and were located at the anterior and posterior sides, respectively, see Figure 3.41. A significant difference between both distributions was the appearance of a larger area of positive strains at the posterior side in the flexion simulation, which did not occur at the opposite side in the extension simulation. The bending simulation to the right and left lateral sides gave similar tendencies, with the largest principal strains also reaching a 20% value, and located at the right and left sides, respectively, see Figure 3.41. The neutral axis ran from the right to the left side when bending in flexion-extension, and ran from the anterior to the posterior side when bending laterally. For the torsion simulation, the presence of adjacent opposite strains suggest that a shear strain was involved, which was mostly seen at the nucleus periphery. Thus, the maximum strain occurred in shear with values reaching 30%, while the principal strains only reach a 20% value. In both distributions, the strain showed a radial growth from zero at the nucleus center to a maximum at the periphery, see Figure 3.41.

The strain distribution in the annulus fibrosus also showed a transition from a negative strain (at the side of the displacement step) to a positive strain at the opposite side, with the appearance of a neutral axis in between. In the forward flexion and in the backward extension simulations, the largest principal strains reached a 30% value and were located at the outer anterior and posterior sides, respectively, see Figure 3.42. Also, the annulus posterior side developed large areas of positive strains or stretching upon simulation of the flexion load. The bending simulation to the right and left sides also showed large strains, which reached a 20% value located at the inner right and left sides, respectively, see Figure 3.42. The lateral bending simulation showed the neutral axis running from the anterior to the posterior side, while in the flexion-extension simulation the neutral axis ran from the right to the left side. For the torsion simulation, the shear strain was maximum with values reaching 40% at the annulus outer wall, while the principal strains reach only a 24 % value, see Figure 3.42.

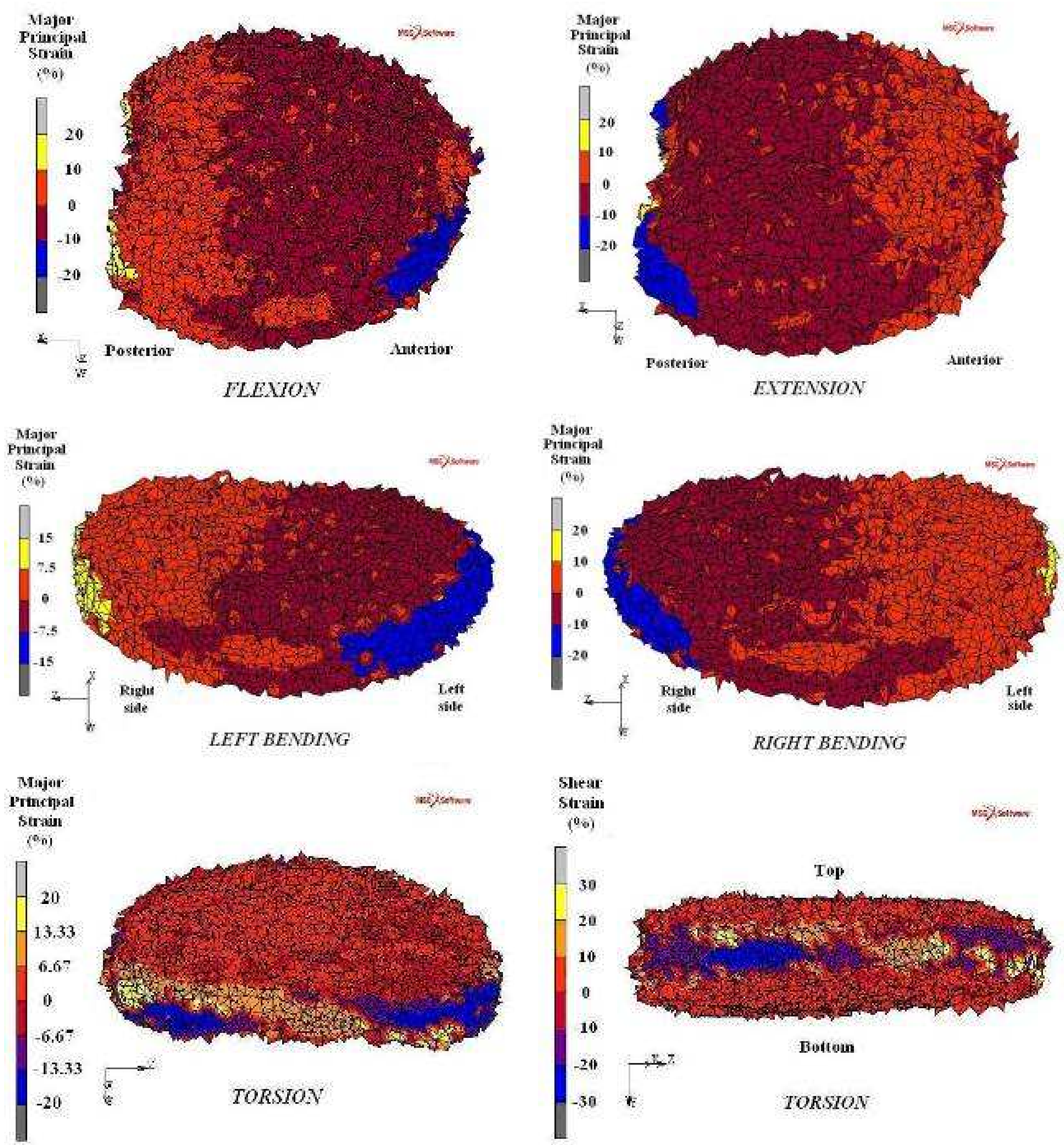

Figure 3.41. Major principal strain distribution in the nucleus pulposus for loading simulations to flexion, extension, right and left lateral bending and torsion, and shear strain distribution for torsion.

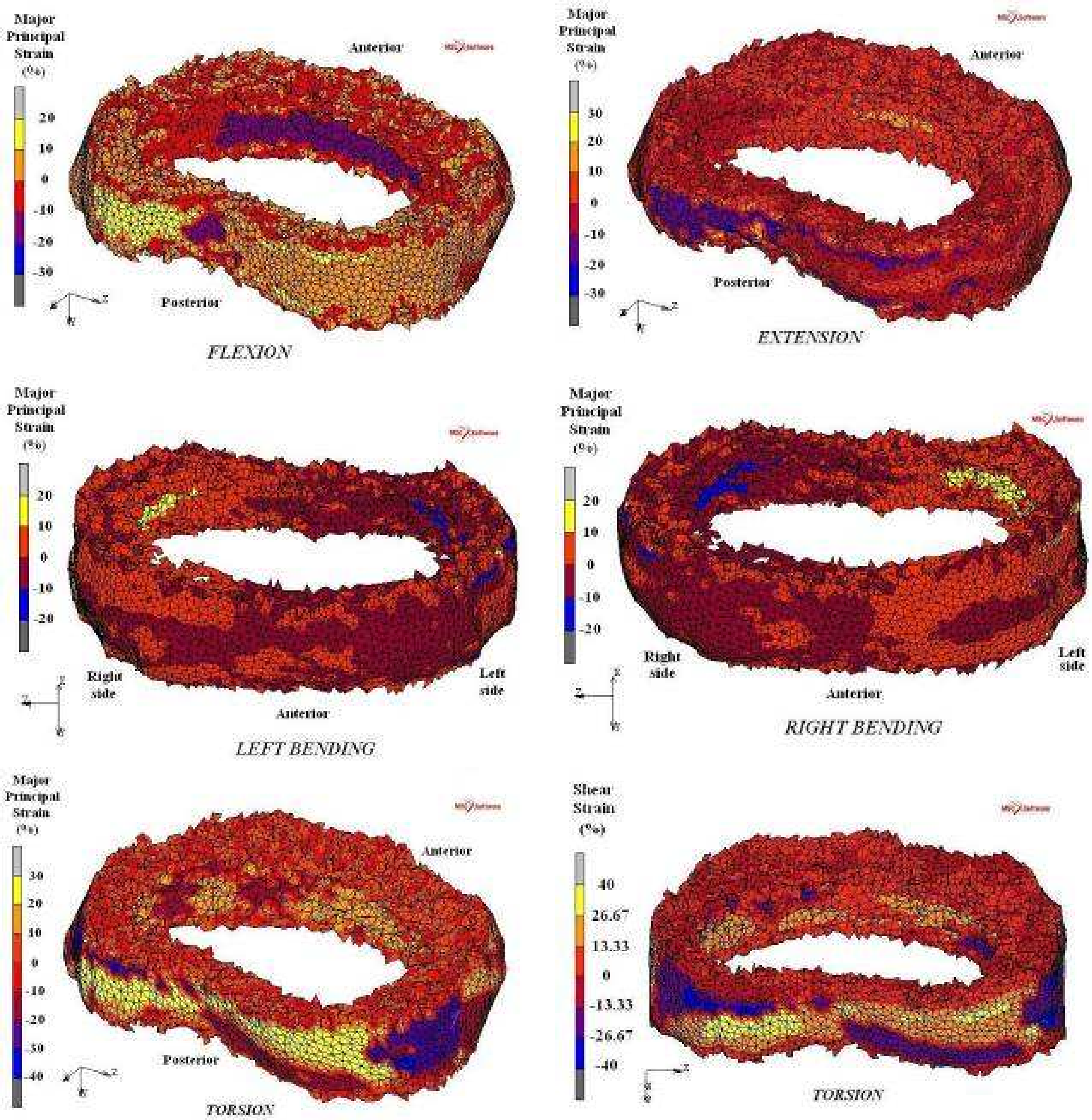

Figure 3.42. Major principal strain distribution in the annulus fibrosus for loading simulations to flexion, extension, right and left lateral bending and torsion, and shear strain distribution for torsion.

ii. Intervertebral disc stresses in flexion-extension, right-left bending and torsion

Results from the bending and torsion simulations showed symmetrical stress distribution between the flexion and extension modes, and also between the right and left lateral bending modes. Also, the stiffer cortical and trabecular bone developed higher stresses, with values reaching 3 and 1.5 MPa, respectively. While in the intervertebral disc, the principal stresses reached only 0.50 MPa. The stress distribution for all loading modes showed a transition of compressive stresses (at the side of the displacement step) to tensile stresses at the opposite side. The neutral axis also ran from the right to the left sides when simulating bending in flexion-extension, and ran from the anterior to the posterior sides when bending to the right or to the left sides, see Figure 3.43.

In the flexion mode simulation, the principal stress distribution showed that the disc model was mostly stressed to compression at the anterior side, with values reaching 0.30 MPa, while at the disc posterior side, traction stresses developed, but only reach 0.20 MPa. In the extension mode simulation, the disc central and posterior areas were the most stressed to compression with values also reaching 0.30 MPa. The lateral right and lateral left bending simulations caused a stress distribution which were higher at the loading side, with values of 0.25 MPa and 0.30 MPa, respectively. The torsion simulation showed that most of the disc model was subjected to shear strains which reach only 0.125 MPa and located at outer walls of the annulus fibrosus, see Figure 3.43.

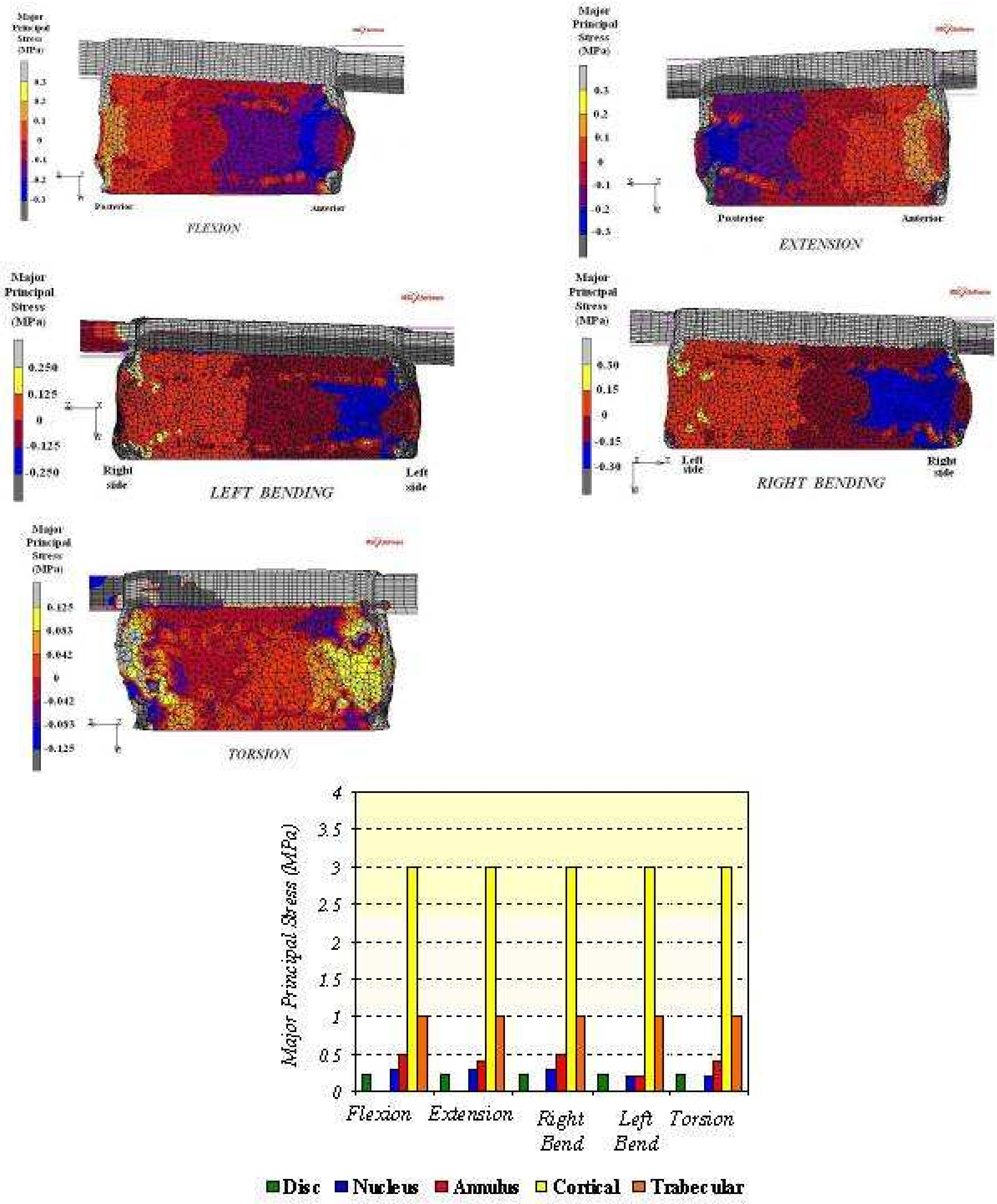

Figure 3.43. Major principal stress distribution in the L2-L3 disc degeneration model for loading simulations in flexion, extension, right and left lateral bending, and torsion. Also shown is a comparison between the disc principal stresses from the mechanical testing and those from the FEM analysis.

When isolating the nucleus pulposus, the stress distribution for all bending modes showed a transition from a compressive stress (at the side of the displacement step) to a tensile stress at the opposite side, with the appearance of a neutral axis in between. In the forward flexion and in the backward extension simulations the principal stresses ran along the nucleus anterior-posterior, or saggital direction with values ranging from -0.30 MPa to 0.20 MPa. The flexion simulation showed large areas of tensile stresses located at the nucleus posterior side; whereas in the extension simulation only a small fraction of the nucleus anterior side was in tension, see Figure 3.44. The bending simulation to the right and left sides gave similar tendencies, with the largest principal stresses occurring at the nucleus right and left lateral sides, with values of 0.20 MPa for both simulations. However, in the left bending simulation the nucleus opposite side showed a large area of tensile stresses of 0.20 MPa, whereas in the right bending simulation only a small fraction of the nucleus anterior side was in tension, see Figure 3.44. The principal stresses ran along the nucleus coronal direction for both lateral bending simulations. For the torsion simulation, the largest stresses were in shear with values reaching 0.20 MPa, while the principal stresses reach only 0.15 MPa. In both cases the stress distribution showed a growth along the radial direction with no tendency of neutral axis formation, and reached a maximum value at the nucleus periphery, see Figure 3.44.

The stress distribution in the annulus fibrosus also showed a transition from a compression to a tension stress, with a neutral axis in between. In the forward flexion simulation the largest principal stresses reached 0.50 MPa, and occurred at the inner anterior and outer posterior annulus side. For the backward extension simulation the magnitudes of the largest stresses were 0.40 MPa and occurred at the outer posterior annulus. The right and left lateral bending simulations showed a symmetrical stress distribution, with principal stress peaks of 0.20 and 0.50 MPa, respectively, see Figure 3.45. The annulus site where these stresses appeared was the inner wall at the lateral sides. For the torsion simulation, the largest stresses reached 0.40 MPa being normal principal and also shear, both occurred at the annulus posterior side, see Figure 3.45.

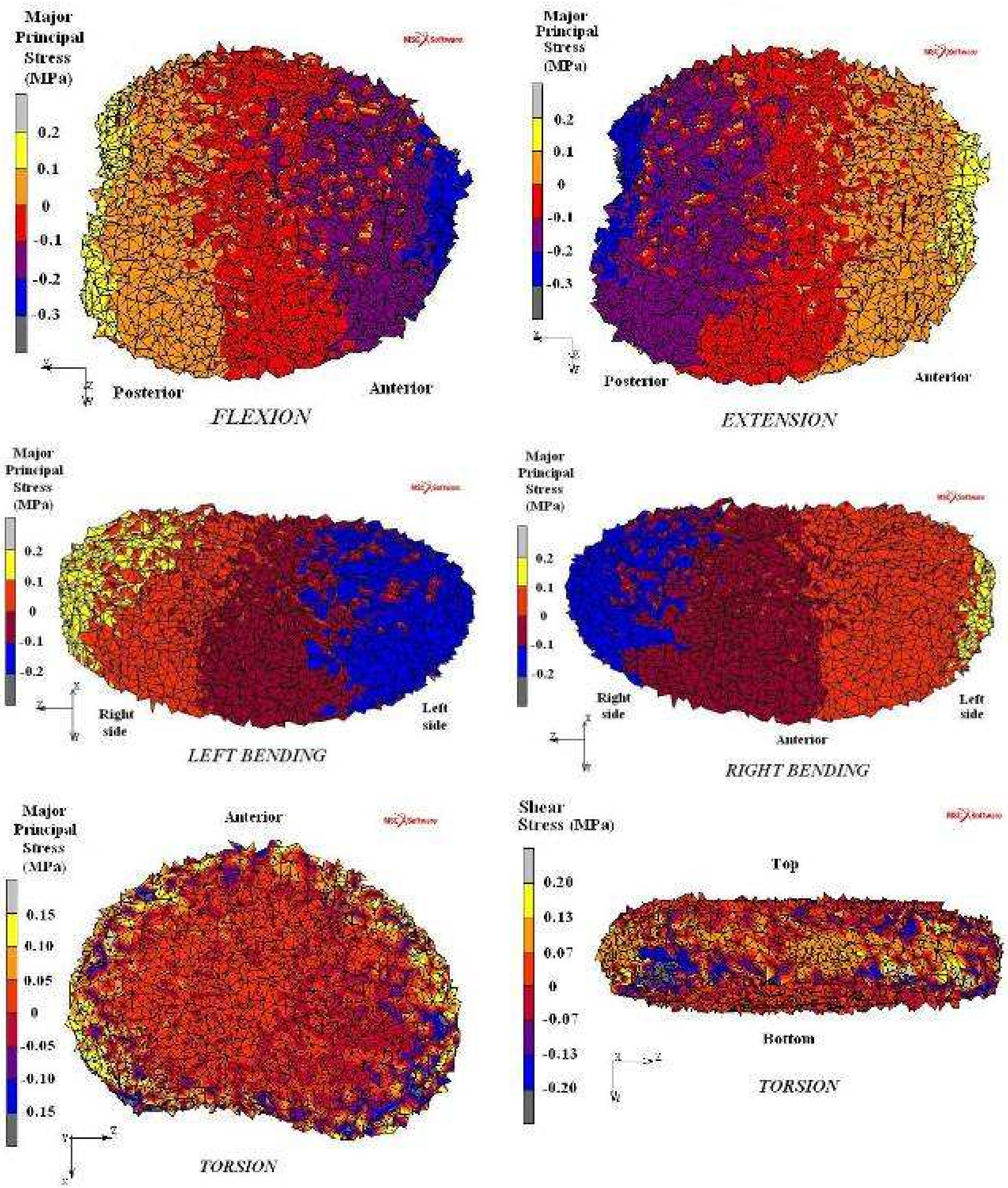

Figure 3.44. Major principal stress distribution in the nucleus pulposus for loading simulations in flexion, extension, right and left lateral bending and torsion, and shear stress distribution for loading in torsion.

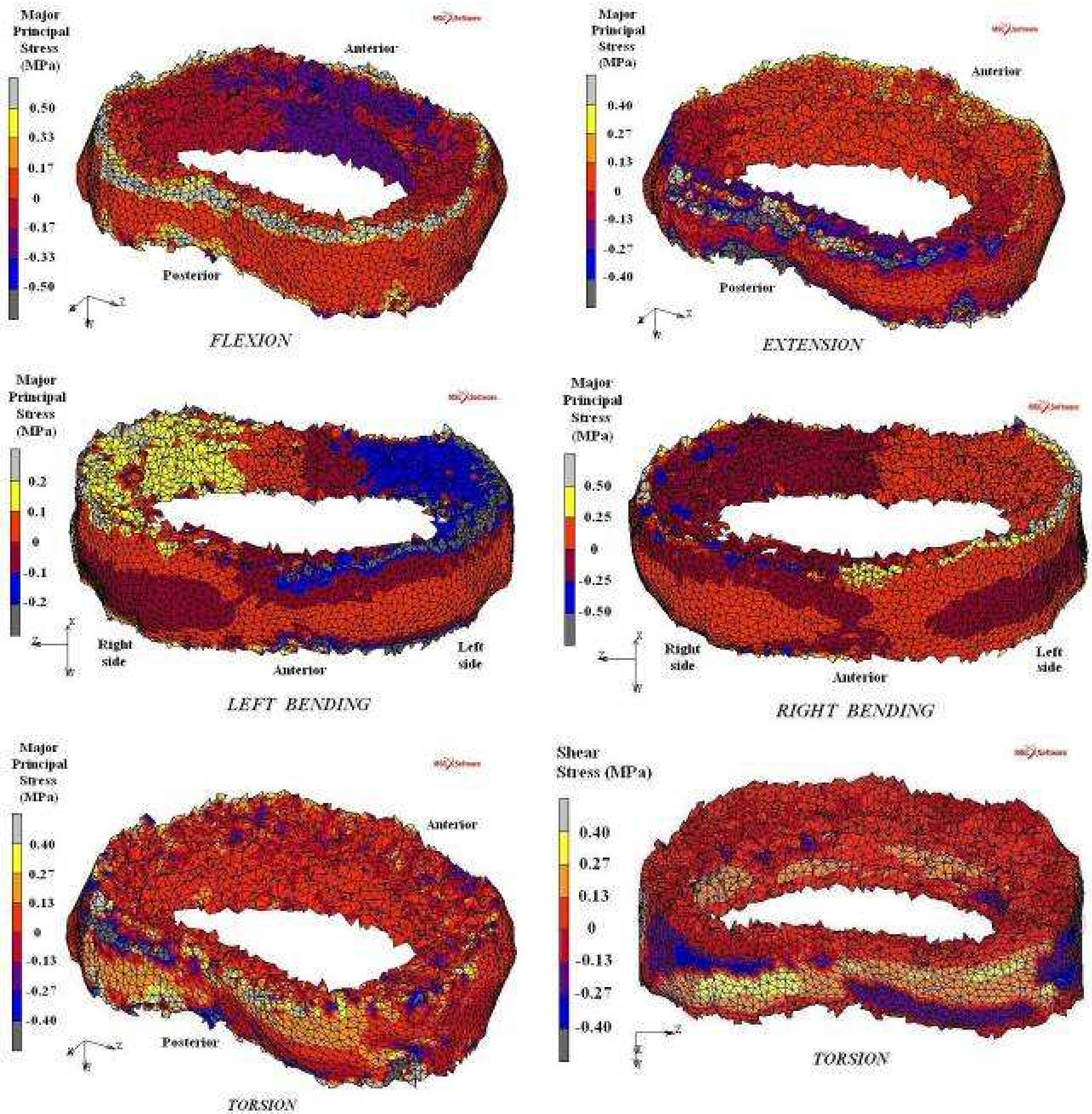

Figure 3.45. Major principal stress distribution in the annulus fibrosus for loading simulations in flexion, extension, right and left lateral bending and torsion, and shear stress distribution for loading in torsion.

IV. References

Adams, M.A., Hutton, W.C., and Stott J.R. (1980). “The Resistence to Flexion of the Intervertebral Joint”. Spine 5(3): pp. 245-253.

Adams, M.A., and Hutton, W.C. (1981). “The relevance of Torsion to the Mechanical Derangement of the Lumbar Spine”. Spine 6(3). pp.241-248.

Allen KD and Athanasiou KA. (2006). “Viscoelastic characterization of the porcine temperomandibular joint disc under unconfined compression”. Journal of Biomechanics 39: 312-322.

Asano S, Kaneda K, Umehara S and Tadano S. (1992). “The Mechanical Properties of the Human L4-5 Functional Spinal Unit During Cyclic Loading: The Structural Effects of the Posterior Elements”. Spine 17(11) pp. 1343-1352.

Banse X, Sims TJ and Bailey AJ (2002). “Mechanical Properties of adult vertebral Cancellous bone: Correlation with collagen intermolecular cross-links”. Journal of Bone and Mineral Research 17(9): pp1621-1628.

Belytschko, T., Kulak, R.F., Schultz, A.B. y Galante, J. O.(May 1974). Finite element stress analysis of an intervertebral disc. Journal of Biomechanics, Vol 7(3): 277-285.

Berkson, M.H., Nachemson, A. and Schultz A.B. (1979). Mechanical Properties of Human Lumbar Spine Motion Segments. Responses in Compression and Shear; Influence of Gross Morphology. Journal of Biomechanichal Engineering. Vol. 101. pp53-57.

Boos N, Rieder R, Schade V, Spratt KF, Semmer N and Aebi M. (1995). “The diagnostic accuracy of magnetic resonance imaging, work perception, and psychosocial factors in identifying symptomatic disc herniations”. Spine 20(24): pp 2613-25.

Brickley-Parson D and Glimcher MJ (1983). “Is the chemistry of collagen in the intervertebral disc an expression of Wolff’s law? A study of the human lumbar spine. Spine 9. 148-163.

Broberg, K.B. y Essen, H.O. (1980). Modeling of intervertebral disc. Spine 5(2) : 155

Buckwalter JA. (1995) “Aging and degeneration of the human intervertebral disc”. Spine 20:1307-14.

Casey K, MacLean J and Iatridis JC. (2008). “Dynamic compression effects on intervertebral disc mechanics and biology”. Spine 33(13): 1403-1409.

Costi JJ, Stokes IA, Gardner-Morse M, Laible JP, Scoffane HM and Iatridis JC. (2007). “Direct measurement of intervertebral disc maximum shear strain in six degrees of freedom: Motions that place disc tissue at risk of injury”. J. Biomechanics 40(11): 2457-66.

Eberlain R, Gerhard AH and Schulze-Bauer C. (2001). “An anisotropic model for annulus tissue and enhanced finite element analysis of intact lumbar disc bodies”.Computer Methods in Biomechanics and Biomedical Engineering, Vol. 4: pp. 209-229.

Edwards WT, Ordway NR, Zheng Y, McCullen G, Han Z and Yuan H. (2001). “Peak stresses observed in the posterior lateral anulus”. Spine 26(16): 1753-1759.

Farfan H., Cossette JW, Robertson G.H., Wells RV, and Kraus H. (1970). “The effects of Torsion on the Lumbar Intervertebral Joints: The role of Torsion in the Production of Disc Degeneration”. The Journal of Bone and Joint Surgery. Vol. 52-A, No. 3. pp.468-497.

Heuer F, Schmidt H and Wilke H. (2008). “The relation between intervertebral disc bulging and annular fiber associated strains for simple and complex loading”. J. Biomechanics 41. pp 1086-1094.

Heuer F, Wolfrom U, Schmidt H and Wilke HJ (2007). “ A method to obtaing surface strains of soft tissues using a laser scanning device”. J Biomechanics 41 (11): pp. 2402-2410.

Heuer F, Schmidt H, Claes L and Wilke HJ. (2008). “A New laser scanning technique for imaging intervertebral disc displacements and its application to modeling nucleotomy”. Clinical Biomechanics 23(3): 260-269.

Iatridis JC, Weidenbaum M, Setton L and Mow V. (1996). “Is the nucleus a solid or a fluis? Mechanical behaviors of the nucleus pulposus of the human intervertebral disc”. Spine 21(10): 1174-1184.

Izambert D, Mitton D, Thourot M and Lavaste F. (2003). “Dynamic stiffness and damping of human intervertebral disc using axial oscillatory displacement under a free mass system”. European Spine Journal 12: 562-566.

Johannessen W, Vresilovic E, Wright A and Elliott D. (2004). “Intervertebral Disc Mechanics are Restored following Cyclic Loading and Unload Recovery”. Annals of Biomedical Engineering, Vol. 32 No.1, January 2004: pp.70-76.

Kemper A, McNally C, McNeely D, Matsuoka F and Duma S. (2006). “Compressive stiffness properties of human lumbar intervertebral discs and the influence of strain rate”. 30 th annual meeting of the American Society of Biomechanics, Blacksburg, VA, 2006.

Kroker P. (1949). “Sichtbare Rissbildungen in den Bandscheiben der Wirbelsaule“. ROFO 72:p.1

Little JP, Adam CJ, Evans JH, Pettet GJ and Pearcy MJ. (2007). “Nonlinear finite element analysis of anular lesions in the L45 intervertebral disc”. J. Biomechanics 40(12): 2744-2751.

Lu YM, Hutton WC, Gharpuray VM. (1996). Do bending, twisting and diurnal fluid changes in the disc affect the propensity to prolapse? A viscoelastic finite element model. Spine 21: 2570-2579.

Mearkin JR and Hukings. (2001). “ Replacing the nucleus pulposus of the intervertebral disc: prediction of suitable properties of a replacement material using finite element analysis”. Journal of Material Science: Material in Medicine 12(2001): 207-213.

Miller, JA; Schultz AB; Wardwick DN, and Spencer DL. (1986). “Mechanical Properties of Lumbar Spine Motion Segments under Large Loads”. J. Biomechanics 19(1) pp. 79-84.

MSC Marc Mentat (2005). Volume B. Element Library.

MSC Marc Mentat (2005). Volume A. Theory and User Guide.

Nachemson A, Schultz, A and Berkson M. (1979). “Mechanical Properties of Human Lumbar Spine Motion Segments: Influence of Age, Sex, Disc Level and Degeneration”. Spine 4(1): pp. 1-8.

Natali AN, and Meroi EA. (1990). “The mechanical behavior of bony endplate and annulus in prolapse disc configuration”. J. Biomedical Engineering 15: 235-239.

Noailly j. “ Model developments for in silico studies of the lumbar spine biomechanics” (2009). PhD Tesis. Technical University of Catalonia.

Noailly J, Lacroix D and Planell J. (2003). “The mechanical significanse of the lumbar spine components – A finite element stress analysis”. 2003 Summer Bioengineering Conference, June 25-29, Sonesta Beach Resort in Key Biscayne, Florida.

Noailly J, Wilke H-J, Planell J and Lacroix D. “ How does the geometry affect the internal biomechanics of a lumbar spine bi-segment finite element model ? Consequences on the validation process. Journal of Biomechanics 40(11): 2414-2425.

Panagiotacopulos ND, Bloch R, Knauss WG, Harvey P and Patzakis M (1977). “Viscoelastic behavior of the human intervertebral disc under consideration of moisture migration”. Project Report. California Institute of Technology, Pasadena CA USA, Grant No. 77-3139.

Panjabi, M., Krag M.H., White A, and Southwick, W. (1977). “Effects of Preload on Load Displacement Curves of the Lumbar Spine”. Orhopedic Clinics of North America. Vol.8, N. 1. pp 181-193.

Rao A, and Dumas G. (1991). “Influence of material properties on the mechanical behavior of the L5-S1 intervertebral disc in compression: A nonlinear finite element element study”. J. Biomedical Engineering 13: 139-151.

Resnick D. (1994). “Diagnosis of Bone and Joint Disorders: Degenerative Disease of the Spine”. W.B. Saunders. Vol.2, Chapter 35: p.1382-1471.

Rohlmann A, Zander T, Schmidt H, Wilke HJ, and Bergmann G. (2006). “Analysis of the influence of disc degeneration on the mechanical behavior of a lumbar motion segment using the finite element method”. Journal of Biomechanics 39: 2484-2490.

Schmidt H, Kettler A, Rohlmann A, Claes L and WilkeHJ. (2007). “The risk of disc prolapses with complex loading in different degrees of disc degeneration – A finite element analysis”. Clinical Biomechanics, 22(9) pp 988-998.

Schmorl’s C and Junghans H (1932). “Die gesunde und kranke wirbelsaule (The healthy and sick spine) ”. Fortchritte auf dem gebiete der röntgenstrahlen, supplementary volume 43, Leipzig.

Schultz, A.B., Warwick, D.N., Berkson, M.H. and Nachemson, A.L. (1979). “Mechanical Properties of Human Lumbar Spinal Motion Segments Part I: Responses in Flexion, Extension, Lateral Bending, and Torsion. Journal of Biomechanical Engineering Vol. 101: pp 46-52.

Shirazi-Adl, A.A., Shivasta, S.C. y Ahmed, A.M., (1984). Stress analysis of the lumbar disc-body unit in compression: A three-dimensional nonlinear finite element study. Spine 9(2): 120-134.

Shirazi-Adl, A.A., Ahmed, A.M. y Shivasta, S.C. (1986). Mechanical response of a lumbar motion segment in axial torque alone and combine with compression. Spine 11(9): 914-927.

Shirazi-Adl , A. A., Ahmed M. and S. C. Shrivastava. (1986). A finite element study of a lumbar motion segment subjected to pure sagittal plane moments. Journal of Biomechanics, Vol 19(4):331-350.

Smit, TH, Odgaard A and Schneider E (1997). “Structure and function of vertebral trabecular bone”. Spine 22, pp 2823-2833.

Smit TH. (1996). “The mechanical significance of the trabecular bone architecture in a human vertebra (Ingenieur) ”. PhD Thesis. Technische Universitat Hamburg-Harburg, Hamburg-Harburg, pp. 49-53.

Spilker R.L., Daugirda, D.M. y Schultz A.B. (1984). Mechanical response of a simple finite element model of the intervertebral disc under complex loading. Journal of Biomechanics, Vol. 17(2): 103-112.

Stokes I. (1987). “Surface strains on human intervertebral discs”. Journal of Orthopeadic Research 5(3): 348-55.

Tanaka N; An HS; Lim T; Fujiwara A; Jeon C; and Haughton V. “The relationship between disc degeneration and flexability of the lumbar spine”. The Spine Journal, Vol. 1(1): pp. 47-56.

Tanaka E, Aoyama , J, Tanaka M, Murata H, Hamada T and Tanne K. (2002). “Dynamic Properties of Bovine Temporomandibular Joint Disks Change with Age”. Journal of Dentresty Research 81(9): 618-622.

Ueno, K. (1987). A three dimensional nonlinear finite element model of lumbar intervertebral joint in torsion. Journal of Biomechanical Engineering. 109: 200-209.

Viera, A and Garret J. (2005). “Understanding Interobserber Agreement: The Kappa Statistic”. Family Medicine. Vol. 37, No.5 p. 360-363.

Wang, Jaw-Lin, Parnianpour, Mohamad, Shirazi-Adl, Aboulfazl, y Engin, Ali E. (Feb 2000). Viscoelastic Finite-Element Analysis of a Lumbar Motion Segment in Combined Compression and Sagittal Flexion: Effect of Loading Rate. Spine. 25(3):310-318.

Wehrli FW, Leonard MB, Saha PK and Gomberg B. (2004). “Quantitative high resolution magnetic resonance imaging reveals structural implications of renal osteodystrophy on trabecular and cortical bone”. Journal of magnetic resonance imaging 20: 83-89.

Yamamoto, I, Panjabi, M., Crisco T and Oxland T. (1989). “Three-Dimensional Movements of the Whole Lumbar Spine and Lumbosacral Joint”.Spine 14(11). Pp. 1256-1259.

Zheng W and Haiyun L. (2005). “A novel 3D finite element modeling based on medical image for intervertebral disc biomechanical analysis”. Proceedings of the 2005 IEEE Engineering in Medicine and Biology 27 th Annual Conference, Shanghai, China September 1-4, 2005.

Chapter 4

Discussion

Chapter 4

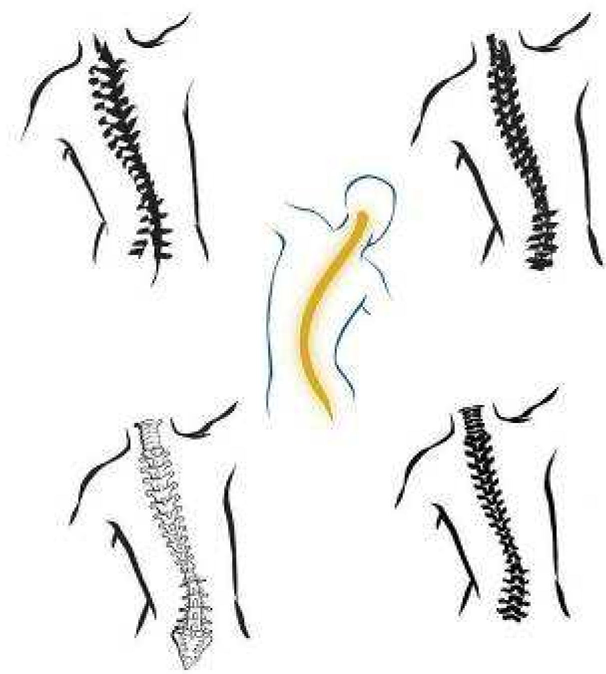

Discussion

I. Testing results

a. Analysis of disc stiffness and bulging

The results show that the stress-strain (σ-ε) relationship is highly nonlinear, which are characteristical of soft biological tissues. This is in part because of the behavior of the long polymeric chains in the collagenous tissues of the intervertebral disc, in particular type I and II collagen. Also, the high water content in the nucleus pulposus (which is up to 90% of its weight in the normal state, and 60 to 70% in degenerated discs, Buckwalter, 1995) serves as a medium for large deformations. Even in the stiffer sections of the intervertebral disc (outer portion of the annulus fibrosus) the water content is high, leading to the disc nonlinear behavior.

The polynomial function proved to be suitable for fitting the nonlinear relationship of stress-strain (mean R^2 = 0.98, n = 10), which initial trajectory resembles a parabola with the toe region included. The first rate of change of $\sigma(\varepsilon)$ gave the *Young's modulus:* $E = d\sigma/d\varepsilon$, which defines the disc stiffness. Normally, a higher order polynomial will imply a larger *E modulus*. It was found that the L4-L5 disc set had a smaller and narrow range of values for the main coefficient A of the polynomial fit than those for the L2-L3 disc set. Also, the MRI from the L4-L5 group clearly reveals a collapse of disc height and a more uniform physical stage of advance degeneration. This agreement was not always clear in the L2-L3 group because of a lesser degenerative stage. The presence of excessive vacuum in the nucleus may explain the low modulus in the L4-L5 disc set, while osteophyte formation seen in the anterior side of discs A and F may stiffen the outer disc tissue leading to a high modulus, see the MRI on Figure 3.1. Hardness is a common feature of bony outgrowths or osteophytes that forms along the disc periphery and adjacent vertebral bone (Banse et al., 2002). The harden surfaces in the anterior and posterior sides of disc F may also explain the poor bulging response. Such occurrence was limited to disc F, while in the rest of the discs radial bulging took place.

Size differences between lower and upper lumbar discs had also been reported as causes of stiffness differences (Nachemson et al., 1979). Thus, from the testing results, it was difficult to obtain significant differences in the *stiffness* or the *Young`s modulus* between discs because of similarities in the degenerated anatomy. In general, individual differences in cadaver lumbar motion segment mechanical behavior usually overshadow any class differences with respect to disc level, degree of degeneration, age or gender (Nachemson et al., 1979). Thus, it was even more difficult to recognize significant differences in the *Young's modulus* among degeneration grade sets than between lumbar level sets due to the larger scatter data. However, discs with a clear height collapse (severe degeneration) showed a low *mean stiffness* and *E modulus* (measured in the vertical direction) than those with a clear height.

The reported range of stiffness from the present study is in agreement with previous results (Panjabi et al., 1977; Nachemson et al., 1979; Edwards et al., 2001; and Gardner-Morse et al., 2004) in which they reported stiffness in the range of 800 to 2400 N/mm using a similar protocol. As a guideline, at around 500 to 1000 N load a normal lumbar disc should exhibit a stiffness value of around 1500 to 3000 N/mm (Adams et al., 1995). Thus, the set of degenerated discs tested showed a 25% decreased in stiffness value when compared with data from healthy discs. This was also evident for the disc Young's moduli E, which decreased between degeneration scoring. The value of the disc E moduli reported here were also in agreement with previous results (Lin et al., 1978; Adams et al. 1996) in which they reported values between 10 MPa (severe degeneration) and 25 MPa (Normal disc), see Table 4.1.

The stress generated in the disc cross section by the compressive load was mainly *normal* σ and range from 0.43 to 0.69 MPa, with no distinction between degeneration scoring. The results showed also agreement with previous mean values of stress distribution across the disc (Adams at el., 1996; Oloyede et al., 1998). Any shear involved in the axial loading due to an inclined plane was discarded.

During the specimen cutting, the disc height profile was irregular, which upon compressive loading could also generate an additional *shear stress* τ. Thus, in the calculations it was assumed a cross section area at the middle of the disc height, where the height profile was more uniform with only a normal stress component. Also, the cross section of the disc resembles an elliptic shape (Farfan et al., 1970) with a long and a short axis, where the larger stiffness occurs along its saggital axis, as this can explain in part the differences in stiffness among movement in forward-backward direction and right-left direction (lateral bending) for a specimen without the posterior assembly.

The bulging results suggest that the set of discs from the L4-L5 group had lost their ability to develop hydrostatic pressure at least between the anterior and posterior site upon compression. This did not happen in the discs from the L2-L3 group where an almost symmetrical bulging occurred. Intervertebral discs that show a height collapse, such as most of the L4-L5 set, will exhibit non symmetrical bulging between the anterior and posterior side. This is mainly because of a decline in water content in the nucleus and annulus, which reduces the disc ability to develop hydrostatic pressure upon axial loading (Nachemson et al., 1960). With advance degeneration, the thinner sections of the disc are first affected due to a lesser water content, such as the disc posterior side which no longer develop a define bulge. As the load continues to be applied, its resulting bulge progressively changes of orientation from a radial to a vertical direction which contributes to an eventual lost of disc height (Brinckmann et al., 1991). This may explain why the bulging response was much higher in the anterior side (0.871 mm) than in the posterior side (0.334 mm) for the L4-L5 set. The clinical relevance of this asymmetrical bulge can be used to try to explain in part the disc hernias most seen in the adulthood and elderly. In contrast, the symmetrical bulge exhibited by the L2-L3 disc group confirms the higher water content shown in the MRI. As these discs developed a more a-like hydrostatic pressure they confirm the anatomical evaluation of moderate degeneration.

Measurement of the radial bulging was limited to only two sites, the middle anterior and the posterior. Because the nucleus pulposus expands in all radial directions upon compression, it is relevant to investigate the bulging along the entire annulus periphery and the posterolateral borders as these sites are known for develop slipped disc. Measuring devices for such a task now use a belt with a laser scanner approach (Heuer et al., 2008) who recorded bulge values in the range of 0.7 to 0.9 mm when applying 500 N in axial compression to healthy discs. The bulging results also suggest that healthy discs develop hydrostatic pressure upon compression. From the present study, the lower bulging results can be explain by the use of different discs with different loading history, degenerated discs, number of discs tested, and measurement technique.

In summary, the severe degeneration group of discs from the present study deforms axially more upon compression, than the lesser degeneration group, which in turn lead to a higher Young's moduli in the latter group. However, the larger deformation seen in the former set of discs did not occur along the radial direction (bulging), implying loss of functionality from the nucleus pulposus and annulus fibrosus.

A summarize of the main results of the compression protocol from the present study and a comparative with previous studies are shown in Table 4.1.

Table 4.1. Main results of the compression protocol from the present study and comparative with previous studies.

Compression response		*Normal disc*	*Degenerated disc*
Stiffness (N/mm)	*Present study*	*1277*	*973*
	Gardner-Morse et al. (2004)	*2420*	*1800*
	Panjabi et al.(1984)	*750*	*600*
	Nachemson et al. (1979)	*571*	*500*
Bulge (mm)	*Present study*	*0.69*	*0.51*
	Heuer et al. (2008)	*0.70*	*0.87*
	Brinckmann et al. (1991)	*0.15*	*0.50*
	Klein et al. (1983)	*0.60*	*0.90*
Young's modulus, E (MPa)	*Present study*	*14.08*	*10.63*
	Adams et al. (1996)	*15*	*10*
	Keller et al. (1987)	*7.5*	*4.5*
	Lin et al. (1978)	*25*	*15*

b. Analysis of the disc relaxation response

The stress relaxation response in all the intervertebral discs shows their viscoelastic behavior which was obtained in a collection of three degenerated stages and also two different lumbar locations. Overall, discs from the L2-L3 set tend to relax at longer times than discs from the L4-L5 set with about 15% higher relaxation stress for the former discs.

The longer *relaxation time t(r)* and higher *relaxation modulus E(t)* of the L2-L3 disc set over those of the L4-L5 disc set suggest that the former set of discs had better capacity of dampers and load carriers. Also, discs with a define height (seen in the MRI) showed a longer relaxation time than those with a height collapse, which confirms the anatomical evaluation in the MRI of these discs.

As long as there is relaxation in a spring-dashpot assembly, the viscous part in the system dissipates the load or the stress, and the assume ratio E_2/η will have a significant value. As the relaxation decreases, the damper also decreases its dissipation, until it ceases and gives the characteristic relaxation parameter (Fung YC, 1993). Results from the exponential fit shows that the ratio E_2/η of the Maxwell arm decreases linearly in accordance with the standard linear solid *SLS* model. Thus, the viscosity η and the *viscous modulus* E_2 represent the viscoelastic parameters of the nucleus pulposus and the intervertebral disc. Also, since the nucleus is composed of a mixture of 70 to 90% of water and disorganized collagen type II, the ratio E_2/η gives insights of the materials constants.

The second order exponential function proved to be suitable for fitting the nonlinear relationship of stress-time (mean $R^2 = 0.98$, $n = 10$). However, the initial stress decay was poorly predictive with $\sigma(t)$ due to the disc unstable stress state cause by the sudden load removal at the end of the loading ramp. This led to a sharp and fast decline of stress which lasted during the first three minutes of the relaxation stage, after which a smoother decline occurred and a better prediction was achieved. This behavior was observed in all the discs, but was most evident in those from the L4-L5 set, especially with a height collapse. Except for disc F, the stress decline and the stress at the relaxation time gave similarities among individual discs and disc classifications. The advance osteophytosis seen in the MRI of the anterior and lateral margins in disc F may explain why this disc showed the smoothest slope of *stress decay* $\sigma(t)$ which gave the slowest relaxation with the lowest α value of 0.00067 sec^{-1} and the largest *relaxation time* $t(r)$ equal to 1500 s. Thus, the slow relaxation caused its low ratio E_2/η equal to $2x10^{-4}$ sec^{-1}, meaning that this disc tend to relax like a solid viscoelastic, which corroborates its high stiffness. In contrast, the rest of the discs with exceptions of discs A and D showed similar relations for the ratio E_2/η versus time, meaning an overall solid viscoelastic relaxation. The shorter relaxation times shown in discs A and D (below 450 s) may be explained by size differences and by the severe collapse of the disc height.

The relaxation results in the present study are in agreement with previous values (Johannessen et al., 2004, 2005; Holmes et al., 2006) in which they reported relaxation times of 290 sec, stresses of 0.150 MPa and α values between 0.0010 and 0.0030 after applying a 200 N initial load to a disc and recorded the force decay during 30 minutes. Some differences with the present results are the use of a lower magnitude load and the maintenance of the posterior elements.

Additionally, the mean value of the ratio E_2/η for the entire set of discs was in the order of one thousandth, which suggests that the viscosity is the dominant part of the dissipation. This tendency was also observed for the rest of the classifications, which means that the overall viscoelastic behavior of the discs does not change with lumbar level or with degeneration scoring. The reported values of the ratio E_2/η differ from previous studies (Li et al., 1995; Pollintine et al., 2010) within one order of magnitude due to the presence of the posterior elements assembly in their specimens. Using the stiffness values for the nucleus pulposus in the proposed range of $0.5\ \text{MPa} \leq E_2 \leq 1\ \text{MPa}$ (Smit et al. 1996) the equivalent viscosity of the nucleus pulposus from the present study ranges from $0.41\ \text{GPa-s} \leq \eta \leq 0.82\ \text{GPa-s}$ (moderate degeneration) to a value in the range of $0.50\ \text{GPa-s} \leq \eta \leq 1\ \text{GPa-s}$ (severe degeneration). Although these values were not statistically different, there magnitudes suggest that all intervertebral discs showed a solid viscoelastic behavior. This was also evidenced by the reduced stiffness of the discs after 20 minutes of relaxation, where the value of the $E(t)$ modulus represented only one quarter of the Young's modulus value calculated in the loading phase.

In summary, discs with a well define height did relax at longer times than those with a collapse height. Even degenerated discs have some capacity of stress relaxation due to their relative water content. This cause difficulty to distinguish significant differences between discs sets. With age and degeneration the discs dehydrate but do not loss entirely their water content which is still around 60 to 70% of their original levels. Thus, it seems that the presence of low quality bone in the vertebrae, vacuum phenomena in the nucleus pulposus, new bone formation in the outer margins of the annulus fibrosus or radial fissures are overwhelm, and any difference in the relaxation response between discs sets was attributed more on size differences.

A summarize of the main results of the relaxation protocol from the present study and a comparative with previous studies are shown in Table 4.2.

Table 4.2. Main results of the relaxation protocol from the present study and comparative with previous studies.

Relaxation response		*Normal disc*	*Degenerated disc*
Relaxation time, t(r) (sec)	*Present study*	*895*	*762*
	Allen et al.,(2006)	*150*	*50*
	Johannessen et al., (2000)	*315*	*290*
	Holmes et al., (1996)	*1680*	*570*
Relaxation modulus, E(t) (MPa)	*Present study*	*3.29*	*2.36*
	Allen et al.,(2006)	*0.83*	*0.60*
	Johannessen et al., (2000)	*1.60*	*1.30*
	Holmes et al., (1996)	*13.33*	*7.62*
Relaxation stress, $\sigma(t)$ (MPa)	*Present study*	*0.215*	*0.186*
	Allen et al.,(2006)	*0.13*	*0.100*
	Johannessen et al., (2005)	*0.70*	*0.26*
	Holmes et al., (1996)	*0.47*	*0.27*
Elastic modulus, E_1, (MPa)	*Present study*	*14.1*	*10.6*
	Pollintine et al., (2010)	*10.43*	*7.08*
	Li et al., (1995)	*9.25*	*6.63*
	Keller et al., (1987)	*7.04*	*6.30*
Viscous modulus, E_2, (MPa)	*Present study*	*0.5*	*0.5*
	Pollintine et al., (2010)	*4.57*	*4.98*
	Li et al., (1995)	*6.35*	*4.29*
	Keller et al., (1987)	*1.55*	*2*
Viscosity η, (GPa-s)	*Present study*	*0.40*	*0.80*
	Pollintine et al., (2010)	*45.1*	*30.2*
	Li et al., (1995)	*27.4*	*15*
	Keller et al., (1987)	*8.29*	*6*

c. Intervertebral disc flexibility

Testing of the intervertebral discs to bending and torsional loads gave input data about the vertebra-disc-vertebra flexibility, which is one of the basic functions in the spine. Flexibility is defined as the amount of motion (rotation) done in the saggital, coronal or axial plane that results from applying a moment load, and decreases with age (Panjabi, 1977).

The results showed that there was no statistical difference in motion response to 5 Nm in bending or torsion between lumbar levels L2-L3 and L4-L5 or between degeneration scoring grades 3, 4 and 5. The small population of discs (n=10), and the absence of normal discs with none degeneration in this study may explain the large scatter data and similarities obtained. The deflection response in forward, backward and lateral bending fall all in the range of values reported from previous studies (Schultz et al., 1979; Adams, et al., 1980; and Panjabi et al., 1977, 1989) with mean rotations in the range of 4° to 7° for Flexion, 2° to 7° for Extension and 2° to 4° for Lateral Bending for a moment load of 5 Nm applied to degenerated and non degenerated discs. They also reported a large scatter in the results which implies that large individual variations exist in the stresses internal to a motion segment resulting from a given load during an activity. The motion responses in Torsion are also in agreement with early studies (Farfan et al., 1970; Adams et al. 1981; and Panjabi et al. 1989) who reported rotations in the range of 3° to 7 ° for a torque of 5 Nm. They also indicated that torsion stiffness depended mainly on disc size differences (shape and area of the cross section) and to a lesser extent to the annulus fibrosus integrity (degeneration), and on the loading rate.

The stiffness response to bending or torsion for the entire set, or any disc classification, did not show a clear nonlinear tendency as it did in the case of compression loading. However, for bending in flexion-extension and torsion, the stiffness curve showed a toe at the beginning, and its slope grew as the deflection angle θ increased, this nonlinearly was observed in discs which showed a clear height, such as, in A, G and H from the L2-L3 set and B, C and D from the L4-L5 set. For lateral bending the initial toe also occur in the same discs but was smaller and almost showed a constant slope which gave a higher stiffness. Because of its elliptic shape, the intervertebral disc has a longer axis along the right-left side over that of the anterior-posterior side, resulting in a higher bending stiffness. Also, because the human gait is done mostly along the spine anterior-posterior direction leading to high deformations in the disc anterior side, it is reasonable to suggest that these may explain the stiffness differences among bending modes.

Degeneration has been associated with the reduction of disc motion in Flexion, Extension and Lateral Bending (Nachemson et al. 1979) and with an increase in Torsion rotation (Farfan et al. 1970). However, results in bending shows that the advanced degenerated L4-L5 discs deflect more than the moderated degenerated L2-L3 discs. The cause of these differences can be explained by the anatomical evaluation from the MRI of the set of discs. For the L4-L5 disc group, the presence of a collapse disc height with little osteophyte formation resulted in a group with a mean stiffness to compression and bending lower than that of the L2-L3 group which showed a more define disc height with larger amount of osteophytes.

Osteophyte formation has been related with reduction of intervertebral disc motion response in flexion-extension (Tanaka et al. 2001). In a biomechanical and imaging study of over 100 human cadaver lumbar discs they related the kinematics properties of the lumbar spine with disc degeneration. They reported that discs with radial tears in the annular fibrosus (degenerated grade III and IV, Thomson's scale) had increased the motion response to flexion-extension. Also, discs with the presence of a total space collapse and large osteophyte formation (grade V) were most likely to experience a decrease of motion response. Because intervertebral osteochondrosis can be present with spondylosis deformans (Schmorl's, 1932) this supports the idea that moderate to large osteophyte formation mostly seen in the anterior-posterior side of the L2-L3 group causes the inferior motion response.

The differences between stiffness values in bending, such as in flexion-extension and that in torsion arise from the way the stress is applied throughout the annulus fibrosus and also by the presence of osteophytes. In bending loading, the annulus is put one half to compression (at the side of loading) and the other half to tension (at the opposite side). Thus, the stress is applied normally to the upper thin surface of the annulus laminas which at the outer rim consist also of osteophytes. In the compression side, the resulting deformation of a lamina is a radial bulge which is similar to that shown by a column when placing a vertical load at its top surface. Because annulus laminas are much taller than thicker, their slenderness ratio is high, they tend to bend. But because they are also attaching to each other, they resist, in the same way that a bundle of paper sheets do.

In torsion, the annulus is put to axial rotation and the stress is a shear applied tangentially to the laminas surface causing a relative displacement between them. The largest deformations always occur at the outer annulus where the longest arch of rotation takes place, according to the elastic theory of torsion. Resistance to this rotation is given by the attachment between laminas which are bonded together by the ground substance. Thus, the lower disc stiffness response in torsion mode suggests that the attachment between laminas are more susceptible to a shear than to a normal stress as was reported by Farfan et al. (1970). The analysis of the shear and normal stress in the annulus fibrosus and nucleus pulpous due to the bend and torsion loads will be presented in the section of the Finite Element Model.

A summarize of the main results of the bending and torsion protocols from the present study and a comparative with previous studies are shown in Table 4.3.

Table 4.3. Main results of the bending and torsion protocol from the present study and comparative with previous studies.

Stiffness response (N-m/rad)		*Normal disc*	*Degenerated disc*
Flexion	*Present study*	*118*	*102*
	Van der Veen et al. (2010)	*32*	*12*
	Guan et al., (2007)	*82*	*51*
	Adams et al., (1980)	*60*	*46*
	Nachemson et al., (1979)	*110*	*110*
Extension	*Present study*	*138*	*97*
	Van der Veen et al. (2010	*32*	*12*
	Guan et al., (2007)	*153*	*61*
	Nachemson et al., (1979)	*210*	*210*
Lateral bending	*Present study*	*158*	*153*
	Van der Veen et al. (2010	*26*	*15*
	Guan et al., (2007)	*76*	*81*
	Nachemson et al., (1979)	*110*	*110*
Axial rotation	*Present study*	*44*	*42*
	Van der Veen et al. (2010	*72*	*40*
	Adams et al., (1981)	*189*	*78*
	Nachemson et al., (1979)	*405*	*608*
	Farfan et al., (1970)	*78*	*98*

d. Dynamic response

Loading the intervertebral disc to cyclic compression gave input data about the disc dynamic properties in a collection of three degenerated stages and also two different lumbar locations.

Results show that at frequencies lower than 1 Hz the stress and strain signals were nearly in phase with an *angle* β difference below 10°. As the *phase angle* β decreases and approaches a zero value, it means that the applied energy to the disc was used totally to deform it and minimum losses appeared as a result of heat, noise, vibration, etc. Thus, under a low frequency loading a solid viscoelastic best defined the disc behavior. For such condition to take place in a biological tissue the duration of load application has to be sufficiently large to allow deformation and partial recovery before the next loading cycle was applied. Loading the disc at 0.2 Hz frequency (5 seconds period) gave the necessary time for the stress and strain to be closely in phase (mean value $\beta = 2.13°$). In contrast, as the load *frequency* ω was increased to the upper limit of 5 Hz (0.2 second period with a mean β value of 19°) the rate of deformation did not gave time for recovery and the disc showed considerable dissipation, meaning that at higher frequencies the disc decreases its “solid-like” viscoelastic behavior.

The reported increase of the *phase angle β* with the *frequency ω* from the Figures 3.18 and 3.19 has been suggested as the result of internal fluid flow and the disc capacity to absorb and dissipate loads (Iatridis et al. 1996). They reported *β* values up to 35˚ using a wider range of frequencies which cover up to 20 Hz; however, their testing protocol and material preparation were specifically aimed to characterize the nucleus pulposus, and not the entire vertebra-disc-vertebra segment, as these differences can led to significant changes since the annulus fibrosus structure is stiffer, and behaved more elastically due to their structurally collagen type I content.

Characterization of the *phase angle β* shows rate similarities among L2-L3 and L4-L5 disc sets which can be explained by the low population (n=10) tested, the moderated to severe stage of disc degeneration in all the discs, and also by the narrow range of study frequencies. The higher mean value of *β* in the L4-L5 set over the L2-L3 set, and degeneration scoring grade 5 set over the other two degenerative sets can be explained more by the size differences.

Smaller discs deformed more than larger ones under the same conditions, with a reduction of the disc capacity to shock absorbed loads and an increased dissipation ratio (E''/E'). Thus, the increasing values of the *phase difference angle β* with frequency in all intervertebral discs shows their viscoelastic and dissipation tendency which were defined by the *loss moduli E"* and the *tangent of δ*.

The increasing value of the *storage E'* and *loss E" moduli* with *frequency ω* shown in Figures 3.20 and 3.21 implies that at higher frequencies, a larger load is required to produce the same strain. Thus, at higher frequencies the disc is better able to resist higher loads than at low frequencies. The wavy structure or crimping of collagen type I fibers in the annulus fibrosus under unstrained conditions may explain this property. The reported values for the *E'* and *E"* moduli are in agreement with those reported by Costi et al., (2008); Korecki et al., (2008); Holmes et al., (1996); and Hansson et al., (1987) in a range from 3 MPa to 30 MPa for the storage modulus, and from 1 MPa to 5 MPa for the loss modulus, considering a loading around 500 N with a frequency in the range of 1 to 5 Hz.

The maximum *dissipation ratio (tanδ)* for any classification only reach a value of 0.45, which implies that the *storage moduli E'* dominates over the *loss moduli E"*, and means that the intervertebral disc behaves more like a viscoelastic solid with considerable dissipation than a viscoelastic fluid. In overall, about 70% of the maximum dynamic response (10.7 MPa) was given by the disc *storage* component with the remaining 30% given by its *loss* component. The stiffer collagen type I mostly seen in the degenerated annulus fibrosus and the dehydrated nucleus pulposus may explain the solid-like performance. Again, the small disc population and similarities in disc degeneration anatomy did not permit a clear distinction in dissipation between severe and moderated degeneration.

The increase value of the dynamic parameters under increased frequency has been previously reported in testing other collagenous tissues (Van Eijden et al., 2006; Allen et al., 2006; Tanaka et al., 2002). They tested mature-adult temperomandibular disc joints (TMJ) to cyclic compression covering a wide frequency range from 0.1 to 100 Hz and reported mean values for the *storage, loss* and *dynamic modulus* of 1.5, 0.3 and 2 MPa respectively. The *phase angle β* and the *dissipation ratio tan δ* were reported to be 15° and 0.20 respectively. Although the TMJ disc joint is smaller in size than the intervertebral disc, the cartilaginous and collagenous tissue from both joints share common features in their annular arrangements and pathologies.

The *disc dissipation* (*hysteresis)* was found to been sensitive to *frequency ω*. For the majority of the testing, the dissipation grew with increased frequency, but was kept low with the resulting relationship showing a "banana-like" shape, as shown in Figure 3.24. The small hysteresis values imply the importance of the imbibition of tissue fluid by the disc (Virgin et al., 1951) and the well maintenance of bone quality and hyaline cartilage in the vertebral bodies and endplate. However, results of *disc dissipation* showed no statistically difference neither for lumbar level or degeneration scoring sets ($p>0.05$). Thus, discs with height collapse (disc D, I and J) or a define height (G or H) did not show any common tendency. The anatomical similarities of advanced degeneration and the small population may explain these results. Increased values of disc dissipation with increased frequency using a similar protocol have been reported previously (Asano et al., 1992; Hansson et al., 1987) with values ranging from 0.1 and 1 Joule. They also indicated that the overall behavior of the disc under cyclic compression resembles a solid viscoelastic. A summarize of the main results of the dynamic testing protocol from the present study and a comparative with previous studies are shown in Table 4.4.

Table 4.4. Main results of the dynamic protocol from the present study and comparative with previous studies.

Dynamic compression response at 5 Hz		*Normal disc*	*Degenerated disc*
Storage modulus, E' (MPa)	*Present study*	*6.90*	*6.50*
	Costi et al., (2008)	*31.80*	*25*
	Holmes et al., (1996)	*19.70*	*11.80*
	Hansson et al., (1987)	*24.60*	*9.80*
Loss modulus, E"(MPa)	*Present study*	*2.12*	*2.99*
	Costi et al., (2008)	*3.20*	*2.50*
	Holmes et al., (1996)	*3.50*	*2.10*
	Hansson et al., (1987)	*4.30*	*1.80*
Dissipation ratio, tanδ	*Present study*	*0.32*	*0.46*
	Costi et al., (2008)	*0.15*	*0.10*
	Ohshima et al., (1989)	*0.20*	*0.10*
	Hansson et al., (1987)	*0.20*	*0.18*
Hysteresis (Joules)	*Present study*	*2.92*	*2.89*
	Costi et al., (2008)	*0.60*	*0.40*
	Hansson et al., (1987)	*0.50*	*0.75*
	Koeller et al., (1986)	*0.86*	*0.40*

From the foregoing, mechanical evaluation of unit vertebral functions (UVF) with normal or degenerated discs serves to investigate its macroscopic properties: Young's modulus, stiffness, bulging, flexibility, storage, damping and dissipation which in turn account for the entire spinal segment: vertebrae and disc. As these spinal material properties unveils, a collection of data is generated which usefulness is evidenced by the increasing number of biomechanical and numerical studies eager to use novel input data.

In this regard, the outcome of the relaxation and dynamic testing gave data that can be used as an input for a future validation of a finite element model of intervertebral cyclic loading. Daily activities such as walking or sitting, which are typical light tasks in the office, workshop or at home, involve repeated compression loading. Degeneration involves a prolonged loading history that eventually leads to tissue deformation and jeopardize disc functionality. Thus, any remains of the disc ability as shock absorber can be evaluated and used to assess low back pain therapies related to light work injuries in the elderly.

Finally and in overall, ex-vivo testing of biological tissues, such as the intervertebral disc, under compression, flexion or torsion loading in static or dynamic conditions should consider observance of tissue dehydration and degradation, since the mechanical properties of collagen, cartilage or bone are sensitive (Galante 1967). The used of water spray and cotton tissue to prevent direct air exposure and maintain a high relative humidity during the testing was satisfactory for this study. However, for tissue evaluation on a micro scale level, then a custom chamber should be used which include temperature and humidity control. When performing mechanical testing and analyzing deflections in soft biological tissues, couple motions should be considered. Because in real life the intervertebral disc shows compression upon twisting or torsion (Schultz et al. 1979), the reported deflections from the present study were limited to measure main motions and any additional couple motion which may occur were neglected. Therefore, when evaluating spinal segments deflection, couple motions should be observed.

II. Simulation results

a. Analysis of the compression load simulation

Overall it was possible to validate the FEM of disc degeneration with the experimental results and obtained a fair approximation. However, variations always arise because of differences between the "real" disc and the model, such as in geometry, material properties, loading history, and evaluation of multiple loadings: compression, bending and torsion.

Selection of an elastomeric material formulation for the disc materials was justified on evaluating the gross behavior of the unit under the loading phase conditions. In general, the elastomeric properties of the disc were adjusted on the premise of equilibrium of forces, between those from the testing and those from the simulation.

In this regard, a displacement step procedure in the simulation of compression proved to be the most realistic approach for reproducing the testing results, and therefore the reaction forces were check. Of these forces, the compression was the dominant component for adjusting the Mooney coefficients and gave a moderate relative difference (18%), while for the rest of the bending modes the relative differences with the testing were greater (up to 70%). The absence of collagen I fibers in the annulus fibrosus model and the non pressurization in the nucleus pulposus may explain these differences.

The smallest difference of relative forces (D.F.) achieved corresponded to the lowest Mooney coefficients used (C_1= 0.10 and C_2= 0.025) from the literature, and gave a Young's modulus E of 750 KPa for the annulus fibrosus, which value match the description for an annulus with minimum degeneration. Also, this was the smallest difference possible when considering disc bulge. The annular bulge was considerable large in all radial directions, being as high as 4 times that of the experimental value (0.9 mm). These differences suggest that a higher elastic modulus should have been used, due to the absence of fiber modelization.

The absence of fibers (truss elements or 3D rebar element technology) in the annulus fibrosus lead to a single model structure based only on stereo lithography *STL* tetrahedrals. It was difficult to integrate these elements into the tetrahedral mesh, because of the nodes incompatibility and the large number of elements involve. Although, the use of these elements gives better prediction of bulge and fiber stress they need hexahedral solids for their implementation, and not tetrahedrals. Thus, the bulges from the present study also differ from those obtained previously with models that include truss elements (Smit at al., 1996) and rebar elements with stiffness gradient along the radial direction, Little et al., (2007), Meakin et al., (2001) and Eberlain et al., (2001) whom they reported bulges in the range from 0.3 to 0.5 mm. However, when comparing bulging results with early studies with models without rebar technology (Belytscho et al., 1974; Kulak et al., 1976 and Spilker et al., 1980) there is a good agreement. Hence, the simulated bulging from the present study shows its profile, form and location in the disc and its components, which is in agreement with the previous studies and may explain in part the biomechanics of disc protrusions and hernias, mostly seen in the elderly.

The large strains of the annulus fibrosus and nucleus pulposus over that of the vertebrae bone shows the relevance of soft tissue deformation, such as disc collapse, bulging and bending that led to geometric changes, which are mostly seen in advanced degeneration. In contrast, the higher stress state in the stiffer vertebrae bone over those of the softer disc tissues shows the relevance of bone predisposition to fracture. In general, this is in agreement with the findings of Kulak et al., (1976) and Shirazi-Adl et al., (1984) who reported that for a normal disc with an incompressible nucleus, the most vulnerable elements under compression load are the cancellous bone and endplate. While for a severe degeneration disc case it is the annulus bulk material which is susceptible to failure, but not the fibers.

The negative strain state of the nucleus pulposus contrast with that of the annulus fibrosus which showed negative and positive strains. However, in both cases the larger strains were negative and where located posteriorly at the annulus-nucleus boundary. The occurrence of large strains at these sites have been reported by Costi et al., (2007) and Stokes (1987) as the result of a combination of geometrical (the thinner wall of the annulus fibrosus and the posterior position of the nucleus pulposus), mechanical (bone formation at the posterior side) and biochemical factors that eventually leads to stress concentrations at these sites.

Overall, the larger deformations at the nucleus and annulus periphery are mainly because they are soft tissues and were treated as incompressible. The disc degeneration model was developed on the assumption of a reasonable amount of water content in the low degeneration stages (around 70% of its original level) which is still a large amount.

The appearance of positive strains in the annulus fibrosus have been suggested as the result of redistribution of strains in the disc (Panagiotacopulos et al., 1977). As the disc is compressed the nucleus pulposus develops pressure that tends to move and expand the annulus radially, like when a balloon is inflated, but this expansion is limited by the collagen fibers. Then, the strains at the outer surface will be positive and will represent a planar strain state in traction. Such a case corresponds to the outer wall deformation of a thinner pressure vessel, in which the radial deformation (due to pressure) changes to tangential and longitudinal surface strains. Recently, (Noailly et al., 2007) develop and validated a L3-L5 bi segment finite element model and interpreted the load transfer in the disc as a combination of interactions between (a) the stiffer cortical bone and the annulus fibrosus, (b) the annulus fibrosus and the nucleus pulposus, (c) the nucleus and the endplate with the cancellous bone. The report emphasizes the predisposition of the nucleus pulposus to be the main load carrier for most physiological loads, especially in axial loading. Thus, from the present results it appears that the complete negative strain state of the nucleus pulposus implies that under axial loading, the nucleus pulposus is the main load carrier. Thus, the larger of the principal stresses and strains were projected along the craneo-caudal direction where the compression loading was applied.

The larger values of the principal stresses and principal strains in the model over those obtained in the compression testing can be explained by the geometry of the disc model which included stress concentrations in the cavities and along the cortical shell. At these concentration sites the stress increased sharply with respect to the test data. The cavitations appear mostly in the nucleus pulposus also lead to stress concentration, since there is less surface contact. Also, the irregular profile of the cortical shell periphery led to rough bumpy surfaces. Differences of stiffness between the bone tissues and the soft disc tissues range between two and three orders of magnitude, leading to large deformations and stresses. The stress distribution in the nucleus pulposus confirms that the highest stresses were negative and occurred at the posterior side where the largest strains took place. While in the annulus fibrosus the stresses varied from positive to mostly negative values, as it did with its strain distribution and are due to the disc bulging.

The stress values reported in the range of 0 to -1 MPa are within a reasonable prediction, since in the experimentation a compression load of 1000 N was applied over a cross sectional disc area of 1880 mm^2, thus giving a mean stress of 0.53 MPa. Also these values are within the range of early studies (Yang et al., 1983; Shirazi et al., 1983, 1984; Natarajan et al., 1994).

The occurrence of large stresses in the outer annulus fibrosus has been reported previously by Noailly et al., (2007) and occurred in the fibers, suggesting as the result of a pathway of load transfer from axial in the cortical shell to fiber oriented in the outer annulus were the laminae are thinner, as described by Brickley-Parsons et al., (1983). They also reported that the nucleus pulposus was very susceptible to be compress for most of the spine movement, except in axial rotation, while the annulus fibrosus was mostly loaded in traction at the anterior side. In another biomechanical study using MRI Zheng et al., (2005) simulated a 300 N axial compression loading and also reported a maximum principal stress of 1 MPa in the outer annulus and a lower stress between 0.1 and 0.5 MPa in the central nucleus.

From the foregoing, the reported occurrence of large strains and stresses in the posterior annulus side of the degeneration model agrees with previous studies and the clinical observation of herniated discs, which takes place at the common posterolateral side. Thus, the results from the computational simulation and validation allows a better understanding of the biomechanics of disc bulging upon disc loading, which can aid the researcher in the design of spine implants, and also to the physician in improving therapy implementation and administration.

b. Analysis of the bending and torsion load simulation

The simulation results for the four modes of bending and that in torsion loading show the intervertebral disc ability to sustain large deformations and stresses. The principal strain distribution for all load cases showed that the peripheral region of the nucleus pulposus and annulus fibrosus bore the highest deformation. In the case of saggital flexion and extension, the presence of high strains across a large area at the posterior side of the annulus fibrosus, and the absence of positive strains at the disc anterior side, suggest a susceptible location for stress concentration at the posterior and posterolateral disc side. Such condition can be interpreted as the result of the position of the nucleus pulposus, being more close to the posterior side than to the anterior side. When bending the disc backward (extension), the nucleus is pushed frontward towards the annulus anterior side, where the wall thickness is greater. While in forward bending (flexion) the nucleus is pushed backward towards the annulus posterior side, where the wall thickness is much thinner, creating stress concentration. Thus, the irregular thickness of the annulus fibrosus leads to differences in the level of principal strains and stresses in the saggital plane. These anatomical and geometrical factors for stress concentration occur at the same place that the common discs bulging and protrusions occur.

The stress distribution due to flexion and torsion near the boundary between the nucleus and annulus was investigated by Little et al., (2007) and reported that in flexion, the nucleus pressure contributed in deforming the annulus inner wall, causing large deformations and stresses in the disc anterior side. While for torsion loading the maximum shear occurs at the outer wall of the annulus fibrosus with no prefer location along the periphery, suggesting that the annulus outer wall is the part of the disc that acts as the principal load carrier.

These results have implication in disc degeneration, since degenerated discs show a clear collapse of disc height with a distorted annulus fibrosus, showing tears and disrupted collagen fibers in the network, and in the case of severe degeneration, the presence of delaminations. Such occurrence jeopardizes the disc ability to resist twisting movement. Thus, the stress distribution in flexion and torsion reaffirms the findings by Farfan et al., (1970) in regard of the role of the intervertebral disc in resistance torsion loading. In degeneration, the annulus ground substance is also affected, but mechanically less than the collagen fibers network, but still the disc carried a small portion of the original torsional load.

The lateral bending simulations show that the disc is 40 % stiffer to bend it laterally (coronal plane) than to bend it forwardly or backwardly (saggital plane). This comes from considering an elliptic shape of the disc which was seen wider from the right to the left side than from the anterior to the posterior side. Here, the wall thickness of the annulus is more symmetrical than in the saggital plane, where the nucleus arrangement is closer to the posterior side.

These observations were reported by Belytschko et al., (1974) using a nonlinear elastomer formulation, and reported principal stresses as high as 0.30 MPa in the annulus wall when conducting flexion and extension. While for bending the disc to the lateral sides they reported stress values around 20 to 40 % lower than those done in the saggital plane, suggesting that reasonable predictions of variations of disc stiffness with vertebra level or integrity can be made on the basis of geometry. We think that the morphological condition of spondylosis deformans in the left side of the annulus may also explain this regional stiffening of the disc model among the coronal and saggital directions.

The occurrence of the highest tensile stresses at the outer wall of the posterior annulus during flexion and at the inner wall of the anterior annulus during extension agrees with the findings by Shirazi-Adl et al., (1986) and more recently with those of Noailly et al., (2003), whom they reported that upon flexion, the largest tensile stresses in the disc occur in the inner annulus fibers located at the posterior and posterolateral sides. They suggest the way the load transfer path occur in the unit vertebra function (UVF) model. In flexion the ligaments are the means of load transfer, while in extension the load is transmitted through the pedicles, laminae and articular processes. The posterior elements limits backward movement, thus they also suggest that upon removal of these elements the remaining vertebra-disc-vertebra gain mobility in the saggital plane. They reported that flexion-extension movement to the remaining disc caused a stress distribution in which the nucleus and annulus showed a transition of stresses from tension to compression.

The stresses reported in the present study falls below the values reported by Ruberté et al., (2009); Rohlmann et al., (2006); Noailly et al., (2003); and Wang et al., (2000) which reported principal stresses in the range of 3.5 MPa to 13 MPa, and from 1 to 6 MPa for shear stresses. Again, the use of a L3-L5 bi segment finite element model with the posterior elements included along with the implementation of 3D rebar technology and the use of larger moments (7.5 N-m) may explain the large differences.

Finally, the stress-strain distribution gives some insights of the way a degenerated disc deforms upon movement by twisting or bending. Such movements are common practice in normal physical activities such as, lifting weights, running, exercising, and even sitting and walking, but in the majority of the elderly are difficult tasks to perform. Thus, the present results assess common failure sites and should serve to acknowledge the researcher in the design of implants and medical devices. Likewise, in the clinical field, these results can assess the physiologist and therapist for a better implementation of their treatments.

III. References

Adams, M. Hutton, W.C., and Stott J.R. (1980). “The Resistence to Flexion of the Intervertebral Joint”. Spine 5(3): pp. 245-253.

Adams, M. and Hutton, W.C. (1981). “The relevance of Torsion to the Mechanical Derangement of the Lumbar Spine”. Spine 6(3). pp.241-248.

Adams M. and Dolan P. (1996). “Time dependent changes in the lumbar spine resistance to bending “ Clinical Biomechanics Vol. 11 (4) pp. 194-200.

Adams MA, McNally DS and Dolan P. (1996). “Stress distribution inside intervertebral discs: The effects of age and degeneration”. The journal of bone and joint surgery, Vol. 78-B, No.6: 965-972

Allen KD and Athanasiou KA. (2006). “Viscoelastic characterization of the porcine temperomandibular joint disc under unconfined compression”. Journal of Biomechanics 39: 312-322.

Asano S, Kaneda K, Umehara S and Tadano S. (1992). “The Mechanical Properties of the Human L4-5 Functional Spinal Unit During Cyclic Loading: The Structural Effects of the Posterior Elements”. Spine 17(11) pp. 1343-1352.

Banse X, Sims TJ and Bailey AJ (2002). “Mechanical Properties of adult vertebral Cancellous bone: Correlation with collagen intermolecular cross-links”. Journal of Bone and Mineral Research 17(9): pp1621-1628.

Belytschko, T., Kulak, R.F., Schultz, A.B. y Galante, J. O.(May 1974). Finite element stress analysis of an intervertebral disc. Journal of Biomechanics, Vol 7(3): 276-285.

Berkson, M.H., Nachemson, A. and Schultz A.B. (1979). Mechanical Properties of Human Lumbar Spine Motion Segments. Responses in Compression and Shear; Influence of Gross Morphology. Journal of Biomechanichal Engineering. Vol. 101. pp53-57.

Boos N, Rieder R, Schade V, Spratt KF, Semmer N and Aebi M. (1995). “The diagnostic accuracy of magnetic resonance imaging, work perception, and psychosocial factors in identifying symptomatic disc herniations”. Spine 20(24): pp 2613-25.

Brickley-Parson D and Glimcher MJ (1983). “Is the chemistry of collagen in the intervertebral disc an expression of Wolff’s law? A study of the human lumbar spine”. Spine 9. 148-163.

Brinckmann P and Grootenboer H (1991). “Change of disc height, radial bulge, and intradiscal pressurefrom discectomy: An in vitro investigation of human lumbar discs” . Spine 16(6), pp. 641-646.

Broberg, K.B. y Essen, H.O. (1980). Modeling of intervertebral disc. Spine 5(2) : 155

Buckwalter JA. (1995) “Aging and degeneration of the human intervertebral disc”. Spine 20:1307-14.

Costi J, Stokes I, Gardner-Morse MS, Iatridis J. (2008). “Frequency-Dependent Behavior of the Intervertebral Disc in Response to Each of the Six Degree of Freedom Dynamic Loading: Solid Phase and Fluid Phase Contributions”. Spine 33 (16): pp1731-1738.

Costi JJ, Stokes IA, Gardner-Morse M, Laible JP, Scoffane HM and Iatridis JC. (2007). “Direct measurement of intervertebral disc maximum shear strain in six degrees of freedom: Motions that place disc tissue at risk of injury”. J. Biomechanics 40(11): 2457-66.

Eberlain R, Gerhard AH and Schulze-Bauer C. (2001). “An anisotropic model for annulus tissue and enhanced finite element analysis of intact lumbar disc bodies”.Computer Methods in Biomechanics and Biomedical Engineering, Vol. 4: pp. 209-229.

Edwards WT, Ordway NR, Zheng Y, McCullen G, Han Z and Yuan H. (2001). “Peak stresses observed in the posterior lateral anulus”. Spine 26(16): 1753-1759.

Farfan H., Cossette JW, Robertson G.H., Wells RV, and Kraus H. (1970). “The effects of Torsion on the Lumbar Intervertebral Joints: The role of Torsion in the Production of Disc Degeneration”. The Journal of Bone and Joint Surgery. Vol. 52-A, No. 3. pp.468-497.

Galante J. (1967). “Tensile Properties of the human lumbar annulus fibrosus”. Acta Orthopedica Scandinavika (Supp) 100.

Gardner-Morse MG and Stokes I. (2004). “Structural behavior of human lumbar spinal motion segments”. Journal of Biomechanics 37. pp. 205-212.

Guan Y, Yoganandan N, Moore J, Pintar FA, Zhang J, Maiman DJ and Laud P. (2007). “Moment – rotation responses of the human lumbosacral spinal column”. Journal of Biomechanics 40:1975-1980.

Hansson TH, Keller TS and Spengler DM. (1987). Mechanical Behavior of the Human Lumbar Spine. II. Fatigue Strength During Dynamic Compressive Loading. Journal of Othopaedic Research Vol.5(4) pp.479-487.

Heuer F, Schmidt H and Wilke H. (2008). “The relation between intervertebral disc bulging and annular fiber associated strains for simple and complex loading”. J. Biomechanics 41. pp 1086-1094.

Heuer F, Wolfrom U, Schmidt H and Wilke HJ (2007). “ A method to obtaing surface strains of soft tissues using a laser scanning device”. J Biomechanics 41 (11): pp. 2402-2410.

Heuer F, Schmidt H, Claes L and Wilke HJ. (2008). “A New laser scanning technique for imaging intervertebral disc displacements and its application to modeling nucleotomy”. Clinical Biomechanics 23(3): 260-269.

Holmes AD, Hukins DWL. (1996). “Analysis of load-relaxation in compressed segments of lumbar spine. Med. Eng. Physics 18: 99-104.

Iatridis JC, Weidenbaum M, Setton L and Mow V. (1996). “Is the nucleus a solid or a fluis? Mechanical behaviors of the nucleus pulposus of the human intervertebral disc”. Spine 21(10): 1174-1184.

Izambert D, Mitton D, Thourot M and Lavaste F. (2003). “Dynamic stiffness and damping of human intervertebral disc using axial oscillatory displacement under a free mass system”. European Spine Journal 12: 562-566.

Johannessen W, Vresilovic E, Wright A and Elliott D. (2004). “Intervertebral Disc Mechanics are Restored following Cyclic Loading and Unload Recovery”. Annals of Biomedical Engineering, Vol. 32 No.1, January 2004: pp.70-76.

Johannessen W, Elliot D (2005). “Effects of degeneration on the biphasic material properties of human nucleus pulposus in confined compression” Spine 30(24), pp. E724-E729.

Keller, TS., Spengler, D.M. y Hansson, T.H. (1987). Mechanical behaviour of the human lumbar spine. I Creep analysis during static compressive loading. J. Orthop. Research, Vol. 5, No. 4. pp.467-478.

Keller TS, Holmes S, Hansson T and Spengler D. (1990). “The dependence of intervertebral disc mechanical properties on physiological conditions” Spine 15(8) pp. 751-761.

Kemper A, McNally C, McNeely D, Matsuoka F and Duma S. (2006). “Compressive stiffness properties of human lumbar intervertebral discs and the influence of strain rate”. 30 th annual meeting of the American Society of Biomechanics, Blacksburg, VA, 2006.

Klein JA, Hickey DS, and Hukins DWL. (1983). “ Radial bulging of the annulus fibrosus during compression of the intervertebral disc”. J Biomechanics 16(3): pp.211-217.

Korecki C, MacLean J and Iatridis JC. (2008). “Dynamic compression effects on intervertebral disc mechanics and biology”. Spine 33(13): 1403-1409.

Kroker P. (1949). “Sichtbare Rissbildungen in den Bandscheiben der Wirbelsaule”. ROFO 72:p.1

Kulak RF, Belytschko T, Schultz AB, Galante JO. (1976). “Nonlinear behavior of the human intervertebral disc under axial load”. Journal of biomechanics Vol. 9: pp. 377-386.

Li S, Patwardhan AG, Amirouche FML, Havey R and Meade K. (1995). “Limitations of the standard linear solid model of intervertebral disc subject to prolonged loading and low-frequency vibration in axial compression”. Journal of Biomechanics Vol. 28(7): pp. 779-790.

Lin HS, Liu YK, Gautman R, Nikravesh P. (1978). “Systems identification for material properties of the intervertebral joint”. Journal of Biomechanics 11: pp. 1-14.

Little JP, Adam CJ, Evans JH, Pettet GJ and Pearcy MJ. (2007). “Nonlinear finite element analysis of anular lesions in the L45 intervertebral disc”. J. Biomechanics 40(12): 2744-2751.

Lu YM, Hutton WC, Gharpuray VM. (1996). Do bending, twisting and diurnal fluid changes in the disc affect the propensity to prolapse? A viscoelastic finite element model. Spine 21: 2570-2579.

Mearkin JR and Hukings. (2001). “ Replacing the nucleus pulposus of the intervertebral disc: prediction of suitable properties of a replacement material using finite element analysis”. Journal of Material Science: Material in Medicine 12(2001): 207-213.

Miller, JA; Schultz AB; Wardwick DN, and Spencer DL. (1986). “Mechanical Properties of Lumbar Spine Motion Segments under Large Loads”. J. Biomechanics 19(1) pp. 79-84.

MSC Marc Mentat (2005). Volume B. Element Library.

MSC Marc Mentat (2005). Volume A. Theory and User Guide.

Nachemson A, Schultz, A and Berkson M. (1979). “Mechanical Properties of Human Lumbar Spine Motion Segments: Influence of Age, Sex, Disc Level and Degeneration”. Spine 4(1): pp. 1-8.

Natali AN, and Meroi EA. (1990). “The mechanical behavior of bony endplate and annulus in prolapse disc configuration”. J. Biomedical Engineering 15: 235-239.

Natarajan RN, Ke JH, Anderson GBJ. (1994). “A model to study the disc degeneration process”. Spine 19: 259-265.

Noailly j. “ Model developments for in silico studies of the lumbar spine biomechanics” (2009). PhD Tesis. Technical University of Catalonia.

Noailly J, Lacroix D and Planell J. (2003). “The mechanical significanse of the lumbar spine components – A finite element stress analysis”. 2003 Summer Bioengineering Conference, June 25-29, Sonesta Beach Resort in Key Biscayne, Florida.

Noailly J, Wilke H-J, Planell J and Lacroix D. “ How does the geometry affect the internal biomechanics of a lumbar spine bi-segment finite element model ? Consequences on the validation process. Journal of Biomechanics 40(11): 2414-2425.

Oleyede A, Broom ND and Martinez JB. (1998). “Experimental factors governing the internal stress state of the intervertebral disc”. Medical Engineering & Physics 20, pp. 631-637.

Panagiotacopulos ND, Bloch R, Knauss WG, Harvey P and Patzakis M (1977). “Viscoelastic behavior of the human intervertebral disc under consideration of moisture migration”. Project Report. California Institute of Technology, Pasadena CA USA, Grant No. 77-3139.

Panjabi, M., Krag M.H., White A, and Southwick, W. (1977). “Effects of Preload on Load Displacement Curves of the Lumbar Spine”. Orhopedic Clinics of North America. Vol.8, N. 1. pp 181-193.

Panjabi MM, Krag MH and White AA (1984). “Effects of disc injury on mechanical behavior of the human spine”. Spine 9(7) pp. 707-713.

Pearcy, M.J. y Tibrewal, S.B. (1984). Axial rotation and lateral bending in the normal lumbar spine measured by three-dimensional radiography. Spine Vol 9 (6) pp.582-587.

Pollintine P, Van Tunen M, Luo J, Brown M, Dolan P and Adams M. (2010). “Time-dependent compressive deformation of the ageing spine: Relevance to spinal stenosis” Spine 35(4): 386-394.

Rao A, and Dumas G. (1991). “Influence of material properties on the mechanical behavior of the L5-S1 intervertebral disc in compression: A nonlinear finite element element study”. J. Biomedical Engineering 13: 139-151.

Resnick D. (1994). “Diagnosis of Bone and Joint Disorders: Degenerative Disease of the Spine”. W.B. Saunders. Vol.2, Chapter 35: p.1382-1471.

Rohlmann A, Zander T, Schmidt H, Wilke HJ, and Bergmann G. (2006). “Analysis of the influence of disc degeneration on the mechanical behavior of a lumbar motion segment using the finite element method”. Journal of Biomechanics 39: 2484-2490.

Ruberté LM, Natarajan R, Andersson GBJ. (2009). “Influence of single-level lumbar degenerative disc disease on the behavior of the adjacent segments - A finite element study”. Journal of Biomechanics 42, pp. 341-348.

Schmidt H, Kettler A, Rohlmann A, Claes L and WilkeHJ. (2007). “The risk of disc prolapses with complex loading in different degrees of disc degeneration – A finite element analysis”. Clinical Biomechanics, 22(9) pp 988-998.

Schmorl’s C and Junghans H (1932). “Die gesunde und kranke wirbelsaule (The healthy and sick spine) ”. Fortchritte auf dem gebiete der röntgenstrahlen, supplementary volume 43, Leipzig.

Schultz, A.B., Warwick, D.N., Berkson, M.H. and Nachemson, A.L. (1979). “Mechanical Properties of Human Lumbar Spinal Motion Segments Part I: Responses in Flexion, Extension, Lateral Bending, and Torsion. Journal of Biomechanical Engineering Vol. 101: pp 46-52.

Shirazi-Adl A, Shrivastava SC and Ahmed AM. (1983). “ A 3-D nonlinear finite element analysis of a lumbar disc with annulus modeled as a composie”. Applied mechanics, bioengineering and fluids engineering conference: biomechanical symposium, Houston TX, June 19-22, 1983. pp. 137-140.

Shirazi-Adl, A.A., Shivasta, S.C. y Ahmed, A.M., (1984). Stress analysis of the lumbar disc-body unit in compression: A three-dimensional nonlinear finite element study. Spine 9(2): 120-134.

Shirazi-Adl, A.A., Ahmed, A.M. y Shivasta, S.C. (1986). Mechanical response of a lumbar motion segment in axial torque alone and combine with compression. Spine 11(9): 914-927.

Shirazi-Adl , A. A., Ahmed M. and S. C. Shrivastava. (1986). A finite element study of a lumbar motion segment subjected to pure sagittal plane moments. Journal of Biomechanics, Vol 19(4):331-350.

Smit, TH, Odgaard A and Schneider E (1997). “Structure and function of vertebral trabecular bone”. Spine 22, pp 2823-2833.

Smit TH. (1996). “The mechanical significance of the trabecular bone architecture in a human vertebra (Ingenieur) ”. PhD Thesis. Technische Universitat Hamburg-Harburg, Hamburg-Harburg, pp. 49-53.

Spilker RL. (1980). “Mechanical behavior of a simple model of an intervertebral disc under compressive loading”. Journal of biomechanics Vol. 13. pp 895-901.

Spilker R.L., Daugirda, D.M. y Schultz A.B. (1984). Mechanical response of a simple finite element model of the intervertebral disc under complex loading. Journal of Biomechanics, Vol. 17(2): 103-112.

Stokes I. (1987). “Surface strains on human intervertebral discs”. Journal of Orthopeadic Research 5(3): 348-55.

Tanaka N; An HS; Lim T; Fujiwara A; Jeon C; and Haughton V. “The relationship between disc degeneration and flexability of the lumbar spine”. The Spine Journal, Vol. 1(1): pp. 47-56.

Tanaka E, Aoyama , J, Tanaka M, Murata H, Hamada T and Tanne K. (2002). “Dynamic Properties of Bovine Temporomandibular Joint Disks Change with Age”. Journal of Dentresty Research 81(9): 618-622.

Ueno, K. (1987). A three dimensional nonlinear finite element model of lumbar intervertebral joint in torsion. Journal of Biomechanical Engineering. 109: 200-209.

Van der Veen A, Busscher I, van Dieën J, Kingma I, Verkerke G and Veldhuizen A. (2010). “In vitro biomechanical characteristics of the spine: A comparison between human and porcine spinal”. Spine 35(2): E35-E42.

Van Eijden T, Tanaka E (2003). “Biomechanical behavior of the temperomandibular joint disc” Critical review in Oral Biology and Medicine. Publisher SAGE 14(2): 138-150.

Viera, A and Garret J. (2005). "Understanding Interobserber Agreement: The Kappa Statistic". Family Medicine. Vol. 37, No.5 p. 360-363.

Wang, Jaw-Lin, Parnianpour, Mohamad, Shirazi-Adl, Aboulfazl, y Engin, Ali E. (Feb 2000). Viscoelastic Finite-Element Analysis of a Lumbar Motion Segment in Combined Compression and Sagittal Flexion: Effect of Loading Rate. Spine. 25(3):310-318.

Wehrli FW, Leonard MB, Saha PK and Gomberg B. (2004). "Quantitative high resolution magnetic resonance imaging reveals structural implications of renal osteodystrophy on trabecular and cortical bone". Journal of magnetic resonance imaging 20: 83-89.

Yamamoto, I, Panjabi, M., Crisco T and Oxland T. (1989). "Three-Dimensional Movements of the Whole Lumbar Spine and Lumbosacral Joint".Spine 14(11). Pp. 1256-1259.

Yang KH, Khalil T, Tzeng R and King AI. (1983). "Finite element model of a functional spinal unit". Applied mechanics, bioengineering and fluids engineering conference: biomechanical symposium, Houston TX, June 19-22, 1983. pp. 137-140.

Zheng W and Haiyun L. (2005). "A novel 3D finite element modeling based on medical image for intervertebral disc biomechanical analysis". Proceedings of the 2005 IEEE Engineering in Medicine and Biology 27 th Annual Conference, Shanghai, China September 1-4, 2005.

Chapter 5

Conclusions

Chapter 5

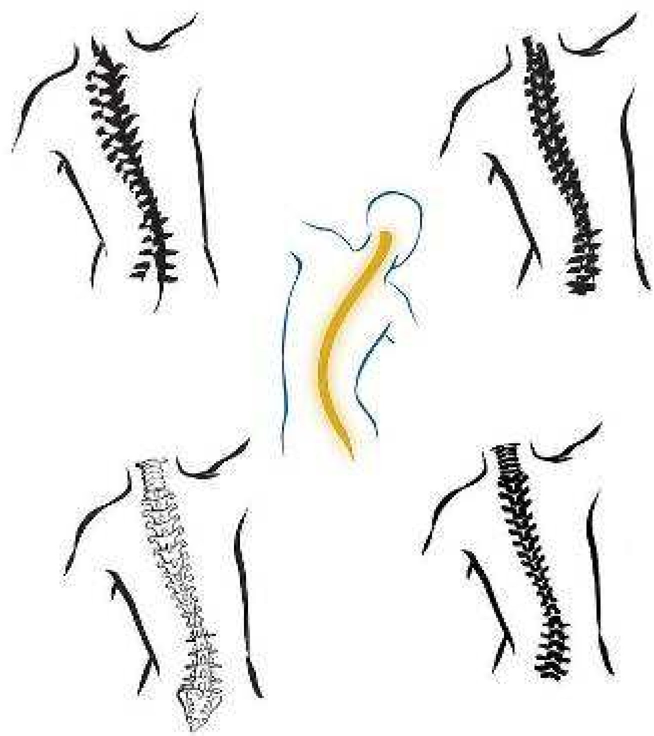

Conclusions

I. Summary of results

The gross anatomy of ten elderly cadaveric intervertebral discs from lumbar levels L2-L3 and L4-L5 was characterized in 3D using magnetic resonance imaging (MRI). Intervertebral osteochondrosis and spondylosis deformans were studied. All the discs showed signs of vacuum phenomena, mostly seen in the nucleus pulposus region, and grew in discs with a clear height collapse. Intervertebral discs with loss of disc space were more prevalent in the L4-L5 disc set. Anterior and lateral marginal osteophytes were identified in all the discs, but were more notorious in discs from the L2-L3 set. In general, the scoring of disc degeneration gave a range covering from mild degeneration (Thomson scale 3) to severe degeneration (Thompson scale 5).

When the discs were tested under static load conditions their mean stiffness showed a nonlinear tendency and a decrease with degeneration. Discs with severe degeneration were 24 % less rigid in compression, 22 % less rigid in flexion-extension, and showed similar stiffness in lateral bending and in torsion in comparison with mild degeneration discs. The disc bulge response was 75% higher in mild degeneration discs, implying the importance of the maintenance of the disc space and water content in these discs. The stress relaxation response showed that the relaxation modulus and time needed for the discs to achieved stable conditions were 40% and 17 % greater in mild degeneration discs, which means that they are better capable of sustaining and cushioning the load.

When the discs were tested under dynamic compression, the dynamic stiffness and dissipation increased with frequency, suggesting that at higher frequencies (5 Hz) the disc is better able to resist higher loads than at low frequencies (0.2 Hz), but also has to dissipate more. For all the discs tested at all the study frequencies, the storage modulus gave around 70 % of the dynamic response and the remaining 30% was given by the loss modulus, implying that the overall behavior of the discs resembles that of a viscoelastic solid, rather than a viscoelastic fluid.

A magnetic resonance image (MRI) based finite element model of disc degeneration was developed using the anatomical background from one MRI T2 weighted sequence of a L2-L3 disc, and validated with the stiffness response gained from the biomechanical testing. Adjustment of material properties was performed on the basis of annulus fibrosus integrity. The minimum difference between the reaction forces of the testing and those from the simulation was used to obtained the Mooney coefficients, which define annulus stiffness, and the results showed that it matched a mild degeneration case, as previously described.

When compression load was simulated, most of the disc was under compressive strains with peak values of 40% predicted at the inner posterior and posterolateral sides of the annulus and nucleus respectively. Tensile strains of 10% were predicted at the outer wall of the annulus fibrosus, suggesting a consistency with the architecture and behaviour of a pressure vessel. The stress distribution showed similar tendencies, with peak compressive stresses of 2 MPa and peak tensile stresses of 0.50 MPa. Disc bulge showed symmetry in all radial directions consistent with the reported behaviour of normal discs; however the prediction was four times larger than the test values.

When bending load was simulated, the disc underwent a transition from compressive strains at the loading side to tensile strains at the opposite side. For each bending mode, the predicted stress and strain in the nucleus grew radially, reaching maximums of 0.2 MPa and 20 % at the periphery. The stress and strain in the annulus showed a ring-like distribution with maximum values of 0.5 MPa and 30% at the outer wall. The torsion load simulation predicted shear stress and strain with maximum values of 0.20 MPa and 30% in the nucleus, and 0.40 MPa and 40% in the annulus. The study showed the relevance of large deformation in the disc, in contrast with negligible deformation of the vertebrae, which shows large stresses, implying bone predisposition to fracture.

II. Limitations

Only degenerated discs corresponding to elderly donors were used in the present study. For a clear comparison of the disc anatomy and the mechanical response, with age or degeneration, it would be desirable to include young and healthy discs.

The resolution of the MRI images were 0.406 x 0.406 x 0.400 mm^3, therefore, anatomical features of smaller size such as collagen fibers, laminae, endplate thickness, bone marrows, proteoglicans and cells were not detected. Nonetheless, the larger anatomical features that also account for disc degeneration: disc collapse, osteophytes, schmorol's nodes and vacuum cavities were well detected by the MRI.

Mechanical characterization of intervertebral discs in this study was based on the methods by Panjabi and White (1976) and Schultz et al. (1979). However, the methodology applied in this study included technical modifications, such as the use of rigid arms instead of strings and pulleys for applying moments, which lead to inaccuracies in the bending angle determination, especially when using small loads. In spite of initial inaccuracies, the disc flexibility showed a nonlinear tendency. Only main motions were measured and any motion coupling or secondary motions that resulted as a consequence of applying a bending or torsion were disregarded.

In loading to compression, the disc bulge was measured at two sites, giving only a partial description of the disc radial distortion. Also, since degeneration affects the disc ability to develop intradiscal pressure, its measurement is taken as a reliable indicator and consequently helps to sort out differences among degeneration stages. Thus, another limitation of this study was the absence of pressure measurements. The advanced degeneration of most discs used in this study favored stress relaxation testing, over creep testing, giving an incomplete description of the viscoelastic effects of the disc. Disc viscoelasticity was analytically modeled using a linear solid model which is more ideal for predicting behavior of rubber, plastics and elastomers. Still, the predictions by the Maxwell arm gave a ratio of stiffness to viscosity of the nucleus within documented values.

The finite element simulation performed using only one sample disc was the main limitation of the numerical simulation. Thus, no clear explanation was provided regarding differences observed between the experimental results and the results obtained from the FE simulation. The stress and strains were calculated changing the material properties: Mooney properties, Bulk modulus, Young's moduli, Shear moduli and Poisson's ratios. Since the development of constitutive equations assumes continuity at the material properties, this approximation represents a limitation.

III. Contributions

This study investigated the distribution of stress and strains in a degenerated intervertebral disc when loaded to compression, bending and torsion using the finite element method. Additionally, the anatomical relevance of disc degeneration and the biomechanical characterization of ten degenerated intervertebral human discs when loaded to static and dynamic conditions were studied. The majority of biomechanical studies of disc degeneration have investigated the stress and strains distribution using a simplification of the disc geometry without giving any anatomical features associated with degeneration. Moreover, because the intervertebral disc undergoes large deformations, any geometrical changes to the configuration have to be analyzed in detail. Therefore, lack of reliable geometrical inputs can lead to an improper strain distributions and can posed questionable results. Furthermore, the studies of discs degeneration that had considered the distribution of stress and strains had been limited to include validation. In this thesis, which is one o few studies implementing medical images of disc degeneration, a finite element model of disc degeneration based on magnetic resonance imaging (MRI) was developed and validated to evaluate the stress and strains acting on the nucleus pulposus and annulus fibrosus when the disc is loaded under compression, bending and torsion.

The methodology presented in this thesis allows extending it not only to other intervertebral discs, but also to bone and organs. The results of this approach could not have been obtained without using a finite element model and an assessment from MRI.

The results obtained help to clarify that:

1) Biomechanical evaluation of intervertebral discs requires knowledge of disc anatomy and geometry, boundary conditions and material properties. The first two were treated by MRI and by mechanical testing, and the latter was treated by material formulations and adopting an adjustment procedure based on the annulus fibrosus integrity.

2) Loading history, postures, properties and integrity of tissues influence the profile of stress and strains inside the intervertebral disc. For healthy and mild degenerative discs, the distribution of stress and strain across the disc section is uniform for all loads, and the formation of disc bulge under compression is symmetric. The nucleus pulposus is the principal load carrier under compressive load, while the annulus fibrosus is the main carrier under bending and torsion load. Discs with severe degeneration show irregular distributions of stress and strain with formation of large stress concentrations, recognized at the posterior side, which is the weakest part of the disc.

3) The large scatter in the mechanical response of the intervertebral discs is normal. Individual differences between discs are obvious (size, age, loading history, gender, race, occupation, habits, lifestyle, etc.) and overtake any class differences with respect to disc level or degree of degeneration.

4) Intervertebral discs with severe degeneration are less rigid in compression, they are less flexible under bending and torsion, they show less disc bulge under compression, and are less solid viscoelastic and dampers. The main degenerative features of these discs were: loss of the disc space (Intervertebral osteochondrosis) and osteophyte formation (spondylosis deformans) at the anterior and lateral margins.

5) A proposed guideline for analyzing other intervertebral discs or other biological tissues has been developed. First, a collection of medical images with good resolution is obtained. Next, a segmentation of materials is performed and a finite element mesh is created to account for the complex geometric shapes. Assignment of regional material properties and application of boundary conditions are made. Finally, validation of the FE model with the experimental testing is performed, or in its absence uses values documented.

IV. Future work

The main objective of this thesis was achieved, *i.e.* to predict the biomechanical response of human degenerated intervertebral discs. However, the process of disc degeneration remains with uncertainties and future efforts should be directed towards improving the understanding of its mechanobiology. Regarding the extension of this study, an integration of numerical models with in vitro and in vivo approaches is a perspective that should be consider. In particular, future work should be aim at the following:

1) Adapt the proposed methodology to the clinical field for the diagnosis of low back pain and other spine disorders in patients.

2) Model the collagen fibers of the annulus fibrosus for a better prediction of the disc bulge and distribution of stress and strains, especially in the outer walls of the annulus.

3) Simulate the load conditions in the model of advance degeneration, to verify the stress concentrations at the disc posterior side. Also, simulate the stress relaxation and the dynamic compression in the current model to verify the viscoelastic response.

4) Include poroelastic and osmotic material formulations to take into account the intradiscal pressure and diffusion of the disc, as these are known to decay with age and degeneration. Additionally validate the model with intradiscal pressure measurements in vitro.

5) Develop a more automatic and patient specific method to analyze all discs.

Appendix

Appendix

I. Instrumentation for measuring disc bulge and deflections in the MTS Bionix 858 system.

This work was done motivated at improving the Bionix versatility for measuring external signals for a broad range of testing types. In the case of the testing protocols in compression, flexion and torsion the measurements of bulging and torque needed the implementation of an interface to connect the sensors (BNC) to the LPT (dB25) port entrance of the Bionix console. Additionally more external signals were incorporated and included: pressure, temperature and an LVDT (linear variable differential transformer) position sensor. Such task represents the possibility of conducting testing with multiple data acquisition.

In order to measure the disc bulge, two displacement sensors were used. Also, when loading the discs to axial rotation a cell for the measuring of torque was required. These external signals had to be first treated and then introduced through the back panel of the MTS Bionix control console, see Figure A1.1.

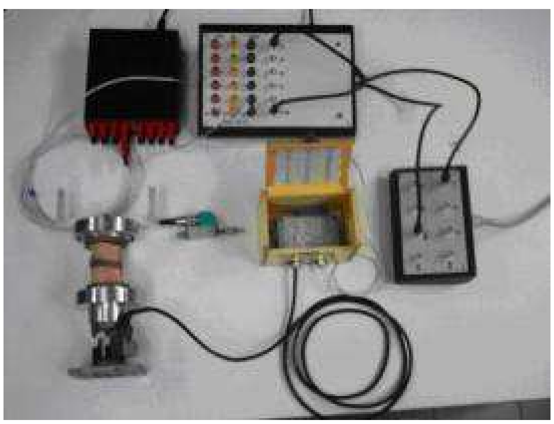

(A)

(B)

Figure A1.1. (A) Instrumentation for the sensors of displacement and torque. (B) Connection of the sensors signals through the back panel of the Bionix controller.

All the sensors had to be calibrated first before any connections to the console. The calibration of the torque cell was done using a lever arm and masses applied at each end, see Figure A1.2.

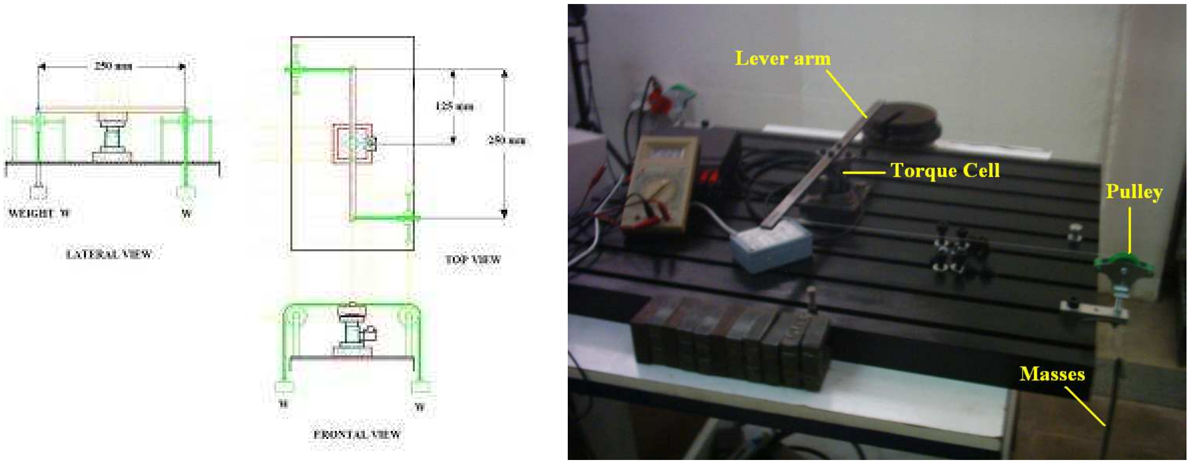

Figure A1.2. (A) Calibration of the torque cell using masses.

For each mass applied a torsion moment was produced and the cell emitted a voltage which was recorded to be linear for the full scale, see the graphic of Figure A1.3.

Torque (N-m)	Voltage (volts)
0.00	0.000
2.45	0.901
4.91	1.828
7.36	2.748
9.81	3.681
12.26	4.591
14.72	5.518
17.17	6.445
19.62	7.338
22.07	8.305
24.53	9.238
26.98	10.138
26.61	10

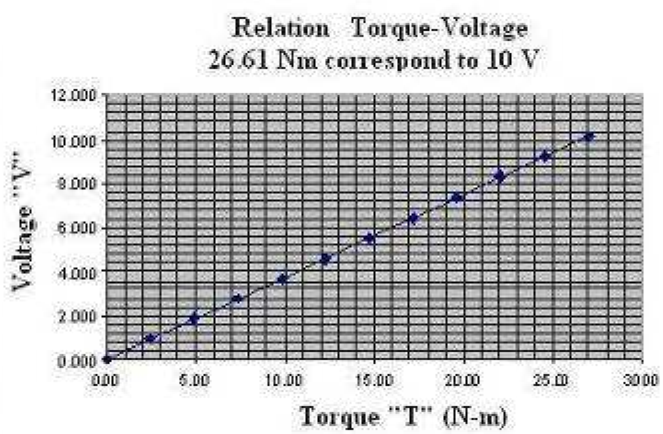

Figure A1.3. Linearity of the torque cell.

The calibration of the displacement sensors were done directly by applying a displacement through length gauges and the potentiometer emitted a voltage which was also recorded, see Figure A1.4.

After calibration, the displacement sensors were connected to a ± 5 V power source, while the torque cell was connected to a + 10V power source. The output signal of the transducers were sent to a connector box and then to the J42 port of the MTS console using a db25 pin connector, see Figure A1.5.

Finally, all the external signals coming from the J42 port were activated and configured in the signals menu of the TestStar Software of the Bionix system.

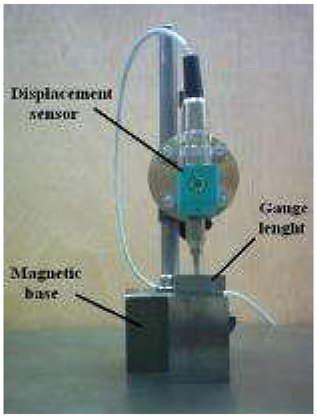

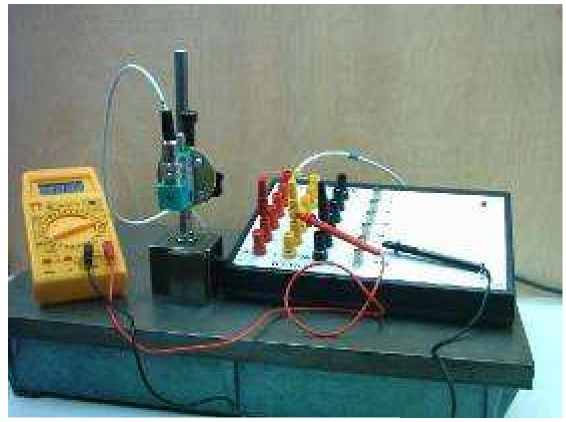

Range (mm)	Voltage
0	4.82
1	3.89
2	2.98
3	2.07
4	1.16
5	0.23
6	-0.67
7	-1.59
8	-2.52
9	-3.42
10	-4.33

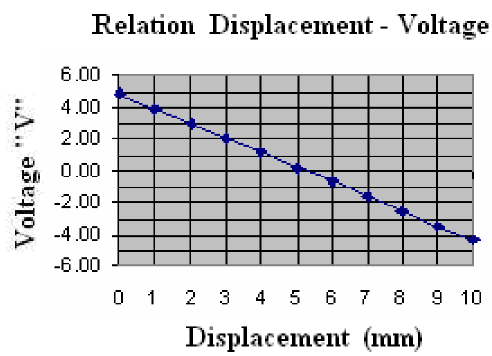

Figure A1.4.Calibration and linearity of the displacement sensors.

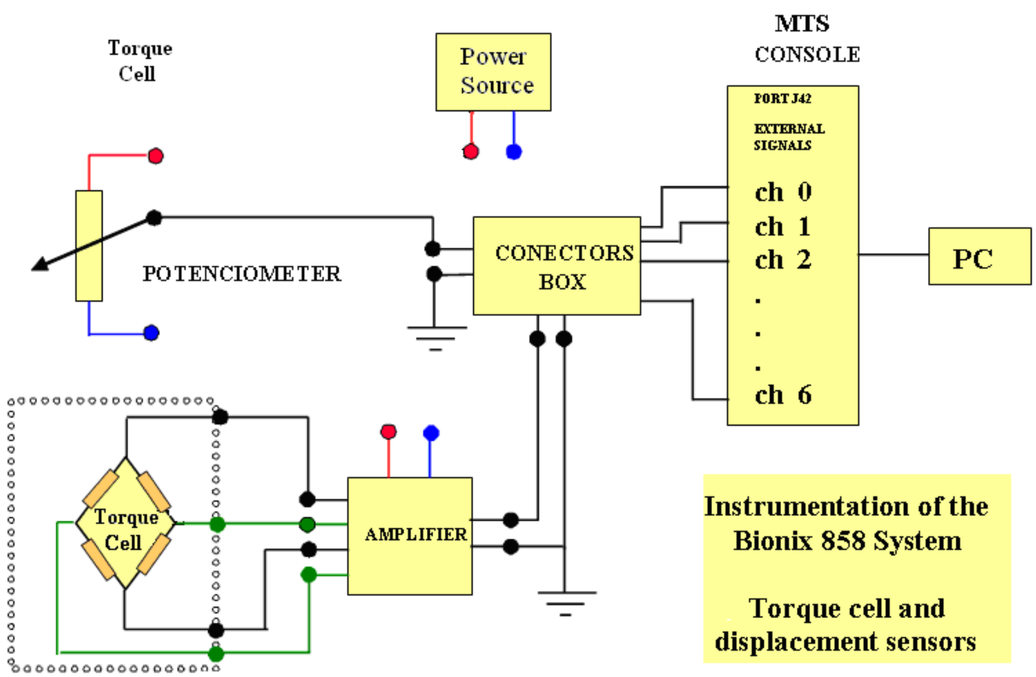

Figure A1.5. Flow chart of the torque and displacement sensors instrumentation.

II. Orthotropy, hyperelasticity and viscoelasticity

The basic fundamentals of orthotropy, hyperelasticity with incompressibility and viscoelasticity are needed for a comprehensive understanding of the mechanical behavior of the vertebral bone and the intervertebral disc. These formulations are described next based on the stiffness matrix.

When the mechanical properties of a material are directional dependent, then it will exhibit anisotropy. The stiffness matrix of an anisotropic material is defined by 36 constants, we can write the direct stiffness method equation as:

$$\begin{bmatrix}\sigma_{11}\\ \sigma_{22}\\ \sigma_{33}\\ \sigma_{12}\\ \sigma_{23}\\ \sigma_{31}\end{bmatrix}=\begin{bmatrix}k_{11} & k_{12} & k_{13} & k_{14} & k_{15} & k_{16}\\ k_{21} & k_{22} & k_{23} & k_{24} & k_{25} & k_{26}\\ k_{31} & k_{32} & k_{33} & k_{34} & k_{35} & k_{36}\\ k_{41} & k_{42} & k_{43} & k_{44} & k_{45} & k_{46}\\ k_{51} & k_{52} & k_{53} & k_{54} & k_{55} & k_{56}\\ k_{61} & k_{62} & k_{63} & k_{64} & k_{65} & k_{66}\end{bmatrix}\begin{bmatrix}\varepsilon_{11}\\ \varepsilon_{22}\\ \varepsilon_{33}\\ \varepsilon_{12}\\ \varepsilon_{23}\\ \varepsilon_{31}\end{bmatrix} \tag{A2-1}$$

however, $k_{12}=k_{21}$, $k_{23}=k_{32}$,… and in general $k_{mn}=k_{nm}$, and therefore only 21 constants are independent, then Eq (A2-1) reduces to:

$$\begin{bmatrix}\sigma_{11}\\ \sigma_{22}\\ \sigma_{33}\\ \sigma_{12}\\ \sigma_{23}\\ \sigma_{31}\end{bmatrix}=\begin{bmatrix}k_{11} & k_{12} & k_{13} & k_{14} & k_{15} & k_{16}\\ & k_{22} & k_{23} & k_{24} & k_{25} & k_{26}\\ & & k_{33} & k_{34} & k_{35} & k_{36}\\ & & & k_{44} & k_{45} & k_{46}\\ & & & & k_{55} & k_{56}\\ & & & & & k_{66}\end{bmatrix}\begin{bmatrix}\varepsilon_{11}\\ \varepsilon_{22}\\ \varepsilon_{33}\\ \varepsilon_{12}\\ \varepsilon_{23}\\ \varepsilon_{31}\end{bmatrix} \tag{A2-2}$$

The left side of Eq (A2-2) correspond to the stress tensor σ_{ij} which contains the normal stress and the shear stress. The far right side contains the strain tensor ε_{ij} and the stiffness matrix. The former contains the normal strain and the shear strain, while the latter contains the 21 independent constants k.

If assuming that no shear strain is involve, then the stress tensor σ_{ij} will contain only normal components and the stiffness matrix of Eq (A2-2) reduces to 9 constants, of which only 6 are independent:

$$\begin{bmatrix}\sigma_{11}\\ \sigma_{22}\\ \sigma_{33}\end{bmatrix}=\begin{bmatrix}k_{11} & k_{12} & k_{13}\\ & k_{22} & k_{23}\\ & & k_{33}\end{bmatrix}\begin{bmatrix}\varepsilon_{11}\\ \varepsilon_{22}\\ \varepsilon_{33}\end{bmatrix} \tag{A2-3}$$

where k_{11}, k_{22}, and k_{33} are the material stiffness in the normal directions 1, 2 and 3 respectively. The constants k_{12}, k_{23}, and k_{13} are the material stiffness in the tangential directions.

Materials that do not exhibit shear deformation upon loading are called orthotropic, thus, there is no change in form of the cross sectional area, but only its volume. These materials are defined by three stiffness constants, or Young´s modulus E, and three tangential stiffness or shear moduli G. Thus, we can rewrite Eq (A2-3) as:

$$\begin{bmatrix} \sigma_{11} \\ \sigma_{22} \\ \sigma_{33} \end{bmatrix} = \begin{bmatrix} E_{11} & G_{12} & G_{13} \\ & E_{22} & G_{23} \\ & & E_{33} \end{bmatrix} \begin{bmatrix} \varepsilon_{11} \\ \varepsilon_{22} \\ \varepsilon_{33} \end{bmatrix} \tag{A2-4}$$

Bone structure (see Figure 2.7) resembles an orthotropic material. Therefore, in practice cancellous and cortical bone are formulated with only two independent moduli E, a longitudinal E_{22} and a radial in which $E_{11}=E_{33}=E$. Also the maximum shear modulus occurs in the normal plane to the stiffer axis, which for the orientation of the two proposed disc models is the vertical axis #2. Then, $G_{12}=G_{23}=G$ is the maximum and the other value is G_{13} and Eq (A2-4) is rewritten as

$$\begin{bmatrix} \sigma_{11} \\ \sigma_{22} \\ \sigma_{33} \end{bmatrix} = \begin{bmatrix} E & G & G_{13} \\ & E_{22} & G \\ & & E \end{bmatrix} \begin{bmatrix} \varepsilon_{11} \\ \varepsilon_{22} \\ \varepsilon_{33} \end{bmatrix} \tag{A2-5}$$

If a material exhibits the same behavior in the three directions, then the stiffness matrix of Eq (A2-5) will reduce to only two independent constants, E and G and the material is called isotropic, thus we can write:

$$\begin{bmatrix} \sigma_{11} \\ \sigma_{22} \\ \sigma_{33} \end{bmatrix} = \begin{bmatrix} E & G & G \\ & E & G \\ & & E \end{bmatrix} \begin{bmatrix} \varepsilon_{11} \\ \varepsilon_{22} \\ \varepsilon_{33} \end{bmatrix} \tag{A2-6}$$

Anisotropy is a common feature in biological soft tissue structures. However, values of the constants for a particular tissue is a challenging task that requires skills and specific testing under physiological conditions, that sometimes is not possible to reproduce in ex-vivo. Thus, it was decided to treat the nucleus pulposus and annulus fibrosus as isotropic nonlinear materials. Also, since collagen is the principal solid material of the nucleus and annulus, the hyperelastic behavior was considered for stress analysis. The high water content of the nucleus and annulus favors the use of an incompressible material formulation based on the Mooney-Rivlin and Neo-Hookean solid. The two solid models are an extension of Hooke's law for large deformations (hyperelasticity) and are usable for plastics and rubber-like substances.

The response of a hyperelastic material, to an applied stress differs from that of a linear elastic material. While a linear elastic material has a linear relationship between applied stress and strain, a hyperelastic material will initially be linear, but at a certain point, the stress-strain curve will flatten due to the release of energy as heat while straining the material. Then, at another point, the elastic modulus of the material will change again.
This hyperelasticity, or rubber elasticity, is often observed in polymers organic and non-organic. Cross-linked polymers will act in this way because initially the polymer chains can move relative to each other when a stress is applied. However, at a certain point the polymer chains will be stretched to the maximum point that the covalent cross links will allow, and this will cause an increase in the elastic modulus of the material.

The model of *Mooney-Rivlin* solid assumes that the extra stresses due to deformation are proportional to the deformation tensor:

$$\sigma = 2C_1 B + 2C_2 B^{-1} + (-p)I \quad \text{(A2-7)}$$

where σ is the stress tensor, C_1 is a constant obtained using the statistical theory for rubber and is related to the molecular network structure (Treloar et al. 1943), the second constant C_2 comes from a purely phenomenological model of elastomers originally proposed by Mooney (1940), B is the deformation tensor, p pressure and I is the unit tensor.
Stress calculation in an elastomer material requires the existence of a strain energy function W, which is usually defined in terms of invariants $\bar{I}$ or stretch ratios λ. Shown on Figure A2.1 is a rectangular block where λ_1, λ_2 and λ_3 are the principal stretch ratios along the edges of the block defined by:

$$\lambda = \frac{L_i + \Delta L_i}{L_i} = 1 + \varepsilon_i \quad \text{(A2-8)}$$

where $\varepsilon_i = \frac{\Delta L_i}{L_i}$ is the deformation.

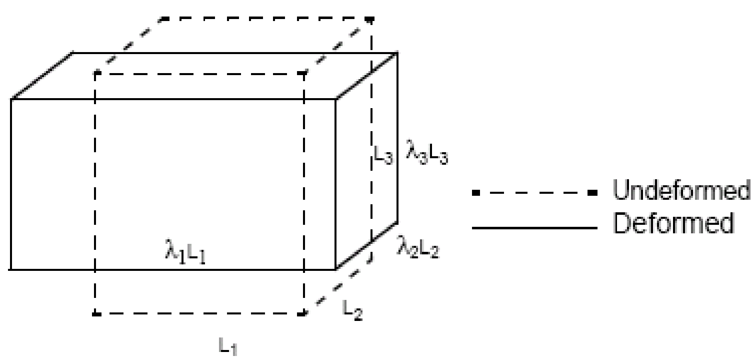

Figure A2.1. Rectangular rubber block. In incompressibility the initial volume remains unchanged and only shape changes are taken into account.

In practice, the elastomer behavior under compression is approximately incompressible, thus $\sum_{i=1}^{3} \varepsilon_i = 0$, leading to the constraint equation:

$$\lambda_1 \lambda_2 \lambda_3 = 1 \qquad \text{(A2-9)}$$

then, the strain invariants are defined as:

$$\begin{aligned} I_1 &= \lambda_1^{\,2} + \lambda_2^{\,2} + \lambda_3^{\,2} \\ I_2 &= \lambda_1^{\,2}\lambda_2^{\,2} + \lambda_2^{\,2}\lambda_3^{\,2} + \lambda_3^{\,2}\lambda_1^{\,2} \\ I_3 &= \lambda_1^{\,2}\lambda_2^{\,2}\lambda_3^{\,2} \end{aligned} \qquad \text{(A2-10)}$$

Strain energy calculations in solids are made using the lagrange formulation, either using a reference configuration (at $t = 0$) called total lagrange or a current ($t = n+1$) named updated lagrange. In any case the strain energy will be the same since its a scalar and an invariant. Also, to account for the incompressibility condition of Eq (A2-9), the strain energy function W is split into deviatoric and volumetric parts as follows:

$$W = W_{deviatoric} + W_{volumetric} \qquad \text{(A2-11)}$$

thus, the deviatoric part of W will take into account energy only as a result of changes in the block *shape*, while the volumetric part of W will consider only the energy that result from changes in the block *volume*. The shape changes in a body are related to its shear modulus G while the volume changes are referred to its bulk modulus K. Therefore, Eq (A2-11) can be rewritten as:

$$W = C_1\left(\bar{I}_1 - 3\right) + C_2\left(\bar{I}_2 - 3\right) + \frac{1}{d}(J-1)^2 \qquad \text{(A2-12)}$$

where $\bar{I}_1, \bar{I}_2$ are the first and the second invariant of the deviatoric component of the strain tensor. Also, the volumetric component of the strain tensor is given by the third term in Eq (A2-12) and by the following relationships:

$$d = \frac{K}{2} \qquad J = \frac{V}{V_0} \qquad \text{(A2-13)}$$

where d is the material incompressibility parameter and J is the local volume ratio. It can be shown from Eq (A2-12) that a material with a high value of K can be treated as incompressible since its volumetric contribution of the strain energy diminishes. Then, Eq (A2-12) reduces to only the deviatoric part

$$W = C_1\left(\bar{I}_1 - 3\right) + C_2\left(\bar{I}_2 - 3\right) \qquad \text{(A2-14)}$$

Thus, *W* for the *Mooney-Rivlin* solid model is a linear combination of two invariants of the deformation or finger tensor *B.*

When working with incompressible materials Marc Mentat™ calculates the corresponding *Young´s module E* using the following relationships:

$$E = 6(C_1+C_2) \qquad \text{(A2-15)}$$

$$C_2 = \frac{1}{4} C_1 \qquad \text{(A2-16)}$$

If in Eq (A2-14) $C_1 = \frac{1}{2} G$ and $C_2=0$, we obtain a *Neo-Hookean solid*, a special case of a *Mooney-Rivlin* solid and Eq (A2-14) reduces to

$$W = \frac{1}{2} G I_B \qquad \text{(A2-17)}$$

where *W* is the potential energy and $I_B=tr(B)$ is the trace or the first invariant of the deformation tensor *B.*

Finally, in the simulation of the loading stage the intervertebral was formulated as a hyperelastic material. Whereas in the stress relaxation simulation, - not included in this study -, a viscoelastic formulation should be used. Compressing statically and dynamically the disc is accompanied by hysteresis, relaxation and creep. But, because the experimental protocols were carried out under a constant strain, only the stress relaxation and hysteresis were analyzed. Also, it was assumed that small to moderated deformations were present, and thus a linear relationship for stress relaxation was employed using the Volterra equation (A2-18):

$$\sigma(t) = E_{inst,relax}\varepsilon(t) + \int_0^t F(t-t')\overset{\circ}{\varepsilon}(t')dt' \qquad \text{(A2-18)}$$

where *t* is the time, $\sigma(t)$ is the stress, $\varepsilon(t)$ is the strain, $E_{inst,relax}$ is the instantaneous elastic modulus for relaxation, and $F(t)$ is the relaxation function refer to the decay of stress which occurs after reaching the peak compressive stress. A more familiar expression of Eq (A2-18) was presented in the stress relaxation protocol section; see section 3.II.b and Eq (3-17).

$$\sigma = E_1\varepsilon + E_r \cdot e^{-\left(\frac{E_2}{\eta}\right)\cdot t} \qquad \text{(3-17)}$$

III. Stress analysis and the meaning of stress

The behavior of the different modeled disc tissues will be studied by using a stress and strain analysis of the model. The use of a *Mooney-Rivlin* elastomeric formulation permits analysis of large strains, stress distribution and bulging response, which occur in the testing.

In continuum mechanics, the stress in a body is continuous, and it results from the action of external loads (traction, compression, transversal, eccentric load, etc…). Physically, the stress σ is a measure of the average force per unit area of a surface within a deformable body on which internal forces act. These internal forces are produce as a reaction to external forces *F* applied to the body, and are distributed within the volume of the material body. Thus, the resulting stress distribution in the body is continuous, and can be represented as a function of space coordinates and time.

In general, the stress σ in not uniformly distributed across the area of a body, and consequently the stress at two different points *P* and *Q* are different than the average stress in the whole area, see Figure A3.1.

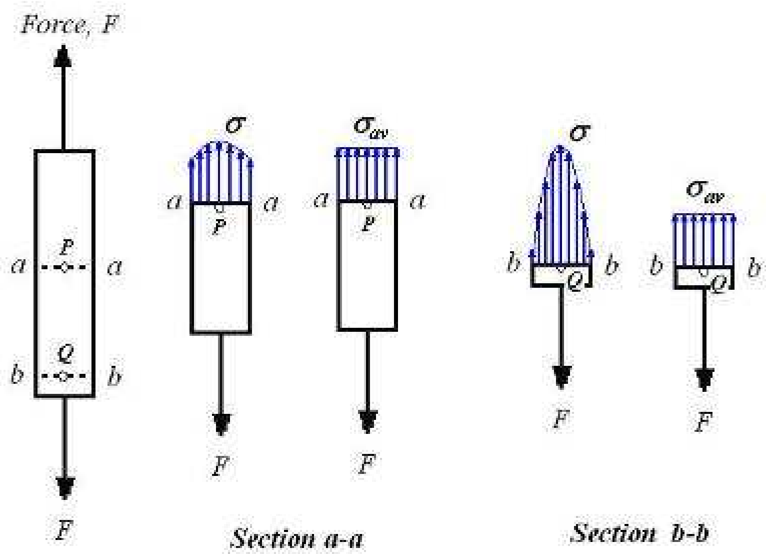

Figure A3.1. Normal stress σ profile in a prismatic bar. The stress in the cross section is not necessary uniform. However, an average normal stress σ_{av} can be used. Observe the closer proximity of point Q (section b-b) to the load application, which causes a higher stress profile than that of point P, as suggested by the Saint-Venant's principle.

Therefore, it is relevant the determination of the stress in a specific point *P*. Such task can be made by analyzing a small area ΔA and using a cubic volume, where a representation of a state of stress holds nine stress components, of which six are independent: three correspond to normal stresses $(\sigma_{11}, \sigma_{22}, \sigma_{33})$ and three to shear stresses $(\sigma_{12}, \sigma_{23}, \sigma_{31})$, as indicated by *Cauchy*, see Figure A3.2.

Thus, the stress of each point in the body is continuous and each point is defined by the six independent stress components σ_{ij} of the second order tensor, known as the *Cauchy stress tensor*, see Eq (A3-1).

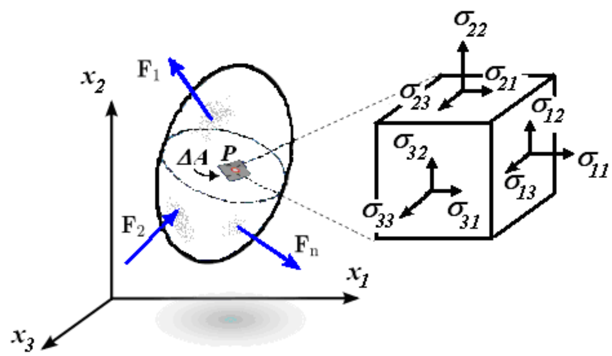

Figure A3.2. A continuous body with external forces F and a general state of stress at point P for a small cubic volume. The nine stress components define the Cauchy stress tensor σ_{ij}.

$$\sigma_{i_j} = \begin{bmatrix} \sigma_{11}\sigma_{12}\sigma_{13} \\ \sigma_{21}\sigma_{22}\sigma_{23} \\ \sigma_{31}\sigma_{32}\sigma_{33} \end{bmatrix} \equiv \begin{bmatrix} \sigma_{xx}\sigma_{xy}\sigma_{xz} \\ \sigma_{yx}\sigma_{yy}\sigma_{yz} \\ \sigma_{zx}\sigma_{zy}\sigma_{zz} \end{bmatrix} \equiv \begin{bmatrix} \sigma_{x}\tau_{xy}\tau_{xz} \\ \tau_{yx}\sigma_{yy}\tau_{yz} \\ \tau_{zx}\tau_{zy}\sigma_{zz} \end{bmatrix} \equiv \begin{bmatrix} \sigma_x & \tau_{xy} & \tau_{xz} \\ & \sigma_y & \tau_{yz} \\ & & \sigma_z \end{bmatrix} \qquad \text{(A3-1)}$$

Replacing the subscripts *1*, *2* and *3* for *x*, *y* and *z* respectively, the three normal stresses are now shown in the principal diagonal of the tensor as σ_x, σ_y and σ_z, and the three shear stresses as τ_{xy}, τ_{yz} and τ_{xz}.

The general case of stress analysis is the *3D* or *spatial problem*, and involves all six independent stress components, $\sigma_x,\sigma_y,\sigma_z,\tau_{xy},\tau_{yz}$ and τ_{xz} of the *Cauchy stress tensor*, which is a three-by-three symmetric matrix, see Figure A3.3.

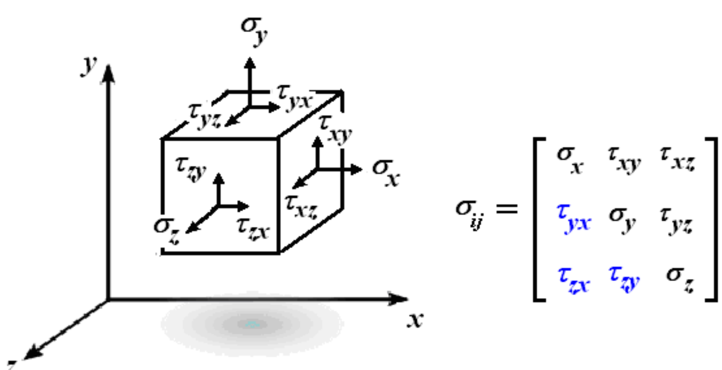

Figure A3.3. Stress condition for a 3D or spatial case. The six independent stress components are shown in black.

The solution of the 3 x 3 matrix of the stress tensor involves the determination of the principal stresses (condition in which the shear stress component vanishes, and $\tau = 0$). Thus, their determination resolves the following problem:

$$(\boldsymbol{\sigma}_{ij} - \lambda \boldsymbol{I}_3)\boldsymbol{n} = 0 \qquad \text{(A3-2)}$$

where $\boldsymbol{\sigma}_{ij}$ is the stress tensor, λ is the normal stress on the plane of analysis, $\boldsymbol{I}_3$ is the identity matrix of order three and $\boldsymbol{n}$ is the normal vector.

The solution of Eq (A3-2) implies that $(\boldsymbol{\sigma}_{ij} - \lambda \boldsymbol{I}_3) = 0$, which can be written as:

$$\begin{bmatrix} \sigma_{11} - \lambda & \sigma_{12} & \sigma_{13} \\ \sigma_{21} & \sigma_{22} - \lambda & \sigma_{23} \\ \sigma_{31} & \sigma_{32} & \sigma_{33} - \lambda \end{bmatrix} = 0 \qquad \text{(A3-3)}$$

The solution of Eq (A3-3) gives three eigenvalues: λ_1, λ_2 and λ_3 which are the principal stresses: σ_1, σ_2, and σ_3 respectively, and are the roots of the following characteristic polynomial equation:

$$det\,(\boldsymbol{\sigma}_{ij} - \lambda \boldsymbol{I}_3)\boldsymbol{n} = \lambda^3 - A\lambda^2 + B\lambda - C = 0 \qquad \text{(A3-4)}$$

where:

$$\left.\begin{aligned} A &= \sigma_x + \sigma_y + \sigma_z \\ B &= \sigma_x \sigma_y + \sigma_y \sigma_z + \sigma_x \sigma_z - \tau_{xy}^2 - \tau_{yz}^2 - \tau_{xz}^2 \\ C &= \sigma_x \sigma_y \sigma_z + 2\,\tau_{xy}\tau_{yz}\tau_{xz} - \sigma_x \tau_{yz}^2 - \sigma_y \tau_{xz}^2 - \sigma_z \tau_{xy}^2 \end{aligned}\right\} \qquad \text{(A3-5)}$$

A graphical representation of the principal stresses, and in general of the stress transformation, is the *Mohr circle*. Since the *Cauchy stress tensor* also undergoes a transformation when a change is made to the system of coordinates, any change to the state of stress can also be view in the *Mohr circle*, see Figure A3.4.

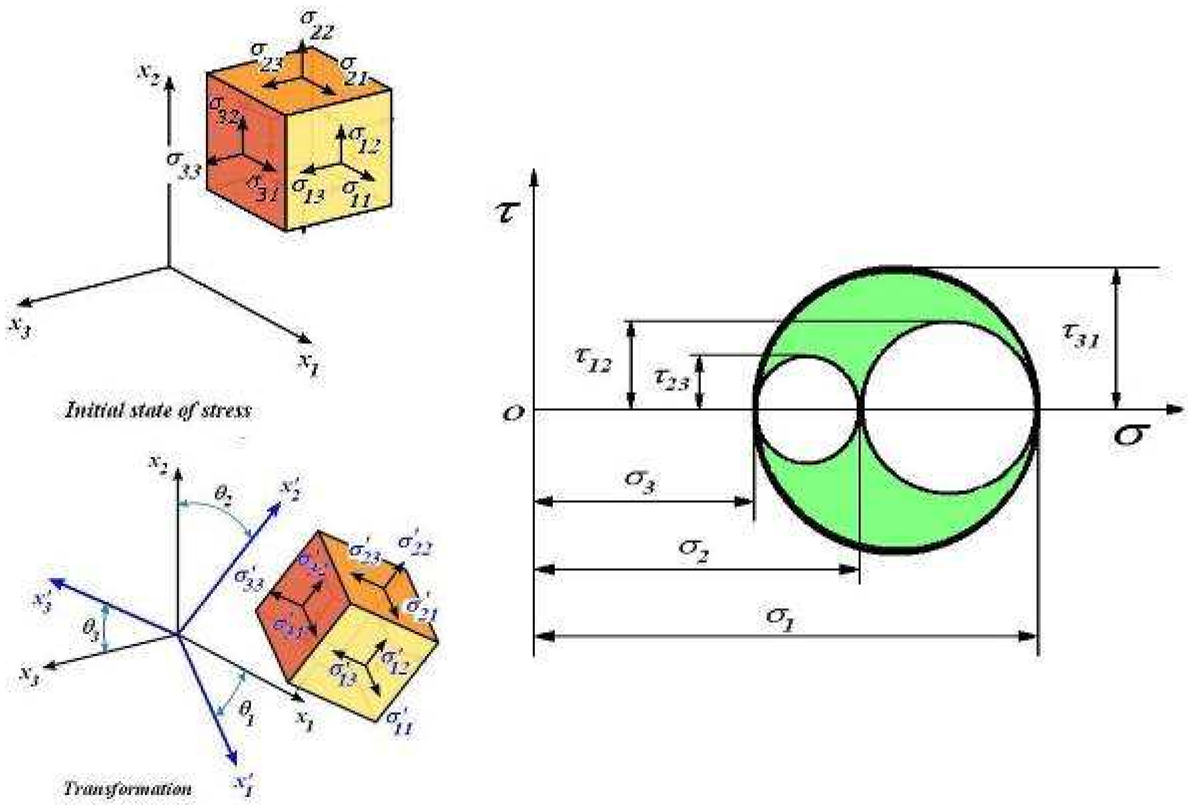

Figure A3.4. Stress transformation and Mohr circle for a 3D stress analysis.

Therefore, the maximum - minimum normal stresses (σ_1, σ_3) and the maximum shear stress *(τ_{3-1})* can be obtain from the *Mohr circle* for 3D stress as follows:

$$\left.\begin{aligned}\sigma_{\max} &= \sigma_1 \\ \sigma_{\min} &= \sigma_3 \\ \tau_{31} &= \frac{\sigma_1 - \sigma_3}{2}\end{aligned}\right\} \qquad \text{(A3-6)}$$

For a *biaxial or plane stress analysis*, the stress state is defined by only three components: two normal (σ_x, σ_y) and a shear (τ_{xy}). Physically, it represents the condition of a stretch surface or of a contraction area, which occurs on the walls of a pressure vessel (*Shigley*, *1979*). The two principal stresses are the hoop stress σ_h, and the longitudinal stress σ_l which act over the surface of the pressure vessel, when an internal pressure *P* develops. The hoop stress is the stress component that makes the vessel grows in diameter, while the longitudinal stress is the stress component that makes the vessel grows in longitude. In the case of a thick wall pressure vessel, there is a third stress component called the radial stress σ_r, which acts across the wall thickness, see Figure A3.5.

A *Mohr circle* for this surface condition is characterized by having both principal stresses with the same sign. These observations were used by *White et al (1990)* to calculate the stresses in the intervertebral disc.

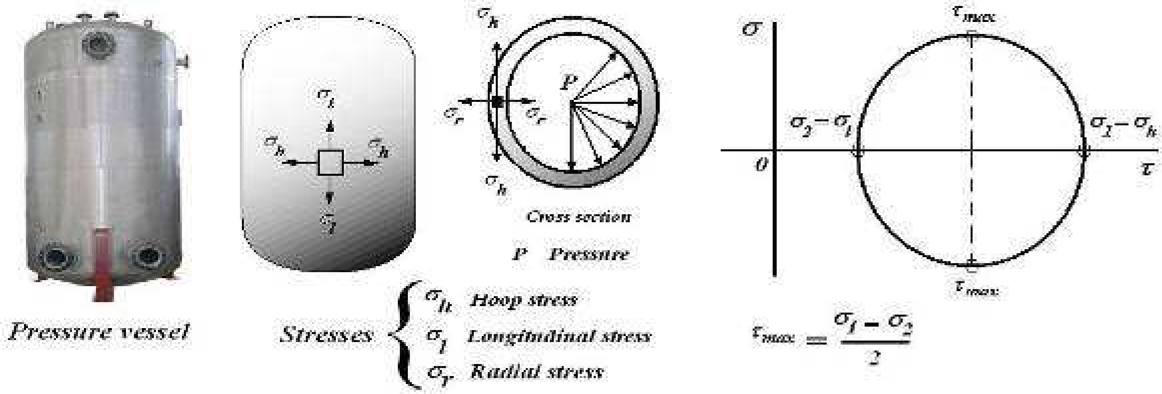

(A) (B)

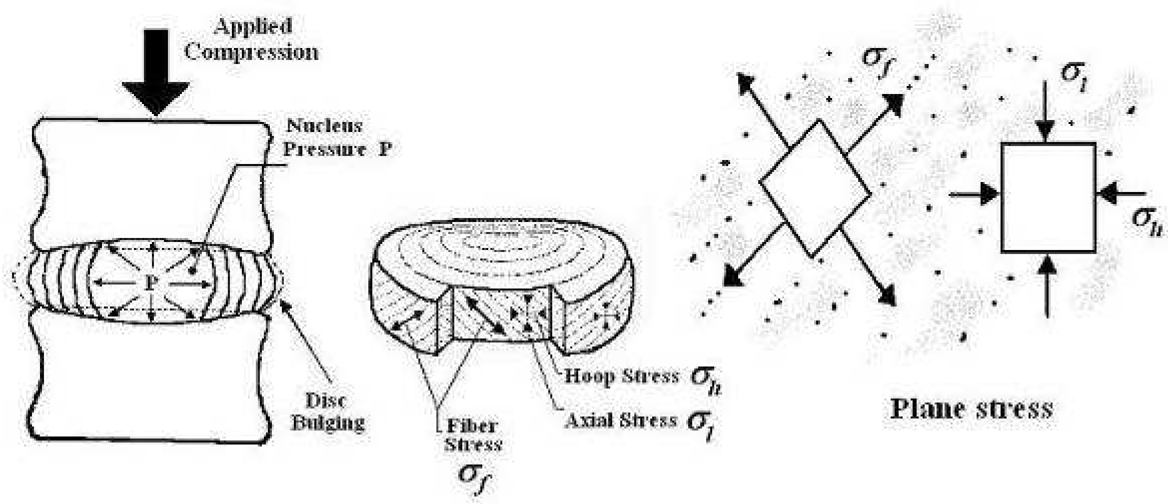

(C)

Figure A3.5. (A) Stresses in a pressure vessel. (B) The corresponding Mohr circle for the condition of plane stress. (C) The stresses in the intervertebral disc, as suggested by White and Punjabi (1990).

For uniaxial loads, such as compression, traction, torsion and bending, the principal stresses and maximum shear are given solely by the respective loads. The *Mohr circles* for these conditions are shown in Figure A3.6.

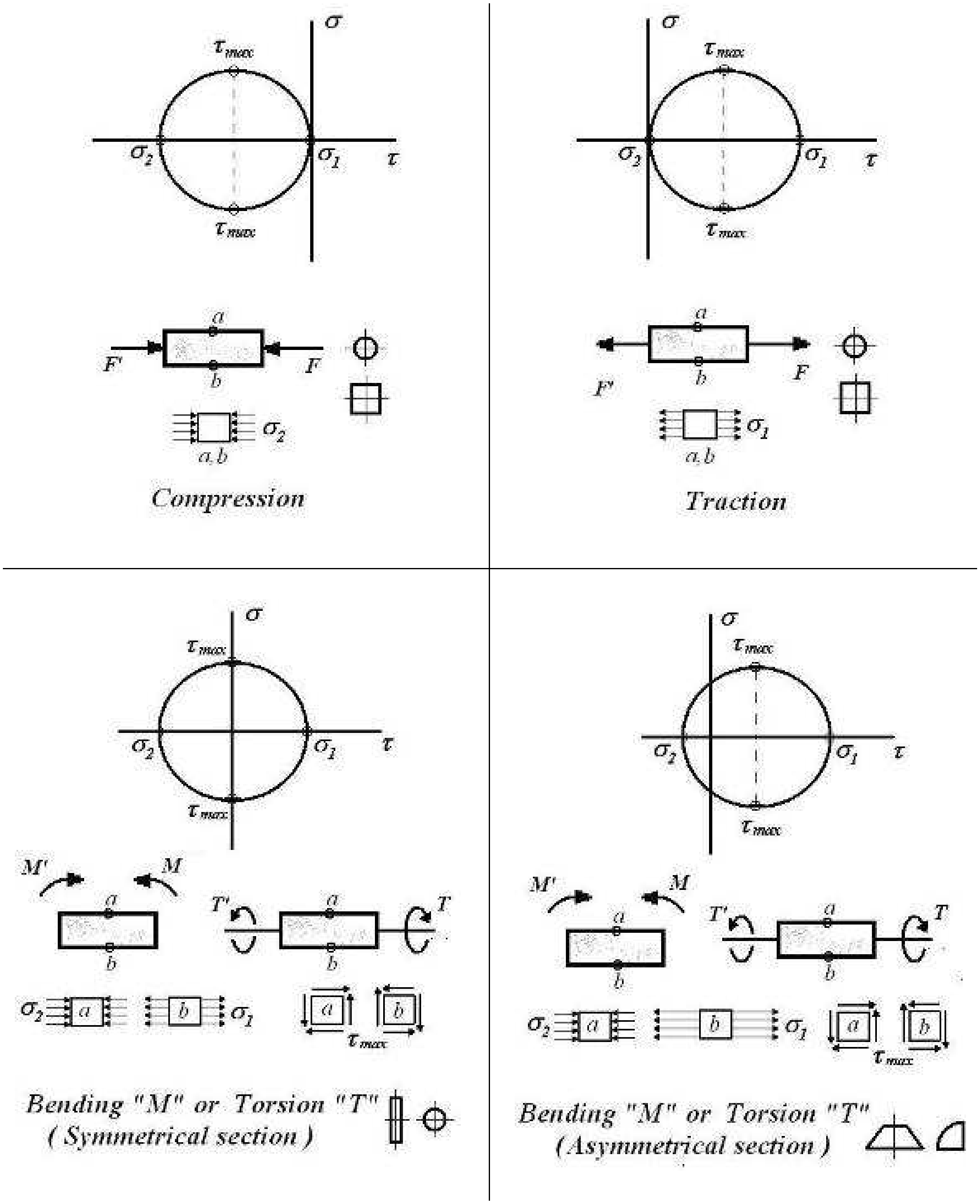

Figure A3.6. Mohr circles for uniaxial loads in compression, traction, torsion and bending.

IV. Lagrangian formulation for the description of the kinematics of deformation

In the Lagrangian method, the finite element mesh is attached to the material and moves through space along with the material. In this case, there is no difficulty in establishing stress or strain histories at a particular material point and the treatment of free surfaces is natural and straightforward.

The Lagrangian approach also naturally describes the deformation of structural elements; that is, shells and beams, and transient problems, such as the indentation problem shown in Figure A4.1.

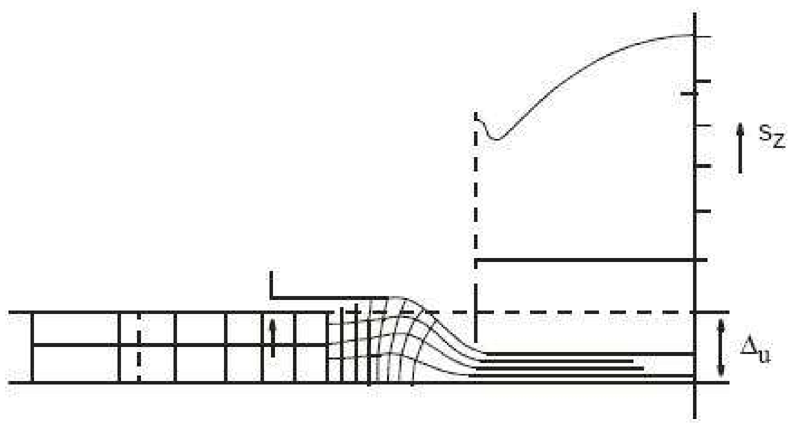

Figure A4.1 Indentation Problem with Pressure Distribution on Tool.

This method can also analyze steady-state processes such as extrusion and rolling. Shortcomings of the Lagrangian method are that flow problems are difficult to model and that the mesh distortion is as severe as the deformation of the object. Severe mesh distortion is shown in Figure A4.2b. However, recent advances in adaptive meshing and rezoning have alleviated the problems of premature termination of the analysis due to mesh distortions as shown in Figure A4.2c.

The Lagrangian approach can be classified in two categories: the total Lagrangian method and the updated Lagrangian method. In the total Lagrangian approach, the equilibrium is expressed with the original undeformed state as the reference; in the updated Lagrangian approach, the current configuration acts as the reference state. The kinematics of deformation and the description of motion are given in Figure A4.3 and Table A4.1.

Depending on which option is used, the stress and strain results are given in different form as discussed below. If the large displacement (LARGE DISP) or large strain (LARGE STRAIN) parameters are not used, the program uses and prints "engineering" stress and strain measures. These measures are suitable only for analyses without large incremental or total rotation or large incremental or total strains.

Using the LARGE DISP parameter, MSC.Marc uses the total Lagrangian method. The program uses and prints the second Piola-Kirchhoff stress and Green-Lagrange strain. These measures are suitable for analysis with large incremental rotations and large incremental strains.
With the LARGE STRAIN, MSC.Marc uses Cauchy stresses and true strains. This is suitable for analyses with large elastic and plastic strains. Stress and strain components are printed with respect to the current state.

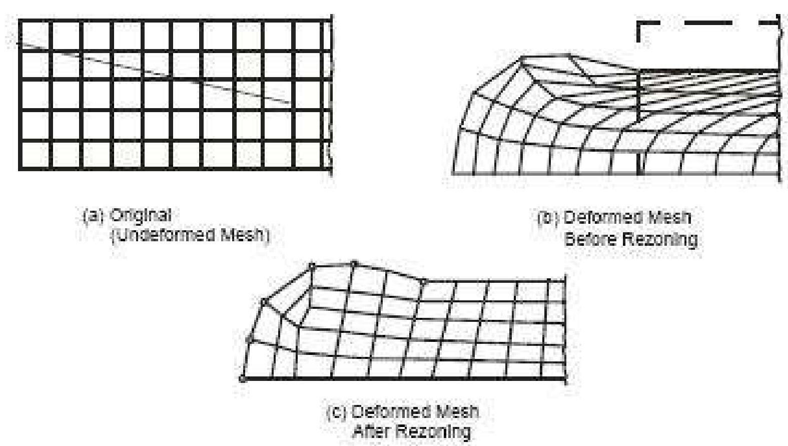

Figure A4.2 Rezoning Example.

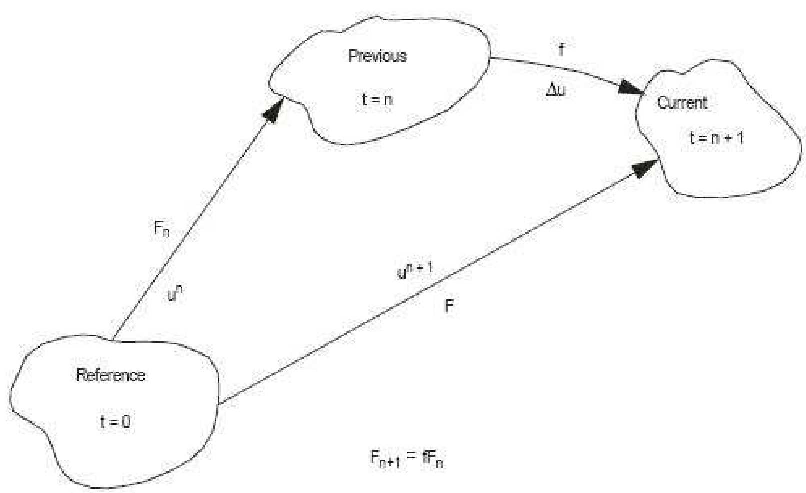

Figure A4.3 Description of motion.

Theoretically and numerically, if formulated mathematically correct, the two formulations yield exactly the same results. However, integration of constitutive equations for certain types of material behavior (for example, plasticity) makes the

implementation of the total Lagrange formulation inconvenient. If the constitutive equations are converted back to the original configuration and proper transformations are applied, then both formulations are equivalent. However, for deformations involving excess distortions, ease of rezoning favors the updated Lagrangian formulation.
This is reflected in the fact that a rezoned mesh in the current state is mapped back to excessively distorted mesh leading to negative Jacobian in the total Lagrangian formulation.

Table A4.1. Kinematics and Stress-Strain Measures in Large Deformation.

Configuration Measures	Reference (t= 0 or n)	Current (t = n+1)
Coordinates	X	x
Deformation tensor	C (Right Cauchy-Green)	b (Left Cauchy-Green)
Strain Measure	E (Green-Lagrange) F (Deformation Gradient)	e (Logarithmic)
Stress Measure	S (Second Piola-Kirchhoff) P (First Piola-Kirchhoff)	σ (Cauchy)

Total Lagrangian Procedure

The total Lagrangian procedure can be used for linear or nonlinear materials, in conjunction with static or dynamic analysis. Although this formulation is based on the initial element geometry, the incremental stiffness matrices are formed to account for previously developed stress and changes in geometry.

This method is suitable for the analysis of nonlinear elastic problems (for instance, with the Mooney or Ogden material behavior or hyperelastic ones. The total Lagrangian approach is also useful for problems in plasticity and creep, where moderately large rotations but small strains occur. A case typical in problems of beam or shell bending. However, this is only due to the approximations involved.

In the total Lagrangian approach, the equilibrium can be expressed by the principle of virtual work as:

$$\int_{V_0} S_{ij}\delta E_{ij}\,dV = \int_{V_0} b_i^0\,\delta\eta_i\,dV + \int_{A_0} t_i^0\,\delta\eta_i\,dA \tag{A4-1}$$

Here S_{ij} is the symmetric second Piola-Kirchhoff stress tensor, E_{ij}, is the Green-Lagrange strain, b_i^0 is the body force in the reference configuration, t_i^0 is the traction vector in the reference configuration, and η_i is the virtual displacements. Integrations are carried out in the original configuration at t = 0. The strains are decomposed in total strains for equilibrated configurations and the incremental strains between t = n and t = n+1 as:

$$E_{ij}^{\ n+1} = E_{ij}^{\ n} + \Delta E_{ij} \tag{A4-2}$$

while the incremental strains are further decomposed into linear, $\Delta E^{l}{}_{ij}$ and nonlinear, $\Delta E^{nl}{}_{ij}$ parts as:

$$\Delta E_{ij} = \Delta E^{l}{}_{ij} + \Delta E^{nl}{}_{ij}$$

where ΔE^{l} is the linear part of the incremental strain expressed as:

$$\Delta E^{l} = \frac{1}{2}\left[\frac{\partial \Delta u_i}{\partial X_j} + \frac{\partial \Delta u_j}{\partial X_i}\right] + \frac{1}{2}\left[\left(\frac{\partial u_k{}^{n}}{\partial X_i}\right)\left(\frac{\partial \Delta u_k}{\partial X_j}\right) + \left(\frac{\partial u_k{}^{n}}{\partial X_j}\right)\left(\frac{\partial \Delta u_k}{\partial X_i}\right)\right] \tag{A4-3}$$

The second term in the bracket in Equation (A4-3) is the initial displacement effect. ΔE^{nl} is the nonlinear part of the incremental strain expressed as:

$$\Delta Enl = \frac{1}{2}\left[\left(\frac{\partial \Delta u_k}{\partial X_i}\right)\left(\frac{\partial \Delta u_k}{\partial X_j}\right)\right] \tag{A4-4}$$

Linearization of equilibrium of Equation (A4-4) yields:

$$\{K_0 + K_1 + K_2\}\delta_u = F - R \tag{A4-5}$$

where K_0 is the small displacement stiffness matrix defined as:

$$(K_0)_{ij} = \int_{V_0} \beta^{0}{}_{imn} D_{mnpq} \beta^{0}{}_{pqj} dV$$

K_1 is the initial displacement stiffness matrix defined as:

$$(K_1)_{ij} = \int_{V_0} \{\beta^{u}{}_{imn} D_{mnpq} \beta^{u}{}_{pqj} + \beta^{u}{}_{imn} D_{mnpq} \beta^{0}{}_{pqj} + \beta^{u}{}_{imn} D_{mnpq} \beta^{u}{}_{pqj}\} dV \tag{A4-6}$$

in the above equations, $\beta^{0}{}_{imn}$ and $\beta^{u}{}_{imn}$ are the constant and displacement dependent symmetric shape function gradient matrices, respectively, and D_{mnpq} is the material tangent, and K_2 is the initial stress stiffness matrix:

$$(K_2)_{ij} = \int_{V_o} N_{i,k} N_{j,l} S_{kl} dV$$

in which S_{kl} is the second Piola-Kirchhoff stresses and $N_{i,k}$ is the shape function gradient matrix. Also, δ_u is the correction displacement vector. F and R are the external and internal forces, respectively.

This Lagrangian formulation can be applied to problems if the undeformed configuration is known so that integrals can be evaluated, and if the second Piola-Kirchhoff stress is a known function of the strain. The first condition is not usually met for fluids, because the deformation history is usually unknown. For solids, however, each analysis usually starts in the stress-free undeformed state, and the integrations can be carried out without any difficulty.

For viscoelastic fluids and elastic-plastic and viscoplastic solids, the constitutive equations usually supply an expression for the rate of stress in terms of deformation rate, stress, deformation, and sometimes other (internal) material parameters. The relevant quantity for the constitutive equations is the rate of stress at a given material point.

It, therefore, seems most obvious to differentiate the Lagrangian virtual work equation with respect to time. The rate of virtual work is readily found as:

$$\int_{V_0} \left[\dot{S}_{ij}\, \delta E_{ij} + S_{ij} \frac{\partial v_k}{\partial X_i} \frac{\partial \delta\eta_k}{\partial X_j} \right] dV = \int_{V_0} \dot{b}_i\, \delta\eta_i dV + \int_{A_0} \dot{t}_i\, \delta\eta_i dA \qquad \text{(A4-7)}$$

This formulation is adequate for most materials, because the rate of the second Piola-Kirchhoff stress can be written as:

$$\dot{S}_{ij} = \dot{S}_{ij}\left(\dot{E}_{kl}, S_{mn}, E_{pq} \right) \qquad \text{(A4-8)}$$

For many materials, the stress rate is even a linear function of the strain rate

$$\dot{S}_{ij} = D_{ijkl}(S_{mn}, E_{pq})\, \dot{E}_{kl} \qquad \text{(A4-9)}$$

Equation (A4-7) supplies a set of linear relations in terms of the velocity field. The velocity field can be solved noniteratively and the displacement can be obtained by time integration of the velocities.

The second Piola-Kirchhoff stress for elastic and hyperelastic materials is a function of the Green-Lagrange strain defined below:

$$S_{ij} = S_{ij}\left(E_{kl} \right) \qquad \text{(A4-10)}$$

If the stress is a linear function of the strain (linear elasticity) then:

$$S_{ij} = D_{ijkl} E_{kl} \qquad \text{(A4-11)}$$

the resulting set of equations is still nonlinear because the strain is a nonlinear function of displacement.

Updated Lagrangian Procedure

The Updated Lagrange formulation takes the reference configuration at $t = n+1$. True or Cauchy stress and an energetically conjugate strain measure, namely the true strain, are used in the constitutive relationship.

The updated Lagrangian approach is useful in:

a. Analysis of shell and beam structures in which rotations are large so that the nonlinear terms in the curvature expressions may no longer be neglected.

b. Large strain elasticity and plasticity analysis.

In general, this approach can be used to analyze structures where inelastic behavior (for example, plasticity, viscoplasticity, or creep) causes the large deformations. The (initial) Lagrangian coordinate frame has little physical significance in these analyses since the inelastic deformations are, by definition, permanent.

For large strain analysis for rubber-like materials with incompressibility (such as materials defined with MOONEY, OGDEN, GENT, and ARRUDA and BOYCE model definition options), MSC.Marc uses a mixed formulation, in which both the displacement and the hydrostatic pressure are independent variables, to overcome the numerical difficulties resulting from the volumetric constraints. For compressible hyperelastic materials defined with FOAM model definition option, MSC.Marc uses conventional displacement formulation.

For large strain elastic-plastic analysis, the default procedure in MSC.Marc uses a procedure based on an additive decomposition of incremental strain into an elastic part and a plastic part, together with a mean normal return-mapping algorithm. In this case, volumetric strain in a lower-order plane strain, axisymmetric or 3-D brick element is assumed to be constant for von Mises plasticity to overcome volumetric locking because of the possible large and incompressible plastic deformation. MSC.Marc uses Cauchy stress (true stress) and logarithmic strain with Updated Lagrange formulation.

It is instructive to derive the stiffness matrices for the updated Lagrangian formulation starting from the virtual work principle in Equation A4-1.

Direct linearization of the left-hand side of Equation A4-1 yields:

$$\int_{V_0} S_{ij}\left(d\left(\delta E_{ij}\right)\right)dV = \int_{V_{n+1}} \nabla\eta_{ik}\sigma_{kj}\nabla\Delta u_{ij}\,dv \qquad \text{(A4-12)}$$

where Δu and η are actual incremental and virtual displacements respectively, and σ_{kj} is Cauchy stress tensor.

$$\int_{V_0} dS_{ij}\delta E_{ij}dV = \int_{V_{n+1}} \nabla^S \eta_{ij} L_{ijkl} \nabla^S (\Delta u_{kl}) dv \qquad \text{(A4-13)}$$

∇^S denotes the symmetric part of ∇, which represents the gradient operator in the current configuration. Also, in Equation A4-12 and Equation A4-13, three identities are used:

$$\begin{aligned} \sigma_{ij} &= \frac{1}{J} F_{im} S_{mn} F_{jn} \\ \delta E_{ij} &= F_{mi} \nabla^S \eta_{mn} F_{nj} \\ L_{ijkl} &= \frac{1}{J} F_{im} F_{jn} F_{kp} F_{lq} D_{mnpq} \end{aligned} \qquad \text{(A4-14)}$$

in which D_{mnpq} represents the material moduli tensor in the reference configuration which is converted to the current configuration, L_{ijkl}. This yield:

$$\{K_1 + K_2\}\delta u = F - R \qquad \text{(A4-15)}$$

where K_1 is the material stiffness matrix written as:

$$(K_1)_{ij} = \int_{V_{n+1}} \beta_{imn} L_{mnpq} \beta_{pqj} \qquad \text{(A4-16)}$$

in which β_{imn} is the symmetric gradient operator-evaluated in the current configuration and σ_{kl} is the Cauchy stresses and K_2 is the geometric stiffness matrix written as:

$$(K_2)_{ij} = \int_{V_{n+1}} \sigma_{kl} N_{i,k} N_{j,l} dv \qquad \text{(A4-17)}$$

while F and R are the external and internal forces, respectively.

Keeping in view that the reference state is the current state; a rate formulation analogous to Equation A4-7 can be obtained by setting:

$$F_{ij} = \delta_{ij}, \qquad \delta E_{ij} = \delta d_{ij}, \qquad \frac{\partial}{\partial X_i} = \frac{\partial}{\partial x_i}, \qquad S_{ij} = \sigma_{ij} \qquad \text{(A4-18)}$$

where F is the deformation tensor, and d is the rate of deformation. Hence,

$$\int_{V_{n+1}} \left[\overset{\nabla}{\sigma_{ij}} \delta d_{ij} + \sigma_{ij} \frac{\partial v_k}{\partial x_i} \frac{\partial \delta \eta_k}{\partial x_j} \right] dv = \int_{V_{n+1}} \dot{b}_i \delta \eta_i dv + \int_{A_{n+1}} \dot{t}_i \delta \eta_i da \qquad \text{(A4-19)}$$

in which b_i and t_i are the body force and surface traction, respectively, in the current configuration. In this equation, $\overset{\nabla}{\sigma}_{ij}$ is the Truesdell rate of Cauchy stress which is essentially a Lie derivative of Cauchy stress obtained as:

$$\overset{\nabla}{\sigma}_{ij} = F_{in}\left(JF_{nk}^{-1}\sigma_{kl}F_{ml}^{-1}\right)F_{mj} \tag{A4-20}$$

The Truesdell rate of Cauchy stress is materially objective implying that if a rigid rotation is imposed on the material, the Truesdell rate vanishes, whereas the usual material rate does not vanish. This fact has important consequences in the large deformation problems where large rotations are involved. The constitutive equations can be formulated in terms of the Truesdell rate of Cauchy stress as:

$$\overset{\nabla}{\sigma}_{ij} = L_{ijkl}d_{kl} \tag{A4-21}$$